JOURNAL OF APPLIED PHYSICS

FOR MATERIALS

TESTING

destructive duet

with constructive overtones

Corresponding reactions of two materials to the same destructive environment are shown in these selections from two sets of pictures. Jet formations produced by shock waves passing over conical depressions in the surfaces of a sheet of Lucite and an aluminum plate were photographed with a Model 189 Beckman & Whitley framing camera.

In the original sequence, in each case, the time between frames was 1.6 microseconds and the exposure time 0.58 microsecond. Reflection illumination was used.

Many laboratories are being provided with the sharp-edged research facilities of Beckman & Whitley framing cameras. There are types and auxiliary units available to meet various specialized requirements. Ask us about the possibilities of applying these techniques to your problems—either with equipment of your own or through investigations made for you by our special service department.

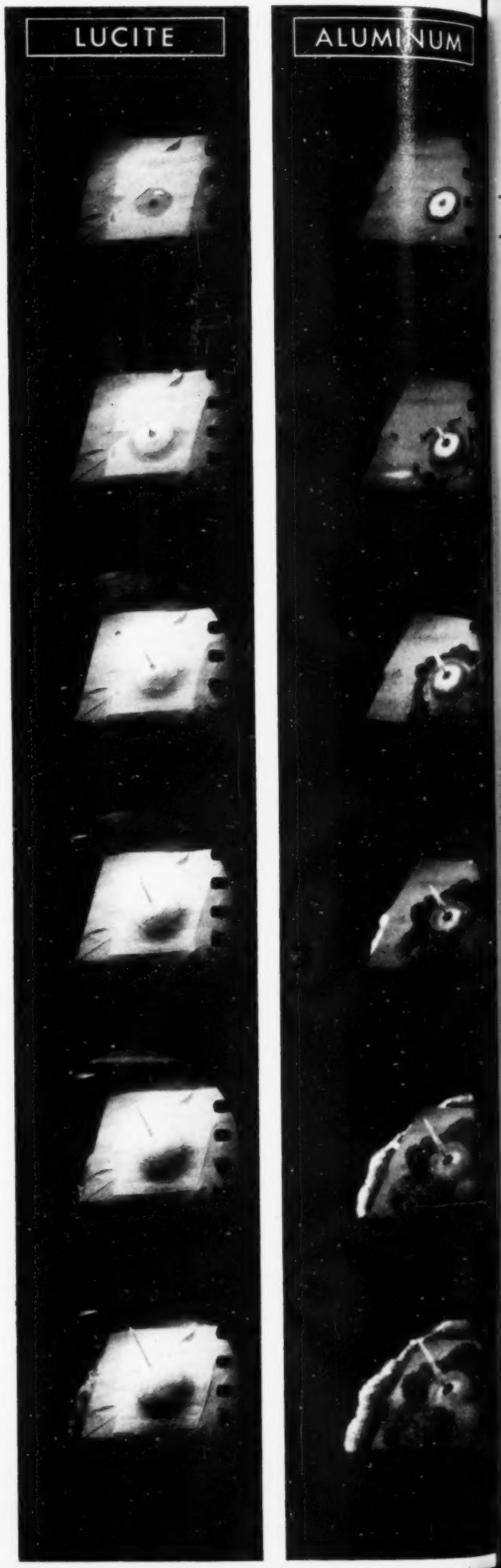

Beckman & Whitley INC.

SAN CARLOS 8 CALIFORNIA

instruments for 4-dimensional documentation

JOURNAL OF APPLIED PHYSICS

Vol. 26, No. 12 DECEMBER, 1955

In This Issue

Dielectric Constant of Quartz as a Function of Frequency and Temperature . . . . . Malcolm R. Stuart 1399

High Field Electron Emission from Irregular Cathode Surfaces . . . . . T. J. Lewis 1405

New Active Circuit Element Using the Magnetoresistive Effect . A. Aharoni, E. H. Frei, and G. Horowitz 1411

Hexagonal Microstructure of Ice Crystals Grown from the Melt . . . . . Frank K. Truby 1416

Space-Charge Distribution in a Static Magnetron . . . . . Howard C. Nedderman 1420

Application of the Engravement Method to the Study of Particle Velocity Distribution in Explosively Loaded Cylinders . . . . . John Pearson and John S. Rinehart 1431

Thickness-Shear and Flexural Vibrations of Rectangular Crystal Plates . . . . . R. D. Mindlin and H. Deresiewicz 1435

Space-Charge Waves in Crossed Electric and Magnetic Fields . . . . . Salim S. Solomon 1443

Theory of Scattering by an Inhomogeneous Solid Possessing Fluctuations in Density and Anisotropy . . . . . Martin Goldstein and E. R. Michalik 1450

Low Shear Capillary Viscometer with Continuously Varying Pressure Head . . . . . Samuel H. Maron and Robert J. Belner 1457

Space-Charge Effects in Electron Optical Systems . . . . . K. T. Dolder and O. Klemperer 1461

Dynamic Determination of the Compressibility of Metals . Roy W. Goranson, Dennison Bancroft, Blendin L. Burton, Theodore Blechar, Edwin E. Houston, Elisabeth F. Gittings, and Stanley A. Landeen 1472

Ferroelectric Hysteresis in Barium Titanate Single Crystals . . . . . H. H. Wieder 1479

Total Emissivities and Absorptivities of Some Commercial Surfaces at Room and Liquid-Nitrogen Temperatures . . . . . F. J. Zimmermann 1483

Gettering of Gas by Titanium . . . . . Virgil L. Stout and Martin D. Gibbons 1488

Stress-Strain Relations in Snow under Uniaxial Compression . . . . . Joseph K. Landauer 1493

Calculation of the Complex Modulus of Linear Viscoelastic Materials from Vibrating Reed Measurements . . . . . D. R. Bland and E. H. Lee 1497

Angular Distribution of Multiply Scattered Gamma Radiation from a Plane Isotropic Source . . . . . Martin J. Berger 1504

Method for Obtaining Complete Quantitative Pole Figures for Flat Sheets Using One Sample and One Sample Holder . . . . . Milton Schwartz 1507

Capacitance Measurements on Alloyed Indium-Germanium Junction Diodes . . . . . D. R. Muss 1514

Letters to the Editor:

Guide to the Successful Propulsion of a Solid Object by an Explosive Charge . . . . . John S. Rinehart 1518

Stress Relaxation in Gold Wire . . . . . O. L. Anderson and P. Andreatch 1518

Comments on Limiting Pressure on Hydrofoils . . . . . E. V. Laitone 1519

Removal of Copper from Germanium . . . . . Katharine B. Blodgett 1520

Preferred Orientation in Stark Rubber Studied with an Automatic Integrating Pole Figure Goniometer . . . . . C. J. Newton, L. Mandelkern, and D. E. Roberts 1521

Comments on "Transformations in Plain Carbon Steels" . . . F. C. Frank and K. E. Puttick 1522

Errata: On the Space-Charge-Limited Current between Nonsymmetrical Electrodes . . . . . George D. O'Neill 1522

Erratum: Ferromagnetic Resonance in Magnesium-Manganese Aluminum Ferrite between 160 and 1900 Mc . . . . . H. Suhl, L. G. Van Uitert, and J. L. Davis 1523

Erratum: Cross Correlation between Velocity and Current Fluctuations in Tube Noise . . . . . S. V. Yadavalli 1523

Books Reviewed 1523

Books Received 1524

Announcements 1524

Author Index to Volume 26 1525

Subject Index to Volume 26 1533

Index to Advertisers xxxii

JOURNAL OF APPLIED PHYSICS

A journal of applications of physics to other sciences and to industry

Published by the

American Institute of Physics

GOVERNING BOARD

Allen V. Astin
Robert F. Bacher
H. A. Bethe
J. W. Buchta
S. A. Goudsmit
Deane B. Judd
Hugh S. Knowles
W. H. Markwood, Jr.
William F. Meggers
Philip M. Morse
Brian O'Brien
Harry F. Olson
R. F. Paton
Eric Rodgers
Ralph A. Sawyer
Frederick Seitz
William Shockley
H. D. Smyth
J. H. Van Vleck
Mark W. Zemansky

OFFICERS AND STAFF

Frederick Seitz
Chairman, Governing Board

Henry A. Barton
Director

George B. Pegram
Treasurer

Wallace Waterfall
Executive Secretary

Theodore Vorburger
Advertising Manager

Ruth F. Bryans
Publication Manager

Edith I. Neftel
Circulation Manager

Kathryn Setze
Assistant Treasurer

Melvin Loos
Consultant on Printing

Editor
Robert L. Sproull

Editorial Board

Maurice A. Biot
Walker Bleakney
Wallace J. Eckert
Elmer Hutchisson
D. O. North
Louis A. Pipes
W. R. Smythe
Arthur V. Tobolsky
A. M. Weinberg

THE JOURNAL OF APPLIED PHYSICS is devoted to the application of physics to other sciences, to engineering, and to industry. Previous to 1937, this journal was called PHYSICS.

The JOURNAL OF APPLIED PHYSICS welcomes articles of two distinct kinds: (1) Descriptions of new results in experimental or theoretical physics which are of general interest to applied physicists. The author should explain his contribution in such a way that a physicist or engineer in another field of specialization can appreciate its objectives and essential features. (2) Critical reviews of particular areas of applied physics. Authors contemplating writing such reviews should correspond with the Editor before they begin writing.

The JOURNAL OF APPLIED PHYSICS welcomes letters to the editor which describe in a few words the content of laboratory reports and theses and which tell readers how they may obtain copies of such reports.

Manuscripts should be submitted to the Editor, Rockefeller Hall, Cornell University, Ithaca, New York. Authors should read the "Information for Contributors," facing page 1 of the January issue, before writing articles or letters. The *Style Manual* of the American Institute of Physics is also helpful to writers preparing manuscripts for journals published by the American Institute of Physics. It can be obtained for $1.00 from the American Institute of Physics, 57 East 55th Street, New York 22, New York.

Corrected proofs and all correspondence concerning papers in the process of publication should be addressed to the Publication Manager, American Institute of Physics, 57 East 55 Street, New York 22, New York.

Subscriptions, renewals, and orders for back numbers should be addressed to the American Institute of Physics, 57 East 55 Street, New York 22, New York.

Subscription Price	U.S. and Canada	Elsewhere
To members of the American Institute of Physics and Affiliated Societies	$10.00	$11.00
To all others	12.00	14.00

Back Number Prices

Yearly back number rate when complete year is available: $15.00.
Single copies: $1.50 each.

Changes of address should be sent to the American Institute of Physics.

Advertising rates supplied on request. Orders, advertising copy, and cuts should be sent to the American Institute of Physics.

Entered as second class matter January 22, 1937, at the Post Office at Lancaster, Pennsylvania, under the Act of March 3, 1879. Accepted for mailing at the special rate of postage provided for in paragraph (d-2), section 34.40, P. L. & R. of 1948, authorized May 2, 1932.

Copyright © 1955 by the American Institute of Physics

Journal
of
Applied Physics

Volume 26, Number 12 December, 1955

Dielectric Constant of Quartz as a Function of Frequency and Temperature*

MALCOLM R. STUART†
Department of Physics, The State University of Iowa, Iowa City, Iowa
(Received June 3, 1955)

Measurements of dielectric constant and power loss were made from 1 to 90 kc/sec and from 20°C to 400°C. The dielectric constant parallel to the optic axis for all frequencies shows a sharp rise, which occurs at successively higher temperatures for higher frequencies. The loss at a given frequency has a temperature maximum which is higher, the higher the frequency. The results are partially explained by assuming that ions are present in "tunnels" parallel to the optic axis. The density and mobility of these ions are obtained. The density is temperature dependent in such a way as to lead to an activation energy of 17.7 kcal per mole. Lithium ions were introduced into the crystals, and the effects caused by these ions were at least compatible with the assumption that lithium ions were originally present. Perpendicular to the optic axis none of the above effects exist.

I. INTRODUCTION

MUCH previous work has been done measuring the static dielectric constant of quartz in the direction of the optic axis.[1] An accurate measurement of the true dielectric constant of the quartz lattice in this direction is difficult because of the anomalously high conductivity along the optic axis. The structure of alpha quartz is such that there exist passages or "tunnels" parallel to the optic axis of about 1 A in radius.[2] The conductivity in this direction has been interpreted as being due to migration of ions along these "tunnels." The polarization induced by a static field thus depends upon the period of application of the field. Thornton's[3] results show that an apparent dielectric constant of 500 can be observed at the end of a period of 5000 minutes.

Relatively little work has been done on the dynamic values of the dielectric constant, particularly as a function of temperature. Gagnebin[4] made measurements at 20 kilocycles per second at temperatures ranging from room temperature to about 500°C. He reported that the dielectric constant began to rise at 100°C, from the room temperature value of 4.65, and reached a value of 13 at 300°C. There it leveled off and remained essentially constant for higher temperatures. There exists some doubt as to this leveling off, and the investigation of this point in part prompted the present research.

The internal friction studies of G. A. Alers[5] done previously in this laboratory on quartz single crystals are also of interest. The results of his work were interpreted in terms of two relaxation processes simultaneously operating to give a double peak in the logarithmic decrement curve when plotted as a function of temperature. The fundamental longitudinal vibration of the quartz crystals was perpendicular to the optic axis. The distortions in the lattice resulting from this vibration might force particles residing in the optic axis "tunnels" to seek new equilibrium positions by moving parallel to the axis. The mechanical losses then could be interpreted as being due to the motion of those particles.

In the present work the electric field is directed along the optic axis so that a similar motion might be induced. If the dissipation of the condenser is the result of such ion motion, then certain similarities in the behavior with frequency and temperature of the logarithmic decrement and the dissipation factor, tanδ, of the condenser might be expected to appear.

* This is based on a thesis submitted in partial fulfillment of the requirements for the degree of Doctor of Philosophy in the Department of Physics of the Graduate College of the State University of Iowa.

† Now at the Westinghouse Electric Corporation, Atomic Power Division, Bettis Field, Pittsburgh, Pennsylvania.

[1] R. B. Sosman, *The Properties of Silica* (Chemical Catalog Company, New York, 1927), p. 515.

[2] G. Gibson and R. C. Vogel, J. Chem. Phys. **18**, 1094 (1950).

[3] Sosman, see reference 1, p. 530.

[4] See reference 1, p. 523.

[5] G. A. Alers, J. Appl. Phys. **24**, 324 (1953).

The dielectric constant and loss were investigated at selected frequencies between 1 and 90 kilocycles per second with the majority of the measurements in the 20 to 90 kilocycle per second range. Measurements were made from room temperature to 400°C.

II. METHOD AND APPARATUS

The dielectric constant of the quartz crystals was found by measuring the capacitance of a condenser in which the crystals were used as a dielectric. The condenser consisted of two outer brass plates separated by a "sandwich" of two quartz crystals and a third brass plate separating them. Either side of this condenser could be examined by the bridge by connecting the appropriate outside plate and the center plate to the bridge. In addition, the two sides could be placed in parallel by connecting the outside plates together. The outside plates had attached to them small brass rods which passed through the uprights of a U-shaped piece of transite which served as a base and support. The condenser assembly was placed in a horizontal tubular furnace in which the temperature could be varied.

The capacitance measurements between 1 and 12 kilocycles per second were made on a General Radio Bridge, Type 650-A. From 20 to 90 kilocycles per second they were made on a bridge used previously in this laboratory and described elsewhere.[5]

The crystals were of natural Brazilian alpha quartz purchased from the E. B. Lewis Precision Crystal Company and Monitor Products Company. They were 2 cm on a side and 1 mm thick. The main interest was in crystals in which the optic axis was oriented perpendicular to the broad face of the crystals. Some X- and Y-cut crystals were also used for comparison purposes. All crystals were cleaned with dilute hydrochloric acid and etched with 50% hydrofluoric acid before measurements were made.

In the latter part of the research the crystals were subjected to a lithium ion current in a manner described by Gibson and Vogel.[2] Metallic lithium was forced through the crystals by electrolytic conduction in an attempt to introduce impurities into them. The results of the dielectric constant measurements, and the effect of the above lithium treatment on them, are discussed below.

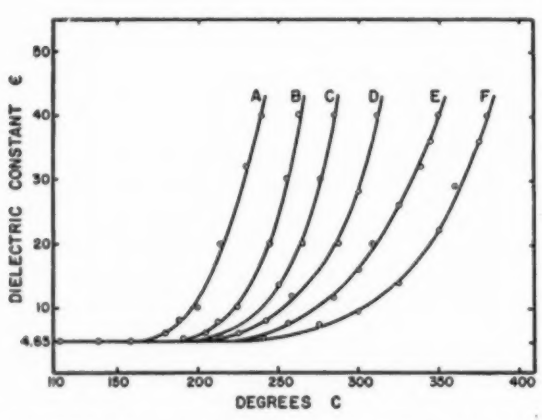

FIG. 1. Dielectric constant *vs* temperature. Frequency in kilocycles per second. *A*, 1; *B*, 4; *C*, 8; *D*, 20; *E*, 40; *F*, 90; crystal *E*−1.

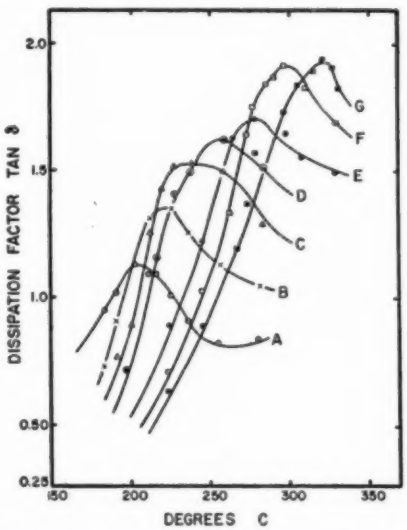

FIG. 2. Dissipation factor *vs* temperature. Frequency in kilocycles per second. *A*, 1; *B*, 2; *C*, 4; *D*, 8; *E*, 20; *F*, 40; *G*, 60; Crystal *M*−1.

III. RESULTS AND DISCUSSION

The general form of the results is shown in Fig. 1. For 1 kilocycle per second the dielectric constant rises only slightly above its room temperature value of 4.65 until the temperature reaches about 175°C. There it rises quickly, increasing from there for higher temperatures. The behavior at other frequencies is essentially the same, except that the sharp rise occurs at increasingly higher temperatures for the higher frequencies. Accompanying this change in the dielectric constant, the parallel resistance of the quartz condenser decreases and the power consumption rises. The dissipation factor of the condenser, or $\tan\delta$, defined as $1/RC\omega$ is shown in Fig. 2. It can be seen that the dissipation factor of a single frequency passes through a maximum. This maximum shifts with increasing frequencies to higher temperatures. In this connection, the present work is in agreement with the previous internal-friction work of Alers.[5] The dissipation factor curves however cannot be represented by a single or even by two relaxation processes as was done by Alers. If the dissipation factor is plotted at a single temperature as a function of frequency and compared with a simple relaxation-type curve, the observed points form a much broader curve with a less well-defined maximum. In spite of the fact that the individual dissipation curves cannot be fitted with a relaxation-type curve, the relationship between the frequency and the temperature at which a given curve has a maximum has a simple form. This is shown

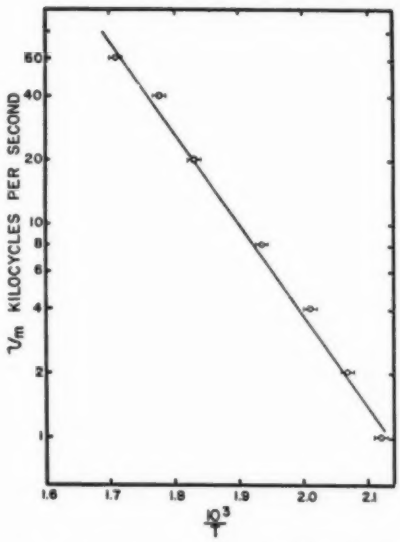

FIG. 3. $\ln\nu_m$ *vs* $10^3/T$. T in degrees Kelvin. Crystal $M-1$.

in Fig. 3 and can be represented by

$$\nu_m = \nu_0 e^{-a/T}, \tag{1}$$

in which ν_m is the frequency at which the maximum dissipation occurs at absolute temperature, T, and ν_0 and a are constants. If one assumes that $a=H/R$, where R is the gas constant and H is an activation energy for the process, the value of H turns out to be 21.6 kilocalories per mole.

By interpolation on the graph of Fig. 3 it is found that the temperatures at which the dissipation factor would peak for 21 and 42 kilocycles per second are 276°C and 295°C, respectively. In the internal-friction work of Alers the logarithmic decrement at 21 kilocycles per second peaked at about 273°C and for 42 kilocycles per second at 305°C. This is about the extent of agreement between the present work and the internal-friction work.

Recently Cook and Breckenridge[6] have reported on a study of internal friction of quartz single-crystal rods. The fundamental frequency of oscillation of their rods was about 35 kilocycles per second and they made observations at various overtone frequencies, up to and including the fifth, as a function of temperature. The effective resistance of the fundamental mode was found to peak at about 300°C with the resistances measured at the overtone frequencies peaking at higher temperatures. They also found that the relationship between the frequency of oscillation and the temperature at which the series resistance reached a maximum had the following form:

$$\nu = \text{const} e^{-H/RT}.$$

The value of H was found to be 22 kilocalories per mole. This agrees very well with the activation energy of 21.6 kilocalories given above.

[6] R. K. Cook and R. G. Breckenridge, Phys. Rev. **92**, 1419 (1953).

In order to interpret the observed results of the dielectric constant measurements a very simple model has been adopted. It has been shown that ions of small atomic number can migrate along the optic axis "tunnels." It is assumed that the motion of an individual ion may be described by the equation,

$$m\ddot{x}+k\dot{x}=eE_0\cos\omega t, \tag{2}$$

where $E_0\cos\omega t$ is the applied field and $-k\dot{x}$ is a resisting force. From the periodic solution for the velocity multiplied by the charge on the ion, assumed positive in this case, and by the number of ions per cm³, the current density is obtained. The ions are assumed to be independent of one another. From the in-phase component of this current the conductivity is obtained and from the component 90 degrees out of phase the contribution to the dielectric constant. The dielectric constant and the conductivity are then given by the following expressions

$$\epsilon' = \frac{4\pi ne^2 m/k^2}{1+(m/k)^2\omega^2} \quad \sigma = \frac{ne^2/k}{1+(m/k)^2\omega^2}. \tag{3}$$

The quantity n is the number of ions per cm³, k is the parameter appearing in Eq. (2), e is the charge on the ion, m is the mass of the ion, and ω is the angular frequency of the applied field.

The parameter k is related to the mobility, μ, cm²/sec volt, by the relation $k=e/\mu$ as may be seen by considering the motion in a static field. Equations (3) can then be rewritten as

$$\epsilon' = \frac{4\pi nm\mu^2}{1+(m\mu/e)^2\omega^2} \quad \sigma = \frac{ne\mu}{1+(m\mu/e)^2\omega^2}. \tag{4}$$

There is also a contribution to the polarization and, thus, to the dilectric constant from the quartz lattice itself. It will be denoted as ϵ_∞, and the value of it is assumed to be 4.65. At any temperature this quantity is the high-frequency limit of the dielectric constant.

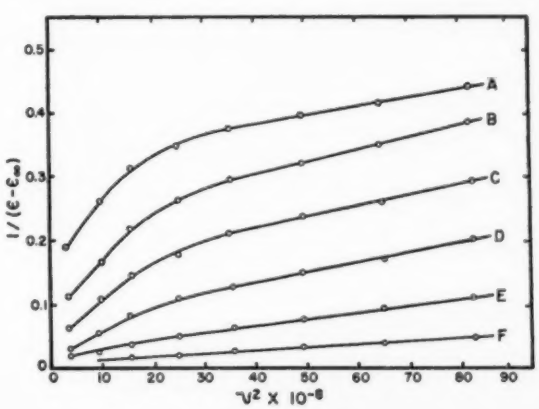

FIG. 4. $1/(\epsilon-\epsilon_\infty)$ *vs* ν^2. Temperature in degrees C. *A*, 269; *B*, 286; *C*, 304; *D*, 324; *E*, 353; *F*, 389. Crystal $E-1$.

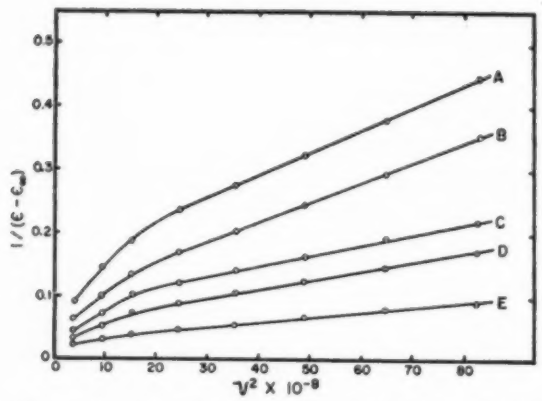

FIG. 5. $1/(\epsilon-\epsilon_\infty)$ *vs* ν^2. Temperature in degrees C. *A*, 272; *B*, 278; *C*, 296; *D*, 306; *E*, 329. Crystal $M-1$.

The full expression for the dielectric constant is then,

$$\epsilon=\epsilon_\infty+\frac{4\pi nm\mu^2}{1+(m\mu/e)^2\omega^2}. \tag{5}$$

According to Eq. (5) the quantity $1/(\epsilon-\epsilon_\infty)$ should be a linear function of ω^2. To test this some of the results are plotted in this manner in Figs. 4 and 5. In the temperature region about 250°C to 325°C, this relationship is satisfied at the higher frequencies. At higher temperatures the relationship is fairly well satisfied over the whole frequency range of 20 to 90 kilocycles per second. At the present time the extra contribution to the dielectric constant at the lower frequencies has not been interpreted. If the difference between the observed values and the extrapolation of the high-frequency straight line is examined it is found that it cannot be fitted by an additional term of the same form as ϵ' in Eqs. (4).

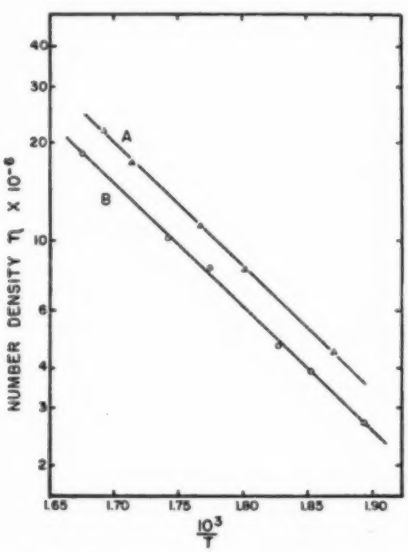

FIG. 6. Variation of number density, n, with temperature. T in degrees Kelvin. Curve *A*, run $C-1$, crystal $E-4$; Curve *B*, run $A-1$, crystal $M-1$.

The parameters n and μ can be found from the slope and intercept of the lines in Figs. 4 and 5. In order to obtain numerical values for these parameters, it is necessary to assume an ionic mass and charge. The mass of the lithium ion, $m=1.1\times10^{-23}$ g, and a charge, $e=4.8\times10^{-10}$ esu are assumed. The temperature variations of these quantities are shown in Figs. 6 and 7. The mobility has unusually high values and no apparant simple temperature dependence. The rise in the mobility curve which follows the minimum may, however, be qualitatively interpreted as being due to the expansion of the lattice permitting greater velocities. It is assumed that this effect would then predominate over the increase of scattering due to thermal vibration of the lattice atoms. The values of n are lower than one might expect, and the temperature dependence appears at first unexpected. It may, however, be explained by supposing that the ions are situated in the "tunnels" in such a way that they require a certain activation energy before their motion can be described by Eq. (2).

TABLE I. Calculated and observed resistances.[a]

Temp. deg C	20 kc		Observed resistance		
	R(calc)[b]	R(obs)	30 kc	60 kc	90 kc
239	194.0	175.0	164.0	134.0	112.0
255	152.0	106.0	99.6	87.3	76.7
270	101.0	66.0	63.2	57.2	52.6
279	80.4	48.0	46.4	43.2	40.7
291	70.5	35.0	33.2	30.8	29.2
308	47.5	23.4	21.7	20.3	19.4
328	30.7	16.7	15.3	13.3	12.6
344	19.1	12.2	11.3	9.8	9.2

[a] All resistances in kilo-ohms.
[b] R(calc) is calculated from dielectric constant data.

The curve of Fig. 6 may be represented by:

$$n=n_0e^{-H/RT}, \tag{6}$$

where n_0 is a constant, R is the gas constant, T the absolute temperature, and H is the activation energy. The value of H is found to be 17.7 kilocalories per mole. This may be compared to the value of the activation energy of from 17 to 21 kilocalories per mole found by Gibson and Vogel[2] for the migration of lithium ions along the optic axis in their migration studies. The agreement may be largely fortuitous.

The conductivity given by Eq. (4) decreases with increasing frequency. The observed conductivity, however, increases with increasing frequency. It is possible, nevertheless, to obtain an order of magnitude estimate of the resistance of a crystal from the dielectric measurements alone. The denominator in Eq. (4) for the conductivity does not vary more than five or ten percent from unity over the whole temperature range for a frequency of 20 kilocycles per second. Thus the conductivity can be approximately set equal to $ne\mu$. Now the dielectric constant expression of Eq. (5) can be written in the parametric form of $\epsilon-\epsilon_\infty=a/(1+b\omega^2)$

with a and b set equal to the quantities given in Eq. (5). Then from the observed values of a and b the conductivity can be computed by writing the conductivity as $\sigma \simeq ne\mu = a/4\pi b^4$. The conductivity can thus be found without assuming specific values for the charge and mass of the ion. This has been done and the comparison with the observed values is given in Table I. Also given in Table I are the observed values of resistance for some selected frequencies for this same crystal. The frequency and temperature dependence of the resistance of the other crystals examined in this research is of the same form. It should be noticed that the higher temperature resistances agree rather well with the calculated ones, and it is in the high-temperature region that the dielectric constant is given closely by the form of Eq. (5).

The frequency dependence of the resistance is in qualitative agreement with that reported by Ambronn.[7]

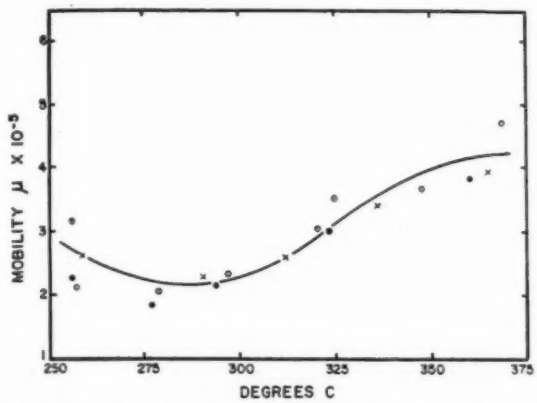

FIG. 7. Variation of mobility, μ, with temperature. The symbols are associated with the following runs and crystals; ⊙, run $A-2$, crystal $M-1$; ○, run $A-4$, crystal $E-1$; ● run $C-1$, crystal $E-4$; ×, run $A-4$, crystal $E-1$.

His work was done in the frequency range of from 1 to 130 cycles per second. He reported that the resistance was proportional to the square root of the period of the applied field. The present measurements only roughly agree with this relation.

The work of Gibson and Vogel, and others, has shown that it is possible to cause a migration of ions along the optic axis under the influence on an external field. It has previously been supposed that the drifting of ions along the optic axis is responsible for the relatively high conductivity in this direction. The conductivity perpendicular to the optic axis is from one-hundredth to one-thousandth of that parallel to the optic axis. Assuming the present model to be correct, it was thought that if one placed a crystal in an external static field it might be possible to "drain" out the ions residing in the "tunnels." After such a treatment the dielectric constant and the conductivity should both decrease. This was done and the results are shown in Figs. 8 and

[7] See reference 1, p. 536.

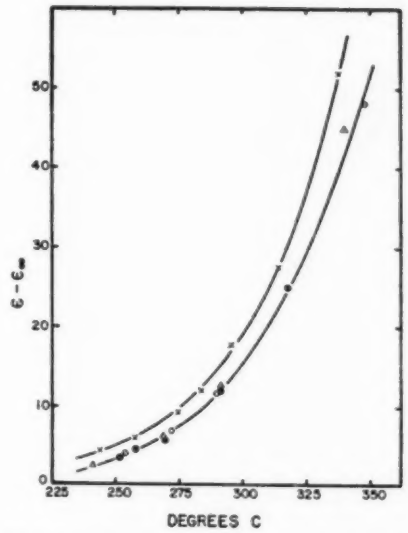

FIG. 8. Dielectric constant *vs* temperature at 20 kc. Δ, before "draining"; ○ and ●, after "draining"; ×, after lithium treatment, crystal $E-1$.

9. The effect of this treatment, if any, is very small. Since this procedure did not produce results of a noticeable amount it was decided to introduce lithium into the crystals. The cell used by Gibson and Vogel consists of two glass cups, one on each side of the crystal, filled with mercury to serve as electrodes. Metallic lithium was amalgamated with the mercury of the anode and this served as the source of ions. Mercury ions do not diffuse through the crystals. A similar device was used with, however, a thin piece of aluminum as the cathode in an effort to prevent the ions from leaving the crystal once they had entered. An ion current was run through the crystal for eight hours. Upon completion of this treatment the aluminum cathode was examined and a deposit was found, indicating that some of the lithium had escaped from the crystal. The results of the dielectric constant and resistance measurements after this treatment are also shown in Figs. 8 and 9. It can be seen that the dielectric constant and conductivity increased.

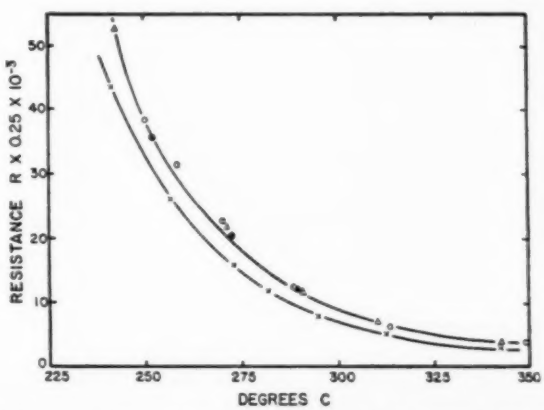

FIG. 9. Resistance *vs* temperature at 20 kc. Δ, before "draining"; ○ and ●, after draining; ×, after lithium treatment. Crystal $E-1$.

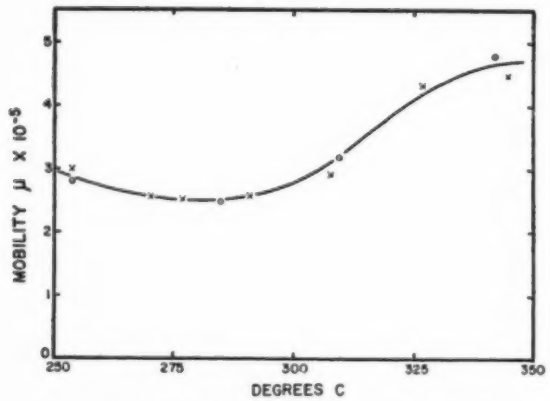

FIG. 10. Effect of lithium treatment on mobility, μ. ○, before lithium treatment; ×, after. Crystal $E-1$.

These results support the interpretation that ionic migration is responsible for the effects observed in natural quartz. It is felt, however, that the changes observed in the dielectric constant and resistance are not large enough to indicate that the lithium ion specifically is responsible for the effects observed in natural quartz.

The mobilities calculated before and after the lithium treatment are compared in Fig. 10. They are essentially the same. In addition, the number density, n, of ions before and after treatment are compared in Fig. 11. The number of ions per cm³ is seen to be increased by a constant factor at all temperatures above that in the previous run, but the activation energy is unchanged. This appears to support the ionic migration picture.

It should also be reported that runs were made on X- and Y-cut crystals, which have the optic axis oriented perpendicular to the applied electric field. No such effects as the above were observed. The dielectric constant was practically constant at all frequencies above the temperature range from room temperature to 350°C, there being noted only a slight rise of from 4.5 to 5. The resistance of the crystals was too high to be accurately measured and may have shown a very small decrease with rising temperature.

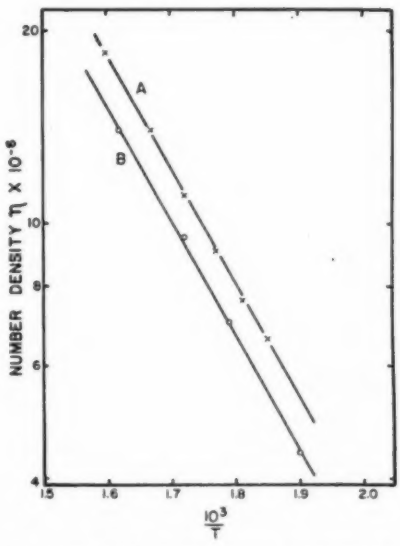

FIG. 11. Effect of lithium treatment on number density, n. Curve B is before and A is after the lithium treatment. Crystal $E-1$.

IV. CONCLUSION

Certain aspects of the present work are in good agreement with the simple picture that has been used to interpret the results. It is felt that the present model should be modified in order to account for the points of disagreement. One such modification is to take account of the fact that in natural quartz there are probably "tunnels" of various lengths. This, however, would tend to depress the polarization at the lower frequencies where the amplitude of oscillation is relatively greater. It would also depress the conductivity at the lower frequencies. The former effect is not observed, while the latter is.

Finally, the results of the present work do not support the work of Gagnebin. On the contrary, the results show no leveling off up to a temperature of 400°C at any frequency.

V. ACKNOWLEDGMENTS

The author wishes to thank Professor E. P. T. Tyndall for his assistance during the performance of this research.

JOURNAL OF APPLIED PHYSICS VOLUME 26, NUMBER 12 DECEMBER, 1955

High Field Electron Emission from Irregular Cathode Surfaces

T. J. LEWIS
Department of Electrical Engineering, Queen Mary College, London, England
(Received May 6, 1955)

Electron emission from a cathode surface produced by an applied field E is enhanced by the presence of projections on the emitter surface which cause a local increase in E. The nature of this enhancement factor $\mu(z)$, which is a function of the distance z from the cathode, is discussed more fully than hitherto and its magnitude is calculated for certain ideal but realistic geometries. Although such a factor may be large on the surface ($z=0$), it decreases rapidly as z increases so that the mean field magnification $\bar{\mu}(z)$, which is required in the Schottky thermionic emission theory, is unlikely to be >2 and is probably near to unity even for fields as great as 5×10^5 v/cm. This fact will mean that the Fowler-Nordheim theory frequently used to explain emission results at these fields is not applicable and that a Schottky theory should be used.

It is also shown that $\bar{\mu}(z)$ is itself field dependent and produces departures from the Schottky law in such a way that the slope of the current *vs* $E^{\frac{1}{2}}$ plot increases rapidly for $E<10^3$ v/cm, remains approximately constant for $10^3<E<10^4$ v/cm, and then increases again at higher fields. A similar reasoning shows that deviations from the Fowler-Nordheim law for fields $>10^6$ v/cm can also be expected.

Finally, the assumption of a constant emitting area for rough cathodes is also shown to give departures from the emission laws in such a manner that the estimated current density at high fields is appreciably less than the expected values.

These deductions help to explain some of the anomalous results frequently found in many conduction experiments in gases and liquids.

I. INTRODUCTION

THERE are two principal mechanisms by which an applied field may increase electron emission from a cathode surface. The first is that of Schottky[1] emission in which a suitable field in the range 10^3-10^6 v/cm reduces the potential barrier at the surface and permits an increased thermionic emission. The second or field-emission mechanism[2] requires fields of $\sim10^7$ v/cm to enable electrons from below the Fermi level to tunnel through the greatly reduced barrier. In both cases the emission is controlled by the field-dependent energy barrier near the surface. Any surface irregularity will distort the macroscopic applied field E in the neighborhood of the cathode and so influence the emission. It has been usual to write $m\underline{E}$ for this distorted field, in which m is a local magnification factor, and to express the emitted current density J for the Schottky and field-emission mechanisms, respectively, as

$$J=AT^2\exp-\{[\phi-e^3(mE)^{\frac{1}{2}}]/kT\}, \quad (1)$$

$$J=B(mE)^2\exp-D/mE, \quad (2)$$

in which A, B, and D are essentially constants, ϕ is the work function of the surface, and e is the electronic charge.

Experimental results have commonly been interpreted in terms of Eqs. (1) or (2) by choosing a value of m so that acceptable values of the other quantities such as ϕ result. This procedure assumes not only that m is independent of E but also introduces assumptions concerning the emitting area. The total current I from the cathode surface S is given by

$$I=\int JdS, \quad (3)$$

which in practice cannot be evaluated, since J is a function of m and will therefore vary with the surface irregularity. Thus it has been necessary to write

$$I=JS', \quad (4)$$

where J is a current density estimated for a particular value of m and S' is an equivalent emitting area which may be much less than S.

In the present paper, the nature of the field enhancement will be investigated more fully than hitherto. More correct versions of Eq. (1) and Eq. (2) will be given, and the experimental interpretation of Eq. (3) and Eq. (4) will be discussed. These matters are of particular importance in certain aspects of the theory of breakdown and conduction in both gases[3-7] and liquids[8-10] in which irregular cathode surfaces have probably been used.

II. SURFACE IRREGULARITY

Before considering the field magnification in detail it is useful to know the probable microgeometry of the cathode surfaces commonly used in the study of break-

[1] W. Schottky, Physik. Z. **15**, 872 (1914).
[2] R. H. Fowler and L. Nordheim, Proc. Roy. Soc. (London) **A119**, 173 (1928).
[3] F. Llewellyn Jones and E. T. de la Perrelle, Proc. Roy. Soc. (London) **A216**, 267 (1953).
[4] F. Llewellyn Jones and C. G. Morgan, Proc. Roy. Soc. (London) **A218**, 88 (1953).
[5] C. Grey Morgan and D. Harcombe, Proc. Phys. Soc. (London) **B66**, 665 (1953).
[6] K. Kerner and H. Raether, Z. angew. Phys. **6**, **212** (1954).
[7] A. H. Howell, Trans. Am. Inst. Elec. Engrs. **58**, 193 (1939).
[8] E. B. Baker and H. A. Boltz, Phys. Rev. **51**, 275 (1937).
[9] W. R. Le Page and L. A. DuBridge, Phys. Rev. **58**, 61 (1940).
[10] D. W. Goodwin and K. A. Macfadyen, Proc. Phys. Soc. (London) **B66**, 85 (1953).

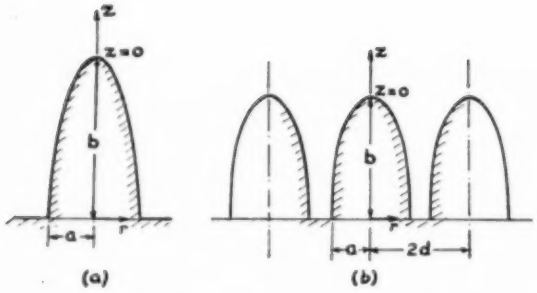

FIG. 1. Surface projections: (a) spheroidal projection, (b) ridge-like projections of elliptic cross section.

down of gases and liquids.[3–10] Detailed information is provided by Bowden and Tabor,[11] who give the following typical values for the heights of surface irregularities:

Finely turned copper, 5×10^{-4} cm,
Steel surface lapped with 150-grade carborundum, 5×10^{-5} cm,
Steel surface polished with 600-grade carborundum, 10^{-5} cm,
Optically polished aluminum, $10^{-6}-10^{-5}$ cm.

The general effect of polishing is to cause the peaks to flow into the valleys of the surface so that serrated peaks are replaced by smoother undulations. Photographs of the surface cross section show that isolated peaks rarely occur and, thus, the effect of neighboring projections on the field magnification must be considered. Since it is extremely unlikely that surfaces of the highest polish have been used for the majority of breakdown measurements, it would seem reasonable to consider field enhancement for surfaces having microgeometries in the range listed above.

III. FIELD ENHANCEMENT

At a distance z from an irregular cathode, the distorted applied field can be written as $\mu(z)E$, where the factor $\mu(z)$ is a decreasing function of z such that $\mu(z)\geqslant1$ or $\leqslant1$ above a surface projection or valley, respectively. This field distortion is quite distinct from that which might be produced by the large-scale geometry of the electrode system, as in a point-plane arrangement for example. Except for brief discussions by Baker and Boltz[8] and Hung[12] it has been assumed generally that the field distortion factor is independent of z, in which case Eqs. (1) and (2) result. This assumption is not correct and the use of a constant field magnification can lead to erroneous results as this paper will show.

Several estimates of the field magnification resulting from projections of simple geometry have been made. For instance, Schottky[13] has shown that for a hemispherical boss on an otherwise plane surface $\mu(0)=3$. By treating the boss itself as a further infinite plane and superimposing another boss of much smaller size, $\mu(0)$ then becomes equal to 3^2.[14] The projection that is built up by a repetition of this process becomes of infinite sharpness and is most unlikely in practice. Compton and Langmuir[15] have calculated the field near the summit of a ridge elevation formed by two intersecting planes, but since the plane of the cathode was not a natural boundary in such a system the result was very approximate.

Two cathode geometries will be considered in the present paper, the first consisting of a single prolate hemispheroid on an otherwise smooth plane and the second of a system of uniform ridges each having a semi-elliptical cross section. Both of these geometries are more realistic than those previously considered and can be made to cover a wide range of surface irregularity.

A. Spheroidal Projections

For a spheroidal projection of height b and base radius a Fig. 1(a), the field enhancement $\mu(z)$ along the axis can be obtained directly from the analytic expression for the potential given by Smythe.[16] The result is

$$\mu(z)=1-\left(\coth^{-1}\eta-\frac{1}{\eta}\right)\Big/\left(\coth^{-1}\eta_1-\frac{1}{\eta_1}\right)+\eta(\eta^2-1)\left(\coth^{-1}\eta_1-\frac{1}{\eta_1}\right), \quad (5)$$

where

$$\eta=(z+b)(b^2-a^2)^{-\frac{1}{2}},\ \eta_1=b(b^2-a^2)^{-\frac{1}{2}}.$$

Values of $\mu(z)$ and of $\bar{\mu}(z)$, the mean magnification factor defined as

$$\bar{\mu}(z)=z^{-1}\int_0^z\mu(z)dz, \quad (6)$$

are shown in Fig. 2 for a range of projections of unit height. The quantity $\bar{\mu}(z)$ is important since, as will be shown presently, it will be required in the corrected versions of Eq. (1) and Eq. (2). The results show that increased sharpness of the projection produces large values of $\mu(0)$, but that the resultant increase in $|d\mu(z)/dz|$ causes $\bar{\mu}(z)$ to decrease rapidly as z increases. For positions away from the axis of the projection, the values of $\bar{\mu}(z)$ will be less than those shown in Fig. 2, this being important in the discussion of Eqs. (3) and (4) in Sec. V.

B. Elliptic Ridges

The values of $\bar{\mu}(z)$ applicable in practice are likely to be considerably less than those obtained from Eqs.

[11] F. P. Bowden and D. Tabor, *The Friction and Lubrication of Solids* (Clarendon Press, Oxford, England, 1950).
[12] C. S. Hung, J. Appl. Phys. **21**, 37 (1950).
[13] W. Schottky, Z. Physik **14**, 63 (1923).
[14] Stern, Gossling, and Fowler, Proc. Roy. Soc. (London) **A124**, 699 (1929).
[15] K. T. Compton and I. Langmuir, Revs. Modern Phys. **2**, 123 (1930).
[16] W. R. Smythe, *Static and Dynamic Electricity* (McGraw-Hill Book Company, Inc., New York, 1950), second edition, p. 168.

(5) and (6) since the existence of a single isolated projection is improbable.[11] Unfortunately the effect of neighboring projections cannot be investigated for the spheroidal geometry since there is no natural coordinate system. However this important effect may be judged by using a system of uniform elliptic ridges on a plane surface as in Fig. 1(b). The potential distribution for such a system has been obtained by Richmond[17] using a Schwarz-Christoffel transformation. Using his analysis, the field distortion along the axis of a particular ridge, Fig. 1(b) is given by the two equations

$$\mu(z)=d\left\{\pi\left[Pt^{\frac{1}{2}}\sinh\left(\frac{\pi z\bar{\mu}(z)}{2d}\right)\times\left(t\cosh^2\frac{\pi z\bar{\mu}(z)}{2d}-1\right)^{-\frac{1}{2}}+Q\right]\right\}^{-1} \quad (7)$$

and

$$z=2P\cosh^{-1}\left[t^{\frac{1}{2}}\cosh\left(\frac{\pi z\bar{\mu}(z)}{2d}\right)\right]+Q\pi z\bar{\mu}(z)d^{-1}. \quad (8)$$

The auxiliary equations which determine the geometry of the ridges are

$$b=2P\cosh^{-1}t^{\frac{1}{2}}$$
$$a=2Q\cos^{-1}t^{-\frac{1}{2}}$$
$$d=\pi(P+Q),$$

in which the parameter t is varied over a wide range. Values of $\bar{\mu}(z)$ for ridges of unit height calculated from Eqs. (6), (7), and (8) are shown in Fig. 3 where again it is seen that $\bar{\mu}(z)\rightarrow 1$ rapidly as z increases.

For both geometries, extreme examples such as the spheroidal projection of base radius 0.1 and the ridge of half-width 0.06 and half-spacing 2.20 have been included. Even for such cases it is found that $\bar{\mu}(z)<2$ when $z=1$. It is important to notice that with an approximately constant ridge width, reduction in d greatly reduces both $\mu(z)$ and $\bar{\mu}(z)$. For instance, with $a\simeq 0.23$, reduction in d from 5.74 to 0.29 reduces $\mu(0)$ by a factor of five. Thus for well-polished surfaces having irregularities of order 10^{-5} cm high in close proximity as shown by Bowden and Tabor,[11] an estimate that $\mu(0)\simeq 2$ and that $\mu(z)$ decreases to unity within 5×10^{-6} cm from the surface would be reasonable. Such surfaces are commonly used as cathodes in gas and liquid breakdown measurements. For these cathodes, values of m, [corresponding approximately to $\bar{\mu}(z)$ in Eq. (6)] as great as 10 have frequently been assumed.[4,6] The errors involved are indicated in Fig. 2 where lines for constant field magnifications $m=3$ and $m=10$ have been drawn. Such assumptions concerning the nature and the degree of field enhancement render Eqs. (1) and (2) inaccurate and necessitate their reconsideration.

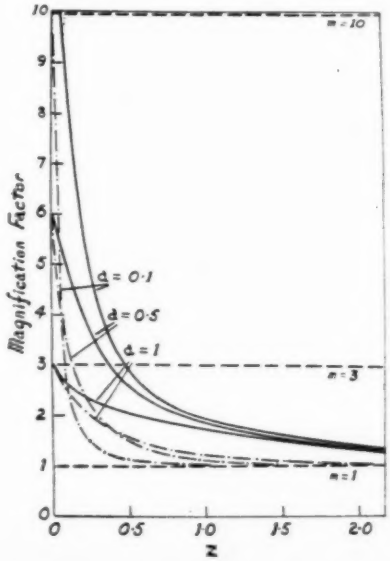

FIG. 2. Field enhancement factors $\mu(z)$ and $\bar{\mu}(z)$ for spheroidal projections having unit height b and various radii a. Constant field magnification factors $m=3$ and $m=10$ are also shown. [—·—·— $\mu(z)$, ——— $\bar{\mu}(z)$].

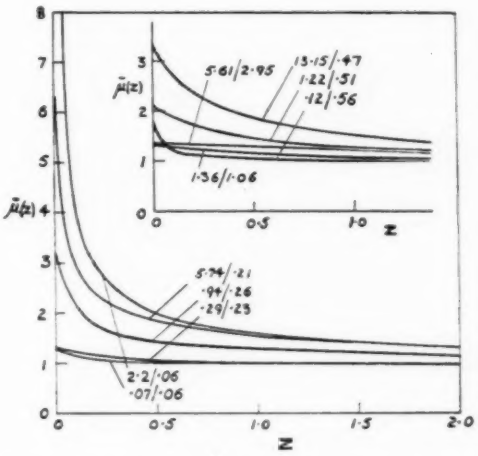

FIG. 3. Mean field enhancement factor $\bar{\mu}(z)$ for ridge projections. (Values on each curve give half-spacing d and half-width a, respectively. Note families of curves having a approximately constant.)

IV. EMISSION PROCESSES

A. Schottky-Type Emission

Equation (1) has been obtained by using a normal image-law for the motive of an electron outside the surface and by assuming that the applied field is uniform and of magnitude mE. If the correct magnification factor $\mu(z)$ is used, a maximum of the electron potential will occur at a distance z_m for which the image and applied fields are of equal magnitude, i.e.,

$$e/4z_m^2=\mu(z_m)E. \quad (9)$$

The lowering of the potential barrier ΔV is then given by

$$\Delta V=e/4z_m+E\int_0^{z_m}\mu(z)dz \quad (10)$$

which, using Eq. (6), becomes

$$\Delta V=\tfrac{1}{2}e^{\frac{1}{2}}E^{\frac{1}{2}}\gamma_m, \quad (11)$$

[17] H. W. Richmond, Proc. London Math. Soc. **22**, 389 (1924).

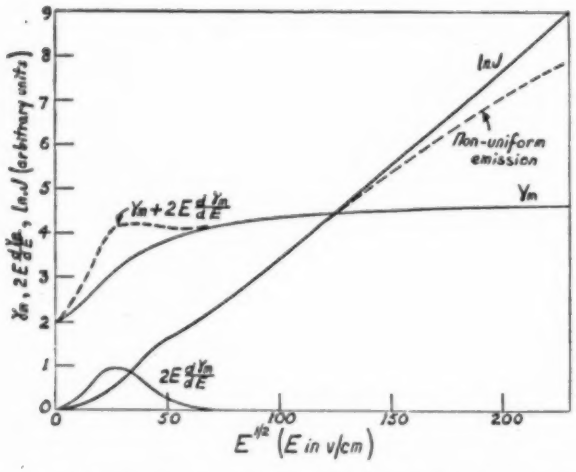

FIG. 4. Approximate Schottky emission for a spheroidal projection having $b=10^{-5}$ cm and $a=5\times10^{-6}$ cm. The variation of γ_m and $2Ed\gamma_m/dE$ in Eq. (13) for the Schottky slope are given, as well as the behavior of $\ln J$ deduced graphically from these. The decrease in the slope due to nonuniform emission at high fields (Sec. V) is also indicated.

in which

$$\gamma_m=[\mu(z_m)+\bar{\mu}(z_m)]\mu(z_m)^{-\frac{1}{2}}.$$

Equation (11) reverts to the usual Schottky lowering $e^{\frac{1}{2}}(mE)^{\frac{1}{2}}$ as in Eq. (1) if it is assumed that the field intensification is independent of z. This is equivalent to the arbitrary condition $\mu(z)=\bar{\mu}(z)=m$.

Using the correct ΔV from Eq. (11), Eq. (1) becomes

$$J=AT^2\exp-\{[\phi-\tfrac{1}{2}e^{\frac{1}{2}}\gamma_mE^{\frac{1}{2}}]/kT\}, \tag{12}$$

from which the Schottky slope is

$$\frac{d\ln J}{dE^{\frac{1}{2}}}=\frac{e^{\frac{1}{2}}}{2kT}\left(\gamma_m+2E\frac{d\gamma_m}{dE}\right), \tag{13}$$

and should be compared with the usual but incorrect value $e^{\frac{1}{2}}m/kT$. The form of the terms γ_m and $2Ed\gamma_m/dE$ in Eq. (13) for a single spheroidal projection of height 10^5 cm and base radius 5×10^{-6} cm is shown approximately in Fig. 4 using values of $\mu(z)$ from Fig. 2. Also shown in Fig. 4 is the $\ln J$ vs $E^{\frac{1}{2}}$ plot obtained graphically from the values of γ_m and $2Ed\gamma_m/dE$. Although the slope of this plot increases as γ_m increases, an inflection can be produced by the behavior of the term $2Ed\gamma_m/dE$ in Eq. (13) which, for the projection chosen, has a maximum at a field of about 10^3 v/cm. At higher fields γ_m slowly tends to a limiting value and the corresponding slope is then a factor $\frac{1}{2}\gamma_m$ greater than the undistorted Schottky value. In practice, the slope may tend to decrease rather than increase slowly in this upper range.[12] This can be caused by patches on the cathode surface[18] or by increased nonuniformity in the emission due to surface irregularities. The latter effect will be discussed in Sec. V when considering Eq. (4) in more detail.

[18] J. A. Becker, Revs. Modern Phys. **7**, 95 (1935).

If the cathode surface has patches of differing work function, the resultant patch fields produce a departure from the image-law motive assumed in Eqs. (1), (9), and (12). Becker and Mueller[19] have shown how the modified motive may be investigated experimentally for a smooth cathode as follows. If no field magnification occurs, i.e., $m=1$ in Eq. (1) then using Eq. (9) with $\mu(z)=1$

$$\frac{d\ln J}{dE}=\frac{ez_m}{kT}, \tag{14}$$

where z_m is now the distance from the cathode at which the motive field strength E_s is equal to the applied field E. If experimental values of J are known for given values of E, Eq. (14) will yield the required relationship between E_s and z_m. If the surface is rough the condition for a maximum of the potential barrier corresponding to Eq. (9) becomes

$$E_s=\mu(z_m)E \tag{15}$$

and the lowering of the barrier ΔV is then

$$\Delta V=\int_{z_m}^{\infty}E_s dz+E\int_0^{z_m}\mu(z)dz. \tag{16}$$

Using Eqs. (15) and (16) to correct Eq. (1), it may be shown directly that

$$\frac{d\ln J}{dE}=\frac{ez_m\bar{\mu}(z_m)}{kT}. \tag{17}$$

The experimental slope $d\ln J/dE$ can no longer be interpreted in terms of z_m as in Eq. (14) and further, as Eq. (15) shows, the motive E_s cannot be determined. The method which was intended to detect a departure from the normal image law is seen to be quite unreliable unless both $\mu(z_m)$ and $\bar{\mu}(z_m)$ are close to unity. This would only occur at low values of the applied field, i.e., in a range in which the surface patch fields are of little interest.

B. Field Emission

Similar arguments concerning field enhancement apply to field emission. This type of emission occurs when the potential barrier at the surface is reduced by the field so that it becomes transparent to electrons from below the Fermi level. Fields of approximately 10^7 v/cm, extending over distances of about 10 A from the surface are required[2] so that for an irregular surface a suitable criterion is that

$$\bar{\mu}(z_0)E\simeq10^7\text{ v/cm}, \tag{18}$$

where $z_0(\simeq10$ A) is the distance at which the barrier is reduced to the Fermi level. Figures 2 and 3 show that true field emission is unlikely to occur therefore until E is significantly greater than 10^6 v/cm. Furthermore the increase of $\bar{\mu}(z_0)$ as E increases will cause the $\ln(JE^{-2})$

[19] J. A. Becker and D. W. Mueller, Phys. Rev. **31**, 431 (1928).

vs E^{-1} plot to depart from linearity at the higher fields. A simple and explicit correction to Eq. (2) cannot be obtained, since the emission depends on the height and width of the barrier in a complicated way. A correction was possible for the Schottky-type emission in Eq. (1) because in that case the emission depended on the height of the barrier alone. However an approximate expression could be obtained by replacing m by $\bar{\mu}(z_0)$ in Eq. (2) and by suitably choosing a mean value for $\bar{\mu}(z_0)$ according to the nature of the emitting surface and the magnitude of E. Thus, Eq. (2) becomes

$$J=B\bar{\mu}(z_0)^2E^2\exp[-D/\bar{\mu}(z_0)E]. \quad (19)$$

V. EMITTING AREA

Ultimately the measured current I from a given cathode surface has to be related as in Eq. (4) to the current density in either Eq. (12) or Eq. (19).

The difficulties in this procedure for a rough cathode have already been mentioned in Sec. I, although the subsequent treatment has so far ignored the fact that $\mu(z)$ is a function of surface position. The expressions given in Eqs. (5) and (7) are for values of $\mu(z)$ along a normal through the tip of a projection. Away from such a normal the decrease in $\mu(z)$ will cause an appreciable decrease in J, since $\mu(z)$ occurs effectively in the exponential terms of the emission laws. As a result, the emission will be concentrated in regions of maximum curvature of the microsurface. If conditions in the neighborhood of a particular projection are considered and r is the distance along the surface measured perpendicularly to the axis of a projection (Fig. 1) then for Schottky emission, using Eq. (12)

$$\frac{dJ}{dr}=AT^2\exp-[(\phi-\tfrac{1}{2}e^{\frac{1}{2}}\gamma_m E^{\frac{1}{2}})/kT]\frac{e^{\frac{1}{2}}E^{\frac{1}{2}}}{2kT}\frac{d\gamma_m}{dr}, \quad (20)$$

and for field emission using Eq. (19)

$$\frac{dJ}{dr}=BE(2\bar{\mu}(z_0)E+D)\exp[-D/\bar{\mu}(z_0)E]\frac{d\bar{\mu}(z_0)}{dr}. \quad (21)$$

It is tedious to calculate values for $d\gamma_m/dr$ and $d\bar{\mu}(z_0)/dr$ since it is difficult to obtain values of $\mu(z)$ other than along the axis of a projection. However the general behavior can be ascertained by the following qualitative argument which is restricted to Schottky emission, Eq. (20).

When E is small, $\mu(z_m)$ along the axis of a projection will be close to unity so that $d\gamma_m/dr$ and therefore dJ/dr from Eq. (17) will be small. The emitted current will be uniform and the effective emitting area S' in Eq. (4) could be considered to be constant although not necessarily equal to the cathode area. As the field is increased γ_m and $|d\gamma_m/dr|$ will increase, making dJ/dr significant. Ultimately as $z_m\to 0$ $\gamma_m\to 2\mu(0)$ and $d\gamma_m/dr\to 2d\mu(0)/dr$ and although such conditions could not be reached in practice, an investigation of $\mu(0)$ as a function of r will indicate possible magnitudes of the terms involved. A typical example for a ridge geometry, Fig. 5, shows that $d\mu(0)/dr$ is considerable near the tip. In addition to the increase of $|d\gamma_m/dr|$ other terms in Eq. (20) will also show a marked increase as E increases. Thus, an appreciable increase in $|dJ/dr|$ can be expected as E increases making the current distribution over the surface more localized. If a constant emitting area S' is assumed, then estimates of J will be too small at the higher fields and a decrease in the Schottky slope as shown in Fig. 4 will result. These deductions show striking agreement with the experimental $\ln J$ vs $E^{\frac{1}{2}}$ curves obtained by Hung[12] using a rough oxide cathode and fields up to 5×10^4 v/cm. All the features indicated in Fig. 4 appear in the experimental curves, including the initial increase in Schottky slope and the small inflection at fields of the order of 10^3 v/cm due to the behavior of the term $2Ed_{\gamma m}/dE$ in Eq. (13), the subsequent linear region for fields ($\sim10^4$ v/cm) at which γ_m tends to remain constant or increase slowly and finally the decrease in slope at fields approaching 5×10^4 v/cm due to the nonuniform emission just described.

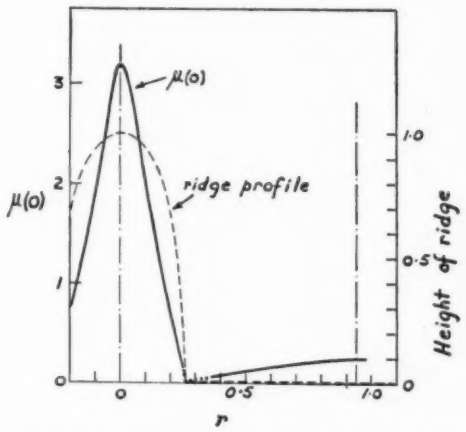

FIG. 5. Variation of surface field $\mu(0)$ for a typical ridge geometry. (Profile of ridge having $a=0{\cdot}26$, $b=1$, $d=0{\cdot}94$ is also shown.)

A similar behavior is predicted by Eq. (18) for field emission and since the applied fields will be in the range 10^6-10^8 v/cm, $|d\bar{\mu}(z_0)/dr|$ will be large and the nonuniformity of the emission accentuated. Under these conditions nonuniform emission may still occur from cathodes which have been carefully polished till the remaining roughness is due solely to the crystalline nature of the surface. Experiments by Dyke and others[20,21] using smooth tungsten cathodes and fields as great as 7×10^7 v/cm have shown marked departures from the Fowler-Nordheim law. At such high field strengths the equivalent z_0 will be <5 A so that such departures can be attributed in part at least to the variation of $\bar{\mu}(z_0)$ in Eq. (19) and to nonuniform emis-

[20] Barbour, Dolan, Trolan, Martin, and Dyke, Phys. Rev. **92**, 45 (1953).
[21] W. P. Dyke and J. K. Trolan, Phys. Rev. **89**, 799 (1953).

sion produced by the microcrystalline structure of the surfaces of the emitters.[22]

VI. DISCUSSION

The present paper has indicated two main factors concerning field enhancement produced by surface roughness. Firstly, calculations for certain ideal geometries indicate that the degree of enhancement for typical cathode surfaces is much less than has been generally assumed by previous workers and, secondly, the effective field enhancement factor to be employed is not constant but is field dependent. These effects can profoundly affect any deductions made from emission experiments.

For instance, by employing magnification factors as as great as 10, Llewellyn Jones and others[3–5] have attempted to use a field emission theory for fields less than 10^5 v/cm when investigating the emission from cathode surfaces in air and other gases. Using this theory these workers found difficulty in obtaining reasonable values for the emitting areas and work function involved. The present calculations using Eq. (9) and Figs. 2 and 3 show that a mean magnification [Eq. (6)] much closer to unity would be more appropriate, in which case a Schottky-type theory employing accepted values of the work function will yield reasonable estimates of the emitting areas.[23] The same criticism can be made of the similar work reported by Kerner and Raether[6] in which a constant magnification factor $m=10$ has been used with a Schottky emission theory. The implicit acceptance of considerable field magnification has led Goodwin and Macfadyen[10] also to suggest that field emission, according to Eq. (2), occurred during their conductivity measurements in *n*-hexane at fields up to approximately 2×10^5 v/cm. In common with Llewellyn Jones and Morgan,[4] their results give an effective emitting area and a work function ($S'\sim10^{-13}$ cm^2, $\phi\sim0{\cdot}01$ *eV*) which are too small to be realistic. These results, together with the fact that the well-polished cathode surfaces used would produce a magnification factor near to unity suggests that Schottky rather than field emission was occurring.

The deduction that $\bar{\mu}(z_m)$ will be close to unity for a roughened surface unless the field is appreciably greater than 10^6 v/cm may also explain the results of Howell[7] for the electric strength of compressed gases. Using fields of 4×10^5 v/cm, Howell found no significant change in the breakdown strength when rough and smooth cathodes were used. This result might be expected if a Schottky theory was employed since z_m could be large enough to render γ_m in Eq. (12) only slightly dependent on the surface roughness, especially if the motive is distorted by patch fields as in Eq. (15).

Baker and Boltz[8] investigating conduction in toluene report increased Schottky slopes for fields in the range 10^4–10^5 v/cm, but closer agreement with the undistorted slope e^3/kT for fields above 10^5 v/cm. Le Page and DuBridge[9] correct certain aspects of the theory of Baker and Boltz and give further similar results for toluene. Treating the dielectric liquid as a continuous medium of dielectric constant K modifying the image-law motive, Eq. (9) becomes

$$e/4Kz_m^2=\mu(z_m)E \tag{22}$$

and the Schottky law corresponding to Eq. (12) is then

$$J=AT^2\exp-[(\phi_D-\tfrac{1}{2}e^{\frac{3}{2}}\gamma_mK^{-\frac{1}{2}}E^{\frac{1}{2}})/kT],$$

in which ϕ_D is the work function into the dielectric. Equation (22) indicates that for a given surface geometry and field E, z_m will be a factor $K^{-\frac{1}{2}}$ less than in a vacuum so that the surface microgeometry becomes more important for emission into a dielectric liquid. The conclusions reached in Sec. IV A and in Sec. V therefore become particularly applicable to these results for toluene. In fact Le Page and DuBridge conclude that the emission comes from discrete spots on the cathode and show that the quantity AS' [Eqs. (1) and (4)] decreases in the range 10^4–10^5 v/cm. This is precisely what might be expected as a result of the variation of dJ/dr in Eq. (20).

VII. ACKNOWLEDGMENTS

The author wishes to thank Professor W. J. John for facilities provided and the University of London for the award of a Turner and Newall Fellowship.

[22] T. J. Lewis, Proc. Phys. Soc. (London) (to be published shortly).
[23] T. J. Lewis, Proc. Phys. Soc. (London) **B68**, 504 (1955).

JOURNAL OF APPLIED PHYSICS VOLUME 26, NUMBER 12 DECEMBER, 1955

New Active Circuit Element Using the Magnetoresistive Effect

A. Aharoni, E. H. Frei, and G. Horowitz
Weizmann Institute of Science, Rehovoth, Israel

(Received March 8, 1954; revised version received July 30, 1955)

A new multistable element is described, and the conditions under which it may operate are discussed. It is found that a bistable element (flip-flop) with reasonable resolving time may be achieved, though it might be necessary to operate it at low temperatures. A tristable element is found to be possible, but not practical. A slowly operating model is described.

I. GENERAL

ALL metals show a change of resistance when brought into a magnetic field; in most cases the resistance rises monotonically with the field. The change is strongly dependent on temperature: the lower the temperature, the greater the change. This effect has been known for many years[1] and has been thoroughly investigated, especially on bismuth,[2,3] since its magnetoresistive effect has one of the highest values known.

We can design an electric network containing magnetoresistive elements. If such a network is designed so that the change of the magnetic field is produced by a changing current, and the resulting change of resistance in turn produces a change of current, this arrangement would represent an amplifier, provided the final change of current were greater than the primary change. Inherently, an element that represents an amplifier could be used in different circuits as an "active element." The use of the magnetoresistive effect in the construction of a simple toggle circuit is considered below (see Fig. 1).

In the bridge R_1, R_2, R_3, and R_4 are resistances constructed of a material whose resistance changes considerably in a magnetic field. L is a coil with resistance r. The coil is so constructed that R_1, R_2, R_3, and R_4 are in a uniform field h produced by the current in the coil. In addition to this field there is a constant field H_0. The field H_0 and R_1, R_2, R_3, and R_4 are so chosen that for $I=0$ $(h=0)$, $R_1=R_2=R_3=R_4=R$. With $I\neq 0$ the arrangement is such that resistors R_1 and R_4 are in a field $H=h+H_0$, while R_2 and R_3 are in a field $H=h-H_0$. ρ represents the lumped external series resistance of the system. We have then:

$$\begin{aligned}(R_1+r+R_3)i_1 \quad & -ri_2 \quad -R_3i_3=-L\partial I/\partial t\\ -ri_1+(R_2+R_4+r)i_2 \quad & -R_4i_3=+L\partial I/\partial t \qquad (1)\\ -R_3i_1 \quad -R_4i_2+(R_3+R_4+\rho)i_3 &= V.\end{aligned}$$

Assuming further $R_3=R_2$, $R_4=R_1$, and solving algebrically, we get

$$I=i_1-i_2=\frac{(R_1-R_2)V-(R_1+R_2+2\rho)L\partial I/\partial t}{(r+\rho)(R_1+R_2)+2(R_1R_2+r\rho)}$$

$$-L\frac{\partial I}{\partial t}=\varphi(I)$$

$$\equiv\frac{(R_2-R_1)V+I[(r+\rho)(R_1+R_2)+2(R_1R_2+r\rho)]}{R_1+R_2+2\rho}. \qquad (2)$$

This equation may be solved explicitly to give $I=I(t)$, but this solution yields very little information, except the rate of descent to a state of equilibrium which will be essentially of the order of L/R. What is more interesting, however, are the values of the states of current equilibrium, which are given by $\partial I/\partial t=0$, and are therefore the roots of φ.

As the magnetoresistive effect is quadratic for all practical cases, we assume:

$$R_1=R_0(1+CH^2)=R_0[1+C(H_0+KI)^2]$$

$$R_2=R_0[1+C(H_0-KI)^2],$$

i.e.,

$$R_1=R(1+2MI+NI^2),\ R_2=R(1-2MI+NI^2)$$

where

$$M=CKH_0/(1+CH_0^2),\ N=CK^2/(1+CH_0^2).$$

Equation (2) yields

$$-L\frac{\partial I}{\partial t}=\frac{[rR+R\rho+\rho r+R^2-2MVR]I+[NR(r+\rho)+2R^2(N-2M^2)]I^3+N^2R^2I^5}{R(1+NI^2)+\rho},$$

which means that the roots of φ are given by the solutions of the quintic equation

$$AI^5+BI^3+DI=0, \quad \text{with} \quad A>0. \qquad (3)$$

The stability of the solutions can be readily determined as follows: If φ is positive, $\partial I/\partial t$ is negative, and the current will decrease; while if φ is negative, $\partial I/\partial t$ is positive, and the current will increase. There are 4 cases to be considered (see Fig. 2); arrows are drawn according to these stability considerations.

(a) $D>0$ $B>0$

(b) $D<0$ $B>0$

(c) $D<0$ $B<0$

(d) $D>0$ $B<0$.

[1] D. K. C. MacDonald and K. Sarginson, Phys. Soc. (London), Repts. Progr. in Phys. **15**, 249 (1952).
[2] H. Jones, Proc. Roy. Soc. (London) **A155**, 653 (1936).
[3] B. Donovan and G. K. T. Conn, Phil. Mag. **40**, 283 (1949).

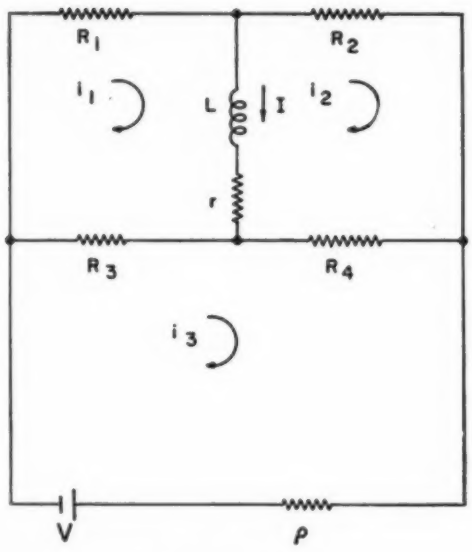

FIG. 1. Basic circuit.

The arrows show in which direction the system changes until it reaches a stable equilibrium. (a) gives a monostable solution, $I=0$, which is trivial. (b) represents 3 solutions; one ($I=0$) is unstable while the two solutions that are symmetric about zero represent the stable configurations. This then produces a bistable system. (c) is also a bistable system as (b) above, but under different conditions of operation. As for (d), examining these five solutions for stability, it is found that there are three stable values of current, $I=0$ and $I=\pm I_0$. Three solutions or one solution may also appear in this case.

Thus, under suitable conditions this circuit is able to produce 1, 2, or 3 positions of stable equilibrium. (b) appears to be the only practical case, and will be the chief subject of discussion. It might be remarked here that (c) appears to have no particular advantage over (b) but rather has the disadvantage of being more difficult to achieve, while (d) can only be achieved under extremely limited circumstances, possibly even prohibitively limited when capacity effects, etc., are taken into account.

The question then arises: Under what conditions is it possible to achieve the bi- (and tri-) stable states? The roots of Eq. (3) are:

$$I=0,\ \pm\{4M^2R-N(r+\rho+2R)\pm\{[4M^2R-N(r+\rho+2R)]^2-4N^2(rR+R\rho+\rho r+R^2-2MVR\}^{\frac{1}{2}}\}^{\frac{1}{2}}/(2N^2R)^{\frac{1}{2}}. \quad (4)$$

From above: $M=CKH_0/(1+CH_0^2)$, $N=CK^2/(1+CH_0^2)$ or, if instead, $k=KC^{\frac{1}{2}}$ and $h_0=H_0C^{\frac{1}{2}}$, then $M=kh_0/(1+h_0^2)$ and $N=k^2/(1+h_0^2)$. If we make $2V/(R+r)=1$, $\rho=0$, and plot parametric curves of the solutions of φ as function of parameter k, we obtain the curves in Fig. 3 with the free parameter h_0.

II. DESIGN CONSIDERATIONS

Case (b):

$$D=(r+\rho)R+r\rho+R^2-2MVR<0$$

and

$$B=NR(r+\rho)+2R^2(N-2M^2)>0$$

$$MV>\tfrac{1}{2}(r+R+\rho)+\tfrac{1}{2}r\rho/R$$

$$(r+\rho+2R)/R>4CH_0^2/(1+CH_0^2)$$

$$\frac{CKH_0V}{1+CH_0^2}>\frac{r+R+\rho}{2}+\frac{r\rho}{2R},\qquad CH_0^2<\frac{2R+r+\rho}{2R-r-\rho}.$$

Case (c):

$$\frac{CKH_0V}{1+CH_0^2}>\frac{r+R+\rho}{2}+\frac{r\rho}{2R}\text{ and }CH_0^2>\frac{2R+r+\rho}{2R-R-\rho}.$$

Case (d):

$$\frac{CKH_0V}{1+CH_0^2}<\frac{r+R+\rho}{2}+\frac{r\rho}{2R}\text{ and }CH_0^2>\frac{2R+r+\rho}{2R-r-\rho}.$$

For 5 solutions in this case the following condition must also be fulfilled:

$$B^2>4AD,$$

i.e.,

$$N^2(r-\rho)^2+8N^2MVR+16M^4R^2>8NM^2R(2R+r+\rho)$$

$$8CKH_0VR(1+CH_0^2)>8CH_0^2R\times[r+\rho+2R+CH_0^2(r+\rho)]-(r-\rho)^2(1+CH_0^2)^2$$

which makes $CKH_0V/(1+CH_0^2)$ greater than an expression of the same order as the previous expression $\frac{1}{2}(R+\rho+r)+\frac{1}{2}r\rho/R$.

For every bistable solution, $CKH_0V/(1+CH_0^2)$ must then be greater than $\frac{1}{2}(R+r+\rho)+r\rho/2R$, for every tristable solution it must be very slightly less. In every case then $2CKH_0V/(1+CH_0^2)$ must be at least of the order of magnitude of $r+R+\rho$. The second condition on the parameters differentiates between two types of solutions: for $CH_0^2<(2R+r+\rho)/(2R-r-\rho)$ it yields a bistable system in which the bridge never

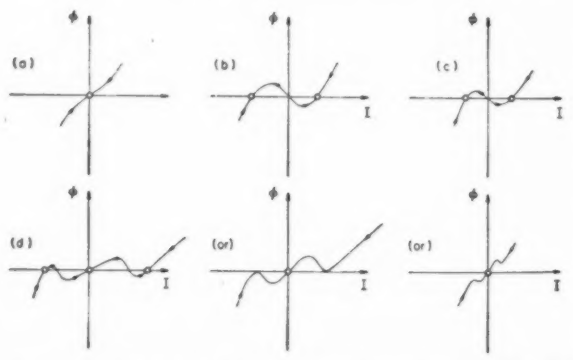

FIG. 2. Graph of the function $\varphi=AI^5+BI^3+DI$, with $A>0$, for (a) $D>0$, $B>0$; (b) $D<0$, $B>0$; (c) $D<0$, $B<0$; (d) $D>0$, $B<0$. o denotes a stable equilibrium point.

departs too far from linear operation about the zero current point, and the amount of current through the coil remains a relatively small fraction of total current of the bridge, that is that the fraction of the bridge current which changes is a small pact of the dc. On the other hand, the condition CH_0^2, greater than a number which is not smaller than one (dependent on the value of $r+\rho$, which is hereby limited to a number less than $2R$), yields two or three stable solutions characterized by changes of current approaching the value of the direct current. In practice this type of solution would present special difficulties including the accentuation of temperature problems due to the wide variation of current through the conductor. There is the additional problem that rather larger energies will be required to effect the transfer from one stable state to the other. For this reason the tristable state, though possible of obtainment, appears to be only of theoretical interest.

From the above general discussion of the conditions on the parameters it is possible to arrive at fairly detailed conclusions as to the values necessary for the parameters. It is immediately obvious that the parameter of the magnetoresistive effect, C, i.e. the change in resistance, must be as large as possible. This implies the choice of a material with the greatest possible C. On the basis of the value of C, the parameters chosen for H_0 and K must be greater than some minimum value and, in addition, that chosen for H_0 must also be less than some maximum value.

It is generally desirable that r be as small as possible, since it effectively reduces the size of C. R may be increased if V is also increased, but the choice of R, V, and as a rule R/V is determined by considerations of the amount of energy which can be dissipated by the Bi resistors.

Another design consideration arises from the fact that for all temperatures K is limited by the following: too many turns cannot be used because this results in larger r, and larger inductance ($H \propto n$, $L \propto n^2$), which means slow operation of the circuit. The problem lies in making K large enough to produce the requisite magnetic field without producing an inductance which is prohibitively large. The result will be an element of small size whose magnetoresistive part consists of thin layers.

III. BISMUTH AS A POSSIBLE MATERIAL

As was noted above, the chief consideration governing the choice of a material is the value of its magnetoresistive coefficient C. Bismuth is the "classical" material in this respect.[4,5] It has been recently found that indium antimonide,[6,7] has also a very large value

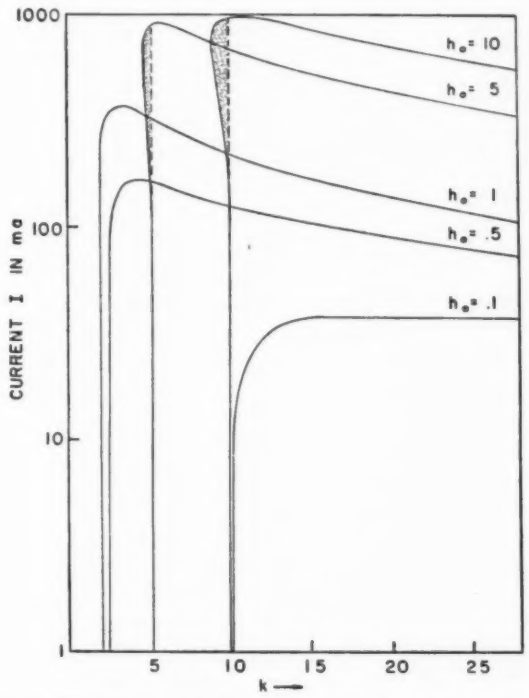

FIG. 3. The current I in the coil L, as a function of k and h_0 for $r=R$, $\rho=0$, $V/R=1$. The shaded region represents tristable states.

of C, even larger than that of bismuth at some temperatures. Germanium[8] has also a relatively large value of C, though smaller than that of bismuth. In all materials the effect is very sensitive to temperature and purity, usually increasing with lower temperature and higher purity.

As outlined above, it will be necessary to use thin layers of the magnetoresistive material. It is known that the magnetoresistive effect decreases with the thickness of the layer (size effect).[9–11] Since the literature does not contain sufficient data on the size effect of germanium or indium antimonide, it is hard to tell which will have the larger C, when thin layers are considered. This discussion will therefore be limited to consideration of the effect in bismuth. In the following the magnitude of this effect will be discussed along with an analysis of the values of the parameters under various temperatures, especially room temperatures.

Impurities in bismuth which generally seem to reduce the size of the resistive change,[2,4] show increasingly greater effect as the temperature is reduced. In spectroscopically pure bismuth, C has the following values for the transversal effect (H being perpendicular both to current and to the Bi layer).

The above analysis of parameters indicated that the

[4] N. Thompson, Proc. Roy. Soc. (London) **A164**, 24 (1938).
[5] P. Kapitza, Proc. Roy. Soc. (London) **A123**, 292 (1929).
[6] G. L. Pearson and M. Tanenbaum, Phys. Rev. **90**, 153(L) (1953).
[7] H. Weiss, Z. Naturforsch. **8a**, 463 (1953).
[8] G. L. Pearson and H. Suhl, Phys. Rev. **83**, 768 (1951).
[9] R. G. Chambers, Proc. Roy. Soc. (London) **A202**, 378 (1950).
[10] D. K. C. MacDonald and K. Sarginson, Proc. Roy. Soc. (London) **A203**, 223 (1950).
[11] E. H. Sondheimer, Phys. Rev. **80**, 401 (1950).

TABLE I. The coefficient of magnetoresistive effect for spectroscopically pure bismuth.

C (gauss^{-2}) / Temp.	Rolled layers 10μ thick[a]	Evaporated layers 0.2–1.3μ thick[b]	Single crystal with current parallel to trig. axis and H parallel to binary axis[c]
Room temperature	6×10^{-9}	$4.9\times10^{-10}-1.5\times10^{-9}$	1.7×10^{-8}
0°C	9×10^{-9}	...	2.5×10^{-8}
Dry ice	3.3×10^{-8}	...	1.2×10^{-7}
Liquid air	3.5×10^{-7}	...	3.1×10^{-6}

[a] Measured by the authors.
[b] Measured by W. F. Leverton and A. J. Dekker, Phys. Rev. **81**, 156(L) (1951).
[c] Measured by S. Meiboom and B. Abeles (unpublished paper).

critical factor would appear to be the design of an element whose magnetic field is sensitive to small changes, and which has an inductance small enough to yield a small resolving time. It is therefore desirable to analyze dimensionally the arrangement of the element under optimum conditions, and to see if, with such dimensions, the heat can be dissipated adequately.

Let us consider the following arrangement: a circular coil with one toroidal ferromagnetic core of very high permeability having a small air gap completely filled with bismuth. The energy W in the magnetic field (assumed to be uniform for simplicity), is given by the following expressions:

$$W=\tfrac{1}{2}LI^2 \tag{5}$$

$$W=\left[V\int H'dB'+v\int HdB\right]\Big/8\pi = (V/\mu+v)H^2/8\pi, \tag{6}$$

where v is the volume of gap and V is the volume of the core. Equating (5) and (6):

$$L=(v+V/\mu)(H/I)^2/4\pi=A(l_g+l/\mu)(H/I)^2/4\pi,$$

where A is the cross section, l is the length of the core, and l_g is the length of the Bi gap. For such a coil the field is given by the expression:

$$H=4\pi nI/10(l/\mu+l_g), \tag{7}$$

and so

$$L=4\pi n^2A/(l/\mu+l_g)10^9$$

(when H is measured in gausses, I in amperes, L in Henries). Let us consider a set of practicable values, say at room temperature, where we may assume $C=5\times10^{-9}$ gauss^{-2}. $H_0=10^4$ gauss, may be easily attained. The condition for operation of a bistable system for $\rho=0, r=R$ is then

$$CKH_0/(1+CH_0^2)=\tfrac{1}{3}\times10^{-4}K>R/V.$$

Take

$$K=4\pi n/10(l_g+l/\mu)=4\times10^4R/V,$$

take

$$l_g=2\times10^{-4}\text{ cm}, l=2\text{ cm}, \mu=2\times10^4,$$

then $n=10\,R/V$. If the toroid is made of a thin strip, one can easily have $A=5\times10^{-3}$ cm^2, which makes $L=2\times10^{-5}(R/V)^2$. If one considers reasonable power dissipation, $V^2/R\sim0.2$ watt, the resolving time will be of the order:

$$L/R=1.0\times10^{-4}\text{ sec, with } n\sim20\text{–}30.$$

This indicates that theoretically the element might successfully be built at room temperatures.

If because of the technical difficulty of making such an element or because of problems of heat dissipation etc., such an arrangement does not prove practical, very much can be accomplished by lowering the temperature. This will permit larger heat dissipation and fewer turns. However, problems arise in two directions: First of all the gap, which still cannot be enlarged too much, approaches the dimensions of the mean free path at which the magnetoresistive effect diminishes (size effect).[9–11] As is seen from Table I, even at room temperature there is a considerable reduction of C for layers of 1μ thickness, as compared to those of 10μ. Secondly, the permeability is never constant in ferromagnetic materials, and the calculation becomes much more complicated when permeability changes with the field H are taken into account. Even more trouble is caused by the remanence in these materials, and these problems become much more acute at lower temperatures. However, it might be possible to construct such an element at liquid-helium temperature without using a ferromagnetic material, but not enough data are published on the magnetoresistive effect at this temperature to decide if such a construction is possible.

The disadvantage of having to produce a low temperature would not however be prohibitive in a large system such as that of a computer where many of these elements are used, and where a liquid-helium cryostat may be considered as additional equipment in the same sense as a power supply. As these elements might work at low power dissipation, the power necessary to drive the whole instrument, including the helium supply, might prove to be less than that needed when conventional vacuum tubes are used. Such a system would have the advantage that its elements can be connected together without any other components, thereby increasing the reliability of the system. This paper, however, deals only with the states of one single element. In order to combine elements in a large system like a

computer several other problems would have to be investigated, especially the question of connecting the elements and the analysis of their transfer properties between different states.

IV. CONSTRUCTION OF MODEL

In building an experimental model to test the principles involved, the question of a short resolving time was ignored, and only an element with two states of equilibrium was sought.

The model consisted of 2 U-shaped electromagnets, each leg of which was 9 cm long×1 cm wide. The legs were 2 cm apart and consisted of 30 foils of 0.5-mm transformer iron with $\mu\sim10^4$. A 4-cm I piece of the same material was attached to a plate; the plate was moved by means of screws to the minimum possible distance from the U piece, both the U and the I pieces being well polished to reduce air gap. The pole pieces of a few mm were made to strengthen the fields, and to provide space for point contacts to which the bismuth layers were soldered (see Fig. 4).

For the preparation of the bismuth layers the method proposed by Heaps,[12] was first tried but the thicknesses obtainable by this method were rather large. The layers used were hot-rolled at the temperature of 150–180°C, (from Johnson and Matthey's "spectroscopically pure" material) to the thickness of $(10\pm0.2)\mu$ (determined by weighing and measuring the area), and then cut to about 15×1.5 mm, making $R\sim1\Omega$. A sheet of mica 0.8 mg/cm² thick was introduced on each side of each Bi layer to isolate it from the iron.

V was a 2-volt battery being adjusted to give 0.6 amp through the bridge.

L was 725 turns of 0.70-mm enameled wire on each of the magnets, the coils being connected in series to yield $r=6.1\Omega$ including the connecting leads.

$(r+R+\rho)/2V+r\rho/2RV$ was thus less than 2, while K by (7) was at least 2.5×10^5 gauss/amp (not taking pole pieces into account).

H_0 was created by 300 turns of the same wire on each magnet wound on one magnet in the same direction as L, and on the other one in the opposite direction, having thus, two of the Bi resistances in the field H_0+KI, and the two others in the field H_0-KI. The coils of H_0, connected in series were connected to a battery through a potentiometer, and it was found that a current of 50 ma through them [making H_0 a few kilogausses by (7), which for $C=6\times10^{-9}$ gauss^{-2} makes $CKH_0/(1+CH_0^2)$ certainly greater than 2] was sufficient to give 2 distinguishable states of equilibrium. These states were wider separated the larger this current. At about 300–400 ma the separation between the 2 positions was large enough to ascertain that a flip-flop was obtained.

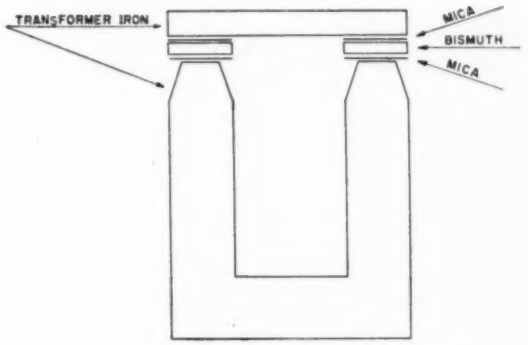

FIG. 4. Schematic representation of the room temperature slow operating model.

With pulses of the order of 0.3 amp through 150 turns on one of the magnets only, it would transfer from one position of equilibrium to the other (measured by the voltage across r)—pulses of the same polarity always bringing back to the same position. The states of equilibrium themselves were, however, not exactly reproducible, and different magnitudes of pulses, or repeated pulses of the same polarity could shift them slightly, due undoubtedly to the change in H_0 which was caused by remanence in the transformer iron.

ACKNOWLEDGMENTS

One of the authors (E.H.F.) is much indebted for valuable discussions to Professor J. von Neumann and Mr. J. Bigelow, of the Institute for Advanced Study, Princeton, New Jersey, where he first started to work on this paper, and to Professor J. B. Wiesner of the Massachusetts Institute of Technology, for his kind interest.

[12] C. W. Heaps, Phys. Rev. **29**, 332 (1927).

JOURNAL OF APPLIED PHYSICS VOLUME 26, NUMBER 12 DECEMBER, 1955

Hexagonal Microstructure of Ice Crystals Grown from the Melt*

FRANK K. TRUBY
New Mexico Institute of Mining and Technology, Socorro, New Mexico
(Received March 7, 1955; revised version received July 27, 1955)

Electron microscopy of etched and nascent surfaces of single ice crystals shows a characteristic microstructure of elongated, hexagonal prisms. The small hexagonal units vary greatly in size with an expected width of the order of 3 microns and a length of 6 microns. The coordination among microcrystalline units characterizes a particular single crystal, the size of which may be determined by processes of freezing and subsequent history, but the sizes of the microcrystalline units of which they are composed appear to be independent of the rates of freezing. The etched surfaces show that the center of the hexagonal unit etches to a greater depth than does the outer area, indicating a higher degree of crystal disorder along the axis of symmetry.

Ice surfaces in process of growing from the melt also appear to consist of hexagonal pyramidal pits which are built up by concentric steps around the *C*-axis. This structure appears to be consistent with that of the etched surfaces. Observations of growing-ice surfaces formed from cesium fluoride solutions reveal that the fluoride impurity tends to reduce the prominence of the pyramidal microstructure in a manner dependent upon concentrations such that the structure disappears for concentrations greater than 10^{-3} M.

1. INTRODUCTION

ELECTRON-MICROSCOPE studies were undertaken in an effort to discern structural manifestation of the role played by the energetic incorporation of certain ionic impurities as described by Workman and Reynolds.[1] The program of investigation here reported included two phases. The first consisted of the development of techniques for etching ice-crystal surfaces and the subsequent production of surface replicas. The second phase consisted of the development of methods for producing surface replicas of the ice during growth.

The investigation was carried out using an RCA electron microscope, model EMC, which had been modified to give a resolving power of about 75 A.

2. EXPERIMENTAL

(a) Etched Ice Surface

A procedure for etching and making replicas of ice surfaces involves, first, breaking or cutting to expose the desired crystal plane and subsequent etching by a blast of cold, dry air. In the etching process the bulk of the ice crystal is maintained at a temperature of about −15°C, and optimum results are obtained when the air flows (about 0.8 cu ft/min) from a $\frac{3}{16}$-inch diameter orifice mounted one inch above the surface. Samples are etched for about 20 minutes under these conditions, and immediately after etching a few drops of chilled and filtered solution of 1% Formvar in ethylene dichloride are spread over the surface. After the Formvar film is dried the sample is melted in water. The replica floats on the water, and the usual techniques of mounting and observing are followed.

(b) Examination of Etched Ice Sample Replicas

An examination of different ice specimens formed under widely varying growth conditions was undertaken using the techniques described. Studies were first carried out using fast-grown ice samples which consist of parallel bundles of small single crystals having cross sections of the order of 1 mm². Secondly, observations were carried out using slow-grown, large single crystals prepared by the Bridgman method. These crystals, from 2 to 5 cm² in cross-sectional area, were grown at rates of approximately 1 mm/hr—a rate one-hundred times slower than that used for the bundles of small crystals. Finally, observations were made on prepared surfaces of Alaskan glacier crystals,[2] which presumably represented an extremely slow rate of formation. Except for the glacier ice,[3] all specimens were frozen from water having a specific conductivity of 3.10^{-7} mho/cm.

Many samples of each of the types listed above were examined, and all revealed a microstructure of bundles of coordinated, hexagonal prisms.[4] The size of these units ranged in width from about $\frac{1}{2}$ to 20 microns and in length between 1 and 10 microns. Though the above-mentioned size range seemed to exist on all three types of specimens, no relationship could be found relating size distribution and growth rate. In Fig. 1, (a) through (f), are shown electron photomicrographs of surface replicas of the bulk crystals. Figure 1(a) shows a cross section perpendicular to the *C*-axis, and it illustrates the hexagonal "honeycomb" boundaries of the microstructure. The centers of the hexagonal units have etched to a greater depth than the outer areas. Figure 1(b) similarly shows the starlike structure of hexagonal symmetry within the single units, and Fig. 1(c) also shows this starlike pattern, but here the boundaries have not assumed a hexagonal outline. Figures 1(d), (e), and (f) show replicas of ice surfaces parallel to the

* The work herein reported was supported in part by the Office of Naval Research.

[1] E. J. Workman and S. E. Reynolds, Phys. Rev. **78**, 254 (1950).

[2] The Alaskan glacier ice was obtained through the courtesy of Professor D. Griggs, UCLA Geophysical Laboratory.

[3] By comparing with the amount of impurities ordinarily found in rainwater it was estimated that the total impurity concentration for the Alaskan glacier ice was less than 10^{-4} M.

[4] A discussion of this microstructure was first presented by E. J. Workman, Phys. Rev. **92**, 544 (1953).

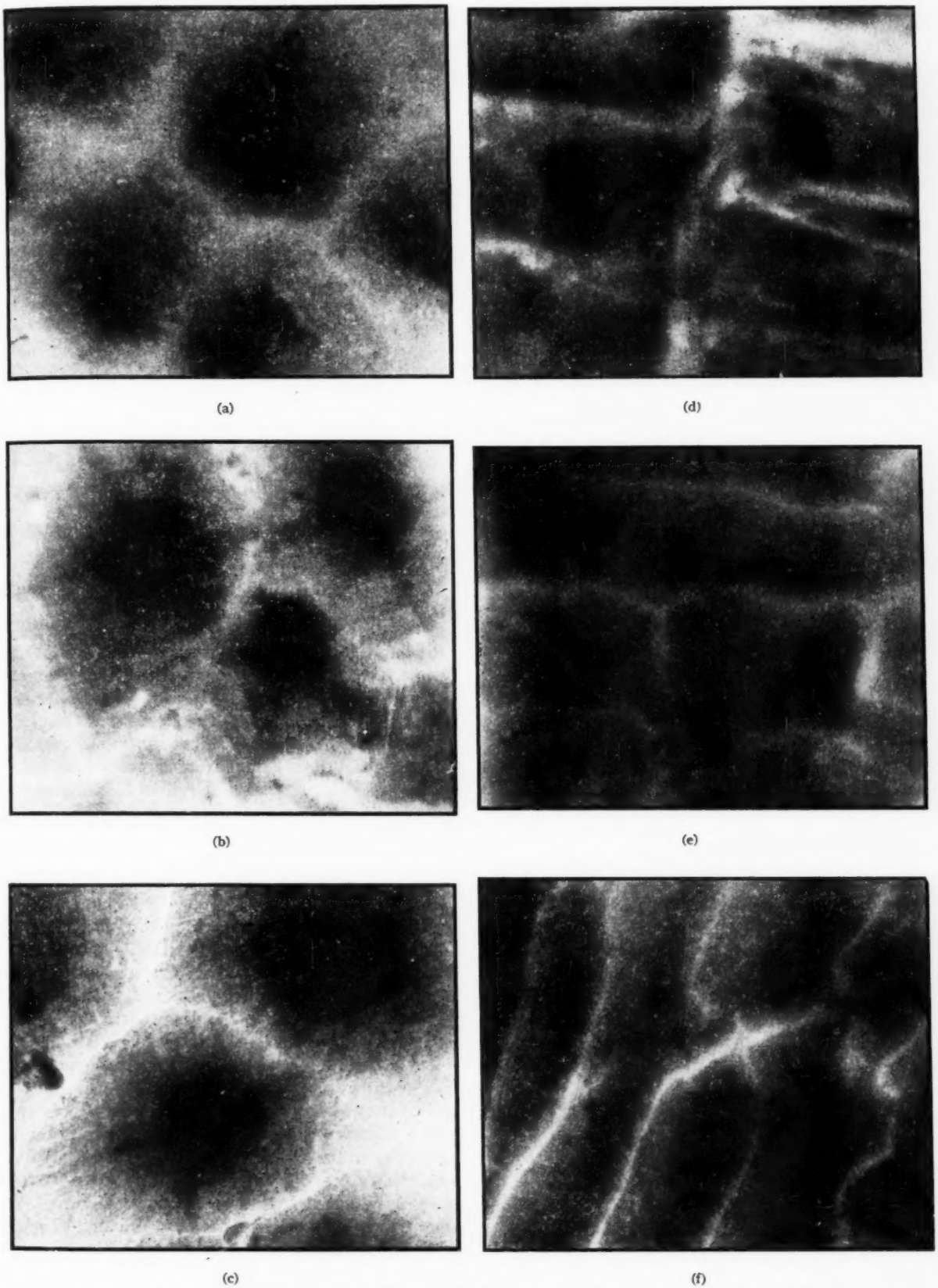

(a) (d)

(b) (e)

(c) (f)

FIG. 1. Etched ice surface replicas; (a), (b), and (c) taken perpendicular to *C*-axis. (d), (e), and (f) taken parallel to *C*-axis. Magnification ×1000.

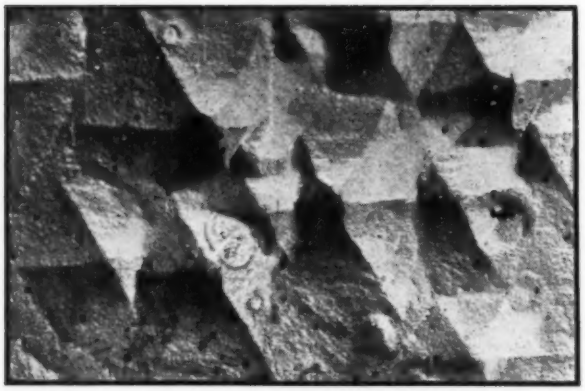

(a)

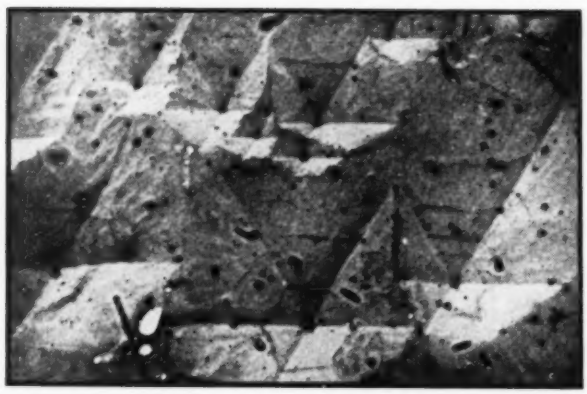

(b)

FIG. 2. Replicas of growing ice surfaces. (a) Magnification ×10 000. (b) Magnification ×1500.

C-axis of the bulk crystal in which a cross section of the "honeycomb"etch pattern is seen. The dimensions of the microcrystalline units deviate considerably from mean values, and no dependence upon growth rate or manner of formation has been detected.

(c) Growing Ice Surfaces

Replicas considered representative of the growing ice surfaces were prepared as follows. The freezing was carried out in cylindrical Teflon cups provided with heavy, platinum-covered copper bases, which acted as the refrigerating surface; under these conditions the *C*-axis of the crystal is perpendicular to the base of the cup. As the growing ice surface advances upwards into the melt, a heavy organic liquid at 0°C is poured into the cup. In this manner the advancing ice surface is abruptly separated from the supernatant liquid. The water above the liquid separation layer is then allowed to freeze and can now be removed mechanically as a plug of ice. The organic separation material should have the following characteristics: (1) be appreciably more dense than water, (2) be insoluble in water, (3) be able to wet the surface of the ice, and (4) have a freezing point below the lowest temperature to which the ice samples will be subjected. Of the group of commercially available organic liquids only a few have all of the required properties. Pentachloroethane appeared to be most satisfactory as a separator, though *o*-bromotoluene may be used successfully.

After the upper ice plug has been removed, any excess of the separation material is poured off and only a thin film wetting the surface is left. A cold solution of 0.75% Formvar in pentachloroethane is finally applied, leaving a relatively thick surface replica after evaporation of the solvent. In the conduct of the critical processes of replica production, which are carried out at about −20°C, it is necessary to guard against the condensation of water vapor from the cold-box atmosphere.

Since the Formvar replicas are too thick for direct observation in the electron microscope, a second negative-replica is prepared. The Formvar film, after being melted from the ice, is mounted on support grids (replica side up) and placed in a vacuum chamber, after which SiO is evaporated onto the surface to give a second negative-replica 50 to 75 A thick. Finally, the SiO replica is shadow cast with chromium, before being removed from the vacuum system.[5] After removal from the vacuum system the thick Formvar film is dissolved away from the SiO, using ethylene dichloride as a solvent, leaving the shadowed SiO replica on the mounting screen.

(d) Examination of Growing Ice Surfaces Replicas

Using the two-step, negative-replica process, growing ice surfaces of pure and fluoride-contaminated ice were studied. Pure ice samples were grown from water having a specific conductivity of 2.5×10^{-7} mho/cm at 20°C, whereas the fluoride-contaminated samples were frozen from CsF solutions in the range of concentrations from 10^{-5} to 10^{-3} M. In the procedure of freezing used,[1] the cesium ions are rejected from the water-ice interface during growth, while the fluoride ions are incorporated into the ice structure. The growth rates for both samples used ranged from 2 mm/hr to about 3 mm/min.

The surface of the advancing ice, characterized by hexagonal, pyramidal pits, often showed a hexagonal, stepped-layer formation concentric with the *C*-axis. The bases of the pyramids range generally from ½ to 20 microns in width, although a few have been observed to be up to 40 microns. These findings are consistent with the findings from the etched samples, and here also there was a lack of correlation between size and growth rate.

Figure 2(a) is a representative electron photomicrograph showing the SiO replica—being negative, the pyramids extend outward. From the length of the shadows (the shadowing angle being about arc tan=⅛) it is seen that the depth of the pyramids ranges from about ¼ micron to about ½ micron. In Fig. 2(b) a low-magnification electron photomicrograph is shown of an

[5] The increased definition obtained by shadowing directly on the Formvar and then depositing the SiO was offset by an observed lack of durability of the replica for use in the 30-kev beam of the EMC electron microscope.

exceptionally coarse structure, in which the concentric step formation can be seen. Figure 3(a) shows a typical electron photomicrograph of a replica heavily shadowed at a higher angle (arc tan=$\frac{1}{3}$) in order that the heights of the step formations could be determined by measuring the length of their shadows. For pure ice samples average step height of the pyramids was of the order of 500 A. Figure 3(b) shows a section of a relatively large pyramid where the steps are split up into two closely adjacent steps.

Studies of growing surfaces of fluoride-contaminated samples reveal that this impurity affects the surface structure in the following manner: As the fluoride concentration is increased the pyramidal microstructure appears to become less prominent, leaving areas in which no pyramidal structure is observed. For concentrations greater than 10^{-3} M, the formation of the pyramidal structure is completely inhibited. From a limited number of observations in the concentration range of from 1 to 5×10^{-5} M, the step height of the pyramidal formations appears to be reduced from 500 A to about 200 A.

3. DISCUSSION

Studies of etched ice surfaces have revealed the existence of a microstructure in the bulk material. This structure—which it is believed is characteristic of *all* ice—is a coordinated system of prisms of hexagonal symmetry, and, unlike the bulk single crystal, its dimensions are independent of the growth rate. Since the centers of the hexagonal units [as shown in Fig. 1(a)–(d)] etch to a greater depth than do the outer areas, it appears that the centers have a higher degree of disorder than the boundaries. The starlike pattern of the etched crystal, best shown in Fig. 1(b), also shows the area of lower bond energy to extend from the center of the hexagonal units outward in the (110) directions. These regions of lower energy occur at the planes of intersection of the linear growth of the (100) planes and can be compared with the lateral edges of the inverted pyramids of the growing ice structure (Fig. 2). There is a slight suggestion, as in Fig. 1(b), that a step structure, concentric about the center of the micro unit, may sometimes occur in the pattern of the etched crystal. This step formation is much less evident than that found in the growing ice surface structure—a fact which may, however, relate only to the different techniques of sample preparation.

The structure of the growing ice reveals the same general characteristics as observed for etched samples. Thus, in both cases the size and size distribution of the hexagonal units are the same, and neither shows any dependence upon growth rate of the bulk crystal. Many of the pyramidal pits of the growing ice surface do not have a perfect apex, as illustrated in Fig. 4, which is a typical micrograph of such a surface. It is believed that the imperfect apices occur because of the existence of cylinders of disorder extending from the interior of the microcrystal unit outward toward the apices of the inverted pyramids. This idea of a cylinder of disorder (parallel to the *C*-axis) at the center of the hexagonal units is consistent with the etch patterns, both perpendicular and parallel to the *C*-axis, as shown in Fig. 1(a)–(f)—the interior of the cellular units etched to a greater depth than the boundaries.

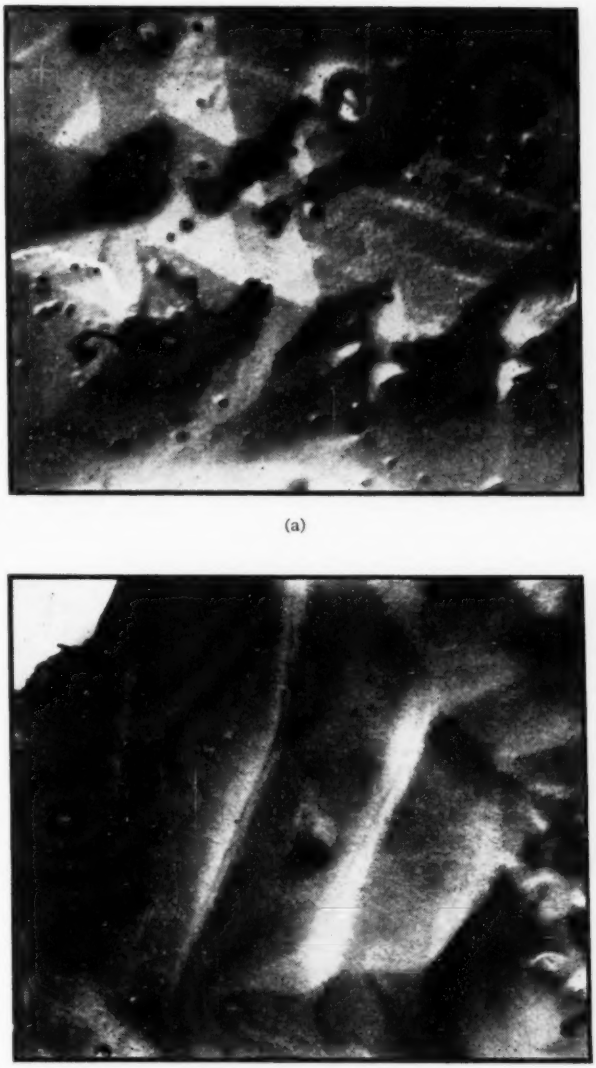

(a)

(b)

FIG. 3. (a) Replica of growing ice surface showing typical step formation. (b) Replica of double step formation. Magnification ×10 000.

The single- and double-step formations shown in Fig. 3(a), (b) are quite typical of a number of observations made using the high-angle, heavy-shadowing technique. There are some indications that the faces of the pyramidal steps of the growing ice surface are not necessarily parallel to the (100) planes but may be parallel to (10*C*) planes, where *C* can take on integral values greater than zero. Insufficient evidence, however, is available from the present observations to establish definitely the Miller indices of the *C*-axis intercepts of these step faces.

FIG. 4. Replica of growing ice surface showing pyramids having imperfect apices. Magnification ×17 500.

Observations of growing ice surfaces frozen from cesium fluoride solutions reveal that this contamination causes two pronounced changes to occur at the ice surface during growth. It apparently reduces the frequency of occurrence of the pyramid formation, leaving areas in which no structure is observed; also, it reduces the heights of the pyramid steps. For concentrations of 10^{-3} M the formation of all characteristic microstructure is completely inhibited. It is surprising to find that the addition of such slight fluoride contamination (less than one F^- per 50 000 water molecules) affects the formation of the pyramidal microstructure of the growing ice surface to such a drastic extent. It should be noted, however, that other prominent effects occur on ice containing small amounts of certain ionic impurities. As an example, the electrical resistivity of ice containing 10^{-6} M fluoride is of the order of a few megohm-cm, while that of relatively pure ice is about 10^6 times as great.

The microstructure in ice reported in this paper resembles in appearance structures seen on metals grown from the melt.[6] However, the resemblance undoubtedly is more apparent than real. Contrary to the explanations most frequently advanced to explain the origin of substructures in metals, it has been proposed that in the case of ice a dislocation mechanism is involved.[7]

[6] For a review of such structures, see Ursula M. Martius, Progr. Metal Phys. **5**, 279 (1954).

[7] W. Drost-Hansen, "On dislocation mechanisms in ice," paper read at meeting of American Association for the Advancement of Science, Santa Fe, April 1955, and E. J. Workman and W. Drost-Hansen, Trans. Am. Geophys. Union **36**, 534 (1955).

JOURNAL OF APPLIED PHYSICS VOLUME 26, NUMBER 12 DECEMBER, 1955

Space-Charge Distribution in a Static Magnetron*

HOWARD C. NEDDERMAN†
Columbia Radiation Laboratory, Columbia University, New York, New York

(Received July 27, 1955)

The space-charge distribution in a static magnetron was investigated by a method involving measurement of the radiation intensity from excited gas atoms at low pressure. Results of the measurements show that space charge extends to the anode under all conditions. Evidence is presented to show that a considerable fraction of the space charge consists of electrons that are trapped for exceedingly long times within the interaction space.

I. INTRODUCTION

ALTHOUGH the solid anode cylindrical magnetron diode as an electron tube has been known and studied since at least 1921, its behavior even under presumably static conditions is still very poorly understood. The available theory is known to be unrealistic and until recently there has been little experimental work of the type that gives direct information about the space-charge distribution.

Hull,[1] Brillouin,[2] Page and Adams,[3] Twiss,[4] and others have published theories based on ordinary potential flow of the electrons. These theories assign a common cut-off voltage to the anode current but differ as to space-charge distribution.‡ Results of the Brillouin theory are given in Fig. 1 as applied to the particular magnetron discussed in this paper.

The most obvious departures from theory of magnetron performance are the well-known violation of current cutoff and the phenomenon of cathode backheating. Observations on the first anomaly have been summarized by Harvey.[5] Jepsen and Muller[6] have

* Work supported by the Signal Corps, the Office of Naval Research, and the Air Research and Development Command.

† Present address: Electronics Laboratory, General Electric Company, Syracuse, New York. Submitted in partial fulfillment of the requirements for the degree of Doctor of Philosophy at Columbia University.

[1] A. W. Hull, Phys. Rev. **18**, 31 (1921).

[2] L. Brillouin, AMP Report 129.2R, Applied Mathematics Group, Columbia University, February 1945.

[3] L. Page and N. I. Adams, Phys. Rev. **69**, 492 (1946).

[4] R. Q. Twiss, Technical Report No. 117, Research Laboratory of Electronics, Massachusetts Institute of Technology, November 20, 1949.

‡ Twiss's theory includes the effect of finite emission velocity so that cutoff is "smeared out" instead of being sharp.

[5] A. F. Harvey, *High Frequency Thermionic Tubes* (John Wiley and Sons, Inc., New York, 1943).

[6] R. L. Jepsen and M. W. Muller, J. Appl. Phys. **22**, 1196 (1951).

reported a comprehensive set of measurements on the second effect. They observed that as much as 60% of the input power was returned to the cathode as back-heating.

It was also determined that the back-heating was independent of the anode material conductivity so that it is unlikely that the effect has anything to do with the rf properties of the magnetron circuit.

Recently an electron optical method has been employed by Reverdin[7] in order to obtain direct information about the space-charge density in a cut-off magnetron. Owing to technical difficulties the experiments were not absolutely conclusive. Some of his results are shown in Fig. 2.

In the experiments to be described the collimated radiation from atoms excited by electronic collisions is used to obtain information about the space-charge density. The excitation cross sections are of course energy dependent so that only an approximate interpretation of the experimental results directly in terms of space-charge density is possible. Furthermore, electrons with energy below threshold are not detected at all, although their importance can be estimated by means of potential calculations. On the other hand, the energy dependence of the cross sections makes it possible to obtain some information concerning the energy distribution of the electrons.

II. EXPERIMENTAL METHOD

A. Theory of Method

The method of sampling the decay radiation from the magnetron is shown in Fig. 3. Since circular symmetry of the space charge is assumed, it is appropriate to use collimating slits that are narrow in the radial direction, in order to get adequate resolution, and long in the azimuthal direction, in order to obtain as much signal as possible. It is of course necessary to have the slits movable along the radius so that a complete set of measurements can be obtained within the interaction space (i.e., the region between cathode and anode).

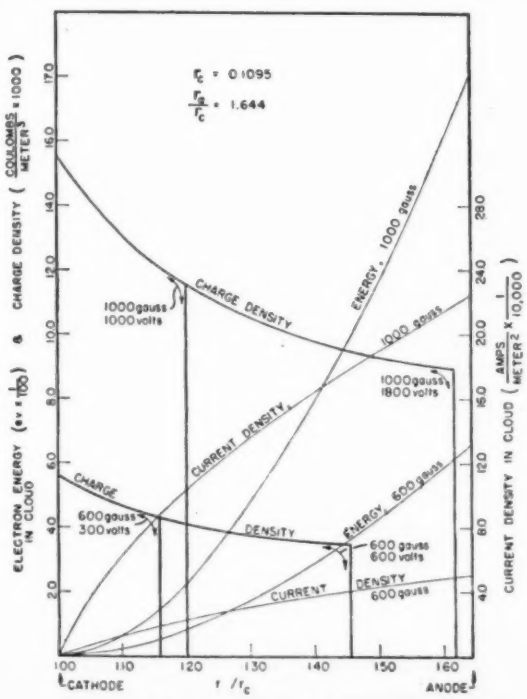

FIG. 1. Brillouin distribution appropriate to magnetron used in this experiment.

The radiation is detected by means of its photoelectric effect. Space charge is assumed to extend uniformly over the length l of the anode (i.e., end effects are ignored). The photoelectric current at low gas pressures is given by the integral:

$$i=\frac{\tau\omega n}{4\pi}\int\sum_j \eta_j\xi_j\sigma_j(v)vd\rho,$$

where the following notation is used:

n = gas density, atoms/meter^3,

$d\rho$ = charge density of electrons with speeds, between v and $v+dv$, coulombs/meter^3,

v = electron speed ($v\gg$atom speed), meters/sec,

$\sigma_j(v)$ = cross section for excitation to jth radiative state, meters^2,

ξ_j = fraction of radiation not absorbed between source and detector,

τ = volume sampled by slit system (length is l),

ω = average solid angle available for detected radiation,

η_j = photoelectric efficiency of detector for jth kind of radiation.

In the foregoing expression it is assumed that the lifetime of the radiative excited states is smaller than the time for an atom to cross the volume τ. Cascade modes of decay are neglected but these will not change the over-all form of the expression provided the total decay time remains small.

In actual practice the photoelectric current is amplified, the resultant signal being a galvanometer deflection. The measured quantity can then be written as

$$S=\int\sigma^*(v)vd\rho,$$

where

$$\sigma^*(v)=\mu\tau\frac{\omega}{4\pi}n\sum_j\eta_j\xi_j\sigma_j(v)$$

with: μ = sensitivity of amplifier, cm deflect./amp photo current.

Most of the measurements reported here make use of helium as the probe gas. In this case there are three major classes of excitation-decay processes which can lead to signal.

[7] D. L. Reverdin, J. Appl. Phys. 22, 257 (1951).

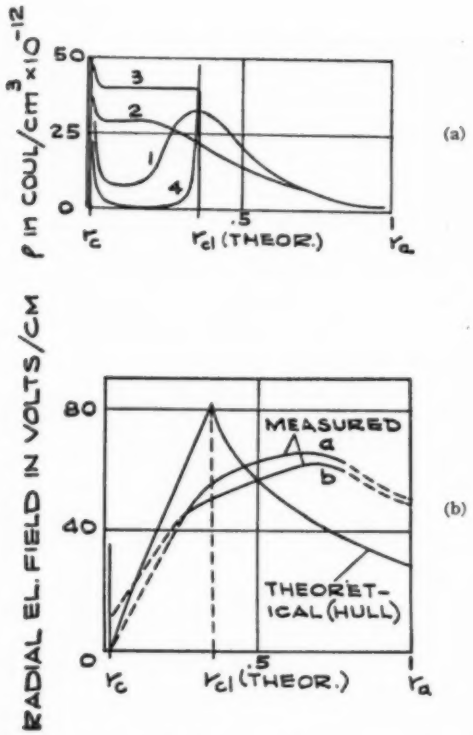

FIG. 2. Reverdin's results for a cut-off magnetron. Top: Typical space-charge distributions: (1) observed for well-aligned magnetron cathode, (2) observed for poorly aligned magnetron cathode, (3) according to the Hull-Brillouin theory, and (4) according to the Page and Adams theory. Bottom: Radial field distribution, $V_a=45$ volts, $r_c=0.0125$ cm. (a) Space-charge saturated magnetron, (b) temperature-limited magnetron.

Class 1. Excitation to Optical Levels

These levels revert to the ground state in about 10^{-10} seconds with the emission of 600 A resonance radiation. With this decay time the error due to motion of the atoms is completely negligible. Owing to self-absorption the importance of these levels is somewhat lessened. The photoelectric efficiency may be of the order of 10%.

Class 2. Excitation to Optically Forbidden Levels

The important levels here are the metastable 2^1S_0 and 2^3S_1 states. These excited atoms undergo collimation just as do photons. On striking the detector they eject electrons with an efficiency that may approach 50%. At the pressures used in this experiment less than 1% of the metastables is lost from the beam as a consequence of scattering.

Class 3. Excitation to Ionic Levels

The important states here are the $n^2P_{\frac{1}{2}}$ states and the $2^2S_{\frac{1}{2}}$ state. The first group decays in about 10^{-10} seconds with the emission of 300 A radiation. The S state tends to be metastable with a lifetime dependent on the local fields within the interaction space. Unfortunately, the decay time is usually longer than the transit time of the ion across the slit volume so that excitation to this state contributes error. However, the signal due to this process can generally be neglected since it contributes not more than 5% of the total.

The "radiation" from helium gas is expected to be differentially absorbed by a thin film, such as collodion, placed in the path of the collimated beam. The 600 A and 300 A radiations are aborbed by different amounts while the metastable atoms are completely stopped. The ratio of signal with the film to signal without the film is then a function of the energy of the electrons causing the excitation. This method was used to obtain an estimate of the electron energy in the magnetron.

Figure 4 gives an estimate of the function $\sigma^*(v)$ as well as the expected transmission through a 200 A collodion film. A brief discussion of the classes of signal and the calculation are given in the Appendix. The computation is too crude to be safely used for interpreting the magnetron data; consequently, $\sigma^*(v)$ must be measured in a separate experiment.

B. Apparatus

Magnetron and Collimation Arrangement

Figure 5 shows a schematic diagram of the apparatus used in this experiment. When it was desired to measure cross sections the magnetron was removed and an electron-gun structure substituted.

The three slits shown in the figure were arranged to be movable along the same projected magnetron radius. The left-hand slit and the associated quartz window aided in lining up the slit system parallel to the anode surface and had nothing to do with the actual measurements.

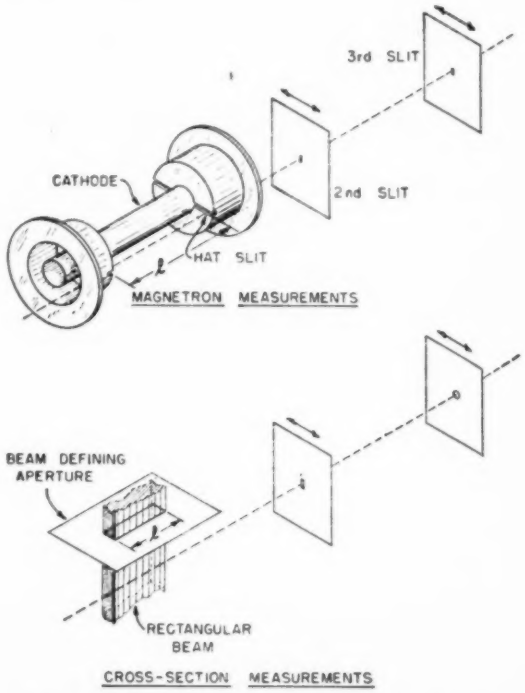

FIG. 3. Method of sampling radiation. The arrows indicate direction of motion of slits.

The slit dimensions were 0.0054 in. by 0.0275 in. Measured by the fraction of the cathode-anode spacing covered at each slit setting the resolution of the system was approximately 9%.

After several trials the magnetron cathode finally adopted was of the nickel matrix variety.§ This consists essentially of a molybdenum cylinder on which is sintered a fairly coarse nickel powder. The final surface is quite porous and capable of absorbing large amounts of the standard barium-strontium carbonate emitter material. The resulting cathode has a very smooth, highly conducting surface capable of dissipating large amounts of back-heating without too much local heating and sparking. The usual operating temperature was approximately 1200°K.

As with all magnetrons, end hats were installed on the cathode in order to confine the space charge. Since an unobstructed view of the radiation was necessary a radial slot 0.040 in. wide was cut from each hat as shown in Fig. 3. Some experiments to be described indicate that a negligible amount of space charge found its way out through these slots.

The support for the cathode and the hats consists of two ceramic plates mounted on the end surfaces of the anode. This type of support, rather than the more conventional axial stem support, is necessary since movable slits are needed on both pole pieces. The cathode heater was bifilar wound in order to reduce disturbance to the magnetic field.

The electromagnet for the magnetron was of conventional construction calibrated to an accuracy of ±2%. Shaped pole pieces gave a field which varied less than 1% over the interaction space.

The pertinent magnetron dimensions are as follows:

anode length	0.600 in.
anode diameter	0.3605 in.
cathode length (active)	0.600 in.
cathode length (hat to hat)	0.800 in.
cathode diameter	0.2185 in.

Detector

The photoelectric currents stimulated by the collimated radiation from the interaction space were in the range from about 7×10^{-15} amperes on down. A photomultiplier was used to obtain most of the gain followed by an electrometer amplifier of the Penick[8] type. The average output current was read with a sensitive wall type galvanometer. The over-all sensitivity of the system was 6.6×10^{-18} photoelectric amp/cm with a time constant of approximately 7 seconds.

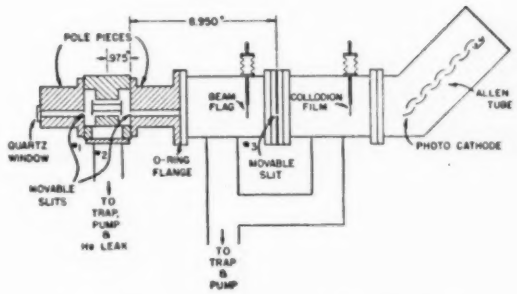

FIG. 5. Schematic diagram of the apparatus.

The photomultiplier followed closely the design of Allen.[9] The dynodes and the photo cathode were all of the same Be Cu alloy. Activation was done in hydrogen according to the procedure of Dare and Rowen.[10]

Stray field in the multiplier region was reduced to less than four gauss by means of iron shielding. The photocathode was operated at minus 2850 volts under which condition the measured gain was 270 000±20 000.

Moorish *et al.*,[11] measured the efficiency of the Allen tube to ultraviolet light and found that the tube was completely insensitive to wavelengths above 3000 A. This fact was important in this experiment since thereby background due to cathode light was reduced. Signal due to cathode light was in fact never observed. The average dark current was quite small, being about 0.1 cm. The fluctuating component plus inherent instabilities of the system amounted to about ±0.3 cm with occasional larger deflections.

Cross-Section Measurements

In order to measure the function $\sigma^*(v)$ an electron gun of the rectilinear Pierce[12] type was substituted for the magnetron. The orientation of the beam with respect to the slits is shown in Fig. 3. In order to avoid contamination by secondary electrons the beam was allowed to traverse a long, wide section of vacuum manifold before being collected. The geometry of the situation duplicated the magnetron arrangement as nearly as possible so as to insure the equivalence of self-absorption effects. The accelerating aperture measured 0.050 in.×0.600 in. and was at ground potential.

The beam charge density in the cross-section meas-

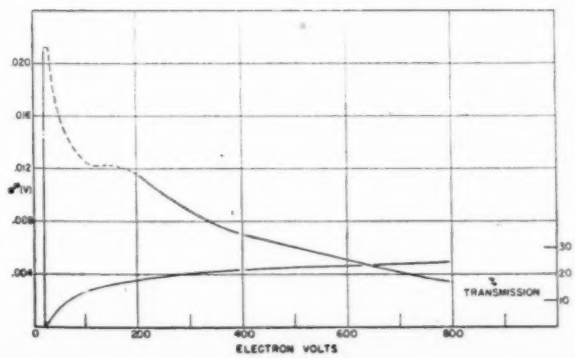

FIG. 4. Estimate of the cross-section function for helium.

§ Developed at Bell Telephone Laboratories.

[8] D. B. Penick, Rev. Sci. Instr. **6**, 115 (1935).
[9] J. S. Allen, Rev. Sci. Instr. **18**, 739 (1947).
[10] J. A. Dare and W. H. Rowen, Tech. Report #6, Laboratory for Nuclear Science and Engineering, Massachusetts Institute of Technology (1948).
[11] Moorish, Williams, and Darby, Rev. Sci. Instr. **21**, 884 (1950).
[12] J. R. Pierce, *Theory and Design of Electron Beams* (D. Van Nostrand Company, Inc., New York, 1949).

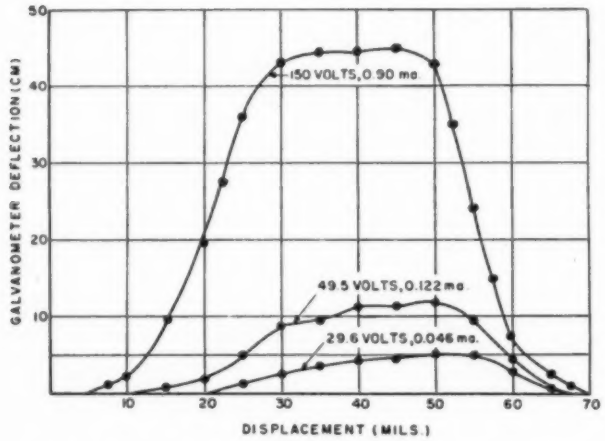

FIG. 6. Sample data for helium leading to cross-section values.

urements was very small so that to obtain a conveniently readable signal in the presence of background noise it was necessary to increase the size of the last (No. 3) slit. A round hole 0.125 in. in diameter was therefore used. Owing to the larger opening the resultant signal was increased by a factor 71.5±5 over what it would have been with the standard slit system. The two sizes of slits were interchangeable in vacuum for ease in determining this ratio. In order to check this number with any kind of accuracy over the range of beam voltages needed it was necessary to increase the gun pressure by a factor of about 10.

Cross-section data were obtained by moving the slit-system across the path of the beam for various beam voltages and currents. The area under the curve of signal *versus* displacement determines $\sigma^*(v)$ through the following relation:

$$\text{area (cm galv. defl.} \times \text{meters displacement)} = 71.5\sigma^*(v)I/l,$$

where I = beam current in amperes, and l = long dimension of beam (0.600 in. = 1.52×10^{-2} m) (same as magnetron anode height).

The need for using the integrated beam signal was of course because the actual beam density could not be known accurately.

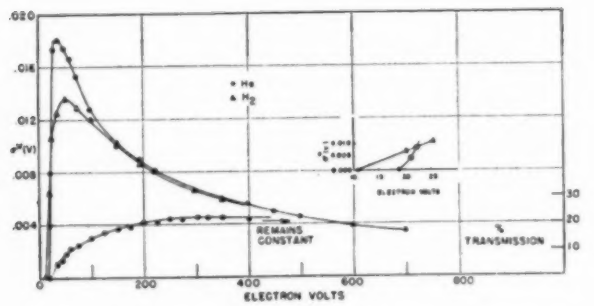

FIG. 7. Experimental cross-section functions for hydrogen and helium resulting from data like that shown in Fig. 7.

C. Operating Conditions and Precision

The system was pumped continuously in order not to spoil the activation of the oxide cathode and the Allen tube. The residual pressure in the magnetron was below 10^{-6} mm with up to about 400 watts dissipation. The signal due to this pressure was not more than 1% of the signal with helium.

During a run the partial pressure of helium in the magnetron was held at approximately 1.1×10^{-4} mm. Unavoidable fluctuations in pressure amounted to ±5%. The pressure in the detector side of the apparatus, determined by the leak rate from the magnetron through the first slit, was below 10^{-6} mm.

The day-to-day precision of the measurements was approximately ±5% except at low signal levels. The transmission measurements through the 200 A collodion film were, of course, considerably less precise so that transmissions below 5% were not reliable.

Pressure measurements were made with the aid of an uncalibrated ionization gauge, the readings, therefore, having only relative accuracy.

III. RESULTS

Figure 6 is a sample of the cross-section measurements for helium. Figure 7 shows the function $\sigma^*(v)$ resulting from data of this type for both helium and hydrogen as well as the transmission for helium. Threshold voltages can be determined only roughly with this apparatus because of the unfavorable background noise at low signal levels. The variation of signal at beam center for voltages near threhold served to place the thresholds at 21.5 and 13.5 volts, respectively, for helium and hydrogen. For helium the true threshold appears to be 19.3 volts.[13] The 2.2 volt difference is to be accounted for primarily by the low work function of the oxide cathode and by small effects due to thermionic energy of emission and space-charge reduction of potential. The last two effects amount to about 0.1 volt each and nearly cancel out. For an oxide cathode and a molybdenum anode the first effect can easily amount to the required correction. In plotting the cross sections 2.2 volts was subtracted from all the meter readings, the voltage-current dependence being negligible. Applying the same correction to hydrogen gives a threshold of 11.3 volts. The first optical level is usually placed at 11.5 volts, the continuum starting at 11.8 volts. Possibly the work function correction is in actual fact not a constant because of differential effects of the gases on the composite cathode as well as on the surface of the molybdenum aperture.

Figure 8 is the performance chart determined for this magnetron. Some crude measurements of cathode backheating, taken by adjustment of heater input to maintain constant cathode temperature, are shown in Fig. 9.

Figure 10 through Fig. 12 show signal and transmission as a function of distance from anode for various

[13] R. Dorrestein, Physica 9, 433 (1942).

operating conditions. These data were taken under space-charge limited conditions in the experimental sense that increase of cathode temperature had no influence on signal.

Some data taken with a severely temperature-limited cathode are shown in Fig. 13. The cathode temperature was estimated to be 850°K, the saturated current for zero magnetic field being approximately 15 ma.

Figure 14 is a representative comparison of hydrogen and helium signal. The particular low-voltage curves shown illustrate about the largest variation observed. Above 300 volts the two gases give nearly identical results except near the cathode and near the anode.

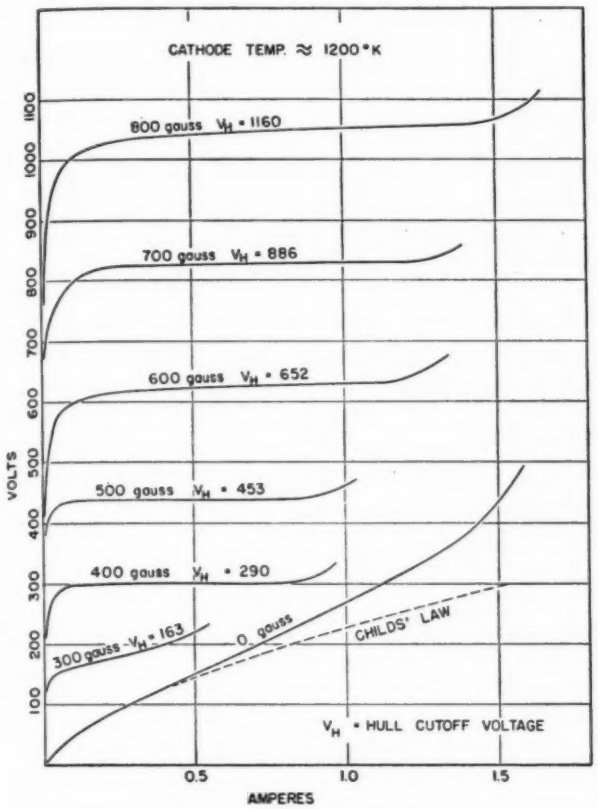

FIG. 8. V–I curves for magnetron.

The variation of signal with helium pressure is illustrated in Fig. 15. The detector pressure was very nearly constant at 10^{-6} mm over this range of magnetron pressures. Because of self-absorption within the magnetron this type of data is not suitable to check the linearity of source signal with pressure. On the other hand, hydrogen gas gives a detected signal showing practically no absorption. The signal was strictly linear with magnetron pressure for pressures below about 5×10^{-4} mm and was unaffected by a change in hydrogen pressure in the detector chamber. The reason for the apparent lack of absorption is partly due to the reduced probability for the stable molecular excited states to return to the lowest vibrational level of the ground state (Franch-Condon principle) and partly due to the differential sensitivity of the detector. Moorish *et al.*,[11]

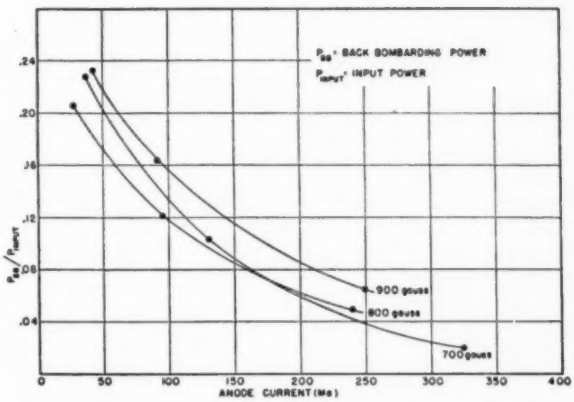

FIG. 9. Observed cathode back-heating of magnetron.

have shown that the Allen tube has maximum sensitivity around 2200 A, decreasing sharply with decreasing wavelength. Kenty[14] found that for several metals the photoelectric efficiency is increasing sharply below 800 A. In all probability the Allen tube has a minimum in sensitivity in the region covered by the radiation from the stable molecular states (around 1000 A) so that observation of the continuous spectrum (2000 A and higher) tends to be preferred.

It was of some importance to establish the fact that the end spaces of the magnetron were not contributing signal due to the presence of leakage current through the hat slots or to thermionic emission from the hats. A wire probe placed in the end space collected a saturated current of only about ten microamperes at a potential as high as 1000 volts positive with respect to the cathode. End space as a source of signal can therefore be dismissed.

IV. INTERPRETATION

This experiment is essentially of the nature of a cross-section measurement. The validity of such measurements usually depends on establishing that the signal is proportional to both pressure and current. Although it has been demonstrated clearly that the signal is strictly proportional to pressure it is not possible to

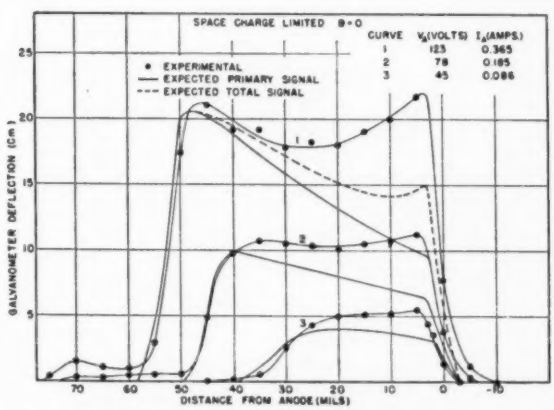

FIG. 10. Observed signal for zero magnetic field compared with expected signal on the basis of primary emission alone. Dashed curve includes effect of secondary emission from copper anode.

[14] C. Kenty, Phys. Rev. 44, 891 (1933).

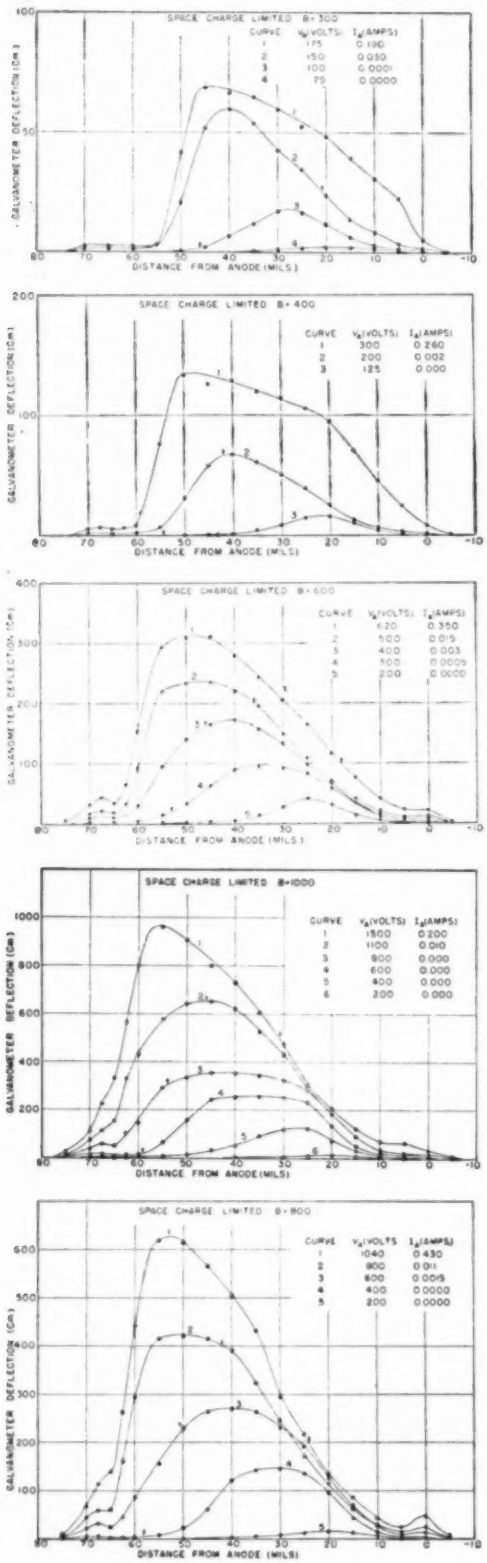

FIG. 11. Signal *versus* distance from anode for various magnetic fields and anode voltages. The arrows on some of the curves indicate the position of space-charge cutoff according to Brillouin.

complete the demonstration because of the unknown relation between current, density, potential, and magnetic field. For the $B=0$ case the relationship between current and anode region signal was found to be linear at all anode voltages covered in this experiment. The current densities are, however, much smaller than in most of the $B=0$ cases so that this test cannot be extrapolated safely. More pertinent information was obtained by some tests on a 10-cm oscillating version of the solid anode magnetron used in this research. It was found that the power output of this magnetron was not influenced by a helium pressure as high as 10^{-3} mm. The efficiency of a magnetron is a rather delicate function of the space-charge distribution (for instance, small changes in cathode diameter have a large effect on efficiency); consequently, this experiment indicated that the helium atoms had little effect on this distribution. Although these tests are admittedly incomplete there seems to be little reason to doubt the validity of the method.

The observed signal curves for the $B=0$ case depend of course on the secondary emission properties of the anode. The solid curves in Fig. 10 represent the expected signal on the basis of primary emission alone. The dashed curve is an estimate of the expected signal for the $V_a=123$ volt case with the effect of secondary emission included. For this part of the calculation a cosine distribution law for the secondaries[15] was assumed and the data on copper by Farnsworth[16] ($\delta=1.1$) were used. The calculated signal is seen to be too low by a factor as large as 2.5 (near anode). This disagreement is not surprising in view of the following considerations. The cosine law is valid only for low-energy

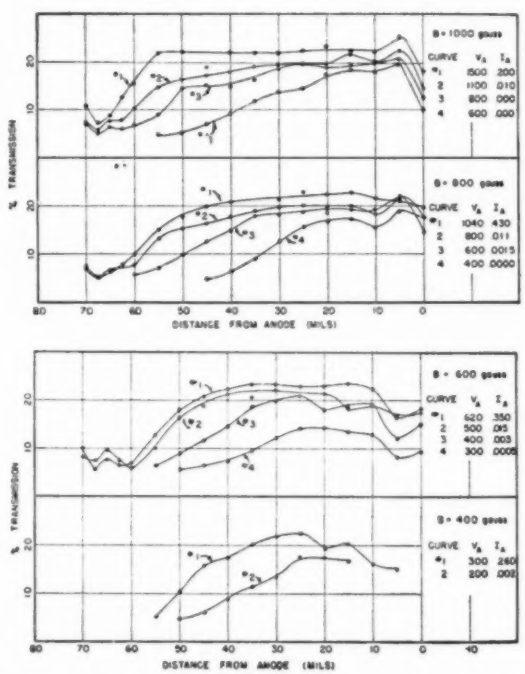

FIG. 12. Transmission of signal through a 200 A collodion film. These curves provide a rough estimate of the local electron energy.

[15] J. L. H. Jonker, Phillips Research Repts. **6**, 372 (1951).
[16] H. E. Farnsworth, Phys. Rev. **25**, 41 (1925).

secondaries. An entirely perpendicular distribution tends to be approached for the electrons in the tail of the energy distribution function. In the calculation, the spike in the energy distribution function at primary energies has been ignored for convenience. Also neglected is the effect of secondaries produced by returning secondaries. An estimate of these three effects results in a total signal which is still too low by a factor of about 2.1 in the anode region. By far the largest error in the estimate lies in the assumption of copper as the emitter. It is well known that oxide cathodes readily contaminate adjacent electrodes, an effect aggravated in magnetrons. The contaminating materials can be expected to have a δ well in excess of 2.0 and the corresponding increase in height of the secondary distribution function must be held responsible for the still remaining discrepancy.

The analysis of the $B \neq 0$ data is complicated by the natural threshold for helium at 19.3 volts. For this reason the signal data cannot follow the space-charge density down to zero energy, and it becomes necessary to account properly for these "missing" electrons.

An apparent space-charge density can be computed from the relation $\rho = S/[v\sigma^*(v)]$ with v calculated from the transmission measurements. The results of this calculation are shown in Fig. 16. It is clear, of course, that the resultant densities include only electrons of energy greater than about 20 ev. The width of the energy distribution is unknown, but since the product $v\sigma^*(v)$ varies only slowly with energy above 45 ev the curves must be reasonably correct in the region where transmission measurements indicate an "average" energy at least as great as this. Where the transmission falls below approximately 7% (corresponding to 45 ev) there is probably considerable inaccuracy depending on the width of the local energy distribution.

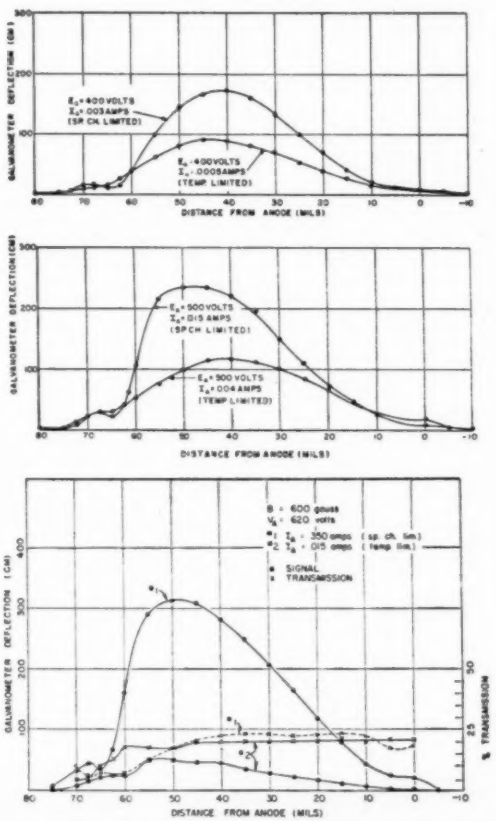

FIG. 13. Effect of temperature limitation of cathode emission on signal. Analysis of these curves shows that a large fraction of the space charge is due to trapped electrons.

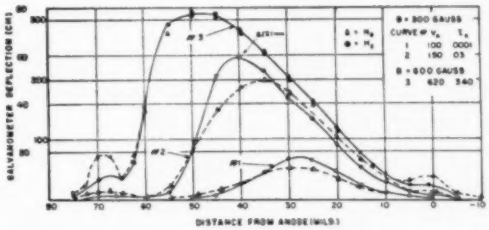

FIG. 14. Comparison of helium and hydrogen signal at a pressure of about $10^{3\frac{1}{4}}$ mm. Outside ordinate refers to 300 gauss, inside ordinate to 600 gauss.

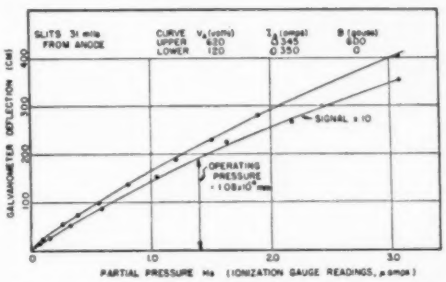

FIG. 15. Nonlinearity of helium signal with pressure owing to self-absorption. Similar curves for hydrogen are linear.

It now becomes necessary to estimate the importance of those electrons that are completely missed by the signal curves (i.e., those electrons with energy below 20 ev). Physically, the logical place for these to be situated is in the region immediately surrounding the cathode. Experimentally, the observation that transmission is more or less monotonic increasing from cathode to anode indicates that electrons of very low energy are not important on the anode side. Some data taken with hydrogen support this conclusion. It has been noted earlier that helium and hydrogen give nearly the same signal curve for $V_a \geq 300$ volts. For lower voltages the large difference in cross sections centered around 50 volts begins to manifest itself in the region where transmission indicates it should (see Fig. 14). In the Figure the curve for $V_a = 150$ volts shows somewhat larger signal for hydrogen than for helium. The experimental inaccuracy is such that it would be presumptuous to assume that this difference is owing to a concentration of 11 to 20 ev electrons [$\sigma^*(v)$ is nonzero for hydrogen, zero for helium, in this region].

It seems reasonably safe to assume that any nondetected electrons are predominantly located in the cathode region. Unfortunately, little can be gleaned from the hydrogen signal concerning the cathode space-charge distribution. The magnitude of the cross section below 20 ev is not large enough to warrant any clear-cut conclusions.

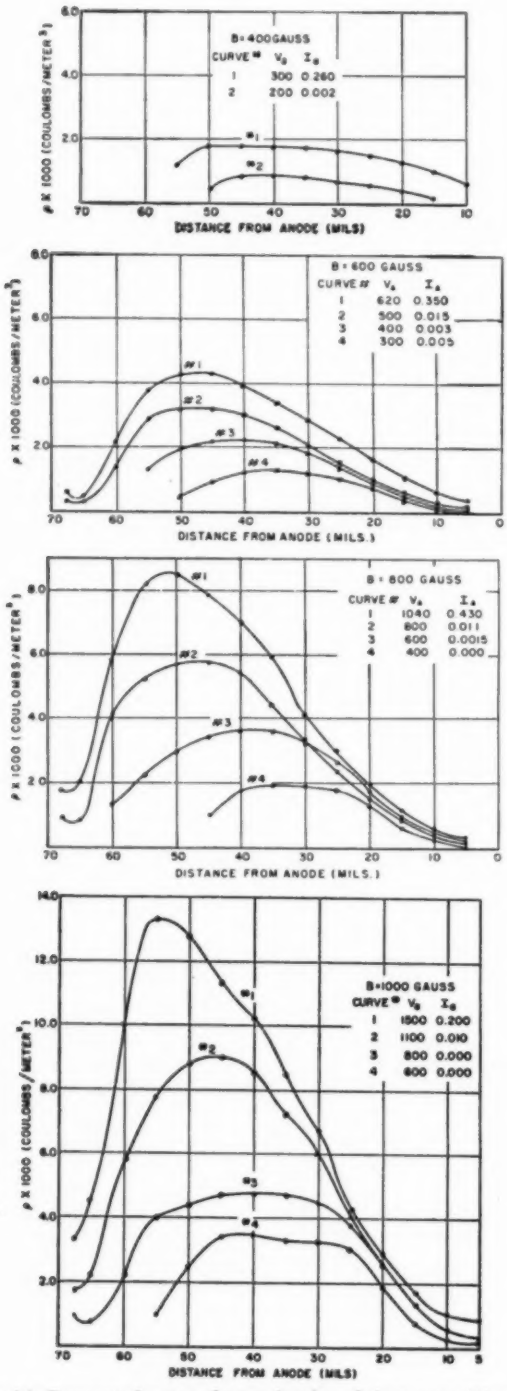

FIG. 16. Computed space-charge density of electrons with energy greater than about 20 ev. The experiment gives no direct information about electrons with energy less than this.

From potential calculations an approximate answer can be given as to just how much space charge is missing from the curves of Fig. 16. Figure 17 shows how the potential varies according to these charge densities.‖ The gradient at the cathode is seen to be nonzero though it should be no larger than zero since the signal data is for the space-charge-limited case. The additional amount of space charge necessary to bring the cathode gradient to zero can be estimated easily. For each curve in Fig. 16 the mean radius between cathode and maximum was chosen as a basis for the calculation. Table I gives the fraction of the total space charge that is missing for various fields and voltages on the basis that the actual cathode gradient should be zero.

It is immediately evident that a large amount of space charge is unaccounted for in the density curves. The missing space charge is undoubtedly situated mainly in the cathode region, but its exact configuration remains open to speculation insofar as the present experiment is concerned. It is seen that a continuation of the density curves from the neighborhood of the peak to the cathode surface with nearly zero slope would account for most, if not all, of the necessary extra space charge. The density at the cathode would then not be much different from the density elsewhere. On the other hand, it is possible that the density goes through a minimum somewhere between the peak of the apparent density curves and the cathode with the result that the actual density at the cathode can be quite large. This is the type of distribution found by Reverdin (see Fig. 2) but in apparently only one instance out of numerous trials.

A comparison with the Brillouin theory is of considerable interest. It is a simple matter to locate the cut-off radius for each magnetic field and anode voltage. When this is done it is found that the amounts of space charge outside and inside this radius are comparable except when considerable anode current is being drawn. For voltages far below cutoff there is, in fact, more space charge outside the Brillouin radius than there is inside. This result agrees with the conclusions of Peterson who attempted to determine actual electron trajectories by passing an electron beam longitudinally through the interaction space.[17] His beam spot deflections were explainable only by assuming a large density outside the Brillouin radius.

The results of the temperature-limited measurements throw a good deal of light on the nature of the observed distribution. In Fig. 13 the cathode temperature for the temperature-limited cases was such that at zero magnetic field not more than about 15 ma of anode current could be drawn. The observed signal cannot possibly be the result of direct thermionic emission from the cathode since the emission density is far too low. Secondary emission cannot be responsible since the input power is too low. The transmission measurements do not reveal any large concentration of energetic electrons at the cathode surface and such would be necessary if secondary emission were important. The only remaining possibility is that the observed signal is due to "trapped" electrons. These are electrons whose energy and momentum are such that they can reach neither cathode nor anode.

‖ The author wishes to thank Z. Fraenkel, Columbia Radiation Laboratory, for computation of these curves.

[17] W. W. Peterson, Tech. Report #18, "The trajectron—an experimental d.c. magnetron," Electron Tube Laboratory, Department of Electrical Engineering, University of Michigan (May, 1954).

A possibility that the cloud of trapped electrons results from ionizing collisions rather than from electron interactions can be disposed of on the following grounds. Current flow in a magnetron below cutoff must be associated with the release of electrons from this cloud at a rate equal to the observed current; consequently, in the steady state, the process that supplies the cloud with electrons must occur at the same rate. In a typical case ($B=600$ gauss, $V_a=400$ volts, $I_a=3$ ma) the estimated ionization rate is too small by a factor in excess of 100.

In the temperature-limited cases the $B=0$ current of 15 ma is nearly the minimum required for a measurable density. For lower cathode temperatures the cloud was observed to collapse almost immediately. It should be mentioned that under some conditions it was possible to maintain a cloud with a room temperature cathode (starting hot, however) but this situation was only rarely duplicated.

The curious behavior of the signal and transmission curves in the vicinity of the anode and cathode is difficult to explain and, in view of the smallness of the signal, it is hard to say whether or not the observations are fundamental to magnetron operation or are due simply to extraneous effects.

The maxima in signal at the anode and cathode surfaces observed in nearly all cases are at least partly a result of reflected ultraviolet. If the reflected radiation is perfectly diffuse (i.e., all reflected angles equally probable) the expected signal at either surface is of order:

$$S \approx 1500 r \bar{S},$$

where r is the reflection coefficient and $\bar{S}$ is an average signal measured in the interaction space.¶ Since r may be as high as 5 to 10% for helium radiation, it is seen that a reasonable assumption about the angular distribution of the reflected light can explain the observations. It may be remarked that the humps in the case of hydrogen are approximately twice as great (at the same pressure) which is not unexpected in view of the wavelength of the hydrogen radiation together with the observation that helium and hydrogen give nearly the same signal within the interaction space.

TABLE I. Fraction of undetected space charge.

Missing fraction	Gauss	Volts
0.21	1000	1500
0.23	1000	1100
0.40	1000	800
0.53	1000	600
0.26	800	1040
0.34	800	800
0.45	800	600
0.61	800	400
0.38	600	620
0.44	600	500
0.56	600	400
0.73	600	300
0.45	400	300
0.68	400	200

¶ In this estimate no allowance has been made for the fact that part of $\bar{S}$ is due to metastables.

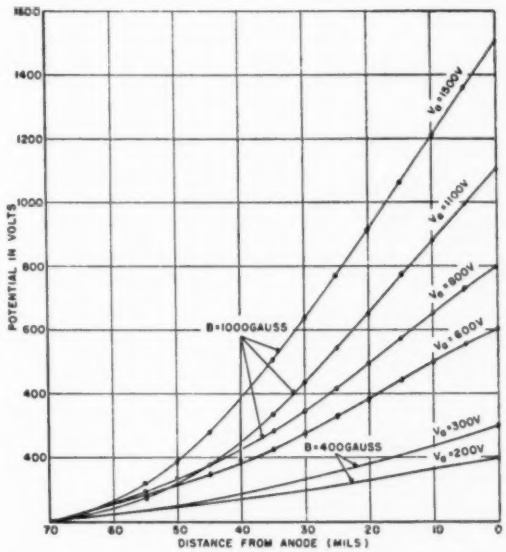

FIG. 17. Variation of potential across the interaction space computed from the curves of Fig. 16. The gradient at the cathode is nonzero owing to exclusion of electrons of energy less than about 20 ev. These curves are used to estimate the amount of space-charge unaccounted for in Fig. 16.

The peak of the reflected signal should be located half a slit width from the surface assuming perfect line-up. This does not appear to be the case but it is possible that the line-up is not as good as indicated and/or the cathode is off center. The anode shoulder can also result in an apparent shift of the peak.

Signal is observed for the $B=0$ cases in regions where the electron energy is certainly below threshold. This effect probably contributes a general background to all the data and may be due to a number of individually small causes. Among these are the presence of low threshold residual molecules, and diffusion of long-lived excited atoms or ions (e.g., the 2^2S_1 ion state of He).

It is unlikely that the peculiar oscillations in the transmission curves near the anode are due strictly to magnetron action. For a given magnetic field the curves have the same shape regardless of anode voltage; consequently, it seems likely that this effect is due to longitudinal motion of electrons. It is probable therefore that a small amount of emission from the end hats is responsible. The higher-than-average field strength existing at the sharp corners of the hat slits may possibly account for such emission.

V. CONCLUSION

In spite of the uncertainties of interpretation discussed in the preceding section at least two significant features of the space-charge distribution have been firmly established. These are:

(1) There appears to be no connection between the theoretically computed cut-off radii and the observed location of the space charge. In all cases a substantial fraction of the space charge is outside the cut-off radius.

Furthermore, as the operating parameters are changed so as to move the theoretical cut-off radius toward or away from the cathode, there is no pronounced trend for the space charge to follow its motion.

(2) Over a wide range of radii a substantial fraction of the electrons have kinetic energies which differ significantly from what would be expected under the hypothesis of energy conservation for the electrons individually. That is, if each electron can be regarded as moving in a mean static potential, the kinetic energy at each radius would be determined uniquely by this potential. It is clear from the transmission measurements that this cannot be the case. There must therefore be large-scale interchanges of energy between electrons. It is probable that these interchanges require long periods of time. An electron can, however, become trapped as the result of a very small deflection.

After becoming trapped it may remain in the interaction space for a very long period of time, thus affording the opportunity for a large exchange of energy. Direct evidence for the existence of trapped electrons in large numbers is provided by the temperature limited case.

It would appear that there are two main groups of electrons in a cut-off magnetron; the organized group of electrons that undergo potential flow from the cathode back to the cathode and the partially disorganized group of secular electrons trapped within the interaction space. Most of the signal observed in these experiments is believed to be produced by these trapped electrons. As noted previously such electrons can be formed from electrons of the first group as the result of small deflections. One would then expect that in the mean a trapped electron, as a result of many subsequent small deflections, would move slowly towards the anode. It would be expected that many Larmor periods would be required for an electron to work its way to the anode. Estimates of the transit time can of course be made from the measurements in which a measurable current is drawn. For example, the case $B=1000$ gauss, $V_a=1100$ volts yields a transit time of approximately 500 Larmor periods. The lower voltages for the $B=1000$ gauss case would clearly yield much longer transit times, implying that the effectiveness of trapping increases rapidly with decreasing electric field strength. The occasional observation of space charge with a cold cathode indicates that exceedingly long transit times are possible.

Quantitative theories of the static magnetron have been based on an entirely different view of what basic phenomena are significant, in particular, on the idea that the situation can be adequately described in terms of a self-consistent field with unique electron trajectories. It seems clear that such a description of the behavior of the magnetron used in these experiments is not possible, and it is therefore not surprising that the observed space-charge distribution bears no apparent connection with that predicted by these theories. A qualitative description of the steady state which bears a strong resemblance to that given in the preceding paragraph has been given by G. Hok.[18]

ACKNOWLEDGMENTS

The author wishes to express appreciation to N. M. Kroll for his valuable guidance and discussions on the main part of this experiment, and to W. E. Lamb, Jr., who suggested and initially guided the topic. It is a pleasure to acknowledge the help of the staff of the Columbia Radiation Laboratory, particularly, C. Deckert and M. Bernstein.

APPENDIX. SIGNAL CLASSES AND CROSS SECTIONS

With regard to lifetime the only process that can cause trouble is that involving the 2^3S_1 state of the ion. This ion is essentially metastable with lifetime dependent, however, on the local diode fields. A formula due to Lamb and Rutherford[19] indicates that under most magnetron conditions the ion will radiate after it leaves the volume τ. Fortunately, the cross section is small so that not more than about 5% of the total signal is concerned. It seems reasonable to neglect this mode altogether although it is possible that it is responsible for some of the signal observed near the cathode.

The estimate of $\sigma^*(v)$ (Fig. 4) involved a variety of isolated data with uncertain application so that the calculation must be considered as rather crude.

Cross sections for the optical levels were taken from the theoretical compilation of Massey and Burhop.[20] This was also the source for the metastable atom states except near threshold where the experimental values of Maier-Leibnitz[21] were used. A single, rough cross-section estimate by Lamb and Skinner[19] together with some unpublished relative measurements taken in these laboratories[22] sufficed for the P states of the ion.

The photoelectric efficiency of the radiation was more or less arbitrarily taken as 10%. The electron ejection efficiency of helium metastable was taken as 48% for the singlets and 24% for the triplets.[13]

Self-absorption of the optical radiation was computed from some formulas given by Holstein.[23] About 16% of the 2^1P_1 radiation and about 50% of the 3^1P_1 radiation reaches the detector while, for the higher states, nearly 100% is transmitted.

According to a paper by O'Bryan[24] a 200 A collodion film transmits about 17% of the 600 A radiation and about 40% of the 300 A radiation.

The remaining factors in the expression for $\sigma^*(v)$ have the values $\mu=1.52\times10^{17}$ cm/amp, $\omega=1.52\times10^{-4}$, $\tau=1.96\times10^{-9}$ meter^3, and $n=3.47\times10^{18}$ atoms/meter^3.

[18] G. Hok, J. Appl. Phys. **23**, 983 (1952).
[19] W. E. Lamb, Jr., and Miriam Skinner, Phys. Rev. **78**, 539 (1950).
[20] H. S. W. Massey and E. H. S. Burhop, *Electronic and Ionic Impact Phenomena* (Oxford University Press, New York, 1952), p. 172.
[21] Maier-Leibnitz, Z. Physik **95**, 499 (1935).
[22] Measurements in connecting with Lamb shift in ionized helium by P. Yergin *et al.* (private communication).
[23] T. Holstein, Phys. Rev. **72**, 1212 (1947).
[24] H. M. O'Bryan, J. Opt. Soc. Am. **22**, 739 (1932).

Application of the Engravement Method to the Study of Particle Velocity Distribution in Explosively Loaded Cylinders*

JOHN PEARSON AND JOHN S. RINEHART
Michelson Laboratory, U. S. Naval Ordnance Test Station, China Lake, California
(Received October 23, 1954)

Application of the engravement method to the study of particle velocity distribution in the wall of a thick-walled metal cylinder internally loaded with an explosive charge is described. Tests were conducted with this method on modified cylinders of annealed low-carbon steel and of brass. Even though each of the modified cylinders broke into a number of fragments, the engravements were well enough preserved to furnish considerable data. Many measurements were obtained from each cylinder by using a large number of pellets of several thicknesses. Particle velocity data were obtained to within $\frac{1}{16}$ inch from the metal-explosive interface. Temporal particle velocity distribution curves are presented for each of the cylinders.

INTRODUCTION

IT has been extremely difficult in many cases to obtain good quantitative data regarding the particle velocity distribution which exists in an impulsively loaded body. The very nature of impulsive loading generally precludes the possibility of obtaining data by the usual test methods. The extreme magnitudes of the pressures, the short durations for which they act, and the fact that the loaded body frequently breaks up under the action of the load are factors which enter into the problem of obtaining data.

In a previous paper by the authors,[1] the theory and technique were described for measuring high-intensity transient stress wave particle velocities in impulsively loaded bodies by a method of engravement. The simplicity of the scheme and the fact that particle velocity data were obtainable even though the test body deformed and broke into fragments indicated the applicability of the method to particle velocity studies in impulsive loading work. The present paper describes the application of the method to the study of particle velocity distribution in a thick-walled metal cylinder internally loaded with an explosive charge.

GENERAL APPLICATION OF THE ENGRAVEMENT METHOD

The engravement method of obtaining high-intensity transient stress wave particle velocities consists essentially of measuring the depth of the engravement or indentation which is left on the surface of an impulsively loaded body by a pellet that had been previously affixed to the surface. The depth of the impression is used to determine the average particle velocity of the wave during the engravement process. Average particle velocity v_{Av} is obtained from the equation

$$v_{Av}=cd/2L, \qquad (1)$$

where c is the velocity of propagation of the wave, d is the depth of the impression, and L is the thickness of the pellet.

To measure particle velocity distribution, a series of pellets of increasing thicknesses are affixed to the body at a given distance from the load and the depths of the respective engravements measured. Average particle velocities are determined from Eq. (1) and the temporal particle velocity distribution at a given distance from the load constructed by means of a histogram.[2] Variation of particle velocity distribution with distance from the load is obtained by repeating the above process at different distances from the load.

When using the engravement method it is usually desirable to limit the maximum thickness of pellets used for a given pellet diameter. If the length of the transient disturbance is less than twice the thickness of the pellet,

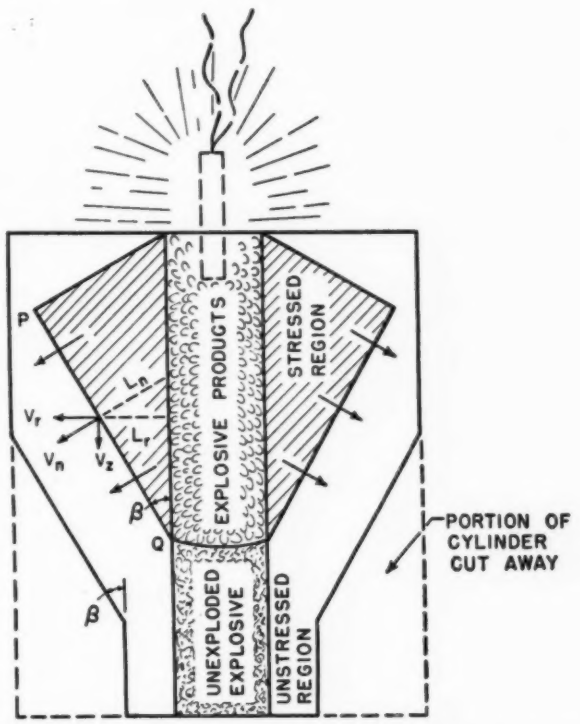

FIG. 1. Generation of stress wave in an internally loaded modified cylinder.

* Partially supported by the Office of Naval Research.
[1] J. S. Rinehart and J. Pearson, J. Appl. Phys. 24, 462 (1953).
[2] J. S. Rinehart, J. Appl. Phys. 22, 555 (1951).

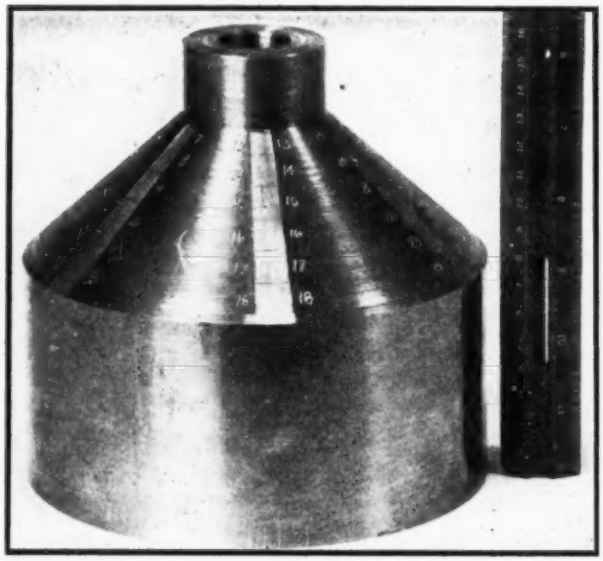

FIG. 2. Modified thick-walled steel cylinder before loading.

the average particle velocity obtained from the engravement is misleading since the actual time of engravement is less than the time represented by the thickness of the pellet. Also, if the pellet is long compared to its diameter it should probably be treated as a rod and consideration given to the problems of wave propagation in rods and their possible effect on the engravement process. It was felt that to obtain adequate data in the present work the pellet thickness should not exceed the pellet diameter.

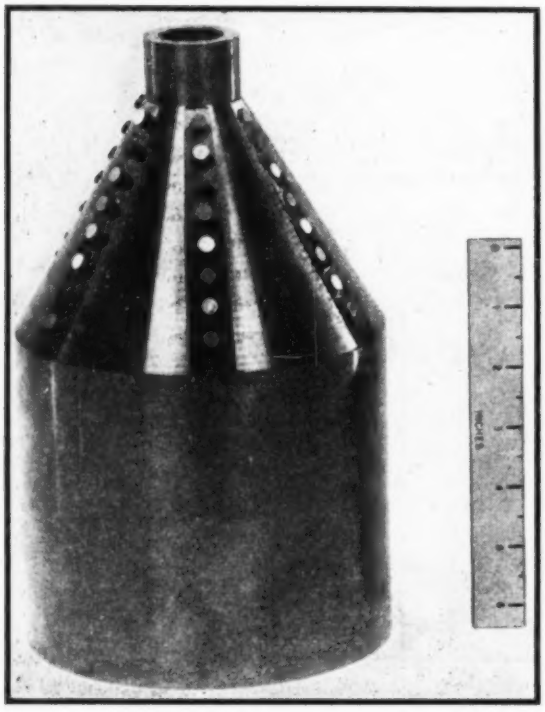

FIG. 3. Modified thick-walled brass cylinder with pellets affixed to conical surface.

Another factor to consider is the possibility of scabbing in the test body and its effect on the engravement. When scabbing occurs beneath the engravement area the produced fracture is liable to cut off a portion of the incident wave and thus prevent completion of the normal engravement process. In that event, a misleading value for the average particle velocity would be obtained.

Consideration should also be given to the geometry of the load and to the shape of the test body since particle motion at the free surface of a body which results from the oblique incidence of a longitudinal wave is not perpendicular to the surface but varies depending on the value of Poisson's ratio for the material and on the angle of incidence.[3] To simplify engravement analysis, it is desirable, therefore, to have the incident wave strike

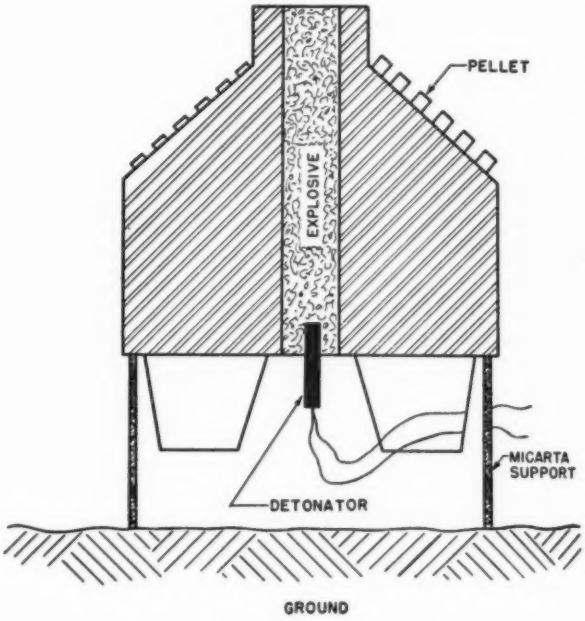

FIG. 4. Firing arrangement for internally loaded modified cylinders.

normal to the surface under study. In the present work normal incidence was obtained by machining one end of the cylinder to the shape of the induced wave front.

ENGRAVEMENT OF THICK-WALLED CYLINDERS

Application of the engravement method to an actual problem is well illustrated by its use in the study of the particle velocity distribution in the wall of an internally loaded thick-walled cylinder. In studies of the deformation and break-up of thick-walled cylinders subjected to internal explosive loading[4,5] it was found desirable to study the particle velocity distribution within the expanding wave that is generated by the explosive charge.

[3] J. Pearson and J. S. Rinehart, J. Acoust. Soc. Am. **25**, 217 (1953).
[4] J. Pearson and J. S. Rinehart, J. Appl. Phys. **23**, 434 (1952).
[5] J. S. Rinehart and J. Pearson, J. Appl. Phys. **23**, 685 (1952).

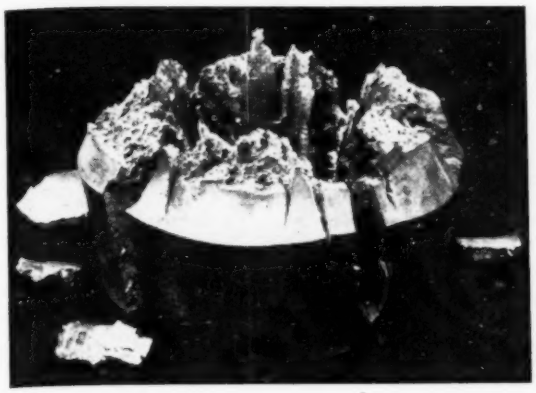

FIG. 5. Fragments of modified steel cylinder after firing.

One approach to the problem was by means of the engravement method.

The simplified situation in the wall of an internally loaded cylinder shortly after detonation of the explosive from one end is illustrated in Fig. 1. When detonated in contact with the metal, the charge initiates a sharp-fronted high-intensity stress wave in the wall of the cylinder. The loading produced by the detonating explosive is asymmetrical since the detonation proceeds through the explosive with a finite velocity D. The induced wave moves both outward and downward through the cylinder wall so that after a time interval t a conical portion of the cylinder wall will be in a stressed condition, and the remaining portion will be at rest in an unstressed condition. For a purely elastic wave the velocity of propagation c of the disturbance would be given by

$$c^2=3K(1-\nu)/\rho(1+\nu) \qquad (2)$$

where K is the bulk modulus, ρ is the density, and ν is the Poisson's ratio of the material. The wave front PQ (Fig. 1) will be inclined at an angle β to the axis of the cylinder, where β is given by[5,6]

$$\beta=\sin^{-1}(c/D). \qquad (3)$$

As the front of the conically expanding wave advances through the cylinder wall particle motion will be perpendicular to the wave front.

By cutting away part of the cylinder to form a conical surface, the advancing compression wave can be made to strike normal to a surface. The angle of the cone can be determined from Eq. (3). For steel and brass cylinders internally loaded with Composition C-3 explosive, the value of β was taken as 48 degrees for the steel, and 30 degrees for the brass. The velocity of wave

(a)

(b)

FIG. 6. Fragments of modified brass cylinders after firing; (a) ½-in. i.d. cylinder and (b) ¾-in. i.d. cylinder.

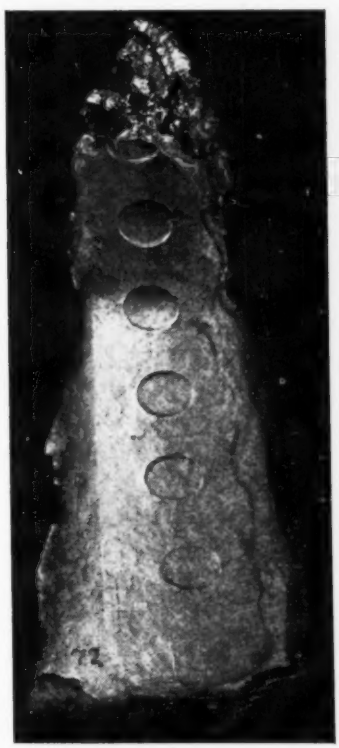

FIG. 7 Fragment of ¾-in. i.d. modified brass cylinder showing pellet engravements.

[6] W. M. Evans, Research 5, 502 (1952).

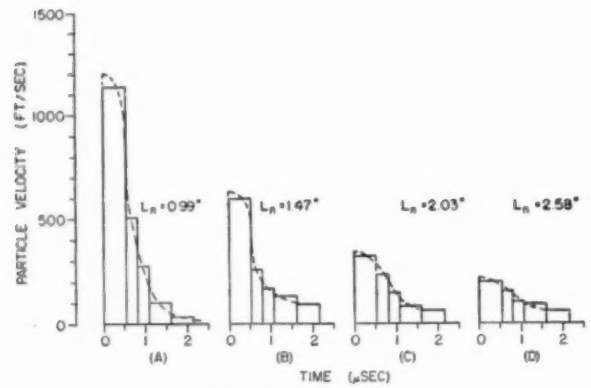

FIG. 8. Temporal particle velocity distributions acting normal to the conical surface of the modified steel cylinder.

propagation c was taken as 19 300 ft/sec for steel and 14 050 ft/sec for brass. The depth of the engravement made by a pellet affixed to the conical surface gives a measure of the average particle velocity of a given portion of the impinging wave.

TEST PROCEDURE

Three thick-walled cylinders, one of annealed low-carbon steel and two of naval brass, were used in the tests. Each cylinder was machined with a conical end using the values of β previously mentioned. Dimensions for the steel cylinder were 1 in. i.d.$\times 6\frac{1}{2}$ in. o.d.$\times 6$ in. long with a minimum wall thickness of $\frac{1}{2}$ in. at the cone end. The two brass cylinders were both $5\frac{7}{8}$ in. o.d.$\times 10$ in. long with a minimum wall thickness of $\frac{1}{4}$ in. One brass cylinder had a $\frac{1}{2}$-in. i.d., the other a $\frac{3}{4}$-in. i.d.

To assure good contact between pellets and cylinder, six narrow flat surfaces equally spaced were ground on the original conical surface of each cylinder. A series of pellets of equal thickness was placed on each flat ground surface with a different pellet thickness being used for each of six flat surfaces. Thirty-six pellets were placed on the steel cylinder, fifty-four pellets on each of the brass cylinders. Pellet thicknesses of $\frac{1}{32}$, $\frac{1}{16}$, $\frac{3}{32}$, $\frac{1}{8}$, $\frac{3}{16}$, and $\frac{1}{4}$ inch were used for the steel cylinder, and of $\frac{1}{32}$, $\frac{1}{16}$, $\frac{3}{32}$, $\frac{1}{8}$, $\frac{5}{32}$, and $\frac{3}{16}$ inch for both brass cylinders. All pellets were $\frac{1}{4}$ inch in diameter and were of the same material as the cylinder to which they were affixed. The contact surface of each pellet was carefully ground and care taken to insure a sharp corner. Pellets were attached to the ground flat surfaces by means of a thin layer of grease. All engravement areas were numbered for later identification. Figure 2 shows the modified steel cylinder before the pellets were affixed. Figure 3 shows a modified brass cylinder similar to the ones used in the tests with a number of pellets in place.

Each cylinder was loaded with Composition C-3 explosive and placed in an upright position in a celotex recovery pit. An Engineer Special Cap was inserted in the bottom end as shown in Fig. 4. A small stand was used to support each cylinder about six inches from the ground. No external constraints were imposed on the specimens. Pellets were placed in position just prior to firing.

TEST RESULTS

Even though each of the modified cylinders broke into a number of fragments, the engravements were well enough preserved to furnish considerable data. Fragments recovered for the steel cylinder are shown in Fig. 5, for the brass cylinders in Fig. 6. The greater degree of fragmentation suffered by the steel cylinder

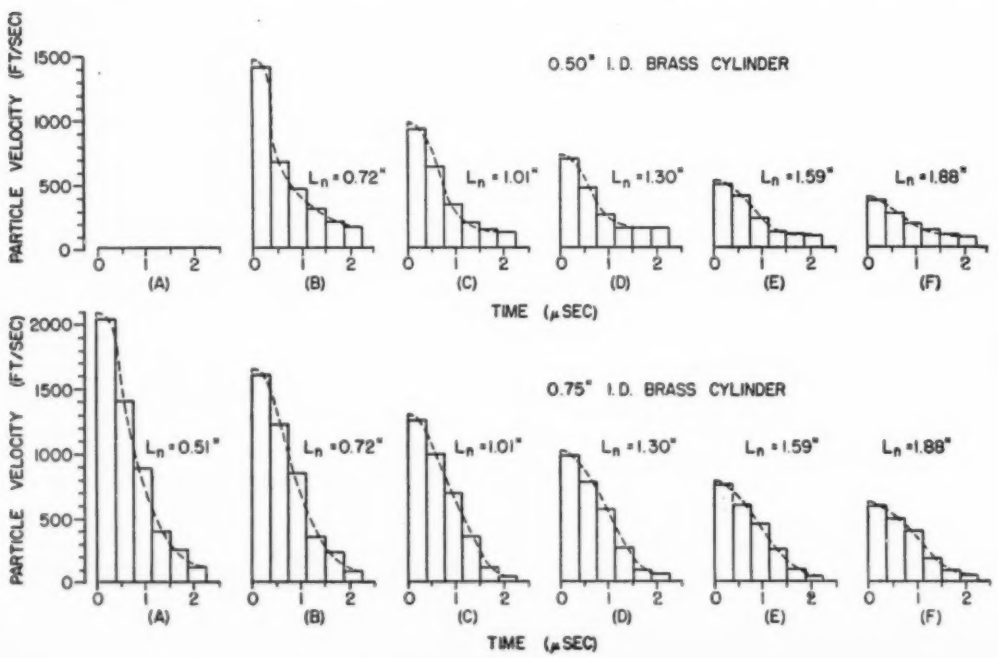

FIG. 9. Temporal particle velocity distributions acting normal to the conical surface of the modified brass cylinders.

was due mainly to the larger explosive charge used. An engraved fragment from the $\frac{3}{4}$-in. i.d. brass cylinder is shown in Fig. 7. The engravements are clearly visible. Engravements were obtained for 86% of the pellets used on the steel cylinder, and for 78% and 89% of the pellets used on the $\frac{3}{4}$-in. i.d. and $\frac{1}{2}$-in. i.d. brass cylinders, respectively. In a few cases the pellet was too thin and the particle velocity too low to give a measureable engravement; in others, the fragment containing the engravement was not recovered.

Engravement measurements were made using a plaster cast and shadowgraph technique.[1] As was to be expected, for a given pellet thickness the engravement depth decreased as the wall thickness increased. Similarly, for a given wall thickness the depth of the engravement increased as the thickness of the pellet increased. Data were obtained to within about $\frac{11}{16}$ in. radially from the explosive for the steel cylinder, and to within about $\frac{7}{16}$ in. for the brass cylinders.

Each histogram curve represents the temporal particle velocity distribution at the conical surface of a cylinder at a given distance from the explosive. The dashed curve on each histogram represents the probable shape of the actual particle velocity distribution. Figure 8 shows a series of such curves for the steel cylinder at four different distances from the explosive. Figure 9 shows similar curves for the two brass cylinders. The value of L_n (see Fig. 1) indicates the distance from the explosive in the direction of wave propagation. The histograms give an indication of the progressive change that occurs in the shape of the wave as it passes through the cylinder wall.

JOURNAL OF APPLIED PHYSICS VOLUME 26, NUMBER 12 DECEMBER, 1955

Thickness-Shear and Flexural Vibrations of Rectangular Crystal Plates*

R. D. MINDLIN AND H. DERESIEWICZ
Department of Civil Engineering and Engineering Mechanics, Columbia University, New York, New York
(Received July 1, 1955)

Equations governing thickness-shear and flexural vibrations of crystal plates are solved for the infinite plate, the simply-supported rectangular plate and the rectangular plate with one pair of parallel edges free and the other pair simply-supported. The equations permit three types of sinusoidal waves, with sinusoidal crests, in an infinite plate. Each of these undergoes a simple reflection upon normal incidence at a simply-supported straight edge, so that the frequency spectrum of a simply-supported rectangular plate has a relatively simple character. The results of a typical computation are given for the AT-cut of quartz. At a free edge each type of incident wave gives rise, in general, to all three types of reflected wave. Consequently, the frequency spectrum of a plate with a pair of parallel, free edges exhibits an intricate coupling of three infinite systems of modes. The development of the coupling is traced continuously by means of a solution involving elastically supported edges.

1. PLATE EQUATIONS

IN a previous paper[1] (referred to in the sequel as I) there are derived approximate equations governing the flexural and first thickness-shear modes of motion of a crystal plate having an axis of monoclinic symmetry in the plane of the plate. The essence of the approximation is the restriction of the components of displacement to the forms

$$u_1=y\psi_x(x,z,t), \quad u_2=\eta(x,z,t), \quad u_3=y\psi_z(x,z,t), \tag{1}$$

where the y-axis is normal to the plane of the plate and u_1, u_2, u_3 are the components of displacement parallel to x,y,z, respectively. Then ψ_x,η,ψ_z are governed by

$$D_1\partial^2\psi_x/\partial x^2+D_5\partial^2\psi_x/\partial z^2+D_7\partial^2\psi_z/\partial x\partial z - D_6(\psi_x+\partial\eta/\partial x)=(\rho h^3/12)\partial^2\psi_x/\partial t^2,$$

$$D_6(\partial\psi_x/\partial x+\partial^2\eta/\partial x^2)+D_4(\partial\psi_z/\partial z+\partial^2\eta/\partial z^2) =\rho h\partial^2\eta/\partial t^2, \tag{2}$$

$$D_3\partial^2\psi_z/\partial z^2+D_5\partial^2\psi_z/\partial x^2+D_7\partial^2\psi_z/\partial x\partial z - D_4(\psi_z+\partial\eta/\partial z)=(\rho h^3/12)\partial^2\psi_z/\partial t^2,$$

where ρ is the density and h is the thickness of the plate. Further,

$$D_1=(c_{11}-c_{12}^2/c_{22})h^3/12, \quad D_2=(c_{13}-c_{12}c_{23}/c_{22})h^3/12,$$
$$D_3=(c_{33}-c_{23}^2/c_{22})h^3/12, \quad D_4=\kappa^2c_{44}h, \tag{3}$$
$$D_5=c_{55}h^3/12, \quad D_6=\kappa^2c_{66}h, \quad D_7=D_2+D_5,$$

in which $\kappa^2=\pi^2/12$ and the c_{ij} are elastic constants referred to x,y,z axes fixed in the plate. (Note that the definition of D_4 has been corrected.)

Boundary conditions sufficient to assure unique solutions of Eq. (2) are obtained by specifying, at each point of the edge of the plate, one member of each of the three products

$$M_\nu\partial\psi_\nu/\partial t, \quad M_{\nu s}\partial\psi_s/\partial t, \quad Q_\nu\partial\eta/\partial t, \tag{4}$$

where ν and s are coordinates normal and tangential, respectively, to the edge. In rectangular coordinates,

* This investigation was supported by the U. S. Army Signal Corps and the Office of Naval Research.
[1] R. D. Mindlin, J. Appl. Phys. **22**, 316 (1951).

the couples M_x, M_{xz} and the force Q_x are given by

$$\begin{aligned} M_x &= D_1\partial\psi_x/\partial x + D_2\partial\psi_z/\partial z, \\ M_z &= D_3\partial\psi_z/\partial z + D_2\partial\psi_x/\partial x, \\ M_{xz} &= D_5(\partial\psi_z/\partial x + \partial\psi_x/\partial z), \\ Q_x &= D_6(\psi_x + \partial\eta/\partial x), \quad Q_z = D_4(\psi_z + \partial\eta/\partial z). \end{aligned} \tag{5}$$

In I a solution was given for the case $\psi_x = \psi_x(x,t)$, $\eta = \eta(x,t)$, $\psi_z = 0$ and a pair of free edges parallel to z. Results of computations were compared with experimental data obtained by Sykes for modes in which η is odd in x. In a subsequent paper[2] (II) the computations were extended to include η even in x and were compared with additional measurements by Sykes. Dependence of ψ_x, η and ψ_z on both x and z is considered in the following sections.

2. INFINITE PLATE

Equations (2) have a solution

$$\begin{aligned} \psi_x &= A\ \cos\xi x\ \sin\zeta z\ \cos\omega t \\ \eta &= Bh\ \sin\xi x\ \sin\zeta z\ \cos\omega t \\ \psi_z &= C\ \sin\xi x\ \cos\zeta z\ \cos\omega t \end{aligned} \tag{6}$$

provided

$$\begin{aligned} AP + B\pi f\alpha \quad + Cd_{71}\alpha\gamma &= 0 \\ A\alpha + B\pi fQ \quad + Cd_{46}\gamma &= 0 \\ Ad_{71}\alpha\gamma + B\pi fd_{46}\gamma + CR &= 0 \end{aligned} \tag{7}$$

where

$$\begin{aligned} &\alpha = \xi h/\pi, \quad \gamma = \zeta h/\pi, \quad d_{k1} = D_k/D_1 \\ &P = \alpha^2 + d_{51}\gamma^2 + f(1 - \omega^2/\omega_x^2) \\ &Q = (\alpha^2 + d_{46}\gamma^2 - \omega^2/\kappa^2\omega_x^2)/f \\ &R = d_{51}\alpha^2 + d_{31}\gamma^2 + f(d_{46} - \omega^2/\omega_x^2) \\ &\omega_x = (\pi/h)(c_{66}/\rho)^{\frac{1}{2}}, \quad f = c_{66}/(c_{11} - c_{12}^2/c_{22}). \end{aligned} \tag{8}$$

Note that α and γ are the ratios of the thickness of the plate to the distances between nodes in the x- and z-directions, respectively; f is the ratio of the xy thickness-shear modulus to the xy flexure modulus; ω_x is the frequency of the first xy thickness-shear mode of an infinite plate.

Equations (7) determine amplitude ratios

$$\begin{aligned} B/A &= (d_{46}P - d_{71}\alpha^2)/\alpha\pi f(d_{71}Q - d_{46}) \\ C/A &= \gamma(d_{46}P - d_{71}\alpha^2)/\alpha(R - d_{46}d_{71}\gamma^2) \end{aligned} \tag{9}$$

and a relation between the wave numbers ξ, ζ and the frequency ω, according to the determinantal equation

$$\begin{vmatrix} P & \alpha & d_{71}\alpha\gamma \\ \alpha & Q & d_{46}\gamma \\ d_{71}\alpha\gamma & d_{46}\gamma & R \end{vmatrix} = 0. \tag{10}$$

This is a bicubic equation in ω as a function of ξ and ζ. For given real, positive ξ and ζ, there are three real, positive roots $\omega_1, \omega_2, \omega_3$ to each of which there corresponds a set of amplitude ratios, in accordance with Eq. (9). Thus, for a given pair of wavelengths, there are three modes of vibration of an infinite plate. In general, each mode has its own frequency and requires the coupling of all three components of displacement ψ_x, η, ψ_z. An understanding of the physical significance of the modes is gained by examining several special cases, which, moreover, are required for the subsequent analysis of rectangular plates.

For the limit $\xi h = 0$, $\zeta h = 0$ (long wavelengths), the positive roots of Eq. (10) and the corresponding amplitudes are

$$\begin{aligned} &\omega_1 = 0 = \omega_y, && A = C = 0, \\ &\omega_2 = (\pi/h)(c_{66}/\rho)^{\frac{1}{2}} = \omega_x, && B = C = 0, \\ &\omega_3 = (\pi/h)(c_{44}/\rho)^{\frac{1}{2}} = \omega_z, && A = B = 0. \end{aligned} \tag{11}$$

The second and third of these are, respectively, the first xy and the first zy thickness-shear modes of an infinite plate. The first mode in Eq. (11) is flexural ($B \neq 0$). Its frequency is more recognizable, in its next higher order approximation,

$$\omega_y = \{[D_1\xi^4 + D_3\zeta^4 + 2(D_2 + 2D_5)\xi^2\zeta^2]/\rho h\}^{\frac{1}{2}}, \tag{12}$$

as the frequency of flexural vibration of an orthotropic plate according to the classical theory of thin plates. In the isotropic case,

$$\begin{aligned} &D_1 = D_3 = D = Eh^3/12(1-\nu^2), \\ &D_2 = \nu D, \quad D_5 = (1-\nu)D/2, \end{aligned} \tag{13}$$

where ν is Poisson's ratio and E is Young's modulus. Equation (12) then reduces to the usual form

$$\omega_y = (\xi^2 + \zeta^2)(D/\rho h)^{\frac{1}{2}}. \tag{14}$$

Thus, when the wavelengths in both the x- and z-directions are very long, in comparison with the thickness of the plate, the three components of displacement ψ_x, η, ψ_z essentially uncouple and produce two simple thickness-shear modes and one flexural mode. In general, $\omega_y < \omega_x, \omega_z$ and, for the AT-cut of quartz, $\omega_y < \omega_x < \omega_z$. The latter inequality is adopted in what follows.

Consider, now, the case in which only the wavelength in the z-direction becomes large ($\zeta = 0$). Then the bicubic Eq. (10) has three real roots $\omega_1, \omega_2, \omega_3$ given by

$$\begin{aligned} 2(\omega_{1,2}/\omega_x)^2 &= 1 + k\alpha^2 \pm [(1 + k\alpha^2)^2 - 4\kappa^4\alpha^4/g]^{\frac{1}{2}} \\ (\omega_3/\omega_x)^2 &= (c_{44}/c_{66})[1 + (c_{55}/c_{44})\alpha^2] \end{aligned} \tag{15}$$

where

$$\begin{aligned} g &= \kappa^2 c_{66}/(c_{11} - c_{12}^2/c_{22}) \\ k &= \kappa^2(1+g)/g. \end{aligned} \tag{16}$$

The corresponding amplitudes are

$$\begin{aligned} &\omega_{1,2}: \quad C = 0, \quad A/B = [(\omega_{1,2}/\kappa\alpha\omega_x)^2 - 1]\pi\alpha \\ &\omega_3: \quad A = B = 0. \end{aligned} \tag{17}$$

Hence, when $\zeta = 0$, the displacement ψ_z is not coupled with ψ_x or η and forms a simple yz thickness-shear mode which varies sinusoidally with x. In each of the other

[2] R. D. Mindlin, J. Appl. Phys. 23, 83 (1952).

two modes the displacements ψ_x and η are coupled. For the mode with the lower frequency $|A/B|<1$ whereas the mode with the higher frequency has $|A/B|>1$. Thus, the mode with frequency ω_1 is essentially flexural while the mode with frequency ω_2 is essentially thickness-shear. These are the two types of motion that were considered in I.

Coming, now, to the case of arbitrary ξ and ζ, we observe that the three roots $\omega_1,\omega_2,\omega_3$ of Eq. (10) are associated with modes which are essentially flexural, xy thickness-shear and zy thickness-shear, respectively, although each mode contains all three components of displacement to some degree. For a fixed ζ, all three frequencies approach infinity as the wavelength in the x-direction approaches zero (i.e., as $\xi\to\infty$). On the other hand, as $\xi\to 0$, all three frequencies diminish monotonically and approach, asymptotically, cut-off values $\omega_1^*,\omega_2^*,\omega_3^*$ obtained as the roots of Eq. (10) with $\xi=0$. Thus

$$2(\omega_{1,3}^*/\omega_x)^2=(c_{44}/c_{66})\{1+k'\gamma^2 \mp[(1+k'\gamma^2)^2-4\kappa^4\gamma^4/g']^{\frac{1}{2}}\} \quad (18)$$
$$(\omega_2^*/\omega_x)^2=1+(c_{55}/c_{66})\gamma^2$$

where

$$g'=\kappa^2 c_{44}/(c_{33}-c_{23}^2/c_{22})$$
$$k'=\kappa^2(1+g')/g'. \quad (19)$$

The behavior of the three roots of Eq. (10) is shown in Fig. 1 for the AT-cut of quartz[3] with $\zeta h/\pi=0.2$. Note that, if d is the distance between nodes in the z-direction, $\zeta h/\pi=h/d$.

It may be observed that, when the displacement components have phase reversals in the z-direction, the cut-off frequencies are higher than otherwise. Thus, $\omega_1^*>\omega_y$, $\omega_2^*>\omega_x$, $\omega_3^*>\omega_z$ when $h/d>0$. Cut-off frequencies for a range of values of h/d are given in Table I for the AT-cut of quartz.

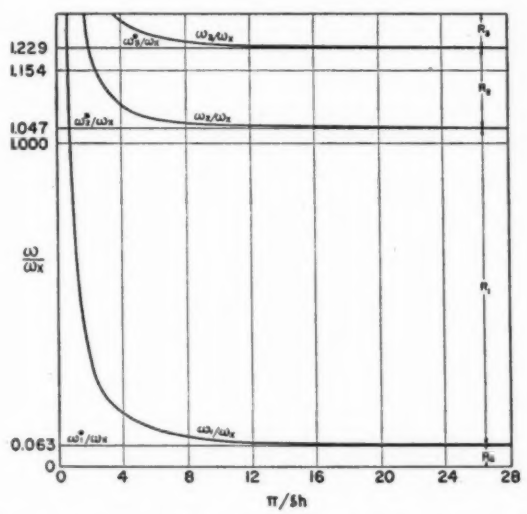

FIG. 1. Frequencies of vibration of an infinite plate. Variation with wavelength in x-direction for fixed wavelength in z-direction. AT-cut of quartz; $\zeta h/\pi=0.2$.

[3] The elastic constants used in the computations are those given by W. P. Mason, *Piezoelectric Crystals and Their Applications to Ultrasonics* (D. Van Nostrand Company, Inc., New York, 1950), p. 84.

TABLE I. Cut-off frequencies as functions of the ratio (h/d) of plate thickness to nodal spacing along z for the AT-cut of quartz.

h/d	Flexure ω_1^*/ω_x	Thickness-shear xy ω_2^*/ω_x	Thickness-shear zy ω_3^*/ω_x
0	0	1	1.154
0.1	0.016	1.012	1.173
0.2	0.063	1.047	1.229
0.3	0.134	1.102	1.313
0.4	0.220	1.175	1.419
0.5	0.316	1.263	1.540
0.6	0.420	1.363	1.673
0.7	0.527	1.472	1.814
0.8	0.636	1.589	1.962
0.9	0.747	1.711	2.115
1.0	0.858	1.839	2.272

3. SIMPLY-SUPPORTED RECTANGULAR PLATE

In the classical theory of plates, a simply-supported edge is characterized by vanishing bending moment (M_x) and displacement (η) normal to the plane of the plate. With these boundary conditions, the modes of vibration of a rectangular plate are described by simple product functions such as those in Eq. (6). Equations (2), however, require an additional boundary condition. Referring to Eq. (4), this may be a condition on the twisting couple M_{xz} or the associated rotation ψ_z. It is when the latter is set equal to zero that the solutions of Eq. (2), for the modes of vibration of a rectangular plate, are analogous to those of classical plate theory, i.e., ψ_x,η, and ψ_z are expressible as simple product functions. Accordingly, for a plate bounded by $x=\pm a$, $z=\pm c$, the boundary conditions for simply-supported edges are taken to be

$$\begin{aligned} &M_x=0, \quad \partial\eta/\partial t=0, \quad \partial\psi_z/\partial t=0, \quad \text{on} \quad x=\pm a;\\ &M_z=0, \quad \partial\eta/\partial t=0, \quad \partial\psi_x/\partial t=0, \quad \text{on} \quad z=\pm c. \end{aligned} \quad (20)$$

We consider three solutions (one for each of $i=1,2,3$)

$$\begin{aligned} \psi_x^i&=A_i\cos\xi_i x\sin\zeta_i z\cos\omega_i t,\\ \eta^i&=B_i h\sin\xi_i x\sin\zeta_i z\cos\omega_i t,\\ \psi_z^i&=C_i\sin\xi_i x\cos\zeta_i z\cos\omega_i t. \end{aligned} \quad (21)$$

To satisfy the equations of motion, Eq. (2), the wave numbers and frequency must again satisfy Eq. (10) with ξ,ζ,ω replaced by ξ_i,ζ_i,ω_i. Then, inserting Eq. (21) into Eq. (5), where necessary, and then into Eq. (20), the boundary conditions reduce to

$$\sin\xi_i a=0, \quad \sin\zeta_i c=0, \quad i=1,2,3. \quad (22)$$

It may be seen that the boundary conditions do not induce coupling between the three types of motion $i=1,2,3$, since each satisfies Eq. (22) separately. Hence, any nodal line of the vibrating infinite plate may be

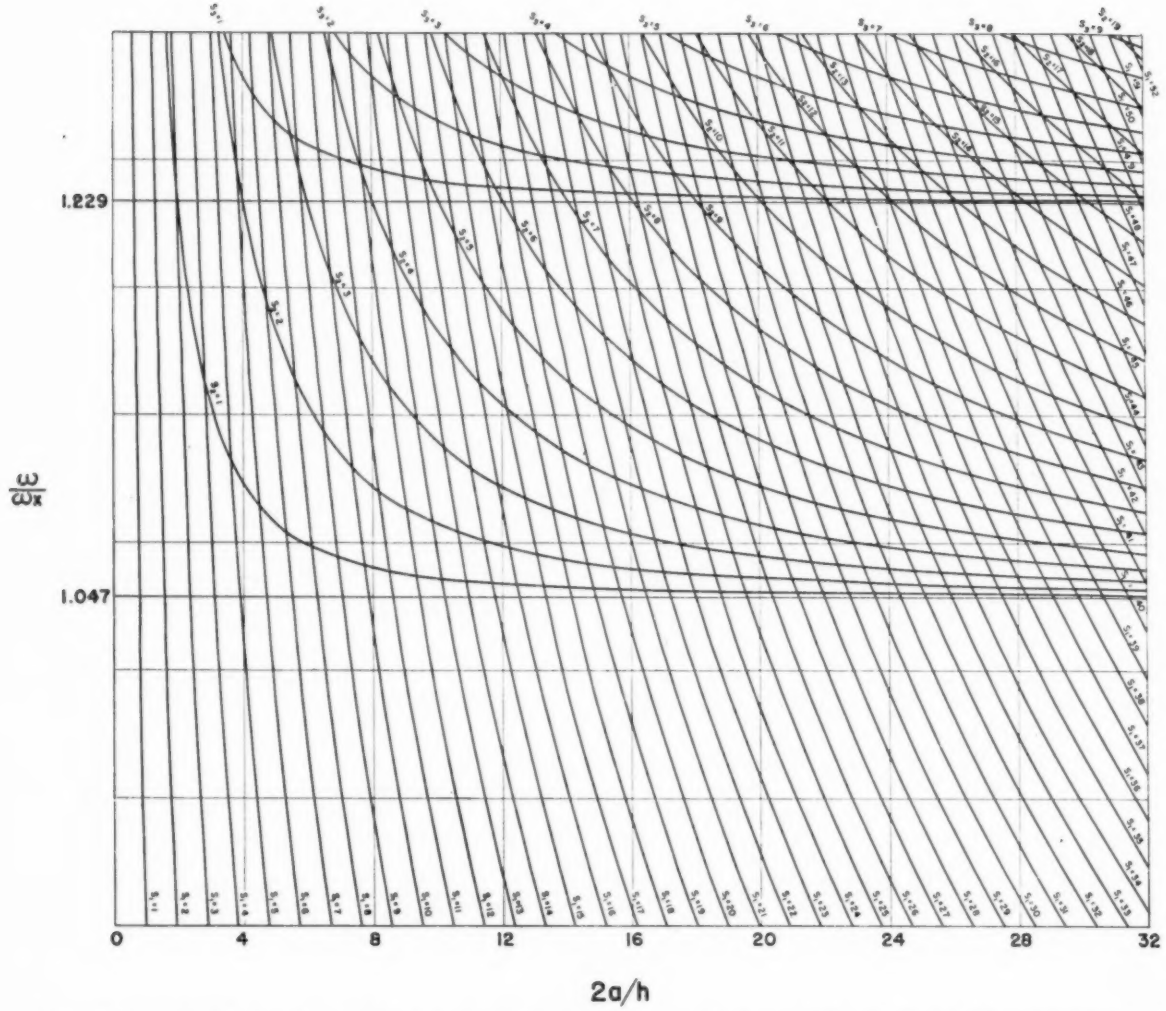

FIG. 2. Frequencies of vibration of a simply-supported rectangular plate. Variation with ratio $(2a/h)$ of length-to-thickness for fixed ratio $(h/d=0.2)$ of thickness-to-distance between nodes along width. Curves s_1, s_2, s_3=constant give frequencies of flexural, xy thickness-shear and zy thickness-shear, respectively. Curves s_i odd, even, are for modes even and odd, respectively, in x and either even or odd in z (AT-cut of quartz).

taken as a simply-supported edge and the resulting vibrations may be regarded as superposed sinusoidal waves, with sinusoidal crests, undergoing simple reflections at these edges.

The symmetry of the modes (i.e., oddness or evenness in x and z) may be identified with the symmetry of η. In Eq. (21), η is odd in both x and z. Modes even in x and odd in z are obtained by interchanging $\sin\xi_i x$ and $\cos\xi_i x$ in all three of Eq. (21). The boundary conditions then reduce to

$$\cos\xi_i a=0, \quad \sin\zeta_i c=0, \quad i=1,2,3. \tag{23}$$

Similarly, for modes odd in x and even in z,

$$\sin\xi_i a=0, \quad \cos\zeta_i c=0, \quad i=1,2,3 \tag{24}$$

and, finally, for modes even in both x and z,

$$\cos\xi_i a=0, \quad \cos\zeta_i c=0, \quad i=1,2,3. \tag{25}$$

The solutions of all of Eqs. (22) to (25) may be written as

$$\xi_i=s_i\pi/2a, \quad \zeta_i=p_i\pi/2a, \quad i=1,2,3, \tag{26}$$

where the s_i are even integers for modes odd in x and odd integers for modes even in x. Similarly, the p_i are even integers for modes odd in z and odd integers for modes even in z.

Hence, the frequencies of vibration of a simply-supported plate are given by the roots of

$$\begin{vmatrix} P_i & \alpha_i & d_{71}\alpha_i\gamma_i \\ \alpha_i & Q_i & d_{46}\gamma_i \\ d_{71}\alpha_i\gamma_i & d_{46}\gamma_i & R_i \end{vmatrix}=0, \tag{27}$$

where

$$\begin{aligned} &\alpha_i=s_i h/2a, \quad \gamma_i=p_i h/2c \\ &P_i=\alpha_i^2+d_{51}\gamma_i^2+f(1-\omega_i^2/\omega_z^2) \\ &Q_i=(\alpha_i^2+d_{46}\gamma_i^2-\omega_i^2/\kappa^2\omega_z^2)/f \\ &R_i=d_{51}\alpha_i^2+d_{31}\gamma_i^2+f(d_{46}-\omega_i^2/\omega_z^2). \end{aligned} \tag{28}$$

The associated amplitude ratios are

$$B_i/A_i=(d_{46}P_i-d_{71}\alpha_i^2)/\alpha_i\pi f(d_{71}Q_i-d_{46})$$
$$C_i/A_i=\gamma_i(d_{46}P_i-d_{71}\alpha_i^2)/\alpha_i(R_i-d_{46}d_{71}\gamma_i^2). \quad (29)$$

The frequency spectrum determined by Eq. (27) is plotted in Fig. 2 for the AT-cut of quartz and $\gamma_i=0.2$. It may be observed that the three families of curves in Fig. 2 may be obtained from the three curves in Fig. 1 by multiplying the abscissas of the latter by 1,2,3,4...etc. The curves $s_1,s_2,s_3=$constant give the frequencies of flexural, xy thickness-shear and zy thickness-shear modes, respectively. s_i odd, even are for modes even and odd, respectively, in x. All the curves apply to modes either odd or even in z.

4. COMPARISON WITH SYKES'S FORMULA

Sykes[4] has given a formula for the frequencies of thickness-shear vibrations:

$$f=\tfrac{1}{2}\left[\frac{c_{jj}}{\rho}\left(\frac{m^2}{l^2}+k\frac{n^2}{l^2}+k_1\frac{(p-1)^2}{w^2}\right)\right]^{\frac{1}{2}} \quad (30)$$

where k and k_1 are empirical coefficients. To convert to the notation of the present paper, note that

$$t=h, \quad l=2a, \quad w=2c$$
$$m=1, \quad n=s_2, \quad p-1=p_2 \quad (31)$$
$$(\pi/l)(c_{jj}/\rho)^{\frac{1}{2}}=\omega_x, \quad f=\omega_2/2\pi.$$

Then Eq. (30) becomes

$$(\omega_2/\omega_x)^2=1+ks_2^2h^2/4a^2+k_1p_2^2h^2/4c^2. \quad (32)$$

This is to be compared with the root of Eq. (27) corresponding to $i=2$.

Now, a frequency of the same form as Eq. (32) can be obtained from the equations of motion, Eq. (2), if we assume $\eta=\psi_z=0$ and if the presence of ψ_x in the second and third of Eq. (2) is ignored. As a result, Eq. (27) reduces to $P_2=0$, which has the same form as Eq. (32). Hence, what is contained in Sykes's coefficients k and k_1 is the effect of coupling of η and ψ_z with ψ_x. This coupling arises from two sources, namely, through the elastic constants and as a result of reflections of waves at the plane surfaces $y=\pm h/2$. The source of the second type of coupling is not apparent in the equations of motion, Eq. (2), since it has been masked as a result of the integration through the thickness. The effects of both types of coupling are contained in the frequencies and amplitude ratios given by Eqs. (27) and (29).

5. ONE PAIR OF PARALLEL EDGES FREE, THE OTHER PAIR SIMPLY-SUPPORTED

In the presence of a free edge, a third type of coupling occurs. If we consider waves of the type that generate the three solutions ($i=1,2,3$) in Eq. (21), then, on incidence at a free edge, each wave gives rise, in general, to reflected waves of all three types.[5] Hence, in a vibrating plate with free edges, the modes are composed of coupled modes of a plate with simply-supported edges.

TABLE II. Real and imaginary character of wave numbers.

Frequency range	Real	Imaginary
$R_3(\omega>\omega_3^*)$	ξ_1,ξ_2,ξ_3	
$R_2(\omega_2^*<\omega<\omega_3^*)$	ξ_1,ξ_2	ξ_3
$R_1(\omega_1^*<\omega<\omega_2^*)$	ξ_1	ξ_2,ξ_3
$R_0(\omega<\omega_1^*)$		ξ_1,ξ_2,ξ_3

For a plate free along $x=\pm a$ and simply-supported along $z=\pm c$, the boundary conditions are

$$M_x=0, \quad Q_x=0, \quad M_{xz}=0 \quad \text{on} \quad x=\pm a$$
$$M_z=0, \quad \partial\eta/\partial t=0, \quad \partial\psi_z/\partial t=0 \quad \text{on} \quad z=\pm c. \quad (33)$$

We consider displacements

$$\psi_x=\sum_{i=1}^{3}A_i\cos\xi_i x\sin\zeta z\cos\omega t$$
$$\eta=\sum_{i=1}^{3}B_i h\sin\xi_i x\sin\zeta z\cos\omega t \quad (34)$$
$$\psi_z=\sum_{i=1}^{3}C_i\sin\xi_i x\cos\zeta z\cos\omega t.$$

This is a solution of Eq. (2) provided that

$$\begin{vmatrix} P_i & \alpha_i & d_{71}\alpha_i\gamma \\ \alpha_i & Q_i & d_{46}\gamma \\ d_{71}\alpha_i\gamma & d_{46}\gamma & R_i \end{vmatrix}=0 \quad (35)$$

and

$$B_i/A_i=(d_{46}P_i-d_{71}\alpha_i^2)/\alpha_i\pi f(d_{71}Q_i-d_{46})$$
$$C_i/A_i=\gamma(d_{46}P_i-d_{71}\alpha_i^2)/\alpha_i(R_i-d_{46}d_{71}\gamma^2), \quad (36)$$

where

$$\alpha_i=\xi_i h/\pi, \quad \gamma=\zeta h/\pi$$
$$P_i=\alpha_i^2+d_{51}\gamma^2+f(1-\omega^2/\omega_x^2)$$
$$Q_i=(\alpha_i^2+d_{46}\gamma^2-\omega^2/\kappa^2\omega_x^2)/f \quad (37)$$
$$R_i=d_{51}\alpha_i^2+d_{31}\gamma^2+f(d_{46}-\omega^2/\omega_x^2).$$

Equation (35) is to be regarded as a bicubic in ξ with ζ and ω as parameters. For positive, real ζ and ω there are three roots ξ_i that are positive real or imaginary depending on the frequency range, as shown in Table II. These are the ξ_i which appear in Eqs. (34) to (37). The frequencies ω_1^*, ω_2^*, ω_3^* at which ξ_1, ξ_2, ξ_3, respectively, change from real to imaginary are those given in Eq. (18).

The boundary conditions, Eq. (33), on $z=\pm c$ are satisfied if

$$\zeta=p\pi/2c, \quad (38)$$

[4] R. A. Sykes in *Quartz Crystals for Electric Circuits*, edited by R. A. Heising (D. Van Nostrand Company, Inc., New York, 1946), chap. VI, p. 218, Eq. 6.9.

[5] This is shown for the isotropic plate by T. R. Kane, J. Appl. Mech. **21**, 213 (1954).

where p is an even integer. For modes even in z, $\sin\zeta z$ and $\cos\zeta z$ are interchanged in Eq. (34). Then the boundary conditions on $z=\pm c$ are satisfied if ζ is given by Eq. (38) and p is an odd integer.

To find the requirements imposed by the boundary conditions on $x=\pm a$ substitute Eq. (34) first in Eq. (5) and then in Eq. (33), with the result

$$\begin{aligned} &A_1\beta_{11}\sin\xi_1 a+A_2\beta_{12}\sin\xi_2 a+A_3\beta_{13}\sin\xi_3 a=0,\\ &A_1\beta_{21}\cos\xi_1 a+A_2\beta_{22}\cos\xi_2 a+A_3\beta_{23}\cos\xi_3 a=0,\\ &A_1\beta_{31}\cos\xi_1 a+A_2\beta_{32}\cos\xi_2 a+A_3\beta_{33}\cos\xi_3 a=0, \end{aligned} \tag{39}$$

where

$$\begin{aligned} \beta_{1i}&=d_{12}\alpha_i+\gamma C_i/A_i,\\ \beta_{2i}&=\gamma+\alpha_i C_i/A_i,\\ \beta_{3i}&=1+\pi\alpha_i B_i/A_i. \end{aligned} \tag{40}$$

Equations (39) determine amplitude ratios $A_1: A_2: A_3$. Thus, except for special cases to be considered later, all three types of the modes of a simply-supported plate are coupled as a result of introducing free edges. For a nontrivial solution, the determinant of Eq. (39) must vanish. This condition yields the transcendental equation

$$L_1\tan\varphi+L_2\tan M\varphi+L_3\tan N\varphi=0, \tag{41}$$

where

$$\begin{aligned} L_1&=\beta_{11}(\beta_{22}\beta_{33}-\beta_{23}\beta_{32}),\\ L_2&=\beta_{12}(\beta_{23}\beta_{31}-\beta_{33}\beta_{21}),\\ L_3&=\beta_{13}(\beta_{21}\beta_{32}-\beta_{31}\beta_{22}),\\ \varphi&=\xi_1 a,\quad M=\xi_2/\xi_1,\quad N=\xi_3/\xi_1. \end{aligned} \tag{42}$$

For modes even in x, tangent is replaced by cotangent in Eq. (41).

The frequency spectrum may be computed in the following manner. The ratios of elastic constants d_{kl} are computed for the material of the plate and orientation of cut. Then choose a value of γ, the ratio of plate thickness to distance between nodes in the z-direction. The further choice of ω/ω_x permits the calculation of the α_i from Eq. (35) and the B_i/A_i and C_i/A_i from Eq. (36), so that the β_{ki} may be found from Eq. (40). With these results, the L_i and M and N may be computed from Eq. (42). Hence, all the coefficients in Eq. (41) are known and the equation becomes a transcendental equation in the single variable φ. A sequence of roots of Eq. (41) may then be computed by successive approximations. To each root there corresponds a length-thickness ratio according to the relation

$$2a/h=2\varphi/\pi\alpha_1. \tag{43}$$

Thus, a set of length-thickness ratios is found for the chosen value of ω/ω_x. The computation may be repeated for successive values of ω/ω_x until sufficient points can be plotted (ω/ω_x *vs* $2a/h$) to enable the curves of the frequency spectrum to be drawn for the chosen value of γ. The process may then be repeated for a new value of γ.

Before proceeding to an analysis of the frequency spectrum, it is advisable to study the relation between the uncoupled spectrum for simply-supported edges and the coupled spectrum for free edges in a simpler case.

6. CYLINDRICAL VIBRATIONS OF A STRIP

Returning to the problem of the rectangular plate simply-supported on all edges, we consider the limiting case ($\zeta h=0$) of motion independent of z. The asymptotic frequencies, Eq. (18), degenerate to $\omega_1^*=0$, $\omega_2^*=\omega_z$, $\omega_3^*=\omega_x$ and the frequencies themselves [from Eq. (27) with $\gamma_i=0$] become

$$\begin{aligned} 2(\omega_{1,2}/\omega_x)^2&=1+k\alpha_{1,2}^2\mp[(1+k\alpha_{1,2}^2)^2-4\kappa^4\alpha_{1,2}^4/g]^{\frac{1}{2}}\\ (\omega_3/\omega_x)^2&=(c_{44}/c_{66})[1+(c_{55}/c_{44})\alpha_3^2]. \end{aligned} \tag{44}$$

The expressions for ω_1 and ω_2 are the same as those given by Eqs. (53) and (52), respectively, of I. (Note that r,n,l and $\bar{\omega}$ of I are s_1, s_2, $2a$ and ω_x, respectively, here.) Hence, Fig. 4 of I is a part of the frequency spectrum of a simply-supported strip, of width $l=2a$, vibrating in modes whose shapes do not vary along the length. A typical portion of the spectrum of the xy thickness-shear and flexural modes, in the range $\omega>\omega_x$, is shown by the curves $s_i=$constant in Fig. 3. The curves s_i even are for modes odd in x and derive from the boundary conditions

$$\sin\xi_1 a=0,\quad \sin\xi_2 a=0. \tag{45}$$

The curves s_i odd are for modes even in x and derive from

$$\cos\xi_1 a=0,\quad \cos\xi_2 a=0. \tag{46}$$

Next, consider the limiting case $\zeta h=0$ in the problem solved in Sec. 5. The boundary conditions, Eq. (39), reduce to

$$\begin{aligned} A_1(\sigma_1-1)\xi_1^2\sin\xi_1 a+A_2(\sigma_2-1)\xi_2^2\sin\xi_2 a&=0\\ A_1\sigma_1\xi_1\cos\xi_1 a+A_2\sigma_2\xi_2\cos\xi_2 a&=0\\ A_3\xi_3\cos\xi_3 a&=0, \end{aligned} \tag{47}$$

where

$$\sigma_i=\omega^2/(\kappa^2\alpha_i^2\omega_x^2), \tag{48}$$

and Eq. (41) becomes

$$(M^2-g)\tan\varphi+M(gM^2-1)\tan M\varphi=0. \tag{49}$$

Since A_3 occurs only in the last boundary condition, the zy thickness-shear modes are not coupled with the xy thickness-shear and flexural modes. However, the latter two are coupled with each other, since A_1 and A_2 appear in both of the first two conditions. This is the case which was treated in I. The frequency spectrum for modes odd in x appears as Fig. 1 of I and a typical portion of it, in the range $\omega>\omega_x$, is shown here as the curve marked K=0 in Fig. 3. (The spectrum for modes even in x is given in Fig. 1 of II).

We note that the first two of Eqs. (47) have the solutions Eqs. (45) and (46). Hence, the curve K=0,

in Fig. 3, passes through the intersections of the curves s_1 even and s_2 even, and also through the intersections of the curves s_1 odd and s_2 odd. Between these intersections, however, the condition $\omega_1=\omega_2$, required by the boundary conditions for free edges, is not satisfied and hence the spectrum of the strip with free edges (K=0) does not coincide with the spectrum of the strip with simply-supported edges (s_i=constant). The development of the coupling, which produces this result, may be traced by considering the elastically supported strip, which contains the free and simply-supported strips as limiting cases.[6]

For elastically supported edges, the boundary conditions on $x=\pm a$ are

$$M_x=0, \quad Q_x=\mp K\eta, \tag{50}$$

where K is the spring constant of the elastic support. Accordingly, for xy thickness-shear and flexural modes odd in x, the boundary conditions become

$$A_1(\sigma_1-1)\xi_1^2 \sin\xi_1 a+A_2(\sigma_2-1)\xi_2^2 \sin\xi_2 a=0,$$

$$D_6(A_1\sigma_1\xi_1 \cos\xi_1 a+A_2\sigma_2\xi_2 \cos\xi_2 a) = -K(A_1 \sin\xi_1 a+A_2 \sin\xi_2 a). \tag{51}$$

When $K=\infty$, Eqs. (51) reduce to Eqs. (45) and when K=0, Eqs. (51) reduce to the first two of Eqs. (47). When $0<K<\infty$, Eqs. (51) still have the roots determined by Eqs. (45), so that the curves giving the frequencies of modes odd in x of the elastically supported strip pass through the intersections of the curves s_1 even, s_2 even of the spectrum of modes odd in x of the simply-supported strip. The portions of the curves (for $0<K<\infty$) between these intersections do not, however, pass through the intersections of s_1 odd, s_2 odd because Eqs. (51) are not satisfied by Eqs. (46). In fact, these portions of the curves may be expected to fall above the intersections s_1 odd, s_2 odd, because the introduction of the elastic support is an additional constraint which serves to raise the frequencies above those of the strip with free edges. Calculation of the roots and corresponding frequencies shows that this is indeed the result. A typical portion of the spectrum for modes odd in x is shown by the dashed lines in Fig. 3 for two values of $0<K<\infty$.

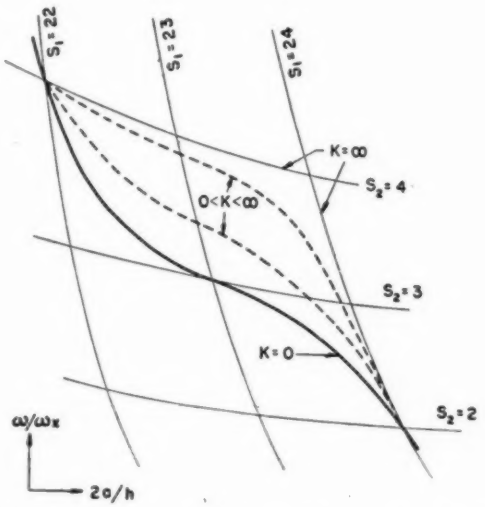

FIG. 3. Typical portion of spectrum of frequencies of cylindrical vibrations of a strip in range $\omega>\omega_x$, illustrating development of coupling. Curves s_i=constant are for simply supported edges; s_1 flexure, s_2 thickness-shear; s_i odd, even, are for modes even and odd, respectively, in x. Curve K=0 is for a mode, odd in x, of a strip with free edges. Curves $0<K<\infty$ are for modes, odd in x, of a strip with elastically supported edges. (K is the spring constant of the elastic support.)

[6] This was suggested by E. Sternberg.

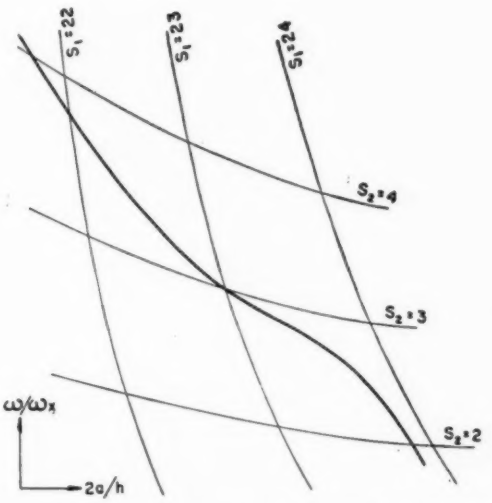

FIG. 4. Typical portion of spectrum, in range R_2, for a mode odd in x, of a plate free along one pair of parallel edges and simply supported along the other pair.

The transition from the simple frequency spectrum of uncoupled modes of the simply-supported strip to the frequency spectrum of the coupled modes of the free strip may now be traced continuously in Fig. 3, for modes odd in x. For modes even in x, the situation is similar. The only alteration required in the explanation in the preceding paragraphs is the interchange of "odd" and "even."

7. FREQUENCY SPECTRUM OF A PLATE WITH A PAIR OF PARALLEL EDGES FREE AND THE OTHER PAIR SIMPLY-SUPPORTED

The frequency spectrum governed by Eqs. (41) and (43) has a different character in each of the four ranges listed in Table II.

Range R_0, $\omega<\omega_1^*$.—In this range all three ξ_i are imaginary so that all three transcendental functions in Eq. (41) are hyperbolic. Accordingly, Eq. (41) has no roots in this range, i.e., there are no frequencies of vibration $\omega<\omega_1^*$.

Range R_1, $\omega_1^*<\omega<\omega_2^*$.—Here ξ_1 is real and ξ_2 and ξ_3 are imaginary. Only one of the three transcendental functions in Eq. (41) is oscillatory and the remaining two are almost unity. Hence, the spectrum is very much like that in the same range for the simply-sup-

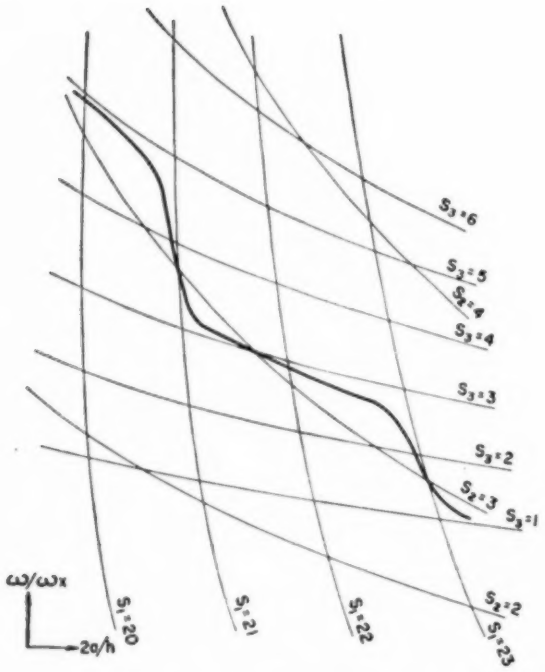

FIG. 5. Typical portion of spectrum, in range R_3, for a mode odd in x, of a plate free along one pair of parallel edges and simply supported along the other pair.

ported plate, as shown in Fig. 2. Near $\omega=\omega_2^*$ the curves are slightly lower than those in Fig. 2, but approach the latter asymptotically as $\omega\rightarrow\omega_1^*$.

Range R_2, $\omega_2^*<\omega<\omega_3^*$.—Both ξ_1 and ξ_2 are real while ξ_3 is imaginary in this range. Thus there are two trigonometric functions in Eq. (41) just as there are in Eq. (49) for the free strip. However, the presence of the third term causes the spectrum to differ from that illustrated by the heavy line in Fig. 3. Referring to Eq. (39), from which Eq. (41) was derived, it may be seen that the equations have a solution

$$\cos\xi_1 a=0, \quad \cos\xi_2 a=0 \tag{52}$$

$$A_3=0, \quad A_1/A_2=\pm\beta_{12}/\beta_{11} \tag{53}$$

but not a solution $\sin\xi_1 a=0$, $\sin\xi_2 a=0$. Hence, the frequency curve for a mode odd in x passes through the intersections of curves s_1 odd, s_2 odd but not through the intersections of s_1 even, s_2 even. The curve may be expected to fall below, rather than above, the latter, because the relaxation of the condition $\zeta h=0$ is a relaxation of a constraint. Hence, instead of the curve $K=0$ in Fig. 3, we have the curve shown by the heavy line in Fig. 4. It is to be noted that the curve for a mode odd in x, of a plate with a pair of free edges, passes through the intersections s_i odd, which are points on the spectrum for modes even in x of a simply-supported plate. It is also evident, from Eq. (53), that at these intersection points the zy thickness-shear mode is absent.

Range R_3, $\omega>\omega_3^*$.—Here all three ξ_i are real. Hence Eqs. (39) and (41) again have the solutions Eqs. (52), (53) and, in addition, two sets of solutions obtained by cyclical permutation of the subscripts in Eqs. (52) and (53). (Only the second subscript in β_{ki} is to be permuted.) Accordingly, all that was said of the intersections of curves s_1, s_2 constant in range R_2 applies to the intersections of s_1, s_2 constant, s_2, s_3 constant, and s_3, s_1 constant in range R_3. Note that, in each case, it is the zy thickness-shear mode, the flexure mode, and the xy thickness-shear mode, respectively, that is absent at the intersection points. A typical curve of the spectrum is illustrated by the heavy line in Fig. 5.

On the basis of these results, a set of rules may be formulated for sketching the frequency spectrum of the plate, with one pair of parallel edges free and the other pair simply-supported, on the network of curves $s_i=$ constant of the simply-supported plate (Fig. 2). For modes odd in x the rules are:

(1) Starting at the low-frequency end of the spectrum, proceed to sketch a line upward. (The line should tend to the left, since, for a given mode, increasing frequencies correspond to decreasing length-thickness ratios.)

(2) The line cannot cross a curve s_i odd except at an intersection with another curve s_i odd.

(3) On approaching a curve s_i odd, the line must bear upward and to the left until it crosses the curve at the nearest intersection with another curve s_i odd.

(4) The line may cross curves s_i even, but must not pass through intersections of curves s_i even.

For modes even in x, it is only necessary to interchange odd and even in the rules.

JOURNAL OF APPLIED PHYSICS VOLUME 26, NUMBER 12 DECEMBER, 1955

Space-Charge Waves in Crossed Electric and Magnetic Fields*

SALIM S. SOLOMON†
Electronics Research Laboratory, University of California, Berkeley 4, California
(Received May 15, 1955)

The problem of space-charge waves propagating along a neutralized electron stream moving in a medium pervaded by crossed static electric and magnetic fields is discussed. From energy considerations it is shown that gain can be realized either by conversion of the electron kinetic or potential energy into electromagnetic energy. A small signal analysis shows that for the first case the *TE* and *TM* modes are coupled in general. However, when the electron velocity is much smaller than the velocity of light the coupling coefficients are negligible and the gain realized is identical with that of the conventional traveling-wave tube. A similar analysis for the second case, which is that of the traveling-wave magnetron tube, yields the interesting result that the *TE* and *TM* modes separate even when the electron velocity is comparable with the velocity of light.

I. INTRODUCTION

THE propagation of electromagnetic waves along an electron beam has been studied by Hahn[1] and Ramo[2] as early as 1939. Two cases were treated:

(a) A very high focusing longitudinal magnetic field is present such that the motion of electrons in any but the axial direction may be neglected.

(b) No focusing magnetic field is present so that the electrons may move in all directions. In both of the above two cases a separation of the space-charge waves into *TE* and *TM* waves is possible.

The more general case when the focusing magnetic field is finite and the velocity of the electrons exists in all directions has been studied recently by Parzen[3] and Sollfrey.[4] Sollfrey gives a complete and clear two-dimensional analysis neglecting relativistic effects. In this case separation of the waves into *TE* and *TM* modes is no longer possible.

A number of valuable articles have already been devoted to the study of space-charge waves in crossed electric and magnetic fields in both the American and French literature. Pierce[5] has developed the equations of the traveling-wave magnetron tube by assuming a stream of electrons coupled to a circuit in crossed electric and magnetic fields. Recently, Muller[6] has published a solution of Pierce's equations. Warnecke and Guénard[7] have discussed the applications of magnetron amplifiers and Brossart and Doëhler[8] have presented a theory for such devices.

A classical analysis of space-charge waves in crossed electric and magnetic fields analogous to that made by Hahn and Ramo in discussing space-charge waves in an infinite or zero longitudinal focusing magnetic field does not appear in the literature. In what follows we demonstrate that such an analysis is possible and yields some interesting results.

We first study the propagation of plane waves. We show that when the electron velocity is comparable with the velocity of light growing plane waves are possible. An analysis similar to that made to develop the theory of the resistive-wall amplifier[9] shows that the magnetic field may be used as an independent parameter to control the value of the gain in the resistive-wall traveling-wave magnetron amplifier. We then assume an electron velocity oblique to the direction of propagation of the plane wave. We find that the component of velocity transverse to the direction of propagation does not affect the nature of the wave.

We then proceed to a two-dimensional analysis of space-charge waves in crossed electric and magnetic fields. From energy considerations it is easy to see that there are two cases possible. The derivation of the differential equations for each case is followed by a typical boundary value solution. We denote special attention to one of the two cases, namely, that of the traveling-wave magnetron tube.

II. PLANE SPACE-CHARGE WAVES IN CROSSED ELECTRIC AND MAGNETIC FIELDS

Consider a medium pervaded by crossed static electric and magnetic fields such that in the absence of the waves the medium has a uniform density of electrons, ρ_0, all traveling at the same constant velocity,

* The work described in this article has been supported by the U. S. Air Force, Wright Air Development Center under Contract No. AF 33(616)-495 with the University of California and is part of a thesis submitted by the author to the Graduate Division of the University of California at Berkeley in partial fulfillment of the requirements for the degree of Doctor of Philosophy in electrical engineering.

† Now with Lenkurt Electric Company, San Carlos, California.

[1] W. C. Hahn, Gen. Elec. Rev. **42**, 258 (1939).

[2] S. Ramo, Phys. Rev. **56**, 276 (1939).

[3] P. Parzen, "The theory of propagation of electromagnetic waves in cylindrical wave guides with longitudinal magnetic focusing fields," Federal Telecommunication Laboratories, Inc., Contract W36-039-SC-44561, Report No. 1338 (November, 1951).

[4] W. Sollfrey, "Magnetic field effects in traveling-wave tubes," New York University, Mathematics Research Group, Report No. TW-18 (May, 1952).

[5] J. R. Pierce, *Traveling-Wave Tubes* (D. Van Nostrand Company, Inc., New York, 1950).

[6] M. Muller, Proc. Inst. Radio Engrs. **42**, 1651 (1954).

[7] R. Warnecke and P. Guénard, Ann. radioélec. compagn. franc. assoc. T.S.F. **3**, 259 (1948).

[8] J. Brossart and O. Doëhler, Ann. radioélec. compagn. franc. assoc. T.S.F. **3**, 259 (1948).

[9] Birdsall, Brewer, and Haeff, Proc. Inst. Radio Engrs. **41**, 865 (1953).

v_0. This condition is made a possible one by certain additional assumptions. Sufficient positive ions are supposed to be contained in the beam to nullify the average current. Assuming small signal theory, let us define our field quantities as follows:

$$\begin{aligned}\mathbf{v}&=\mathbf{a}_z v_0+\mathbf{v}_1 e^{j(\omega t-\beta z)}\\ \mathbf{H}&=\mathbf{a}_y H_0+\mathbf{h}e^{j(\omega t-\beta z)}\\ \mathbf{E}&=\mathbf{a}_z E_0+\mathbf{E}_1 e^{j(\omega t-\beta z)}\\ \rho&=\rho_0+\rho_1 e^{j(\omega t-\beta z)}\\ \mathbf{E}_0&=\mu v_0 H_0,\end{aligned} \tag{1}$$

where $\mathbf{v}$ is the velocity of the electrons, $\mathbf{E}$ and $\mathbf{H}$ are the electric and magnetic fields vectors, respectively, ρ is the charge density, and $\mathbf{a}_z$, $\mathbf{a}_y$, and $\mathbf{a}_z$ are unit vectors along the axes of a rectangular coordinate system. v_0, H_0, E_0, and ρ_0 are steady-state quantities, while $\mathbf{v}_1$, $\mathbf{h}$, $\mathbf{E}_1$, and ρ_1, are small ac quantities with $\exp(j(\omega t-\beta z))$ dependence alone. In the relativistic range, subject to the restriction that $|v_1|\ll v_0$ the mass of the electron and the charge density may be considered to depend upon the axial velocity alone Eq. (1), i.e., $m=m_0K$, and $\rho=\rho' K$ where $K=[1-(v_0/c)^2]^{-\frac{1}{2}}$. Other symbols frequently used in this article are:

$\omega_b=\omega-\beta v_0$

$\omega_0^2=e\rho_0/\epsilon m_0$

$\omega_c=\mu H_0 e/m_0$

$\omega_0/\omega=\xi$

$\omega_c/\omega_0=\eta$

$\beta=\beta_0(1+\delta)$; $|\delta|\ll 1$

e = charge of the electron

m_0 = rest mass of the electron

ρ' = charge density in a frame where such charges are at rest

ϵ = permittivity

μ = permeability

$j=\sqrt{-1}$.

For the model described by Eq. (1) it is easy to derive from Maxwell's equations the inhomogeneous wave equations in $\mathbf{h}$ and $\mathbf{E}_1$, which may be written as

$$-\frac{\partial^2\mathbf{h}}{\partial z^2}+\mu\epsilon\frac{\partial^2\mathbf{h}}{\partial t^2}=\nabla\times\rho\mathbf{v} \tag{2}$$

$$-\frac{\partial^2\mathbf{E}_1}{\partial z^2}+\mu\epsilon\frac{\partial^2\mathbf{E}_1}{\partial t^2}=-\nabla\frac{\rho_1}{\epsilon}-\mu\frac{\partial}{\partial t}(\rho\mathbf{v}). \tag{3}$$

By suitable substitution from the Lorentz force equation for the electron there results

$$\left(\frac{K^3\omega_b^2}{\omega_0^2}-1\right)=\left(\frac{\omega_c}{\omega_0}\right)^2\times\left[\frac{\omega_b^2-2\omega\omega_b+(\omega/K)^2}{K\omega_b^2-2K\omega\omega_b+\omega_0^2\left(1-\frac{1}{K^2}\right)+\frac{\omega^2}{K}}\right]. \tag{4}$$

In the special case when the steady-state electron velocity is much smaller than the velocity of light we let $K\rightarrow 1$ and Eq. (4) reduces to

$$\omega_b^2=\omega_0^2+\omega_c^2. \tag{5}$$

It is interesting to remark at this point that Eq. (5) specifies a pair of space-charge waves which reduces to the known pair in the case when $\omega_0^2\ll\omega_c^2$, namely, $\omega_b=\pm\omega_c$. In the case when the steady-state velocity is comparable with the velocity of light Eq. (4) is a quartic in ω_b, since the solution of a quartic equation is a complicated matter in general, we limit ourselves to an investigation of the nature of the roots only. Because we usually deal with cathodes which emit a fixed number of electrons, there corresponds for a "proper" charge density ρ' in a frame where such charges are at rest, a relativistic charge density $\rho=\rho' K$. Also as we chose to use the value of the relativistic charge density in our derivation, it is proper now to refer all quantities to a frame which is at rest. This means that in Eq. (4) we have to let

$$\omega_0^2\rightarrow(\omega_0')^2K.$$

From the theory of a biquadratic equation it may be shown that Eq. (4) has complex roots if the following inequality holds:

$$K^4\left[\left(\frac{\omega_0'}{\omega}\right)^2-\tfrac{3}{2}\right]+K^2\left[1-2\left(\frac{\omega_0'}{\omega}\right)^2\right]-\left(\frac{\omega_c}{\omega}\right)^2>0. \tag{6}$$

It is evident that Eq. (6) is only valid when the charge density is large.

Thus the foregoing approximate analysis shows that it is possible for growing plane waves to propagate, if the charge density and the electron velocity are large enough, conditions which might be difficult to obtain practically. Bailey[10] has already demonstrated that in an ionized medium moving with a velocity comparable with the velocity of light, growing ac perturbations are possible in the presence of general static electric and magnetic fields.

It is of interest to find how the space-charge waves will be modified if the electron stream is made to flow with a velocity much smaller than the velocity of light through a porous resistive medium pervaded by crossed focusing electric and magnetic fields. If we restrict ourselves to the same assumptions made by Birdsall[9] in his one-dimensional treatment of the resistive wall amplifier with an infinite focusing longitudinal magnetic field, it is easy to derive that for the resistive-wall amplifier with crossed focusing electric and magnetic fields

$$\omega_b^2=\omega_c^2+\frac{\omega_0^2}{\left(1-j\frac{\sigma}{\omega\epsilon}\right)}. \tag{7}$$

[10] V. A. Bailey, Phys. Rev. 83, 489 (1951).

If $\omega_0^2 \ll \omega_c^2$, then, Eq. (7) reduces to

$$\omega_b \simeq \pm\omega_c\left[1+\tfrac{1}{2}\left(\frac{\omega_0}{\omega_c}\right)^2\left[\frac{1}{1+\dfrac{\sigma^2}{\epsilon^2\omega^2}}\right]\left(1+j\frac{\sigma}{\omega\epsilon}\right)\right]. \quad (8)$$

It is evident that Eq. (8) represents a pair of space-charge waves, one growing and the other decaying. The gain specified by Eq. (8) may be varied over a wide range by simply varying the transverse focusing magnetic field as an independent parameter. It is, however, always smaller than the gain obtainable from Birdsall's analysis for the resistive-wall amplifier.

III. SPACE-CHARGE WAVES IN AN ELECTRON STREAM HAVING A DRIFT VELOCITY OBLIQUE TO THE DIRECTION OF PROPAGATION

In their study of plane waves in an ionized gas, with and without static magnetic and electric fields present first Bailey[11] and then Roberts[12] appeared to believe that even when the stream velocity is much smaller than the velocity of light, growing plane space-charge waves can be made to propagate along the stream. In a brief note Walker[13] has pointed out that such is not the case. Bailey conceded that his theory was in error and worked out a new theory where relativistic effects were taken into consideration.

If we define our field quantities as follows:

$$\begin{aligned}
\mathbf{v} &= \mathbf{a}_x v_{02} + \mathbf{a}_z v_{01} + v_1 e^{j(\omega t-\beta z)} \\
\mathbf{H} &= \mathbf{a}_y H_0 + \mathbf{h} e^{j(\omega t-\beta z)} \\
\mathbf{E} &= \mathbf{a}_z E_{02} - \mathbf{a}_z E_{01} + \mathbf{E}_1 e^{j(\omega t-\beta z)} \\
\rho &= \rho_0 + \rho_1 e^{j(\omega t-\beta z)} \\
E_{01} &= -\mu v_{02} H_0 \\
E_{02} &= \mu v_{01} H_0,
\end{aligned} \quad (9)$$

then it may be shown that for a neutralized stream of electrons drifting with a velocity much smaller than the velocity of light in a direction oblique to that of wave propagation, no growing plane waves are possible. The same pair of space-charge waves defined by Eq. (5) is obtained. It has been pointed out to us by L. Brillouin in an informal discussion, that the velocity of the electron stream perpendicular to the direction of propagation of the wave does not affect the nature of the space-charge waves. This becomes apparent, Brillouin mentioned, if one treats the propagation of space-charge waves from a wave mechanics point of view.

IV. TWO-DIMENSIONAL ANALYSIS

In our one-dimensional analysis we have demonstrated the existence of space-charge waves in the presence of crossed focusing electric and magnetic fields.

[11] V. A. Bailey, Australian J. Sci. Research **1**, 351 (1948).
[12] J. A. Roberts, Phys. Rev. **76**, 340 (1949).
[13] L. R. Walker, Phys. Rev. **76**, 1721 (1949).

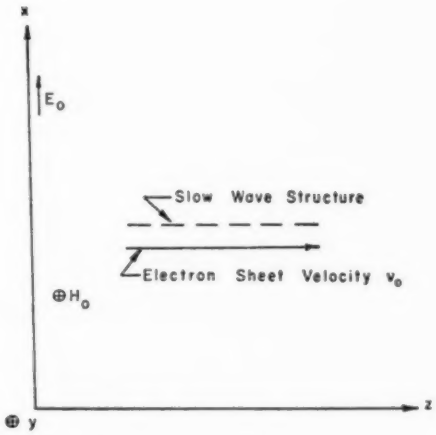

FIG. 1. Electron sheet near a slow wave structure in crossed electric and magnetic fields.

We now proceed to a two-dimensional analysis of the same problem. From energy considerations it is easy to see that there are two different cases possible. Consider a thin plane sheet of electrons, moving with a velocity v_0 in crossed electric and magnetic fields, as shown in Fig. 1, such that $E_0=\mu v_0 H_0$. A slow wave structure is placed near the electron stream.

An electromagnetic wave impressed on the circuit will cause the plane surface of the electron stream to be perturbed. If we assume all ac quantities to have no y, dependence, then the electrons may change their potential energy by approaching or receding from the circuit while their velocity in the direction of propagation remains constant. If on the average the electrons deliver energy to the wave, we have conversion of potential energy into electromagnetic energy. This is actually the physical process by which gain is obtained in the traveling-wave magnetron amplifier.[14] We show later that this is only true when the static magnetic field is large enough.

If in Fig. 1 we interchange the static electric and magnetic fields, such that the electron stream when perturbed will approach and recede from the circuit by moving in a uniform magnetic field, then it is clear that through such a process there can be no conversion of potential energy into electromagnetic energy. Therefore, this is a case different from that of the traveling-wave magnetron tube. However, since our argument does not exclude the possibility of obtaining gain through conversion of kinetic energy into electromagnetic energy, we find it of interest to present the following analysis which yields, indeed, some useful results.

Let a stream of electrons move along the z-axis with a uniform velocity, which may be comparable with the velocity of light, in the presence of crossed static electric and magnetic fields oriented along the x- and y-axes, respectively. We assume that all derivatives in

[14] W. W. Harman, *Fundamentals of Electronic Motion* (McGraw-Hill Book Company, Inc., New York, 1953).

the direction of static electric field to vanish. Such a state of affairs may be expressed mathematically as follows:

$$\begin{aligned}\mathbf{v}&=\mathbf{a}_z v_0+\mathbf{v}_1(y)e^{j(\omega t-\beta z)}\\ \mathbf{H}&=\mathbf{a}_y H_0+\mathbf{h}(y)e^{j(\omega t-\beta z)}\\ \mathbf{E}&=\mathbf{a}_z E_0+\mathbf{E}_1(y)e^{j(\omega t-\beta z)}\\ \rho&=\rho_0+\rho_1(y)e^{j(\omega t-\beta z)}\\ E_0&=\mu v_0 H_0.\end{aligned} \tag{10}$$

The pertinent components of the inhomogeneous wave equations are

$$-\frac{\nabla^2 h_y}{\partial t^2}+\mu\epsilon\frac{\partial^2 h_y}{\partial t^2}=-j\beta\rho_0 v_{1z} \tag{11}$$

$$-\nabla^2 E_{1z}+\mu\epsilon\frac{\partial^2 E_{1z}}{\partial t^2}=-\frac{1}{\epsilon}\frac{\partial\rho_1}{\partial z}-\mu\frac{\partial}{\partial t}(\rho_0 v_{1z}+v_0\rho_1). \tag{12}$$

By making suitable substitutions from the Lorentz force equation and Maxwell's equations, the inhomogeneous parts of Eqs. (11) and (12) may be expressed in terms of the field quantities h_y and E_{1z} alone. Thus, we obtain the following two linear simultaneous differential equations:

$$\frac{d^2 h_y}{dy^2}+A_1 h_y+A_2 E_{1z}=0, \tag{13}$$

where

$$A_1=\left(\mu\epsilon\omega^2-\beta^2+\frac{\mu\epsilon K^2\omega_0^2\omega_b^2}{\omega_c^2-K^4\omega_b^2}\right) \tag{13a}$$

$$A_2=j\frac{\epsilon\beta\omega_c\omega_0^2}{\omega_c^2-K^4\omega_b^2}, \tag{13b}$$

and

$$\frac{d^2 E_{1z}}{dy^2}+A_3 E_{1z}+A_4 h_y=0, \tag{14}$$

where

$$A_3=\left[\mu\epsilon\omega^2-\beta^2+\frac{\mu\epsilon K\omega\omega_b\omega_0^2}{\omega_c^2-K^4\omega_b^2}-\frac{S_2}{\epsilon v_0 K^2}(\omega-K^2\omega_b)\right] \tag{14a}$$

$$A_4=j\left[\frac{S_1}{\epsilon v_0 K^2}(\omega-K^2\omega_b)-\frac{\mu^2\epsilon\omega\omega_b\omega_c\omega_0^2}{\beta(\omega_c^2-K^4\omega_b^2)}\right] \tag{14b}$$

$$S_1=\frac{\mu\epsilon\omega_c\omega_b\omega_0^2[\omega_b K^3(\omega-\omega_b)-\omega_0^2(K^2-1)]}{\beta v_0(\omega_c^2-\omega_b^2K^4)(\omega_b^2K^3-\omega_0^2)} \tag{14c}$$

$$S_2=\frac{\epsilon\omega_0^2[\omega_c^2(\omega-K^2\omega_b)+K\omega_b(K^3\omega_b^2-\omega_0^2)(K^2-1)]}{v_0(\omega_c^2-K^4\omega_b^2)(K^3\omega_b^2-\omega_0^2)}. \tag{14d}$$

The remaining field quantities may be determined in terms of E_{1z} and h_y.

In the formulation of the boundary value problem we restrict ourselves to the case when the electron velocity is much smaller than the velocity of light, i.e., we let $K\to 1$. We assume the following simple model: a sheet beam of electrons extends between $-b<y<b$ in the region bounded at $y=\pm a$ by the slow wave structure formed by slitting a plane conductor with many infinite parallel cuts, making an angle θ with the x-axis as shown in Fig. 2. We need three solutions: one in the region $0<y<b$, a second in the region $b<y<a$, and a third in the region $a<y<\infty$. In the particular case when the electron velocity is much smaller than the velocity of light it is easy to show that $4A_2A_4\ll(A_1-A_3)^2$. Hence an approximate solution to Eqs. (13) and (14) inside the beam may be chosen as follows:

$$h_{y_i}=M\sin k_1 y, \tag{15}$$

$$E_{1z_i}=N\cos k_2 y, \tag{16}$$

where $k_1^2=A_1$, $k_2^2=A_3$, and M and N are arbitrary constants. In the application of the boundary conditions at $y=b$ we make use of Hahn's[1] idea of replacing the perturbed surface at the beam by a sheet of charge, ρ_S, given by

$$\rho_S=-j\frac{\rho_0}{\omega_b}v_{1y}\bigg|_{y=b}. \tag{17}$$

Hence, at $y=b$ the normal component of the electric field is discontinuous while the tangential component of the electric field suffers no discontinuity. Therefore, we must have two different solutions for the TM mode, one valid inside the beam and another in the middle region. However, because the TE mode is the same inside the beam as in free space, we need only one solution up to $y=a$. Suitable solutions in the middle

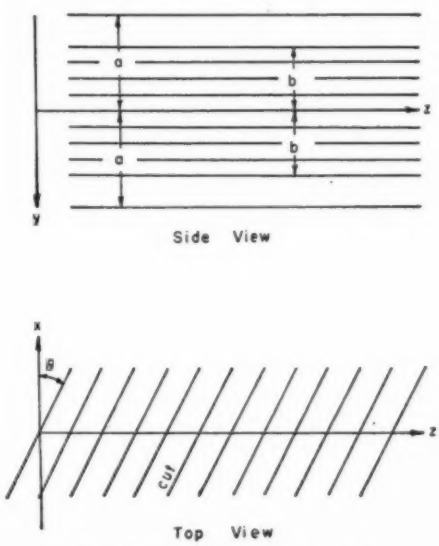

FIG. 2. Two-dimensional model.

region are

$$E_{1z_m}=A_m e^{-\beta y}+R_m e^{\beta y}, \tag{18}$$

$$h_{ym}=h_{yi}. \tag{19}$$

In the region $\infty > y > a$, a solution which satisfies the boundary conditions at $y=a$ and vanishes at infinity may be chosen as follows:

$$E_{1z_0}=D_1 e^{-\beta y} \tag{20}$$

$$h_{z_0}=D_2 e^{-\beta y}. \tag{21}$$

A_m, R_m, D_1, and D_2 are arbitrary constants.

At $y=a$ we apply the usual boundary conditions, namely,

(1) The electric field along the cut vanishes.
(2) The electric field normal to the cut is continuous.
(3) The magnetic field along the cut is continuous.

Application of the boundary conditions at $y=a$ and $y=b$ yields the following characteristic equation:

$$(1+\delta)^2(1+d)^2=\frac{1}{1+\psi e^{2\beta(b-a)}}, \tag{22}$$

where

$$\psi=\frac{\delta(\delta^2-\eta^2\xi^2)^{\frac{1}{2}}-[(\delta^2-\xi^2)(\delta^2-\xi^2-\eta^2\xi^2)]^{\frac{1}{2}}}{\delta(\delta^2-\eta^2\xi^2)^{\frac{1}{2}}+[(\delta^2-\xi^2)(\delta^2-\xi^2-\eta^2\xi^2)]^{\frac{1}{2}}}. \tag{22a}$$

Equation (22) is derived subject to the assumption that

$$\tan^2\theta=\mu\epsilon(v_0{}^1)^2,$$

where

$$v_0{}^1=v_0(1+d);\ d\ll 1 \text{ and } \beta a\gg 1;\ \beta b\gg 1.$$

For a beam filling the region up to a height a and neglecting powers of δ and d higher than the first compared to unity Eq. (22) reduces to

$$1+4(\delta+d)\simeq\frac{1}{\delta}\left[\frac{(\delta^2-\xi^2)(\delta^2-\xi^2-\eta^2\xi^2)}{(\delta^2-\eta^2\xi^2)}\right]^{\frac{1}{2}}; \tag{23}$$

when the magnetic field is large $\eta\xi>\xi$ and Eq. (23) is further simplified to

$$\delta^2(\delta+d)=-\xi^2/8. \tag{24}$$

It is to be remarked that Eq. (24) describes a gain identical to that of a traveling-wave tube with an infinite longitudinal focusing magnetic field. Also when the magnetic field is zero we let $\eta\xi\to 0$ and Eq. (23) reduces to

$$\delta^2(\delta+d)=-\xi^2/4. \tag{25}$$

When the magnetic field is finite Eq. (25) is a quintic and therefore its complete solution is rather complicated. However, the solution to Eq. (24) is very well known and has been solved by Pierce[5] in detail. The solution to Eq. (25) can be easily deduced from that of Eq. (24). We expect the solution for finite magnetic field to be something in between. We thus have described a model for a novel traveling-wave tube with crossed focusing electric and magnetic fields which promises to have a performance almost identical to that of the traveling-wave tube with a longitudinal focusing magnetic field. It is evident that a physical realization of the model we propose is more complicated than that of the conventional traveling-wave tube. However, it has the potential advantage that the magnetic field can be more easily supplied from a permanent magnet.

V. TWO-DIMENSIONAL ANALYSIS OF THE LINEAR MAGNETRON AMPLIFIER

Here we imagine a stream of electrons flowing along the axis with a uniform velocity which may approach the velocity of light. As in the preceding paragraph we assume the medium to be pervaded by crossed static electric and magnetic fields. We study the small signal interaction between an ac electromagnetic field and the stream of electrons assuming all derivatives in the direction of the static magnetic field to vanish. In mathematical terms our field quantities may be written as follows:

$$\begin{aligned}\mathbf{v}&=\mathbf{a}_z v_0+\mathbf{v}_1(x)e^{j(\omega t-\beta z)}\\ \mathbf{H}&=\mathbf{a}_y H_0+\mathbf{h}(x)e^{j(\omega t-\beta z)}\\ \mathbf{E}&=\mathbf{a}_z E_0+\mathbf{E}_1(x)e^{j(\omega t-\beta z)}\\ \rho&=\rho_0+\rho_1(x)e^{j(\omega t-\beta z)}\\ E_0&=\mu v_0 H_0.\end{aligned} \tag{26}$$

For this case it can be shown that the inhomogeneous parts of Eq. (12) may be expressed in terms of E_{1z} alone and that the TM and TE modes do separate. The field components h_y and E_{1x} can be derived in terms of E_{1z} and its derivatives, while the components h_z, h_x, and E_{1y} form an independent set whose differential equation may be readily obtained. The two differential equations which describe our model of the traveling-wave magnetron are thus found to be

$$-\nabla^2 E_{1z}+\mu\epsilon\frac{\partial^2 E_{1z}}{\partial t^2}=\frac{\omega_0^2\left(1-\frac{1}{K^2}\right)(\omega_0^2-K^3\omega_b^2)}{v_0^2(K^4\omega_b^2-K\omega_0^2-\omega_c^2)}E_{1z} \tag{27}$$

$$-\nabla^2 h_z+\mu\epsilon\frac{\partial^2 h_z}{\partial t^2}=-\frac{\mu\epsilon\omega_0^2}{K}h_z. \tag{28}$$

For the boundary value solution using the same model shown in Fig. 2 and applying the same boundary conditions as in Sec. IV we find that, for an electron stream traveling with a velocity much smaller than the velocity of light, the characteristic equation is

$$(1+\delta)^2(1+d)^2=\frac{1}{1+\psi' e^{2\beta(b-a)}}, \tag{29}$$

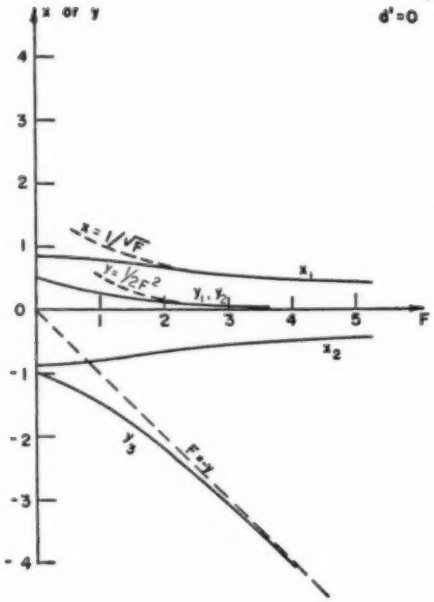

FIG. 3. Graphical solution of Eqs. (32a) and (32b).

where

$$\psi'=\frac{\xi^2}{2\delta^2+2\delta\eta\xi-\xi^2}. \tag{29a}$$

For a beam filling the region up to a height a, Eq. (29) reduces to

$$\delta(\delta+d)(\delta+\eta\xi)=-\xi^2/4, \tag{30}$$

where all powers of δ and d higher than the first are neglected compared to unity. Equation (30) can be handled more conveniently if we make the following substitutions:

$$\begin{aligned}\delta&=(\xi/2)^{\frac{1}{3}}(y+jx),\\ \eta\xi&=(\xi/2)^{\frac{1}{3}}f,\\ d&=(\xi/2)^{\frac{1}{3}}d'.\end{aligned} \tag{31}$$

Hence Eq. (30) becomes

$$y(y+d')(y+f)-x^2(3y+f+d')=-1, \tag{32a}$$

$$x[y(y+d')+y(y+f)+(y+d')(y+f)-x^2]=0. \tag{32b}$$

To find the dependence of the gain on the magnetic field when the electron velocity is in synchronism with the wave velocity, i.e., $d'=0$ Eqs. (32a) and (32b) are solved graphically in Fig. 3. For this particular case when the magnetic field is large Eq. (30) reduces to

$$y\simeq\frac{1}{2f^2};\quad x^2=\frac{1}{f}. \tag{33}$$

Additional solutions of the x part of Eqs. (32a) and (32b) when $f=0$, 1, 2, and 4 are given in Fig. 4 showing the variation of the gain as a function of d'. We deduce from Eq. (30) that if the magnetic field is large, i.e., $\delta\ll\eta\xi$; $d\ll\eta\xi$, then very approximately:

$$\frac{(d')^2}{(4/f)}+\frac{x^2}{1/f}=1. \tag{34}$$

From Eq. (34) we see that varying the wave velocity with respect to the electron velocity when the magnetic field is large will result in the gain describing an ellipse centered at the origin.

At the beginning of the preceding paragraph we mentioned that the physical process by which gain is obtained in the magnetron type traveling-wave tube is through conversion of potential energy into electromagnetic energy. Because at any instant there is a charge q moving in the x-direction in an electric field E_0 then the work done per second is qE_0v_{1x}. At the same time the same charge moves in the z-direction with velocity v_0 in an electric field E_{1z} doing, or having work done on it, at the rate of $qE_{1z}v_0$. Assuming $\delta\ll\eta\xi$ and substituting for E_{1z} and v_{1x} their values at $x=a$, it may be shown that

$$qE_0v_{1x}\big|_{x=a}=-qv_0E_{1z}\big|_{x=a}. \tag{35}$$

Equation (35) is equivalent to saying that the rate of potential energy lost by the electrons is equal to the rate of energy carried by the wave.

VI. BACKWARD WAVE OSCILLATIONS

In this paragraph we extend our analysis to the study of the propagation of backward waves in our prototype model of Fig. 2. We limit ourselves to a discussion analogous to that made by Pierce,[5] for the traveling-wave tube with a longitudinal focusing magnetic field.

Let us assume that at $z=0$ an unmodulated beam of electrons is injected into the circuit, and at a distance l to the right of the origin we apply a voltage, V_l, to the circuit. We assume, furthermore, that the circuit is terminated at $z=l$ so that power can only flow to the left. If at $z=0$ and $x=a$ the voltages associated with the waves are V_{01}, V_{02}, and V_{03}, respectively, and $v_{1z}=\rho_S=0$

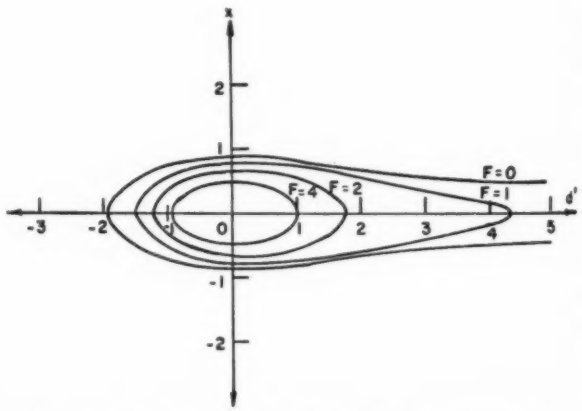

FIG. 4. Gain as a function of the difference between the circuit phase velocity and the electron velocity.

then the characteristic equation which describes the propagation of the backward waves is

$$\frac{V_l}{V_0}e^{j\beta_0 l}=\frac{\delta_1(\delta_1+f)e^{-j\phi\delta_1}}{(\delta_1-\delta_2)(\delta_1-\delta_3)}+\frac{\delta_2(\delta_2+f)e^{-j\phi\delta_2}}{(\delta_2-\delta_1)(\delta_2-\delta_3)}+\frac{\delta_3(\delta_3+f)e^{-j\phi\delta_3}}{(\delta_3-\delta_2)(\delta_3-\delta_1)}, \quad (36)$$

where

$$\phi=\beta_0 l(\xi/2)^{\frac{1}{2}},$$
$$V_0=V_{01}+V_{02}+V_{03},$$

for the special case of large magnetic field Eq. (36) reduces to

$$\frac{V_l}{V_0}e^{j\beta_0 l}=\frac{1}{\delta_1-\delta_2}(\delta_1 e^{-j\phi\delta_1}-\delta_2 e^{-j\phi\delta_2}). \quad (37)$$

In order that our model may operate as a backward wave oscillator we must have $|V_l/V_0|=0$; thus we deduce from Eq. (37) that for backward wave oscillations to start in the presence of a large magnetic field we must have:

$$\cosh\left\{\frac{\phi}{2}[(4/f)-(d')^2]^{\frac{1}{2}}\right\}=\frac{f^{\frac{1}{2}}d'}{2}. \quad (38)$$

It is easy to see that Eq. (38) cannot be satisfied for real values of the parameters. Hence, we have shown that backward wave oscillations are not likely to start in the presence of a large magnetic field in the traveling-wave magnetron tube. However, if we make a comparison with Pierce's discussion on backward wave oscillations, it becomes evident that our tube may oscillate when the magnetic field is made zero. To determine the value of the magnetic field which will make backward-wave oscillations unlikely we have solved Eq. (36) for $\phi=2$ and $f=0$, 1, 2, and 4, respectively. The results are plotted in Fig. 5 from which it is evident that for $f>2$ backward-wave oscillations are unlikely to occur. An important tube called the Carcinatron has been developed in France[15] in which these oscillations have been observed experimentally and predicted theoretically.

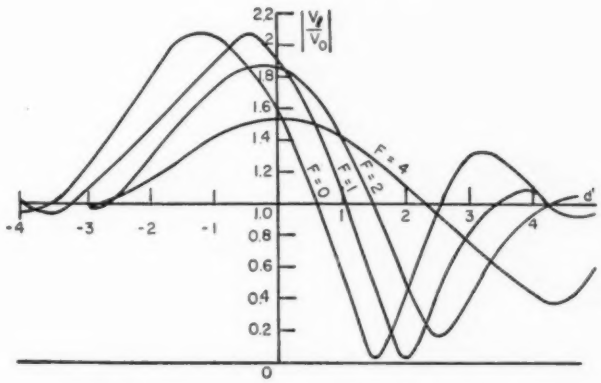

FIG. 5. Graphical solution of Eq. (36) for $\phi=2$ and $f=0,1,2$, and 4, respectively.

ACKNOWLEDGMENTS

The author would like to express his sincere thanks and gratitude to Professor J. R. Whinnery for his helpful suggestions and continuous encouragement to him.

[15] R. R. Warnecke, Ann. radioélec. compagn. franc. assoc. T.S.F. 9, 107 (1954).

Theory of Scattering by an Inhomogeneous Solid Possessing Fluctuations in Density and Anisotropy

MARTIN GOLDSTEIN AND E. R. MICHALIK
Glass Science Fellowship and Applied Mathematics Division, Mellon Institute, Pittsburgh 13, Pennsylvania
(Received August 10, 1955)

The theory of Debye and Bueche for the scattering of light by an amorphous solid is extended to the case where fluctuations in anisotropy as well as density are considered. A generalized correlation function is defined, which gives the probability of a simultaneous occurrence of fluctuations in polarizability in two volume elements a distance r apart. The fluctuations are specified by the magnitudes of the polarizabilities and the directions of the optic axes. The correlation function is assumed to depend on r, on the angle between the axes of the fluctuations, and on the angle giving the position of the second element with respect to the optic axis of the first. The intensities of the horizontal and vertical components of the scattered light are expressed as integrals over the correlation function of explicit functions of r and the two angles. From the initial slopes and intercepts of the intensities plotted against $\sin^2(\theta/2)$ where θ is the scattering angle, one can obtain average values and average dimensions of the fluctuations, and a measure of the extent to which fluctuations in density and anisotropy are correlated. The theory is applicable to glasses, gels, and liquid crystals.

THIS paper is an extension of the theory of Debye and Bueche[1] for scattering by an inhomogeneous solid to include the possibility of fluctuations in anisotropy as well as density.

As a pattern for the development to follow, we summarize briefly their treatment, which considers density (or refractive index) fluctuations alone. The scattering medium (a glass, gel, liquid crystal, or polymer) is assumed to have an average dielectric constant ϵ on which are imposed local fluctuations η. A correlation function $\gamma(r)$ is defined that gives the mean value of simultaneous fluctuations η_1 and η_2 in dielectric constant at two volume elements a distance r apart. This function is, by its definition, a function of r, that goes to zero at large values of r. They (and we) use the Rayleigh-Gans-Born (RGB) assumption that the incident beam is propagated, unperturbed by the fluctuations, with a velocity determined by the macroscopic refractive index of the medium. The limitations of this assumption will be discussed later.

The intensity of scattered light is then shown to be proportional to the integral $\int(\sin krs/krs)\gamma(r)4\pi r^2dr$ where $k=2\pi/\lambda$, $s=2\sin(\theta/2)$, with λ the wavelength of the light (in the medium) and θ the angle between the direction of propagation of the incident beam and the direction of observation.

Experimental data may be interpreted, using this theory, in three ways. First, the correlation function $\gamma(r)$ may be expressed formally as an integral transform of the scattered intensity. It is well known, though, that the inversion of the intensity to obtain $\gamma(r)$ requires experimental data of greater range and precision than is usually available from light scattering. Second, a form for $\gamma(r)$ may be assumed, and a theoretical curve for scattered intensity may be calculated, with which the observed scattering may be compared. A third method, appropriate when the size of the fluctuations is small, is to expand the function $(\sin krs/krs)$ in a power series, then integrate the successive terms over $\gamma(r)$. The result is an even power series in ks, the coefficients of the nth term depending on the $2n$th moments of r over $\gamma(r)$:

$$\langle r^{2n}\rangle=\int r^{2n}\gamma(r)4\pi r^2dr.$$

The first term in the series, that independent of ks, can be shown to be proportional to the mean-square fluctuation $\langle\eta^2\rangle$, and the second term has in the coefficient of k^2s^2 the second moment $\langle r^2\rangle$ of $\gamma(r)$. The second moment may be regarded as a kind of radius of gyration of the fluctuations. The higher moments $\langle r^{2n}\rangle$ give more detailed information about the form of $\gamma(r)$, and if a large number of them were available, a picture of $\gamma(r)$ could be obtained.

To extend this theory to include anisotropy fluctuations, a more general correlation function is defined. We deal with polarizability fluctuations rather than dielectric constant fluctuations to be consistent with the language previously used by others in considering the influence of anistropy in light scattering.[2] We assume that the fluctuations are small enough for the relation $\eta_i=4\pi\alpha_i$ to hold. We make the assumption that the local fluctuations have the symmetry of a uniaxial crystal, to avoid a highly cumbersome result. Then the specification of a local fluctuation requires two angles to orient the unique optic axis, plus values for the polarizabilities parallel to and perpendicular to this axis. The correlation function Γ then gives the probability of simultaneous occurrence of two specified fluctuations in two different volume elements.

This function is not quite analogous to Debye's, in that his correlation function gives the mean value of $\eta_1\eta_2$ directly, rather than giving the probability of occurrence of a specified $\eta_1\eta_2$. The relation between our

[1] P. W. Debye and A. M. Bueche, J. Appl. Phys. **20**, 518 (1949).

[2] S. Bhagavantam, *Scattering of Light and the Raman Effect* (Chemical Publishing Company, Inc., Brooklyn, New York, 1942).

Γ and his γ is, except for a constant,

$$\gamma=\int\int \alpha_i\alpha_j\Gamma d\alpha_i d\alpha_j d\delta_i d\delta_j d\theta d\varphi,$$

where $d\theta d\varphi$ denotes integration over all angles, but *not* over r.

We may therefore write the polarizability fluctuation matrix of the ith volume element, expressed in a coordinate system based on the optic axes of this element, as

$$\alpha_i=\begin{bmatrix}\alpha_i-\frac{1}{3}\delta_i & 0 & 0\\ 0 & \alpha_i-\frac{1}{3}\delta_i & 0\\ 0 & 0 & \alpha_i+\frac{2}{3}\delta_i\end{bmatrix}, \qquad (1)$$

where α_i is the fluctuation in mean polarizability at i, and δ_i the fluctuation in anisotropy. If all δ_i were zero, we obtain the Debye-Bueche formula, as will be seen. The location of the jth element with respect to the ith element is given by a distance r_{ij}, and the polar and azimuthal angles θ_i and φ_i, θ_i being measured from the optic axis of the element at i. The orientation of the polarizability axes at j will be given by the angle pair θ_{ij}, φ_{ij}, again using the optic axis of i as polar axis.

In the spirit of the assumption of uniaxial symmetry for the fluctuations, we further assume that the generalized correlation function Γ depends on the coordinates r_{ij}, θ_i, and θ_{ij} only, being independent of φ_i and φ_{ij}. We note, in partial justification, that the interaction energy between two dipoles has this property also.

We take now the well-known expression[3] for the intensity of light scattered from two elements i and j

$$I_{ij}=A_iA_j\cos(k\mathbf{r}_{ij}\cdot\mathbf{s}). \qquad (2)$$

A_i,A_j are the amplitudes (in a particular reference direction) scattered by the i and j elements; they are calculable from the amplitude of the incident beam and the polarizability matrices at i and j. $\mathbf{r}_{ij}$ is the vector from the i to the j particle, and $\mathbf{s}$ is a vector defined as $\mathbf{s}_0-\mathbf{s}_s$, where $\mathbf{s}_0$ is a unit vector in the direction of propagation of the incident beam and $\mathbf{s}_s$ a unit vector in the direction of the scattered beam. Elementary geometrical considerations lead to the relation $s=2\sin(\theta/2)$.

The total scattered intensity is obtained by summing Eq. (2) over all volume elements i and j, and over all values of the polarizabilities.

$$I=\int\cdots\int A_iA_j\cos(k\mathbf{r}_{ij}\cdot\mathbf{s})\Gamma d\tau_i d\tau_j d\alpha_i d\alpha_j d\delta_i d\delta_j. \qquad (3)$$

Throughout this work we will be dealing with a multiplicity of coordinate systems, six to be precise,

[3] R. W. James, *The Optical Principles of the Diffraction of X-Rays* (The MacMillan Company, New York, 1948).

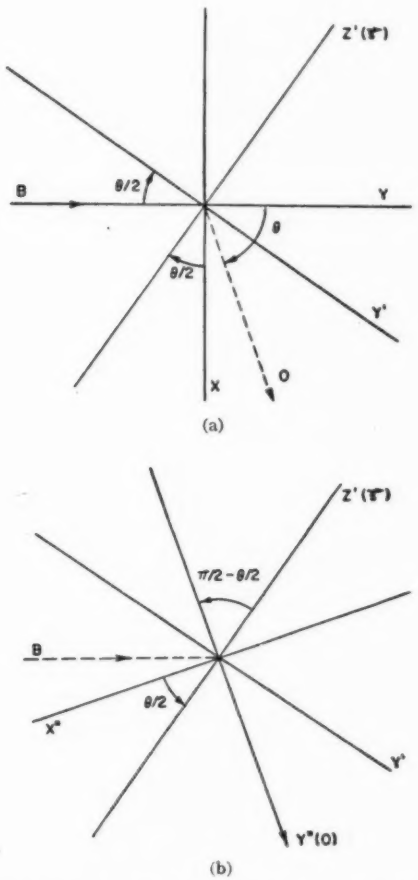

FIG. 1. (a) Relationship between the beam coordinate system and the scattering coordinate system (primed axis). B denotes the direction of the light source. z' is in the direction of the vector $\mathbf{s}$. 0 is in the direction of observation. (b) Relationship between the scattering coordinate system and the observation coordinate system (double primed axes). B and 0 represent, as before, the directions of the light source and of observation, respectively.

and we will endeaver to define them carefully enough to prevent confusion.

(1) The coordinate system of the incident beam. The z-axis is taken vertically, the y-axis as the direction of propagation. The electric vector $\mathbf{E}$ of the incident beam is then either $E_0(1, 0, 0)$ for horizontally polarized light, or $E_0(0, 0, 1)$ for vertically polarized light.

(2) A coordinate system based on the scattering vector $\mathbf{s}$ as a new z-axis [Fig. 1(a)]. The new x-axis is taken vertically. The matrix transforming a vector from the incident beam system to the scattering system is given by

$$M=\begin{bmatrix}0 & 0 & 1\\ \sin\frac{\theta}{2} & \cos\frac{\theta}{2} & 0\\ -\cos\frac{\theta}{2} & \sin\frac{\theta}{2} & 0\end{bmatrix}. \qquad (4)$$

This coordinate system is used to specify the orientation of $\mathbf{r}_{ij}$ in space by the angles θ_r and φ_r; all orientations of $\mathbf{r}_{ij}$ are equally probable, since the system is macroscopically isotropic. $\mathbf{r}_{ij}\cdot\mathbf{s}$ is seen to be given by $r_{ij}s\cos\theta_r$.

(3) A coordinate system based on $\mathbf{r}_{ij}$ as polar axis. The orientation of the unique optic axis at i is given by θ_i measured from $\mathbf{r}_{ij}$, and φ_i measured from an axis perpendicular to $\mathbf{r}_{ij}$ but otherwise arbitrary.

(4) A coordinate system based on the optic axis of i as polar axis. The polarizability matrix of the element i is in its diagonal form in this system. The orientation of the axis of j is given by θ_{ij}, φ_{ij}.

(5) A system in which the polarizability matrix of the element i is in its diagonal form [Eq. (1)]. The transformations 2 to 3, 3 to 4, and 4 to 5 are all given by matrices of the form

$$T=\begin{pmatrix}\cos\theta\cos\varphi & \cos\theta\sin\varphi & -\sin\theta\\ -\sin\varphi & \cos\varphi & 0\\ \sin\theta\cos\varphi & \sin\theta\sin\varphi & \cos\theta\end{pmatrix} \tag{5}$$

with appropriate subscripts r, i, and ij attached to the θ's, φ's, and T. All of these matrices are orthogonal matrices, whose reciprocals are obtained by exchanging rows and columns. Any product of these or their reciprocals, being itself a rotation of coordinates, is also an orthogonal matrix.

(6) The matrix that converts from system 2 to a system based on the direction of observation, in which the z-axis is once more vertical, and the y-axis the direction of propagation of the scattered beam [Fig. 1(b)]. The matrix converting from system 2 to system 6 is given by

$$M'=\begin{pmatrix}0 & -\sin\frac{\theta}{2} & -\cos\frac{\theta}{2}\\ 0 & \cos\frac{\theta}{2} & -\sin\frac{\theta}{2}\\ 1 & 0 & 0\end{pmatrix}. \tag{6}$$

We may now obtain the amplitudes scattered by the i and j elements by expressing the incident beam in the coordinate system of the polarizability matrix, multiply the coordinates of this vector by the components of the polarizability matrix to obtain the vector of the scattered beam, then convert this vector into the observation coordinate system 6. The x- and z-components of the scattered beam give, respectively, the amplitudes of the horizontally and vertically scattered light.

Symbolically:

$$\begin{aligned}\mathbf{A}_i&=M'T_r^{-1}T_i^{-1}\alpha_iT_iT_rM\mathbf{E}\\ \mathbf{A}_j&=M'T_r^{-1}T_i^{-1}T_{ij}^{-1}\alpha_jT_{ij}T_iT_rM\mathbf{E}.\end{aligned} \tag{7}$$

By averaging as in Eq. (3) we obtain the total horizontally and vertically polarized intensities.

The three or four matrix multiplications required to express the incident beam in the coordinate system of the polarizability matrix of the scattering element could of course be represented as a single matrix operation. The formidable character of Eq. (7) is required to obtain the explicit dependence on the angles of which Γ is assumed to be a function.

We note as the first step in evaluating the intensities that the coordinates θ_{ij} and φ_{ij} appear in $\mathbf{A}_j$ only, and that therefore we may perform the averaging over φ_{ij} on the product $T_{ij}^{-1}\alpha_jT_{ij}$. On integrating the elements of this product over $d\varphi_{ij}$ from 0 to 2π, it is reduced to diagonal form:

$$\int_0^{2\pi}T_{ij}^{-1}\alpha_jT_{ij}d\varphi_{ij}=\pi\begin{pmatrix}2\alpha_j-\delta_j(\cos^2\theta_{ij}-\frac{1}{3}) & 0 & 0\\ 0 & 2\alpha_j-\delta_i(\cos^2\theta_{ij}-\frac{1}{3}) & 0\\ 0 & 0 & 2\alpha_j+2\delta_j(\cos^2\theta_{ij}-\frac{1}{3})\end{pmatrix}. \tag{8}$$

We see that both $\mathbf{A}_i$ and $\mathbf{A}_j$ are given by expressions of the form

$$\mathbf{A}_l=M'T_r^{-1}T_i^{-1}\alpha_lT_iT_rM\mathbf{E}=M'P_lM\cdot\mathbf{E} \tag{9}$$

with α_l of the form

$$\begin{pmatrix}X_l-Y_l & 0 & 0\\ 0 & X_l-Y_l & 0\\ 0 & 0 & X_l+2Y_l\end{pmatrix}.$$

l can be either i or j. α_l can be expressed as the sum of two matrices, one of which is a constant:

$$\alpha_l=X_l\begin{pmatrix}1&0&0\\0&1&0\\0&0&1\end{pmatrix}+Y_l\begin{pmatrix}-1&0&0\\0&-1&0\\0&0&2\end{pmatrix}. \tag{10}$$

Let us abbreviate T_iT_r as Q, $T_r^{-1}T_i^{-1}$ as Q^{-1}. Clearly the operation of the identity matrix on Q, followed by multiplication by Q^{-1}, gives the identity matrix back again:

$$Q^{-1}\cdot\alpha_l\cdot Q=X_l\begin{pmatrix}1&0&0\\0&1&0\\0&0&1\end{pmatrix}+Y_lQ^{-1}\begin{pmatrix}-1&0&0\\0&-1&0\\0&0&2\end{pmatrix}Q.$$

TABLE I. The table gives those elements and products of elements of the matrix R [defined in Eq. (11)] which arise in the multiplications of Eq. (15) and do not vanish on averaging.[a]

$\langle R_{11}\rangle_{Av}=\langle q_{31}^2\rangle_{Av}$	$\langle R_{22}\rangle_{Av}=\langle q_{32}^2\rangle_{Av}$	$\langle R_{33}\rangle_{Av}=\langle q_{33}^2\rangle_{Av}$
2002 | 2200	2002 | 0220	0022 | 0200
0002 | 0022	0002 | 2002	2200 | 0000
0220 | 2000	0220 | 0020	

$\langle R_{11}^2\rangle_{Av}=\langle q_{31}^4\rangle_{Av}$	$\langle R_{22}^2\rangle_{Av}=\langle q_{32}^4\rangle_{Av}$	$\langle R_{33}^2\rangle_{Av}=\langle q_{33}^4\rangle_{Av}$
4004 | 4400	4004 | 0440	0044 | 0400
2004 | 2222 | 6	2004 | 2222 | 6	2222 | 0200 | 6
2222 | 4200 | 6	2222 | 0240 | 6	4400 | 0000
0004 | 0044	0004 | 4004	
0222 | 2022 | 6	0222 | 2022 | 6	
0440 | 4000	0440 | 0040	

$\langle R_{12}^2\rangle_{Av}=\langle q_{31}^2q_{32}^2\rangle_{Av}$	$\langle R_{13}^2\rangle_{Av}=\langle q_{31}^2q_{33}^2\rangle_{Av}$	$\langle R_{22}R_{33}\rangle_{Av}=\langle q_{32}^2q_{33}^2\rangle_{Av}$
4004 | 2420	2024 | 2400	2024 | 0420
2004 | 4202	4202 | 2200	4202 | 0220
2222 | 2220 | 6	0024 | 0222	2222 | 0220 | −4
2004 | 0242	2202 | 0022	0024 | 2202
0004 | 2024	0242 | 2200	2202 | 2002
0222 | 0042	2420 | 2000	0242 | 0220
0222 | 4002	2222 | 2200 | −4	2420 | 0020
0440 | 2020		
2004 | 2222 | −4		
0222 | 2022 | −4		

[a] 0000 | 0000 appears in $P_{11}^{(i)}P_{11}^{(j)}$, $P_{22}^{(i)}P_{22}^{(j)}$, $P_{33}^{(i)}P_{33}^{(j)}$, and $P_{22}^{(i)}P_{33}^{(j)}+P_{22}^{(j)}P_{33}^{(i)}$.

If the fact that the three columns of the orthogonal matrix Q form a set of three orthogonal normalized vectors, as do the three rows, is taken into account,[4] it can easily be shown that

$$Q^{-1}\begin{pmatrix}-1&0&0\\0&-1&0\\0&0&2\end{pmatrix}Q=3\begin{pmatrix}q_{31}^2&q_{31}q_{32}&q_{31}q_{33}\\q_{31}q_{32}&q_{32}^2&q_{32}q_{33}\\q_{31}q_{33}&q_{32}q_{33}&q_{33}^2\end{pmatrix}-\begin{pmatrix}1&0&0\\0&1&0\\0&0&1\end{pmatrix}=3R-I \quad (11)$$

with q_{mn} the mnth element of Q. This gives for P_l [defined in Eq. (9)]:

$$P_l=(X_l-Y_l)I+3Y_lR,$$

Specifically:

$$P_i=(\alpha_i-\tfrac{1}{3}\delta_i)I+\delta_iR$$
$$P_j=[2\pi\alpha_j-\pi\delta_j(\cos^2\theta_{ij}-\tfrac{1}{3})]I+3\pi\delta_j(\cos^2\theta_{ij}-\tfrac{1}{3})R. \quad (12)$$

In the cases of incident light vertically polarized, the operation $M'P_lM$ gives rise to a scattered vector

$$\begin{pmatrix}-P_{21}^{(l)}\sin\frac{\theta}{2} & -P_{31}^{(l)}\cos\frac{\theta}{2}\\ P_{21}^{(l)}\cos\frac{\theta}{2} & -P_{31}^{(l)}\sin\frac{\theta}{2}\\ P_{11}^{(l)}\end{pmatrix} \quad (13a)$$

with P_{mn} the mnth component of the P_i or P_j matrix.

Horizontally polarized light gives rise to

$$\begin{pmatrix}-P_{22}^{(l)}\sin^2\frac{\theta}{2}+(P_{23}^{(l)}-P_{32}^{(l)})\sin\frac{\theta}{2}\cos\frac{\theta}{2}+P_{33}^{(l)}\cos^2\frac{\theta}{2}\\ (P_{22}^{(l)}+P_{33}^{(l)})\sin\frac{\theta}{2}\cos\frac{\theta}{2}-P_{23}^{(l)}\cos^2\frac{\theta}{2}-P_{32}^{(l)}\sin^2\frac{\theta}{2}\\ P_{12}^{(l)}\sin\frac{\theta}{2}-P_{13}^{(l)}\cos\frac{\theta}{2}\end{pmatrix} \quad (13b)$$

which with use of the Eqs. (11) and (12) reduces to

$$\begin{pmatrix}-P_{22}^{(l)}\sin^2\frac{\theta}{2}+P_{33}^{(l)}\cos^2\frac{\theta}{2}\\ (P_{22}^{(l)}+P_{33}^{(l)})\sin\frac{\theta}{2}\cos\frac{\theta}{2}-P_{23}^{(l)}\cos^2\frac{\theta}{2}-P_{32}^{(l)}\sin^2\frac{\theta}{2}\\ P_{12}^{(l)}\sin\frac{\theta}{2}-P_{13}^{(l)}\cos\frac{\theta}{2}\end{pmatrix}. \quad (14)$$

This gives for the scattered intensities

$$\begin{aligned}V_v&=\langle P_{11}^{(i)}P_{11}^{(j)}\rangle_{Av}\\ H_v&=\left\langle\left(-P_{21}^{(i)}\sin\frac{\theta}{2}-P_{31}^{(i)}\cos\frac{\theta}{2}\right)\left(-P_{21}^{(j)}\sin\frac{\theta}{2}-P_{31}^{(j)}\cos\frac{\theta}{2}\right)\right\rangle_{Av}\\ V_h&=\left\langle\left(P_{12}^{(i)}\sin\frac{\theta}{2}-P_{13}^{(i)}\cos\frac{\theta}{2}\right)\left(P_{12}^{(j)}\sin\frac{\theta}{2}-P_{13}^{(j)}\cos\frac{\theta}{2}\right)\right\rangle_{Av}\\ H_h&=\left\langle\left(-P_{22}^{(i)}\sin^2\frac{\theta}{2}+P_{33}^{(i)}\cos^2\frac{\theta}{2}\right)\left(-P_{22}^{(j)}\sin^2\frac{\theta}{2}+P_{33}^{(j)}\cos^2\frac{\theta}{2}\right)\right\rangle_{Av}\end{aligned} \quad (15)$$

[4] H. Jeffreys and B. S. Jeffreys, *Methods of Mathematical Physics* (Cambridge University Press, New York, 1946), Chap. 4.

with the symbol $\langle\cdots\rangle_{Av}$ denoting averages of products of elements of P_i and P_j over the correlation function Γ and the factor $\cos(kr_{ij}s\cos\theta_r)$. The capital letters on the left of the above equations denote the scattered intensities observed for the vertical and horizontal directions of polarization; the subscripts denote the polarization of the incident beam.

To obtain the averages the elements of the matrix R of Eq. (11) were obtained by multiplication of the appropriate elements of the matrices Eq. (5). These multiplications were performed by expressing the matrix elements from Eq. (5) in the form of a coded nine digit number, in which the first eight digits represented the power to which the sine or cosine of each angle appeared, and the ninth the numerical factor necessary. The order was $\cos\theta_r\cos\theta_i\sin\theta_r\sin\theta_i|\cos\varphi_r\cos\varphi_i\sin\varphi_r\sin\varphi_i|$factor: for example, an element $-\cos^2\theta_r\sin\theta_i\sin^2\varphi_r$ is coded $2001|0020|-1$. Multiplication is then effected by adding the first eight digits and multiplying the ninth. The averaging over the randomly distributed angles $\varphi_i\varphi_r$, and θ_r is performed by integrations

$$\int_0^\pi\int_0^{2\pi}\int_0^{2\pi}\cdots\cos(kr_{ij}s\cos\theta_r)d\varphi_i d\varphi_r\sin\theta_r d\theta_r.$$

Odd powers of $\sin\varphi$ and $\cos\varphi$ lead to vanishing integrals. By inspection, it is seen that $P_{13}^{(l)}=P_{31}^{(l)}$, $P_{12}^{(l)}=P_{21}^{(l)}$, and by multiplication it is found that $\langle P_{12}^{(i)}P_{13}^{(j)}\rangle_{Av}$ vanishes on averaging. This gives for V_h and H_v

$$V_h=H_v=\langle P_{12}^{(i)}P_{12}^{(j)}\rangle_{Av}\sin^2\frac{\theta}{2}+\langle P_{13}^{(i)}P_{13}^{(j)}\rangle_{Av}\cos^2\frac{\theta}{2}. \quad (16)$$

All elements giving rise to nonvanishing contributions are tabulated in Table I. Integration over θ_r leads to integrals of the form

$$F_m(krs)=\int_0^\pi\cos(krs\cos\theta_r)\cos^{2m}\theta_r\sin\theta_r d\theta_r \quad (17)$$

with $m=0$, 1, or 2. These are readily found to be

$$\begin{aligned}
F_0&=\frac{2}{krs}\sin krs,\\
F_1&=\left(\frac{2}{krs}-\frac{4}{(krs)^3}\right)\sin krs+\frac{4}{(krs)^2}\cos krs,\\
F_2&=\left(\frac{2}{krs}-\frac{24}{(krs)^3}+\frac{48}{(krs)^5}\right)\sin krs\\
&\quad+\left(\frac{8}{(krs)^2}-\frac{48}{(krs)^4}\right)\cos krs.
\end{aligned} \quad (18)$$

It is useful to have series expansions of these integrals; they are found most easily by expanding the $\cos(krs\cos\theta_r)$ term in the integral of Eq. (17) and integrating termwise

$$\begin{aligned}
F_0(x)&=2-\frac{1}{3}x^2+\frac{1}{60}x^4\cdots\\
F_1(x)&=\frac{2}{3}-\frac{1}{5}x^2+\frac{1}{84}x^4\cdots\\
F_2(x)&=\frac{2}{5}-\frac{1}{7}x^2+\frac{1}{108}x^4\cdots.
\end{aligned} \quad (19)$$

Considerations of symmetry require, after averaging over the correlation function Γ, that $\langle\alpha_i\delta_j\rangle_{Av}=\langle\alpha_j\delta_i\rangle_{Av}$.

We obtain, after various algebraic and trigonometric simplifications, the functions listed below. These functions of r_{ij}, θ_{ij}, θ_i, and the polarizabilities, on integration over Γ, give quantities proportional to the ratio of the scattered intensities to the incident intensity, in the same way that $(2\sin krs/krs)$, integrated over γ, gave the ratio of the scattered intensity to the incident intensity at a distance R from the scattering volume V in the Debye-Bueche treatment. A normalization factor of $\pi^4V/16\epsilon^2\lambda^4R^2$ is omitted from the formulas. ϵ=dielectric constant of the medium; λ is the wavelength of light in it. The use of polarizability rather than dielectric constant fluctuations must be remembered here.

$$\begin{aligned}
V_v&=\langle 128F_0\alpha_i\alpha_j\\
&\quad+48F_3(\cos^2\theta_i-\tfrac{1}{3})\alpha_i\delta_j(\cos^2\theta_{ij}+\tfrac{1}{3})\\
&\quad+[49F_0-42F_1+81F_2+(-42F_0+612F_1-810F_2)\\
&\qquad\times\cos^2\theta_i+27F_4\cos^4\theta_i]\tfrac{1}{3}\delta_i\delta_j(\cos^2\theta_{ij}-\tfrac{1}{3})\rangle_{Av},\\
H_v&=V_h=\Big\langle\sin^2\frac{\theta}{2}[(27F_0+18F_1+27F_2)\\
&\quad+(18F_0+108F_1-270F_2)\cos^2\theta_i+9F_4\cos^4\theta_i]\\
&\quad+\cos^2\frac{\theta}{2}[(36F_0+72F_1-108F_2)\\
&\quad+(72F_0-864F_1+1080F_2)\cos^2\theta_i\\
&\qquad-36F_4\cos^4\theta_i]\tfrac{1}{3}\delta_i\delta_j(\cos^2\theta_{ij}-\tfrac{1}{3})\Big\rangle_{Av}, \quad (20)\\
H_h&=\Big\langle V_v\sin^4\frac{\theta}{2}+\{128F_0\alpha_i\alpha_j-96F_3(\cos^2\theta_i-\tfrac{1}{3})\alpha_i\delta_j\\
&\quad\times(\cos^2\theta_{ij}+\tfrac{1}{3})+[88F_0-240F_1+216F_2\\
&\quad+(-240F_0+2016F_1-2160F_2)\cos^2\theta_i\\
&\quad+72F_4\cos^4\theta_i]\tfrac{1}{3}\delta_i\delta_j(\cos^2\theta_{ij}-\tfrac{1}{3})\}\cos^4\frac{\theta}{2}\\
&\quad-\{256F_0\alpha_i\alpha_j-48F_3(\cos^2\theta_i-\tfrac{1}{3})\alpha_i\delta_j(\cos^2\theta_{ij}+\tfrac{1}{3})\\
&\quad+[(-88F_0+240F_1-216F_2)\\
&\quad+(240F_0-2016F_1+2160F_2)\cos^2\theta_i\\
&\qquad-72F_4\cos^4\theta_i]\tfrac{1}{3}\delta_i\delta_j(\cos^2\theta_{ij}-\tfrac{1}{3})\}\cos^2\frac{\theta}{2}\sin^2\frac{\theta}{2}\Big\rangle_{Av},
\end{aligned}$$

with

$$F_3=F_0-3F_1$$

$$F_4=3F_0-30F_1+35F_2$$

$$F_3(x)=\frac{4}{15}x^2-\frac{2}{105}x^4+\cdots$$

$$F_4(x)=\frac{16}{945}x^4+\cdots.$$

We see that the scattering due to fluctuations in anisotropy enters through the expression $\delta_i\delta_j(\cos^2\theta_{ij}-\frac{1}{3})$, which contains explicit dependence on the extent of correlation between the optic axes of fluctuations in neighboring volumes. Likewise, we find a scattering dependent on the extent to which fluctuations in anisotropy and density are correlated. This factor, $(\cos^2\theta_{ij}+\frac{1}{3})\alpha_i\delta_j(\cos^2\theta_i-\frac{1}{3})$, contains explicit dependence on both the correlation between optic axes and the shape of the fluctuation. We note further that H_v depends only on anisotropy fluctuations. For 90° scattering, H_v is found to be

$$H_v(\text{at } 90°)=\Big\langle\tfrac{1}{2}[63F_0+90F_1-81F_2$$

$$+(90F_0-756F_1+810F_2)$$

$$\times\cos^2\theta_i-27F_4\cos^4\theta_i]\frac{\delta_i\delta_j}{3}(\cos^2\theta_{ij}-\tfrac{1}{3})\Big\rangle_{Av}. \quad (21)$$

At 90° H_h turns out to depend only on anisotropy fluctuations.

$$H_h(\text{at } 90°)=\Big\langle\tfrac{1}{4}[225F_0-522F_1+513F_2$$

$$+(-522F_0+4644F_1-5130F_2)$$

$$\times\cos^2\theta_i+171F_4\cos^4\theta_i]\frac{\delta_i\delta_j}{3}(\cos^2\theta_{ij}-\tfrac{1}{3})\Big\rangle_{Av}. \quad (22)$$

We now take up several special cases of interest. First of all, let us consider the situation when the fluctuations have a constant strength and orientation up to their boundaries. For this case $\cos^2\theta_{ij}=1$ within the fluctuation, and the factor $(\delta_i\delta_j/3)(\cos^2\theta_{ij}-\frac{1}{3})=(2/9)\delta^2$. Similarly $\alpha_i\alpha_j=\alpha^2$ and $\alpha_i\delta_j(\cos^2\theta_{ij}+\frac{1}{3})=(4/3)\alpha\delta$. In this form the theory is formally valid for some solutions of large molecules possessing anisotropy, but not for moderately flexible chain molecules in which the chain elements possess anisotropy. In this case Eqs. (20) are of course still formally correct.

For certain shapes of fluctuations satisfying the restrictive conditions of the preceding paragraph, we can evaluate the mean values of $\cos^2\theta_i$ and $\cos^4\theta_i$ readily: for a sphere

$$\langle\cos^2\theta_i\rangle_{Av}=\int_0^\pi\cos^2\theta_i\sin\theta_i d\theta_i\Big/\int_0^\pi\sin\theta_i d\theta_i$$

$$=\tfrac{1}{3},\quad\langle\cos^4\theta_i\rangle_{Av}=1/5,$$

for an anisotropic rod $\langle\cos^2\theta_i\rangle_{Av}=\langle\cos^4\theta_i\rangle_{Av}=1$, and for an anisotropic disk, whose unique axis is perpendicular to the plane of the disk $\langle\cos^2\theta_i\rangle_{Av}=\langle\cos^4\theta_i\rangle_{Av}=0$.

$\Gamma(r)$, after the substitutions indicated in the two preceding paragraphs, is the ordinary pair distribution function for spheres, rods, or disks, as the case may be, and the scattering function for anisotropic particles of these shapes may in principle be found by the appropriate integration. These functions for rods[5] and spheres[6] have already been found by more direct methods than by the use of this theory, which pays a price in cumbersomeness for its generality.

When the fluctuations are small, the RGB approximation is most likely to be valid. An experimental criterion for its validity will be discussed later. It is just under the condition of small fluctuations that the power series expansions are permitted, and a great deal of simplicity is introduced.

We note however that the intensities H_v and H_h depend on $\sin^2(\theta/2)$ both implicitly, through μ, and explicitly. While in principle it is possible to separate the two dependencies from measurements of angular dependence, it seems to us likely that the explicit dependence will always be the stronger, and the separation would require unusual experimental precision. However, at specified values of θ, μ can be varied by varying λ. We give therefore series expansions for V_v (which is not explicitly dependent on θ) and for H_h and H_v only at 90 degrees. We find thus:

$$V_v=\Big\langle\alpha_i\alpha_j\Big(256-\frac{128}{3}x^2+\frac{32}{15}x^4+\cdots\Big)$$

$$+\alpha_i\delta_j(\cos^2\theta_{ij}+\tfrac{1}{3})(\cos^2\theta_i-\tfrac{1}{3})\Big(\frac{64}{5}x^2-\frac{32}{35}x^4+\cdots\Big)$$

$$+\tfrac{1}{3}\delta_i\delta_j(\cos^2\theta_{ij}-\tfrac{1}{3})\Big[\Big(\frac{512}{5}-\frac{2048}{105}x^2+\frac{16}{15}x^4-\cdots\Big)$$

$$+\cos^2\theta_i\Big(\frac{256}{35}x^2-\frac{32}{35}x^4+\cdots\Big)$$

$$+\cos^4\theta_i\Big(\frac{16}{945}x^4+\cdots\Big)\Big]\Big\rangle_{Av}. \quad (23)$$

[5] Horn, Benoit, and Oster, J. chim. phys. **48**, 530 (1951).
[6] P. Chatelain, Acta Cryst. **4**, 453 (1951).

At 90°:

$$H_v=\left\langle\frac{\delta_i\delta_j}{3}(\cos^2\theta_{ij}-\tfrac{1}{3})\left[\frac{384}{5}-\frac{96}{7}\left(1-\frac{\cos^2\theta_i}{5}\right)x^2+\left(\frac{24}{35}-\frac{8}{35}\cos^4\theta_i\right)x^4+\cdots\right]\right\rangle_{Av},$$

$$H_h=\left\langle\frac{\delta_i\delta_j}{3}(\cos^2\theta_{ij}-\tfrac{1}{3})\left[\frac{384}{5}-\frac{384}{35}\left(1+\frac{\cos^2\theta_i}{2}\right)x^2+\left(\frac{4}{7}-\frac{8}{35}\cos^2\theta_i+\frac{76}{105}\cos^4\theta_i\right)x^4+\cdots\right]\right\rangle_{Av}. \quad (24)$$

With the aid of the series expansions, we may make several checks on the correctness of the formulas: we find that $V_v=H_h$ at $\theta=0$ or 180°, that $H_v=H_h$ at $\theta=90°$ and $\lambda\to\infty$, and that the formulas reduce to those for the scattering from a gas of anisotropic molecules as $\lambda\to\infty$.

When the fluctuations have constant strength and orientation to their boundaries, we can evaluate the coefficients for certain shapes, as has been done by Gans[7] to the first power in $x^2(x=krs)$. We find for the ratio $\rho_h=H_v/H_h$ to terms of order x^2.

$$\rho_h=\frac{\frac{384}{5}-\left\langle\frac{96}{7}\left(1-\frac{\cos^2\theta_i}{5}\right)x^2\right\rangle_{Av}+\cdots}{\frac{384}{5}-\left\langle\frac{384}{35}\left(1+\frac{\cos^2\theta_i}{2}\right)x^2\right\rangle_{Av}+\cdots}. \quad (25)$$

The cases rod ($\langle\cos^2\theta_i\rangle_{Av}=1$), sphere ($\cos^2\theta_i=1/3$) and disk ($\cos^2\theta_i=0$) give

$$\begin{aligned}\rho_h\text{ rod}&>1,\\ \rho_h\text{ sphere}&=1,\\ \rho_h\text{ disk}&<1.\end{aligned} \quad (26)$$

For the sphere we can compute the x^4 term, using $\langle\cos^4\theta_i\rangle_{Av}=1/5$ and we find

$$\rho_h(\text{sphere})=\frac{\frac{384}{5}+\langle 0.129x^4\rangle_{Av}}{\frac{384}{5}+\langle 0.640x^4\rangle_{Av}}, \quad (27)$$

i.e., the first influence of size on ρ_h of a sphere is to decrease it below unity. This serves to indicate that the effect of anisotropy is to produce more often $\rho_h<1$ rather than the reverse.

We now wish to consider the influence of the breakdown of RGB behavior on scattering. A complete and rigorous solution of the problem of scattering from isotropic spheres was worked out by G. Mie in 1908.[8]

In recent years extensive tables of the functions arising in his theory have been prepared, by Lowan[9] and others. One of the important results of the Mie theory is that the light scattered is partially depolarized, H_h being finite with H_v remaining zero. The effect is greater the greater the size of the sphere, and the greater its refractive index relative to the medium. Some approximate calculations on shapes other than spherical have been carried out by Gans and others.[10] These treatments have been summarized by W. Lotmar.[11] They indicate that deviation from spherical shape results in a finite H_v; however it is extremely small. This suggests that the equations derived here for H_v have a greater range of validity than those for H_h.

It would be desirable to have some method of estimating how much of an observed H_h is the result of anisotropy and how much the result of the influence of the size and relative mean refractive index of the particles.

The condition for the RGB approximation to be valid has been given by Van de Hulst[12] as $(4\pi r/\lambda)(m-1)\ll 1$, with r the sphere radius and m the relative refractive index. There is a difficulty in applying this test however, in that measurement of the scattered light does not permit one to distinguish between the composite effect of the relative refractive index m and the number of fluctuations. r can be determined from the dependence of intensity on angle of observation or wavelength, but for m one can only make such an estimate as seems reasonable for the system under study.

We have therefore sought for criteria that can be applied to the experimental data itself. We had hoped that one would be provided by plotting the values of $\rho_v/\rho_h=H_h/V_v$ as a function of dissymmetry, defined as the ratio of V_v at 45° to V_v at 135°, for spheres of different sizes and refractive indices. This gives an indication of the contribution made to ρ_h by size alone. The data plotted in Fig. 2 were calculated from Lowan's tables, and are approximate, linear interpolation having been used to obtain V_v at 45° and 135° from tabulated values at 40°, 50°, 130° and 140°. However, the values of ρ_v/ρ_h for a given dissymmetry can be seen to depend strongly on the relative refractive index m. In many amorphous solids fluctuations in m of as much as 1.33 in an appreciable volume are unlikely. For ρ_v/ρ_h of the order of a percent or more, and dissymmetry less than 2, RGB theory for H_h should still be valid.

An additional consequence of the Mie theory is that the scattered light is elliptically polarized. We had thought that a test of deviation from the RGB approximation not requiring *a priori* knowledge of m might be

[7] R. Gans, Phys. Zeitschrift **37**, 19 (1936).
[8] G. Mie, Ann. Physik **25**, 377 (1908).
[9] Lowan, "Tables of scattering functions for spherical particles," Natl. Bur. Standards, Appl. Math. Series, 4.
[10] R. Gans, Ann. Physik **62**, 331 (1920); **65**, 97 (1921).
[11] W. Lotmar, Helv. Chim. Acta, **21**, 792 (1938).
[12] H. C. Van de Hulst, in "Optics of spherical particles," *Recherches Astronomiques de L'Observatoire D'Utrecht* (J. F. Duwaer, Amsterdam, 1946).

provided by a measurement of the phase difference (if any) between horizontally and vertically polarized scattered light at some one angle of observation, but examination of Lowan's tables revealed that phase difference is a rapidly oscillating function of particle size even for small radii and low m values. It may be, though, that measurement of ellipticity as a function of scattering angle would provide a test. Experimental methods and theoretical considerations are discussed by Kerker and LaMer.[13] and ellipticity in glasses has been studied by Krishnan[14] and others.[15]

An alternative but tedious test of the validity of the theory may be performed in the following way. Including moments of r_{ij} up to the second, there are six independent quantities that may be determined from experimental data: $\langle\alpha_i\alpha_j\rangle_{Av}$, $\langle\alpha_i\alpha_j r^2\rangle_{Av}$, $\langle(\cos^2\theta_{ij}+\frac{1}{3})\alpha_i\delta_j(\cos^2\theta_i-\frac{1}{3})r^2\rangle_{Av}$, $\langle\delta_i\delta_j(\cos^2\theta_{ij}-\frac{1}{3})\rangle_{Av}$, $\langle\delta_i\delta_j(\cos^2\theta_{ij}-)\frac{1}{3}r^2\rangle_{Av}$, and $\langle\delta_i\delta_j(\cos^2\theta_{ij}-\frac{1}{3})r^2\cos^2\theta_i\rangle_{Av}$. If one measures the three components of the scattered light at any arbitrary angle θ as a function of $(1/\lambda^2)$, it is in principle possible to obtain the intercepts and initial slopes. This would give us six experimental quantities (except at 90°, where the intercepts for H_h and H_v are equal), sufficient to determine the six quantities listed previously. If we made a measurement at a different scattering angle, we sould obtain a new set of values, permitting the self-consistency in the data to be tested.

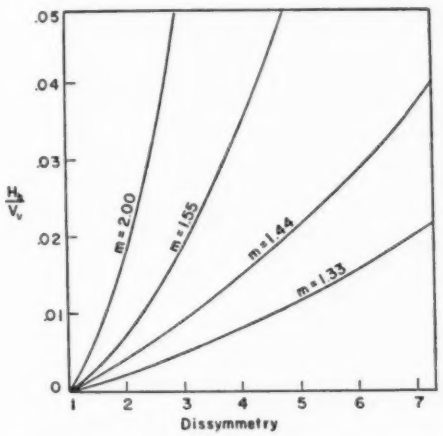

FIG. 2. Ratio of H_h to V_v plotted as a function of dissymmetry for spheres of different relative refractive indices m, from the Mie theory.

[13] M. Kerker and V. K. LaMer, J. Am. Chem. Soc. **72**, 3516 (1950).
[14] R. S. Krishnan and P. Venkata Rao, Proc. Indian Acad. Sci. **A20**, 109 (1944).
[15] A. George, Current Sci. (India) **19**, 239 (1950).

JOURNAL OF APPLIED PHYSICS VOLUME 26, NUMBER 12 DECEMBER, 1955

Low Shear Capillary Viscometer with Continuously Varying Pressure Head

SAMUEL H. MARON AND ROBERT J. BELNER
Department of Chemistry and Chemical Engineering, Case Institute of Technology, Cleveland, Ohio
(Received July 12, 1955)

A capillary viscometer is described for the study of the flow behavior of non-Newtonian fluids at shear stresses of 0.06–20 dynes/cm². The all-glass instrument consists of two units connected by a ball joint, one unit of which contains the capillary while the second is essentially a manometer. As the test fluid moves through the capillary, the rate of rise of the fluid in the manometer is observed. This measurement of the column height as a function of time allows calculation of both pressure drop and rate of flow. Different combinations of capillary and manometer units can be employed interchangeably to study liquids of widely varying viscosities. Data and methods are presented which show that the instrument can be used to determine the absolute viscosities of Newtonian liquids and the flow curves of non-Newtonian fluids over the indicated shear stress region.

INTRODUCTION

MARON, Krieger, and Sisko[1] have described a capillary viscometer with continuously varying pressure head which employs mercury, or liquids of lower density, to drive the test fluids through the capillary. This instrument has proved to be satisfactory for measurements of Newtonian and non-Newtonian liquid systems at shear stresses ranging from about 20 to 800 dynes/cm². At shear stresses below 20 dynes/cm² the errors in the measurement of effective height become more pronounced. Further, it has been observed that at the low shear stresses the interfacial tension between mercury and the water drive fluid seems to appear and give results which are incorrect.

For many rheologic measurements on non-Newtonian systems it is necessary to have a viscometer which will go below the lower limit of the instrument referred to and which will retain to a large degree the absolute character, precision, versatility, and convenience of the continuously varying pressure head viscometer. The instrument described below meets these conditions, and covers a shear stress range of 0.06–20 dynes/cm².

[1] Maron, Krieger, and Sisko, J. Appl. Phys. **25**, 971 (1954).

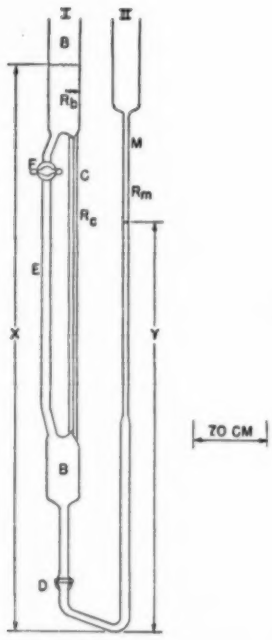

FIG. 1. Diagram of low F_m viscometer.

DESCRIPTION AND OPERATION OF VISCOMETER

Figure 1 shows a sketch of the new apparatus, which is made of glass and is composed of two main parts. Part I is a capillary unit, consisting of a precision-bore capillary C, precision-bore upper and lower bulbs B, and a sidearm by-pass tube E. Part II, in turn, is a manometer unit, which has essentially a precision-bore tube or capillary M. The two units are joined by a ball-and-socket joint at D which is spring clamped, as is also stopcock F.

The instrument is versatile in that various capillary and manometer units can be assembled interchangeably. The proper selection of capillary and manometer unit pairings to be used is governed by two factors, namely, (a) the ratio $(R_c/R_m)^4$, where R_c is the radius of the capillary and R_m that of the manometer, and (b) the viscosity of the fluid to be measured. In the present work $(R_c/R_m)^4$ was arbitrarily kept in all instances below 0.004 in order to make the resistance to flow in the manometer unit negligible compared to that in the capillary. Again, although a particular combination of capillary and manometer is suitable for a given viscosity region, the time for flow may become prohibitive when the viscosity increases. For this reason several combinations of different capillary and manometer units must be used in order to cover the desired range in a reasonable time of measurement. In the present study three different capillary and manometer units were employed in combination but always under conditions where $(R_c/R_m)^4$ was less than 0.004. The upper limit of shear stress of the various capillary-manometer pairings varied from about 11.0 to 20.0 dynes/cm^2.

For operation the units are joined and the assembly held together rigidly by a split-clamp device attached to the upper bulbs. The sample is next introduced through B until, with stopcock F open, the liquid extends approximately 1–2 cm into bulb B. The entire apparatus is then immersed in a constant temperature bath and allowed to come to thermal equilibrium. It is essential that the bath have one face made of a good quality plate glass, as the change of the liquid height in the manometer unit with time is measured with a cathetometer. Optical distortions caused by the glass are very undesirable under such conditions.

After thermal equilibrium has been reached stopcock F is closed, and a slight pressure is applied to the manometer unit to depress slowly the liquid height. When the level of the meniscus in the manometer unit has been lowered about 20–22 cm a short period is allowed for complete drainage, after which the applied pressure is removed, and the liquid level allowed to rise to hydrostatic balance. During this rise, readings at fixed heights are made by cathetometer to the nearest 0.01 cm, and the times corresponding to these are recorded to the nearest 0.1 second. Finally, at the end of the run, stopcock F is opened, and the height of the meniscus in the manometer unit is read. This reading gives the position of hydrostatic equilibrium.

The relationship between the instrumental dimensions and the experimentally measurable quantities can be derived as follows: Referring to Fig. 1, when the sample is flowing through the capillary, and the meniscus is at a point such as y in the manometer, then the pressure drop P across the capillary is

$$P=\rho g(x-y), \tag{1}$$

where ρ = density of fluid and g = gravitational constant. At hydrostatic balance $x=x_0$, $y=y_0$, and $P=0$. Therefore,

$$P=\rho g[(x-x_0)-(y-y_0)]. \tag{2}$$

Since the same volume is flowing through each unit,

$$(x-x_0)=R_m^2/R_b^2(y_0-y),$$

and

$$P=\rho g(y_0-y)[(R_m^2/R_b^2)+1]. \tag{3}$$

If we let now $h=(y_0-y)$, then

$$P=\alpha\rho h \tag{4}$$

where

$$\alpha=g[(R_m^2/R_b^2)+1]. \tag{5}$$

Furthermore, the volume rate of flow Q and the shear stress at the capillary wall F_m are given by

$$Q=-\pi R_m^2 dh/dt, \tag{6}$$

$$F_m=R_cP/2L, \tag{7}$$

TABLE I. Dimensions of capillary and manometer units.

Capillary	R_c (cm)	R_b (cm)	L (cm)	Manometer	R_m (cm)
A	0.02563	1.196	29.22	I	0.1022
B	0.05001	1.191	29.26	II	0.2016
C	0.1022	1.189	29.53	III	0.4194

where L = length of the capillary. Thus, by use of Eqs. (4), (6), and (7) P, Q, and F_m can be determined if h is available as a function of t, and if ρ and the instrumental dimensions are known.

The instrumental dimensions which are required are R_m, R_b, and R_c, and L. The radii were obtained as follows. The capillary, manometer, and bulb B were filled with mercury, and a given length of mercury was removed from these and weighed. The lengths taken were measured to 0.01 cm, and knowing the temperature and weight of mercury, the radii could be calculated. The actual length of the capillaries was measured directly with a cathetometer, and also by resistance measurement with a Mueller bridge on the mercury-filled capillaries when the radii of these were small enough. The direct and the resistance results checked very well. The values of the instrumental dimensions thus obtained for the capillaries and manometers used are listed in Table I.

FLOW OF NEWTONIAN FLUIDS IN VISCOMETER

According to Poiseuille's equation the viscosity η of a Newtonian fluid is given by

$$\eta=\pi R_c^4 P/8LQ. \tag{8}$$

Substituting the expressions for P and Q from Eqs. (4) and (6) we get

$$\eta=-\frac{R_c^4\alpha\rho h}{8LR_m^2(dh/dt)}$$

or

$$\frac{d\log_{10}h}{dt}=m=-\left[\frac{R_c^4\alpha}{8(2.303)LR_m^2}\right]\frac{\rho}{\eta}=-B\left(\frac{\rho}{\eta}\right), \tag{9}$$

where

$$B=\frac{R_c^4\alpha}{8(2.303)LR_m^2}. \tag{10}$$

From Eq. (9) it follows that for a Newtonian fluid a plot of $\log_{10}h$ *vs* t should be linear, and the viscosity should be recoverable from the slope of the line, the density, and the instrumental dimensions.

Typical plots of $\log_{10}h$ *vs* t obtained with Newtonian liquids are shown in Fig. 2. Table II, in turn, shows data observed on the flow behavior of a number of liquids of known viscosity in three different capillary-manometer combinations, the values of B calculated from these by means of Eq. (9), and also the values of B calculated from the instrumental dimensions by means of Eq. (10). The agreement between the experimental and calculated B values is in all instances within 0.40%, and hence within this accuracy the instrument can be used as an absolute viscometer.

TABLE II. Flow data for Newtonian liquids at 30°C.

Viscometer Capillary	Viscometer Manometer	η poises	ρ g/cc	$-m\times10^3$	$B\times10^5$ Exper.	$B\times10^5$ Calculated	% Deviation
A	I	0.007983	0.9957	9.421	7.554		
		0.008473	1.577	14.07	7.559		
					7.557	7.583	−0.34
B	II	0.06247	0.8195	3.753	28.62		
		0.1164	0.8403	2.048	28.36		
					28.49	28.56	−0.24
C	III	0.4073	0.9427	2.896	125.1	125.6	−0.40

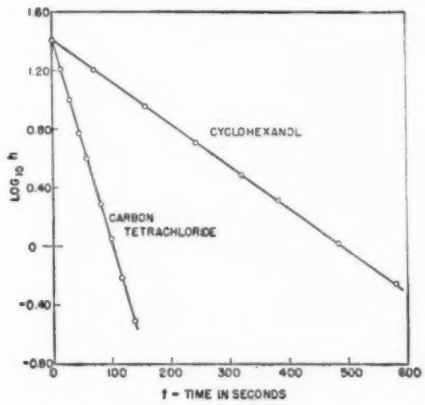

FIG. 2. Typical plots of $\log_{10}h$ *vs* t for Newtonian liquids.

FLOW OF NON-NEWTONIAN FLUIDS IN VISCOMETER

When non-Newtonian fluids are run in the low F_m viscometer, the plots of $\log_{10}h$ *vs* t are nonlinear. Such nonlinear plots can be used to obtain the relation between rate of shear G and shear stress F_m by the method of Krieger and Maron,[1,2] who showed that for capillary viscometers

$$\frac{G}{F_m}=\phi_a\left[1+\frac{1}{4}\frac{d\ln\phi_a}{d\ln F_m}\right], \tag{11}$$

where $\phi_a=1/\eta$ as given by Eq. (9), namely,

$$\phi_a=-\frac{1}{B}\frac{m}{\rho}. \tag{12}$$

Now m is the slope of the $\log_{10}h$ *vs* t plot at any given point on the curve. On substitution of Eq. (12) into Eq. (11) G/F_m becomes, with the aid of Eqs. (4) and (7),

$$\frac{G}{F_m}=\frac{-m}{\rho B}\left[1+\frac{1}{4(2.303)m^2}\frac{dm}{dt}\right]. \tag{13}$$

To convert then the experimental data into G/F_m, the first and second derivatives of the $\log_{10}h$ *vs* t plots are required at various points.

However, many fluids do not show appreciable deviation from Newtonian flow at low shear stresses. For such systems the $\log_{10}h$ *vs* t plots do not give much curvature, as may be seen from the solid line in Fig 3, and hence the foregoing procedure cannot be applied directly with accuracy. To obviate this difficulty, the following treatment of the data was employed. First, a known straight line lying close to the $\log_{10}h$ *vs* t plot,

[2] I. M. Krieger and S. H. Maron, J. Appl. Phys. **23**, 147 (1952); **25**, 72 (1954).

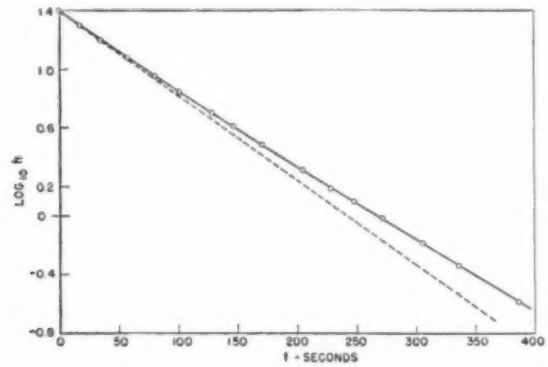

FIG. 3. $\text{Log}_{10}h$ *vs* t plot for a 39.7% solids Latex at 30°C.

such as the dotted line in Fig. 3, was assumed. Next differences, δ, were calculated between the $\log_{10}h$ curve and the assumed line at the experimental values of t. If we designate the equation of the straight line by

$$\log_{10}H = a + bt, \tag{14}$$

where a and b are constants, then

$$\begin{aligned}\delta &= \log_{10}h - \log_{10}H \\ &= \log_{10}h - a - bt.\end{aligned} \tag{15}$$

On differentiation with respect to t we get

$$\frac{d\delta}{dt} = \frac{d\log_{10}h}{dt} - b, \tag{16}$$

and hence

$$\frac{d\log_{10}h}{dt} = m = \frac{d\delta}{dt} + b. \tag{17}$$

Consequently, on plotting δ *vs* t and differentiating the curve at various points, $d\delta/dt$ is obtained; and, this quantity added to b yields m. The latter quantity can then be plotted directly against t to obtain the second derivative.

Figure 4 shows a plot of δ *vs* t for the same data as given in Fig. 3. The curvature is now more pronounced, and hence the differentiation is easier. Furthermore, since $d\delta/dt$ is a correction to b, the differentiation need not be performed as accurately as in the direct determination of m from the $\log_{10}h$ *vs* t plots.

In Fig. 5 is given the plot of G/F_m *vs* F_m deduced in this manner from the data given in Fig. 3. For a Newtonian fluid this plot would be a straight line parallel to the abscissa. Here, however, the latex shows Newtonian flow only up to a shear stress of about two dynes/cm², and non-Newtonian behavior at higher stresses. A more detailed discussion of these and similar results at low shear stresses will be given in a future publication.

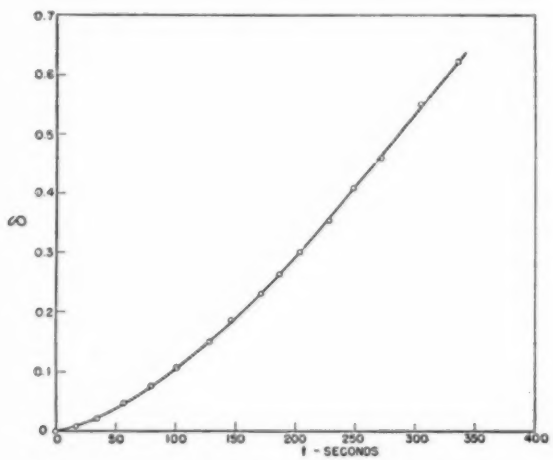

FIG. 4. δ *vs* t plot for 39.7% solids Latex at 30°C.

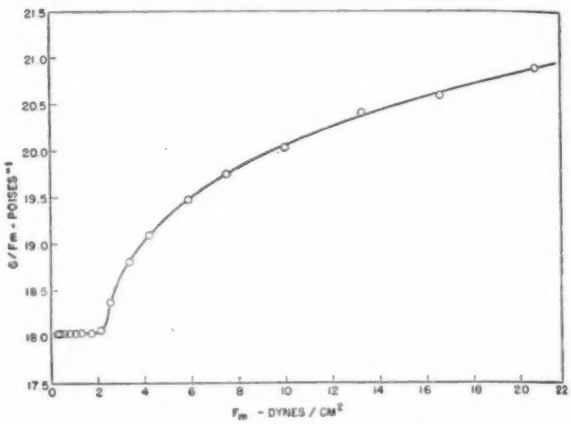

FIG. 5. G/F_m *vs* F_m plot for 39.7% solids Latex at 30°C.

CONCLUSIONS

The data presented in this paper show that the capillary viscometer described for use at low shear stresses is capable of giving excellent results with both Newtonian and non-Newtonian fluids. For Newtonian fluids the viscometer can be used as an absolute instrument with an accuracy of 0.4% or better. For non-Newtonian fluids the data can be used to obtain the flow curve at shear stresses which, depending on the assembly used, range from $F_m = 0.06$ to $F_m = 20$ dynes/cm².

ACKNOWLEDGMENTS

This work was performed as part of a research project sponsored by the Office of Synthetic Rubber, Federal Facilities Corporation, in connection with the Government Synthetic Rubber Program.

JOURNAL OF APPLIED PHYSICS VOLUME 26, NUMBER 12 DECEMBER, 1955

Space-Charge Effects in Electron Optical Systems

K. T. DOLDER* AND O. KLEMPERER
Imperial College, University of London, London, England

(Received May 31, 1955)

Beams consisting of charged particles which are all directed towards a given virtual focus will generally not reach this focus but, due to their mutual repulsion, they will pass through a waist and then become divergent. Ray tracing shows that either positive or negative spherical aberration is introduced in a beam passing through a waist. This aberration is caused by the interaction of the electrons; its sign depends on voltage, current, and on the angle of initial convergence of the beam. For sufficiently high voltages or low currents, waist formation no longer occurs, but the electron rays cross the axis of the beam. With decreasing current density, the transition from waist to crossover is found to occur first for the inner rays of the beam while the outer rays still form a waist. All experimental results are found to be in approximate agreement with theoretical predictions.

1. INTRODUCTION

THE spreading of an electron beam due to its own space charge has been discussed by Watson[1], Thompson and Headrick,[2] Field, Spangenberg, and Helm,[3] and many other authors. In the theoretical analysis the beam is usually treated as a continuous flow of electric charge. Under this assumption it is found that the rays in an initially homogeneous, homocentric, convergent beam of circular cross section could never cross the axis; they would approach the axis, reach a minimum distance from it, the so called "waist," and then would spread again under the influence of their mutual repulsion. Waist formation is believed to occur in beams of high current density, such as are used, for instance, in klystron tubes. On the other hand, in every electron optical image-projection, for instance, in the electron microscope, an inverted image is observed; this implies that the rays must have formed a true crossover.

Barford and Klemperer (see Klemperer[4]) pointed out that the continuum theory of space charge is expected to fail when the waist radius decreases below a certain critical value which should be of the order of the mutual distance of the electrons in the beam. On this assumption the ray in an aberration-free, convergent electron beam of circular cross section is expected to cross over when

$$\left(0.3\times10^{12}y\frac{I}{V^{\frac{1}{2}}}\right)\exp\left(-33\times10^{-6}\frac{\Theta^2V^{\frac{1}{2}}}{I}\right)\leqq1 \qquad (1)$$

where y is the initial semiaperture of a ray with a slope-angle Θ, I is the current flowing in that inner part of the beam which contains the above ray in its envelope, and V is the voltage corresponding to the initial electron energy.

Experimental evidence will be given below that in convergent beams of very low current density all electrons cross the axis. With increased current, a transitional state is observed in which the inner beam electrons still cross over while the outer beam electrons already form a waist. With further increase in current, the transition region moves more and more inwards until practically the whole beam passes through a waist.

The waist of a convergent electron beam corresponds to the disk of least confusion of the *actual* beam focus. This waist, however, must be distinguished from the *virtual* focus towards which the rays are aiming while they pass through a given aperture. Only for beams of very small current density are both foci identical. According to Klemperer[4] the coordinates of the waist (Z_W) and of the virtual focus (Z_{FA}) with respect to the axial coordinate Z_A of a given entrance aperture of the beam are given by the relation

$$\frac{z_W-z_A}{z_{FA}-z_A}=-\frac{2\sqrt{\sigma}\,D(\sqrt{\sigma})}{\exp\sigma} \qquad (2)$$

where

$$\sigma=2\epsilon\pi\left(\frac{2e}{m}\right)^{\frac{1}{2}}\frac{V^{\frac{1}{2}}}{I}\tan^2\Theta=33\times10^{-6}\frac{V^{\frac{1}{2}}}{I}\tan^2\Theta \qquad (3)$$

and where the dielectric constant ϵ, the specific electron charge e/m, the beam current I, and the voltage V are all expressed in rationalised mks units. The "Dawson function" D is given by

$$D(x)=\int_0^x\exp\zeta^2d\zeta \qquad (4)$$

and its values can be found in tables (e.g., Jahnke and Emde[5], or Terrill and Sweeny[6]).

A curve presenting Eq. (2) is plotted in Fig. 1. Auxiliary sketches 1(a), 1(b), 1(c), and 1(d) in this figure show four characteristic stages of the initially convergent electron beam. In each sketch is drawn the

* Now at the Atomic Energy Research Establishment, Harwell, Didcot, Berkshire, England.

[1] E. E. Watson, Phil. Mag. **3**, 849 (1927).

[2] B. J. Thompson and L. B. Headrick, Proc. Inst. Radio Engrs. **28**, 319 (1940).

[3] Field, Spangenberg, and Helm, Elec. Commun. **24**, 108 (1947).

[4] O. Klemperer, *Electron Optics* (The Cambridge University Press, London, England, 1953), second edition.

[5] E. Jahnke and F. Emde, *Tables of Functions* (New York, 1945).

[6] H. M. Terrill and L. Sweeny, J. Franklin Inst. **237**, 495 and 238, 220 (1944).

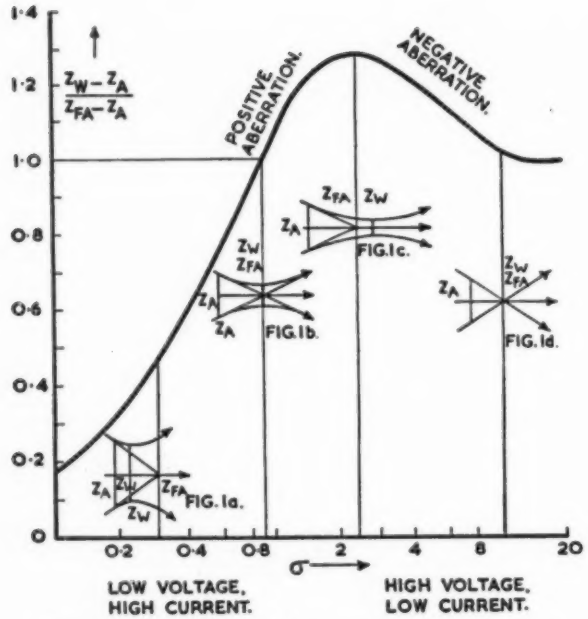

FIG. 1. Beam spread coefficient and shift of beam waist.

beam envelope with its tangents at the entrance aperture (coordinate z_A). These tangents intersect at the virtual focus with the coordinate z_{FA}. The beam waist is marked in each sketch by z_W.

From Eq. (2) it follows that, for small values of σ, the entrance aperture should be nearer to the waist than to the virtual focus [see Fig. 1(a)]. Now, when at a given constant slope angle Θ, an increase in voltage (or decrease in current) leads to an increase in σ, the virtual focal distance $(z_{FA}-z_A)$ remains constant but the waist distance (z_W-z_A) varies. For $\sigma=0.86$ [see Fig. 1(b)] z_W and z_{FA} coincide. For $\sigma=\sigma_0=2.3$ [Fig. 1(c)], (z_W-z_A) reaches a maximum. For large values of σ [see Fig. 1(d)] the waist should again coincide with the virtual focus; in this region, however, the charge density is generally low enough for the beam to cross over as predicted by Eq. (1).

The first-order theory which we have discussed so far deals with beams of homogeneous velocity. There, the waist of every single ray of the beam moves in the manner described and homocentricity of the beam is preserved. In other words, according to the first-order theory, space charge effects are not expected to produce spherical aberration in an initially homocentric, homogeneous electron beam. However, homogeneity of velocities cannot be maintained in beams of relatively large current density. Already Borries and Dosse[7] pointed out that, due to space charge, the potential V_0 at the axis should always be more negative than the potential V_1 of a marginal ray. The potential difference is to a first approximation calculated to be

$$V_0-V_1=\frac{I/V_1^{\frac{1}{2}}}{(2e/m)^{\frac{1}{2}}}=1.5\times10^4 I/\sqrt{V_1}. \qquad (5)$$

[7] B. v. Borries and J. Dosse, Arch. Elektrotech. 32, 221 (1938).

Due to this voltage difference the paraxial electrons should be expected to have smaller velocities than the marginal electrons. Klemperer[4] has pointed out that, for the following reasons, a loss of homogeneity must lead to spherical aberration. As the paraxial part of the beam is slowed down its current density is decreased; this in turn will lead—according to Eq. (2)—to an increase of σ in the paraxial region. Therefore the coefficient σ always decreases with increasing ray aperture y, thus

$$\sigma_{Pa}>\sigma_{Ma}$$

where the suffix Pa stands for the paraxial region and Ma stands for the marginal region of the beam. Now, from the fact that the shift of the waist, as shown in Fig. 1 as a function of σ, has a maximum at $\sigma_0=2.3$, the following conclusion has been drawn by Klemperer[4]:

If $\sigma_{Pa}<\sigma_0$, then $(z_W-z_A)_{Pa}>(z_W-z_A)_{Ma}$ and the beam passing through the waist should exhibit positive spherical aberration. On the other hand, if $\sigma_{Ma}>\sigma_0$ the aberration of the beam should be negative.

2. EXPERIMENTAL METHOD

The apparatus used to determine the effects of space charge on the properties of initially convergent electron beams is represented diagrammatically in Fig. 2. Emission was drawn from an oxide cathode Ca which was shielded by an apertured grid electrode Gr. The electrons were accelerated by a tubular anode An 1 and retarded by a second anode An 2. The focal length of the resulting electron lens was conveniently reduced by a diaphragm Dm 1. A second diaphragm Dm 2 marked the entrance of the beam, it was situated in a field-free space, but it did not necessarily limit the aperture of the beam.

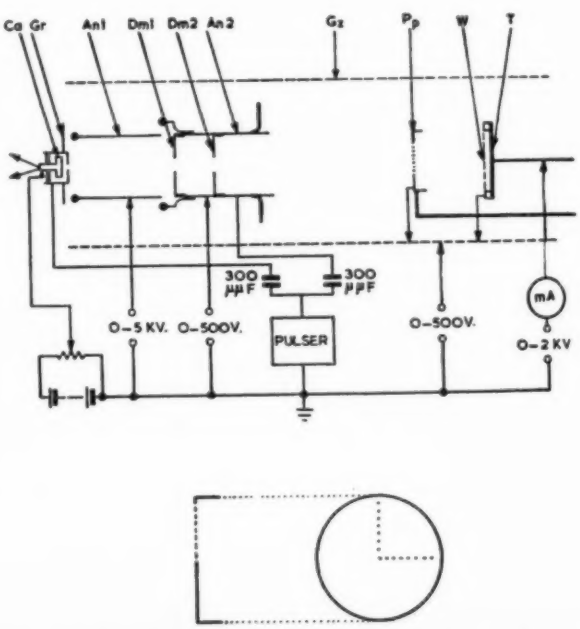

FIG. 2. Apparatus for ray tracing. (a) Pepperpot diaphragm.

The electron lenses produced by the fields between Gr and An 1 and between An 1 and An 2 projected a converging beam into the field-free space between the second anode An 2 and a pepperpot-diaphragm Pp. This diaphragm is illustrated in Fig. 2(a); it is seen to contain a number of circular holes of 0.1 mm diameter drilled accurately at 1.0 mm intervals along two mutually perpendicular straight lines. The whole arrangement was shielded by a wire gauze cylinder Gz maintained at the potential of the pepperpot diaphragm Pp.

The pepperpot diaphragm selected discrete electron pencils from the beam. Each pencil produced a bright spot on the fluorescent target T. A fine wire gauze W was mounted on the target and, a fraction of a millimeter in front of it. This gauze which was electrically insulated from the target, was maintained at the potential of the pepperpot diaphragm. The target potential was about one kilovolt positive with respect to W. The field between W and T therefore served for a post-acceleration of the electrons which, in the present experiments, were too slow to give sufficient excitation of the fluorescent substance on T.

Provision was made to slide the target along the axis of the beam, so that the position of each spot marked by the electron pencils, selected by the pepperpot diaphragm, could be determined with a measuring microscope. In this way virtual foci and aberrations of the pencils could be traced.

Modulation of the beam current was effected either by changing the grid bias or by a micrometer control of the grid to cathode spacing. These changes, however, were kept small enough to avoid substantial effects in the geometry of rays in the emission system.

In order to reduce the neutralization of electron space charge by residual positive ions, formed by ionising collisions in the beam, a pulsing technique was employed. A blocking oscillator was used to produce rectangular 100-volt negative pulses of 5-μsec duration at 15-μsec intervals. These pulses could be applied simultaneously to both the grid electrode and to the second anode. Pulses applied to the grid electrode caused periodic interruptions of the beam, these interruptions coincided with the production of a potential gradient between the second anode and the pepperpot diaphragm which served to sweep the ions from this region while the beam was interrupted. According to investigations of Linder and Hernqvist[8] the chosen timing of the pulses was expected to be adequate for avoiding a substantial "buildup" of positive ions in electron beams of a few hundred volts at pressures of the order of 10^{-6} mm Hg.

Experiments showed that the size of the pattern produced on the fluorescent target by a high current density beam increased sharply when the above pulses were applied. We therefore concluded that the technique

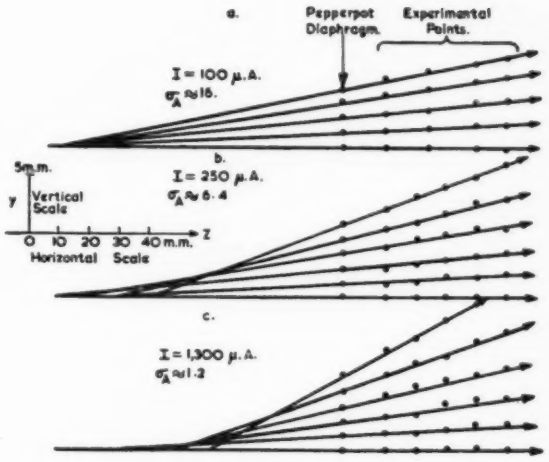

FIG. 3. Experimental ray tracings.

outlined substantially reduces the neutralization of space charges by positive ions and consequently increases the beam spread. The pulsing technique was therefore employed in all experiments described, though it should be emphasized that the aberration effects discussed in Sec. 3 could also be noticed without the pulsing.

When tracing rays, it was desirable to suppress secondary emission from the pepperpot diaphragm. The potential of the pepperpot, target and gauze Gz was accordingly maintained 12 volts positive with respect to second anode and target so that slow electrons could not escape from the pepperpot diaphragm.

A further precaution became necessary when experimenting with high current density beams. If the beam was intercepted by a conductor, e.g. the pepperpot diaphragm, any radial potential gradients set up by the space charge of the beam were destroyed at the conducting surface, and the character of the beam would consequently become modified. Hence the pepperpot was always kept at least a few centimeters beyond the beam waist. There, the rays had spread sufficiently and the current density had become too low to leave any detectable potential gradients across the beam.

In order to obtain quantitative information it was necessary to measure, for each tracing, the beam energy, beam current and initial semiangle of convergence. Provision was therefore made to swing the pepperpot in and out of line with the beam. When the pepperpot was removed, the whole beam current was collected by the post-accelerating target and its average value was indicated by a milliammeter. However, since the current was pulsed, its actual magnitude was then calculated from the known frequency and duration of the pulses. The initial angle of semiconvergence Θ_A could be determined approximately by tracing the beam envelope at low intensity with the sliding target and a measuring microscope. Since the propagation of low-

[8] E. G. Linder and K. G. Hernqvist, J. Appl. Phys. **21**, 1088 (1950).

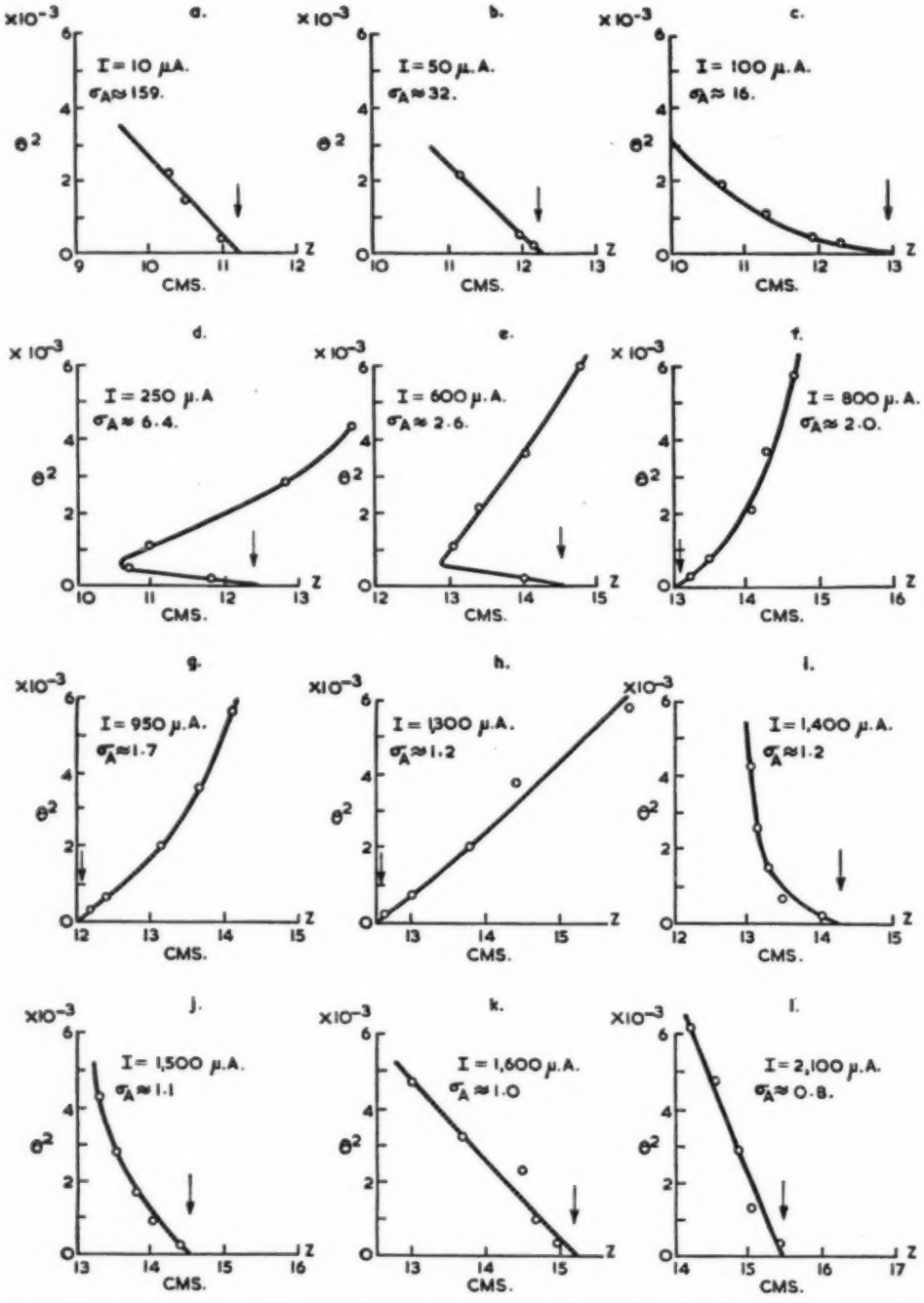

FIG. 4. Aberration curves at 360 ev. [*Note:* The ordinates of these curves should be marked $(\Theta')^2$ instead of Θ^2.]

intensity beams is rectilinear, Θ_A was found as the semivertical angle $\Theta_A'(=\Theta_A)$ of the conical envelope of the diverging beam.

3. SPHERICAL ABERRATION PRODUCED IN AN ELECTRON BEAM BY SPACE CHARGE

Experiments were first performed with beams directed towards a given point on the beam axis. The potentials of the electrodes were kept constant so that changes in the beam caused solely by increases of beam current could be investigated.

Figure 3 shows three tracings obtained for 360-volt beams of different beam current but of the same initial semiconvergence ($\Theta_A = 8.4 \times 10^{-2}$ rad). The total beam current I and the approximate value of σ_A are stated in each case. These values of σ_A are calculated according to Eq. (3) from the initial inclination of the beam envelope (Θ_A), the beam voltage (V) and the total current (I); they therefore represent an average value for the various radial zones in the beam. Figure 3 shows that both positive and negative spherical aberration can occur in electron beams; of further interest is the coexistence of the different types of aberration in different zones of the beam illustrated in Fig. 3(b).

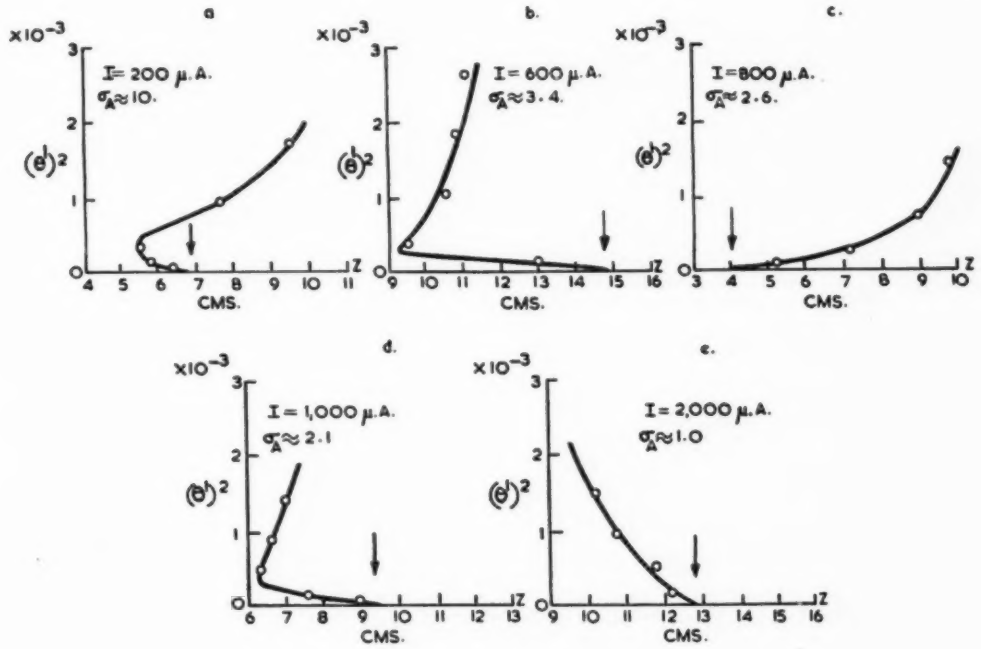

FIG. 5. Aberration curves at 240 ev.

The results of a number of ray tracings are presented as aberration curves in Figs. 4–6. These curves show the square of the angle which an electron pencil makes with the beam axis $(\Theta')^2$ plotted against the axial coordinate of the virtual focus of the pencil (z), the origin of the scale being the entrance aperture (Dm 2 in Fig. 2).

Figures 4(a) to 4(l) refers to beams of initial semiconvergence $\Theta_A = 8.4 \times 10^{-2}$ radian and of $V = 360$ volts electron energy. The total currents I and the coefficient σ_A calculated from these three values are noted for each graph. The aberration curves in Figs. 4(a) and 4(b) have been taken with small beam currents of 10 μA and 50 μA respectively. The positive aberration shown by these curves is due to the emission system and to the electron lens which was used to converge the beam. Figure 4(c), taken at 100 μA, shows the first effects of space charge on the aberration of the beam; the decreased slope of the aberration curve in the region of small apertures indicates an increase in positive spherical aberration produced by space charge.

A further increase in beam current to 250 and 600 μA, as shown in Figs. 4(d) and 4(e) respectively, causes a substantial change in the character of the aberration curves. Now, only the region of the beam near the axis shows positive spherical aberration. The marginal region, on the other hand, shows considerable negative spherical aberration. In Sec. 1 we saw, according to Barford and Klemperer, that when with increasing current a waist is forming in an electron beam, it will be initially confined to the marginal region. We also saw that if a waist is formed in a beam for which σ_A is sufficiently large, the spherical aberration of the diverging beam should be negative. Theoretical considerations, therefore, lead us to expect the possible coexistence of a crossover for zonal rays exhibiting positive spherical aberration and of a waist for marginal rays which exhibit negative spherical aberration.

When the beam current was raised beyond 600 μA, the region with positive aberration decreased until it could no longer be detected by the pepperpot diaphragm which only allowed us to trace pencils which made an angle greater than about 10^{-2} radian with the axis. Figures 4(f), 4(g), and 4(h) therefore only show negative aberration.

With a current greater than 1300 μA we arrive at the second major change in the character of the beam. It was pointed out in Sec. 1 that the spherical aberration

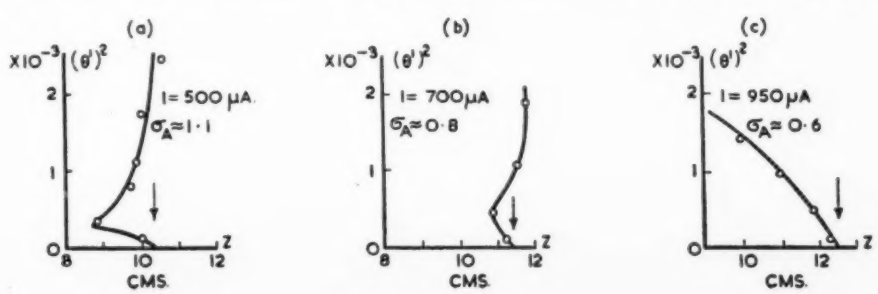

FIG. 6. Aberration curves at 480 ev.

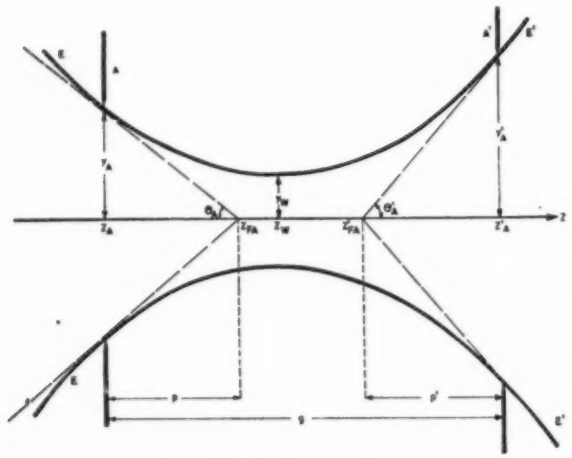

FIG. 7. Homocentric electron beam under the influence of its own space charge.

of a beam diverging from an electron waist should be positive for $\sigma \lesssim \sigma_0$. Now, the value of σ may be taken as the measured average value σ_A, moreover, $\sigma_0 = 2.3$. Hence in the present experiments we expect a change in sign of the spherical aberration somewhere for $\sigma_A \approx 2.3$. This transition was observed. Figures 4(i) and 4(j), taken at 1400 μA and 1500 μA respectively, represent an intermediate region; Figures 4(k) and 4(l) show the complete establishment of positive spherical aberration for beam currents of 1600 μA and 2100 μA.

Further aberration measurements over a wide range of beam currents have been carried out at 240 volts with a beam of initial semiconvergence of $\Theta_A = 0.128$ radian; only a few tracings are shown in Figs. 5(a) to 5(e). Attention should be drawn here to the very large positive spherical aberration measured at the relatively low voltage for beams of high current density which continue to cross over [see rays close to the axis in Fig. 5(b)].

Results obtained at 480 volt and with $\Theta_A = 4.1 \times 10^{-2}$ radian are given in Figs. 6(a) to 6(c). The aberration curves in Fig. 6 seem to differ from those of Figs. 4 and 5, insofar, as with increasing beam current the transition from crossover to waist and again from waist with negative aberration to waist with positive aberration seem to follow much more closely in the experiments at the relatively higher voltages. At 300 μA all rays still seem to cross over, since they all show positive aberration. At 500 and 700 μA respectively [Figs. 6(a) and 6(b)] waist formation with introduction of some negative spherical aberration has already started in the marginal region. However, when the crossover of the rays nearest to the axis is hardly converted into a waist, there seems to follow already [Fig. 6(c)] the region of the waist with positive aberration.

Comparison of Figs. 4, 5, and 6 reveals also that the spherical aberration produced by space charge is much greater in lower energy beams. This result could have been expected from the discussions in Sec. 1. We saw there that the spherical aberration of a beam diverging from a waist results from radial potential gradients in the beam. The magnitude of these gradients increases with decreasing beam voltage [see Eq. (5)]. Moreover, since a given radial potential difference will have greater relative importance in a low-energy beam we would expect that the magnitude of the spherical aberration of a beam diverging from a waist should increase with decreasing beam voltage.

It can also be seen from Figs. 4–6 that the relation between $(\Theta')^2$ and z is, in general, not linear. We therefore conclude that the spherical aberration produced by space charge at a waist or crossover contains relatively large terms of higher order. At the present stage, however, it seems not to be worthwhile to attempt a quantitative analysis of the aberration curves, since the aberration contributions due to the electron gun cannot be properly separated from those due to the electron beam.

At the discussion of Figs. 4(a) and 4(b) we drew attention to the lack of initial homocentricity of the investigated electron beam and we pointed out that initial aberrations are introduced by the electron gun. These aberrations, however, are not quite the same in all subsequent measurements, since with increasing current the aberrations in the gun itself are modified by space charge effects. Now, the emission system and the projecting lens of which the gun consists are known (see Klemperer[4]) to suffer always from a positive (never negative) spherical aberration which is not greatly modified by changes in the transmitted current density. For this reason we can conclude that the changes in aberration due to increased current density as shown in

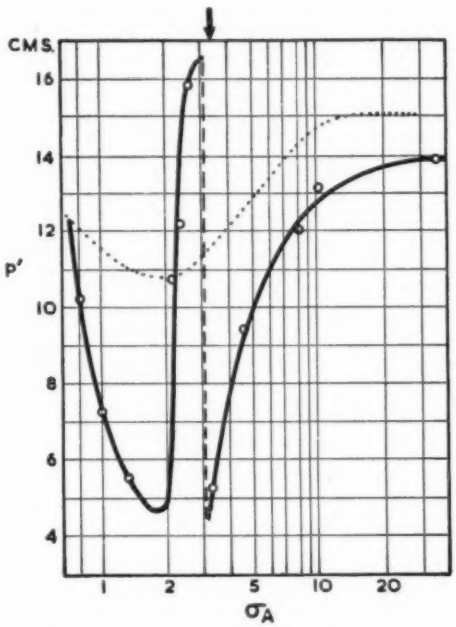

FIG. 8. Beam spread coefficient and paraxial focus shift at 360 ev.

Figs. 4–6, are essentially produced by space charges in the beam. However, since we have not been able to separate the two contributions, we have here to be content with a qualitative analysis of the aberration curves.

4. THE SHIFT OF THE BEAM FOCUS BY SPACE CHARGE

The "first-order" theory of space charge effects in an electron beam is concerned with homocentric rays of homogeneous velocity. The beam is shown in Fig. 7. Its envelope is represented by the curves EE'. The beam passes through an entrance aperture A where all electron trajectories are directed towards a virtual focus z_{FA}. The beam radius subsequently reaches a minimum value y_W at the axial coordinate z_W, finally the beam passes through an exit aperture A' where all electron trajectories appear to diverge from the virtual focus z_{FA}'.

Experimental values for the distance of the paraxial virtual focus from the exit aperture $p'=(z_A'-z_{FA}')$ as a function of the coefficient σ_A can be taken from the aberration curves Figs. 4–6. The origin of the abscissas in these figures is the fixed position z_A of the entrance aperture A; we obtain the paraxial foci z_{FA}' as intercepts of the aberration curves with the abscissa. Moreover, the distances p' refer to the exit aperture, hence, they can be obtained by subtraction of the values of the abscissas in Figs. 4–6 from the given distance $g=z_A-z_A'$ between the entrance and exit aperture. The exit aperture is presented by the pepperpot diaphragm which, for the purpose of ray tracing, could be placed in any position far enough from the beam-waist to be in the region of substantially rectilinear propagation of the rays. A constant distance $g=20$ cm was taken here for all tracings.

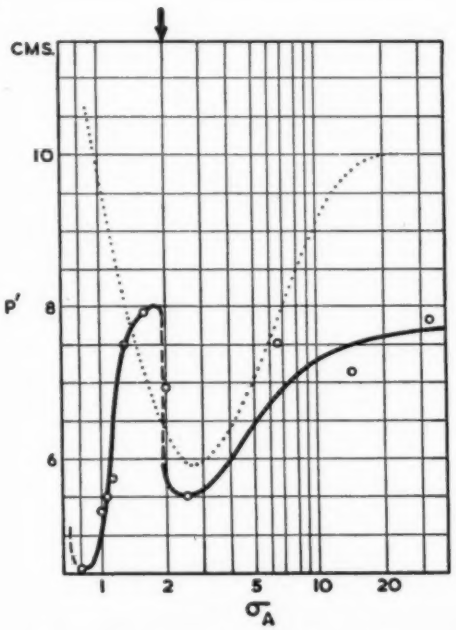

FIG. 9. Beam spread coefficient and paraxial focus shift at 240 ev.

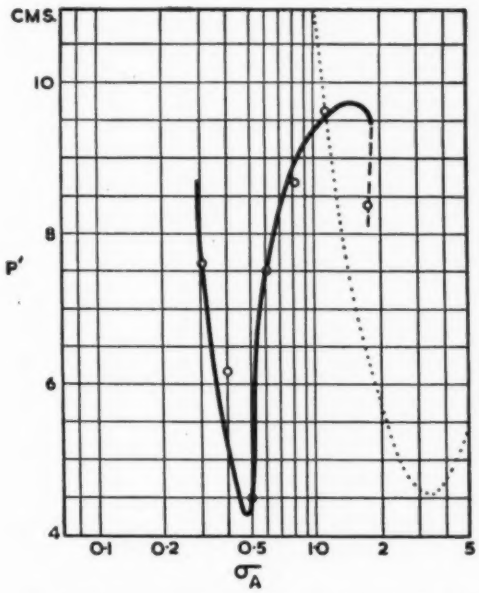

FIG. 10. Beam spread coefficient and paraxial focus shift at 480 ev.

Figure 8 shows curves for p' as a function of σ_A for an electron energy of $V=240$ ev. Figures 9 and 10 show corresponding curves for $V=360$ ev and for $V=480$ ev respectively. The distances $p=z_{FA}-z_A$ of the focus from the entrance aperture were measured to be 5 cm, 10 cm, and 11.5 cm respectively for these three figures.

The experimental points (ooo) are connected by solid curves; they can be compared with theoretical values which are presented by dotted curves. Let the calculation of these theoretical values be explained with a few examples given in Table I.

The beam spread coefficient σ_A given in line (1) of Table I can be calculated from Eq. (3) for any given voltage V, current I and angle of semiconvergence Θ_A. Line (2) contains the ratio $(z_W-z_A)/(z_{FA}-z_A)$ which, for any σ_A value can be obtained from the graph in Fig. 1. (z_W-z_A) in line (3) is obtained by multiplying line (2) with $p=(z_{FA}-z_A)$, the distance of the virtual focus of the converging beam from the entrance aperture. The value of p is noted at the head of the table; it was obtained from a low intensity tracing as described at the end of Sec. 2. The values in line (4) are given (as seen from Fig. 7) by

$$(z_A'-z_W)=g-(z_W-z_A). \tag{6}$$

The values of the Dawson function of the square root of the σ_A values of line (1), as written down in line (5), are obtained from the tables by Terrill and Sweeny (1944), while the Dawson function in line (6) is calculated from the simple formula

$$D(\sqrt{\sigma_A'})=\frac{g-(z_W-z_A)}{z_W-z_A}D(\sqrt{\sigma_A}). \tag{7}$$

TABLE I. Calculation of the distance p' of the virtual focus of the diverging beam from the exit aperture—as a function of the spread-coefficient σ_A of the converging beam at the entrance aperture A. Given: $g=20$ cm, $p=5$ cm.

(1)	σ_A	given by V, I, Θ_A	1	2	5	7
(2)	$\frac{z_W-z_A}{z_{FA}-z_A}$	See Fig. 1	1.09	1.28	1.17	1.08
(3)	z_W-z_A	line (2) × p	5.45	6.40	5.85	5.40
(4)	$z_A'-z_W$	See Eq. (6)	14.55	13.60	14.15	14.60
(5)	$D(\sqrt{\sigma_A})$	Dawson tables and line (1)	1.46	3.31	38.9	221
(6)	$D(\sqrt{\sigma_A'})$	See Eq. (7)	3.91	7.05	93	610
(7)	σ_A'	Dawson tables and line (6)	2.2	2.96	6.0	8.1
(8)	$\frac{z_A'-z_W}{z_A'-z_{FA}'}$	See Fig. 1	1.25	1.26	1.11	1.05
(9)	$p=z_A'-z_{FA}'$	line (4)/line (8)	11.6	10.8	12.8	13.8

This Eq. (7) can be derived in the following way. According to the first-order theory (see Field, Spangenberg, and Helm[3], or Klemperer,[4] p. 202) the coordinates (y, z) of points on the beam envelope can be presented in the form

$$\frac{z-z_W}{y_W}=\frac{4(\pi\epsilon)^{\frac{1}{2}}(e/2m)^{\frac{1}{4}}}{\sqrt{I/V^{\frac{1}{2}}}}D\left[\left(\sqrt{\log\frac{y}{y_W}}\right)\right]^{\frac{1}{2}} \tag{8}$$

where y_W is the beam radius at the waist and D is again the Dawson function given in Eq. (4). Applying Eq. (8) to a beam, as it passes through the aperture A, and recalling that

$$\log\frac{y_A}{y_W}=\sigma_A \tag{9}$$

we obtain

$$\frac{z_W-z_A}{y_W}\propto D(\sqrt{\sigma_A}). \tag{8a}$$

Applying Eq. (8) to the same beam as it passes through the aperture A' we have

$$\frac{z_A'-z_W}{y_W}\propto D(\sqrt{\sigma_A'}). \tag{8b}$$

If we now divide Eq. (8b) by Eq. (8a) and subsitute for $(z_A'-z_W)$ from Eq. (6), we obtain immediately Eq. (7) as given above.

σ_A' in line (7) can be determined from $D(\sqrt{\sigma_A'})$ of line (6) with the help of Dawson function tables. The values in line (8) are obtained from the curve in Fig. 1 for the σ_A' values of line (7). Finally the p' values of line (9) follow as the ratio of the values given in line (4) and line (8) respectively.

The calculated values of p' reach a minimum for certain σ_A values, the position of this minimum depends upon the magnitude of p.

When we now compare the experimental results with the calculated values, we see that the predicted minimum of p' did in fact occur. However, in all experimental curves the minimum is seen to occur at smaller σ_A values than in the theoretical curves. Exact agreement between the experimental and theoretical curves is not to be expected, since the position of the paraxial virtual focus should depend on σ_{Pa}; but in Sec. 1 we saw that in a given beam σ_{Pa} will generally differ from σ_A. Moreover, the theory applies to initially homocentric beams while a certain amount of positive spherical aberration cannot be avoided in an experimental beam.

For lower current densities (greater σ_A), however, the experimental curves do not show even qualitative agreement with the continuum theory prediction. This may be understood if we refer to the vertical arrows shown in Figs. 8 and 9. These arrows are inserted according to the results of Figs. 4–6 in order to mark the transition from negative to positive spherical aberration which is caused, in zones near the axis, by decreasing the beam current. According to previous arguments this change in aberration indicates the transition from waist to crossover. On the right of the arrows, therefore, the focus shift curves refer to beams which are believed to crossover. For such beams the continuum theory should fail.

The curves in Figs. 8 and 9 show at the arrows a sudden movement of the paraxial focus away from the electron source when the beam current is gradually decreased. This movement was expected to coincide with the transition from a waist to a crossover and its observation provides a further confirmation of the view that a transition from crossover to waist did occur in the investigated electron beams.

5. TRANSITION FROM WAIST TO CROSSOVER INSIDE THE BEAM

The appearance of negative spherical aberration in a beam with increasing current was explained to be an indication for the formation of an electron waist. It has been pointed out here in Sec. 1, and confirmed by experiments described in Sec. 3 that the waist can already be formed in the marginal region when the trajectories nearer to the axis still cross over.

The coexistence of waist and crossover in a beam is illustrated in Fig. 11. There, the shaded region indicates the zone in which the rays cross over while the rays in the unshaded zone form a waist.

Let the semivertical angle of the cone of rays forming

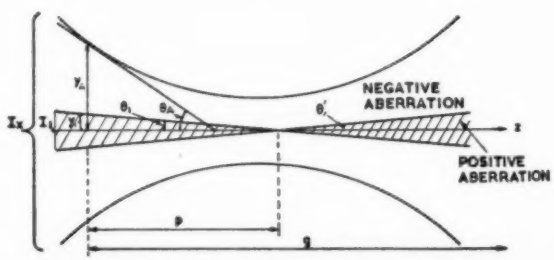

FIG. 11. Co-existence of crossover and waist.

the crossover be Θ_1 and the current flowing in this cone be I_1. If we assume uniform current density in the beam we can write

$$\frac{I_1}{I_z} \approx \frac{\Theta_1^2}{\Theta_A^2} \tag{10}$$

where I_z is that total current in the beam which is just large enough to cause all rays with initial semiconvergence greater than Θ_1 to form a waist (i.e., to show negative spherical aberration), and where Θ_A is the initial angle of semiconvergence of the beam at the entrance aperture.

Let the divergent beam be intercepted by a pepperpot diaphragm selecting a series of pencils. One pencil close to the axis, arbitrarily chosen for sake of argument may have the slope angle Θ_1'. If we assume the first-order theory to be valid so that $\Theta_1=\Theta_1'$ the total beam current I_z will be just large enough to cause all traced pencils with $\Theta \geq \Theta_1$ to exhibit negative spherical aberration; on the other hand, all rays in the beam which converge at angles smaller than Θ_1 will cross over.

Now, I_z, Θ_A, and $\Theta_1(\approx\Theta_1')$ are accessible to direct measurement (see Sec. 2). On the other hand, $I_z=f(\Theta_A,\Theta_1')$ can be calculated from the Barford-Klemperer criterion which, in the form of Eq. (1) allows us to determine I_1 for any given beam voltage V and entrance aperture y_1 of rays with slope angle Θ_1. However, y_1 can be calculated from the known radius y_A of the entrance aperture of the beam, since

$$\frac{y_1}{y_A} \approx \frac{\Theta_1}{\Theta_A}. \tag{11}$$

Figure 12 shows experimental values (circles; solid curve) and theoretical results (dotted curve) for I_z as a function of Θ_A. The directly measured values of I_z which are plotted as ordinates, represent currents which were just large enough to produce negative spherical aberration in every obtainable pencil. This implies that Θ_1 was taken as the initial semiconvergence of a pencil which passed through the pepperpot hole nearest to the axis. It was measured as the ratio.

$$\Theta_1=\Theta_1'=\frac{y_1'}{g-p}$$

where $y_1'=1$ mm was the ray aperture given by the distance of the first hole of the pepperpot diaphragm from the axis. g was again the distance between entrance and exit aperture (=20 cm, see Sec. 4), and p was the distance of the entrance aperture from the focus found by low-intensity beam tracing (see Sec. 2).

The initial angles of semiconvergence which are plotted in Fig. 12 as abscissas, were obtained as the ratio $\Theta_A=y_A/p$, where $y_A=1.5$ mm was the fixed entrance semiaperture of the beam, and p was the focal distance as above. The angles Θ_A were varied by changing the potential of the first anode (An 1 in Fig. 2) while the potential of the second anode (An 2) remained constant in order to keep the energy (V) of the electrons unchanged. The results of Fig. 12 were obtained at $V=360$ ev.

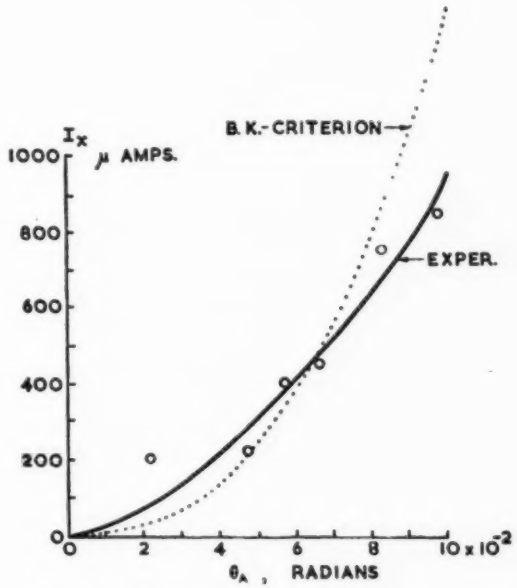

FIG. 12. Minimum beam current to produce negative spherical aberration at 360 ev.

The theoretical curve in Fig. 12 was obtained from the Barford-Klemperer criterion (Eq. (1)) which, for the present purpose, may be expressed in the following form: for a beam current $I=I_1$ at which rays of slope angle Θ_1 present a boundary between crossover and waist formation, the function

$$\sigma_1=33\times10^{-6}\frac{\Theta_1^2V^{\frac{1}{2}}}{I} \tag{12a}$$

will be about equal to the function

$$\tau_1=\log_e(0.3\times10^{12}y_1I/V^{\frac{1}{2}}). \tag{12b}$$

Hence, the required current I_1 can be calculated from given values of y_1, Θ_1, and V. I_1 was obtained here, for instance, graphically by finding the intersection of the two curves presenting σ_1 and τ_1 respectively as a function of I.

For example, the typical values $y_A=1.5$ mm, $\Theta_A=8\times10^{-2}$ radian and $\Theta_1=5.5\times10^{-3}$ lead with Eq. (11) to $y=0.10$ mm. By substitution in Eqs. (12a) and (12b) these values yield an intersection of the relevant σ_1 and τ_1 curves at the critical current $I_1=3.75\times10^{-6}$ amp. From Eq. (10) we can then obtain for the required total beam current

$$I_z=I_1\Theta_A^2/\Theta_1^2=7.9\times10^{-4}\text{ amp.}$$

The relation between beam voltage V and minimum total beam current I_z necessary to produce negative

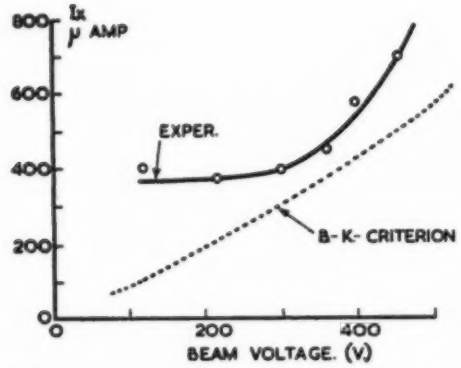

FIG. 13. Minimum beam current to produce negative spherical aberration at 6×10^{-2} radian initial semiconvergence.

spherical aberration in all of the electron pencils selected by the pepperpot diaphragm, is shown in Fig. 13. Here, the initial semiconvergence $\Theta_A=6\times10^{-2}$ radian and the radius of the entrance aperture $y_A=1.5$ mm were both kept constant. Experimental points are again marked by small circles and connected by a solid curve. The dotted curve was calculated as above from the Barford-Klemperer criterion. Both Figs. 12 and 13 show that the theory is able to predict approximately the right magnitude of the experimental values. Complete agreement should, however, not be expected since the present theory applies to homocentric beams, but the actual electron beam never was homocentric owing to an initial positive spherical aberration introduced by the emission system and the lenses of the electron gun, and owing to further aberrations produced by the space charge effects in the beam.

6. PRODUCTION OF NEGATIVE SPHERICAL ABERRATION BY SPACE CHARGE AND THE CORRECTION OF ELECTRON LENSES

Experiments discussed in Sec. 5 have shown that a given electron beam diverging from a waist will begin to exhibit negative spherical aberration for rays near the axis when the beam current I is increased up to a specified limit I_z. On the other hand, it has been shown in Sec. 3 that in a beam diverging from a waist the sign of spherical aberration will always change from negative to positive when the beam current is sufficiently increased. Let us assume this change will occur when the coefficient σ [see Eq. (3)] is decreased to a value σ_2. According to discussions of Sec. 1 we expect that σ_2 should be of the order of $\sigma_0=2.3$ given by the maximum of the curve in Fig. 1.

In order to obtain experimental information about the actual values of σ_2 we have (as in Sec. 5) varied the slope angle Θ_A and for each chosen Θ_A we have increased the beam current up to a value I_t which was, at an electron energy of 360 ev, just sufficient for changing the sign of spherical aberration from negative to positive for the selected pencils nearest to the axis for which the change occurs first. These experimental results for I_t are marked as circles in Fig. 14. The dotted curve in this figure shows values for I_t calculated under the assumption that the change occurs when the coefficient σ of the beam reaches the value σ_0. The experimental values, however, seem to be grouped rather about the solid curve which corresponds to $\sigma_2=1.1$. They fall above this curve only for the smallest investigated convergences Θ_A.

The relation between the transition current I_t and the beam voltage V is shown for a fixed beam convergence $\Theta_A=6.7\times10^{-2}$ radian by Fig. 15. Circle marks again show the experimental values and the dotted curve is again drawn to have a constant parameter $\sigma=\sigma_0=2.3$. The experimental values (excepting for the small voltage) are approximately presented by $\sigma_2=1.3$, and with this parameter we have drawn another dotted curve in Fig. 15.

The possibility of producing negative spherical aberration in an electron beam is obviously of greatest technical interest for the correction of electron lenses

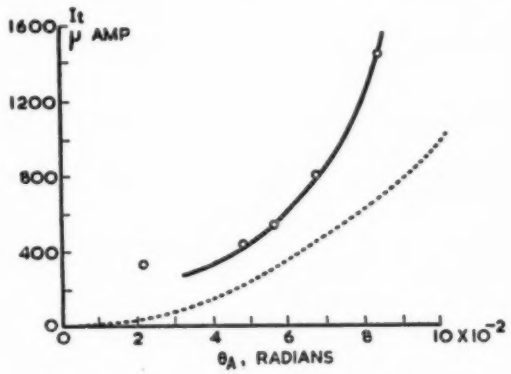

FIG. 14. Beam current necessary to change sign of aberration at 360 ev.

which are known to suffer always from positive spherical aberration. A formulation of the conditions under which the waist of a convergent electron beam produces negative spherical aberration can be derived by considering that beam currents I_n for production of negative aberration must be inside the limits

$$I_z<I_n<I_t.$$

Comparing the experimental values of I_z and I_t given in Figs. 12–15, it is found that I_t is given by the constant parameter $\sigma_2=1.3$ and that I_z is represented by various σ_1 values which generally are greater than 3, hence a fair representation of I_n might be given by $\sigma\approx2$. Substituting this value in Eq. (3) we find

$$I_n\approx\Theta^2V^{\frac{3}{2}}/0.6\times10^5 \qquad (13)$$

i.e., negative spherical aberration will be produced in a beam of initial semiconvergence Θ (radians) and of an electron energy V (volts) for beam currents I (amp) given by values about I_n of Eq. (13). From the experimental results presented in Figs. 12–15 it can be seen,

however, that the interval between I_s and I_t decreases with decreasing initial convergence Θ of the beam and with increasing beam voltage V. Hence Eq. (13) will apply within a given region of Θ and V values only. This region is not critically defined and its boundaries could not be sharply determined by the present measurements. It may only be mentioned that no negative spherical aberration could be detected here in beams of electron energy greater than 500 ev. This limit, however, was to some extent the result of the unavoidable initial positive spherical aberration contained already in the beam while it left the electron gun. The initial positive aberration must, of course, be exceeded by the negative aberration produced in the beam waist before any negative aberration is registered.

An attempt to use space charge for the correction of spherical aberration in projected electron optical images meets serious difficulties. We have tried to observe an erect shadow image projected by an electron beam which passed through a waist. For this purpose a platinum wire of 0.1 mm diameter was welded radially over the circular aperture of a diaphragm which was placed in a field-free space in front of the beam waist. The wire ended at the center of the aperture. For small beam currents an inverted shadow of the wire was observed on the target, indicating that the rays in the beam were crossing the axis. When, however, the beam current was increased the shadow was no longer visible, only a uniform circular fluorescent patch was seen. No better results were obtained when, instead of using the arrangement of Fig. 2, a beam was converged by a magnetic electron lens of particularly small aberration.

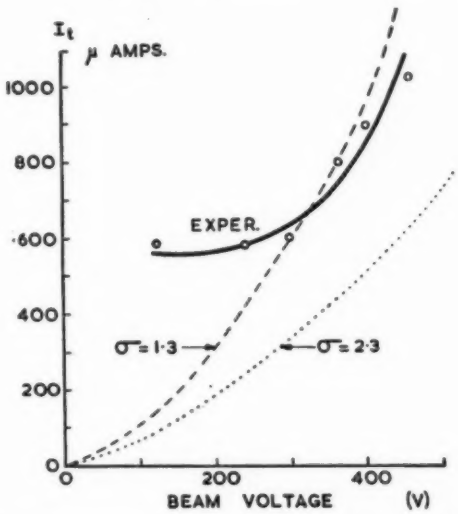

FIG. 15. Beam current necessary to change sign of aberration at 6×10^{-2} radian initial semiconvergence.

It is not unlikely that the disappearance of the shadow was caused by mutual repulsion in the beam which produced a deflexion of the rays into the empty space of the shadow. A correction of errors in the image formation with the aid of space charge effects produced in the beam by its own charge might therefore be impracticable. However, it appears possible to use space charge loaded beams for the correction of spherical aberration in a focused spot.

CONCLUSIONS

1. The transition from crossover to waist has been observed in initially convergent electron beams. It has been found that a waist and a crossover can coexist in the same beam. The waist formation begins when the current density is sufficiently high. While the inner rays still cross over, the outer rays can already form a waist. The smallest waist radii of rays in a beam have been found to be approximately equal to the mean mutual distance between the electrons in the region near the waist.

2. It has been found that, according to the initial conditions either positive or negative spherical aberration can be produced by space charge effects in initially convergent beams. These aberrations indicate the importance of some radial forces in the beam which are responsible for the unexpectedly rapid beam spread that has been observed by other authors.

This investigation, carried out in the Physics Department of the Imperial College, London, formed part of the doctorial thesis of one of us (K.T.D.) who is indebted to the Department of Scientific and Industrial Research for award of a Scholarship.

Dynamic Determination of the Compressibility of Metals*

ROY W. GORANSON,† DENNISON BANCROFT,‡ BLENDIN L. BURTON, THEODORE BLECHAR, EDWIN E. HOUSTON, ELISABETH F. GITTINGS, AND STANLEY A. LANDEEN
Los Alamos Scientific Laboratory of the University of California, Los Alamos, New Mexico
(Received July 16, 1955)

Equation of state data for Duralumin in the pressure range from 0.1 to 0.3 megabar have been determined dynamically by measuring shock and free surface velocity electrically in a plate of 24 ST Duralumin that has been stressed by a high explosive detonation. A theory is presented which allows comparison with data obtained by other experimenters, and which yields the relationship between pressure and compression either at constant entropy or constant temperature. The empirical form chosen for the equation of state ($p=a\mu+\beta\mu^2$) expresses the pressure as a quadratic function of the compression. Experimental techniques are described in detail. Five points are given for the equation of state of Duralumin in the pressure range from approximately 0.15 megabar to 0.33 megabars. Some data are also presented for cadmium and steel.

INTRODUCTION

EARLY in 1945 experimental work was initiated at the Los Alamos Scientific Laboratory for the study of physical properties of materials in the pressure range from 0.1 to 0.3 megabar (10^{12} dynes/cm^2). One-tenth of a megabar had been obtained statically at the Geophysical Laboratory of the Carnegie Institution, but determinations of the equation of state at this pressure become impractical partly because of the elaborate and cumbersome apparatus required and partly because static measurements are subject to uncertainties resulting from creep distortions. An alternative technique, and one particularly suited to the data here desired, is to make the measurements dynamically, thereby eliminating the need for elaborate high pressure equipment with its inherent creep uncertainties.

It is, of course, well known that extreme, though temporary, pressures can be developed by high explosives. With suitably designed apparatus, detonation of a high explosive may be made to produce in the material being investigated a plane shock wave approximately flat-topped in the sense that the pressure in the compressed material is virtually independent of position. The conditions for the existence and stability of such shock waves are discussed in a variety of textbooks.[1]

The theory of propagation of such waves implies that simultaneous determinations of the propagation velocity of the wave and of the mass velocity of the compressed material can be used to infer the equation of state. In addition it is possible under certain conditions to determine shock pressures by means of piezoelectric crystals though this last technique has proved rather difficult to exploit.

THEORY

Detonation of high explosive in contact with a metallic specimen produces pressures in the metal under what are usually termed "Rankine-Hugoniot Shock" conditions. Such conditions will be denoted by appending the subscript D to the symbols appearing in Table I. The mechanical considerations of conservation of mass and conservation of momentum, respectively, lead to the equations:

$$\eta-1=\mu=u/(D-u) \tag{1}$$

$$p_D=\rho_0 Du. \tag{2}$$

The pressures and compressions appearing in Tables II and III were computed by means of Eq. (1) and (2). For many purposes, for example in comparing our data with other data, it is necessary to know the relationship between pressure and compression either at constant entropy or at constant temperature. Such conditions will be specified by the subscripts s and T, respectively. In order to compute the difference between p_D and p_s or

TABLE I. Definitions of symbols and list of units to be used in computation.

Symbol	Definition	Units
p	pressure	megabar = 10^{12} dynes/cm^2
v	specific volume	cm^3/g
ρ	density at pressure p	g/cm^3
ρ_0	initial density	g/cm^3
$\eta-1=\mu$	compression − 1 $=(\rho-\rho_0)/\rho_0$*	.....
e	specific internal energy	cm^3-megabar/g = 10^{12} ergs/g
T	absolute temperature	electron volt = κT = 11,605°C
s	specific entropy	cm^3-megabar/g-ev
C_v	specific heat at constant volume $=(\partial e/\partial T)_v$	cm^3-megabar/g-ev
D	shock wave velocity	cm/μsec = cm/10^{-6} sec
u	particle or mass velocity	cm/μsec = cm/10^{-6} sec
σ	excess of free surface velocity over mass velocity	cm/μsec = cm/10^{-6} sec
c	velocity of sound $=(\partial p/\partial\rho)_s^{\frac{1}{2}}$	cm/μsec = cm/10^{-6} sec
α_s	isentropic bulk modulus at $p=0$	megabar
β_s	second-order coefficient in empirical isentropic equation of state; see Eq. (17)	megabar

* Compression is alternatively defined as $(v_0-v)/v_0=(\eta-1)/\eta$, where v_0 is the normal specific volume.

* Work done under the auspices of the U. S. Atomic Energy Commission.
† Now at University of California Radiation Laboratory, Livermore, California.
‡ Now at Swarthmore College, Swarthmore, Pennsylvania.
[1] e.g., Courant-Friedrichs, *Supersonic Flow and Shock Waves* (Interscience Publishers, Inc., New York, 1948), p. 121 *et seq.*

p_T for some specified compression η, one requires an additional shock condition based on thermodynamic conservation of energy:

$$\Delta e_D = (\tfrac{1}{2}) p_D (v_0 - v), \tag{3}$$

where Δe_D represents the internal energy change required to reach the shock pressure p_D at the final specific volume v. The energy change required to reach this same final volume isentropically may be found by integration:

$$\Delta e_s = \int_v^{v_0} p dv. \tag{4}$$

The energy excess under conditions produced by the shock is thermal energy. This energy difference may be expressed in terms of thermodynamic data by the equation:

$$\Delta e_D - \Delta e_s = \int_{p_s}^{p_D} C_v (\partial T/\partial p)_v dp. \tag{5}$$

Equations (3), (4), and (5) when combined result in an equation from which the difference $p_D - p_s$ may be found. Estimates of the integrand in Eq. (5) are available, and for our immediate purposes, appropriate mean values can be selected with sufficient accuracy. In this case an explicit solution for $(p_D - p_s)$ may be obtained in the simple form:

$$p_D - p_s = \frac{(\tfrac{1}{2}) p_s (v_0 - v) - \int_v^{v_0} p dv}{C_v (\partial T/\partial p)_v - (\tfrac{1}{2})(v_0 - v)}. \tag{6}$$

In order to solve Eq. (6) a preliminary estimate is made for p_s as a function of v at constant entropy, in which case the numerator of Eq. (6) may easily be evaluated. The specified correction may then be applied to the observed shock pressure p_D and a second approximation made for the isentropic pressure-volume relation. Further approximations can readily be made if necessary.

The initial free surface velocity of the target plates with which we have experimented is approximately twice the mass velocity. More precisely, however, the excess σ of the free surface velocity over mass velocity is given by the Riemann velocity

$$\sigma = \int_{\rho_D}^{\rho_1} (c/\rho) d\rho \tag{7}$$

an expression which may be derived on the assumption that the material compressed by the shock expands isentropically to density ρ_1 when traversed by a wave of rarefaction. The difficulty involved in evaluating σ stems from the fact that the entropy of the expanding material, though constant, is different from the original entropy, and accordingly, to determine the isentropic equation of state, the experimental data require correction. Before considering the corrections necessary it is convenient to transform Eq. (7) to the form

$$\sigma = \int_0^{p_D} (-\partial v/\partial p)_s^{\frac{1}{2}} dp. \tag{8}$$

Evaluation of σ as specified in Eq. (8) may be facilitated by the following artifice. First eliminate the shock velocity D between Eqs. (1) and (2) obtaining an expression for the mass velocity u in the form

$$u = \int_0^{p_D} \left(\frac{v_0 - v}{p_D}\right)^{\frac{1}{2}} dp, \tag{9}$$

the integrand of which is constant once a particular volume v corresponding to the extreme pressure has been chosen. Combining Eqs. (8) and (9) there results

$$(\sigma - u)/u = (1/p_D) \int_v^{v_1} \left\{1 - \left[(\partial v/\partial p)_s \frac{p_D}{v_0 - v}\right]^{\frac{1}{2}}\right\} \left(\frac{\partial p}{\partial v}\right)_s dv, \tag{10}$$

where v_1 is the final specific volume after the isentropic expansion. Equation (10) clearly implies that for sufficiently weak shock the free surface velocity approaches twice the mass velocity. Furthermore, approximate values of the integrand of Eq. (10) suffice to provide an estimate of the difference between u and σ.

In order to determine $(\partial p/\partial v)_s$ at the entropy of the shocked material, one may compute the entropy change Δs due to the shock, then estimate from available thermodynamic data the magnitude of $\partial^2 p/\partial s \partial v$, and thus obtain a corrected value of the desired derivative in the form

$$(\partial p/\partial v)_s = (\partial p/\partial v)_{s0} + (\partial^2 p/\partial s \partial v) \Delta s. \tag{11}$$

A formula for $\partial^2 p/\partial s \partial v$ in terms of readily available thermodynamic data is

$$\frac{\partial^2 p}{\partial s \partial v} = -\frac{T}{C_v^2}\left(\frac{\partial p}{\partial T}\right)_v^2 + \frac{T}{C_v}\frac{\partial^2 p}{\partial T \partial v} + \frac{T^2}{C_v^3}\left(\frac{\partial p}{\partial T}\right)_v^2 \left(\frac{\partial C_v}{\partial T}\right)_v - \frac{2T^2}{C_v^2}\left(\frac{\partial p}{\partial T}\right)_v \left(\frac{\partial^2 p}{\partial T^2}\right)_v \tag{12}$$

in which the first term on the right is the most important.

The entropy excess Δs of the shocked material may be computed by integrating with respect to temperature at the final known volume of the compressed material.

The first step in this process is to determine the isentropic temperature T_s at the compressed volume v from the formula

$$\ln(T_s/T_0) = \int_v^{v_0} (1/C_v)(\partial p/\partial T)_v dv. \tag{13}$$

Next one determines the shock temperature T_D at this same volume by means of the relation

$$T_D - T_s = \frac{\Delta e_D - \Delta e_s}{C_v}. \tag{14}$$

The numerator of Eq. (14) may be evaluated by means of Eqs. (3) and (4) which, with the help of Eq. (6), may be put in the form

$$\Delta e_D - \Delta e_s = \frac{(\tfrac{1}{2})p_s(v_0 - v) - \int_v^{v_0} p\,dv}{1 - \dfrac{v_0 - v}{2C_v}\left(\dfrac{\partial p}{\partial T}\right)_v}. \tag{15}$$

Once T_D and T_s are known, it is very simple to compute Δs, for

$$\Delta s = C_v \ln(T_D/T_s). \tag{16}$$

It should perhaps be noted that Eqs. (14) and (16) are both based on processes occurring at constant volume, in which of course no mechanical work is performed by the system. On the other hand, the integrals in Eqs. (13) and (15) are to be evaluated at constant entropy.

It will be clear that all the corrections to be made depend on information about the temperature and volume dependence of the various thermodynamic variables. Fortunately C_v and $(\partial p/\partial T)_v$ do not vary much under the conditions covered by the observations. The calculations for Duralumin have included an estimate of this variation, though it has been found that the final results would not be significantly changed if both quantities were taken as constants.

The necessary calculations are quite straightforward once an approximate expression for p as a function of compression at constant entropy is known. The empirical form chosen is

$$p_s = \alpha_s \mu + \beta_s \mu^2, \tag{17}$$

the entropy being constant. The value of the constant α_s is inferred from known values of the velocity of sound and of the density under standard laboratory conditions. Thus the data derived from shock measurements are used merely to evaluate the constant β_s. Some question naturally arises as to how α_s is related to the observed sound velocity. Equation (17) is intended to apply to material under such great hydrostatic pressure that any shearing stress is completely negligible both in its magnitude and in its effect on the compression η. Accordingly, it would seem natural to evaluate α_s for conditions under which compression occurs without appreciable shearing stress. But determinations of sound velocity in general are made either with bars, for which $c_1 = (E/\rho)^{\frac{1}{2}}$ where E is Young's modulus, or for large masses of material for which $c_2 = [(k + 4G/3)/\rho]^{\frac{1}{2}}$ where k is the bulk modulus and G the shear modulus. It is the isentropic bulk modulus which relates pressure to compression when the shearing stress is negligible, and accordingly we have assumed that

$$\alpha_s = (\partial p/\partial \mu)_s = -v_0(\partial p/\partial v)_s = k_s. \tag{18}$$

A value of α_s may be quickly deduced from c_1, if Poisson's ratio ν is known, or from c_2 if the velocity of shear waves $c_3 = (G/\rho)^{\frac{1}{2}}$ is known. In the latter case, the computation is obvious; in the former,

$$\alpha_s = E_s/3(1 - 2\nu). \tag{19}$$

Most of the currently available data on compressibilities at extreme pressures have been obtained isothermally. These data may likewise be fitted well by an equation similar to Eq. (17):

$$p_T = \alpha_T \mu + \beta_T \mu^2. \tag{20}$$

The relation between α_s and α_T is well known to be

$$\alpha_s - \alpha_T = (v_0 T/C_v)(\partial p/\partial T)_v^2. \tag{21}$$

The corresponding difference between β_s and β_T is not so well known, but may be written

$$\begin{aligned}\beta_s - \beta_T = -(\alpha_s - \alpha_T)\{1 - (\tfrac{1}{2})v_0[&(1/C_v)(\partial p/\partial T)_v \\ &+ 3(\partial^2 p/\partial v \partial T)/(\partial p/\partial T)_v - 3(T/C_v)(\partial^2 p/\partial T^2)_v \\ &- (T/C_v^2)(\partial p/\partial T)_v(\partial C_v/\partial T)_v]\}.\end{aligned} \tag{22}$$

In the course of developing experimental techniques with a view to determining what ultimate precision is possible, it was found convenient to use an alloy of aluminum with superior mechanical properties rather than the pure element for which static compressibilities are available. In order to compare the present work with that of others,[2] it is desirable to estimate the effects of the alloying constituents. This can be done easily if one assumes that the volume of the alloy is equal to the sum of the volumes of its constituents. For many alloys this assumption leads to an excellent estimate of the normal density, and it seems reasonable to expect that its validity is not appreciably worse at high pressures. The subscripts (1) and (2) will be used to denote properties of the constituents; absence of either of these denotes a property of the alloy. The additional subscript (o) refers to a property under standard laboratory conditions. Thus the equations of state involved would be

$$\begin{aligned} p &= \alpha\mu + \beta\mu^2, \\ p &= \alpha_1\mu_1 + \beta_1\mu_1^2, \\ p &= \alpha_2\mu_2 + \beta_2\mu_2^2, \end{aligned} \tag{23}$$

while the equation connecting the various compressions is

$$\frac{1}{\rho_0(\mu+1)} = \frac{X_1}{\rho_{01}(\mu_1+1)} + \frac{X_2}{\rho_{02}(\mu_2+1)}. \tag{24}$$

X_1 and X_2 denote the fractions by mass of the respective constituents. Values of α and β in terms of α_1, α_2, β_1, and

[2] P. W. Bridgman, Proc. Am. Acad. Arts Sci. 77, 189 (1949).

β_2 may be approximated at small compressions by implicit differentiation. This approximation probably does not give very good average values over the extended range of compressions involved, but it should at least suffice to indicate whether or not observed discrepancies are of the sort to be expected because of variation in composition. The required relations are

$$1/\rho_0\alpha = (X_1/\rho_0\alpha_1) + (X_2/\rho_{02}\alpha_2), \tag{25}$$

and

$$\frac{\beta}{\rho_0\alpha^3} = \frac{X_1}{\rho_{01}\alpha_1^2}\left[\frac{\beta_1}{\alpha_1} + 1 - \frac{\rho_0 X_1}{\rho_{01}}\right] + \frac{X_2}{\rho_{02}\alpha_2^2}\left[\frac{\beta_2}{\alpha_2} + 1 - \frac{\rho_0 X_2}{\rho_{02}}\right]. \tag{26}$$

EXPERIMENTAL TECHNIQUES

The essential details of the experimental technique for the necessary velocity determinations may be visualized by reference to Fig. 1. The material to be studied is machined into the form of a plate perhaps 8 inches in diameter and of a thickness governed by considerations to be discussed. A shock wave is induced in this plate by means of a large block of high explosive (H.E.) detonated simultaneously at all points of its upper surface by means of a suitably designed high explosive lens. Detonation of the latter is initiated electrically in the usual way. At the upper surface of the plate, a high pressure pulse is produced, the magnitude of which depends on the type of high explosive used, and the duration of which depends on the size and shape of the high explosive. In order to achieve a condition of fairly constant pressure at the upper surface of the plate for an appreciable length of time the block of H.E. must be large. For although the instantaneous pressure in the detonated H.E. depends primarily on its chemical and physical properties, the pressure generated by the detonation is immediately relieved at the free surfaces by rarefaction waves. These rarefactions limit the time available for the measurements to a few microseconds and also mean that portions of the plate near the sides never receive the full detonation pressure.

Since the block of high explosive is necessarily of finite thickness (usually 3 to 4 inches), the shock wave in the plate resulting from impact by the detonation wave in the explosive is not quite flat-topped. The shock front is followed immediately by a rarefaction from the back surface which results in an exponential decay. This unloading wave, moving through the plate more rapidly than the shock front, is continuously whittling down the peak pressure. In consequence it is necessary to measure the parameters as a function of thickness of the material.

The free surface velocity at the bottom of the plate (Fig. 1) is ascertained by means of externally placed electrical contactors. These contactors, or "pins," shown in Fig. 1, may be arranged to measure either free surface velocity, by spacing them out behind the plate as shown, or compression wave velocity through the plate by insulating and imbedding the pins in holes drilled to various depths. In either case, the oscillograph records the time at which each pin first touches the metallic surface. In order to synchronize the oscillograph, an extra pin is imbedded in the plate at some convenient level, thus providing an electrical pulse for initiation of the sweep.

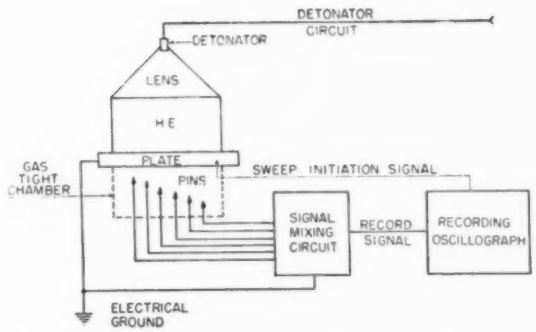

FIG. 1. Apparatus for determining free surface velocity.

Pressure may be measured independently by means of probes made from z-cut tourmaline disks. The calibration constant of the crystals, for the geometry and conditions of these tests, was determined from measurements of u and D in steel. It is advantageous to make these crystals thin. Ours are thicker, about 0.5 mm, than desired but this choice was dictated by practical consideration of existent constructional limitations. Several reverberations are required for equilibrium to be attained between target and crystal and therefore a useful crystal life of about 0.5 μsec is required. If the crystal becomes short circuited before this time a correction factor must be applied for the acoustic mismatch of crystal and specimen plate.

Most of the experimental work on which the present paper is based was performed in 1945. At that time it was realized that elaborate precautions would be required in order to improve the precision of the data. The recent work on Duralumin is inclusive of various improvements in technique which have been discovered over the course of the last five years.

In the first place, if the pins are spaced out behind the plate as shown in Fig. 1, they may be prematurely connected to the plate, and to one another, by ionization of the gas with which they are surrounded. Attempts to insulate the pins from this ionization tend to result in erratic conduction when the metallic surface itself arrives. After much investigation, which included attempted evacuation of the space surrounding the pins, and all sorts of insulations for the pins themselves, it was discovered that little or no preconduction occurs if the gas surrounding the pins is one of the light hydrocarbons, i.e., methane, ethane, propane, or butane. The "gas-tight chamber" in Fig. 1 is always, in the more recent work, filled with one of these gases.

Furthermore, the plane wave of compression as it proceeds through the plate must be exceedingly regular. It is known that in such a compression the pressure rise

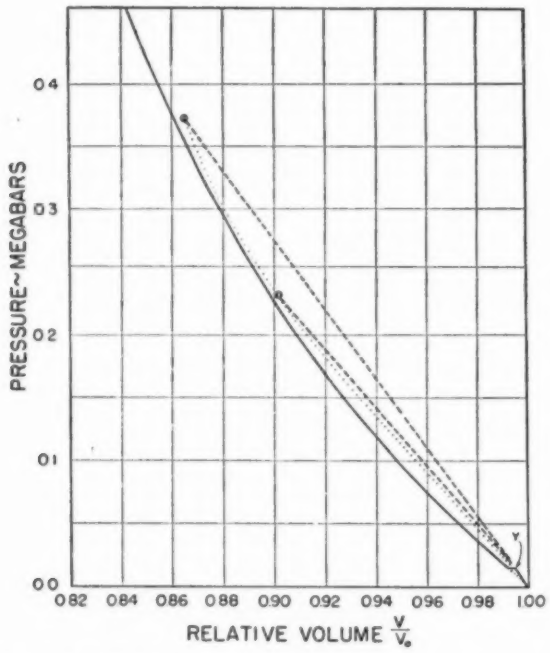

FIG. 2. Solid line represents a hypothetical isentropic equation of state of steel subjected to uniaxial compression, showing effect of shearing stress below the dynamic yield point Y. Shock wave velocity is given by the expression $D=(-\Delta p/\Delta V)^{\frac{1}{2}}V$, where V is the specific volume of the material ahead of the shock; Δp is the incremental shock pressure; and ΔV, the change in specific volume due to the shock.

Below the dynamic yield point, compressional waves are propagated with the sound velocity, proportional to the square root of the slope of the solid line.

Above dynamic yield point, compressional waves are propagated with velocities proportional to the square root of the slope of the dashed lines. By joining the end points of the dashed lines, one obtains the representation of the "Rankine-Hugoniot" equation of state shown by the dotted curve. This lies above the isentropic because of the entropy change under shock conditions. Upper dashed line represents a shock traveling with the velocity of sound at low pressures, i.e., a shock not preceded by an elastic wave.

is exceedingly abrupt and that the amplitude of this abrupt rise is constant provided the material behind the wave is uniformly compressed. Constancy of pressure behind the shock front may be achieved approximately by using a sufficiently large block of high explosive. If, however, the wave is not plane, its space configuration varies as it proceeds, and if the compression behind the front is not uniform, the magnitude of the virtually discontinuous pressure change is not constant. Furthermore, even if the wave is perfect in terms of the above criteria the plane of the waves may not be parallel to the plane of the plate. A variety of special precautions has been introduced to minimize effects of these possible sources of error. Continual improvement in the preparation of the H.E. and the "lens" have virtually eliminated departures from planeness and tilt in the wave itself. A small residual tilt of the front does not affect (to errors of the first order) the inferred velocities if the pins are properly arranged in small circles. In some experiments, as many as nine circles of eight pins each are used to supply simultaneous information.

In addition to the above difficulties it has been found that small irregularities or scratches in the surface of the plate result in jets which may cause erratic pin discharge. Indeed owing to the polycrystalline structure of the metal itself, some irregularities in the moving free surface are invariably present, the magnitude of these irregularities being of the order of the size of the individual metallic crystal grains. Because of this unavoidable roughness, it is not practical to make free surface velocity measurements over extremely short ranges of motion. Experiment has shown, however, that these irregularities are not too serious if the total range covered by the pins exceeds 5 mm.

A further limitation on the method results from the fact that in certain materials (e.g., steel) an elastic wave of compression moves with a higher velocity than the shock wave up to a certain pressure which depends on the dynamic yield point (see Fig. 2). In such cases, the necessary information can be achieved by the use of piezoelectric crystals (see Figs. 3 and 4).

One further technical experimental point deserves brief mention. As has been mentioned, some decay of pressure is encountered with increasing thickness of the plate. It is thus essential that the shock wave velocity and the mass velocity be obtained for an equivalent particle, namely a particle close to the free surface of the plate. But the probes for measuring propagation velocity are perforce distributed through the thickness of the plate, and, since the amplitude of the shock is varying, so also does the propagation velocity vary. The simplest way of finding shock velocity at the free surface is to make the portion of the plate where the shock velocity is measured somewhat thicker than the portion where the free surface velocity is measured, so that an average value for the former will be compatible with the observed value of the latter.

From the measured free surface velocity, the mass velocity of the compressed material may be inferred. It is, of course, necessary to complete the measurement of free surface velocity before reverberations can occur in the target plate. Otherwise, one obtains a measure not of mass velocity but of momentum transfer from explosive to plate. Furthermore because of the decay of pressure behind the shock front, one might expect the *observed* free surface velocity to diminish as the motion proceeds, but such an effect has not been detected. With these considerations in mind each set of 8 contactors is usually spaced over an interval of about 5 mm from the

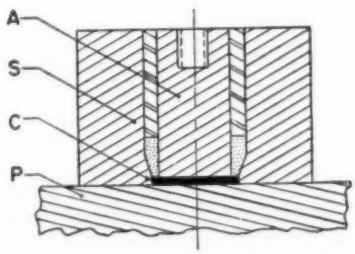

FIG. 3. Assembly for holding piezoelectric crystal in place. *A* Metal electrode and inertial support for crystal. *S* Guard ring. *C* Crystal. *P* Specimen through which shock-wave proceeds.

back surface of the plate, though for very thin plates an even closer spacing may be necessary in spite of the uncertainties caused by roughness of the moving free surface as previously mentioned, and the shorter reverberation time.

In order to obtain extensive data on the equation of state of the material under study, it is necessary to produce in the specimen compressional shock waves of arbitrary amplitude. There are three ways in which this has been accomplished:

(1) By increasing the thickness of the specimen, the pressure decays naturally, because the amplitude of the pressure discontinuity remains constant only if the pressure in the compressed material is everywhere uniform. With blocks of high explosive of finite dimensions, this condition is not satisfied, and a continuous degradation of shock pressure is always encountered.

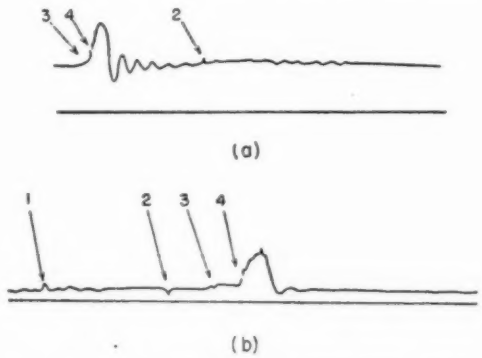

FIG. 4. Oscillograph records of shock-wave profile after moving through (a) 0.25 in. (b) 1.25 in. of SAE 4340 steel. (1) is cross talk from (a); (2) is the synchronizing time pip for the two records; (3) is the elastic-wave front; and (4) is the main shock front. Total sweep length is 10 μsec. Elastic pressure is 0.0157 mb; peak shock pressure in (b) is 0.225 mb; elastic velocity is 0.585 cm/μsec; and shock velocity is 0.510 cm/μsec. (Oscillations in shock front are reverberations in crystal probes.)

(2) The detonation pressure may be varied by using different compositions of high explosive.

(3) The amplitude of the transmitted shock may be adjusted by placing an intermediate metal between the block H.E. and the specimen "plate," as would be possible with acoustic waves.

OBSERVED DATA

The data obtained by the measurements made in 1945 are summarized in the first two columns of Table II. The more recent measurements made on Duralumin are listed in the first two columns of Table III.

In the foregoing two tables, the recorded data represent averages taken from a large number of individual determinations. In Table II the standard deviation for both wave velocities is of the order of 2%. Unfortunately, in the case of steel, the presence of the elastic wave renders the computation of shock pressure and compression somewhat uncertain; the magnitude of the correction appears, however, to be less than 1%. In Table III the standard deviations as computed from the residuals do not exceed 0.5% in any case. In compiling both tables the original oscillographic data were analyzed by the method of least squares. Table II is based on the assumption that the measured free surface velocity is twice the mass velocity. In Table III a correction to this approximation has been made. All units are as specified in Table I.

TABLE II. Early data on aluminum, cadmium, and steel.

Material	Shock velocity	Free surface velocity	$\eta-1$ (computed)	Pressure (computed)	Pressure (crystal)
Aluminum	0.738	0.295	0.250	0.294	——
Cadmium	0.396	0.145	0.224	0.248	0.231
Steel		0.115	0.122	0.223	(calibration)
Shock wave	0.510 (Average)	0.166	0.195	0.332	0.324
Elastic wave	0.588	0.00667	0.006	0.015	0.0157

NUMERICAL COMPUTATIONS AND RESULTS

In order to reduce the shock pressures in Table II to adiabatic pressures, the data of Table IV are required. The data of the first four columns were computed from material to be found in the usual sources, notably Birch's Handbook,[3] the Metals Handbook,[4] and the Handbook of Chemistry and Physics.[5]

The values of β_s in the fifth column are those deduced by correcting the data of Table II to isentropic conditions and then fitting Eq. (17) to the observed point.

In the case of steel, only the point obtained at the lower shock pressure was used in computing the value of β_s. At the higher pressure, the computed value of μ appears to be much too large, and would imply an even smaller value of β_s. Further work will be required to verify the discrepancy between Bridgman's work and ours, but the available data seem worth recording because of the interest which may attach to the peak pressure as recorded by the tourmaline crystal and the relatively good agreement between this pressure and that computed by Eq. (2).

Values of β_s may also be computed by an analysis of Bridgman's more recent work,[2] and for aluminum and iron these appear in the last column of Table IV.

TABLE III. Recent data on 24 ST Duralumin.

Shock velocity	Free surface velocity	Mass velocity (computed)	$\eta-1$ (computed)	Shock pressure (computed)	Isentropic pressure (computed)
0.6460	0.1629	0.0814	0.1442	0.1462	0.1435
0.6850	0.2254	0.1126	0.1967	0.2144	0.2079
0.7005	0.2395	0.1196	0.2059	0.2329	0.2250
0.7426	0.3014	0.1503	0.2538	0.3103	0.2952
0.7520	0.3179	0.1584	0.2668	0.3312	0.3139

[3] Francis Birch, *Handbook of Physical Constants* (Geological Society of America, 1942).

[4] *Americal Society of Metals*, "Metals handbook," 1948.

[5] Charles D. Hodgman, *Handbook of Chemistry and Physics* (Chemical Rubber Publishing Company, Cleveland, 1952).

TABLE IV. Thermodynamic properties of selected elements.

Element	ρ_0	α_s	C_v	$(\partial p/\partial T)_v$	β_s	β_s (Bridgman)
Aluminum	2.699	0.742	0.108	0.56	1.53	1.69±0.04
Cadmium	8.65	0.48	0.014	0.46	2.20	···
Steel	7.84	1.69	0.054	0.46	0.8	2.4 ±0.1

The standard deviations for these values are simply indications of the precision with which the empirical equation of state fits the observed points and should not be taken as an indication of the experimental accuracy. The relatively better precision shown in the case of the aluminum is owing chiefly to the fact that the aluminum is much more compressible, so that a greater range of values of the compression are available for analysis. The correction from β_T to β_s amounts to $+0.01$ for aluminum when computed by Eq. (22); it has not been computed for steel.

The corrections required to reduce the data of Table III are shown graphically in Fig. 4. The plotted values of $(\sigma-u)/u$ are subject to considerable uncertainty, but the values shown for p_D-p_s should be accurate to 5% or better. In analyzing the reduced data, a value $\alpha_s=0.760$ was arbitrarily selected. This value was inferred from measurements of the velocity of sound in Duralumin. The method of least squares was then used to infer the value $\beta_s=1.57\pm0.02$ for this material. Correction for the presence of copper [see Eqs. (25) and (26)] gives corresponding values for pure aluminum of $\alpha_s=0.753$ and $\beta_s=1.53$. Correction of these to isothermal conditions [see Eqs. (21) and (22)] yields $\alpha_T=0.726$, $\beta_T=1.52$. Corresponding coefficients computed from Bridgman's data again by the method of least squares are $\alpha_T=0.715\pm0.001$, $\beta_T=1.68\pm0.04$. The discrepancy between the two values of α is of no immediate concern, since the shock wave measurements are not used for this determination. However, part of the discrepancy between the two values of β_T results from the fact that the α's do not agree. If our arbitrary choice of α is made in such a way as to give agreement with the figure deduced from Bridgman's work, then the discrepancy between the β's drops from 0.16 to 0.11. One might reasonably inquire as to whether a three-term equation of state would better fit our data, and yield better agreement between our results and Bridgman's. Unfortunately if the second-order coefficients were made to agree, the third-order coefficient as deduced from our data would be negative, and hence could hardly be useful for purposes of extrapolation.

It should of course be noted that Bridgman's measurements extend to only 30 000 kg/cm², whereas ours cover roughly ten times this range. Since Eq. (17) is purely empirical, it is to be expected that different sets of coefficients would be required to give the best representations of the data over the two different ranges.

CONCLUSIONS

Determination of shock and mass velocities in material subject to explosive stress yields data for equations of state up to 0.3 megabar or more. With care the precision attainable is about 0.5% on the velocity measurements, but because of the extreme pressures that may be reached, even this precision provides a more precise determination of the second-order term in the equation of state than is possible with static measurements. In the case of aluminum, part or all of the discrepancy between the coefficients determined statically and those determined dynamically may be owing to the different pressure ranges to which the respective measurements apply, though the sign of the discrepancy suggests that this explanation is inadequate.

In Fig. 5 there has been included an estimate of the final temperature increase in the Duralumin after the expansion to atmospheric pressure. [This estimate is based on the entropy change as calculated by Eq. (16), and has been converted to centigrade degrees.] It will be observed that the melting point of the aluminum would be reached by a 0.6-megabar shock, and it seems likely that the measurements would become impracticable under these conditions. In any event the problem of correcting free surface velocity to obtain mass velocity would become much more complicated.

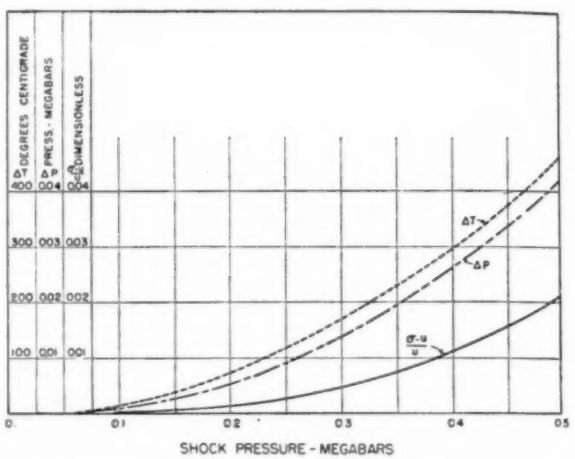

FIG. 5. Excess of shock pressure over adiabatic pressure (ΔP), temperature increase after expansion (ΔT), and fractional excess free surface velocity $(\sigma-u)/u$ as functions of pressure.

A final word about precision seems in order. It might be imagined on casual examination of Eqs. (1) and (2) that D and u must be determined with equal precision in order to obtain useful data on the equation of state. Fortunately, however, u need not be known with as great precision as D. To show this, let us consider the problem of determining β in terms of u and D by means of Eqs. (1), (2), and (17), assuming α to be known. The fractional error $\Delta\beta/\beta$ to be feared in β due to fractional

errors $\Delta u/u$ and $\Delta D/D$ in u and D, respectively, is

$$(\Delta\beta/\beta)=(u/\beta)(\partial\beta/\partial u)(\Delta u/u) +(D/\beta)(\partial\beta/\partial D)(\Delta D/D). \quad (27)$$

Calculation reveals that for the Duralumin, at the highest pressure attained, $(u/\beta)(\partial\beta/\partial u)=-1.9$ and $(D/\beta)(\partial\beta/\partial D)=7.8$ so that four times the precision is required on D to make the errors of equal magnitude. Accuracy of 0.5% on D would imply 4% accuracy on β. In view of the fact that five points were used for our final determination of β, the calculated standard deviation of a little less than 2% appears to be compatible with these considerations.

ACKNOWLEDGMENTS

The authors wish to express their indebtedness to Gordon Waters, S. W. Bale, and Earl Faudree for their care and precision in making the assemblies and to George Cody for checking the thermodynamical calculations.

JOURNAL OF APPLIED PHYSICS VOLUME 26, NUMBER 12 DECEMBER, 1955

Ferroelectric Hysteresis in Barium Titanate Single Crystals

H. H. WIEDER
Naval Ordnance Laboratory, Corona, California
(Received June 15, 1955)

The properties of the dynamic hysteresis loop of a c-domain $BaTiO_3$ single crystal are examined as a function of temperature. Experimental results indicate that the coercivity and hysteresis losses decrease sharply as the crystal passes through a phase transition to a lower order of symmetry. This occurs without a substantial loss in loop rectangularity. The properties of a theoretical model for the hysteresis loop are derived from the Devonshire thermodynamic equations and previously defined experimental parameters. In the tetragonal and orthorhombic crystal phases, good agreement is obtained between the behavior predicted for the theoretical model and the experimental observations made on a c-domain.

INTRODUCTION

THE recently reported method of $BaTiO_3$ crystal[1] growth has made available large crystal plates having a relatively simple domain configuration. It is therefore possible to isolate a crystal area composed only of antiparallel domains (c-domain) whose polarization axis is perpendicular to the crystal plate at room temperature. Such a crystal area is a close approximation of a single domain. Its behavior can therefore be tested against relatively simple concepts in the theory of ferroelectrics.

For ferroelectrics such as barium titanate* the hysteresis loop is a graphical representation of the relation between the polarization and the applied electric field. In analogy with ferromagnetics, the magnitude of the field necessary for the switching of the polarization along the major hysteresis loop is defined as the coercivity. This paper presents some experimental and theoretical relations between the coercivity of a c-domain and the ferroelectric crystal phase of the $BaTiO_3$ unit cell.

EXPERIMENTAL

The barium titanate crystals used for these experiments consisted of selected specimens having a large c-domain area. The thickness of the crystals varied between 0.20 and 0.10 mm. Electrodes, in the form of an evaporated layer of gold, were applied to the center of the crystal faces over an area of 0.15 mm². The well-known circuit of Sawyer and Tower[2] was used for obtaining the dynamic hysteresis loop at 60 cps. Each sample was maintained for five minutes at a given temperature (±0.5°C) allowing it to come to thermal equilibrium. The temperature was then gradually changed to a new stable setting. The temperature range covered the region of −100°C to +100°C. Some of the representative hysteresis loops are shown in Fig. 1 and the calculated values of coercivity are plotted in Fig. 2.

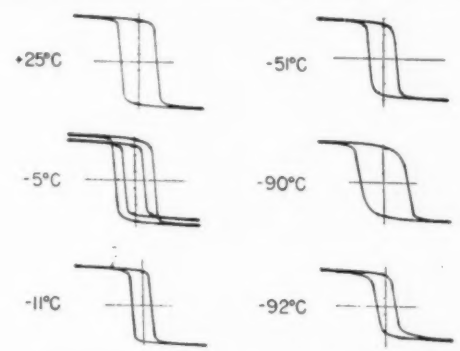

FIG. 1. Representative 60-cps hysteresis loops of a c-domain crystal as function of temperature. Abscissa = 6.6 kv/cm per inch. Ordinate = 58 μcoulombs/cm² per inch.

[1] J. P. Remeika, Proceedings of the 1954 Electronic Components Symposium, 61 (1954).

* For a survey of recent publications on ferroelectrics and their application, see W. P. Mason and R. F. Wick, Proc. Inst. Radio Engrs. 42, 1606 (1954).

[2] C. B. Sawyer and C. H. Tower, Phys. Rev. 35, 269–73 (1930).

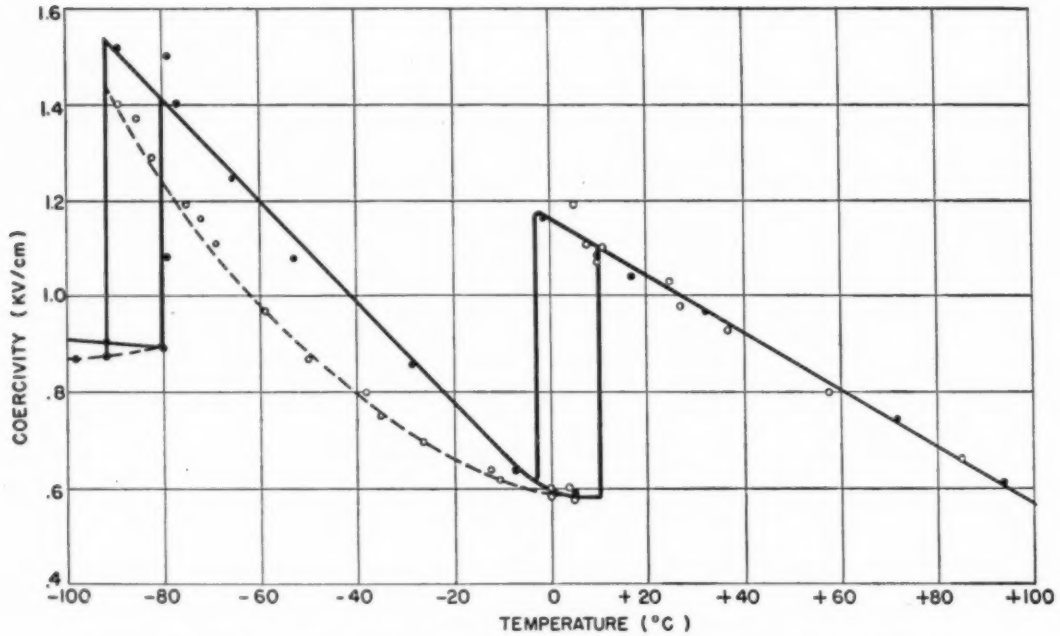

FIG. 2. Coercivity as a function of temperature. Solid curve=c-domain crystal at +25°C. Dashed curve=c-domain crystal having a number of a-domain wedges at +25°C.

It is evident that the coercivity decreases sharply as the crystal goes through a phase transition from higher to lower symmetry. The two ferroelectric transitions correspond to a change in the crystal lattice structure from tetragonal to orthorhombic at −10°C and orthorhombic to trigonal at −90°C. Although generally complicated domain twinning effects occur as a crystal goes through a transition, optical examination indicated that the simple configuration shown in Fig. 3 is obtained for a tetragonal c-domain going through the −10°C transition. The transition to the trigonal phase is generally more complicated and only two crystals from this experimental lot gave the simple domain arrangement described by Kay and Vousden.[3]

DISCUSSION

The theory developed by Devonshire[4] and extended by Slater[5] is a very useful tool in the analysis of the behavior of $BaTiO_3$ single crystals using only simple crystal thermodynamics and experimentally determined changes in lattice parameters as a function of temperature. Merz[6] has used it successfully in explaining the double hysteresis loop in the vicinity of the Curie point and the shift of the Curie point as a function of high applied fields. Other phenomena such as the variation of the spontaneous polarization and of the dielectric constant as a function of temperature have been successfully explained by Devonshire[4] and Kay and Vousden.[3]

In the simplest form, the Devonshire equations define the free energy of a single domain crystal in terms of polarization only, the effects of stresses being neglected. They are presented below in the normalized parameters given by Devonshire:

$$A=0 \tag{a}$$

$$A=\chi_0 P_1^2[\tfrac{1}{2}z^3-z^2+\tfrac{1}{2}zt] \tag{b}$$

$$A=\chi_0 P_1^2[z^3+2(\alpha-1)z^2+zt] \tag{c}$$

$$A=\chi_0 P_1^2[z^3+3(2\alpha-1)z^2+\tfrac{3}{2}zt] \tag{d}$$

where Eqs. (a), (b), (c), and (d) refer, respectively, to the cubic, tetragonal, orthorhombic, and trigonal crystal phases. Here, A is the free energy and χ_0 and P_1 are constants having values of: $\chi_0=8.1\times10^{-4}$ cgs units and $P_1=18\times10^{-6}$ coulombs/cm^2. The temperature parameter t is determined from the relation $t=(T-T_0)/(T_1-T_0)$ where T_1 and T_0 are constants and T is an arbitrary temperature in degrees centigrade. T_1 and T_0

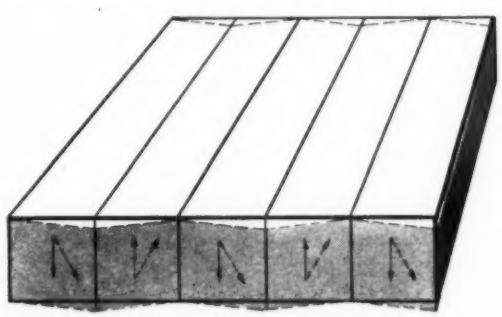

FIG. 3. A tabular c-domain crystal (solid lines) taken through the orthorhombic transition (dotted lines). Note shift in polarization axis.

[3] H. F. Kay and P. Vousden, Phil. Mag. **40**, 1040 (1949).
[4] A. F. Devonshire, Phil. Mag. **40**, 1040 (1949).
[5] J. C. Slater, Phys. Rev. **78**, 748 (1950.
[6] W. J. Merz, Phys. Rev. **91**, 513 (1953).

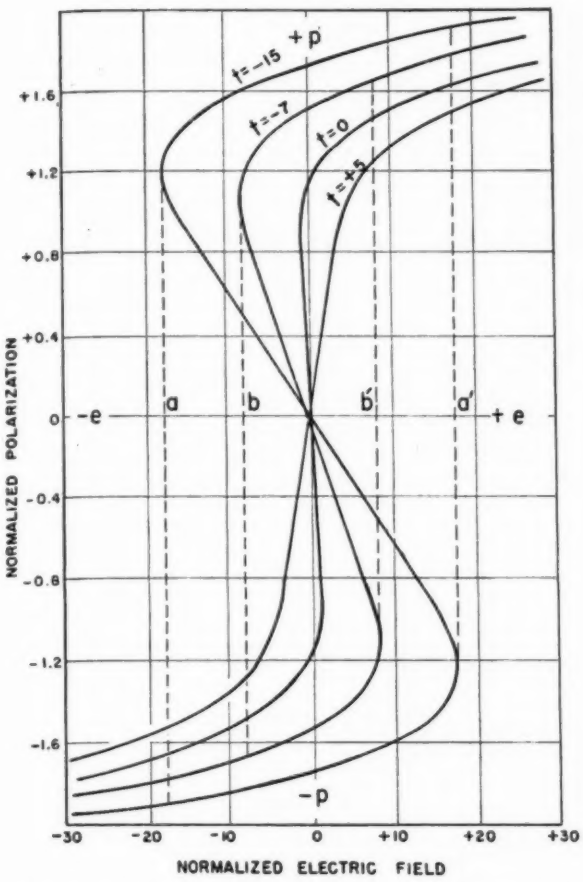

FIG. 4. The idealized hysteresis loop obtained by plotting polarization as a function of electric field for the tetragonal phase of the $BaTiO_3$ crystal using the normalized Devonshire equation for 3e.

have the values of +122°C and +117°C, respectively. The parameter z is determined from the relation $z=(P_z/P_1)^2$ where P_z is the value of the polarization along the Z coordinate axis of a single domain. For a c-domain, $P_z \simeq 26\times10^{-6}$ coulombs/cm^2 at +25°C.[6] The parameter α represents the interaction between the polarizations developed along the a-, b-, c-axis of the unit crystal cell. In the tetragonal phase, α is zero since the elongation of the unit cell along the c-axis restrains the formation of polarizations along either the a- or the b-axis. Devonshire has indicated that a best fit for experimental results can be obtained by assuming $\alpha=1.2$. For the improved crystals used in the previously described experiments a better fit is obtained if α is assumed to have a value of 1.8. The relations between the polarizations along the z coordinate axis of a crystal in its various phases have been determined experimentally as: P_z (tetragonal) $=\sqrt{2}\,P_z$ (orthorhombic) $=\sqrt{3}\,P_z$ (trigonal). Also, since the electric field E_z is obtained from the relation $E_z=dA/dP_z$, one may obtain the equations defining a normalized electric field e in terms of a normalized polarization p and the aforementioned parameters t and α:

$$e=3p^5-4p^3+pt \qquad \text{(e)}$$

$$e=\tfrac{3}{4}p^5+2(\alpha-1)p^3+pt \qquad \text{(f)}$$

$$e=\tfrac{1}{3}p^5+4/3(2\alpha-1)p^3+pt. \qquad \text{(g)}$$

Equations (e), (f), and (g) refer, respectively, to the tetragonal, orthorhombic, and trigonal phases with $e=E_z/\chi_0P_1$ and $p=P_z/P_1$. Figure 4 represents, for Eq. (e), a plot of the function $p(e)$ for constant values of t. The threshold field $de/dp=0$, where the polarization jumps to a new stable value, is represented by the dotted lines in the Figure. For a single domain crystal, one might make the assumption that this threshold field is the theoretical coercivity e_c. One can obtain, therefore, a suitable plot of this coercivity determined from the maxima of the curves of Eqs. (e), (f), and (g). Such a plot is shown in Fig. 5. It can be seen that reasonably good agreement is obtained between the theoretical and experimental curves in the tetragonal and orthorhombic regions. The experimental plot indicates, however, a much larger change in coercivity at the trigonal transition than could have been expected from the theoretical curve. This probably results from the fact that the crystal breaks up into multiple twinned

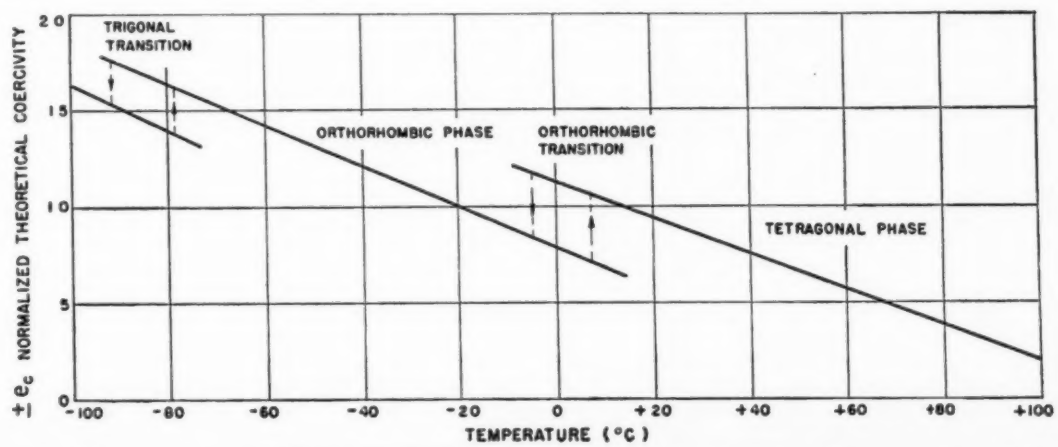

FIG. 5. Theoretical coercivity calculated from the idealized hysteresis loop plots and the Devonshire equations.

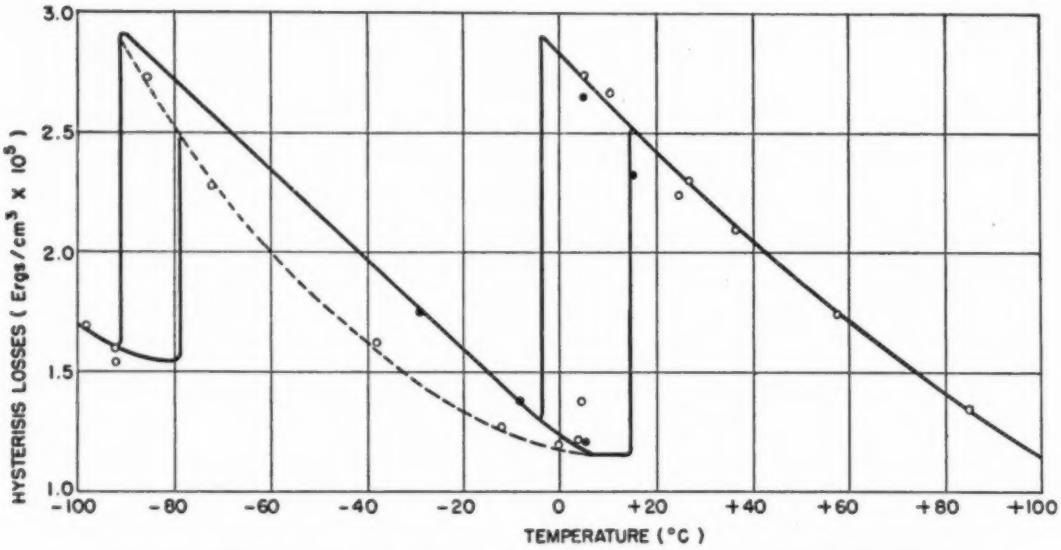

FIG. 6. Hysteresis loss per cycle per cm³ calculated from the area enclosed by experimental 60-cps hysteresis loops.

domains leading to effects which had not been taken into account in this simple theory. Another possibility might be that the interaction factor is not temperature independent as Devonshire had assumed. Recent experimental evidence[7] indicates that an increase of α with temperature is to be expected and, qualitatively, this might bring the experimental and theoretical curves to a better agreement.

Additional experiments were made in order to determine the effect of *a*-domain wedges under the electrode areas. These are domains which have their polarization axis in the plane of the crystal plate. As the domain twinning increases, the departure from the theoretical curve increases; as may be inferred qualitatively from Fig. 5.

Figure 6 is a plot of the hysteresis loss per unit volume as a function of temperature. The latter is obtained from an integration of the area under the experimentally determined 60-cps loops. It is evident that the decrease in coercivity below the phase transitions (Fig. 2) is accompanied by a decrease in hysteresis losses (Fig. 6). This should make this crystal phase of particular interest for circuit and component design.

[7] D. R. Young, IBM Laboratories, private communication (September, 1954).

SUMMARY AND CONCLUSION

The experimental evidence presented in this paper indicates that a satisfactory theoretical model can be obtained for the $p(e)$ hysteresis loop by using the thermodynamic equations of Devonshire. These equations do not, however, take into account the nucleation mechanism of domains and their role in polarization reversal. A better definition of the coercive field will therefore be obtained for a model based on the proper quantum-mechanical considerations and accounting for the domain dynamics involved.

The decrease in the hysteresis losses below the $-10°C$ transition should be of some interest for ferroelectric memory devices and amplifiers. The decrease in coercivity encountered in this region can be obtained without loss (and sometimes with an improvement) of loop "rectangularity." Further work is required in order to clarify many other interesting characteristics of $BaTiO_3$. It is well known, for example, that additives such as strontium and lead titanate lower the Curie point. It is quite likely that by careful control of the crystal growing process, the orthorhombic phase of the single crystal can be shifted to room temperature retaining the advantages enumerated above.

JOURNAL OF APPLIED PHYSICS VOLUME 26, NUMBER 12 DECEMBER, 1955

Total Emissivities and Absorptivities of Some Commercial Surfaces at Room and Liquid-Nitrogen Temperatures

F. J. ZIMMERMANN*
Arthur D. Little, Inc., Cambridge, Massachusetts
(Received February 7, 1955)

The heat transferred by radiation was measured between surfaces at room temperature and liquid-nitrogen temperature. The surfaces used were various combinations of electroplated gold and silver and polished copper sheet. From the test data, the approximate total emissivities of the room-temperature surfaces and the total absorptivities of the liquid-nitrogen surfaces were computed.

The results of these tests indicated that electroplated silver surfaces have lower emissivities and absorptivities than equivalently treated electroplated gold surfaces in this temperature range. The best surface tested was a special, bright, unbuffed silver-plated surface. This surface is known to the trade as "silver lume." The room-temperature emissivity of this surface was approximately 0.017, and the absorptivity at 77.3°K for radiation from a 300°K surface was about 0.0083. These are the lowest values at these temperatures of which we have knowledge.

It was found that the electroplated surfaces were best used without buffing or any mechanical working of the surface. It is believed that cold working of the metal surface increases its emissivity and absorptivity by increasing its electrical resistivity.

I. INTRODUCTION

THE design of low-temperature equipment insulated by high-vacuum jackets—such as liquefied-gas storage vessels and transfer lines—is very dependent on the emissivity and absorptivity of the surfaces lining the vacuum chamber because the major source of heat leakage to such equipment is usually radiation heat transfer. The emissivities or absorptivities of practical commercial surface finishes below room temperature are not generally available. The purpose of the experiments described here was to determine design values for the emissivities and absorptivities of surfaces that could be obtained commercially on reasonably large equipment.

II. APPARATUS

A. Description

To determine the heat transferred between a surface at room temperature and a surface at liquid-nitrogen temperature, the quantity of gas evolved from a vessel containing liquid nitrogen was measured. This vessel was in thermal communication with the ambient by radiation, gas conduction, and conduction through the support system.

Figure 1 is a diagram of the calorimeter used in these tests. A 25-liter, liquid-nitrogen Dewar was disassembled and altered. The circumferential seam of the outer jacket was flanged to permit easy replacement of the inner sphere. All supports for the inner sphere except the filling tube were removed. To reduce the heat transfer by conduction through the neck, the filling tube was extended with a thin-walled stainless-steel tube. The charcoal pot was removed from the inner sphere. A pumping connection, ion gauges, and a thermocouple gauge were added as shown. These openings in the otherwise continuous surface of the outer sphere would tend to radiate energy at a rate approaching that of a blackbody; therefore, radiation shields were installed. The inner surface of the shell and the outer surface of the sphere were treated as indicated in Table I.

Figure 2 shows the calorimeter and the supporting equipment schematically. Ten copper-constantan thermocouples were used to determine the average temperature of the outer jacket. Two ion gauges were used to measure the pressure in the vacuum space. The nitrogen gas evaporated from the liquid by the heat transferred between the surfaces at room and liquid-nitrogen temperatures was measured with a wet-test meter. A water saturator was used to prevent changes in the level of the water in the gas meter during a test.

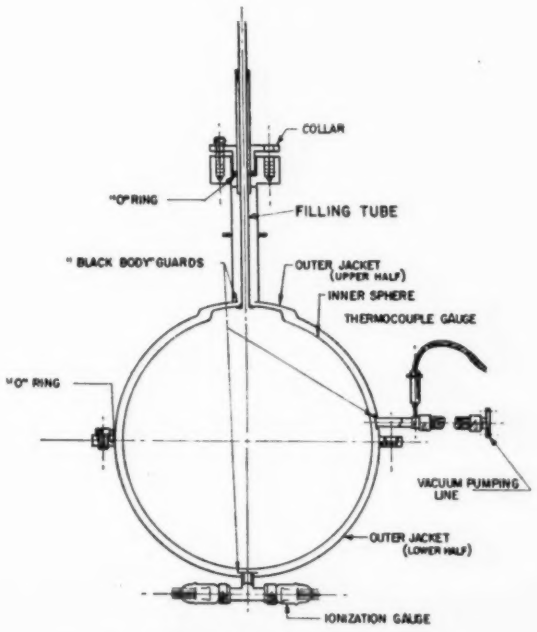

FIG. 1. Radiation study calorimeter.

* Present address: Department of Mechanical Engineering, Yale University, New Haven, Connecticut.

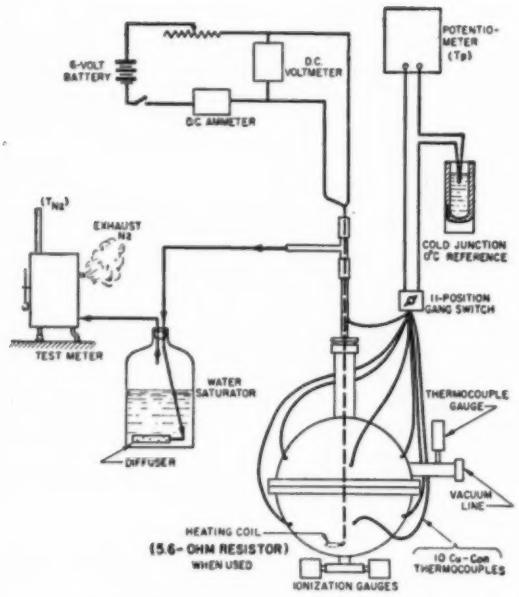

FIG. 2. Radiation study test equipment.

A heater circuit was used in the calibration of the apparatus.

B. Plating Technique

The following procedure was used by the suppliers in plating the calorimeter parts:

(1) Polish base metal to smooth, lustrous finish.
(2) Clean by usual methods.
(3) Nickel strike on stainless steel only.
(4) Copper plate, approximately 0.0003 inch.
(5) Plate with gold or silver, approximately 0.0003 inch.
(6) Rinse and dry; buff if specified.

The silver-lume plating process was done in the Hanson-van Winkle-Munning bath. This is a fairly conventional potassium cyanide plating bath containing organic addition agents to reduce grain size. Under ideal conditions of composition, current density, and agitation, brilliant deposits may be obtained. No buffing was used in any of the silver-lume tests.

The "matte" surfaces were unbuffed, electroplated surfaces. These were, in general, dull or milky in appearance.

C. Calibration

1. Support Conduction

Calculations indicated that the maximum neck conduction (assuming no reduction due to the cooling effect of the evolved gases) would be less than 3% of the boil-off. An experiment was performed in which electrical energy was added at known rates in order to vary the neck cooling effect. The net boil-off, after the part due to the electrical energy was subtracted, was essentially independent of the energy input rate. This result indicated that the neck conduction was negligible compared with the other heat-transfer mechanisms.

2. Gas Conduction

The pressure in the vacuum jacket of the calorimeter was varied by throttling the vacuum pumping line. The heat-transfer rate was plotted as a function of the pressure for two different surfaces in the calorimeter. Figure 3 shows the results of these tests. The data for the gold-plated calorimeter with T_o at 299°K fit the equation

$$q_c = 2.17 \times 10^4 \times P_{cal} \text{ watts},$$

where P_{cal} is in mm Hg.

3. Liquid Level Effect

During the series of tests, both copper and stainless-steel inner spheres were used. Tests were performed with different quantities of liquid in the spheres to see if boil-off varied with level. No difference in boil-off was detected with either type of sphere.

4. Reproducibility of Results

The reproducibility of results in this calorimeter was good. Care had to be taken to insure a very clean system. No volatile materials could be left in any part of the system ahead of the cold trap in the pumping line. It was essential to keep the cold trap supplied with liquid nitrogen; otherwise the boil-off rate would start to rise as the oil back-streaming from the diffusion pump coated the calorimeter surfaces and increased their emissivity.

TABLE I. Emissitivity factors, $F_E = q_R/[\sigma A_i(T_o^4 - T_i^4)]$.

Sphere surface[a] (liquid N_2 temperature)	Shell surface (room temperature)			
	Silver lume	Polished gold	Matte silver	Polished copper
Silver lume	0.0054 (5)[b]	0.0061 (7) 0.0063 (2) 0.0060[c] (3)	0.0059 (5)	
Matte silver		0.0080 (1)		
Dry buffed silver		0.0093 (3)		
Matte gold		0.0087 (9)[3][d]	0.0083 (3)	
Gold wash		0.0092 (3)		
Dry buffed gold		0.0096 (5)[2]		
Polished gold		0.0100 (6)[2] 0.0110 (3)		
Polished copper		0.0092 (3)		0.0087 (2)
Stainless steel Spinning rubbed with fine emery cloth		0.0180[c] (3)		
Drafting tape	0.0170[c] (4)	0.0225 (5)		

[a] All gold and silver surfaces electroplated—see Appendix C.
[b] ( ) = Number of tests performed.
[c] Stainless steel sphere; all others copper.
[d] [ ] = Number of spheres involved, if other than one.

The positioning of the inner sphere relative to the jacket also had to be observed carefully. After the sphere was filled with nitrogen, the unit was disturbed sufficiently to cause the sphere to swing as a pendulum. The stand was then adjusted so that no contact noise could be observed as the sphere oscillated in any direction.

III. RESULTS

A. Emissitivity Factor

We had determined that there was no appreciable neck conduction loss in the apparatus and had devised a method to correct for gas conduction effects. (The pressure in the calorimeter vacuum space was less than 3×10^{-6} mm Hg during most of the radiation tests.) We were therefore able to compute q_R, the heat transferred from the shell to the sphere by radiation alone. According to the theory of radiant heat transmission, this heat quantity can be expressed by an equation of the form,

$$q_R=\sigma A_i F_E(T_0^4-T_i^4) \text{ (for derivation see Appendix),}$$

where

σ = Stefan-Boltzmann constant,
5.67×10^{-12} watt cm^{-2} °K^{-4},
A_i = area of the surface of the inner sphere,
4180 cm^2—copper sphere,
4000 cm^2—stainless-steel sphere,
T_o = temperature of outer sphere—°K,
T_i = temperature of inner sphere—°K,
F_E = emissivity factor.

Table I shows values of the emissivity factor F_E, with various combinations of shell surfaces (at room temperature, or approximately 300°K) and sphere surfaces (at liquid-nitrogen temperature, or 77.3°K). The emissivity factor is a direct ratio of the heat transferred by radiation in the equipment to the heat that would be transferred if both surfaces were blackbodies.

Table I indicates directly the relative merit of various combinations for insulating room-temperature surfaces from liquid-nitrogen temperature surfaces in high-vacuum systems. Two silver-lume surfaces are the best combination, with a heat leakage approximately one-half that of two polished gold-plated surfaces.

Most of the tests combined a polished gold-plated shell with spheres of various treatments, so that the emissivity factor could directly show an indication of the relative emissivities of the nitrogen-cooled surfaces.

B. Emissivity

The emissivity factor for two concentric spheres under the conditions of these tests can be expressed as a function of the emissivity of the outer surface $\mathcal{E}_o$, and the absorptivity of the inner surface for energy emitted by the outer surface $\alpha_{i,o}$. The expression assumes that the reflections are specular in nature.

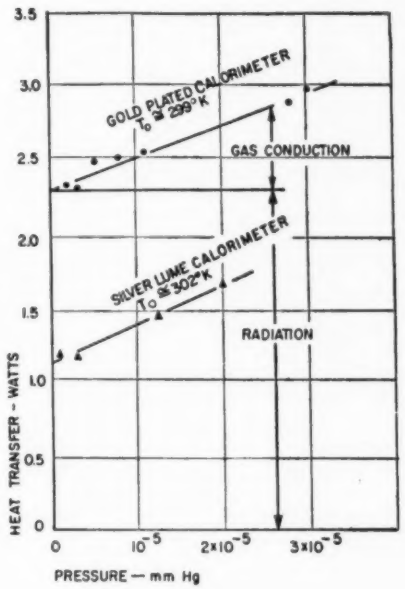

FIG. 3. Heat transfer *vs* calorimeter pressure.

$$F_E=\frac{1}{(1/\alpha_{i,o})+(1/\mathcal{E}_0)-1} \text{ (for derivation see Appendix).}$$

To have a starting value for use in solving for surface emissivities and absorptivities, it was necessary to establish the emissivity of one surface. A sphere was coated with drafting tape in order to approximate a blackbody on the nitrogen-cooled surface. It was necessary to modify the cold surface rather than the warm surface in this manner, because of the volatile materials in the adhesive. The computed emissivity of the room-temperature surface is relatively insensitive to the actual absorptivity of the paper surface. If $\alpha_{i,o}$ varies from 0.5 to 1.0, the corresponding value of $\mathcal{E}_o$ changes by only 2%. For the maximum heat-transfer rate observed in these tests, the temperature drop through the paper was computed to be much less than 1°C. This should have very little effect on the emissivities computed for the room-temperature surface. The taped sphere was used to determine the room-temperature emissivities of polished gold plate and silver-lume plate. With these two values, the absorptivity of silver lume could be calculated from two different tests and compared. From the emissivity factor for the polished gold shell and silver-lume sphere, the absorptivity of silver lume at liquid-nitrogen temperatures was calculated to be 0.0083; from the emissivity factor for the complete silver-lume calorimeter, the absorptivity of silver lume at liquid-nitrogen temperatures was found to be 0.0079, which is different by about 4%. The emissivities and absorptivities of the surfaces tested during this work are given in Table II.

TABLE II. Emissivities and absorptivities of surfaces tested.

Material	$\alpha_{i,o}$ [a]	ε_o [b]
Silver lume	0.0083	0.017
Matte silver	0.012	0.020
Dry buffed silver	0.016	
Matte gold	0.014	
Gold wash	0.015	
Dry buffed gold	0.016	
Polished gold (kerosene buff)	0.018	0.0225
Polished copper (solid copper sheet)	0.015	0.020

[a] $\alpha_{i,o}$ = Absorptivity for a surface at 77.3°K for radiation from a 300°K surface.
[b] ε_o = Emissivity for a 300°K surface.

IV. DISCUSSION

The accuracy of the emissivity factors presented herein is a function of the accuracy of the following data:

	Approximate error (%)
1. Rate of heat transfer (q_R)	±3
2. Shell temperature (T_0)	±0.25%; T_0^4; ±1
3. Sphere area	±1
Total	±5

The computed absorptivity of the liquid-nitrogen-temperature surfaces is a function of two emissivity factors; hence, it is accurate to approximately ±10%. The computed emissivity of the room-temperature surfaces is a function of one emissivity factor, the absorptivity of paper at 77.3°K, and the accuracy of the equation assumed to hold for the surfaces. Therefore, the error in the emissivities for the room-temperature surfaces might be on the order of ±20%. It is unlikely, however, that all the above possible errors would be additive, so the actual accuracy would probably be better than the foregoing figures indicate.

The internal consistency of the results is also of interest. As shown in Sec. II, the absorptivity of silver lume at 77.3°K, calculated from two different sets of data, was 0.0083 and 0.0079.

The absorptivity of matte gold at 77.3°K, also calculated from two different sets of data, yielded values of 0.0143 and 0.0138.

The increase in emissivity and absorptivity with buffing was thought to be at least partly due to cold working of the surface material, with the attendant changes in electrical resistance. The theory for thermal radiation from metal surfaces indicates a dependence on the square root of the resistivity of the material at liquid-nitrogen temperatures. For values less than 0.20 ohm cm °K of resistivity times absolute temperature, the theoretical equation is

$$\mathcal{E}=0.751(r_eT)^{\frac{1}{2}}-0.396r_eT.^{1}$$

Note.—At the same time that this work was in progress at Arthur D. Little, Inc., the Cryogenic Engineering Laboratory of the National Bureau of Standards, at Boulder, Colorado, was carrying out a similar investigation of the absorptivities of metal sheets at liquid-nitrogen temperatures in a cylindrical calorimeter. In order to verify further the low absorptivities we obtained for the silver-lume surface, we sent two stainless-steel sheets plated by the silver-lume process to NBS for testing in their calorimeter. The NBS tests gave absorptivities of 0.007 and 0.009 for the two samples, or an average value of 0.008, which is in good agreement with our results.

[1] M. Jakob, *Heat Transfer* (John Wiley and Sons, Inc., New York, 1949), p. 51.

V. CONCLUSIONS

If electroplated gold or silver surfaces are to be used for radiation shielding, they should not be buffed. If other conditions permit, silver-lume surfaces should be used in preference to any other surface tested by the writer for radiation shielding at or below room temperature. It should be remembered that dirt or oil vapor can do much to ruin an otherwise good radiation shielding surface.

VI. ACKNOWLEDGMENTS

This test work was done between February, 1953 and April, 1954, and was sponsored by the U. S. Atomic Energy Commission under Contract No. AT(29-1)-1358.

The author is indebted to Wayland Bailey, Peter Draffone, and Augustus Ventre, all of Arthur D. Little, Inc., without whose help it would not have been possible to carry on the extended operation of the calorimeter which was necessary to obtain reasonably long runs at equilibrium conditions. The author is also indebted to Howard O. McMahon of Arthur D. Little, Inc., for advice and encouragement in this program.

APPENDIX

The heat transferred by radiation between two concentric spheres can be shown to be expressed by the equations following.

If the reflections from the surfaces are assumed to be specular, the heat transfer is

$$q_R=\sigma A_iT_i^4\left[\frac{1}{(1/\mathcal{E}_i)+(1/\alpha_{o,i})-1}\right]-\sigma A_oPT_o^4\left[\frac{1}{(1/\alpha_{i,o})+(1/\mathcal{E}_o)-1}\right], \quad (1)$$

where subscript i refers to inner sphere, subscript o refers to outer sphere, $\alpha_{o,i}$ = absorptivity of the outer surface for energy emitted by the inner surface, $\alpha_{i,o}$ = absorptivity of the inner surface for energy emitted by the outer surface, and P = the fraction of the total energy emitted by a small area of the outer surface which is radiated into the solid angle subtended by the inner surface.

If the reflections are assumed to be nonspecular and if the reflected energy is assumed to have a distribution, throughout the space above the surface, which is similar to the distribution of the emitted energy, the heat transfer is

$$q_R=\sigma A_i T_i^4\left[\frac{1}{\frac{1}{\mathcal{E}_i}+P\left(\frac{1}{\alpha_{o,i}}-1\right)}\right]$$

$$-\sigma A_o P T_o^4\left[\frac{1}{\frac{1}{\alpha_{i,o}}+P\left(\frac{1}{\mathcal{E}_o}-1\right)}\right]. \quad (2)$$

The evaluation of P requires a knowledge of the distribution of the radiant energy in space. In the case of blackbodies or gray bodies, the radiant energy is diffuse which means equal distribution of radiant flux density in all directions of space. The rate that energy is radiated by a small black or gray area dA in any direction is proportional to the cosine of the angle between the direction of interest and the normal to the surface. Evaluation of P for the case of concentric spheres with black or gray surfaces leads to the value

$$P_g=A_i/A_o.^2$$

Substituting this value into the preceding equations and noting that for a gray body $\alpha_{1,2}=\mathcal{E}_1$ and $\alpha_{2,1}=\mathcal{E}_2$ by definition, the following equations, available in the literature for the case of concentric spheres,[3] are obtained:

$$q_R=\sigma A_i(T_i^4-T_0^4)\left[\frac{1}{(1/\mathcal{E}_i)+(1/\mathcal{E}_o)-1}\right]$$

specular reflection, (3)

$$q_R=\sigma A_i(T_i^4-T_o^4)\left[\frac{1}{(1/\mathcal{E}_i)+(A_i/A_o)(1/\mathcal{E}_o-1)}\right]$$

diffuse reflection. (4)

For metal surfaces both the emissivity and the absorptivity are functions of the angle ϕ between the normal to the surface and the direction of the radiant energy. However, for black or gray surfaces the emissivity is constant, independent of the angle ϕ. The total emissivity of a metal surface of low emissivity is shown by Jakob[1] to approach 4/3 times the normal emissivity. For the case of metal surfaces, evaluation of P_m and substitution into the Eqs. (1) and (2) leads to a physically impossible solution, because the original derivation of the equations did not consider that the absorptivity is a function of the angle ϕ. However, if the emissivities and absorptivities in the equations are, in the case of metal surfaces, taken to be the total values, it is possible to evaluate a factor P by physical reasoning.

In the case of either specular or nonspecular reflections, the heat transfer must approach zero as the temperatures of the two surfaces approach each other. Since $\mathcal{E}_i$ approaches $\alpha_{i,o}$ and $\mathcal{E}_o$ approaches $\alpha_{o,i}$ as T_i approaches T_o, it is necessary for the following to be true for zero heat transfer at $T_i=T_o$:

$$A_i=A_oP \quad \therefore \quad P=A_i/A_o.$$

The equations can be rewritten as follows:

$$q_R=\sigma A_i\left[\frac{T_i^4}{(1/\mathcal{E}_i)+(1/\alpha_{o,i})-1}\right]$$

$$-\sigma A_i\left[\frac{T_o^4}{(1/\alpha_{i,o})+(1/\mathcal{E}_0)-1}\right] \text{ specular reflections,}$$

$$q_R=\sigma A_i\left[\frac{T_i^4}{(1/\mathcal{E}_i)+(A_i/A_o)(1/\alpha_{o,i}-1)}\right]$$

$$-\sigma A_i\left[\frac{T_0^4}{(1/\alpha_{i,o})+(A_i/A_0)(1/\mathcal{E}_0-1)}\right]$$

nonspecular reflections.

It is possible to simplify these equations for use with the calorimeter because of the wide temperature spread between the two emitting surfaces. The temperatures in the calorimeter were approximately $T_o\cong 300°K$ and $T_i\cong 77.3°K$. The ratio of the fourth powers of these temperarures, $(T_i/T_o)^4\cong 0.0044$, is a very small value. The values of $\mathcal{E}_i$ and $\alpha_{i,o}$, and $\mathcal{E}_o$ and $\alpha_{o,i}$ are probably of the same order of magnitude. Therefore, the T_o^4 term is controlling, and rewriting the equations as follows should lead to much less than 1% error:

$$q_R=\sigma A_i F_E(T_o^4-T_i^4),$$

where

$$F_E=\frac{1}{(1/\alpha_{i,o})+(1/\mathcal{E}_o)-1} \text{ specular reflection,}$$

$$F_E=\frac{1}{(1/\alpha_{i,o})+(A_i/A_o)(1/\mathcal{E}_0-1)}$$

nonspecular reflection.

Both of these expressions indicate that the net heat transfer in the calorimeter is a function of the emissivity of the outer surface and the absorptivity of the inner surface of energy of the spectral distribution emitted by the outer surface.

The choice between these two equations is not clear cut. The metal surfaces in the calorimeter were not

[2] A. D. Moore, *Fundamentals of Electrical Design* (McGraw-Hill Book Company, Inc., New York, 1927).
[3] H. C. Hottel, Mech. Engr. 52, 699–704 (1930).

optically smooth or even good mirrors in general. However, at the long wavelengths involved in the 300°K and 77°K radiation, the optical qualities are not necessarily a true picture of the radiation characteristics. In addition, the use of the equation for specular reflections results in higher values for the emissivity of the outer surface than use of the nonspecular equation. Since this is conservative, it was decided to use the specular reflection equation for the calorimeter.

where

$$q_R=\sigma A_i F_E(T_o^4-T_i^4),$$

$$F_E=\frac{1}{(1/\alpha_{i,o})+(1/\mathcal{E}_o)-1}.$$

JOURNAL OF APPLIED PHYSICS VOLUME 26, NUMBER 12 DECEMBER, 1955

Gettering of Gas by Titanium

VIRGIL L. STOUT AND MARTIN D. GIBBONS
General Electric Research Laboratory, Schenectady, New York

(Received May 28, 1955)

Titanium metal has been studied as a getter for oxygen, nitrogen, carbon dioxide, air, water vapor, hydrogen, and methane. Titanium above 700°C will getter oxygen, nitrogen, and carbon dioxide. Hydrogen is absorbed by titanium in the temperature range of 25 to 400°C. Water vapor and methane are readily sorbed when the metal is operated at both elevated and reduced temperatures. Large quantities of gases can be sorbed; sorption of ten to ninety atomic percent is possible. When saturated with gas, the metal becomes brittle and is easily fractured. Hydrogen gas is the only gas which can be released by heating after it has been sorbed by titanium.

INTRODUCTION

THE practice of using getters in sealed-off vacuum bulbs extends back to 1894, when Malignani painted red phosphorous onto the inside of the exhaust tube of a carbon filament lamp. Gettering has progressed from this early start into a practice that now makes possible the mass production of a large number of electronics devices; a survey of gas sorption by metals has been written.[1] Getters that have been commonly used include materials such as aluminum, misch metal, magnesium, barium, thorium, zirconium, and uranium.[2–4]

Titanium metal also possesses certain properties that make it useful as a getter material. As a member of the fourth group of the periodic table, titanium has many properties in common with zirconium, hafnium, and thorium. Zirconium gas reactions have been studied at both elevated and reduced pressures,[5–7] and many studies have been made on titanium gas reactions at elevated pressures.[8] The titanium-hydrogen system has been intensively investigated.[8,9] Oxidation of titanium and its alloys has received much attention.[8,10] As titanium metal has a low vapor pressure at elevated temperatures,[11] it appears to be a reasonable choice for vacuum-tube applications. This study was undertaken to evaluate titanium as a getter.

In evaluating gettering properties, we have tried to find the answers to the following questions about titanium:

(1) Can it be outgassed?
(2) What gases are sorbed?
(3) How much gas can be sorbed?
(4) At what rates are the gases sorbed and how do these rates depend upon the temperature and gas concentration within the metal?
(5) Does the metal retain the sorbed gas?

EXPERIMENTAL

To carry out this investigation, the vacuum system shown in Fig. 1 was constructed. This consisted of a forepump, diffusion pump, and getter bulb with a transfer flask which comprised the principal volume of the system. The gas pressure was measured by a Hg manometer or a McLeod gauge. An auxiliary calibration flask of known volume was used to ascertain the volume of the system. A double-stopcock entry was used to introduce dry gas. Water vapor was removed by the use of a cold trap.

A more complete drawing of the getter bulb is shown

[1] Saul Dushman, *Scientific Foundations of Vacuum Technique* (John Wiley and Sons, Inc., New York, 1949).
[2] Author unknown, Light Metals **7**, 34 (1944).
[3] Author unknown, Light Metals **7**, 77 (1944).
[4] Espe, Knoll, and Wilder, Electronics **23**, 80 (October, 1950).
[5] E. A. Gulbransen and K. F. Andrews, Trans. Am. Inst. Mining Met. Engrs., J. Metals **185**, 515 (1949).
[6] W. G. Guldner and L. A. Wooten, Trans. Am. Electrochem. Soc. **93**, 223 (1948).
[7] S. Wagener, Brit. J. Appl. Phys. **1**, 225 (1950).
[8] E. A. Gulbransen and K. F. Andrews, Trans. Am. Inst. Mining Met. Engrs., J. Metals **185**, 741 (1949).
[9] A. D. McQuillan, Proc. Roy. Soc. (London) **A204**, 309 (1950).
[10] W. A. Alexander and L. M. Pidgeon, Can. J. Research **B28**, 60 (1950).
[11] L. G. Carpenter and W. A. Mair, Proc. Phys. Soc. (London) **B64**, 57 (1951).

in Fig. 2. Iodide titanium was formed into rings 1.5 inches in diameter from metal 0.005 inch thick and $\frac{1}{4}$ inch wide. The weight of each ring was about $\frac{1}{2}$ gram. This was supported by two 0.010-inch-diameter molybdenum wires which in turn were supported by 0.060-inch nickel wires at the glass press. Heating of the getter was accomplished by the use of induced radio-frequency current, while the temperature was measured by use of platinum-platinum 10% rhodium thermocouple. In order to attach the thermocouple to the titanium, a piece of tantalum foil 0.001 inch thick was welded between the two metals. The tantalum prevented the formation of an alloy between titanium and platinum which is produced at about 1200°C. A nickel shield was located between the hot and cold junction of the thermocouple. The reentrant press of the getter bulb was filled with distilled water and a thermometer measured its temperature, which was taken to be the cold junction temperature of the thermocouple.

Titanium samples were cleaned by degreasing with acetone, etching in hot hydrochloric acid, and washing with distilled water. The hydrochloric acid etch produced a mat finish on the titanium, increasing somewhat the effective surface area. In interpreting our results, no attempt was made to correct for this increase in area. The amount of gas sorbed by the metal was measured by the change of pressure-volume relationship and by the total gain in weight of the metal.

MEASUREMENTS

During this study various methods of investigation were employed.

(1) The sorption was studied by measuring the change in pressure of the trapped volume of gas with time for a range of metal temperatures. Several gases were introduced into the system, such as oxygen, nitrogen, carbon dioxide, hydrogen, methane, water vapor, and room air.

(2) The products of the gas-metal reaction were analyzed by x-ray powder patterns.

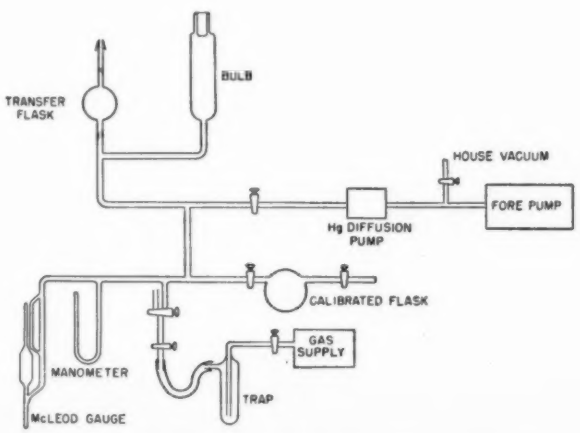

FIG. 1. Vacuum system for gettering experiments.

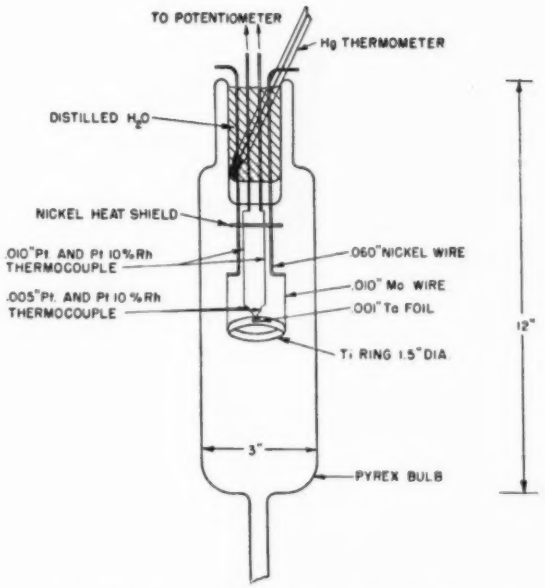

FIG. 2. Getter bulb used for gas sorption studies.

(3) Residual gases from several of the gas sorption runs were identified by mass spectrometry.

The procedure of taking the data can be described with the aid of Fig. 1. The getter bulb and transfer flask were mounted on the glass system. The volume of the vacuum system was determined by letting room air at atmospheric pressure, measured by a barometer, into the calibration flask of known volume. The system was pumped to about 0.1 micron of Hg and closed off from the pump. Then the air from the calibration flask was allowed to expand into the evacuated section. The second pressure reading was taken on the mercury manometer. With this information, the volume of the system was determined.

Following the volume determination, the system was baked at 450°C for one hour. After bakeout, the getter ring was processed by heating the metal to 1150°C until the pressure in the vacuum system was such that the McLeod gauge would readily "stick." The pressure at this time was equal to or less than 10^{-3} micron of Hg. This processing required about ten minutes. During this time two things happened to the metal. First, the surface contamination caused by oxygen, nitrogen, carbon, etc., is dissolved by the metal, and, secondly, hydrogen gas is released by the titanium. P. D. Zemany has shown by a mass-spectrometer analysis that hydrogen is the principal gas evolved by hot titanium.[12] When the processing step was completed, the gas to be gettered was released into the system through the double-stopcock entry. The initial pressure was read with the getter cold; then the getter ring was heated to temperature and the pressure was read with the McLeod gauge at $\frac{1}{2}$- or 1-minute intervals.

[12] P. D. Zemany, private communication.

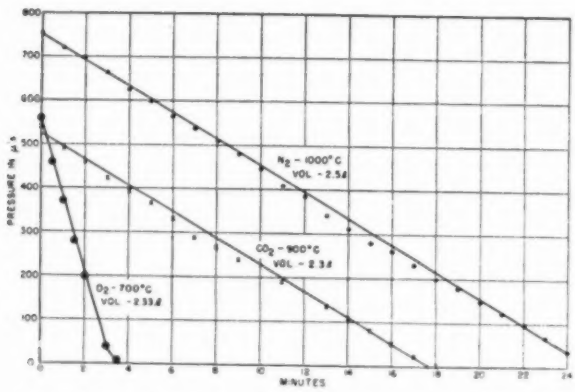

FIG. 3. Linear variation of gas pressure above titanium metal with time.

RESULTS

Reactions at High Temperatures

The gases nitrogen, carbon dioxide, oxygen, and room air were gettered by hot titanium. The gas pressure above the metal decreased nearly linearly with time during the sorption of nitrogen, carbon dioxide, and small concentrations of oxygen. Figure 3 shows typical pressure *versus* time plots. The linear pressure *vs* time relationship was found even after large amounts of nitrogen had been continuously sorbed. The linear decrease of the gas pressure above titanium was accompanied by a change of gas composition when carbon dioxide was being sorbed. Gas samples removed from the system and analyzed by a mass spectrometer, after the initial carbon dioxide pressure had been decreased with the getter by a factor of two, contained a large amount of carbon monoxide. Oxygen gave a linear pressure-time plot as long as the total quantity of sorbed gas per sample was less than about 100 μl/cm^2 at 700°C.

In order to account for the linear pressure-time relation that was so commonly found, we postulate a surface-barrier-limited sorption. The barrier separates a nearly constant number of gas and metal atoms. Under this condition the rate of combination is constant with time, or $dn/dt=c$. As the barrier is limiting the entire gas-sorption process, the number of atoms combining per unit time across the barrier is equal to the number of atoms taken from the gas above the metal per unit time. Thus, from the perfect gas law, $dp/dt=c$ for the entrapped volume of gas.

The rate of sorption is markedly dependent upon temperature. Figure 4 shows a plot of the logarithm of the rate of nitrogen sorption in μl/sec cm^2 *vs* reciprocal temperature. The data fall on two straight lines. The break point that occurs in the temperature range of 900–1000°C is apparently the result of the phase change of the metal. These data were taken by measuring rates at low temperatures and then increasing temperature. As nitrogen is sorbed into the metal structure, we could expect the phase-change temperature to increase and a two-phase region to develop.[13]

In the foregoing, we have discussed initial oxygen sorption by clean metal. When a large amount of oxygen had been previously sorbed by the metal, the pressure decreased according to a parabolic law. Figure 5 shows two gas sorption measurements for oxygen. Run 1 was made with a clean metal surface, while Run 2 was made immediately following Run 1 so that any oxygen buildup within the metal would be present near the surface to inhibit further sorption during the second run. By plotting the data of Run 2 as pressure *vs* the square root of time, one obtains a straight line. This indicates that a diffusion barrier now exceeds the surface barrier limiting the rate of sorption.

A summary of rate of sorption data is shown in Table I. The gettering rate of titanium is given for the gases nitrogen, oxygen, and carbon dioxide in the temperature range of 700–1100°C, inclusive. From this information

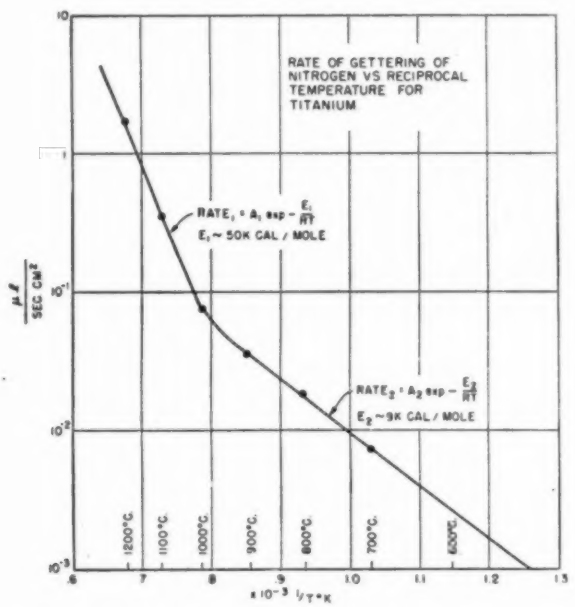

FIG. 4. Temperature dependence of the gettering rate of nitrogen by titanium metal.

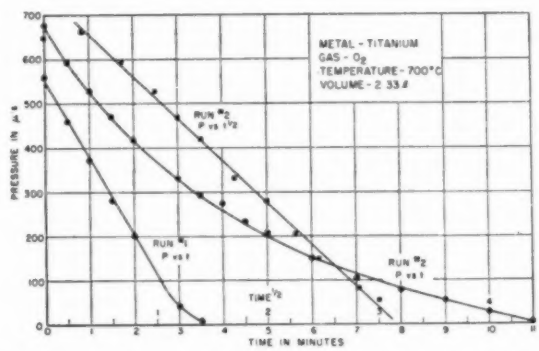

FIG. 5. Linear and parabolic oxygen sorption characteristics.

[13] New York University for Watertown Arsenal, Reports No. 9 and 10 (October and November, 1951).

TABLE I. Gettering properties of titanium.

		Nitrogen	Oxygen	Carbon dioxide	Air
	Temp °C				
Gettering rate (μl/cm² min) at various temperatures	700	0.4	11	0.15	
	800	0.9	127	1.7	
	900	2.0	*	3.9	
	1000	5.0	*	15	
	1100	2.0	*	48	
Residual gases after gettering	Relative quantity	$7/10^4$	$4/10^3$		$9.8/10^3$
	Gas content	50% A, 50% Ne	90% A, 10% Ne		% A in air
Total quantity gettered in μl/mg		160	90	50	

* Too rapid to measure.

it is evident that nitrogen and carbon dioxide are much more difficult to sorb than is oxygen.

Since the rates of sorption are different for various gases, one might expect unusual behavior for the sorption of a gas mixture. Figure 6 shows a pressure-time plot for the sorption of room air by titanium. The initial rate of gas sorption is high as the oxygen attacks the getter; when the oxygen is depleted from the system, nitrogen is sorbed, with argon left as the residual gas in the system. Table I also contains residual gas information, giving as a relative quantity the initial partial pressure and gas composition as measured after the sorption of tank nitrogen, tank oxygen, and atmospheric air. From separate tests we have found that partial pressure of the active gas is reduced to less than $10^{-4}\mu$ by the getter. The noble gases and mercury do not attack or interfere with gettering by titanium.

The total quantity of any one gas sorbed at elevated temperatures before a getter failed because of a crack or break in the metal ring is given in the last line of Table I. The gas concentration of 160 μl/mg that caused failure during the sorption of nitrogen corresponds to 90 atomic percent. After getter failures the metal rings were brittle. X-ray data showed TiN, TiO, and TiC to be present when nitrogen and carbon dioxide had been sorbed. Upon examination under an optical microscope, sections of getter that had been heavily contaminated by nitrogen showed localized TiN concentrations.

Reactions at Low Temperatures

From studies that have been made on the titanium hydrogen system, most investigators have reported that hydrogen is not sorbed by titanium at temperatures less than 300°C. During this investigation, hydrogen has been sorbed by titanium at room temperature. Figure 7 shows a logarithm of pressure *vs* time plot for hydrogen sorption by titanium metal at room temperature. During this one run 5 μl of hydrogen were sorbed per milligram of titanium. The natural law obeyed is $P=P_0e^{-Bt}$, where P_0 is the initial pressure, t the time, and B is a constant. The constant B can be evaluated from the perfect gas law and from thermodynamics to give

$$B=\frac{Aa}{V}\left(\frac{kT}{2\pi m}\right)^{\frac{1}{2}}, \tag{1}$$

where k is Boltzmann's constant, T is the absolute temperature, m is the mass of the gas molecule, a is the area of the getter, V is the volume of the system, and A is the number of molecules sticking to the getter per molecule incident. From the data of Fig. 7, A has been evaluated as being equal to 1.6×10^{-5}. This is an exceedingly small number and may be controlled to a large extent by the fractional part of the surface that is available for hydrogen sorption. Smaller values of A are readily obtained when vacuum conditions are poor before hydrogen is let into the system. From our experiments it seems that a small layer of surface oxide on the titanium can effectively seal it from hydrogen attack. This layer can easily account both for the failure of others to observe hydrogen sorption below 300°C and for the small value of A. Little or no temperature-

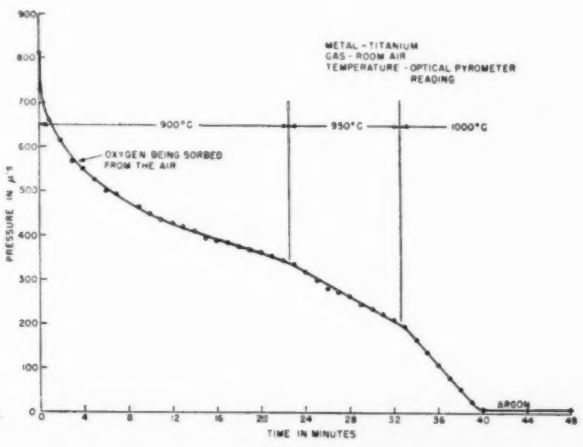

FIG. 6. Gas pressure variation with time for room air above titanium.

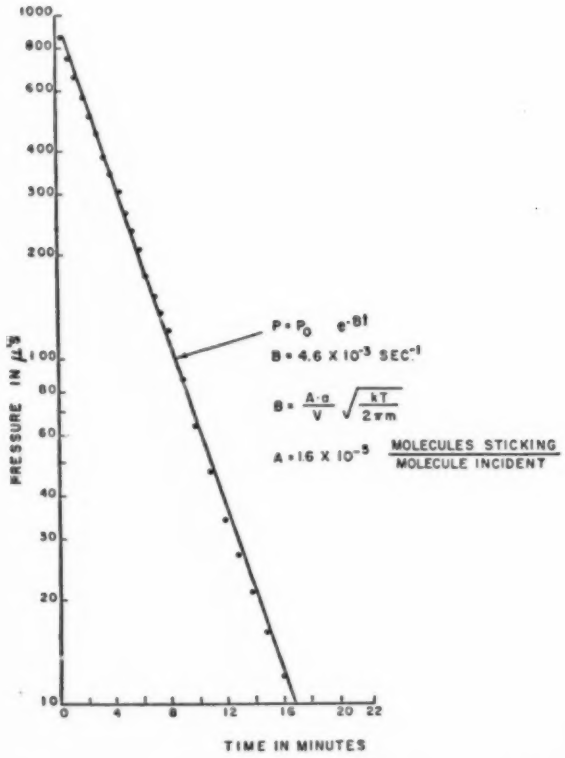

FIG. 7. Change of hydrogen pressure above titanium with time at room temperature.

dependence for hydrogen sorption was measured in the temperature range of 25 to 400°C.

Reactions at High and Low Temperatures

Water vapor and methane can be gettered by using titanium at both high and low temperatures. Titanium at 300–400°C can getter water vapor but is limited in total amount and rate of sorption. Figure 8 shows a methane sorption run. The pressure in the closed system rose from an initial value of 485 to 930μ in a period of 12 minutes when the titanium was heated to 1200°C. The temperature of the titanium was then reduced and the gas pressure dropped abruptly to less than 1μ. While the getter is at the high temperature, methane is decomposed and carbon is sorbed by the titanium. For each atom of carbon sorbed, two molecules of hydrogen are produced. On such a basis the pressure above the metal would double were it not for the small quantity of hydrogen taken on by the titanium. When the temperature of the getter is reduced, hydrogen is rapidly sorbed by the clean titanium.

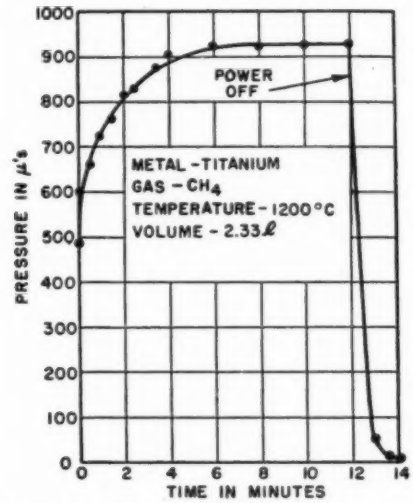

FIG. 8. Pressure characteristic of the methane-titanium reaction at 1200°C and reduced temperatures.

CONCLUSIONS

To report briefly the answers to the originally posed questions, titanium is a desirable metal for vacuum-tube use. Its vapor pressure lies between that of nickel and platinum. The metal can be readily processed for use as a getter. The principal gas released by hot titanium is hydrogen. Ten to ninety atomic percent takeup of gas by the metal is possible. When large quantities of gas are sorbed, the metal becomes brittle and its resistivity increases. In order to continuously getter nitrogen, oxygen, and carbon dioxide, it is desirable to heat titanium above 700°C. Hydrogen gas, which is released by the metal at elevated temperatures is gettered readily between 25 and 400°C. Sorption of hydrogen at room temperature can be stopped by the formation of an oxide film on the getter. The rate of sorption of gases at elevated temperatures depends upon the amount of gas already sorbed by the metal. Once sorbed by titanium, carbon, oxygen, and nitrogen can form stable compounds and are not released when the metal is heated to elevated temperatures.

In order to getter successfully a vacuum device, it is essential that titanium metal operate both at elevated and reduced temperatures. This requires either two separate pieces of metal, or better, one titanium piece that operates with a temperature gradient.

ACKNOWLEDGMENTS

We wish to thank E. D. McArthur for suggesting this problem, and to express our gratitude to J. E. Beggs and R. J. Bondley for many helpful discussions of this work.

JOURNAL OF APPLIED PHYSICS VOLUME 26, NUMBER 12 DECEMBER, 1955

Stress-Strain Relations in Snow under Uniaxial Compression

JOSEPH K. LANDAUER
Snow Ice and Permafrost Research Establishment, Corps of Engineers, U. S. Army, Wilmette, Illinois
(Received June 24, 1955)

Two types of tests were performed on the uniaxial compression of snow; experiments at constant strain rate and at constant load. The strain rate can be represented as the product of functions of density, stress, temperature, and time. For densities between $\gamma \simeq 0.3$ g/cc and $\gamma \simeq 0.6$ g/cc the strain rate is proportional to $(\gamma_{ice}-\gamma)/\gamma$ to the fourth power. The strain rate varies linearly with stress for low stresses ($2<\sigma<100$ g/cm^2) but increases to an approximately cubic relationship at higher stresses ($1<\sigma<5$ kg/cm^2). An activation energy of about 14 000 cal/mole can be derived from the temperature dependence. In the constant load tests the strain is proportional to the time to a power of about 0.8. The effect of snow type is small, being less than the relatively large experimental scatter encountered.

INTRODUCTION

SNOW subjected to uniaxial compression displays deformation behavior characteristic of a viscoplastic material. In order to determine empirical laws describing this behavior, tests at constant strain rate and constant load were performed on various types of snow within a range of stress conditions and temperatures near the melting point.

EXPERIMENTAL

The snows studied were both natural and sifted. The natural snow was cut into blocks in t' e field ard stored at −40°C until used. The sifted snow was formed from the natural snow by mixing and sifting through a coarse sieve. This procedure tended to give a more homogeneous snow than was obtained naturally. Snow cylinders were formed by inserting sharpened stainless steel cylinders of 500 cc vo'ume into the snow block and then carefully removing the snow from the cylinder. The sifted snow was sifted directly into these cylinders and later removed for testing. A several-day waiting period allowed bonding to develop sufficiently for the sample to be removed whole. Variations in density of the sifted snow were obtained by compaction in the cylinder.

New, natural snow has a density ranging from 0.05 g/cc to about 0.30 g/cc but after the snow ages for some time these densities increase. Uncompressed sifted snow has a density in the neighborhood of 0.4 g/cc. At temperatures below −5°C snow of density greater than about 0.2 g/cc can be handled with care without damage. As the density increases the snow becomes harder and correspondingly easier to handle. However, it is not until densities of about 0.8 that snow becomes markedly ice-like.

These experiments were performed in cold rooms. Temperatures were controlled to ±0.5°C.

TESTS AT CONSTANT STRAIN RATE

Compression

Stress-time curves were obtained for cylindrical specimens (diam 55 mm, length approx 100 mm) of various snows, both natural and sifted, under uniaxial compression at constant strain rate. The general characteristics of such curves (Fig. 1) are a short initial slow increase of stress (region I) followed by a sharply increasing stress (II) and finally an approach to an approximately constant stress (III).

The initial region of slow stress increase is probably due to cylinder-end surface irregularities. If a snow sample is compressed slightly and then allowed to relax, this initial region is less prominent on a subsequent test. Therefore, this effect will be neglected in the following discussion.

A significant part of the stress-time curve is an increasing stress at a continuously decreasing rate. Here the stress induced by compression is relieved by a relaxation mechanism. The stress rate decreases until these two processes are equal. The stress rate does not drop to zero, owing to increasing density and perhaps also to strain hardening of the snow. There is, however, a fairly well-defined region where the rate decreases abruptly (Fig. 2) and an equilibrium stress is attained.

If the snow is compressed in a series of increasing velocities, a curve as in Fig. 2 is obtained. An equilibrium stress, σ, is reached for each strain rate, $\dot{e}$. These are related by:

$$\dot{e}=k\sigma^r. \tag{1}$$

k, which will be called the coefficient of plasticity under uniaxial compression, is a function of density and temperature. The strain rates used in these experiments range from 10^{-5} sec^{-1} to 10^{-3} sec^{-1}. Values of r vary be-

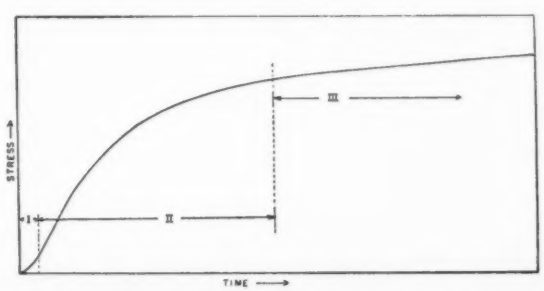

FIG. 1. Stress-time curve for constant strain rate. The regions I, II, and III are explaned in the text.

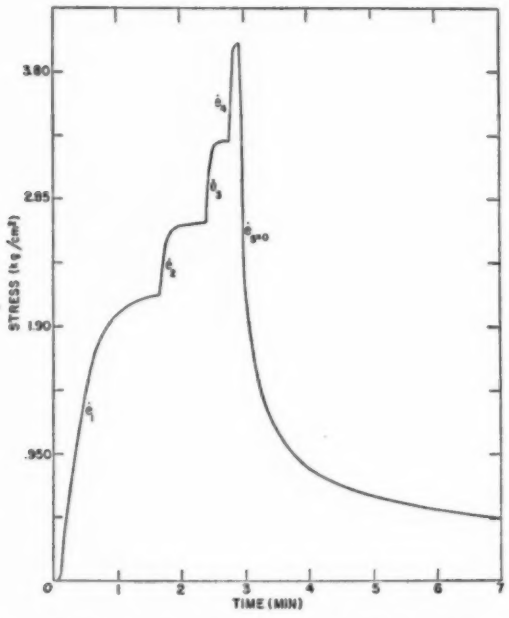

FIG. 2. Stress-time curve for a series of strain-rates. $T=-10°C$, $\gamma=0.42$ g/cm³, $\dot{\epsilon}_1=6.34\times10^{-5}$ sec^{-1}, $\dot{\epsilon}_2=12.8\times10^{-5}$ sec^{-1}, $\dot{\epsilon}_3=25.8\times10^{-5}$ sec^{-1}, $\dot{\epsilon}_4=52.1\times10^{-5}$ sec^{-1}.

tween 2 and 4 but a large majority fall between 3.0 and 3.2. In the region of investigation ($0.3<\gamma<0.6$ g/cc), r does not vary with density; k, however, varies greatly with density and, within the experimental error, can be represented as proportional to the void ratio, $\epsilon=(\gamma_{ice}-\gamma/\gamma)$, to a power, p:

$$k=A\epsilon^p, \tag{2}$$

where γ is the density, for densities between 0.44 and 0.61, p is about 4.

Limited experiments indicate no marked dependence of r or k on snow type. More detailed work would probably show that k, but not r, depends somewhat on snow type. The basis for this prediction is that while various snow types and microcrystalline ice have the same r, the k for snows, when extrapolated using Eq. (2), does not agree with the k for microcrystalline ice.

Relaxation

If the press is stopped after equilibrium pressure is reached, relaxation of stress occurs as in Figs. 2 and 4.

Assuming elastic and plastic flow processes, the total strain rate, $\dot{\epsilon}$, is the sum of an elastic strain rate, $\dot{\epsilon}_E$, and a plastic strain rate, $\dot{\epsilon}_P$:

$$\dot{\epsilon}=\dot{\epsilon}_E+\dot{\epsilon}_P. \tag{3}$$

Since the elastic strain is proportional to the stress, the strain rate is

$$\dot{\epsilon}_E=-\frac{1}{Z}\frac{dZ}{dt}=\frac{1}{M}\frac{d\sigma}{dt}, \tag{4}$$

where M is the elastic modulus. Using Eq. (1) for $\dot{\epsilon}_P$ we get:

$$\dot{\epsilon}=\frac{1}{M}\frac{d\sigma}{dt}+k\sigma^r. \tag{5}$$

Since $\dot{\epsilon}=0$, the slope of the relaxation curve must be:

$$d\sigma/dt=-Mk\sigma^r. \tag{6}$$

Figure 2 is an actual experimental curve traced from a recorder graph. The density is assumed constant throughout. Data from this curve, plotted in Fig. 3, show good agreement with Eqs. (1) and (6). The value of r is 3.4 for the step compression curve and 3.1 for the relaxation curve. These two values are considered equal since the results of many experiments do not indicate consistent differences.

The value of M as calculated from these curves is 1.6×10^9 dyne/cm². This is considerably smaller than the averaged Young's modulus for ice ($E\simeq10^{11}$ dyne/cm²).[1] Further disagreement is found when Eq. (5) is applied to the slope of the compression curve (Fig. 4). The initial slopes do not agree with Eq. (5). Table I shows

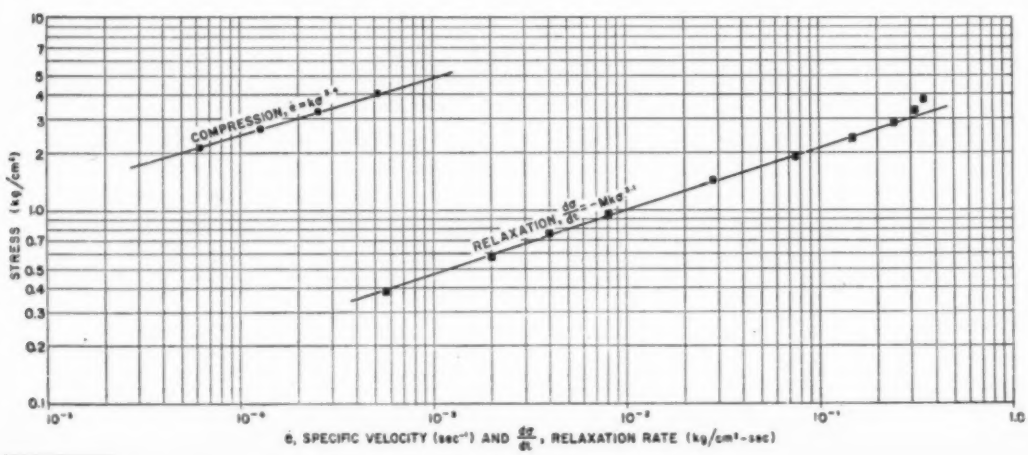

FIG. 3. Snow compression and relaxation data taken from Fig. 2. $T=-10°C$, $\gamma=0.42$ g/cm³.

[1] F. Jona and P. Sherrer, Helv. Phys. Acta **25**, 35 (1952).

the difference in slope between the compression and relaxation curves of Fig. 4 for several pressures. According to Eq. (5), these differences should be constant.

Equation (5) is probably unsatisfactory for increasing stress because of neglect of the dependence of strain rate on time. The equation holds well for relaxation where the strain rate is zero.

CREEP TESTS

A series of creep tests were performed. In these tests the deformation of snow was measured as a function of time for uniaxial compression at constant load. The stress was produced by dead-weight loads and deformation was measured with a dial gauge. A typical series of creep curves is shown in Fig. 5. The strain rate de-

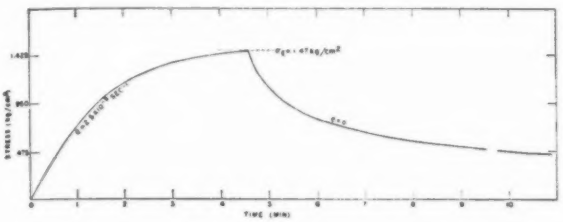

FIG. 4. Compression and relaxation curve. $T=-10°C$, $\gamma=0.42$ g/cm³.

creases continuously with time, having the appearance of asymptotically approaching a linear time dependence. However, the slope of the apparent asymptote decreases with time and, for the longest runs made (~15 000 min), a straight line is not yet attained. A good representation of these creep curves, then, does not involve an appreci-

TABLE I.

σ(kg/cm²)	$(d\sigma/dt)_{comp}-(d\sigma/dt)_{relax}$ (kg/cm²−sec)
0.473	0.311
0.947	0.349
1.42	0.734

able linear term for times less than many thousands of minutes.

One representation of the creep curve appears satisfactory for a large percentage of the cases:

$$\Delta Z/Z_0=B\sigma t^s. \qquad (7)$$

Here $\Delta Z/Z$ is the strain and B is a parameter depending on temperature and density. σ is the stress, which is considered constant for these experiments because of the small changes in cross-sectional area. Values of s are usually near 0.8 although extreme values vary between 0.5 and 1.0. Not all creep curves can be described by Eq. (7) unless two values of s are used in different time regions.

The linear dependence of deformation on stress, indicated in Eq. (7), is good for the range of stress used

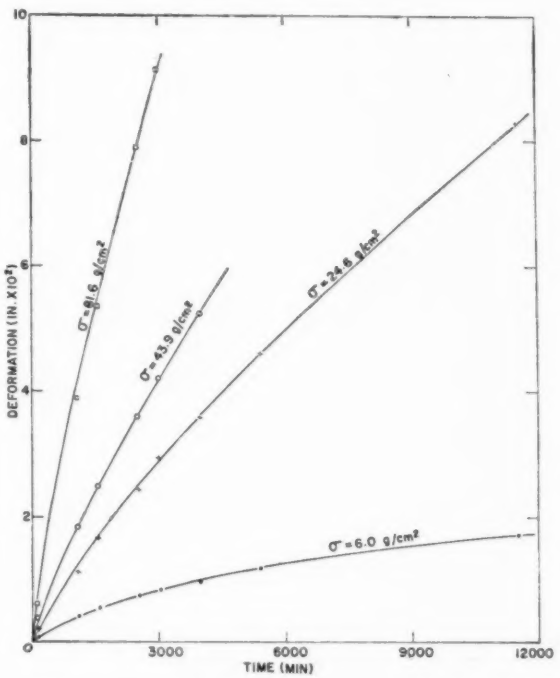

FIG. 5. Creep curves for various stresses at $T=-10°C$, $\gamma=0.42$ g/cm³.

in the creep tests ($2<\sigma<100$ g/cm²). For these low loads, the weight of the upper part of the sample on the lower part contributes appreciably to the deformation. Therefore, the dead-weight load plus one-half the weight

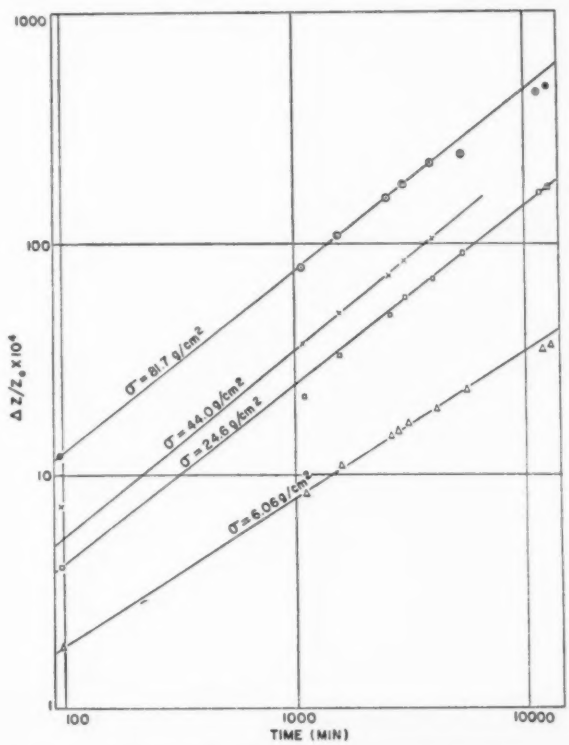

FIG. 6. Double logarithmic plots of deformation *vs* time for various stresses. $T=-10°C$ and $\gamma=0.42$ g/cm³.

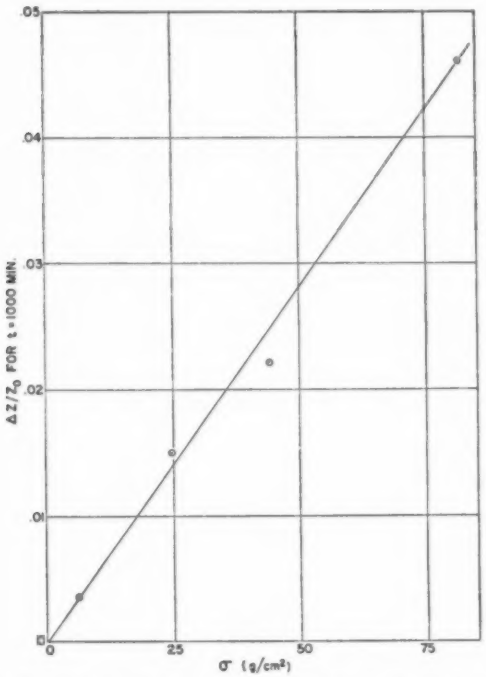

FIG. 7. Creep deformation *vs* stress for identical sifted snows at $T=-10°C$, $\gamma=0.42$ g/cm³.

of the sample is taken as the total load. A typical series of creep curves for identical snows under various loads is shown in Fig. 6. In Fig. 7, the relative deformation at 1000 min is plotted against the total stress. It should be noted that, beside the good experimental agreement, there is some theoretical justification for using the factor $\frac{1}{2}$ for the load contribution due to the weight of the sample.

Creep tests were conducted at $-5°C$, $-10°C$, and $-20°C$. The temperature variation of B can be represented by

$$B=\text{const}e^{-(\Delta H/RK)}, \tag{8}$$

where K is the absolute temperature and R is the gas constant. The activation energy, ΔH, for creep is about 14 000 cal/mole. Several tests indicate that this value may be in error by as much as 20%.

The density dependence of B can be expressed as a function of the void ratio as in Eq. (2). Figure 8 shows that the value of p is about 4, in good agreement with the constant strain rate tests.

Snow type does not appear to have any significant effect on B or s. This means that, if any effect exists, it is masked by the fairly large experimental scatter observed, and that snow type is certainly not a primary factor in these experiments.

CONCLUSIONS

The dependence of uniaxial deformation on stress increases from a linear relationship at low stress to approximately a cubic relationship at high stress. This change occurs roughly in the neighborhood of 1 kg/cm². It is noteworthy that the high stress relationship in snow is similar to that observed in polycrystalline ice.[2] For polycrystalline ice, however, the apparent activation energy for creep is several times larger than for snow. It is possible that stress and activation energy are both involved exponentially as suggested by Kauzmann.[3] Further study should shed light on this matter.

These results are consistent with those of workers in the field of metal creep. For example, the creep curves

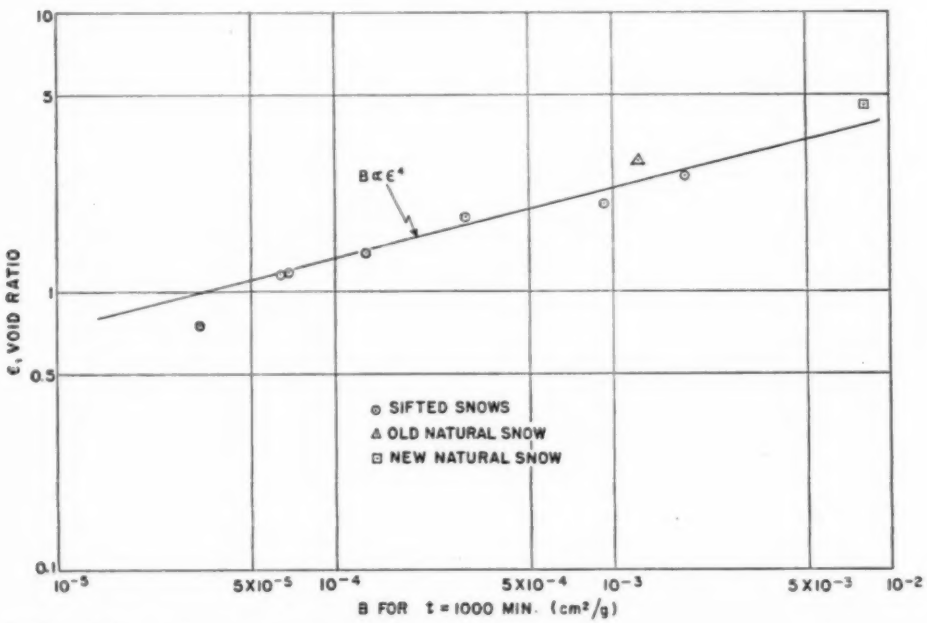

FIG. 8. Creep parameter *vs* void ratio for various snows at $T=-10°C$.

[2] J. W. Glen, Nature **172**, 721 (1953).
[3] W. Kauzmann, Trans. Am. Inst. Mining Met. Engrs. **143**, 57 (1941).

for snow [Eq. (7)] are similar to ones for zinc.[4] The value of the exponent is not seriously different. The observed lack of variation of s with temperature may be attributed to the limited interval studied. The activation energy for creep in snow is not out of line with energies obtained from the creep of soft metals. It can be seen that essentially similar processes must account for creep in metals and in snow. The relative importance of grain boundary and intragrain motion needs further study.

[4] D. O. Thompson, J. Appl. Phys. **26**, 280 (1955).

The empirical relations discussed in the preceding sections appear to be valid in many cases. Reproducibility is erratic, however, and deviations from these relations do occur. When carefully sifted snows are used, greater reproducibility is obtained than for the natural snows. Nevertheless, deviations of 10 to 20% are often observed for supposedly identical sifted snows.

ACKNOWLEDGMENTS

The author wishes to thank Dr. Henri Bader for valuable discussions pertaining to this work.

JOURNAL OF APPLIED PHYSICS VOLUME 26, NUMBER 12 DECEMBER, 1955

Calculation of the Complex Modulus of Linear Viscoelastic Materials from Vibrating Reed Measurements*

D. R. Bland† and E. H. Lee‡
Brown University, Providence, Rhode Island
(Received June 9, 1955)

Two methods of determining the variation of real and complex modulus with frequency from vibrating reed test results are detailed. One is based on measurements of the relative amplitude and phase lag of the motion of the free and driven ends of the reed, the other on amplitude resonance measurements only. The analysis is based on a general linear viscoelastic law, and takes into account the influence of the frequency dependent moduli of the material on the frequency and amplitude of the resonance peaks. This influence has not been correctly accounted for in previous analyses which have included the assumption that the material behaves according to a particular, simple viscoelastic law, which will in general not be borne out by the final results.

The method is applied to a series of tests. For the material and frequency range used the imaginary part of the complex modulus was small compared with the real part, and the influence mentioned in the foregoing was small. A simpler method of analysis might thus be justified, but in other cases it will be necessary to carry out the complete analysis in order to obtain a satisfactory interpretation of test results.

INTRODUCTION

THE purpose of this paper is to describe the calculation of the complex modulus of a linear viscoelastic material from measurements of the steady forced oscillation of a vibrating reed of the material. In a previous paper[1] the authors discussed the significance of this calculation from the general standpoint of the analysis of dynamic tests. In the main, this work differs from previous analysis in that care is taken to base the analysis on the general viscoelastic law, so that the variation of the response with frequency which is used in a resonance test is consistent with the deduced behavior of the material. Previous analyses have based the interpretation of test results on the assumption that the material is represented by a simple viscoelastic model, which may lead to contradictions in the final results.

* Sponsored under Department of Defense Contract, Nord-11496 between the Bureau of Ordnance, Navy Department, and Brown University.
† I.C.I. Research Fellow at Imperial College, London.
‡ Professor of Applied Mathematics, Brown University.
[1] E. H. Lee and D. R. Bland, Soc. Plastic Engrs. 11, No. 7 (September, 1955).

GOVERNING DIFFERENTIAL EQUATION

In experiments with a vibrating reed, one end of the reed is clamped and performs vibrations of constant amplitude and frequency in the direction of the thickness of the reed. The far end of the reed is free and from its motion, the viscoelastic properties of the material are determined. It is assumed that the length of the reed is large compared to its thickness so that the usual assumptions of vibrating beam theory can be made. The analysis differs from that of classical elasticity only in that the stress-strain relation $\sigma=E\epsilon$ is replaced by:

$$P(\partial/\partial t)\sigma=Q(\partial/\partial t)\epsilon, \tag{1}$$

where $P(\partial/\partial t)$ and $Q(\partial/\partial t)$ are polynomials in the operator $(\partial/\partial t)$ with constant coefficients. Since we are concerned with periodic oscillations of angular frequency ω, the operator $(\partial/\partial t)$ can be replaced by $(i\omega)$ using the well-known complex representation. Equation (1) becomes:

$$P(i\omega)\sigma=Q(i\omega)\epsilon \tag{2}$$

or

$$\sigma=(Q/P)\epsilon. \tag{3}$$

Thus, we merely have to replace E in the elastic analysis by Q/P, a complex constant for prescribed ω when the system has settled down to steady-state forced oscillation.

If x denotes the distance along the reed, measured from its clamped end, y the displacement normal to it, M the bending moment, and S the shearing force on any cross section, m the mass per unit length, and I the second moment of the cross section, the well-known results for an elastic reed are:

$$M=-EI\partial^2y/\partial x^2$$
$$S=EI\partial^3y/\partial x^3,$$

and

$$\frac{\partial^4y}{\partial x^4}-\frac{m\omega^2}{EI}y=0.$$

The deflections are assumed to be sufficiently small for $(\partial y/\partial x)\ll 1$. For a viscoelastic reed, these equations become

$$M=-\frac{QI}{P}\frac{\partial^2y}{\partial x^2} \tag{4}$$

$$S=\frac{QI}{P}\frac{\partial^3y}{\partial x^3}, \tag{5}$$

and

$$\frac{\partial^4y}{\partial x^4}-\frac{m\omega^2P}{QI}y=0. \tag{6}$$

Since Q/P is independent of x, the solution of Eq. (6) is similar in form to the solution of the corresponding elastic problem.

PART 1. REED WITH THE FREE END UNLOADED

For the case of a reed clamped at the driven end, and free at the other end, the boundary conditions are $y=Ye^{i\omega t}$ and $\partial y/\partial x=0$ at the clamped end $x=0$, and $\partial^2y/\partial x^2=-(P/QI)M=0$ and $\partial^3y/\partial x^3=(P/QI)S=0$ at the free end, $x=l$.

Here only the motion of the free end is of interest. Solving Eq. (6) with the above boundary conditions and then putting $x=l$, we obtain

$$y=Y\frac{\cosh\psi+\cos\psi}{1+\cosh\psi\cos\psi}e^{i\omega t}$$

where

$$\psi=(m\omega^2P/IQ)^{\frac{1}{4}}l. \tag{7}$$

It is the ratio of amplitudes A between the free and clamped ends and the phase lag θ, of the free end behind the clamped end which are significant. They are given by

$$Ae^{-i\theta}=\frac{\cosh\psi+\cos\psi}{1+\cosh\psi\cos\psi}. \tag{8}$$

Equation (7) will be needed in an inverted form to solve for E_1 and E_2 in terms of ψ. This form is

$$E_1+iE_2=\frac{Q}{P}=\frac{m\omega^2}{I}l^4\psi^{-4}. \tag{9}$$

For a particular length of reed an amplitude-frequency curve is obtained. This will have a series of maxima at the resonance frequencies of the system. From the curve around a particular maximum (usually the first maximum is taken) values of the complex modulus can be deduced. Nolle[2] and Horio and Onogi[3] make use of the frequency at resonance and the width of the resonance curve. This method assumes that the form of the variation of the complex modulus is prescribed according to a simple viscoelastic relation across the width of the curve. The two methods given below do not make this assumption. The second method also uses only amplitude frequency curves. It makes use of the frequency and maximum amplitude and is useful only when the imaginary part of the complex modulus does not exceed one-half of the real modulus. The first method is generally valid. It requires measurements of both amplitude and phase lag of the free end, and one length of reed is sufficient for a whole set of measurements. For all the maximum amplitude methods a whole series of measurements with different lengths is necessary so that the maximum amplitude occurs in turn at different frequencies.

Method 1

This method requires knowledge of both A and θ. We transform Eq. (8) by putting

$$\psi=(1-i)\eta, \tag{10}$$

which leads to

$$Ae^{-i\theta}=\frac{2\cosh\eta\cos\eta}{\cosh^2\eta+\cos^2\eta}, \tag{11}$$

whence

$$\frac{\cosh\eta}{\cos\eta}=\frac{e^{i\theta}}{A}(1+i(A^2e^{-2i\theta}-1)^{\frac{1}{2}})=B+iC, \tag{12}$$

the sign of the square root being chosen so that $(\cosh\eta/\cos\eta)\to i$ as $A\to\infty$. Since A and θ are known, $B+iC$ can be calculated; B and C are both real.

Let us suppose we have an approximate solution $\eta_0=\alpha_0+i\beta_0$ to Eq. (12) and that we wish to improve the approximation. We put $\eta=\eta_0+\epsilon_0$ and neglect powers of ϵ_0 higher than the first. To this order, Eq. (12) gives:

$$\epsilon_0=\frac{(B+iC)\cos\eta_0-\cosh\eta_0}{(B+iC)\sin\eta_0+\sinh\eta_0}.$$

[2] A. W. Nolle, J. Appl. Phys. **19**, 753 (1948).
[3] M. Horio and S. Onogi, J. Appl. Phys. **22**, 977 (1951).

On separating η_0 into its real and imaginary parts,

$$\epsilon_0=\frac{(B+iC)(\cos\alpha_0\cosh\beta_0-i\sin\alpha_0\sinh\beta_0)-(\cosh\alpha_0\cos\beta_0+i\sinh\alpha_0\sin\beta_0)}{(B+iC)(\sin\alpha_0\cosh\beta_0+i\cos\alpha_0\sinh\beta_0)+(\sinh\alpha_0\cos\beta_0+i\cosh\alpha_0\sin\beta_0)}. \quad (13)$$

The method of determining ψ for given A and θ is as follows; from A and θ, B and C are found from Eq. (12). A value of η, $\eta_0=\alpha_0+i\beta_0$, is guessed and ϵ_0 is found from Eq. (13). The next value of η is taken as $\eta_0+\epsilon_0$. The cycle is repeated until ϵ becomes negligibly small. The final value of η is substituted into Eq. (10) to obtain ψ.

Substitute ψ into Eq. (9) to obtain E_1 and E_2. The whole process is then repeated at as many different values of ω as are required.

Method 2

Theory.—

This method assumes that $E_2<\frac{1}{2}E_1$. In this case writing $\psi=a+ib$, $b<\frac{1}{8}a$ and the value of ψ at the maximum amplitude is near to the corresponding value at resonance of an elastic rod, which corresponds to $b=0$. The latter value is known and will be denoted by a_0. The difference $\psi-a_0$ will be denoted by $\chi=\epsilon+ib$. a_0 is a solution of the equation $1+\cosh a_0\cos a_0=0$. The first maximum will be used here. This corresponds to $a_0=1.875$. We now expand the expression on the right-hand side of Eq. (8) as a power series in the small quantity χ, making use of the relations $\sin a_0\cosh a_0=\sinh a_0$ and $\sinh a_0\cos a_0=-\sin a_0$. It can be shown that

$$Ae^{-i\theta}=\frac{\cosh\psi+\cos\psi}{1+\cosh\psi\cos\psi}=-\frac{c}{\chi}(1+c_2\chi^2+0(\chi^3)), \quad (14)$$

where

$$c=\frac{\cosh a_0+\cos a_0}{\sinh a_0+\sin a_0}, \quad (15)$$

and

$$c_2=\frac{\sinh a_0\cosh a_0-\sin a_0\cos a_0+5\sinh a_0+5\sin a_0}{6(\sinh a_0\cosh a_0+\sin a_0\cos a_0+\sinh a_0-\sin a_0)}. \quad (16)$$

For the first maximum $a_0=1.875$, $c=0.734$, $c_2=0.419$.

To obtain an expression for the amplitude A, we substitute $\chi=\epsilon+ib$ in Eq. (14). Whence

$$A^2=\frac{c^2}{\epsilon^2+b^2}(1+2c_2(\epsilon^2-b^2)+0(\epsilon,b)^2). \quad (17)$$

At the maximum amplitude $dA^2/d\omega=0$ giving:

$$\epsilon=-b\frac{db/d\omega}{da/d\omega}(1+4c_2(b^2+\epsilon^2)) \quad (18)$$

using $(da/d\omega)=(d\epsilon/d\omega)$ since $a=a_0+\epsilon$. Since $b\ll a$, it will be assumed for later verification that $(db/da)=0(b/a)$. Then $\epsilon=0(b^2/a^2)$ and Eq. (17) can be written for maximum amplitude A_m

$$A_m=\frac{c}{|b|}\left(1-c_2b^2-\frac{1}{2}\left(\frac{db/d\omega}{da/d\omega}\right)^2+0(b^3)\right). \quad (19)$$

To determine E_1 and E_2, Eq. (9) is used in the form

$$E_1+iE_2=\frac{m\omega^2}{I}l^4a^{-4}\left(1+i\frac{b}{a}\right)^{-4}.$$

when $b\ll a$,

$$E_1=\frac{m}{I}\omega^2l^4a^{-4}\left(1-6\frac{b^2}{a^2}+0\left(\frac{b^4}{a^4}\right)\right) \quad (20)$$

$$E_2=-\frac{m}{I}\omega^2l^4a^{-4}\frac{4b}{a}\left(1-\frac{b^2}{a^2}+0\left(\frac{b^4}{a^4}\right)\right)$$

or

$$E_2=-\frac{4b}{a}E_1\left(1+5\frac{b^2}{a^2}+0\left(\frac{b^4}{a^4}\right)\right). \quad (21)$$

If $E_2>0$, b must be negative. Changing the sign of b only effects the sign of E_2 as b^2 or $b(db/da)$ occurs elsewhere.

Procedure for solution.—

For a first approximation, terms of $0(b^2/a^2)$ are neglected. To this order of accuracy, from Eqs. (18) and (19),

$$\epsilon=0, \quad A_m=\frac{c}{|b|}$$

therefore

$$a=a_0, \quad b=b_1=-\frac{c}{A_m},$$

negative since $E_2>0$. Then from Eqs. (20) and (21),

$$E_1=\frac{m}{I}\omega^2l^4a_0^{-4}\left(1-\frac{6c^2}{a_0^2A_m^2}\right)$$

$$E_2=\frac{4c}{a_0A_m}E_1\left(1+\frac{5c^2}{a_0^2A_m^2}\right).$$

This is the first approximation for E_1 and E_2.

If only one amplitude-frequency curve has been found, it is impossible to proceed further. However, if a series of such curves exist for different lengths or different thicknesses of reed, E_1 and E_2 are found at the maximum of each of these curves. Since each maximum corresponds to a different frequency, curves of E_1 and E_2 against frequency can be drawn and values of $dE_1/d\omega$

and $dE_2/d\omega$ calculated. From Eq. (9) by differentiation, it can be shown that

$$\frac{db/d\omega}{da/d\omega}=\frac{b}{a}\frac{1+\left(\frac{a}{b}\frac{E_2}{E_1^2+E_2^2}-\frac{E_1}{E_1^2+E_2^2}\right)\frac{\omega}{2}\frac{dE_1}{d\omega}-\left(\frac{a}{b}\frac{E_1}{E_1^2+E_2^2}+\frac{E_2}{E_1^2+E_2^2}\right)\frac{\omega}{2}\frac{dE_2}{d\omega}}{1-\left(\frac{E_1}{E_1^2+E_2^2}+\frac{b}{a}\frac{E_2}{E_1^2+E_2^2}\right)\frac{\omega}{2}\frac{dE_1}{d\omega}-\left(\frac{E_2}{E_1^2+E_2^2}-\frac{b}{a}\frac{E_1}{E_1^2+E_2^2}\right)\frac{\omega}{2}\frac{dE_2}{d\omega}}. \tag{22}$$

From Eq. (22) ($db/d\omega/da/d\omega$) is calculated, using the first approximations a_0 and b_1. An approximate form of Eq. (22) which can be utilized is:

$$\frac{db/d\omega}{da/d\omega}=\frac{b}{a}+\frac{\omega}{2}\frac{E_2\frac{dE_1}{d\omega}-E_1\frac{dE_2}{d\omega}}{E_1^2+E_2^2}. \tag{23}$$

The next approximations for a and b, a_2 and b_2, are found from Eqs. (19) and (18) as

$$a_2=a_0+\epsilon_2=a_0-b_2\frac{db/d\omega}{da/d\omega}$$

$$b_2=-\frac{c}{A_m}\left(1-c_2b_1^2-\frac{1}{2}\left(\frac{db/d\omega}{da/d\omega}\right)^2\right).$$

Therefore,

$$\delta a=a_2-a_0=-b_2\frac{db/d\omega}{da/d\omega} \tag{24}$$

and

$$\delta b=b_2-b_1=+\frac{c}{A_m}\left(b_1^2+\frac{1}{2}\left(\frac{db/d\omega}{da/d\omega}\right)^2\right). \tag{25}$$

The second approximation to E_1 and E_2 is obtained from Eqs. (20) and (21). Equation (20) gives

$$\delta E_1=E_1\left(-\frac{4\delta a}{a_0}\right), \tag{26}$$

and Eq. (21) gives

$$\delta E_2=E_2\left(\frac{\delta b}{b_1}-\frac{5\delta a}{a_0}\right). \tag{27}$$

When added to the first approximations for E_1 and E_2, δE_1 and δE_2 determine the second approximations.

The process is carried out for each maximum and a plot of E_1 and E_2 against frequency is made. $dE_1/d\omega$ and $dE_2/d\omega$ are recalculated. If they differ appreciably from the previous values, the calculation for the second approximation should be repeated using the new $dE_1/d\omega$ and $dE_2/d\omega$. Otherwise they represent the correct values of the complex moduli.

Part 2. The Vibrating Reed with the Free End Loaded

It is found experimentally that to measure accurately the motion of the free end of an unloaded reed is difficult. The measurement is simplified if an iron pin is stuck through the end, and the motion of the pin is determined electrically. In this case not only the mass of the pin but its moment of inertia must be taken into account. The motion of the reed in these circumstances is analyzed in the following, and the determination of the complex modulus by the second of the foregoing methods is given. The analysis is the same in principle as in Part 1 but the algebraic details are more complicated.

The differential equation for the vibration of the reed, Eq. (6), is unaltered. The boundary conditions at the end $x=0$, namely, $y=Ye^{i\omega t}$ and $\partial y/\partial x=0$, are unaltered. At the end $x=l$, the bending moment $M=J(\partial^3 y/\partial t^2\partial x)$ and the shearing force $S=W(\partial^2 y/\partial t^2)$, where J and W are the moment of inertia and the mass of the pin, respectively. The moment of inertia is taken about an axis parallel to the breadth of the reed at the end of the reed and at the midpoint of the thickness. Since $M=-I(Q/P)(\partial^2 y/\partial x^2)$ and $S=I(Q/P)(\partial^3 y/\partial x^3)$, for periodic vibrations at angular frequency ω the boundary conditions at $x=l$ become

$$\frac{\partial^2 y}{\partial x^2}=J\frac{\omega^2 P}{IQ}\frac{\partial y}{\partial x} \quad \text{and} \quad \frac{\partial^3 y}{\partial x^3}=-W\frac{\omega^2 P}{IQ}y.$$

Using the above boundary conditions for Eq. (6), and then substituting $x=l$, the equation of motion for the end of the pin becomes

$$\frac{y}{Ye^{i\omega t}}=z_l$$

$$=\frac{\cosh\psi+\cos\psi-B\psi^3(\sinh\psi+\sin\psi)}{1+\cosh\psi\cos\psi+A\psi(\sinh\psi\cos\psi-\cosh\psi\sin\psi)-B\psi^3(\cosh\psi\sin\psi+\sinh\psi\cos\psi)+AB\psi^4(1-\cosh\psi\cos\psi)} \tag{28}$$

where as before

$$\psi=(m\omega^2P/IQ)^{\frac{1}{4}}l \tag{7}$$

and

$$A=W/ml, \tag{29}$$

$$B=J/ml^3. \tag{30}$$

Instead of expanding about real roots of $1+\cosh\psi\cos\psi$ as in Part 1, we now expand about a real root of the denominator of the right-hand side of Eq. (28) which corresponds to the resonance of the loaded elastic reed. Such a root is denoted by γ, and the values of $\cosh\gamma$, $\cos\gamma$, $\sinh\gamma$, and $\sin\gamma$ by C, c, S, and s, respectively. We shall put $\psi=\gamma+\chi$ and $\chi=\epsilon+ib$. The values of the maximum amplitude and its position will be found in terms of ϵ and b. We expand z_l in powers of χ, giving:

$$z_l=\frac{1}{\chi}(c_0+c_1\chi+c_2\chi^2+0(\chi^3)), \tag{31}$$

where

$$c_0=\frac{\alpha_0}{\beta_0},\quad c_1=\frac{\alpha_1}{\beta_0}-\frac{\beta_1}{\beta_0}c_0=\frac{\alpha_1}{\beta_0}-\frac{\alpha_0\beta_1}{\beta_0^2},$$

$$c_2=\frac{\alpha_2}{\beta_0}-\frac{\beta_2}{\beta_0}c_0-\frac{\beta_1}{\beta_0}c_1=\frac{\alpha_2}{\beta_0}-\frac{\alpha_0\beta_2}{\beta_0^2}-\frac{\alpha_1\beta_1}{\beta_0^2}+\frac{\alpha_0\beta_1^2}{\beta_0^3}, \tag{32}$$

and

$$\alpha_0=C+c-B\gamma^3(S+s)$$

$$\alpha_1=S-s-B\gamma^3(C+c)-3B\gamma^2(S+s)$$

$$\alpha_2=\tfrac{1}{2}(C-c)-3B\gamma(S+s)-3B\gamma^2(C+c)-\tfrac{1}{2}B\gamma^3(S-s)$$

$$\beta_0=Sc-Cs+A(Sc-Cs)-2A\gamma Ss-2B\gamma^3Cc$$
$$-3B\gamma^2(Sc+Cs)+4AB\gamma^3(1-Cc)-AB\gamma^4(Sc-Cs)$$

$$\beta_1=-Ss-A\gamma(Cs+Sc)-2ASs-3B\gamma(Sc+Cs)$$
$$-6B\gamma^2Cc-B\gamma^3(Sc-Cs)+6AB\gamma^2(1-Cc)$$
$$-4AB\gamma^3(Sc-Cs)+AB\gamma^4Ss$$

$$\beta_2=-\frac{Sc+Cs}{3}-\frac{2A\gamma Cc}{3}-A(Cs+Sc)+\frac{2B\gamma^3Ss}{3}$$
$$-3B\gamma^2(Sc-Cs)-6B\gamma Cc-B(Sc+Cs)$$
$$+4AB\gamma(1-Cc)-6AB\gamma^2(Sc-Cs)$$
$$+4AB\gamma^3Ss+\tfrac{1}{3}AB\gamma^4(Sc+Cs). \tag{33}$$

We now separate χ into real and imaginary parts so that the value of $|z_l|$ can be determined.

Using

$$\chi=\epsilon+ib, \tag{34}$$

$$|z_l|^2=\frac{c_0^2+2c_0c_1\epsilon+(c_1^2+2c_0c_2)\epsilon^2+(c_1^2-2c_0c_2)b^2+0(\epsilon,b)^3}{\epsilon^2+b^2}. \tag{35}$$

For a maximum of $|z_l|$, $(d|z_l|/d\omega)=0$ or, since $(d\epsilon/d\omega)\neq0$, $(d|z_l|/d\epsilon)=0$. Substituting from Eq. (35):

$$c_0\epsilon+c_1\epsilon^2-c_1b^2-4c_2\epsilon b^2+(c_0+2c_1\epsilon+4c_2\epsilon^2)b\frac{db}{d\epsilon}=0.$$

As before we assume $(db/d\epsilon)=(db/da)$ to be of order b which must be checked from the final results. Then, from the foregoing equation, the maximum amplitude condition gives:

$$\epsilon=\frac{c_1}{c_0}b^2-b\frac{db}{da}+0(b^4) \tag{36}$$

so that ϵ is of order b^2. Substituting back into Eq. (35) to find $|z_l|$ at maximum and denoting this value by A_m, we obtain:

$$A_m=\left|\frac{c_0}{b}\right|\left(1+\frac{c_1^2-c_0c_2}{c_0^2}b^2-\frac{1}{2}\left(\frac{db}{da}\right)^2+0(b^3)\right). \tag{37}$$

The angular frequency and value of maximum amplitude, ω and A_m, are determined experimentally. We must now work back to determine the values of E_1 and E_2 at this frequency. From Eq. (7),

$$\psi=\gamma+\epsilon+ib=\left(\frac{m\omega^2P}{IQ}\right)^{\frac{1}{4}}l$$

$$E_1+iE_2=\frac{Q}{P}=\frac{m}{I}l^4\omega^2(\gamma+\epsilon+ib)^{-4}$$
$$=\frac{m}{I}l^4\omega^2\gamma^{-4}\left(1-\frac{4\epsilon}{\gamma}-10\frac{b^2}{\gamma^2}\right.$$
$$\left.+i\left(-\frac{4b}{\gamma}+\frac{20\epsilon b}{\gamma^2}+\frac{20b^3}{\gamma^3}\right)+0(b^4)\right). \tag{38}$$

From Eq. (37),

$$b=\frac{c_0}{A_m}\left(1+\frac{c_1^2-c_0c_2}{A_m^2}-\frac{1}{2}\left(\frac{db}{da}\right)^2\right)+0\left(\frac{c_0}{A_m}\right)^4. \tag{39}$$

The sign of b is negative since $E_2>0$. $c_0<0$ therefore there is no negative sign at the beginning of the right-hand side of the foregoing equations. Substituting for b from Eq. (39) into Eq. (36)

$$\epsilon=\frac{c_1c_0}{A_m^2}-\frac{c_0}{A_m}\frac{db}{da}+0\left(\frac{c_0}{A_m}\right)^4. \tag{40}$$

Substituting for b and ϵ in Eq. (38),

$$E_1=\frac{m}{I}l^4\omega^2\gamma^{-4}\left\{1-\left(10+\frac{4c_1\gamma}{c_0}\right)\frac{c_0^2}{\gamma^2A_m^2}\right.$$
$$\left.+4\frac{c_0}{\gamma A_m}\frac{db}{da}+0\left(\frac{c_0}{A_m}\right)^4\right\} \tag{41}$$

and

$$E_2=-\frac{4c_0}{A_m}l^4\omega^2\gamma^{-5}\left\{1+\frac{1}{A_m^2}(c_1^2-c_0c_2)-\frac{1}{2}\left(\frac{db}{da}\right)^2 -5\frac{c_0}{\gamma A_m}\left(\frac{c_0}{A_m}-\frac{db}{da}\right)-5\frac{c_0^2}{\gamma^2A_m^2}+0\left(\frac{c_0}{A_m}\right)^4\right\} \quad (42)$$

or

$$E_2=-\frac{4c_0}{\gamma A_m}E_1\left\{1+\frac{1}{A_m^2}(c_1^2-c_0c_2)-\frac{1}{2}\left(\frac{db}{da}\right)^2 +\frac{c_0}{\gamma A_m}\frac{db}{da}+5\frac{c_0^2}{\gamma^2A_m^2}-\frac{c_1c_0}{\gamma A_m^2}+0\left(\frac{c_0}{A_m}\right)^3\right\}. \quad (43)$$

Equations (41) and (42) or (43) enable E_1 and E_2 to be calculated from the experimentally determined ω and A_m. (db/da) is found from Eq. (22) using the first approximation to E_1 and E_2 as explained below.

PROCEDURE FOR SOLUTION

First calculate the two constants A and B, Eqs. (29) and (30). Secondly, calculate γ. If the first maximum of the amplitude-frequency curve is used for the experimental measurements, then the first real root is required of the equation

$$1+\cosh\psi\cos\psi+A\psi(\sinh\psi\cos\psi-\cosh\psi\sin\psi) -B\psi^3(\cosh\psi\sin\psi+\sinh\psi\cos\psi) +AB\psi^4(1-\cosh\psi\cos\psi)=0.$$

For $A=B=0$ this root is 1.875. For A, $B>0$, the root is less than 1.875. If the nth maximum of the curve is used then the nth real root is the required value of γ.

Thirdly, calculate α_0, α_1, α_2, β_0, β_1, and β_2 from Eq. (33) and then c_0, c_1, and c_2 from Eq. (32). Fourthly, calculate the first approximations to E_1 and E_2 from Eqs. (41) and (43). The first approximations are the first terms only on the right-hand sides of these equations. That is

$$E_1\simeq\frac{m}{I}l^4\omega^2\gamma^{-4}$$

$$E_2\simeq-\frac{4c_0}{\gamma A_m}E_1.$$

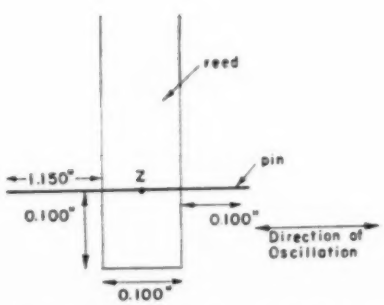

FIG. 1. Geometry of attachment of pin to reed.

If only one pair of values of ω and A_m have been measured, it is impossible to proceed further. When more pairs are known, the first approximations for all these pairs are calculated. From these values of E_1 and E_2, values of $(dE_1/d\omega)$ and $(dE_2/d\omega)$ at each resonance frequency can be calculated and then (db/da) is given by Eq. (22). The remaining terms in Eqs. (41) and (43) are now evaluated and the final values of E_1 and E_2 obtained. Note that in order to allow for the correct variation of material properties with frequency, it is necessary to work with variables such as E_1 and E_2 depending only on the material properties. The variables b and a also depend on the dynamic system and on this account differ at the various resonance frequencies associated with different reed lengths.

EXAMPLE

A series of vibrating reed tests was carried out on a propellant type plastic by the Plastics Research Section at Picatinny Arsenal. A pin was stuck through one end of a reed and the resonant frequency and the amplitude of the pin found for various amplitudes of the damped end. For variations of amplitude of the clamped end of 1000%, the resonant frequency and amplitude ratio varied by less than 5%. The accuracy of the frequency and amplitude measurements were each about 2%. The material of the reed therefore shows but a small departure from linearity.

The mass of the pin was 0.0545 gram. Its dimensions and position with respect to the end of the reed are shown in Fig. 1. The moment of inertia of the pin about an axis through Z, normal to the plane of the diagram is 0.0233 g in.^{2}. To the mass of the pin must be added the mass of the reed projecting beyond Z (its moment of inertia is negligible). The mass of the reed per unit length is 0.477 g/in. and the projecting part has mass 0.0477 g. The total mass at the end of the reed is, therefore, 0.1022 g with moment of inertia 0.0233 g in.^{2}.

For various lengths of reed the resonant frequency and amplitude ratio were found. They are tabulated in Table I (the length is measured from the clamped end to the point Z). The next two columns show the calculated values of A and B from Eqs. (29) and (30). The corresponding values of γ are given in the next line. The α's and β's were calculated from Eq. (33) and c_0, c_1, and c_2 from Eq. (32); the latter values are shown in the next three columns.

It is usually convenient to work with frequencies rather than angular frequencies. The first term in Eqs. (41) and (42) can then be written as $(2\pi)^2(m/I)l^4f^2\gamma^{-4}$. Since $(2\pi)^2(m/I)$ is the same for different lengths of reed, it is evaluated separately

$$(2\pi)^2\frac{m}{I}=1.195\cdot10^6 \text{ g/in.}^5.$$

If l is expressed in inches, f in cycles/sec, then E_1 will be in g in. sec^{-2}/in.^{2}. To convert to lbs force/in.^{2} multiply

TABLE I. Real and complex moduli calculated from experimental results. Thickness of reed = 0.100 in., breadth = 0.189 in., mass = 0.477 g/in., mass at end = 0.1022 g, moment of inertia at end = 0.0233 g-in.^{2}.

Effective length of reed l, in.	Resonant frequency f cps	Resonant amplitude ratio A_m	$\frac{A}{} = \frac{W}{ml}$	$\frac{B}{} = \frac{J}{ml^2}$	γ	c_0	c_1	c_2	$\frac{c_0}{\gamma A_m}$	First approx 10^4 lb force per in.^{2} E_1'	E_2'
3.377	33.5	5.84	0.063	0.001	1.769	−0.640	0.080	−0.951	−0.062	10.19	2.53
3.135	38.9	5.84	0.068	0.002	1.759	−0.629	0.087	−0.894	−0.061	10.45	2.56
2.873	46.9	6.65	0.074	0.002	1.752	−0.623	0.094	−0.890	−0.054	10.88	2.33
2.625	55.0	7.16	0.082	0.003	1.738	−0.609	0.111	−0.858	−0.049	10.73	2.10
2.420	64.2	7.73	0.088	0.003	1.730	−0.605	0.112	−0.848	−0.045	10.79	1.95
2.259	79.7	7.86	0.095	0.004	1.719	−0.594	0.122	−0.805	−0.044	12.96	2.28
2.093	92.7	8.24	0.102	0.005	1.708	−0.583	0.132	−0.786	−0.041	13.25	2.20
1.915	107.3	8.35	0.112	0.007	1.691	−0.568	0.149	−0.734	−0.040	12.95	2.08
1.700	135.1	7.72	0.126	0.010	1.669	−0.546	0.171	−0.663	−0.042	13.44	2.28
1.493	169.0	8.20	0.143	0.015	1.640	−0.517	0.204	−0.562	−0.038	13.41	2.06
1.352	198.6	8.54	0.158	0.020	1.616	−0.492	0.232	−0.473	−0.036	13.21	1.88
1.093	265.2	7.58	0.196	0.037	1.553	−0.428	0.312	−0.228	−0.036	11.80	1.72
0.935	301.0	6.16	0.229	0.060	1.493	−0.368	0.399	+0.076	−0.040	9.53	1.53

Resonant frequency f cps	$\frac{db}{da}$	Final values 10^4 lb force psi E_1	E_2	J_1	J_2	$J_2 f$
33.5	−0.031	9.915	2.375	0.09538	0.02285	0.7655
38.9	−0.026	10.168	2.406	0.09313	0.02204	0.8574
46.9	−0.017	10.637	2.219	0.09009	0.01879	0.8813
55.0	−0.006	10.518	2.013	0.09172	0.01755	0.9653
64.2	0.003	10.598	1.878	0.09148	0.01621	1.0407
79.7	−0.019	12.790	2.212	0.07592	0.01313	1.0465
92.7	−0.022	13.107	2.145	0.07431	0.01216	1.1272
107.3	−0.022	12.826	2.032	0.07606	0.01205	1.2930
135.1	−0.025	13.308	2.224	0.07310	0.01222	1.6509
169.0	−0.023	13.309	2.022	0.07344	0.01116	1.8860
198.6	−0.026	13.139	1.852	0.07467	0.01053	2.0913
265.2	−0.053	11.806	1.705	0.08297	0.01198	3.1771
301.0	—	(9.53)	(1.53)	(0.10230)	(0.01642)	(4.9424)

by $(1/453 \cdot 12 \cdot 32.2)$. Consequently, the first approximation to E_1 is

$$E_1 \simeq \frac{1.195 \cdot 10^6}{453 \cdot 12 \cdot 32.2} l^4 f^2 \gamma^{-4} \text{ lb force/in.}^2$$

$$\simeq 6.84 l^4 f^2 \gamma^{-4} \qquad \text{lb force/in.}^2.$$

The first approximation to E_2 is given by

$$E_2 \simeq -\frac{4c_0}{\gamma A_m} E_1 \text{ lb force/in.}^2.$$

$(c_0/\gamma A_m)$ and the first approximations to E_1 and E_2 are tabulated.

E_1 and E_2 are plotted against frequency and a curve drawn for each. Values of (dE_1/df) and (dE_2/df) are found at each resonance frequency. These are substituted into Eq. (22) to determine (db/da). It is immaterial in Eq. (22) whether ω or f is used provided the same one is used throughout. (db/da) is tabulated. It is seen that (db/da) is the same order as b, that is (c_0/A_m), so that the derivation is satisfactory. The remaining terms in Eqs. (41) and (43) can now be calculated and the final values of E_1 and E_2 obtained.

It is seen that in this case the influence of the variation of E_1 and E_2 with frequency is comparatively small. This will usually be the case when the imaginary part of the modulus is small compared with the real part. In such cases the refinements of the present analysis may be hardly warranted, and the previously suggested method[2] will give satisfactory results since the resonance peak will be comparatively sharp. In other cases in which E_2 is large it may be necessary to carry out the complete analysis in order to obtain a satisfactory interpretation of the test results.

The mathematical development in this paper has been reduced to a minimum. It is given in more detail by Bland and Lee.[4]

[4] D. R. Bland and E. H. Lee, "The calculation of the complex modulus of linear visco-elastic materials from vibrating reed measurement," Brown University Report PA-TR/9, 1955.

Angular Distribution of Multiply Scattered Gamma Radiation from a Plane Isotropic Source

MARTIN J. BERGER
National Bureau of Standards, Washington, D. C.
(Received August 3, 1955)

A method is given for calculating, within the framework of the moment-method of Spencer and Fano, the angular distribution of radiation from a plane isotropic source. Essential use is made of the simplification introduced by a geometrical feature of radiation from such a source. Sample calculations are presented for a 1-Mev source in water.

I. INTRODUCTION

THE moment-method of Spencer and Fano[1] provides a general prescription for calculating the spatial and angular distribution of multiply scattered gamma radiation in an infinite medium. It consists of two distinct steps: (a) the calculation of some of the spatial and angular moments of the radiation flux, and (b) the construction of the flux distribution by moment-fitting. The moments are computed numerically; for practical reasons only a limited number of them can be obtained. Therefore the implementation of the general prescription is not trivial, but the moment-fitting procedure must be selected with care so that a few moments suffice for the accurate determination of the distribution. A large number of calculations have been carried out under various conditions for the flux integrated over all directions.[2] But complications arise in the determination of the joint angular and spatial distribution, so that to date only one detailed application of this kind has been published pertaining to a point isotropic source.[3] It is the purpose of this note to point out that the radiation from a *plane isotropic source* presents a special case, in which the correlation of the spatial and angular distributions of the flux is such that the moment-fitting problem can be reduced from a two-variable problem to one in the space variable only. This makes the treatment both simple and accurate

A. Moments

Let $F(E,x,\omega_x)$ be the energy flux of radiation from a plane isotropic source located in the plane $x=0$ in an infinite homogeneous scattering medium.[4] Consider the expansion of the flux into a Legendre polynomial series:

$$F(E,x,\omega_x)=\sum_{l=0}^{\infty}\frac{2l+1}{2}F_l(E,x)P_l(\omega_x). \quad (1)$$

According to the Spencer-Fano theory, the calculation of the flux is approached indirectly through the calculation of the moments

$$F_{nl}(E)=\int_{-\infty}^{\infty}dx x^n F_l(E,x)$$
$$=\int_{-\infty}^{\infty}dx x^n\int_{-1}^{1}d\omega_x P_l(\omega_x)F(E,x,\omega_x). \quad (2)$$

These joint moments (or correlation coefficients) have the important property that

$$F_{nl}(E)=0 \quad \text{if} \quad l>n. \quad (3)$$

The validity of (3) is rather obvious for the case $n=0$. The quantity $\int_{-\infty}^{\infty}F(E,x,\omega_x)dx$ can be interpreted as the energy and angular distribution of the flux in a medium filled with a uniformly distributed source. Clearly such radiation is isotropic, so that $F_{0l}(E)=0$ for $l\neq 0$.

A formal proof of (3) with the use of a Laplace transformation of the flux distribution has been given by Marshak.[5] It is worth mentioning that one can obtain a more direct and physically more obvious proof based on the fact that the flux from a plane isotropic source can be derived by the superposition of point isotropic sources. If the plane source is at $x=0$, and the point isotropic flux is denoted by $G(E,r,\omega_r)$,

$$F(E,x,\omega_x)=\int_0^{2\pi}d\varphi\int_0^{\infty}\rho d\rho G\left[E,(x^2+\rho^2)^{\frac{1}{2}},\right.$$
$$\left.\frac{x\omega_x+(1-\omega_x^2)^{\frac{1}{2}}\rho\cos\varphi}{(x^2+\rho^2)^{\frac{1}{2}}}\right]. \quad (4)$$

It can be shown[6] that as a consequence of (4) the corresponding Legendre expansion coefficients are related by the equation

$$F_l(E,x)=2\pi\int_{|x|}^{\infty}rdrG_l(E,r)P_l(x/r). \quad (5)$$

[1] L. V. Spencer and U. Fano, J. Research Natl. Bur. Standards **46**, 446 (1951).
[2] H. Goldstein and J. E. Wilkins, Jr., AEC Report NYO-3075 (1954).
[3] L. V. Spencer and F. Stinson, Phys. Rev. **85**, 662 (1952).
[4] By the flux is meant the flow of energy through an isotropic detector at a distance x from the source plane; E is the spectral energy, and ω_x the cosine of the angle between the direction of travel of the radiation and the normal to the source plane.
[5] R. E. Marshak, Revs. Modern Phys. **19**, 201 (1947).
[6] See, e.g., U. Fano, J. Research Natl. Bur. Standards **51**, 95 (1953).

By taking spatial moments, one finds that for even $n+l$

$$F_{nl}(E)=2\pi\int_{-\infty}^{\infty}x^n dx\int_{|x|}^{\infty}r dr G_l(E,r)P_l(x/r)$$

$$=4\pi\int_0^{\infty}r^{n+2}G_l(E,r)dr\cdot\int_0^1 u^n P_l(u)du. \quad (6)$$

We may confine our attention to the case when $n+l$ is even; otherwise $F_{nl}(E)=0$ because of the symmetry of the plane isotropic flux about the source plane. It is a well known property of Legendre polynomials that in this case the factor $\int_0^1 u^n P_l(u)du$ vanishes when $l>n$, which completes the proof of statement (3).

B. Moment Fitting

Consider now the moments of the energy flux in a given direction:

$$M_n(E,\omega_x')=\int_{-\infty}^{\infty}dx x^n F(E,x,\omega_x')=$$

$$=\sum_{l=0}^{n}\frac{2l+1}{2}F_{nl}(E)P_l(\omega_x'). \quad (7)$$

Note that the series *terminates* by virtue of Eq. (3), so that the moments M_n are *exact*.

Suppose that this were not the case (e.g., if the source were point isotropic). Then instead of exact moments only partial Legendre series would be available, the number of terms being small because of the limitation on the number of computed F_{nl}'s. For low-energy components of the flux this would not matter, because they are nearly isotropic and the Legendre series would be rapidly convergent. But there would be trouble at high energies where the angular distribution is peaked and contains many harmonics. It would not do to use a Legendre series; one would have to extract the information contained in the F_{nl}'s in a better way by constructing M_n around a suitable weight function. The choice of a good weight function as initial approximation is not obvious.

For the plane isotropic source we are spared these difficulties and are left with a moment-fitting problem in the space variable x only. This is quite similar to the problem of the flux of radiation from a monodirectional source treated by Spencer and Fano,[1] and so the same method of polynomial expansion is used here. The flux is expressed as the sum of symmetric and antisymmetric parts, which are fitted by polynomial expansions with $e^{-\mu_0|x|}$, respectively, $xe^{-\mu_0|x|}$, as weight functions (where μ_0 is the total linear attenuation coefficient of the source radiation). Sample calculations described in the next section indicate that these weight functions were appropriate, since the polynomial expansions converge rapidly.[7]

To calculate the flux moving in a given angular cone rather than in a specific direction, it is easiest and most accurate to carry out the required angular integrations prior to the moment-fitting. For example, in order to obtain the flux

$$F^{(+)}(E,x)=\int_0^1 F(E,x,\omega_x)d\omega_x$$

of outward-bound photons, one carries out the integration over the moments as given by Eq. (7) and finds

$$M_{2n}^{(+)}(E)=\tfrac{1}{2}F_{2n,0}(E), \quad (8a)$$

$$M_{2n+1}^{(+)}(E)=\sum_{l=0}^{n}\frac{4l+3}{2}\frac{(-1)^l}{2^{2l+1}}\frac{(2l)!}{l!(l+1)!}F_{2n+1,2l+1}(E). \quad (8b)$$

Because of the symmetry of the flux about the source plane, the inward-bound flux

$$F^{(-)}(E,x)=\int_{-1}^{0}F(E,x,\omega_x)d\omega_x=F^{(+)}(E,-x). \quad (9)$$

II. SAMPLE CALCULATION

The angular distribution of the flux has been evaluated for a monoenergetic 1-Mev plane isotropic source in an infinitely extended medium of water. Eight moments $M_n(E,\omega_x')$ ($n=0, 1, \cdots, 7$) were calculated and fitted for $E=0.864$, 0.762, 0.680, 0.561, and 0.477 Mev, and for $\omega_x'=-1.0, -0.9, \cdots 1.0$.

Figures 1(a), (b), (c), and (d) show the angular distribution of the flux at various energies in the source plane ($\mu_0 x=0$) and at distances $\mu_0 x=1$, 4, and 7. It can be seen that in the source plane the distribution is peaked around $\omega_x=0$; this is due mainly to the contribution of singly scattered radiation. As the spectral energy decreases and singly scattered radiation becomes less important the peak flattens out. As one moves away from the source, a different anisotropy of the flux becomes dominant, the peak being shifted toward $w_x=1$. This is so because radiation has the best chance of penetrating to great depths of traveling at right angles to the source plane. In Fig. 1(e), the dependence of the angular distribution on the distance from the source is shown in detail for scattered radiation with an energy of 0.864 Mev. Figure 2 shows the ratio $F^{(+)}/(F^{(+)}+F^{(-)})$, i.e. the proportion of the energy flux that is outward-bound, for scattered radiation with energies of 0.864 and 0.477 Mev plotted as function of the distance from the source plane.

[7] In some trial calculations methods other than polynomial expansions were also used. They gave substantially the same results but were much more cumbersome to apply.

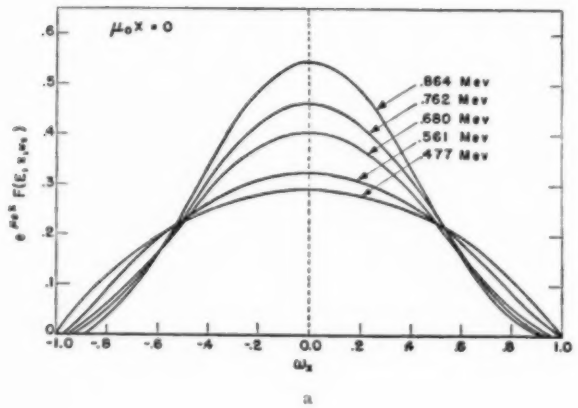

a

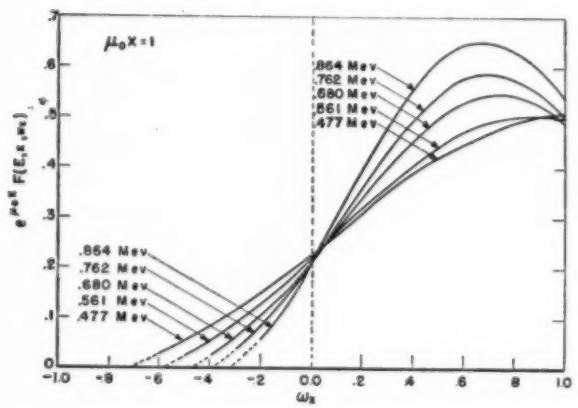

b

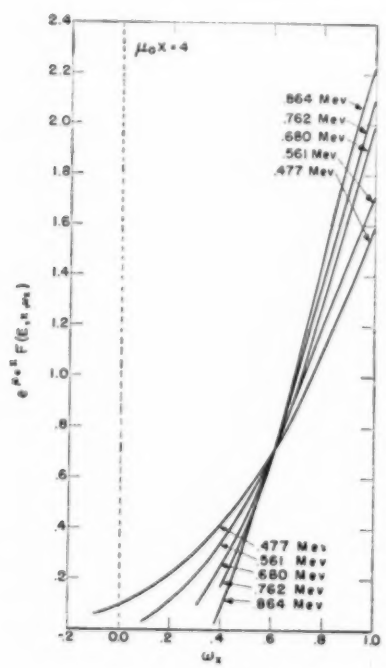

c

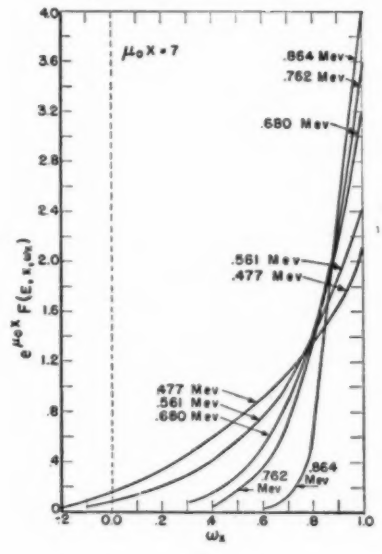

d

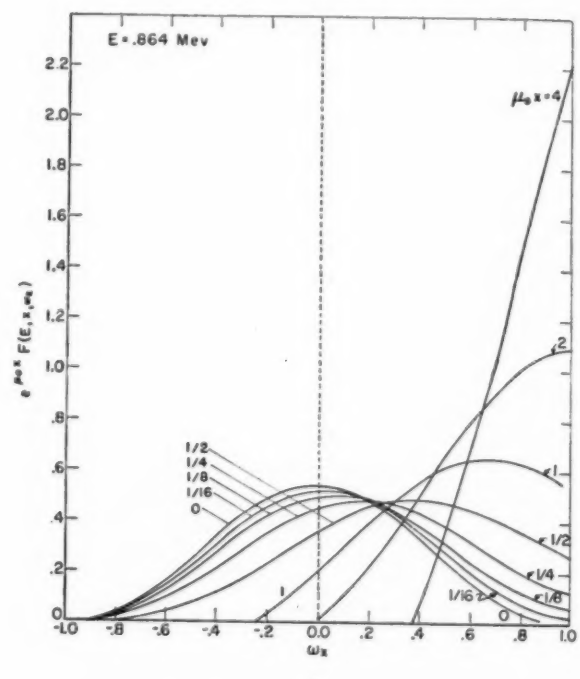

e

FIG. 1. Angular distribution $F(E,x,\omega_x)$ of the energy flux of several spectral components, at various distances from a 1-Mev plane isotropic source in water. The quantity $e^{\mu_0 x}F(E,x,\omega_x)$ shown above is a function of $\mu_0 x$, and is measured in (Mev/sec cm²)/(Mev$\times 2\pi$ steradian). The ordinate is normalized to correspond to a source emitting one photon/sec cm². (a) Spectral components at 0.864, 0.762, 0.680, 0.561, and 0.477 Mev. $\mu_0 x = 0$. (b) Spectral components at 0.864, 0.762, 0.680, 0.561, and 0.477 Mev. $\mu_0 x = 1$. (c) Spectral components at 0.864, 0.762, 0.680, 0.561, and 0.477 Mev. $\mu_0 x = 4$. (d) Spectral components at 0.864, 0.762, 0.680, 0.561, and 0.447 Mev. $\mu_0 x = 7$. (e) Spectral components at 0.864 Mev. $\mu_0 x = 0$, $\frac{1}{16}$, $\frac{1}{8}$, $\frac{1}{4}$, $\frac{1}{2}$, 1, 2, and 4.

III. COMMENTS

The results of the calculations described also remain valid if the scattering medium has a density depending on the distance from the source, and, approximately, for other media of low atomic number, provided all distances are expressed in mean free paths of the primary radiation. Hence the angular distributions obtained also pertain to the flux of radiation in the air above a plane contaminated uniformly with a gamma emitter.

The repeated crossing of a plane by the same photon is unlikely in an infinite medium (except very close to the source) so that the outward-bound flux in an infinite medium is a close approximation to the flux from an interior plane source emerging through the boundary plane of a semi-infinite medium. By summing over plane isotropic sources one can also obtain the emergent flux from a semi-infinite medium filled with a uniform source.

The determination of the angular distribution from a point isotropic source is more difficult than the corresponding problem for the plane source, since no equivalent geometrical simplification exists. It appears promising to calculate first the angular distribution from a plane source, and then to obtain the point source flux by inversion of the integral equations (4) or (5).

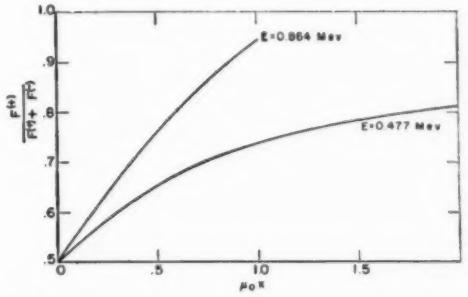

FIG. 2. Ratio of the outward-bound to the total energy flux, for spectral components at 0.864 and 0.477 Mev, at various distances from a 1-Mev plane isotropic source in water.

IV. ACKNOWLEDGMENTS

The author is indebted to Miss Mary Orr for the numerical calculations.

JOURNAL OF APPLIED PHYSICS VOLUME 26, NUMBER 12 DECEMBER, 1955

Method for Obtaining Complete Quantitative Pole Figures for Flat Sheets Using One Sample and One Sample Holder

MILTON SCHWARTZ
Pitman-Dunn Laboratories, Frankford Arsenal, Philadelphia, Pennsylvania
(Received June 10, 1955)

The general expressions for the x-ray absorption corrections in the reflection region for flat sheets in any orientation are derived. These equations contain, as special cases, the correction factors of previously reported pole figure techniques and also correction factors for a new method, permitting a rapid and accurate determination of complete quantitative pole figures of flat sheets using one sample and one sample holder. For the outer regions of the polar net a low-order Bragg reflection is used with the technique of Decker, Asp, and Harker; and for the center region a higher order Bragg reflection from the same set of planes is used with a different set of correction factors. Pole figures, obtained by this method, for cold rolled aluminum and magnesium are presented.

INTRODUCTION

THE accurate determination of preferred orientation in thin flat sheets using a Geiger counter x-ray diffractometer was proposed by Decker, Asp, and Harker[1] in 1948. The correction formula derived permits a standardization of x-ray intensities which takes into account the changes in absorption as the sample is titled in the beam provided the diffracted beam is in the transmission region. Field and Merchant,[2] using a somewhat similar experimental setup, derived a formula to correct diffracted intensities reflected from the surface layers of infinitely thick specimens. Schulz,[3] using a different sample holder, showed that the correction factors can be made constant through wide ranges of angles of tilt by taking into account sample thickness, slit design, and by tilting the specimen in a particular way. None of the above techniques can be used to determine the entire pole figure. This paper proposes a new method of determining quantitative pole figures whereby the entire pole figure is obtained by using the same sample and sample holder.

The sample holder[1,4] for this method permits positioning the sample at different angles of tilt with its plane perpendicular to the plane of the incident x-ray beam and the Geiger tube (see Fig. 1). By means of a small

[1] Decker, Asp, and Harker, J. Appl. Phys. **19**, 388–392 (1948).
[2] Field and Merchant, J. Appl. Phys. **20**, 741–745 (1949).
[3] L. G. Schulz, J. Appl. Phys. **20**, 1030–1036 (1949).
[4] M. Schwartz and G. J. Mills, "Preferred orientation of rolled magnesium solid solution alloys, Part I," Frankford Arsenal Report R-1214 (1954).

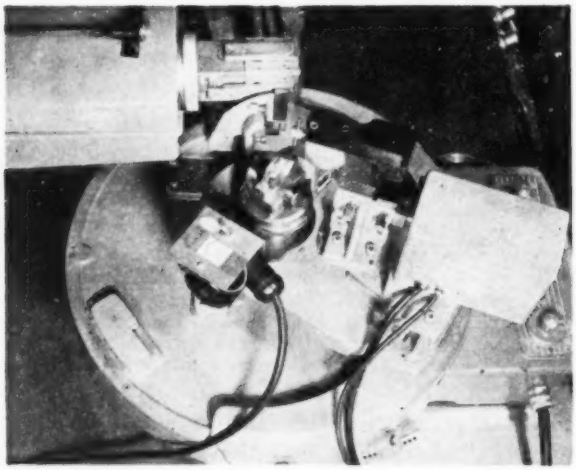

FIG. 1. Experimental setup to determine preferred orientation in flat sheets.

motor, the sample can be rotated in its own plane so that intensities can be recorded continuously. Using this sample rotator for both the reflection region and the transmission region previously mentioned, one can determine the entire quantitative pole figure by overlapping the two regions. For the method to be truly quantitative, it is necessary to standardize the intensities to correct for absorption. A correction formula will be derived for the intensities of x-rays diffracted in the reflection region from a flat sheet of any thickness and in any orientation.

ABSORPTION FACTORS IN THE REFLECTION REGION

Absorption corrections are necessary in quantitative preferred orientation studies of thin sheets, since the path length of the x-rays in the sample varies as the sample is tilted with respect to the incident beam. With the Geiger counter technique[1] in mind, consider a beam of parallel x-rays incident on a flat specimen which has a general orientation with the beam. If a Debye cone is cut by a plane containing its axis and the Geiger counter, then there are, in general, four different path lengths for the rays diffracted from a particular set of planes; two for the transmission case and two for the reflection region. The geometry for the reflection region is shown in Fig. 2, which has the plane of the x-rays and the normal to the diffracting plane in the plane of the paper. The transmission case, with the normal to the sheet in the diffracting plane, is shown in reference 1. Figure 3 shows the orientation of the sample looking along the line LM where it is seen that the normal to the specimen surface makes an angle ϕ with its projection in the plane of the incident and diffracted x-rays. This projected line makes an angle α with the diffracting plane as seen in Fig. 2. The following sign convention, consistent with the transmission region, will be used to differentiate between the two cases;

α is the positive acute angle measured from the projected line described above to the diffracting plane. If this direction is clockwise, α is positive; if counterclockwise, α is negative.

When the incident beam has an intensity A, the intensity after penetrating a distance x is $Ae^{-\mu x}$, where μ is the linear coefficient of absorption. If diffraction now occurs, and if D is the fraction of the radiation diffracted per unit volume at any point in the sample, then the intensity of radiation from an elementary diffracting volume is

$$dI_{\pm\alpha}=ADe^{-\mu x}\exp\left\{-\mu\left[-\frac{x\cos(\alpha\pm\theta)}{\cos(\alpha\mp\theta)}\right]\right\}dv \qquad (1)$$

in the reflection region. If the incident beam has a width w and a height h, then $dv=whdx$. Integrating the foregoing equation for the thickness of a sheet of randomly oriented grains, i.e., where D is a constant, one has

$$I_{\pm\alpha}=ADwh\int_0^{\mp t'/\cos(\alpha\pm\theta)} e^{-\mu M_{\pm\alpha}x}dx \qquad (2)$$

where

$$M_{\pm\alpha}=1-\frac{\cos(\theta\pm\alpha)}{\cos(\theta\mp\alpha)} \quad \text{and} \quad t'=t/\cos\phi,$$

t being the actual thickness of the sheet. When Eq. (2) is integrated, the intensity has the form

$$I_{\pm\alpha}=\frac{ADwh}{\mu M_{\pm\alpha}}\left\{1-\exp\left[\frac{\mu t'}{\cos(\alpha+\theta)}-\frac{\mu t'}{\cos(\alpha-\theta)}\right]\right\}. \qquad (3)$$

If all the intensities are compared to the intensity (I_0) for which $\alpha=\phi=0°$, the standard position of the transmission region,[5] then the following correction factor is used:

$$R_{\pm\alpha}\equiv\frac{I_0}{I_{\pm\alpha}}=\frac{\mu tM_{\pm\alpha}\exp(-\mu t/\cos\theta)}{\cos\theta\left\{1-\exp\left[\frac{\mu t'}{\cos(\alpha+\theta)}-\frac{\mu t'}{\cos(\alpha-\theta)}\right]\right\}}, \qquad (4)$$

where

$$I_0=\frac{ADwht}{\cos\theta}\exp(-\mu t/\cos\theta) \qquad (5)$$

from reference 1. Equation (4) is the set of correction factors which must be applied to the intensity at any α angle in the reflection region to standardize it for $\alpha=\phi=0°$.

If the angle between the pole of the plane and the normal to the specimen is p, then from the law of cosines, the relationship connecting p, ϕ and α is

$$\cos p=\cos\phi\,\sin\alpha. \qquad (6)$$

Equation (6) suggests methods of tilting the sample to cover parts of the pole figure and, at the same time, reducing by one the number of independent variables in

[5] American Society for Testing Materials Committee E-4 on Metallography, "Tentative method for preparing quantitative pole figures of metals," Am. Soc. Testing Materials Standards E81-54T (1954).

Eq. (4). If $\alpha=90°$, then the normal to the specimen traces a plane which is the perpendicular bisector of the incident and diffracted x-ray beams. All of the diffraction is in the reflection region, which is the basis of the Schulz technique. If $\phi=0°$, then the normal to the specimen traces a plane which is the diffraction plane. Here the diffraction can be in the transmission region as in the Decker, Asp, and Harker method; and it can be in the reflection region as in the technique reported by Field and Merchant for infinite thicknesses or that proposed in this report for finite thicknesses.

The general equations (3) and (4) contain, as special cases, all of the reflection methods mentioned previously for obtaining pole figures. These are:

Case I. $\alpha=90°$ and ϕ varies.
Case II. $\phi=0°$ and α varies for "infinitely thick" samples.
Case III. $\phi=0°$ and α varies for "thin" samples.

Case I:

If $\alpha=90°$, then Eq. (3) has the form

$$I_{90°}=\frac{ADwh}{2\mu}\left[1-\exp\frac{-2\mu t}{\sin\theta\cos\phi}\right], \tag{7}$$

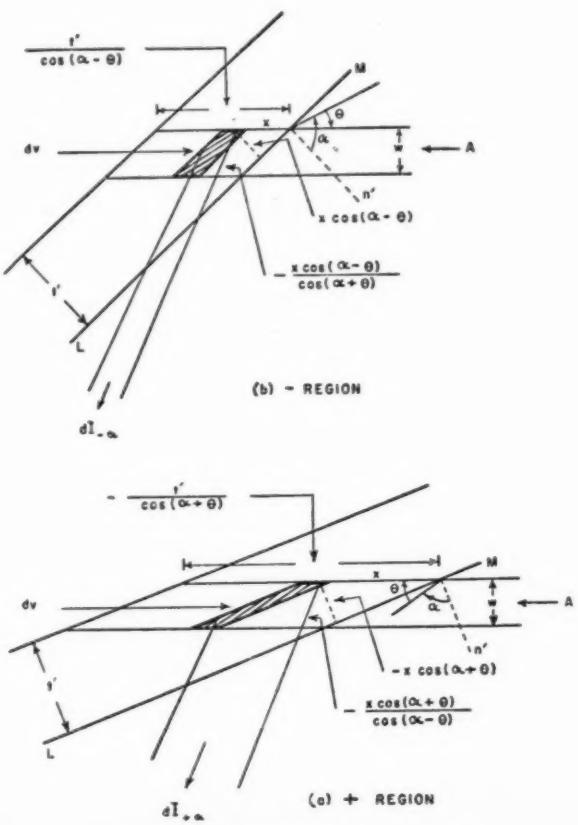

FIG. 2. Geometry for the reflection region.

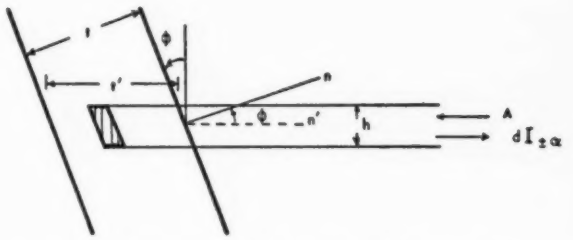

FIG. 3. Geometry parallel to the diffraction plane.

and for "infinitely thick" samples

$$I_{90°}=\frac{ADwh}{2\mu}=\text{constant}. \tag{8}$$

Equations (7) and (8) are presented in reference 3 and their simplicity shows the advantage in using the Schulz technique. In order to correct the intensities of Eq. (7) to the standard position, Eq. (5) must be divided by Eq. (7), resulting in the expression

$$R_{90°}=\frac{2\mu t\exp(-\mu t/\cos\theta)}{\cos\theta[1-\exp(2\mu t/\sin\theta\cos\phi)]}. \tag{9}$$

These, then, are the correction factors which will standardize the intensities for this mode of scanning to that of the standard transmission technique.[5]

Case II:

For $\phi=0°$ and "infinitely thick" samples one obtains from Eq. (3)

$$I_{\pm\alpha}=\frac{ADwh}{\mu\left[1-\dfrac{\cos(\alpha\pm\theta)}{\cos(\alpha\mp\theta)}\right]}, \tag{10}$$

and if $\alpha=90°$ is taken as a standard position, one obtains by dividing Eq. (10) by Eq. (8),

$$\frac{I_{\pm\alpha}}{I_{90°}}=\frac{2}{1-\dfrac{\cos(\alpha\pm\theta)}{\cos(\alpha\mp\theta)}}. \tag{11}$$

Equations (10) and (11) are similar to those used by Field and Merchant.[3]

Case III:

Also for $\phi=0°$, for finite thickness, one obtains from Eq. (4),

$$R_{\pm\alpha}=\frac{\mu t M_{\pm\alpha}\exp(-\mu t/\cos\theta)}{\cos\theta\left\{1-\exp\left[\dfrac{\mu t}{\cos(\alpha+\theta)}-\dfrac{\mu t}{\cos(\alpha-\theta)}\right]\right\}}. \tag{12}$$

Equation (12) will then correct intensities in the reflection region so that by means of it and the standard transmission technique the entire quantitative pole figure can be plotted using the same sample and sample holder.

$R_{\pm\alpha}$ in Eq. (4) has been evaluated as a function of θ, α, and μt for about 4000 points by means of a 409 Remington digital computer so as to include the ranges of these parameters which are encountered in preferred orientation studies. Figures 4 and 5 show $R_{\pm\alpha}$ as a function of μt for various θ angles for $\alpha=+65°$ and $\alpha=-65°$, respectively. The complete set of correction factors in both graph and table form will be published in a Frankford Arsenal R-Report. The accuracy in interpolating between the curves is in general about two percent, and the numbers can be read off the graphs rapidly.

An examination of the complete set of $R_{\pm\alpha}$ *vs* μt curves gives the following information. As μt increases from zero the curves for small θ increase to a maximum which occurs before a μt of one, and then the curves go to zero asymptotically. For larger θ the curves decrease slowly as μt increases; and for large θ, $R_{\pm\alpha}$ falls very sharply toward zero. All the curves approach zero asymptotically for large μt's. At very small values of μt, $R_{\pm\alpha}$ approaches a limit which is given by

$$R_{\pm\alpha}=\mp\frac{\cos(\alpha\pm\theta)}{\cos\theta} \tag{13}$$

for $\mu\ll\cos\theta$ and $\mu t\ll|\cos(\alpha\pm\theta)|$.

EXPERIMENTAL RESULTS

Random samples of aluminum and magnesium were prepared in two different ways. Very small spherical particles of these metals were mixed with Acryloid which had been thinned with xylene and then sprayed with a medical atomizer onto thin paper. The other method was dusting the metal powder through two thicknesses of metallographic silk onto thin paper which had been wetted with Acryloid thinned with xylene. A thickness of any desired μt was produced by repeated application. In both methods the sprayer and dusting bottle were held about one foot from the paper, and the operations were performed in still air so as to help produce uniform deposits. The entire sample produced was a circle of diameter about eight inches, and the specimen used in the experiment was a piece one inch by three-fourths inches cut from the center of the entire sample.

The theoretical curves resulting from Eq. (12) were checked with various random samples of aluminum and

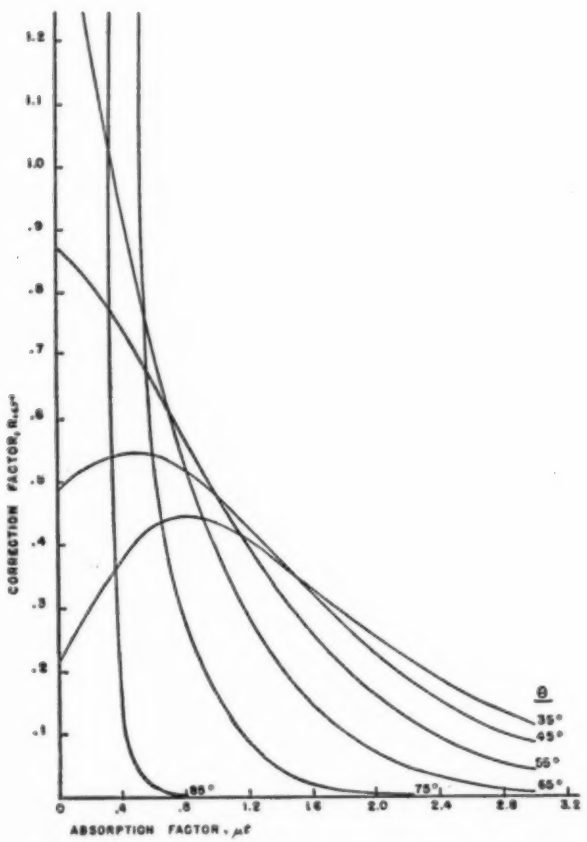

FIG. 4. $R_{+65°}$ *versus* μt for the reflection region for $\alpha=+65°$.

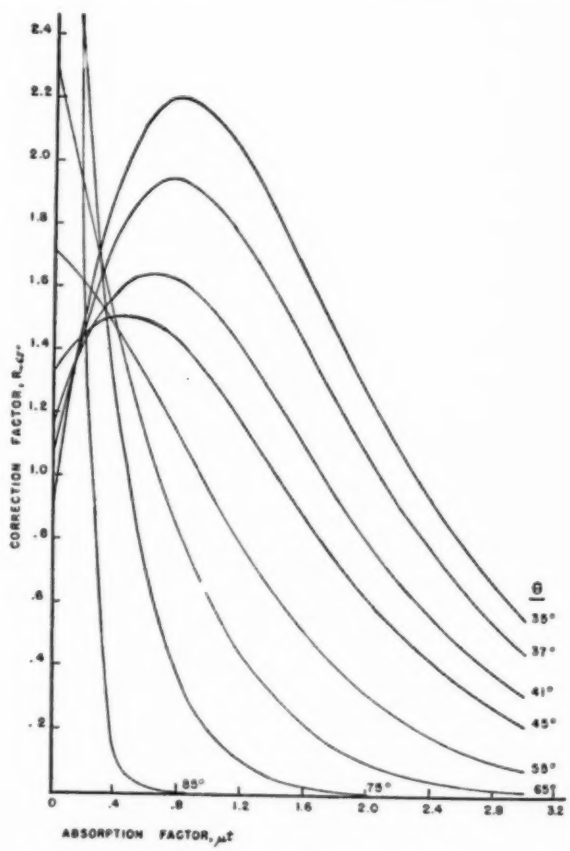

FIG. 5. $R_{-65°}$ *versus* μt for the reflection region for $\alpha=-65°$.

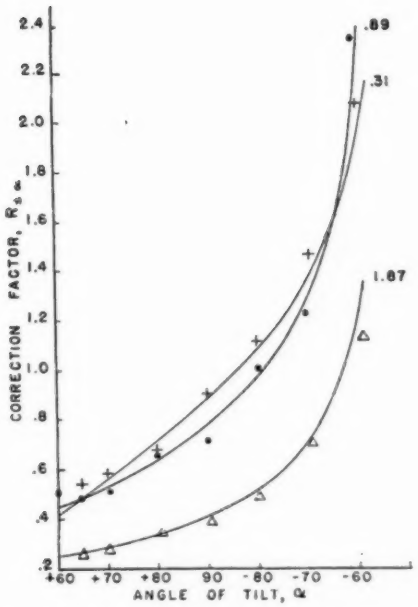

FIG. 6. $R_{\pm\alpha}$ *versus* α for the (222) planes of aluminum random samples. The solid lines are theoretical curves, and Δ, ●, + are experimental points for $\mu l = 1.87$, 0.89, and 0.31 respectively.

magnesium. Figure 6 shows the agreement between the experimental points and the theoretical curves for the (222) planes of three random samples of aluminum. The experimental conditions for these runs were: G.E. XRD-3 x-ray unit, nickel filtered copper radiation, 35 kv and 20 ma; 0.4° beam slit, medium resolution Soller slit, and no detector slit; $2\theta = 82.60°$; the samples were rotated in their own plane at a speed of about one-half a revolution per minute; and background intensities on both sides of the line were averaged and subtracted from the total line intensity. The average deviation of all the points from the three curves is about five percent, and it felt that most of this error is due to the effect of the rough surface. Point checks between the mathematical curves and experimental data for the (111) planes using these three aluminum samples and others with μl's as high as 2.6 resulted in further verification. Data for two magnesium samples also showed agreement for the second- and fourth-order basal planes.

The pole figure of aluminum cold-rolled 98.4% was determined using the curves from Eq. (4). The sample was rotated in its plane at the rate of 10° per minute and intensities corrected for background were read from the calibrated recorder. Figure 7 shows the pole figures for the reflection region for the (222) planes determined with the same experimental conditions described earlier. Figures 7(A) and 7(B) are for the $-\alpha$ and $+\alpha$ regions, respectively, and are uncorrected for intensity. Figures 7(C) and 7(D) are the pole figures which have been corrected by the curves for Eq. (4), and it is seen that these corrected figures are essentially identical.

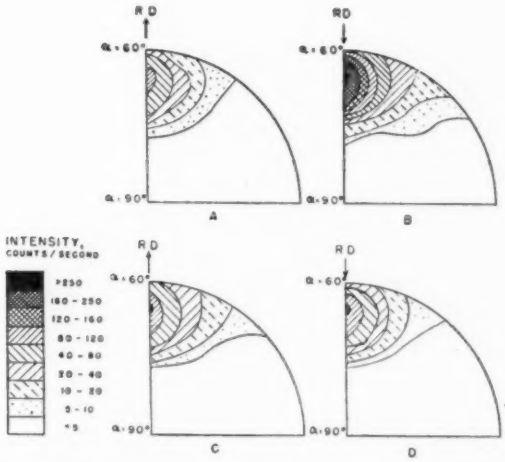

FIG. 7. Pole figure of (222) planes of aluminum cold rolled 98.4% A. $-\alpha$ region, uncorrected B. $+\alpha$ region, uncorrected C. $-\alpha$ region, corrected D. $+\alpha$ region, corrected.

QUANTITATIVE POLE FIGURES FOR FLAT SHEETS

The experimental procedure for obtaining quantitative pole figures in the reflection region is the same as that for the transmission case except for the correction factors and order of diffraction. A random sample of the test material is prepared to any convenient thickness, generally between two and ten mils. This sample is placed in the diffractometer at $\alpha = \phi = 0°$. For this method and the remainder of this paper, ϕ will be equal to zero. The diffracted intensities at these standard positions are determined for two orders of the crystallographic planes of interest. The lower order applies to the transmission region, and the higher one to the reflection case. Since, in general, the thickness of the random sample is different from that of the test specimen, these two intensities must be corrected to give the intensities that they would have if the random sample had the same μl as the test specimen. This can be accomplished by applying Eq. (15) given below. Then the intensities for any angle of tilt (α) of this hypothetical random sample (matched μl) are determined by the corrected intensities for the standard position and the set of correction factors. These values are generally termed 1 × random and they serve as a reference to show the extent of the preferred orientation of the test specimen. The test specimen is now rotated in its own plane while its plane is held stationary at various angles of tilt, and the intensities are recorded continuously. The pole figure is then plotted in terms of multiples of the random sample intensity.

From the preceding discussions, it can be seen that complete quantitative pole figures can be drawn by using the same sample and sample holder. The procedure is simply to use the standard transmission method for the outer portion of the polar net and then use the reflection method previously described for the center of the figure. There are several methods for joining the

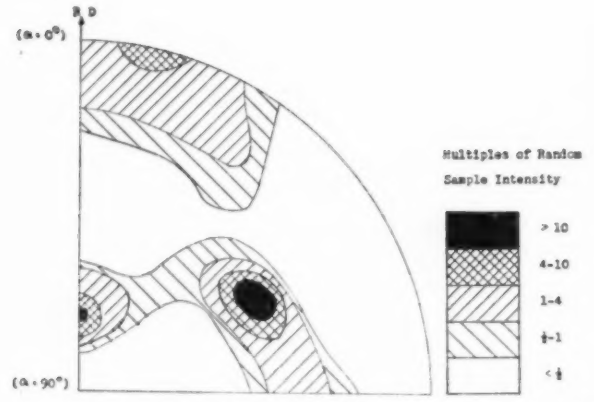

FIG. 8. Pole figure of the octahedral planes of aluminum cold rolled 98.4%. The transmission and reflection regions were joined at $\alpha=-60°$.

reflection region to the transmission region, but that suggested above is recommended; that is, the use of a higher order Bragg reflection in the reflection region. This will permit an overlapping of the two sections of the pole figure, and it will also require two intensity readings from the random sample, I_0 for each order.

The pole figure for 98.4% cold-rolled aluminum of $\mu t=1.28$ is shown in Fig. 8 where the intensities are given in multiples of that from a random sample. From $\alpha=0°$ to $\alpha=-60°$, the (111) planes were used with the standard transmission technique; from $\alpha=-60°$ to $\alpha=90°$, the reflection method described above was used. The experimental conditions are the same as those used for the random samples of aluminum. The following general technique was employed to determine the intensities of a random sample of $\mu t=1.28$ for all of the α angles used.

For a random sample of a given alloy at a given Bragg angle, the diffracted intensity is proportional only to the absorption correction, extinction and other similar effects being neglected. If the sample is placed in the $\alpha=0°$ position, then from Eq. (5) one has

$$I_0=k\frac{t}{\cos\theta}\exp(-\mu t/\cos\theta), \tag{14}$$

and hence the intensity of a different μt of the same alloy is

$$(I_0)_u=(I_0)_k\frac{(\mu t)_u}{(\mu t)_k}\exp\frac{(\mu t)_k-(\mu t)_u}{\cos\theta}, \tag{15}$$

where the subscript k refers to the sample whose μt and I_0 have already been determined and u refers to the unknown. The advantage of Eq. (15) is that the intensity can be determined without either μ or t being known. For thin samples, it may not be possible to determine these quantities with sufficient accuracy, but μt can be determined accurately. Using Eq. (15), the intensities of a hypothetical random sample of aluminum of $\mu t=1.28$ were determined for $\alpha=0°$ for both the (111) and (222) planes from intensity readings on the samples used in determining Fig. 6. The average deviation in the six readings is about 3%. The intensities of the hypothetical random sample of $\mu t=1.28$ at the various α angles were then determined by the correction factors of the standard transmission method[6] and the curves resulting from Eq. (4) for the reflection region.

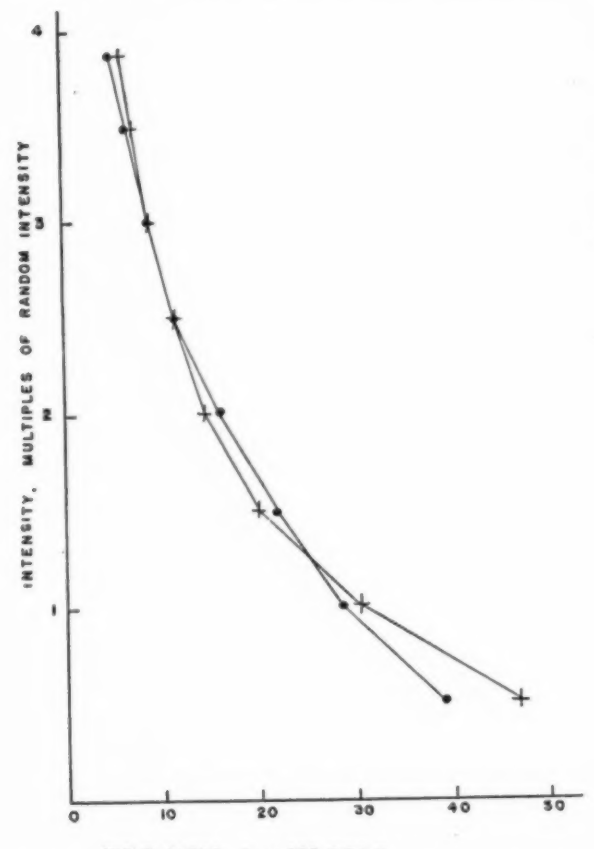

FIG. 9. Comparison of intensities from the transmission and reflection regions at the same α angle ($-60°$) for 98.4% cold rolled aluminum. The + points are for the (222) planes in the reflection region and the ● points are for the (111) planes in the transmission region.

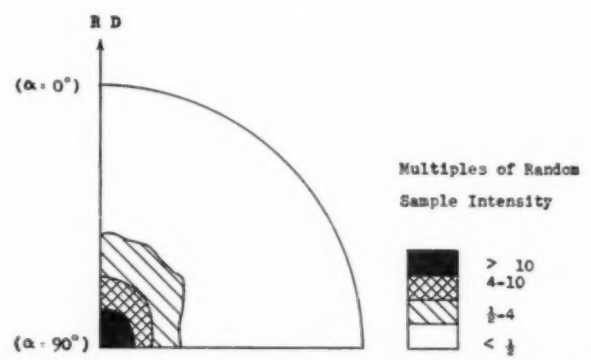

FIG. 10. Pole figure of the basal planes of magnesium cold rolled 75%. The transmission and reflection regions were joined at $\alpha=-65°$.

[6] These are published in the handy booklet "Intensity correction factors for x-ray spectrometer transmission pole figure determinations," Suzanne E. A. Beatty, Scientific Paper 1488, Westinghouse Research Laboratories, East Pittsburgh, Pennsylvania (December 6, 1949).

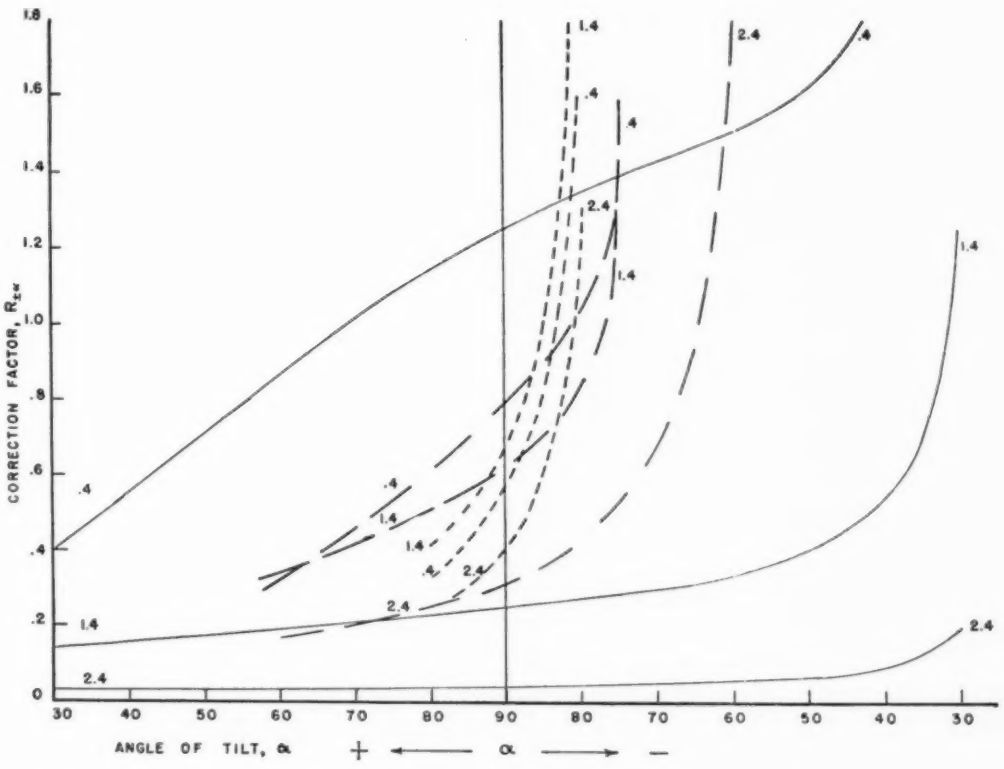

FIG. 11. $R_{\pm\alpha}$ *versus* α for the reflection region. μt is given on each curve, and θ equals 15°, 35°, and 65° for the dotted, dashed, and solid lines, respectively.

Figure 9 shows the variation of intensity, in multiples of the random intensity, along the latitude circle $\alpha=-60°$ where the reflection region overlaps the transmission region. The two curves are almost coincident, except for small values of the intensity where the signal to background ratio is low.

The pole figure for the basal planes of 75% cold-rolled magnesium is shown in Fig. 10 where it is seen that almost the entire intensity is in the reflection region. The (0002) plane was used in the transmission region, and the (0004) plane in the reflection region, the two regions were joined at $\alpha=-65°$. The beam slit was 5-mm high, and the other parameters were the same as stated previously. The rolled sample has a μt of 1.50, and the intensities of a random sample of this μt were determined from a random sample of magnesium of $\mu t=1.21$ and Eq. (15).

The set of curves plotted from Eq. (4) serves not only as a source of correction factors for the reflection region, but also as a guide to sample preparation and experimental technique. Figure 11 shows the variation of the correction factor with the angle of tilt for three Bragg angles and three absorption factors. From an examination of these curves, it can be concluded that, in general, the $+\alpha$ region is less critical; that is, the slope of the curves is smaller. Also, for a larger μt and larger θ, the correction factors become more constant over a large range of α angles so that, for less accurate work, the correction factors for a given θ and μt can be considered constant within the values shown on the curve.

CONCLUSIONS

It can be concluded that quantitative pole figures of flat sheets can be drawn from 0° to 90° in α using the same sample and sample holder. The method employs a low order plane in the transmission region and a higher order plane of the same set in the reflection region. A random sample of convenient thickness of the test alloy is prepared and the diffracted intensities at $\alpha=0°$ for the two orders are obtained. The intensities at the various α angles of a hypothetical random sample, having the same μt as the test sample, are determined from Eq. (15) and the sets of absorption corrections for the two regions. Then quantitative pole figures are drawn expressing the ratio of the intensity of the preferred sample to that of the random sample.

ACKNOWLEDGMENTS

The author wishes to thank Dr. George Mills, of the Metallurgy Laboratory, for his helpful comments and discussions. Also, the author wishes to thank Mr. Salvatore Narisi, of the Mathematics Branch, for the use of the electronic computer in evaluating Eq. (4), and also Mr. William Sipes, of the Metallurgy Laboratory, for his assistance in the work. The author wishes to thank the Ordnance Corps of the United States Army for permission to publish this work.

Capacitance Measurements on Alloyed Indium-Germanium Junction Diodes

D. R. Muss
Westinghouse Research Laboratories, East Pittsburgh, Pennsylvania
(Received May 11, 1955)

Donor densities in the base material of fused junction diodes, inferred from capacitance data, are used to calculate majority carrier mobilities. The dependence of capacitance on reverse bias at very low biases is found to be given by the sum of two terms, a space charge capacitance and a capacitance due to the flow of holes as given by Shockley's low level p-n junction theory.

INTRODUCTION

THE experimental capacitance of alloyed indium-germanium junctions is found to follow a $V^{-\frac{1}{2}}$ dependence at high reverse bias voltages, in general agreement with previous investigations of abrupt junctions.[1,2] At low voltages the capacitance is accounted for by the sum of an extrapolated $V^{-\frac{1}{2}}$ term and an exponential term due to hole current. The junction capacitances were measured at a frequency of 100 kc, using a substitutional twin-T bridge; the amplitude of the ac signal across the diode was held below 10 mv.

It has been customary to take the mobility of electrons in n-type germanium as equal to the drift mobility of electrons in p-type germanium for equivalent values of impurity density. The electron mobility in n-type germanium is determined more directly in this investigation by inferring n-type impurity densities from the capacitance measurements.

THEORY

The approximate dependence of abrupt p-n junction capacitance on applied dc voltage can be derived by solving Poisson's equation on the basis of a simple static model. The transition from n-type to p-type germanium in a fused junction diode is assumed to be abrupt, with a dipole layer in the depletion region as indicated in Fig. 1. The solution for the capacitance ($C=dQ/dV$) as a function of applied reverse bias voltage (V) is given *for this model* by

$$(C/A)^{-2}=(8\pi/q\kappa)[(1/n_n)+(1/p_p)](V+V_0), \quad (1)$$

where (for this simple model) V_0 is a voltage equal to ψ, the internal contact potential, A is the junction area, q is the magnitude of the electronic charge, κ is the dielectric constant, n_n is the electron density in the n-type semiconductor taken as equal to the net donor density N_d, and p_p is the hole density in the p-type semiconductor, taken as equal to the net acceptor density N_a.

Since the concentration of acceptor ions in the redeposited p-type germanium is much higher than the concentration of donor ions in the relatively pure n-type germanium, we may set $p_p \gg n_n$. Equation (1) may then be rewritten as

$$(C/A)^{-2}=m(V+V_0), \quad (1a)$$

where, for germanium,

$$m=(0.884\times10^7/n_n)(\text{cm}^4/\text{volt-}\mu\mu\text{f}^2). \quad (1b)$$

An expression for the low-frequency value of the capacitance, due to hole flow, of a p-n junction with very low bias voltage has been derived by Shockley[3] as a function of the lifetime τ_p of the minority carriers. This capacitance is independent of the nature of the impurity transition. We may neglect the contribution of the electron flow to the capacitance and to the saturation current density j_s, since $p_p \gg n_n$. We can then write

$$(C/A)=(C_0/A)\exp(-qV/kT), \quad (2)$$

where C_0 is the value of C at zero bias. C_0 depends fundamentally on τ_p but may be alternatively expressed in terms of j_s, as follows:

$$(C_0/A)=\rho_n^2\mu_n^3q^4n_i^4/2j_sb. \quad (2a)$$

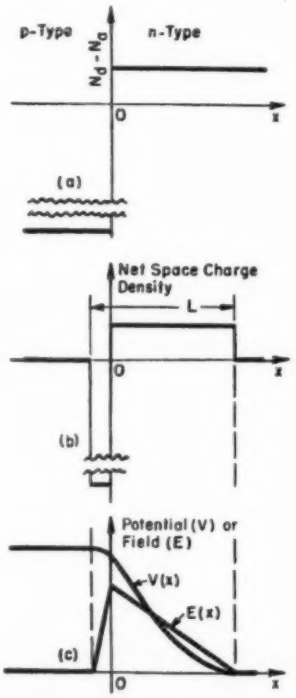

FIG. 1. (a) Impurity density, (b) space charge density, and (c) potential and electric field for idealized abrupt p-n junction.

[1] G. L. Pearson and B. Sawyer, Proc. Inst. Radio Engrs. **40**, 1348 (1952).
[2] H. U. Harten *et al.*, Z. Physik **138**, 336 (1954).
[3] W. Shockley, Bell System Tech. J. **28**, 435 (1949).

Here, μ_n is the mobility of electrons, n_i is the density of electrons in the intrinsic semiconductor, b is the ratio of electron to hole mobility, and ρ_n is the resistivity of n-type base material. For Ge(μ_n=3600 cm²/volt-sec), according to this theory,

$$C_0/A = 2.2\rho_n^2/j_s(\mu\mu f/cm^2). \quad (2b)$$

RESULTS

A. Mobility as a Function of Donor Density

A large group of fused indium-germanium diodes with n-type base resistivities ρ_n varying from 0.03 to 20.0 ohm-cm were studied. A typical plot of $(C/A)^{-2}$ *vs* V for a low resistivity diode at several temperatures is shown in Fig. 2. It can be seen that the room-temperature curve is linear for biases greater than a few tenths of a volt; therefore the assumption of an abrupt model for the fused junction may be considered valid except for low biases. From (1b) it follows that the slope of this curve m provides a direct determination of n_n or N_d.

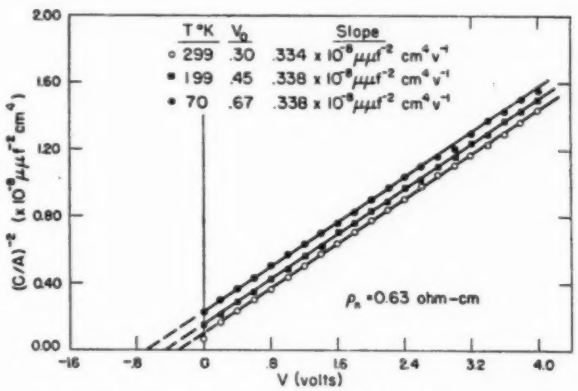
T °K
Vo
Slope
○ 299 .30 .334 x 10⁻⁸ μμf⁻² cm⁴ v⁻¹
● 199 .45 .338 x 10⁻⁸ μμf⁻² cm⁴ v⁻¹
● 70 .67 .338 x 10⁻⁸ μμf⁻² cm⁴ v⁻¹
ρn =0.63 ohm-cm
(C/A)⁻² (x 10⁻⁸ μμf⁻² cm⁴)
V (volts)

FIG. 2. Capacitance per unit area *vs* bias voltage, for low resistivity diode.

Figure 3 shows how this slope varies with base resistivity. Assuming that $n_n \gg p_n$, and knowing ρ_n from four-probe resistivity measurements,[4] we can calculate the majority carrier mobility μ_n in n-type germanium ($\mu_n = 1/\rho_n q n_n$).* In Fig. 4, μ_n is plotted as a function of the donor density N_d or the acceptor density N_a.

The values of μ_n inferred from capacitance measurements are true majority carrier mobilities, as are the values inferred from radioactive tracer data. These data are therefore plotted as a function of N_d. Minority carrier (drift) mobilities of electrons in p-type germanium measured by M. B. Prince,[5] are plotted as a function of N_a. The value of μ_n inferred from these data is 3600 cm²/volt-sec±10%, averaged over the high resistivity range ($\rho_n > 0.3$). Although the scatter in these mobility data is fairly large, there is indication that Prince's

[4] L. B. Valdes, Proc. Inst. Radio Engrs. 42, 420 (1954).

* A correction is made for the contribution of holes to the conductivity of high-resistivity diodes.

[5] M. B. Prince, Phys. Rev. 92, 681 (1953).

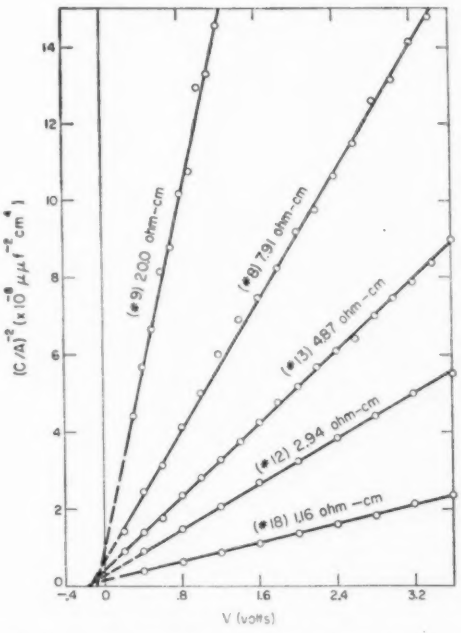

FIG. 3. Capacitance per unit area *vs* bias voltage for representative resistivities.

values for minority carrier mobilities at high impurity densities may be lower than the corresponding majority carrier mobilities.

B. Voltage Intercept (V_0)

For all junctions studied except those made from very high resistivity Ge, it was observed that a change in temperature shifts the intercept V_0 of the C^{-2} *vs* V curves but does not modify the slope. Since n_n is independent of temperature within the range studied and $m \propto 1/n_n$, no change in slope is expected. Figure 2 illustrates the typical behavior.

In a p-n junction at equilibrium, i.e., with no applied voltage, a potential exists across the junction due to the thermal diffusion of carriers across the junction. This

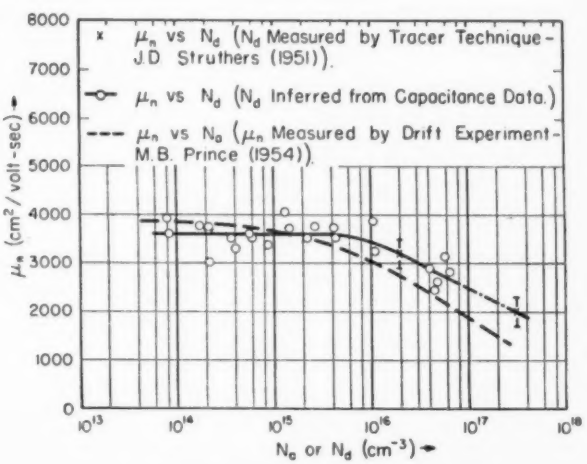
μn vs Nd (Nd Measured by Tracer Technique - J.D Struthers (1951))
μn vs Nd (Nd Inferred from Capacitance Data.)
μn vs Na (μn Measured by Drift Experiment - M.B. Prince (1954))
μn (cm²/volt-sec)
Na or Nd (cm⁻³)

FIG. 4. Electron mobility *vs* N_a or N_d.

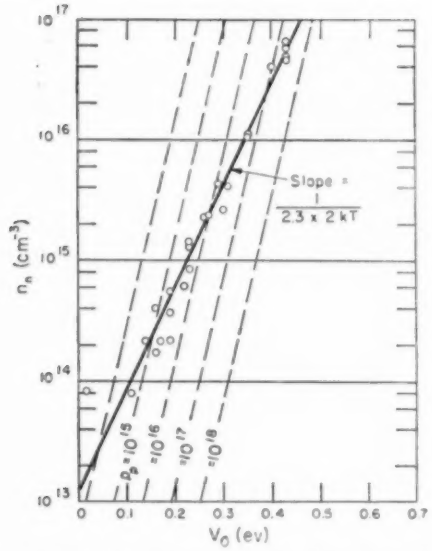

FIG. 5. Logn_n vs V_0, where $C^{-2}=(K/n_n)(V+V_0)$. Dotted lines are given by log $n_n=\log(n_i^2/p_p)+(1/2.3kT)\psi$, where $n_i^2=5.4\times10^{26}$ cm^{-6}, $T=300°$K, and V_0 is set equal to ψ, the internal contact potential.

potential has been termed the internal contact potential ψ. According to the simple model of a fused junction discussed so far, the intercept V_0 is just equal to the internal contact potential.

A thermodynamic relationship between n_n, p_p, and ψ is given by[5]

$$n_n p_p = n_i^2 \exp(q\psi/kT), \tag{3}$$

where n_i is 2.3×10^{13} cm^{-3} for Ge at 300°K. This equation is valid, independent of the model assumed for the transition from p to n concentrations, if neither side is very close to being degenerate. If V_0 and ψ were identical both ψ and n_n could be determined by capacitance measurements, and p_p could then be calculated from (3). In Fig. 5, logn_n is plotted as a function of the intercepts V_0. The dashed lines indicate the theoretical curves for several values of p_p, assuming $V_0=\psi$. It can be seen that the experimental data do not satisfy (3) and that the assumption $V_0=\psi$ is therefore incorrect. This fact has been observed by other workers in the field. Schwarz and Walsh[6] calculated the dependence of capacitance on reverse bias for a metal-semiconductor contact and found for this case that the intercept V_0 should not represent the internal contact potential. Schultz,[7] taking p_p as infinite, has derived an expression for C^{-2} as a function of V in which V_0 is the intercept of a tangent to this curve, and is a slowly varying function of V. (This curvature was too small to be detected in this experiment.) The data in Fig. 5 were compared with his expression in an informal manner by assuming an average value for V. The agreement in slope was found to be excellent, the agreement in intercept was fair. The variation of V_0 with V arises from the presence within the n-type material of holes which diffuse from the p-type material. The space-charge distribution depicted in Fig. 1(b) neglects the contribution due to these holes. The region within the depletion layer where holes are present has been termed the inversion layer. This inversion layer results from the fact that for $p_p \gg n_n$ the voltage drop across the junction appears almost entirely within the n-type material, the drop in the p-type material being very nearly equal to kT/q. It can be seen from Fig. 6 that as the potential rises in the depletion region the n-type material becomes intrinsic at the point where the Fermi level is at the center of the forbidden gap, and therefore holes are present between the intrinsic point and the junction.

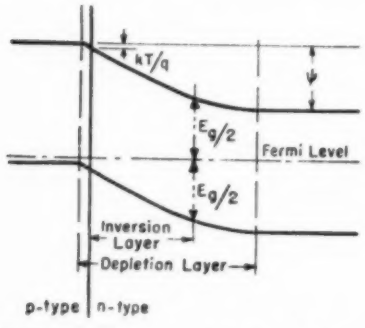

FIG. 6. Potential diagram for p-n junction in equilibrium, with $p_p \gg n_n$ (schematic).

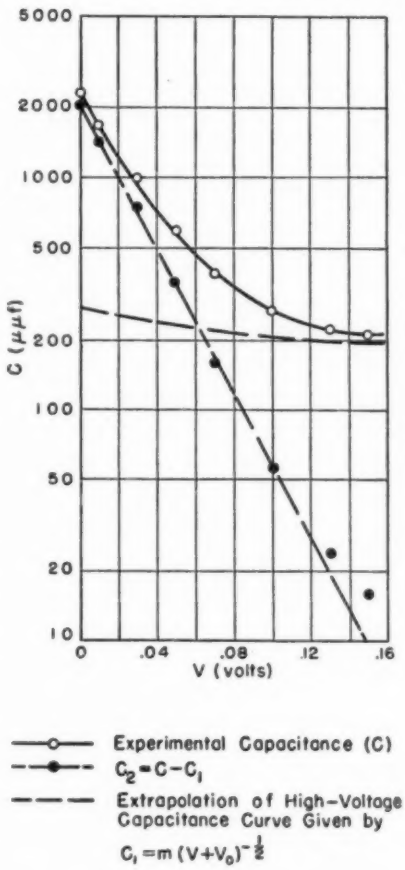

FIG. 7. Representation of the low-voltage capacitance as the sum of an exponential term and a power term. If $C_2=C_{02}\exp(-V/\alpha)$, then $C_{02}=2100$ $\mu\mu$f, and $\alpha=0.0278$. Shockley's low voltage theory gives $\alpha=kT/q=0.0258$, $C_{02}=2530$ $\mu\mu$f.

[5] R. F. Schwarz and J. F. Walsh, Proc. Inst. Radio Engrs. 41, 1715 (1953).

[7] W. Schultz, Z. Physik 138, 598 (1954).

C. Junction Capacitance at Low Voltages

At low reverse biases it is expected that a capacitance due to the flow of holes will become significant.[6,8] (See Fig. 2.) It will be assumed here that the measured junction capacitance has two components:

$$C=C_1+C_2, \tag{4}$$

where C_1 is given by (1a) based on the simple static theory, and C_2 is produced by some other mechanism. It is shown by a plot of log$C$ *vs* V in Fig. 7 that, if values of C_1 taken from the extrapolated linear C^{-2} *vs* V curve are subtracted from C, the result (C_2) is an exponential that may be compared with Eq. (2). It is seen that the slope of the logC_2 *vs* V curve is in good agreement with Shockley's value q/kT; however the extent of agreement between the experimentally determined intercept C_{02} and the calculated value from (2b) is seen from Fig. 8 to be poor. Values for saturation currents required for the comparison were inferred from dc current-voltage characteristics on the assumption that any difference in reverse current at 0.1 v and 1 v is due to an ohmic shunt resistance.

At low temperatures the observed zero bias capacitance is given exactly by (1a) (see Fig. 2). This is entirely consistent with (4) since Shockley's theoretical value of C_{02} decreases very rapidly with decreasing temperature. H.-L. Rath has recently shown that the temperature dependence of the capacitance at zero volts bias is given by (4).[9]

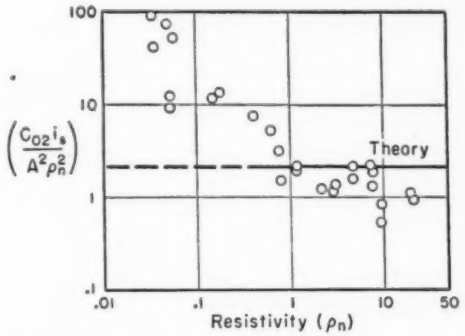

FIG. 8. Comparison of experimental data with a function of the low-level capacitance which is constant according to theory.

SUMMARY

The work reported here has demonstrated that for a fused junction the concept of an abrupt transition of impurity density from p- to n-type semiconductor is valid. This has been done by showing experimentally that for $V>0.2$ volt a linear relationship holds between C^{-2} and V, as predicted by an approximate static solution for this type of transition. For $V<0.2$ volt an additive exponential term predicted by Shockley becomes significant at room temperature. This contribution diminishes rapidly with decreasing temperature.

It has been found that the internal contact potential cannot be determined at this time from capacitance measurements. The value of the donor concentrations may, however, be accurately inferred. From these values the majority carrier mobilities have been calculated using independent measurements of the base resistivity.

ACKNOWLEDGMENTS

The author wishes to express his appreciation to Dr. Harold F. John who prepared the diodes used in this experiment, and to Dr. Richard L. Longini for his many helpful comments and suggestions. The author is indebted to Dr. Frank S. Stein who suggested the project, helped analyze the data, and contributed much to the understanding of the problem.

[8] Goucher, Pearson, Sparks, Teal, and Shockley, Phys. Rev. **81**, 637 (1951).
[9] H.-L. Rath, Z. Naturforsch. **9a**, 699 (1954).

Letters to the Editor

Guide to the Successful Propulsion of a Solid Object by an Explosive Charge

JOHN S. RINEHART
Astrophysical Observatory, Smithsonian Institution, Cambridge 38, Massachusetts
(Received September 7, 1955)

IN a recent paper von Valkenburg and Hendricks[1] describe a scheme for propelling a small missile at high velocity from an explosive charge. The scheme is a specific application of a general principle that seems not to have been described heretofore. The purpose of this note is to bring the principle to the attention of those concerned with the development and use of metal-explosive systems.

Consider a solid object of arbitrary shape with the exception that one surface of the body, the surface against which the accelerating force acts, is assumed to be flat and oriented normal to the direction of the force. If the body is to remain intact after acceleration, all parts of it must be accelerated to the same velocity v. Generally, the force F_s that acts at a particular point on the body will vary rapidly with time.[2] The value of F_s may, and frequently will, vary markedly from point to point on the surface. The impulse I_s that acts on an increment of area dS of the surface will be given by

$$I_s=\int_0^\infty F_s(t)dt.$$

The velocity imparted to that mass m_s which lies below the elemental area dS will be given by

$$v_s=I_s/m_s.$$

If the body is to hold together, the following relationship,

$$\frac{\int_0^\infty F_s(t)dt}{m_s}=\text{constant}$$

must be satisfied for every point on the surface.

Consider specifically the case of a cylindrically symmetrical object that is propelled off of the end of a stick of explosive. A qualitative plot of I_s *versus* radial distance from the axis, deduced from considerations discussed previously by the author,[2] is shown in Fig. 1. It is to be expected, therefore, that the pellet used by

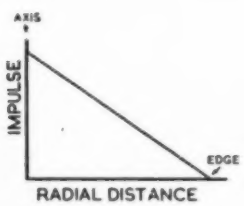

FIG. 1. Graph showing qualitative variation of impulse I_s delivered to a point on the end of a right circular cylinder of explosive.

van Valkenburg would hold together. It is significant that the shape of the identation made in a block of steel[3] is almost a mirror image of the shape of the pellet.

The greatest difficulty in applying this principle to a specific case will arise from lack of knowledge of $\int F_s dt$. Fortunately, the qualitative behavior of this quantity can frequently be surmised from a simple examination of the geometry of the metal-explosive system under consideration.

[1] M. E. van Valkenburg and C. D. Hendricks, Jr., J. Appl. Phys. **26**, 776 (1955).
[2] J. S. Rinehart and J. Pearson, *Behavior of Metals Under Impulsive Loads*, (American Society for Metals, Cleveland, Ohio, 1954), Chap. 5.
[3] J. S. Rinehart, J. Appl. Phys. **22**, 1178 (1951).

Stress Relaxation in Gold Wire

O. L. ANDERSON AND P. ANDREATCH
Bell Telephone Laboratories, Inc., Murray Hill, New Jersey
(Received July 23, 1955)

THE stress relaxation in gold wire has been measured using the technique developed by Mallina,[1] and subsequently used in determining the stress relaxation in copper and aluminum.[2,3] This technique (see Fig. 1)* consists of wrapping the wire under a prescribed tension around a rectangular metal terminal, so as to produce a twist in the terminal, and measuring the angle of twist as a function of time.

In the experiments reported here, a terminal of nickel brass alloy, commonly known as nickel silver, measuring 0.062 by 0.016 by 4 in. long was wrapped with 120 turns of 0.020 in. gold wire (purity 99.97%) tensioned with a two pound weight (6300 psi). This tension produced an angle of twist of about 26° which was read by means of a pointer attached to the terminal. A fixture holding four of these terminals was placed in an oven, whose temperature was controlled to ±2°C, for a period of 16 months. The angle of twist was read periodically through a glass window in the oven. Measurements were conducted at 70°C, 100°C, and 150°C, and also in an atmosphere-controlled room whose temperature is 25°C±0.5°C, and whose relative humidity is 40%. The accuracy of the twist readings is ±2%. In a period of 16 months, after being unwrapped, the creep in the terminals was found to be about 2°. The data, as presented here, are corrected for this creep.

The ratio of the stress to the initial stress is shown in Fig. 2. The points on the curve represent average values of two measurements.

The activation energy of stress relaxation is given by the following equation which is derived in reference 3.

$$H_\sigma=R\ln(t_1/t_2)\Big/\left[\frac{1}{T_1}-\frac{1}{T_2}\right],$$

where t_1 and t_2 are time values corresponding to the temperature T_1 and T_2 at the same stress level, R is the gas constant, and H_σ designates the activation energy at the stress σ. Using the solid lines in Fig. 2, the activation energy for the various stress levels is calculated and graphed in Fig. 3. Using the values of activation

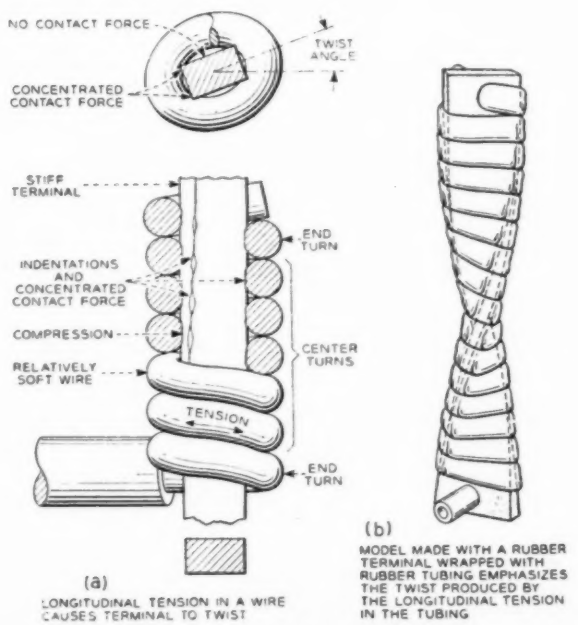

FIG. 1. Illustration of wire wrapped on terminals.

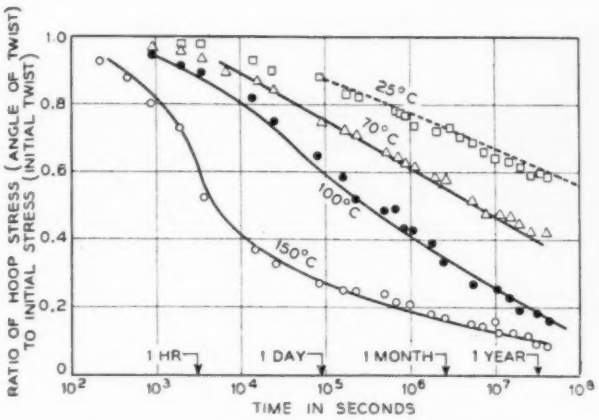

FIG. 2. Relaxation of stress in gold wire as a function of time and temperature.

energy in Fig. 3, the stress relaxation curve at 25°C is predicted and plotted as a dashed line in Fig. 2.

The activation energy associated with stress relaxation in gold decreases as the stress increases which is the same result

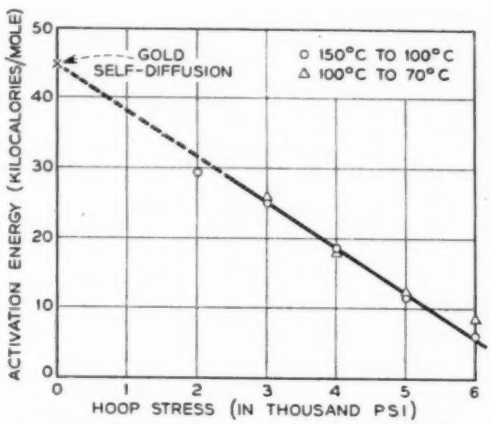

FIG. 3. Activation energy for stress relaxation as a function of hoop stress.

found for similar experiments with copper and aluminum described in reference 3. Furthermore, the extrapolated value of activation energy at zero stress agrees with the activation energy of gold self-diffusion (44 100 cal/mole),[4,5] indicating that the atomic readjustments which relieve persisting tension are similar to those involving self-diffusion.

[1] R. F. Mallina, Bell System Tech. J. **32**, 525 (1953).
[2] W. P. Mason and T. F. Osmer, Bell System Tech. J. **32**, 557 (1953).
[3] W. P. Mason and O. L. Anderson, Bell System Tech. J. **33**, 1093 (1954).
* This figure republished from Bell System Tech. J. [3] **32**, 535 (1953).
[4] W. A. Johnson, Trans. Am. Inst. Mining Met. Engrs. **147**, 107 (1941).
[5] F. Seitz, Phys. Rev. **79**, 1513 (1948).

Comments on Limiting Pressure on Hydrofoils

E. V. LAITONE
University of California, Berkeley, California
(Received August 10, 1955)

PREVIOUSLY the writer[1,2] had pointed out that if hydrostatic conditions are achieved on the upper surface of a thin hydrofoil at small angles of attack as it approaches the free water surface, then there is a limiting maximum surface velocity that is determined by the maximum water depth recovery that can be

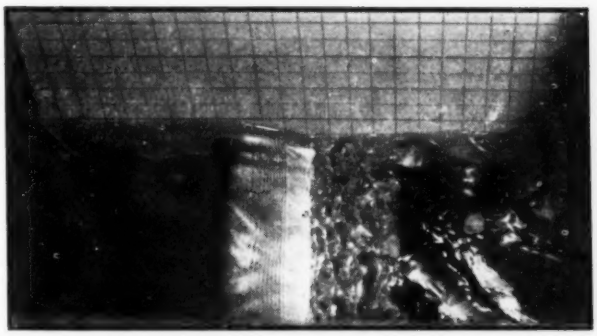

FIG. 1. Hydraulic jump on the hydrofoil ($M_\infty=0.73$, $F=0.5$).

produced by a hydraulic jump. That is, the supercritical flow that can occur if hydrostatic conditions are attained can be converted to subcritical flow only by means of the hydraulic jump that produces the maximum absolute water depth after the jump. This fixes the maximum local Froude number immediately upstream of the hydraulic jump as $M_1=\sqrt{3}=v_1/(gy_1)^{\frac{1}{2}}$. This hydraulic jump always produces a doubling of the water depth ($y_2/y_1=2 \approx y_\infty/y_1$) where the maximum depth after the hydraulic jump (y_2) must be only slightly less than the depth of hydrofoil trailing-edge below the original free water surface (y_∞).

The writer[1,2] pointed out two severe limitations to this theory; namely,

(1) If hydrostatic flow were not established, neither the limiting velocity nor the hydraulic jump could occur. This would be expected for thick hydrofoils or large angles of attack, or *possibly* for large Froude numbers based on the forward speed of the hydrofoil (V_∞) and the depth of submergence since the vertical acceleration may not be negligible. Consequently, the writer[2] restricted the Froude number range for this theory to

$$M_\infty=V_\infty/(gy_\infty)^{\frac{1}{2}}\leqq\sqrt{3}.$$

(2) If the hydrofoil were in a channel of finite depth, then the downstream wave disturbances could not overtake the hydrofoil in order to form a hydraulic jump whenever the Froude number based on the channel depth h became supercritical

$$F=V_\infty/(gh)^{\frac{1}{2}}>1.$$

Unfortunately, the experimental equipment at Berkeley did not permit testing for $M_\infty>\sqrt{3}$ when $F<1$ in order to determine the upper range for the velocity limitation. However, recent experimental and theoretical investigations by Parkin, Perry, and Wu[3] have shown that at high Froude (M_∞) numbers the hydraulic jump and the accompanying velocity limitation do not occur even when $F<1$. Their experimental data, all taken at subcritical channel speeds, indicate that when $M_\infty\leqq1$ the velocity limitation is applicable, but when $M_\infty>\sqrt{3}$ it is definitely no longer valid.

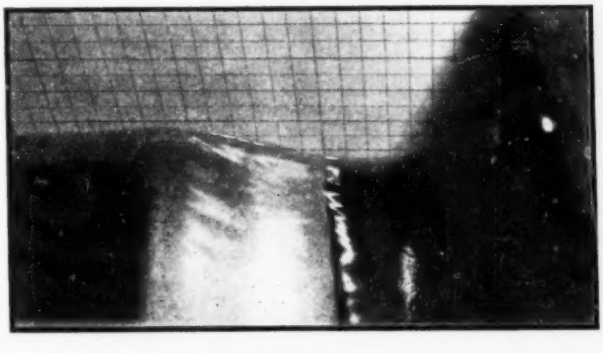

FIG. 2. Hydraulic jump downstream of the hydrofoil ($M_\infty=1.18$, $F=0.79$)

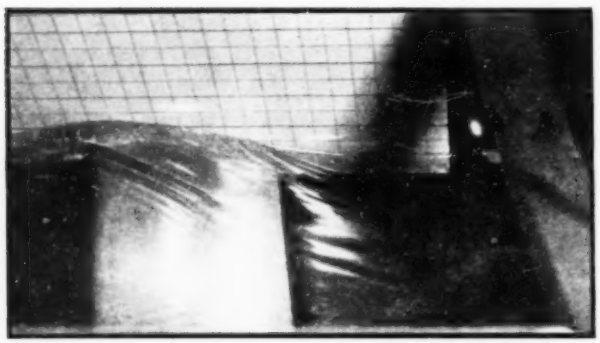

FIG. 3. No hydraulic jump, channel flow supercritical ($M_\infty = 1.73$, $F = 1.18$).

Figure 1 depicts the hydraulic jump over a 4-inch chord hydrofoil with an NACA-0012 profile during tests made at Berkeley by towing the hydrofoil through still water in a 4-inch deep channel. Figure 2 shows that for $M_\infty > 1$ (when $F < 1$) the hydraulic jump has left the hydrofoil surface and appears downstream of the trailing edge. Figure 3 illustrates a case for which no hydraulic jump can occur. Visual observation showed that for $1 < M_\infty < \sqrt{3}$ any supercritical channel flow ($F > 1$) also prevented the formation of a hydraulic jump.

The analogy between the hydraulic jump on the hydrofoil and the normal shock wave occurring on an airfoil flying at a high subsonic freestream Mach number is seen to be valid only for $M_\infty < 1$ when $F < 1$, as previously noted by the writer.[2]

[1] E. V. Laitone, J. Appl. Phys. 25, 623 (1954).
[2] E. V. Laitone, "Limiting velocity by momentum relations for hydrofoils near the surface and airfoils in near sonic flow," Proceedings of the Second U. S. National Congress of Applied Mechanics, pp. 751–753 (June, 1954).
[3] Parkin, Perry, and Wu, "Pressure distribution on a hydrofoil running near the water surface," Hydrodynamics Laboratory Report, California Institute of Technology, Pasadena (to be published).

Removal of Copper from Germanium

KATHARINE B. BLODGETT
General Electric Research Laboratory, Schenectady, New York
(Received August 29, 1955)

SAMPLES of clean n-type germanium were coated with a copper salt and heated at 800°C in hydrogen to allow copper to diffuse into the interior.[1] The samples were then given certain treatments which had results that could be interpreted as meaning that each treatment had drained copper out of the germanium. The treatments consisted in heating a sample at 700°C (1) in an atmosphere of hydrogen, or (2) in an atmosphere of oxygen, or (3) with a coating of an iron salt covering the surface, in hydrogen.

The results of the treatments were measured by means of (a) changes in volume resistivity of the germanium, and (b) use of tracer Cu^{64} which accumulated at the surface during the heat treatment.

The results obtained with Cu^{64} for samples treated in O_2 and H_2 are given in Table I.

The data show that two successive treatments in O_2 removed 0.97 of the copper from a sample, whereas four successive treatments in H_2 removed a fraction 0.36.

A coating of an iron salt on a germanium surface caused more copper to drain out of a sample in hot hydrogen than when the germanium was clean. Tests made with iron salt coatings had two special features (a) the coating could be localized: one-half the length of a bar of copperized germanium could be converted from p- to n-type by a coating on that half, and heat treatment, while the uncoated half remained p-type, and (b) the effect of the amount of iron salt in the coating could be studied.

The data in Fig. 1 give measurements of resistivity obtained with a sample of n-type germanium, 1.3 cm×0.49 cm×0.16 cm in size. The sample was coated on both faces with known amounts of ferric nitrate, deposited from an aqueous solution, and then heated in hydrogen at 700°C for 15 minutes; during this heat treatment the ferric nitrate was reduced to iron. The data show that in each run the p-type resistivity increased with successive treatments. The rate of increase depended on the amount of ferric nitrate on the surface. In the case of Curve (A), which corresponds to the largest amount used, the resistivity reached a maximum value after three treatments, then changed from p- to n-type and diminished in value with further treatments.

TABLE I. Comparison of results for samples of germanium containing Cu^{64}, treated in O_2 and in H_2. Size of each sample 2.8 cm×1.1 cm×0.254 cm.

(1) Amount of Cu in sample (No. of atoms)	(2) Treatment	(3) Amount of Cu that arrived at surface (No. of atoms)	(4) Fraction removed Col. (3)/ Col. (1)
1.01×10^{16}	In O_2 at 700°C 30 min	0.89×10^{16}	0.88
	Again in O_2 at 700°C	0.09×10^{16}	0.09
1.1×10^{16}	In H_2 at 700°C 30 min four successive times	0.39×10^{16}	0.36

These results were interpreted as meaning that an iron coating on the surface serves as a "sink" to hold the copper that diffuses to it, and that copper diffuses to the iron until an equilibrium concentration of copper in iron is built up. Iron that has taken up copper must be cleaned off the surface, and a fresh coating of an iron salt applied, in order to continue removing copper from the sample. The iron was cleaned off by grinding the sample which was 0.063 in. thick so as to remove not more than 0.001 in. thickness from each face. The data in Fig. 1 were not corrected for the decrease of thickness.

A sample of germanium containing only a little Cu^{64} was coated on one face (B) with iron nitrate while the opposite face

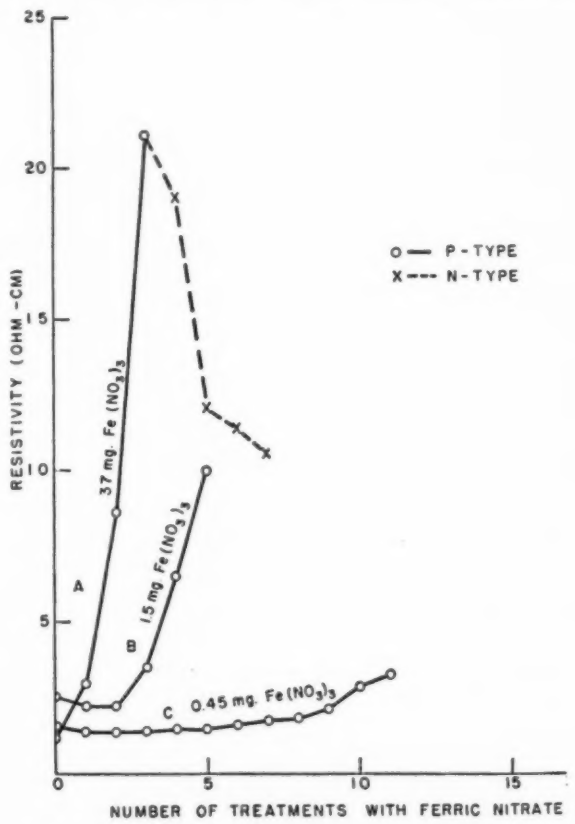

FIG. 1. Resistivity of germanium containing copper after heat treatment with a surface coating of iron nitrate.

(A) was kept clean. After being in hydrogen at 700°C for 20 minutes, the counts for the two faces corresponded to 0.12×10^{16} copper atoms for face (A) and 0.16×10^{16} for face (B). The faces were cleaned, face (B) was coated again and the heat treatment repeated. The counts then corresponded to 0.014×10^{16} copper atoms for (*A*) and 0.056×10^{16} for (*B*).

[1] Fuller, Struthers, Ditzenberger, and Wolfstirn, Phys. Rev. **93**, 1182 (1954).

Preferred Orientation in Stark Rubber Studied with an Automatic Integrating Pole Figure Goniometer

C. J. Newton, L. Mandelkern, and D. E. Roberts
National Bureau of Standards, Washington, D. C.
(Received September 2, 1955)

NATURAL rubber is occasionally found to be hard and inelastic when received or stored in temperate climates; this type of rubber has been popularly designated as "stark rubber." It is known that its unusual physical properties are due to the development of appreciable amounts of crystallinity.[1*] The authors recently demonstrated[2] from x-ray diffraction patterns obtained photographically and interpreted by pole figure analysis[3] the existence of preferred orientation in an accidentally-occurring stark specimen. Recently an automatic integrating pole figure goniometer[4] was made available for a few weeks through the courtesy of the X-ray Department of the General Electric Company. Using this instrument and a Geiger counter diffractometer, the authors made a study of preferred orientation in a sheet of stark rubber, about 2 mm thick. The sheet used for the experiment had been deliberately transformed in the laboratory into stark rubber by compression between flat metal plates for about twenty years. During most of the time it had been kept at a temperature between 0° and 14°C.

Copper $K\alpha$ radiation was employed and the following diffractions from monoclinic natural rubber were studied: (200) at a Bragg angle of 7.0°; (201) and ($\bar{2}$01), not resolved, at 8.9°; and (120) ($\bar{1}$20), single spacing, at 10.5°. The intensity data were corrected for absorption and plotted as pole figures with respect to the plane of the specimen and an arbitrary vertical direction.

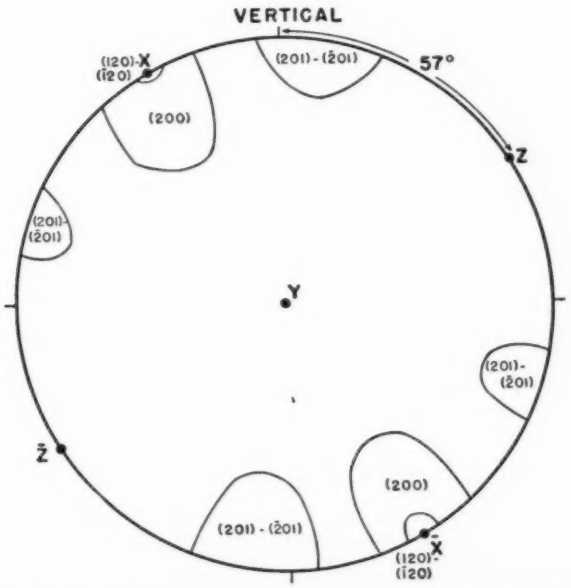

FIG. 1. Combined pole figures of concentrations of normals to (200), (201)–($\bar{2}$01), and (120)–($\bar{1}$20) planes giving rise to diffractions observed in this study of stark rubber.

The areas representing angular regions of maximum preferred orientations were combined on a single stereographic projection as shown in Fig. 1. All three orders showed maxima along the edge of the projection, that is, in the plane of the stark rubber sheet. The (201) and ($\bar{2}$01) maxima appeared four times, two diametrical pairs, separated by 75°, which is the angle between (201) and ($\bar{2}$01) in the monoclinic unit cell of rubber.[5] The (200) maxima appeared as a single diametrical pair oriented with respect to the (201) ($\bar{2}$01) set in such a manner that they may all be referred to one set of crystallographic axes having a single orientation with respect to the sheet. This system of preferred orientation places the *Y*-axis normal to the sheet and the *X*-axis and *Z*-axis (the chain molecule axis) in the plane of the sheet.

The (120) ($\bar{1}$20) diffraction exhibited a single diametrical pair of maxima which did not, however, belong to the texture system described. The maxima here too indicated a concentration of poles in the plane of the sheet, seemingly coinciding with the (200) maxima. Although there was not enough information to ascribe a definite unit cell orientation to this second texture system, it was interesting to notice that the (120) ($\bar{1}$20) maxima fell 90° from the position assigned to the *Z*-axis in the first system. Since the normals to the (120) ($\bar{1}$20) planes are 90° from *Z* in the unit cell, it is possible that the two systems have their *Z*-axis (chain axis) in common.

This preferred direction of the *Z*-axis, which is compatible with the maxima observed in all three cases of diffraction, bears an interesting relationship to a macroscopic feature visible in the stark rubber sheet. There is a pattern of small parallelograms formed by the intersection of two sets of parallel lines, each about 5 mm apart, of slightly darker material, intersecting at an angle of 65°. This is indicated in Fig. 2. Both the dark and light materials were shown by x-ray diffraction to be crystalline with preferred orientation. The source of these lines was a pattern of difference in thickness imparted to the sheet by grooves in the mill rolls during the processing of the smoked rubber. After the long period of laboratory compression, the surfaces of the sheet were smooth and the thickness was uniform; but the trace of the pattern was still visible in the translucency of the sheet. The apparent direction of the *Z*-axis on the pole figures coincides with the direction of the shorter diagonal of the parallelograms in this pattern. It is well known that ordinary rubber while held in simple extension, may exist in a crystalline state at room temperature, and that it has the *Z*-axis parallel to the direction of stress.[6] In the case of the sample of stark rubber, one is led to inquire if there may be some residual or "locked-in" stress in the sheet, bearing an appropriate relationship to the pattern of lines and hence to the preferential crystallization.

In metals, one often finds residual stresses in specimens which have been plastically deformed.[7] Such residual stresses measured with x-rays generally are oppositely directed to the direction of plastic flow. Let us assume that, when the uneven sheet of rubber was placed under compression, plastic flow was directed outward from the ridges whose traces constitute the pattern in the smooth sheet. The material would everywhere be forced from the ridges toward the interiors of the little parallelograms. The system of stresses would be complex, but in the plane of the sheet the maximum effect would obviously be present at the intersection of ridges, parallel to the bisector of the obtuse angle. This means

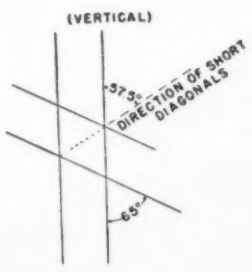

FIG. 2. Schematic diagram of parallelogram pattern on rubber specimen.

that while under load the material would be subjected to compressive stresses in the plane of the sheet with maximum components parallel to the short diagonals of the parallelograms. Then upon release of the external load, there would appear, if in this respect the behavior of the material were analogous to that of metals, a system of locked-in stresses, the principal tensile component of which would be parallel to these short diagonals. As mentioned above, the Z-axis in ordinary stretched rubber is usually oriented in the direction of tension; our observation of the preferred direction of the Z-axis along the short diagonals of the pattern in the stark specimen agrees with this behavior of ordinary rubber.

There is, however, a serious difficulty with this proposed explanation. Any system of locked-in stresses is not complete without a complementary system of balancing stresses. The problem of the nature of these stresses and of the material in which they lie has not been completely resolved in the case of metals; it would seem to be even more difficult to explain in the case of rubber-like materials. Apparently, the high viscosity of rubber at room temperature is sufficient to prevent the complete relaxation of stresses set up thus by the strong compression of several years duration, and hence to maintain the orientation of the molecular chain segments for relatively long periods of time after the removal of the external forces. This is consistent with the observation that, after stark rubber is melted and subsequently recrystallized, the normal behavior of ordinary rubber is observed.[1]

[1] D. E. Roberts and L. Mandelkern, J. Research Natl. Bur. Standards **54**, 167 (1955).
* Numbers in parentheses refer to references at end of paper.
[2] Newton, Mandelkern, and Roberts, J. Research Natl. Bur. Standards **55**, 143 (1955).
[3] B. F. Decker, Proc. Am. Soc. Testing Materials **43**, 785 (1943).
[4] C. G. Suits, Gen. Elec. Rev. **54** (11), 32 (1951).
[5] C. W. Bunn, Proc. Roy. Soc. (London) **A180**, 40 (1942).
[6] S. D. Gehman and J. E. Field, J. Appl. Phys. **10**, 564 (1939).
[7] G. B. Greenough, Progr. Metal Phys. **3**, 191 (1952).

Comments on "Transformations in Plain Carbon Steels"

F. C. Frank and K. E. Puttick
University of Bristol, Bristol, England
(Received September 7, 1955)

Heidenreich's[1] observations by thermionic emission microscopy of transformations in carbon steels present a number of significant features which must ultimately contribute to a better understanding of these processes, but we consider that the experimental evidence he presents neither demands such an unorthodox interpretation as he gives, nor is capable of being adequately explained by it. The principal novel feature in his interpretation is the intervention (in high-temperature transformations) of the phase which he denotes by α', that is, supersaturated ferrite produced by a diffusionless transformation with the same composition as the austenite from which it forms. He first proposes this for a steel of 0.22 weight % carbon, transformed at 810°C, about 10° below the phase boundary, when the new phase grew with a linear velocity of about 5 μ/sec.

The first question that this interpretation raises is what can prevent the diffusion? There can be no doubt that the chemical potential of carbon in the supersaturated ferrite must be higher than in the austenite: there can be little doubt that it must be substantially higher. Carbon must therefore diffuse into the austenite unless the interface is somehow impervious to it. We are unable to conceive how a mobile boundary can possess this property. The calculation of Heidenreich's appendix shows that the carbon must *consequently* diffuse ahead of the boundary for a distance of the order of a micron into the austenite.

The second question is whether the diffusionless transformation is thermodynamically possible at this temperature. The pseudo-equilibrium boundary, $(\alpha/\gamma)'$, for the diffusionless transformation must lie within the two-phase region of the phase diagram. As a reasonable rough estimate we may put it at the geometric mean of the carbon concentrations at the ferritus and austenitus lines. If that is so, 810°C is too high a temperature for the supersaturated ferrite to be stable with respect to austenite. Heidenreich's reason for believing that the transformation took place without diffusion was that he thinks a carbon-rich zone ahead of the growing phase should give enhanced emission, and he was unable to see this. We suppose that this latter inference was at fault. The fact that after the complete history of preparation a carbon-rich specimen has higher emission does not necessarily mean that carbon enrichment by itself immediately raises the emission. If it is growing in previously homogeneous austenite, we believe that the ferrite must have a zone of enhanced carbon content ahead of it. Alternatively, in view of the short austenitizing time (5 minutes at 900°C), we can suppose that the specimen was by no means homogeneous and the transformation was taking place in a region of particularly low carbon content. In either case the conclusion loses its force.

This criticism of the conclusions for the transformation of 0.22% carbon steel at 810°C also weakens the case for the interpretation given for the transformation of 0.77% carbon steel at 670°C. The interpretation is based partly on analogy with the former case, and partly on the fact that it gives one interpretation of the changes in emissivity. Heidenreich supposes that the first visible nucleus of a pearlite nodule is supersaturated ferrite formed by diffusionless transformation. It is once again distinctly dubious whether at the temperature concerned this phase would be stable with respect to austenite, unless the inhomogeneity of composition in the specimen was particularly severe. The polygonal early outline of the nodule is of interest (Fig. 6 of Heidenreich's paper), as is also the elongated form of the transformation product, parallel to an austenite twin, at 640°C (Fig. 8): but neither bears much resemblance to the lenses or parallel sided plates, irrationally oriented, which are usually characteristic of diffusionless transformations. Without suggesting that a final interpretation can be given with certainty on the existing evidence, we would prefer to suppose that the pearlite nucleus seen in Fig. 6 is already normal pearlite, and that the question to be asked is what are the changes in the surface, accompanying pearlitic decomposition, which give it a transient over-all bright emission?

There is an error implicit in the assumption that the velocity of transformation is limited by diffusion of carbon *away from the boundary* in all cases other than growth of a supersaturated phase. For pearlite the controlling factor is, of course, diffusion of carbon to the edges of cementite plates, either through the austenite, through the ferrite, or along the interface boundary.[2] The velocity of transformation of the rod-shaped crystal shown in Heidenreich's Fig. 8(c) is given as approximately 1μ/sec at 640°C, which the author considers to be evidence of growth too rapid for a diffusion controlled transformation. However, this is of the right order of magnitude for the velocity of pearlite growth in steel at this temperature[3]; it is indeed rather low for a high purity alloy. This is further support for the suggestion that pearlite is detected in Heidenreich's experiments before its structure can be resolved.

[1] R. D. Heidenreich, J. Appl. Phys. **26**, 879 (1955).
[2] J. C. Fisher, "Eutectoid decompositions, thermodynamics in physical metallurgy," ASM seminar 1949.
[3] Hull, Colton, and Mehl, Trans. Am. Inst. Mining Met. Engrs. **150**, 185 (1942).

Errata: On the Space-Charge-Limited Current between Nonsymmetrical Electrodes

[J. Appl. Phys. **26**, 1034 (1955)]
George D. O'Neill
Research Laboratories, Sylvania Electric Products, Inc., Bayside, New York

A solidus was accidentally omitted from one equation and a pair of parentheses from another. The correct expressions

are:

$$C=l\left[2\ln\left(\frac{4h^2-r_0^2/2}{\pi hr_0}\right)\right]^{-1}. \quad (17)$$

$$C=l[2\ln(4h/\pi r_0)]^{-1}. \quad (18)$$

The equation occurring in the sentence beginning at the bottom of page 1038 may be confusing because of the break in the line. It is to be read

$$C=1/2p(\mu+1).$$

Erratum: Ferromagnetic Resonance in Magnesium-Manganese Aluminum Ferrite between 160 and 1900 Mc

[J. Appl. Phys. 26, 1180–1182 (1955)]

H. SUHL, L. G. VAN UITERT, AND J. L. DAVIS
Bell Telephone Laboratories, Inc., Murray Hill, New Jersey

THE captions to Figs. 2(a) and 2(b) should be interchanged.

Erratum: Cross Correlation between Velocity and Current Fluctuations in Tube Noise

[J. Appl. Phys. 26, 605 (1955)]

S. V. YADAVALLI
General Electric Microwave Laboratory at Stanford, Palo Alto, California

IN the derivation of Rack's noise velocity under assumption (3)

$$\lim_{n\to\infty}\frac{1}{n}\sum_{j=1}^{n} f_j \underset{\text{a.s.}}{\to} 0$$

should read

$$\text{l. i. m.}_{n\to\infty}\frac{1}{n}\sum_{j=1}^{n} f_j \underset{\text{a.s.}}{\to} 0.$$

This is important mathematically since absolute convergence is a more severe restriction than convergence in the mean.

Books Reviewed

Principles of Meteorological Analysis. WALTER J. SAUCIER. Pp. 438+xvi, Figs. University of Chicago Press, Chicago, 1955. Price $10.00.

This book is an intermediate textbook in weather analysis. The author assumes that the student has an elementary knowledge of climatology, weather observations, statics and thermodynamics, and an understanding of calculus (especially partial differentials). The approach presented here emphasizes the relatively simple airflow patterns of the upper atmosphere. The student is led from this study to the fundamentals of analysis and to an understanding of the lower atmosphere. Detailed discussions of meteorological charts, pressure reduction below the surface, applications of stability concepts, contouring, and graphic, kinematic, and local analysis are presented.

Bericht über den V. Internationalen Astronautischen Kongress. F. HECHT, EDITOR. Pp. 307+vi. Springer-Verlag, Vienna, 1955. Price $13.80.

This volume presents the papers given at a meeting in August, 1954, sponsored by the Austrian Association for Space Research.

Grundzüge der Tensorrechnung in Analytischer Darstellung III. Teil. A. DUSCHEK AND A. HOCHRAINER. Pp. 250+vi. Springer-Verlag, Vienna, 1955. Price $5.70.

This is Part III of the series on tensor analysis and is subtitled "Applications in Physics and Technology." Applications to mechanics, elasticity, fluid mechanics, heat flow, electrodynamics, special relativity, and gravitation are discussed.

Handbook of Engineering Materials. DOUGLAS F. MINER AND JOHN B. SEASTONE, EDITORS. Pp. 1380. John Wiley and Sons, Inc., New York, 1955. Price $17.50.

This is the first edition of a handbook of information on engineering materials. The physical properties, applications, and methods of preparation or fabrication of the principal engineering materials are tabulated. About one-fourth of the handbook is devoted to mathematical and physical tables and to the properties of construction materials such as concrete and timber. The other three-fourths present the properties of metals, alloys, wood, paper, fibers, plastics, organic finishes, fuels, ceramics, lubricants, and other materials. Properties such as creep and corrosion resistance are listed for many alloys. The text was prepared by fifty-one contributors.

An Introduction to the Theory of Aeroelasticity. Y. C. FUNG. Pp. 490+xi. John Wiley and Sons, Inc., New York, 1955. Price $10.50.

This book is a textbook for advanced undergraduates and graduates in aeronautics, but it is addressed also to designers and engineers concerned with flutter. The fundamentals of aerodynamics, elasticity, and vibration theory are reviewed in the first chapter. Chapters 2 to 11 survey aeroelastic problems, their historical background, their basic physics, and the principles of their analysis. Chapters 12 to 15 contain the fundamentals of oscillating airfoil theory and a brief summary of experimental results.

Bearing Lubrication Analysis. R. R. SLAYMAKER. Pp. 108+xiv. John Wiley and Sons, Inc., New York, 1955. Price $5.00.

The lubrication of sleeve bearings is the subject of this book, which is a textbook for a graduate course in machine design. The analysis is illustrated by examples of actual bearing design problems. The hydrodynamic theory of lubrication is presented and the importance of oil viscosity is stressed. There is a short discussion of "oilless" bearings.

Hydrodynamics. GARRETT BIRKHOFF. Pp. 186+xiii. Dover Publications, New York, 1955. Price $1.75 (clothbound $3.50).

The subtitle of this book, which was originally published by Princeton University Press in 1950, is "A Study in Logic, Fact, and Similitude." The book probes the complicated logical relation between theory and experiment in fluid mechanics and it develops symmetry concepts as applied to fluid mechanics.

Non-Euclidean Geometry. ROBERTO BONOLA. Pp. 389+xliv. Dover Publications, New York, 1955. Price $1.90 (clothbound $3.95).

This volume contains translations of three well-known treatises on non-Euclidean geometry: The critical and historical study by Roberto Bonola and the original contributions "The Science of Absolute Space" by John Bolyai and "The Theory of Parallels" by Nicholas Lobachevski.

Theory of Groups of Finite Order. W. BURNSIDE. Pp. 512+xxiv. Dover Publications, New York, 1955. Price $2.00 (clothbound $3.95).

This book is a reprinting of the second edition (1911) of Burnside's book, which was originally published by the Cambridge University Press.

Transmission-Line Theory. RONOLD W. P. KING. Pp. 509+xiii. McGraw-Hill Book Company, Inc., New York, 1955. Price $12.00.

The rigorous and complete treatment of transmission lines is featured in this book. The theory of lines is approached from electromagnetic principles, rather than from assumed equivalent networks, in order to emphasize the conditions under which the theoretical treatment provides a good approximation to the actual physical problem. The infinite line and the terminated line are discussed separately. Impedance, amplitude relations for current and voltage, discontinuities and nonuniformities, transmission-line oscillators, and coupled sections of lines are discussed. The book is intended as a textbook for a graduate course in transmission-line theory.

Principles of Electromagnetism. E. B. MOULIN. Pp. 438+viii. Clarendon Press, Oxford, England, 1955. Third edition. Price $8.00.

The author has tried to bridge the gap between engineering textbooks in electromagnetism and theoretical physics textbooks. The third edition is more than half again as long as the first. The principal additions are the discussions of dielectric loss and of the high-frequency resistance of rods and coils and the extension of the theory of circular cylinder conductors in uniform fields. The book emphasizes the working of examples and is intended as a companion volume to the author's "Electromagnetic Principles of the Dynamo."

Gas Kinetics. A. F. TROTMAN-DICKENSON. Pp. 322+x. Academic Press, Inc., New York, 1955. Price $8.00.

This monograph on the kinetics of homogeneous gas reactions surveys the experimental results and discusses their significance. It is intended for the advanced undergraduate and the graduate chemist undertaking research on gas kinetics. The reactions discussed have been chosen because of the light they shed on the fundamental question of why elementary reactions occur at the rate they do. Thus, combustion reactions receive relatively little attention. The book contains over eight hundred references.

Books Received

Experimental Electronics for the Beginner. L. R. CROW AND L. G. BLEVINS. Pp. 360. Universal Scientific Company, Vincennes, Indiana, 1955. Price $3.50.

Some Aspects of the European Energy Problem. LOUIS ARMAND. Pp. 63. O.E.E.C. Mission Publications Office, Washington, D. C., 1955. Price $1.00.

Sound Barrier. NEVILLE DUKE AND EDWARD LANCHBERY. Pp. 129. Philosophical Library, New York, 1955. Price $4.75.

Principles of Mass and Flow Production. FRANK G. WOOLLARD. Pp. 195. Philosophical Library, New York, 1955. Price $7.50.

Announcements

Symposium on Nonlinear Circuit Analysis. II

The sixth in a series of international symposia on nonlinear circuit analysis will be held at the Microwave Research Institute, Polytechnic Institute of Brooklyn, 55 Johnson Street, Brooklyn 1, New York, April 25–27, 1956. The program will emphasize the use of nonlinear network theory in the analysis of oscillators, switching and discontinuous systems, and nonlinear systems with random inputs. The proceedings of the conference will be published. Requests for the detailed program should be addressed to the Microwave Research Institute.

Author Index to Volume 26

(References with (L) are to Letters to the Editor)

Adler, F. P. Information required for missile guidance—492(L)

Aharoni, A., E. H. Frei, and G. Horowitz. New active circuit element using the magnetoresistive effect—1411

Alexander, L. E., S. Ohlberg, and G. R. Taylor. X-ray diffraction studies of crystallization in elastomers—1068

Allen, W. A. and W. Goldsmith. Elastic description of a high-amplitude spherical pulse in steel—69

——, **J. M. Mapes, and E. B. Mayfield.** Shock waves in air produced by waves in a plate—1173

——, **J. M. Mapes, and E. B. Mayfield.** Shock waves in air produced by elastic and plastic waves in a plate—125(L)

Alperin, H. A. (see Siegel, K. M.)—297

Altschuler, H. M. (see Oliner, A. A.)—214

Anderson, A. G., R. L. Garwin, E. L. Hahn, J. W. Horton, G. L. Tucker, and R. M. Walker. Spin echo serial storage memory—1324

Anderson, J. R., G. W. Brady, W. J. Merz, and J. P. Remeika. Effects of ambient atmosphere on the stability of barium titanate—1387(L)

Anderson, O. L. and P. Andreatch. Stress relaxation in gold wire—1518(L)

Andreatch, P. (see Anderson, O. L.)—1518(L)

Andrew, A. (see Jeppson, M. R.)—365

Andrews, C. L. Collapsed toroidal springs as contact elements in microwave cavities—777(L)

Andrews, R. D. Retraction of oriented polystyrene monofilaments—1061

Andrews, R. D. (see Gurnee, E. F.)—1106

Antal, J. J. (see Keating, D. T.)—1041

Anthony, R. L. (see Baldwin, F. P.)—750

Armstrong, G. M. (see Watson, M. T.)—701

Artman, J. O. and P. E. Tannenwald. Measurement of susceptibility tensor in ferrites—1124

Artman, R. A. (see Tyndall, E. P. T.)—286

Arthurs, E. and L. H. Martin. Closed expansion of the convolution integral (a generalization of servomechanism error coefficients)—58

Ash, E. A. Use of space charge in electron optics—327

Ashenhurst, R. L. (see Minnick, R. C.)—575

Atkins, W. W. Flash associated with high-velocity impact on aluminum—126(L)

Atwater, H. A. and B. Chalmers. Nucleation of lead with preferred orientation—918(L)

—— **and B. Chalmers.** Erratum: Nucleation of lead with preferred orientation—1284(L)

Baba, K. (see Takakura, T.)—185

Baer, W. Spatial distribution of thermal neutrons from a polonium-beryllium source in water-zirconium mixtures—1235

Balas, W., J. N. Dempsey, and E. F. Rexer. Oxide-impregnated nickel-matrix cathode—1163

Baldwin, F. P., J. E. Ivory, and R. L. Anthony. Experimental examination of the statistical theory of rubber elasticity. Low extension studies—750

Bancroft, D. (see Goranson, R. W.)—1472

Barton, Henry A. Editorial—1

Beach, L. A. (see Theus, R. B.)—294

Bean, C. P. Hysteresis loops of mixtures of ferromagnetic micropowders—1381

—— (see Rodbell, D. S.)—1318

—— **and D. S. Rodbell.** Kinetics of magnetization in some square loop magnetic tapes—124(L)

Becker, M. (see Spitzer, Wm. G.)—414

Bekefi, G. (see Buchsbaum, S. J.)—706

Belner, R. J. (see Maron, S. H.)—1457

Berg, M. (see Kingery, W. D.)—1205

Berger, M. J. Angular distribution of multiply scattered gamma radiation from a plane isotropic source—1504

Berkowitz, A. E. Relation to diffusion measurements of some beta-ray absorption phenomena—403

Berry, B. S. Precise investigation of the theory of damping by transverse thermal currents—1221

Berthold, W. (see Rottgardt, K. H. J.)—1180(L)

Bess, L. Relative influence of majority and minority carriers on excess noise in semiconductor filaments—1377

—— (see Maple, T. G.)—490(L)

Bever, M. B. (see Leach, J. S. L.)—728

Bierbower, J. B. (see Thomsen, E. G.)—920

Biot, M. A. Theory of elasticity and consolidation for a porous anisotropic solid—182

Birman, J. L. On zone refining—1195

Bland, D. R. and E. H. Lee. Calculation of the complex modulus of linear viscoelastic materials from vibrating reed measurements—1497

Blechar, T. (see Goranson, R. W.)—1472

Blewitt, T. H. (see Thompson, D. O.)—1188(L)

Blodgett, Katharine B. Removal of copper from germanium—1520(L)

Blois, M. S., Jr. Preparation of thin magnetic films and their properties—975

Bonkowski, R. R. (see Siegel, K. M.)—297

Borneman, E. H., R. F. Schwarz, and J. J. Stickler. Rectification properties of metal semiconductor contacts—1021

Botzen, A. (see Michels, A.)—843

Bourne, H. C., Jr. Composition of the interelectrode prebreakdown current in high vacuum—625

——, **R. W. Cloud, and J. G. Trump.** Role of positive ions in high-voltage breakdown in vacuum—596

Bowman, J. C., J. A. Krumhansl, and J. R. Stock. Interpretation of the strain broadening components in x-ray diffraction patterns—1057(L)

Boyle, W. S. Self-propagating intermittent discharge—584

—— **and L. H. Germer.** Arcing at electrical contacts on closure. Part VI. The anode mechanism of extremely short arcs—571

——, **P. Kisliuk, and L. H. Germer.** Electrical breakdown in high vacuum—720

Brachman, M. K. Note on Kramers-Kronig relations—497

Bradford, E. B. and J. W. Vanderhoff. Electron microscopy of monodisperse latexes—864

Brady, G. W. (see Anderson, J. R.)—1387(L)

Bragg, J. K. (see Crowe, R. W.)—1121

—— (see Sharbaugh, A. H.)—434

Breitman, L. Glass transitions in polymer-plasticizer systems—1092

Bridgers, H. E. and E. D. Kolb. Rate-grown germanium crystal for high-frequency transistors—1188(L)

Briggs, L. J. Maximum superheating of water as a measure of negative pressure—1001

Brode, H. L. Numerical solutions of spherical blast waves—766

Brodnyan, J. (see Philippoff, W.)—846

Brouwer, G. Electrical analog of the eddy-current-limited domain-boundary motion in ferromagnetics—1297

Brubaker, W. M. Influence of space charge on the potential distribution in mass spectrometer ion sources—1007

Bruns, H. B. (see LeCraw, R. C.)—124(L)

Bube, R. H. (see Stripp, K. F.)—251(L)
Buchsbaum, S. J., A. R. Milne, D. C. Hogg, G. Bekefi, and G. A. Woonton. Microwave diffraction by apertures of various shapes—706
Bueche, F. Viscoelasticity of poly methacrylates—738
—— Tensile strength of plastics above the glass temperature—1133
Buehler, E. (see Tanenbaum, M.)—686
Burford, T. M. Qualitative evaluation of correlation coefficients from scatter diagrams—56
Burger, E. E. (see Cobine, J. D.)—895
Burger, R. M. (see Farnsworth, H. E.)—252(L)
Burgess, H. and R. Smoluchowski. Note on self-diffusion of nickel—491(L)
Burgess, R. E. Thermal effects in point-contact rectifiers—1058(L)
Burton, B. L. (see Goranson, R. W.)—1472
Button, K. J. (see Lax, B.)—1184(L)
—— (see Lax, B.)—1186(L)

Carlin, H. J. Theory and application of gyrator networks—643
Carmichael, J. H. (see Varnerin, L. J., Jr.)—782(L)
Carnevale, E. H. (see Litovitz, T. A.)—816
Carter, David. Wide-angle radiation in pencil beam antennas—645
Chabai, A. J. and R. J. Emrich. Measurement of wall temperature and heat flow in the shock tube—779(L)
Chalmers, B. (see Atwater, H. A.)—918(L)
—— (see Atwater, H. A.)—1284(L)
Chatterjee, G. P. Rate of formation of film on metals and alloys—363
Chatterjee, J. S. Radiation characteristics of a conical helix of low pitch angle—331
Cheek, C. (see Linnenbom, V.)—932
Chin, T. N. Electron temperature in the parallel plane diode—418
Chipman, D. R. Mass absorption coefficient of carbon for CuKα radiation—1387(L)
Chodorov, M. and E. L. Chu. Cross-wound twin helices for traveling-wave tubes—33
Chu, E. L. (see Chodorov, M.)—33
Cloud, R. W. (see Bourne, H. C., Jr.)—596
Cobine, J. D. and E. E. Burger. Analysis of electrode phenomena in the high-current arc—895
Cohn, S. B. (see Jones, E. M. T.)—452
Cole, J. D. Acceleration of slender bodies of revolution through sonic velocity—322
Coleman, P. D. and M. D. Sirkis. Harmodotron—a beam harmonic, higher order mode device for producing millimeter and submillimeter waves—1385(L)
Comer, J. J. and J. W. Turley. Replica studies of bulk clays—346
Cook, E. O. and H. S. Heaps. Reflection of sound in the ocean from a continuous stratum containing a velocity extremum—429
Cook, M. A., R. L. Doran, and G. J. Morris. Measurement of detonation velocity by Doppler effect at three-centimeter wavelength—426
Coomes, E. A. (see LaBerge, W. B.)—241
Cox, J. A. M. (see Michels, A.)—843
Cram, K. H. and J. C. Whitwell. Equivalent-radius method for determination of non-Newtonian flow curves from viscometric data—613
Creutz, E. (see Wigner, E. P.)—260
——, **H. Jupnik, T. Snyder, and E. P. Wigner.** Review of measurements of the resonance absorption of neutrons by uranium in bulk—257
——, **H. Jupnik, T. Snyder, and E. P. Wigner.** Effect of geometry on resonance absorption of neutrons by uranium—271
——, **H. Jupnik, and E. P. Wigner.** Effect of temperature on total resonance absorption of neutrons by spheres of uranium oxide—276
Criddle, D. W. and A. L. Meader, Jr. Viscosity and elasticity of oil surfaces and oil-water interfaces—838
Crispin, J. W. (see Siegel, K. M.)—297 and 309
Crowe, R. W. (see Sharbaugh, A. H.)—434
——, **J. K. Bragg, and J. C. Devins.** Semiempirical expression for the first Townsend coefficient of molecular gases—1121
Crowell, C. R. Theoretical basis for measuring the saturation emission of highly emitting cathodes under space-charge-limited conditions—1353
Cusano, D. A. (see Williams, F. E.)—358
Cutler, M. Forward characteristic of germanium point contact rectifiers—949
—— (see Spitzer, Wm. G.)—414

Damask, A. C. and A. S. Nowick. Internal friction peak associated with precipitation in an Al-Ag alloy—1165
Damon, R. W. Magnetically controlled microwave directional coupler—1281(L)
Danos, M. Čerenkov radiation from extended electron beams—2
Darin, S. R. (see Taylor, G. R.)—1075
Davis, J. L. (see Suhl, H.)—1180(L)
—— (see Suhl, H.)—1523
Decker, R. W. and D. W. Stebbins. Photoelectric work functions of the borides of lanthanum, praseodymium, and neodymium—1004
Dempsey, J. N. (see Balas, W.)—1163
Deresiewicz, H. (see Mindlin, R. D.)—1435
Devins, J. C. (see Crowe, R. W.)—1121
DeWitt, T. W. Rheological equation of state which predicts non-Newtonian viscosity, normal stresses, and dynamic moduli—889
Dezoteux, J. A. (see LaBerge, W. B.)—241
Dienes, G. J. (see Fleeman, J.)—652
—— (see Rosenblatt, D. B.)—1044
Dolder, K. T. and O. Klemperer. Space-charge effects in electron optical systems—1461
Domenicali, C. A. and F. A. Otter. Thermoelectric power and electrical resistivity of dilute alloys of silicon in copper, nickel, and iron—377
Doran, R. L. (see Cook, M. A.)—426
Dow, W. G. (see Sicinski, H. S.)—1284(L)
Doyama, M. (see Kuczynski, G. C.)—871
Duffin, R. J. Impossible behavior of nonlinear networks—603
DuMond, J. W. M. (see Henke, B. L.)—903
Dunkerley, H. S. and D. L. Schaefer. Observations of cathode arc tracks—1384(L)
Dunkuls, Annija and Earl Zwicker. Potential distribution as a function of current in the spherical diode—779(L)
Dusenbury, J. H. (see Wakelin, J. H.)—786
Dwork, J. S. and H. Hurwitz, Jr. Neutron absorption in a semi-infinite region—642(L)

Ehrlich, M. J., S. Silver, and G. Held. Studies of the diffraction of electromagnetic waves by circular apertures and complementary obstacles: the near zone field—336
Eichelberger, R. J. Re-examination of the nonsteady theory of jet formation by lined cavity charges—398
Eisner, R. (see Tyndall, E. P. T.)—286
Ekstein, H. Theory of remagnetization of thin tapes—1342
Elliott, R. S. Azimuthal surface waves on circular cylinders—368

Ellis, S. G. Dislocations in germanium—1140
Elsken, R. H. (see Shaw, T. M.)—313
Emrich, R. J. (see Chabai, A. J.)—779(L)
Ernst, E. W. and H. VonFoerster. Time dispersion of secondary electron emission—781(L)
Evans, M. W., F. I. Given, and W. E. Richeson, Jr. Effects of attenuating materials on detonation induction distances in gases—1111
Eyring, H. (see Ree, T.)—793
—— (see Ree, T.)—800

Farnsworth, H. E., R. E. Schlier, T. H. George, and R. M. Burger. Ion bombardment-cleaning of germanium and titanium as determined by low-energy electron diffraction—252(L)
Faust, W. R. (see Theus, R. B.)—294
Feinstein, Joseph. Information theory aspects of propagation through time-varying media—219
Felsen, L. B. Backscattering from wide-angle and narrow-angle cones—138
Feng, I-Ming. Analysis of the effect of various factors on metal transfer and wear between specimen pairs of same metal and same shape. I. Basic scheme of formulation of metal transfer and wear—24
—— Analysis of the effect of various factors on metal transfer and wear between specimen pairs of same metal and same shape. II. Effect of the surrounding atmosphere—28
Fernbach, S. and W. G. Proctor. Spin-echo memory device—170
Ferry, J. D., R. F. Landel, and M. L. Williams. Extension of the Rouse theory of viscoelastic properties to undiluted linear polymers—359
Finch, G. I., K. P. Sinha, and A. Goswami. Transition structure of nickel—250(L)
Findley, Wm. N. and G. Khosla. Application of the superposition principle and theories of mechanical equation of state, strain, and time hardening to creep of plastics under changing loads—821
Fine, M. E. Elastic constants of germanium between 1.7° and 80°K—862
—— Erratum: Elastic constants of germanium between 1.7° and 80°K—1389(L)
Firle, T. E. (see Spitzer, Wm. G.)—414
Firle, T. E. and H. Winston. Noise measurements in semiconductors at very low frequencies—716
Fitch, T. E. (see Hill, J. E.)—1013
—— (see Roberts, L. D.)—1018
Fleeman, J. and G. J. Dienes. Effect of reactor irradiation on the white-to-grey tin transformation—652
Flom, D. G. and N. T. Porile. Friction of teflon sliding on teflon—1088
Flügge-Lotz, I. and W. S. Wunch. On a nonlinear transfer system—484
Ford, C. A. and I. I. Glass. Erratum: On the interaction of two similarly facing plane shock waves—643(L)
Forman, R. Properties of pore conductors—1187(L)
Forster, M. J. Unilateral compression of rubber—1104
Fowler, A. and P. Levesque. Optical determination of base width in grown *n-p-n* silicon crystals—641(L)
Fox, R. H. Extension of nonreciprocal ferrite devices to the 500–3000 megacycle frequency range—128(L)
Fox, T. G. and S. Loshaek. Isothermal viscosity-molecular weight dependence for long polymer chains—1080
Frank, F. C. and K. E. Puttick. Comments on "Transformations in plain carbon steels"—1522(L)
Freeman, J. J. On power spectra and the minimum detectable signal in measurement systems—236
Frei, E. H. (see Aharoni, A.)—1411
Friedman, A. S. (see Michels, A.)—843
Friedmann, N. E. Analog methods for study of transient heat flow in solids with temperature-dependent thermal properties—129(L)
—— Erratum: Analog methods for study of transient flow in solids with temperature-dependent thermal properties—783(L)
Friedrichs, K. O. and J. B. Keller. Geometrical acoustics. II. Diffraction, reflection, and refraction of a weak spherical or cylindrical shock at a plane interface—961
Furney, L. C. (see Zinn, W. H.)—1286

Gans, Paul (see Hoyaux, Max)—110
Garwin, R. L. (see Anderson, A. G.)—1324
Gebbie, H. A. (see Maple, T. G.)—490(L)
George, T. H. (see Farnsworth, H. E.)—252(L)
Germer, L. H. (see Boyle, W. S.)—571
—— (see Boyle, W. S.)—720
Gianola, U. F. Application of the Wiedemann effect to the magnetostrictive coupling of crossed coils—1152
Gibbons, M. D. (see Stout, V. L.)—1488
Gittings, E. F. (see Goranson, R. W.)—1472
Given, F. I. (see Evans, M. W.)—1111
Glass, I. I. (see Ford, C. A.)—643(L)
—— **and W. A. Martin.** Experimental and theoretical aspects of shock-wave attenuation—113
—— **and W. A. Martin.** Errata: Experimental and theoretical aspects of shock-wave attenuation—1187(L)
Glick, H. S. (see Petschek, H. E.)—83
Gold, Louis. On the diffusion of decaying particles—233
—— Errata: Relativistic dynamics of a charged particle in crossed magnetic and electric fields with application to the planar magnetron—253(L)
Goldsmith, W. (see Allen, W. A.)—69
Goldstein, M. and E. R. Michalik. Theory of scattering by an inhomogeneous solid possessing fluctuations in density of anisotropy—1450
Goodenough, J. B. (see Menyuk, N.)—8
Goranson, R. W., D. Bancroft, B. L. Burton, T. Blechar, E. E. Houston, E. F. Gittings, and S. A. Landeen. Dynamic determination of the compressibility of metals—1472
Gossick, B. R. On the transient behavior of semiconductor rectifiers—1356
Goswami, A. (see Finch, G. I.)—250(L)
Granneman, W. W. and R. B. Watson. Diffraction of electromagnetic waves by a metallic wedge of acute dihedral angle—392
Green, W. B. Conduction and breakdown in hexane—1257
Groetzinger, G. (see Wiener, B.)—609
—— (see Wiener, B.)—857
Guldner, W. G. (see Wooten, L. A.)—937
Gunn, J. B. and C. A. Hogarth. Novel microwave attenuator using germanium—353(L)
Gurnee, E. F. Solution of an integral equation arising in optical studies of oriented filaments—918(L)
——, **L. T. Patterson, and R. D. Andrews.** Apparatus for making simultaneous stress and birefringence measurements on polymers—1106

Hagstrum, H. D. Apparatus for studying electron ejection from metals by positive ions—256
Hahn, E. L. (see Anderson, A. G.)—1324
Hall, J. G. Transition through a contact region—698
Haneman, D. Barkhausen noise from a cylindrical core—355(L)
Hannay, N. B. (see Tanenbaum, M.)—686
Hanson, G. H. Shot noise in *p-n-p* transistors—1388(L)
Haus, H. A. Noise in one-dimensional electron beams—560
Heaps, H. S. (see Cook, E. O.)—429

Heidenreich, R. D. Thermionic emission microscopy of metals. I. General—757
—— Thermionic emission microscopy of metals. II. Transformations in plain carbon steels—879
—— **and K. H. Storks.** Note on electron diffraction patterns of CuO—1056(L)
Held, G. (see Ehrlich, M. J.)—336
Hendricks, C. D., Jr. (see Van Valkenburg, M. E.)—776(L)
Henke, B. L. and J. W. M. DuMond. Submicroscopic structure determination by long wavelength x-ray diffraction—903
Hernqvist, K. G. Plasma ion oscillations in electron beams—544
—— Plasma oscillations in electron beams—1029
Heybey, W. H. and S. G. Reed, Jr. Weak detonations and condensation shocks—969
Heyn, A. N. J. Small particle x-ray scattering by fibers, size and shape of microcrystallites—519
—— Small particle x-ray scattering by fibers. II. Radial distribution of microcrystallites—1113
Hill, J. E. (see Roberts, L. D.)—1018
——, **L. D. Roberts, and T. E. Fitch.** Slowing down distribution of U^{235} fission neutrons from a point source in light water—1013
Hines, M. E., G. W. Hoffman, and J. A. Saloom. Positive-ion drainage in magnetically focused electron beams—1157
Hirshfield, Jay L. and C. M. Zieman. Measurement of microwave diffraction from a long slit in a thin conducting plane—135
Hochman, R. F. (see Kuczynski, G. C.)—871
Hoffman, G. W. (see Hines, M. E.)—1157
Hogarth, C. A. (see Gunn, J. B.)—353(L)
Hogg, D. C. (see Buchsbaum, S. J.)—706
Holmes, D. K. (see Thompson, D. O.)—1188(L)
Holonyak, Nick, Jr. Observation of circular patterns in the vicinity of small-area alloyed germanium *p-n* junctions—121
—— **and Harry Letaw, Jr.** Sparked hydrogen treatment of germanium surfaces—355(L)
Horowitz, G. (see Aharoni, A.)—1411
Horowitz, M. (see Tomlinson, N. P.)—229
Horton, J. W. (see Anderson, A. G.)—1324
Houston, E. E. (see Goranson, R. W.)—1472
Hoyaux, M., R. Lemaitre, and Paul Gans. Theory and probe measurements in a magnetic ion source—110
Huang, C., R. D. Kodis, and H. Levine. Diffraction by apertures—151
Hughes, D. S. and J. M. Kennel. Variation of elastic wave velocity with frequency in fused quartz and Armco iron—1307
Hunt, F. V. Elastic-plastic instability caused by the size effect and its influence on rubbing wear—850
Hurwitz, H., Jr. (see Dwork, J. S.)—642(L)
—— **and P. F. Zweifel.** Slowing down of neutrons by hydrogenous moderators—923

Ivory, J. E. (see Baldwin, F. P.)—750

Jan, J.-P. Small-angle x-ray scattering from precipitates in cold-worked Al-Ag and Al-Zn—1291
Jeppson, M. R., R. L. Mather, A. Andrew, and H. P. Yockey. Creep of aluminum under cyclotron irradiation—365
Johnstone, H. F. (see Wong, J. B.)—244
Jones, E. M. T. and S. B. Cohn. Surface matching of dielectric lenses—452
Jones, N. T., R. H. Kingston, and S. F. Neustadter. Anomalous forward switching transient in *p-n* junction diodes—210
Judson, L. V. Units of weight and measure—definitions and tables of equivalents—1284
Jupnik, H. (see Creutz, E.)—257, 271, and 276
—— (see Wigner, E. P.)—260

Kammerer, O. F. (see Levy, P. W.)—1182(L)
Kane, Anne (see Petschek, H. E.)—83
Kane, E. O. Thermionic emission from semiconductors—784
Kantrowitz, A. (see Lin, Shao-Chi)—95
—— (see Petscheck, H. E.)—83
Kaplan, D. E. (see Venable, D.)—639(L)
Karasek, F. W. (see Wherry, T. C.)—682
Keating, D. T. and J. J. Antal. Correlation of diffraction and transmission experiments for x-ray and neutron elastic scattering—1041
Keller, J. B. (see Friedrichs, K. O.)—961
Kennedy, W. D. (see Watson, M. T.)—701
Kennel, J. M. (see Hughes, D. S.)—1307
Kerr, J. and C. Wert. Effect of nitrides on the coercive force of iron—1147
Keyes, R. J. (see Stevenson, D. T.)—190
Khosla, G. (see Findley, Wm. N.)—821
King, Ronold. Gap problem in antenna theory—317
Kingery, W. D. and M. Berg. Study of the initial stages of sintering solids by viscous flow, evaporation-condensation, and self-diffusion—1205
Kingston, R. H. (see Jones, N. T.)—210
—— **and S. F. Neustadter.** Calculation of the space charge, electric field, and free carrier concentration at the surface of a semiconductor—718
Kisliuk, P. (see Boyle, W. S.)—720
Kitchen, S. W. and A. D. Schelberg. Resonant-cavity field measurements—618
Klemperer, O. (see Dolder, K. T.)—1461
Kodis, R. D. (see Huang, C.)—151
Kolb, E. D. (see Bridgers, H. E.)—1188(L)
Kovasznay, L. S. G. (see Uberoi, M. S.)—19
Krafft, J. M. Surface friction in ballistic penetration—1248
Kraus, J. D. Radio map of the center of the galaxy—494
Krumhansl, J. A. (see Bowman, J. C.)—1057(L)
Kubu, E. T. (see McMickle, R. H.)—832
Kuczynski, G. C., R. F. Hochman, and M. Doyama. Study of the kinetics of ordering in the alloy AuCu—871

LaBerge, W. B., R. J. Munick, J. A. Dezoteux, J. F. Whalen, and E. A. Coomes. Patch effect for the thermionic emission from polycrystalline tantalum—241
Laitone, E. V. Comments on limiting pressure on hydrofoils—1519(L)
Landauer, J. K. Stress-strain relations in snow under uniaxial compression—1493
Landeen, S. A. (see Goranson, R. W.)—1472
Landel, R. F. (see Ferry, J. D.)—359
Latter, R. Similarity solution for a spherical shock wave—954
Law, J. T. and P. S. Meigs. Effect of water vapor on grown germanium and silicon *np* junction units—1265
Lax, B. Figure of merit for microwave ferrites at low and high frequencies—919(L)
—— **and K. J. Button.** Theory of new ferrite modes in rectangular wave guide—1184(L)
—— **and K. J. Button.** New ferrite mode configurations and their applications—1186(L)

Leach, J. S. L., E. G. Loewen, and M. B. Bever. Energy relations in cold working an alloy at 78°K and at room temperature—728
LeCraw, R. C. (see Spencer, E. G.)—250(L)
—— (see Spencer, E. G.)—354(L)
—— (see Sullivan, R. F.)—1282(L)
—— **and H. B. Bruns.** Time delay in high-speed ferrite microwave switches—124(L)
Lee, E. H. (see Bland, D. R.)—1497
Lehovec, Kurt. "Gate modulation" of electromagnetic radiation—495
Lemaitre, R. (see Hoyaux, Max)—110
Letaw, Harry, Jr. (see Holonyak, Nick, Jr.)—355(L)
Levesque, P. (see Fowler, A.)—641(L)
Levi, Roberto. Improved "impregnated cathode"—639(L)
Levine, H. (see Huang, C.)—151
Levy, P. W. and O. F. Kammerer. "Spiral polygon" tin whiskers—1182(L)
Lewis, T. J. High field electron emission from irregular cathode surfaces—1405
Li, Yin-Yuan and R. Smoluchowski. Small-angle scattering and surface structure—128(L)
Lieberman, D. S., M. S. Wechsler, and T. A. Read. Cubic to orthorhombic diffusionless phase change—experimental and theoretical studies of AuCd—473
Lin, Shao-Chi, E. L. Resler, and A. Kantrowitz. Electrical conductivity of highly ionized argon produced by shock waves—95
Linhart, J. G. Čerenkov radiation of electrons moving parallel to a dielectric boundary—527
Linnenbom, V., M. Tetenbaum, and C. Cheek. Tracer diffusion of iron in stainless steel—932
Litovitz, T. A. and E. H. Carnevale. Effect of pressure on sound propagation in water—816
Loashaek, S. (see Fox, T. G.)—1080
Loewen, E. G. (see Leach, J. S. L.)—728
Logan, R. A. and M. Schwartz. Restoration of resistivity and lifetime in heat treated germanium—1287
Luborsky, F. E. (see Mendelsohn, L. I.)—1274

Maffett, A. L. (see Siegel, K. M.)—297
Mallory, H. D. Propagation of shock waves in aluminum—555
Mallory, K. B. (see Motz, H.)—1384(L)
Mandelkern, L. Crystallization kinetics in high polymers. II. Polymer-diluent mixtures—443
—— (see Newton, C. J.)—1521(L)
Manson, J. E. X-ray diffraction study of silver iodide aerosols—423
—— Preferred orientation of platelets in x-ray diffractometer powder samples—1254
Mapes, J. M. (see Allen, Wm. A.)—125(L)
—— (see Allen, Wm. A.)—1173
Maple, T. G., L. Bess, and H. A. Gebbie. Variation of noise with ambient in germanium filaments—490(L)
Mapother, D. E., and J. N. Snyder. Axial variation of the magnetic field in solenoids of finite thickness—784
Maron, S. H. and R. J. Belner. A low shear capillary viscometer with continuously varying pressure head—1457
Martin, L. H. (see Arthurs, E.)—58
Martin, W. A. (see Glass, I. I.)—113
—— (see Glass, I. I.)—1187(L)
Mather, R. L. (see Jeppson, M. R.)—365
Mayer, L. On electron mirror microscopy—1228
Mayfield, E. B. (see Allen, Wm. A.)—125(L)
—— (see Allen, Wm. A.)—1173
McCollum, R. (see Wiener, B.)—857
McMickle, R. H. and E. T. Kubu. Diffusion controlled stress relaxation—832
McSkimin, H. J. Measurement of the elastic constants of single crystal cobalt—406
Meader, A. L., Jr. (see Criddle, D. W.)—838
Meigs, P. S. (see Law, J. T.)—1265
Mendelsohn, L. I., F. E. Luborsky, and T. O. Paine. Permanent-magnet properties of elongated single-domain iron particles—1274
Menyuk, N. Magnetic materials for digital computer components. II. Magnetic characteristics of ultra-thin molybdenum-permalloy cores—692
—— **and J. B. Goodenough.** Magnetic materials for digital-computer components. I. A theory of flux reversal in polycrystalline ferromagnetics—8
Merz, W. J. (see Anderson, J. R.)—1387(L)
Michalik, E. R. (see Goldstein, M.)—1450
Michels, A., J. A. M. Cox, A. Botzen, and A. S. Friedman. Contribution to the study of transport phenomena in gases at high densities—843
Milne, A. R. (see Buchsbaum, S. J.)—706
Mindlin, R. D. and H. Deresiewicz. Thickness-shear and flexural vibrations of rectangular crystal plates—1435
Minnick, R. C. and R. L. Ashenhurst. Multiple coincidence magnetic storage systems—575
Minshall, Stanley. Properties of elastic and plastic waves determined by pin contactors and crystals—463
Mitani, H. (see Takakura, T.)—185
Mitchell, F. H. and R. N. Whitehurst. Further remarks on the odd ball problem as an example in information theory—778(L)
Montgomery, D. J. (see Stauff, D. W.)—540
—— (see Wakelin, J. H.)—786
Moore, G. E. (see Wooten, L. A.)—44
—— (see Wooten, L. A.)—937
——, **L. A. Wooten, and J. Morrison.** Excess Ba content of practical oxide coated cathodes and thermionic emission—943
Morris, G. J. (see Cook, M. A.)—426
Morrish, A. H. and S. P. Yu. Dependence of the coercive force on the density of some iron oxide powders—1049
Morrison, J. (see Moore, G. E.)—943
—— **and R. B. Zetterstrom.** Barium getters in carbon monoxide—437
Motz, H. and K. B. Mallory. Generation of submillimeter waves—1384(L)
Müller, E. W. Work function of tungsten single crystal planes measured by the field emission microscope—732
Munick, R. J. (see LaBerge, W. B.)—241
Muss, D. R. Capacitance measurements on alloyed indium-germanium junction diodes—1514

Nedderman, H. C. Space-charge distribution in a static magnetron—1420
Nesbitt, E. A. and H. J. Williams. Shape and crystal anisotropy of Alnico 5—1217
Neustadter, S. F. (see Jones, N. T.)—210
—— (see Kingston, R. H.)—718
Newton, C. J., L. Mandelkern, and D. E. Roberts. Preferred orientation in stark rubber studied with an automatic integrating pole figure goniometer—1521(L)
Newkirk, J. B. and D. Turnbull. Nucleation of ammonium iodide crystals from aqueous solutions—579
Nichols, James L. Orientation and temperature effects on the electrical resistivity of high-purity magnesium—470
Nilan, T. G. (see Paxton, W. S.)—994
Nowick, A. S. (see Damask, A. C.)—1165
Nunogaki, K. (see Takakura, T.)—185

Ohlberg, S. (see Alexander, L. E.)—1068
Oliner, A. A. and H. M. Altschuler. Methods of measuring dielectric constants based upon a microwave network viewpoint—214
O'Neill, G. D. On the space-charge-limited current between nonsymmetrical electrodes—1034; erratum, 1522
Orowan, E. Condition of high-velocity ductile fracture—900
Otter, F. A. (see Domenicali, C. A.)—377

Paine, T. O. (see Mendelsohn, L. I.)—1274
Pao, Yoh-Han. Extension of the Hertz theory of impact to the viscoelastic case—1083
Patterson, L. T. (see Gurnee, E. F.)—1106
Paxton, W. S. and T. G. Nilan. Domain configurations and crystallographic orientation in grain-oriented silicon steel —994
Pearson, J. and J. S. Rinehart. Application of the engravement method to the study of particle velocity distribution in explosively loaded cylinders—1431
Pell, E. M. Reverse current and carrier lifetime as a function of temperature in germanium junction diodes—658
Perkins, J. F. Monte Carlo calculation of gamma-ray albedos of concrete and aluminum—655
—— Some Monte Carlo calculations of gamma-ray penetrations—1372
Petschek, H. E., P. H. Rose, H. S. Glick, Anne Kane, and A. Kantrowitz. Spectroscopic studies of highly ionized argon produced by shock waves—83
Philippoff, W. and J. Brodnyan. Preliminary results in measuring dynamic compressibilities—846
Pierce, J. R. Interaction of moving charges with wave circuits—627
Poole, K. M. Emission from hollow cathodes—1176
Porile, N. T. (see Flom, D. G.)—1088
Powers, D. A. and T. Suita. Prebreakdown current and noise in insulators—1244
Prince, M. B.—Silicon solar energy converters—534
Proctor, W. G. (see Fernbach, S.)—170
Puckett, H. R., Jr. (see Skolnik, M. I.)—74
Purl, O. T. and H. M. VonFoerster. Velocity spectrography of electron dynamics in a traveling field—351(L)
Puttick, K. E. (see Frank, F. C.)—1522(L)

Ranz, W. E. (see Wong, J. B.)—244
Read, T. A. (see Lieberman, D. S.)—473
Ree, T. and H. Eyring. Theory of non-Newtonian flow. I. Solid plastic system—793; II. Solution system of high polymers—800
Reed, S. G., Jr. (see Heybey, W. H.)—969
Reggia, F. (see Spencer, E. G.)—354(L)
Remeika, J. P. (see Anderson, J. R.)—1387(L)
Resler, E. L. (see Lin, Shao-Chi)—95
Rexer, E. F. (see Balas, W.)—1163
Reynolds, C. H. (see Tomlinson, N. P.)—229
Richeson, W. E., Jr. (see Evans, M. W.)—1111
Rinehart, J. S. Deformation of an explosively loaded aluminum single crystal—1315
—— Guide to the successful propulsion of a solid object by an explosive charge—1518(L)
—— (see Pearson, J.)—1431
Roberts, D. E. (see Newton, C. J.)—1521(L)
Roberts, L. D. (see Hill, J. E.)—1013
——, **J. E. Hill, and T. E. Fitch.** Slowing distribution to indium resonance of U^{235} fission neutrons from a point fission source in two aluminum light water mixtures—1018
Robinson, L. B. Effect of delayed fission neutrons on reactor kinetics—52
Rodbell, D. S. (see Bean, C. P.)—124(L)
—— **and C. P. Bean.** Influence of pulsed magnetic fields on the reversal of magnetization in square-loop metallic tapes —1318
Rogosa, G. L. and G. Schwarz. X-ray path through calcite in Laue diffraction—967
Rome, Martin. Relation of antimony transmission and the photoelectric yield of Cs-Sb—166
Rose, P. H. (see Petscheck, H. E.)—83
Rosenblatt, D. B., R. Smoluchowski, and G. J. Dienes. Radiation induced changes in the electrical resistivity of α brass—1044
Rottgardt, K. H. J. and W. Berthold. Sticking potential of CRT screens—1180(L)
Row, R. V. Theoretical and experimental study of electromagnetic scattering by two identical conducting cylinders —666
Rudinger, G. On the reflection of shock waves from an open end of a duct—981
—— Improved wave diagram procedure for shock reflection from an open end of a duct—1339
Ruehle, A. E. (see Wooten, L. A.)—44

Saloom, J. A. (see Hines, M. E.)—1157
Schaefer, D. L. (see Dunkerley, H. S.)—1384(L)
Schelberg, A. D. (see Kitchen, S. W.)—618
Schelkunoff, S. A. On representation of electromagnetic fields in cavities in terms of natural modes of oscillation —1231
Schensted, C. E. Electromagnetic and acoustic scattering by a semi-infinite body of revolution—306
—— (see Siegel, K. M.)—297 and 309
Schensted, I. V. (see Siegel, K. M.)—297
Schlier, R. E. (see Farnsworth, H. E.)—252(L)
Schoening, F. R. L. and J. N. van Niekerk. X-ray measurements of particle size and strain distribution in cold worked silver—726
Schultheis, P. M. (see Steinberg, H.)—195
Schwartz, M. Method for obtaining complete quantitative pole figures for flat sheets using one sample and one sample holder—1507
—— (see Logan, R. A.)—1287
Schwarz, G. (see Rogosa, G. L.)—967
Schwarz, R. F. (see Borneman, E. H.)—1021
Schwed, P. (see Wiener, B.)—609
Seliger, H. H. (see Ziegler, C. A.)—1225
Sellars, John R. Laminar flow in channels with porous walls at high suction Reynolds numbers—489(L)
Sharbaugh, A. H., J. K. Bragg, and R. W. Crowe. Dependence of the electric strengths of liquids on electrode spacing—434
Shaw, T. M. and R. H. Elsken. Techniques for nuclear magnetic resonance measurements on granular hygroscopic materials—313
Shmoys, J. Propagation in semi-infinite wave guides—1284
Shulman, R. G. (see Spitzer, Wm. G.)—414
Sicinski, H. S., N. W. Spencer, and W. G. Dow. Erratum: Rocket measurements of upper atmosphere ambient temperature and pressure in the 30- to 75-kilometer region —1284(L)
Siegel, K. M., H. A. Alperin, R. R. Bonkowski, J. W. Crispin, A. L. Maffett, C. E. Schensted, and I. V. Schensted. Bistatic radar cross section of surfaces of revolution—297
——, **J. W. Crispin, and C. E. Schensted.** Electromagnetic and acoustical scattering from a semi-infinite cone—309
Silver, S. (see Ehrlich, M. J.)—336
Sinha, K. P. (see Finch, G. I.)—250(L)

Sirkis, M. D. (see Coleman, P. D.)—1385(L)
Skinner, S. M. Diffusion, static charges, and the conduction of electricity in nonmetallic solids by a single charge carrier. I. Electric charges in plastics and insulating materials—498
—— Diffusion, static charges, and the conduction of electricity in nonmetallic solids by a single charge carrier. II. Solution of the rectifier equations for insulating layers—509
Skolnik, M. I. and H. R. Puckett, Jr. Relaxation oscillations and noise from low-current arc discharges—74
Skulski, R. W. and D. Weimer. Reflection of a compression wave from a symmetrical wedge—1344
Slepian, J. Failure of the ionic centrifuge prior to the ionic expander—1283(L)
Slichter, W. P. Proton magnetic resonance in polyamides—1099
Smoluchowski, R. (see Li, Yin-Yuan)—128(L)
—— (see Burgess, H.)—491(L)
—— (see Rosenblatt, D. B.)—1044
Snyder, J. N. (see Mapother, D. E.)—784
Snyder, T. (see Creutz, E.)—257 and 271
—— (see Wigner, E. P.)—260
Solomon, S. S. Space-charge waves in crossed electric and magnetic fields—1443
Spencer, N. W. (see Sicinski, H. S.)—1284(L)
Spencer, E. G. and R. C. LeCraw. Wall effects on microwave measurements of ferrite spheres—250(L)
——, **R. C. LeCraw, and F. Reggia.** Circularly polarized cavities for measurement of tensor permeabilities—354(L)
Spinrad, B. I. Anisotropic diffusion lengths in diffusion theory—548
Spitzer, Wm. G., T. E. Firle, M. Cutler, R. G. Shulman, and M. Becker. Measurement of the lifetime of minority carriers in germanium—414
Sponsler, G. C. Trajectory-tracer study of helix- and band-type postdeflection acceleration—676
Stauff, D. W. and D. J. Montgomery. Effect of air damping on transverse vibrations of stretched filaments—540
Stebbins, D. W. (see Decker, R. W.)—1004
Steele, H. L., Jr. Wattage lost in a fluorescent lamp through elastic collisions—1183(L)
Steinberg, H., P. M. Schultheiss, C. A. Wogrin, and F. Zweig. Short-time frequency measurement of narrow-band random signals by means of a zero counting process—195
Stevenson, D. T. and R. J. Keyes. Measurement of carrier lifetimes in germanium and silicon—190
Stewart, John L. Theory of frequency modulation noise in tubes employing phase focusing—409
Stickler, J. J. (see Borneman, E. H.)—1021
Stock, J. R. (see Bowman, J. C.)—1057(L)
Storks, K. H. (see Heidenreich, R. D.)—1056(L)
Stout, V. L. and M. D. Gibbons. Gettering of gas by titanium—1488
Stripp, K. F. and R. H. Bube. Effect of superposing a small alternating excitation on the steady excitation of a luminescent material—251(L)
Stuart, M. R. Dielectric constant of quartz as a function of frequency and temperature—1399
Suhl, H., L. G. Van Uitert, and J. L. Davis. Ferromagnetic resonance in magnesium-manganese aluminum ferrite between 160 and 1900 Mc—1180(L); erratum, 1523
Suita, T. (see Powers, D. A.)—1244
Sullivan, R. F. and R. C. LeCraw. New type ferrite microwave switch—1282(L)
Swanson, D. L. and J. W. Williams. Effect of molecular weight distribution on the creep behavior of cellulose acetate—810
Takakura, T., K. Baba, K. Nunogaki, and H. Mitani. Radiation of plasma noise from arc discharge—185
Tanenbaum, M., L. B. Valdes, E. Buehler, and N. B. Hannay. Silicon *n-p-n* grown junction transistors—686
Tannenwald, L. M. Asymptotic spherical shock decay—551
Tannenwald, P. E. (see Artman, J. O.)—1124
Taylor, G. R. (see Alexander, L. E.)—1068
—— **and S. R. Darin.** Birefringence and crystallization in elastomers—1075
Tetenbaum, M. (see Linnenbom, V.)—932
Theus, R. B., L. A. Beach, and W. R. Faust. Analysis of scintillation spectrometer observations of the penetration of Cs^{137} gamma radiation through water—294
Thompson, D. O. Temperature dependent creep in zinc crystals—280
——, **D. K. Holmes, and T. H. Blewitt.** Neutron irradiation effects upon Young's Modulus and internal friction of copper—1188(L)
Thomsen, E. G., C. T. Yang, and J. B. Bierbower. An experimental investigation of the mechanics of plastic deformation of metals—920
Thomson, W. T. Approximate theory of armor penetration—80
—— Note on "An approximate theory of armor penetration"—919(L)
Tittman, Jay. Moderation of neutrons in SiO_2 and $CaCO_3$—394
Todd, B. J. Outgassing of glass—1238
Tomlinson, N. P., M. Horowitz, and C. H. Reynolds. Analog computer construction of conformal maps in fluid dynamics—229
Truby, F. K. Hexagonal microstructure of ice crystals grown from the melt—1416
Trump, J. G. (see Bourne, H. C., Jr.)—596
Tucker, G. L. (see Anderson, A. G.)—1324
Turley, J. W. (see Comer, J. J.)—346
Turnbull, D. (see Newkirk, J. B.)—579
Twiss, R. Q. Nyquist's and Thevenin's theorems generalized for nonreciprocal linear networks—599
Tyler, R. W., J. H. Webb, and W. C. York. Measurements of electrical polarization in thin dielectric materials—61
Tyndall, E. P. T., R. A. Artman, C. A. Wert, and R. Eisner. Creep of zinc crystals—286

Uberoi, M. S. and L. S. G. Kovasznay. Analysis of turbulent density fluctuations by the shadow method—19

Valdes, L. B. (see Tanenbaum, M.)—686
Vand, V. Methods for the correction of x-ray intensities for primary and secondary extinction in crystal structure analysis—1191
Vanderhoff, J. W. (see Bradford, E. B.)—864
van Niekerk, J. N. (see Schoening, F. R. L.)—726
van Roosbroeck, W. Injected current carrier transport in a semi-infinite semiconductor and the determination of lifetimes and surface recombination velocities—380
Van Uitert, L. G. Low magnetic saturation ferrites for microwave applications—1289
—— (see Suhl, H.)—1180(L); erratum, 1523
Van Valkenburg, M. E. and C. D. Hendricks, Jr. Method for producing high-velocity metallic and plastic pellets—776(L)
Varnerin, L. J., Jr., and J. H. Carmichael. Ionic pumping mechanism of helium in an ionization gauge—782(L)
Venable, D. and D. E. Kaplan. Electron beam method of determining density profiles across shock waves in gases at low densities—639(L)

Vermilyea, D. A. Growth of anodic Ta_2O_5 films during illumination with ultraviolet light—489(L)
Volkin, H. C. Effect of asymmetric oxygen scattering on the slowing-down length of neutrons in water—127(L)
VonFoerster, H. (see Ernst, E. W.)—781(L)
—— (see Purl, O. T.)—351(L)
Voong, E. T. L. (see Wakelin, J. H.)—786

Wainfan, N. (see Walker, W. C.)—1366
Wait, James R. Field produced by an arbitrary slot on an elliptic cylinder—458
Wakelin, J. H., E. T. L. Voong, D. J. Montgomery, and J. H. Dusenbury. Vibroscope measurements of the elastic moduli of nylon 66 and dacron filaments of various draw ratios—786
Walker, L. R. Generalizations of Brillouin flow—780(L)
—— Power flow in electron beams—1031
Walker, R. M. (see Anderson, A. G.)—1324
Walker, W. C., N. Wainfan, and G. L. Weissler. Photoelectric yields in the vacuum ultraviolet—1366
Watkins, D. A. Noise at the potential minimum in the high-frequency diode—622
Watson, M. T., W. D. Kennedy, and G. M. Armstrong. Short-time stress relaxation behavior of plastics—701
Watson, R. B. (see Granneman, W. W.)—392
Wax, Nelson. Signal-to-noise improvement and the statistics of track populations—586
Wayland, H. Streaming birefringence as a hydrodynamic research tool—applied to a rotating cylinder apparatus above the transition velocity—1197
Webb, J. H. Ultrashort light and voltage pulses applied to silver halide crystals by turbine-driven mirror and spark-gap switch—1309
—— (see Tyler, R. W.)—61
Webster, H. F. Breakup of hollow electron beams—1386(L)
Wechsler, M. S. (see Lieberman, D. S.)—473
Weertman, J. Internal friction of metal single crystals—202
—— Theory of steady-state creep based on dislocation climb—1213
Wehner, G. K. Sputtering of metal single crystals by ion bombardment—1056(L)
Weimer, D. (see Skulski, R. W.)—1344
Weissler, G. L. (see Walker, W. C.)—1366
Wert, C. Internal friction of an alloy of 16 percent aluminum in iron—640(L)
—— (see Kerr, J.)—1147
—— (see Tyndall, E. P. T.)—286
Whalen, J. F. (see LaBerge, W. B.)—241
Wherry, T. C. and F. W. Karasek. Performance of the nonmagnetic radio-frequency mass spectrometer tube—682
Whitehurst, R. N. (see Mitchell, F. H.)—778(L)
Whitwell, J. C. (see Cram, K. H.)—613
Wieder, H. H. Ferroelectric hysteresis in barium titanate single crystals—1479
Wiener, B., G. Groetzinger, and R. McCollum. Specification of thermally and mechanically induced nonequilibrium states in AuCu by the resistivity and magnetoresistivity —857
——, **P. Schwed, and G. Groetzinger.** Variation of magnetoresistivity of AuCu with degree of order—609
Wigner, E. P. (see Creutz, E.)—257, 271, and 276
——, **Creutz, H. Jupnik, and T. Snyder.** Resonance absorption of neutrons by spheres—260
Williams, F. E. and D. A. Cusano. Light amplifier—358
Williams, H. J. (see Nesbitt, E. A.)—1217
Wiliams, J. W. (see Swanson, D. L.)—810
Williams, M. L. (see Ferry, J. D.)—359
Winston, H. (see Firle, T. E.)—716
Wogrin, C. A. (see Steinberg, H.)—195
Wong, J. B., W. E. Ranz, and H. F. Johnstone. Inertial impaction of aerosol particles on cylinders—244
Woonton, G. A. (see Buchsbaum, S. J.)—706
Wooten, L. A. (see Moore, G. E.)—943
——, **G. E. Moore, and W. G. Guldner.** Measurement of excess Ba in practical oxide coated cathodes—937
——, **A. E. Ruehle, and G. E. Moore.** Evaporation of barium and strontium from oxide-coated cathodes—44
Wunch, W. S. (see Flügge-Lotz, I.)—484

Yadavalli, S. V. Cross correlation between velocity and current fluctuations in tube noise—605
—— Erratum: Cross correlation between velocity and current fluctuations in tube noise—1523(L)
Yang, C. T. (see Thomsen, E. G.)—920
Yockey, H. P. (see Jeppson, M. R.)—365
York, W. C. (see Tyler, R. W.)—61
Young, F. W., Jr. Oxidized copper single crystal sphere—644
Young, J. R. Deterioration of luminescent phosphors under positive ion bombardment—1302
Yu, S. P. (see Morrish, A. H.)—1049

Zetterstrom, R. B. (see Morrison, J.)—437
Ziegler, C. A. and H. H. Seliger. Hysteresis effect in multiplier phototube noise—1225
Zieman, C. M. (see Hirshfield, Jay L.)—135
Zimmermann, F. J. Total emissivities and absorptivities of some commercial surfaces at room and liquid-nitrogen temperatures—1483
Zinn, W. H. and L. C. Furney. Intentional explosion of a nuclear reactor—1286
Zweifel, P. F. (see Hurwitz, H., Jr.)—923
Zweig, F. (see Steinberg, H.)—195
Zwicker, Earl (see Dunkuls, Annija)—779(L)

Subject Index to Volume 26

(References with (L) are to Letters to the Editor)

Announcements—134, 256, 358, 494, 644, 715, 1060, 1390, 1524

Antennas

Field produced by an arbitrary slot on an elliptic cylinder, James R. Wait—458

Gap problems in antenna theory, Ronold King—317

Measurement of microwave diffraction from a long slit in a thin conducting plane, Jay L. Hirshfield and C. M. Zieman—135

Radiation characteristics of a conical helix of low pitch angle, J. S. Chatterjee—331

Surface matching of dielectric lenses, E. M. T. Jones and S. B. Cohn—452

Wide-angle radiation in pencil beam antennas, David Carter—645

Ballistics

Approximate theory of armor penetration. W. T. Thomson—80

Approximate theory of armor penetration. W. T. Thomson—919(L)

Flash associated with high-velocity impact on aluminum, W. W. Atkins—126(L)

Surface friction in ballistic penetration, J. M. Krafft—1248

Colloids

Inertial impaction of aerosol particles on cylinders, J. B. Wong, W. E. Ranz, and H. F. Johnstone—244

X-ray diffraction study of silver iodide aerosols, James E. Manson—423

Computing Techniques and Machines

Basic circuitry of the MIDAC and MIDSAC, University of Michigan Press—643

Magnetic materials for digital-computer components. I. Theory of flux reversal in polycrystalline ferromagnetics, N. Menyuk and J. B. Goodenough—8

Magnetic materials for digital computer components. II. Magnetic characteristics of ultra-thin molybdenum-permalloy cores, Norman Menyuk—692

Multiple coincidence magnetic storage systems, R. C. Minnick and R. L. Ashenhurst—575

Spin-echo memory device, S. Fernbach and W. G. Proctor—170

Spin echo serial storage memory, A. G. Anderson, R. L. Garwin, E. L. Hahn, J. W. Horton, G. L. Tucker, and R. M. Walker—1324

Crystals and Crystal Growth

Hexagonal microstructure of ice crystals grown from the melt, F. K. Truby—1416

Nucleation of ammonium iodide crystals from aqueous solutions, J. B. Newkirk and D. Turnbull—579

Nucleation of lead with preferred orientation, H. A. Atwater and B. Chalmers—918(L)

Nucleation of lead with preferred orientation, H. A. Atwater and B. Chalmers—1284 (erratum)

Rate-grown germanium crystal for high-frequency transistors, H. E. Bridgers and E. D. Kolb—1188(L)

"Spiral polygon" tin whiskers, P. W. Levy and O. F. Kammerer—1182(L)

Dielectrics and Dielectric Breakdown in Insulators

Conduction and breakdown in hexane, W. B. Green—1257

Dependence of the electric strengths of liquids on electrode spacing, A. H. Sharbough, J. K. Bragg, and R. W. Crowe—434

Dielectric constant of quartz as a function of frequency and temperature, M. R. Stuart—1399

Diffusion, static charges, and the conduction of electricity in nonmetallic solids by a single charge carrier. I. Electric charges in plastics and insulating materials, S. M. Skinner—498

Diffusion, static charges, and the conduction of electricity in nonmetallic solids by a single charge carrier. II. Solution of the rectifier equations for insulating layers, S. M. Skinner—509

Measurements of electrical polarization in thin dielectric materials, R. W. Tyler, J. H. Webb, and W. C. York—61

Methods of measuring dielectric constants based upon a microwave network viewpoint, A. A. Oliner and H. M. Altschuler—214

Prebreakdown current and noise in insulators, D. A. Powers and T. Suita—1244

Ultrashort light and voltage pulses applied to silver halide crystals by turbine-driven mirror and spark-gap switch, J. H. Webb—1309

Diffusion

Diffusion controlled stress relaxation, R. H. McMickle and E. T. Kubu—832

Diffusion of decaying particles, Louis Gold—233

Relation to diffusion measurements of some beta-ray absorption phenomena, A. E. Berkowitz—403

Self-diffusion of nickel, H. Burgess and R. Smoluchowski—491(L)

Study of the initial stages of sintering solids by viscous flow, evaporation-condensation, and self-diffusion, W. D. Kingery and M. Berg—1205

Tracer diffusion of iron in stainless steel, V. Linnenbom, M. Tetenbaum, and C. Cheek—932

Elasticity and Inelasticity

Dynamic determination of the compressibility of metals, R. W. Goranson, D. Bancroft, B. L. Burton, T. Blechar, E. E. Houston, E. F. Gittings, and S. A. Landeen—1472

Elastic constants of germanium between 1.7° and 80°K, M. E. Fine—862

Elastic constants of germanium between 1.7° and 80°K, M. E. Fine—1389 (erratum)

Elastic description of a high-amplitude spherical pulse in steel, W. A. Allen and W. Goldsmith—69

Elastic-plastic instability caused by the size effect and its influence on rubbing wear, F. V. Hunt—850

Experimental examination of the statistical theory of rubber elasticity. Low extension studies, F. P. Baldwin, J. E. Ivory, and R. L. Anthony—750

Internal friction of an alloy of 16 percent aluminum in iron, C. Wert—640(L)

Internal friction of metal single crystals, Johannes Weertman—202

Internal friction peak associated with precipitation in an Al-Ag alloy, A. C. Damask and A. S. Nowick—1165

Measurement of the elastic constants of single crystal cobalt, H. J. McSkimin—406

Neutron irradiation effects upon Young's modulus and internal friction of copper, D. O. Thompson, D. K. Holmes, and T. H. Blewitt—1188(L)

Precise investigation of the theory of damping by transverse thermal currents, B. S. Berry—1221

Properties of elastic and plastic waves determined by pin contactors and crystals, S. Minshall—463

Elasticity and Inelasticity (continued)
Rheological equation of state which predicts non-Newtonian viscosity, normal stresses, and dynamic moduli, T. W. DeWitt—889
Shock waves in air produced by elastic and plastic waves in a plate, Wm. A. Allen, J. M. Mapes, and E. B. Mayfield—125(L)
Stress relaxation in gold wire, O. L. Anderson and P. Andreatch—1518(L)
Stress-strain relations in snow under uniaxial compression, J. K. Landauer—1493
Tensile strength of plastics above the glass temperature, F. Bueche—1133
Theory of elasticity and consolidation for a porous anisotropic solid, M. A. Biot—182
Variation of elastic wave velocity with frequency in fused quartz and Armco iron, D. S. Hughes and J. M. Kennel—1307
Vibroscope measurements of the elastic moduli of nylon 66 and dacron filaments of various draw ratios, J. H. Wakelin, E. T. L. Voong, D. J. Montgomery, and J. H. Dusenbury—786
Viscosity and elasticity of oil surfaces and oil-water interfaces, D. W. Criddle and A. L. Meader, Jr.—838

Electrical Circuits and Networks
Impossible behavior of nonlinear networks, R. J. Duffin—603
Kramers-Kronig relations, M. K. Brachman—497
New active circuit element using the magnetoresistive effects, A. Aharoni, E. H. Frei, and G. Horowitz—1411
Nonlinear transfer system, I. Flügge-Lotz and W. S. Wunch—484
Nyquist's and Thevenin's theorems generalized for nonreciprocal linear networks, R. Q. Twiss—599
Theory and application of gyrator networks, H. J. Carlin—643

Electrical Conductivity
Orientation and temperature effects on the electrical resistivity of high-purity magnesium, James L. Nichols—470
Radiation induced changes in the electrical resistivity of α brass, D. B. Rosenblatt, R. Smoluchowski, and G. J. Dienes—1044
Specification of thermally and mechanically induced nonequilibrium states in AuCu by the resistivity and magnetoresistivity, B. Wiener, G. Groetzinger, and R. McCollum—857
Thermoelectric power and electrical resistivity of dilute alloys of silicon in copper, nickel, and iron, C. A. Domenicali and F. A. Otter—377
Ultrashort light and voltage pulses applied to silver halide crystals by turbine-driven mirror and spark-gap switch, J. H. Webb—1309
Variation of magnetoresistivity of AuCu with degree of order, B. Wiener, P. Schwed, and G. Groetzinger—609

Electrical Contacts
Arcing at electrical contacts on closure. Part VI. The anode mechanism of extremely short arcs, W. S. Boyle and L. H. Germer—571
Collapsed toroidal springs as contact elements in microwave cavities, C. L. Andrews—777(L)
Electrical breakdown in high vacuum, W. S. Boyle, P. Kisliuk, and L. H. Germer—720
Rectification properties of metal semiconductor contacts, E. H. Borneman, R. F. Schwarz, and J. J. Stickler—1021
Self-propagating intermittent discharge, W. S. Boyle—584

Electrical Discharges in Gases
Analysis of electrode phenomena in the high-current arc, J. D. Cobine and E. E. Burger—895
Composition of the interelectrode prebreakdown current in high vacuum, H. C. Bourne, Jr.—625
Electrical conductivity of highly ionized argon produced by shock waves, Shao-Chi Lin, E. L. Resler, and A. Kantrowitz—95
Failure of the ionic centrifuge prior to the ionic expander, J. Slepian—1283(L)
Observations of cathode arc tracks, H. S. Dunkerley and D. L. Schaefer—1384(L)
Radiation of plasma noise from arc discharge, T. Takakura, K. Baba, K. Nunogaki, and H. Mitani—185
Relaxation oscillations and noise from low-current arc discharges, M. I. Skolnik and H. R. Puckett, Jr.—74
Role of positive ions in high-voltage breakdown in vacuum, H. C. Bourne, Jr., R. W. Cloud, and J. G. Trump—596
Self-propagating intermittent discharge, W. S. Boyle—584
Semiempirical expression for the first Townsend coefficient of molecular gases, R. W. Crowe, J. K. Bragg, and J. C. Devins—1121
Sputtering of metal single crystals by ion bombardment, G. K. Wehner—1056(L)
Theory and probe measurements in a magnetic ion source, M. Hoyaux, R. Lemaitre, and Paul Gans—110
Wattage lost in a fluorescent lamp through elastic collisions, H. L. Steele, Jr.—1183(L)

Electromagnetic Waves
Azimuthal surface waves on circular cylinders, Robert S. Elliott—368
Backscattering from wide-angle and narrow-angle cones, L. B. Felsen—138
Bistatic radar cross section of surfaces of revolution, K. M. Siegel, H. A. Alperin, R. R. Bonkowski, J. W. Crispin, A. L. Maffett, C. E. Schensted, and I. V. Schensted—297
Čerenkov radiation from extended electron beams, M. Danos—2
Čerenkov radiation of electrons moving parallel to a dielectric boundary, J. G. Linhart—527
Cross-wound twin helices for traveling-wave tubes, M. Chodorow and E. L. Chu—33
Diffraction by apertures, C. Huang, R. D. Kodis, and H. Levine—151
Diffraction of electromagnetic waves by a metallic wedge of acute dihedral angle, W. W. Grannemann and R. B. Watson—392
Electromagnetic and acoustic scattering by a semi-infinite body of revolution, C. E. Schensted—306
Electromagnetic and acoustical scattering from a semi-infinite cone, K. M. Siegel, J. W. Crispin, and C. E. Schensted—309
Gap problem in antenna theory, Ronold King—317
Interaction of moving charges with wave circuits, J. R. Pierce—627
Measurement of microwave diffraction from a long slit in a thin conducting plane, J. L. Hirshfield and C. M. Zieman—135
Microwave diffraction by apertures of various shapes, S. J. Buchsbaum, A. R. Milne, D. C. Hogg, G. Bekefi, and G. A. Woonton—706
Studies of the diffraction of electromagnetic waves by circular apertures and complementary obstacles: the near zone field, M. J. Ehrlich, S. Silver, and G. Held—336
Surface matching of dielectric lenses, E. M. T. Jones and S. B. Cohn—452

Theoretical and experimental study of electromagnetic scattering by two identical conducting cylinders, R. V. Row—666

Electron and Ion Optics

Relativistic dynamics of a charged particle in crossed magnetic and electric fields with application to the planar magnetron, Louis Gold—253 (errata)

Space-charge effects in electron optical systems, K. T. Dolder and O. Klemperer—1461

Trajectory-tracer study of helix- and band-type post-deflection acceleration, G. C. Sponsler—676

Use of space charge in electron optics, E. A. Ash—327

Velocity spectrography of electron dynamics in a traveling field, O. T. Purl and H. M. VonFoerster—351(L)

Electron Beams

Breakup of hollow electron beams, H. F. Webster—1386(L)

Čerenkov radiation from extended electron beams, M. Danos—2

Čerenkov radiation of electrons moving parallel to a dielectric boundary, J. G. Linhart—527

Electron beam method of determining density profiles across shock waves in gases at low densities, D. Venable and D. E. Kaplan—639(L)

Generalizations of Brillouin flow, L. R. Walker—780(L)

Noise in one-dimensional electron beams, H. A. Haus—560

Plasma ion oscillations in electron beams, K. G. Hernqvist—544

Plasma oscillations in electron beams, K. G. Hernqvist—1029

Positive-ion drainage in magnetically focused electron beams, M. E. Hines, G. W. Hoffman, and J. A. Saloom—1157

Power flow in electron beams, L. R. Walker—1031

Electron Diffraction

Electron diffraction patterns of CuO, R. D. Heidenreich and K. H. Storks—1056(L)

Transition structure of nickel, G. I. Finch, K. P. Sinha, and A. Goswami—250(L)

Electron Emission

Analysis of electrode phenomena in the high-current arc, J. D. Cobine and E. E. Burger—895

Apparatus for studying electron ejection from metals by positive ions, H. D. Hagstrum—256

Composition of the interelectrode prebreakdown current in high vacuum, H. C. Bourne, Jr.—625

Electrical breakdown in high vacuum, W. S. Boyle, P. Kisliuk, and L. H. Germer—720

Emission from hollow cathodes, K. M. Poole—1176

Evaporation of barium and strontium from oxide-coated cathodes, L. A. Wooten, A. E. Ruehle, and G. E. Moore—44

Excess Ba content of practical oxide coated cathodes and thermionic emission, G. E. Moore, L. A. Wooten, and J. Morrison—943

High field electron emission from irregular cathode surfaces, T. J. Lewis—1405

Improved "impregnated cathode," Roberto Levi—639(L)

Measurement of excess Ba in practical oxide coated cathodes, L. A. Wooten, G. E. Moore, and W. G. Guldner—937

Oxide-impregnated nickel-matrix cathode, W. Balas, J. N. Dempsey, and E. F. Rexer—1163

Patch effect for the thermionic emission from polycrystalline tantalum, W. B. LaBerge, R. J. Munick, J. A. Dezoteux, J. F. Whalen, and E. A. Coomes—241

Photoelectric work functions of the borides of lanthanum, praseodymium, and neodymium, R. W. Decker and D. W. Stebbins—1004

Photoelectric yields in the vacuum ultraviolet, W. C. Walker, N. Wainfan, and G. L. Weissler—1366

Properties of pore conductors, R. Forman—1187(L)

Relation of antimony transmission and the photoelectric yield of Cs-Sb, Martin Rome—166

Role of positive ions in high-voltage breakdown in vacuum, H. C. Bourne, Jr., R. W. Cloud, and J. G. Trump—596

Sticking potential of CRT screens, K. H. J. Rottgardt and W. Berthold—1180(L)

Theoretical basis for measuring the saturation emission of highly emitting cathodes under space-charge-limited conditions, C. R. Crowell—1353

Thermionic emission from semiconductors, E. O. Kane—784

Thermionic emission microscopy of metals. I. General, R. D. Heidenreich—757

Time dispersion of secondary electron emission, E. W. Ernst and H. VonFoerster—781(L)

Work function of tungsten single crystal planes measured by the field emission microscope, E. W. Müller—732

Electron Microscope Society of America, Proceedings of the Thirteenth Annual Meeting—pp. 1391–1398

Electron Microscopy

Electron microscopy of monodisperse latexes, E. B. Bradford and J. W. Vanderhoff—864

Electron mirror microscopy, L. Mayer—1228

Replica studies of bulk clays, J. J. Comer and J. W. Turley—346

Thermionic emission microscopy of metals. I. General, R. D. Heidenreich—757

Thermionic emission microscopy of metals. II. Transformations in plain carbon steels, R. D. Heidenreich—879

Transformations in plain carbon steels, F. C. Frank and K. E. Puttick—1522(L)

Electron Tubes

Cross correlation between velocity and current fluctuations in tube noise, S. V. Yadavalli—605

Cross correlation between velocity and current fluctuations in tube noise, S. V. Yadavalli—1523 (erratum)

Cross-wound twin helices for traveling-wave tubes, M. Chodorow and E. L. Chu—33

Electron temperature in the parallel plane diode, T. N. Chin—418

Generation of submillimeter waves, H. Motz and K. B. Mallory—1384(L)

Harmodotron—a beam harmonic, higher order mode device for producing millimeter and submillimeter waves, P. D. Coleman and M. D. Sirkis—1385(L)

Interaction of moving charges with wave circuits, J. R. Pierce—627

Noise at the potential minimum in the high-frequency diode, D. A. Watkins—622

Potential distribution as a function of current in the spherical diode, Annija Dunkuls and Earl Zwicker—779(L)

Space-charge distribution in a static magnetron, H. C. Nedderman—1420

Space-charge-limited current between nonsymmetrical electrodes, G. D. O'Neill—1034

Space-charge waves in crossed electric and magnetic fields, S. S. Solomon—1443

Theoretical basis for measuring the saturation emission of highly emitting cathodes under space-charge-limited conditions, C. R. Crowell—1353

Theory of frequency modulation noise in tubes employing phase focusing, John L. Stewart—409

Velocity spectrography of electron dynamics in a traveling field, O. T. Purl and H. M. VonFoerster—351(L)

Errata
Analog methods for study of transient flow in solids with temperature-dependent thermal properties, N. E. Friedmann—783
Cross correlation between velocity and current fluctuations in tube noise, S. V. Yadavalli—1523
Elastic constants of germanium between 1.7° and 80°K, M. E. Fine—1389 (erratum)
Experimental and theoretical aspects of shock-wave attenuation, I. I. Glass and W. A. Martin—1187
Ferromagnetic resonance in magnesium-manganese aluminum ferrite between 160 and 1900 Mc, H. Suhl, L. G. Van Uitert, and J. L. Davis—1523
Interaction of two similarly facing plane shock waves, C. A. Ford and I. I. Glass—643
Nucleation of lead with preferred orientation, H. A. Atwater and B. Chalmers—1284
Space-charge-limited current between nonsymmetrical electrodes, G. D. O'Neill—1522 (errata)
Relativistic dynamics of a charged particle in crossed magnetic and electric fields with application to the planar magnetron, Louis Gold—253
Rocket measurements of upper atmosphere ambient temperature and pressure in the 30- to 75-kilometer region, H. S. Sicinski, N. W. Spencer, and W. G. Dow—1284

Explosives and Explosions
Application of the engravement method to the study of particle velocity distribution in explosively loaded cylinders, J. Pearson and J. S. Rinehart—1431
Deformation of an explosively loaded aluminum single crystal, J. S. Rinehart—1315
Dynamic determination of the compressibility of metals, R. W. Goranson, D. Bancroft, B. L. Burton, T. Blechar, E. E. Houston, E. F. Gittings, and S. A. Landeen—1472
Effects of attenuating materials on detonation induction distances in gases, M. W. Evans, F. I. Given, and W. E. Richeson, Jr.—1111
Guide to the successful propulsion of a solid object by an explosive charge, J. S. Rinehart—1518(L)
Measurement of detonation velocity by Doppler effect at three-centimeter wavelength, M. A. Cook, R. L. Doran, and G. J. Morris—426
Method for producing high-velocity metallic and plastic pellets, M. E. Van Valkenburg and C. D. Hendricks, Jr.—776(L)
Numerical solutions of spherical blast waves, H. L. Brode—766
Re-examination of the nonsteady theory of jet formation by lined cavity charges, R. J. Eichelberger—398

Ferroelectricity
Effects of ambient atmosphere on the stability of barium titanate, J. R. Anderson, G. W. Brady, W. J. Merz, and J. P. Remeika—1387(L)
Ferroelectric hysteresis in barium titanate single crystals, H. H. Wieder—1479

Ferromagnetic Materials and Ferrites
Circularly polarized cavities for measurement of tensor permeabilities, E. G. Spencer, R. C. LeCraw, and F. Reggia—354(L)
Dependence of the coercive force on the density of some iron oxide powders, A. H. Morrish and S. P. Yu—1049
Domain configurations and crystallographic orientation in grain-oriented silicon steel, W. S. Paxton and T. G. Nilan—994
Effect of nitrides on the coercive force of iron, J. Kerr and C. Wert—1147
Electrical analog of the eddy-current-limited domain-boundary motion in ferromagnetics, G. Brouwer—1297
Extension of nonreciprocal ferrite devices to the 500–3000 megacycle frequency range, R. H. Fox—128(L)
Ferromagnetic resonance in magnesium-manganese aluminum ferrite between 160 and 1900 Mc, H. Suhl, L. G. Van Uitert, and J. L. Davis—1180(L)
Figure of merit for microwave ferrites at low and high frequencies, Benjamin Lax—919(L)
Hysteresis loops of mixtures of ferromagnetic micropowders, C. P. Bean—1381
Influence of pulsed magnetic fields on the reversal of magnetization in square-loop metallic tapes, D. S. Rodbell and C. P. Bean—1318
Kinetics of magnetization in some square loop magnetic tapes, C. P. Bean and D. S. Rodbell—124(L)
Low magnetic saturation ferrites for microwave applications, L. G. Van Uitert—1289
Magnetic materials for digital-computer components. I. A theory of flux reversal in polycrystalline ferromagnetics, N. Menyuk and J. B. Goodenough—8
Magnetic materials for digital computer components. II. Magnetic characteristics of ultra-thin molybdenum-permalloy cores, N. Menyuk—692
Magnetically controlled microwave directional coupler, R. W. Damon—1281(L)
Measurement of susceptibility tensor in ferrites, J. O. Artman and P. E. Tannenwald—1124
New ferrite mode configurations and their applications, B. Lax and K. J. Button—1186(L)
New type ferrite microwave switch, R. F. Sullivan and R. C. LeCraw—1282(L)
Permanent-magnet properties of elongated single-domain iron particles, L. I. Mendelsohn, F. E. Luborsky, and T. O. Paine—1274
Shape and crystal anisotropy of Alnico 5, E. A. Nesbitt and H. J. Williams—1217
Theory of new ferrite modes in rectangular wave guide, B. Lax and K. J. Button—1184(L)
Theory of remagnetization of thin tapes, H. Ekstein—1342
Time delay in high-speed ferrite microwave switches, R. C. LeCraw and H. B. Bruns—124(L)
Wall effects on microwave measurements of ferrite spheres, E. G. Spencer and R. C. LeCraw—250(L)

Fluid Dynamics
Acceleration of slender bodies of revolution through sonic velocity, J. D. Cole—322
Analog computer construction of conformal maps in fluid dynamics, N. P. Tomlinson, M. Horowitz, and C. H. Reynolds—229
Laminar flow in channels with porous walls at high suction Reynolds numbers, John R. Sellars—489(L)
Limiting pressure on hydrofoils, E. V. Laitone—1519(L)
Method for producing high-velocity metallic and plastic pellets, M. E. Van Valkenburg and C. D. Hendricks, Jr.—776(L)
Reflection of a compression wave from a symmetrical wedge, R. W. Skulski and D. Weimer—1344
Streaming birefringence as a hydrodynamic research tool—applied to a rotating cylinder apparatus above the transition velocity, H. Wayland—1197
Transition through a contact region, J. G. Hall—698

Fluid Flow, Low Speed
Laminar flow in channels with porous walls at high suction Reynolds numbers, J. R. Sellars—489(L)

Friction and Wear
Analysis of the effect of various factors on metal transfer and wear between specimen pairs of same metal and same shape. I. Basic scheme of formulation of metal transfer and wear, I-Ming Feng—24

Analysis of the effect of various factors on metal transfer and wear between specimen pairs of same metal and same shape. II. Effect of the surrounding atmosphere, I-Ming Feng—28
Elastic-plastic instability caused by the size effect and its influence on rubbing wear, F. V. Hunt—850
Friction of Teflon sliding on Teflon, D. G. Flom and N. T. Porile—1088
Surface friction in ballistic penetration, J. M. Krafft—1248

Geophysics
Theory of elasticity and consolidation for a porous anisotropic solid, M. A. Biot—182

Heat Transfer
Analog methods for study of transient heat flow in solids with temperature-dependent thermal properties, N. E. Friedmann—129(L)
Analog methods for study of transient flow in solids with temperature-dependent thermal properties, N. E. Friedmann—783 (erratum)
Measurement of wall temperature and heat flow in the shock tube, A. J. Chabai and R. J. Emrich—779(L)

Information Theory and Communication Theory
Information required for missile guidance, Fred P. Adler —492(L)
Information theory aspects of propagation through time-varying media, Joseph Feinstein—219
Odd ball problem as an example in information theory, Further remarks, F. H. Mitchell and R. N. Whitehurst —778(L)
Signal-to-noise improvement and the statistics of track populations, Nelson Wax—586

Liquids
Conduction and breakdown in hexane, W. B. Green—1257
Dependence of the electric strengths of liquids on electrode spacing, A. H. Sharbaugh, J. K. Bragg, and R. W. Crowe—434
Effect of pressure on sound propagation in water, T. A. Litovitz and E. H. Carnevale—816
Maximum superheating of water as a measure of negative pressure, L. J. Briggs—1001

Luminescence
Deterioration of luminescent phosphors under positive ion bombardment, J. R. Young—1302
Effect of superposing a small alternating excitation on the steady excitation of a luminescent material, K. F. Stripp and R. H. Bube—251(L)
Light amplifier, F. E. Williams and D. A. Cusano—358
Sticking potential of CRT screens, K. H. J. Rottgardt and W. Berthold—1180(L)

Magnetic Resonance
Ferromagnetic resonance in magnesium-manganese aluminum ferrite between 160 and 1900 Mc, H. Suhl, L. G. Van Uitert, and J. L. Davis—1180(L)
Ferromagnetic resonance in magnesium-manganese aluminum ferrite between 160 and 1900 Mc, H. Suhl, L. G. Van Uitert, and J. L. Davis—1523 (erratum)
Proton magnetic resonance in polyamides, W. P. Slichter —1099
Spin-echo memory device, S. Fernbach and W. G. Proctor —170
Spin echo serial storage memory, A. G. Anderson, R. L. Garwin, E. L. Hahn, J. W. Horton, G. L. Tucker, and R. M. Walker—1324
Techniques for nuclear magnetic resonance measurements on granular hygroscopic materials, T. M. Shaw and R. H. Elsken—313

Magnetism
Axial variation of the magnetic field in solenoids of finite thickness, D. E. Mapother and J. N. Snyder—784
Barkhausen noise from a cylindrical core, D. Haneman—355(L)
New active circuit element using the magnetoresistive effect, A. Aharoni, E. H. Frei, and G. Horowitz—1411
Specification of thermally and mechanically induced non-equilibrium states in AuCu by the resistivity and magnetoresistivity, B. Wiener, G. Groetzinger, and R. McCollum—857
Variation of magnetoresistivity of AuCu with degree of order, B. Wiener, P. Schwed, and G. Groetzinger—609

Magnetostriction
Application of the Wiedemann effect to the magnetostrictive coupling of crossed coils, U. F. Gianola—1152

Mass Spectrometry
Influence of space charge on the potential distribution in mass spectrometer ion sources, W. M. Brubaker—1007
Performance of the nonmagnetic radio-frequency mass spectrometer tube, T. C. Wherry and F. W. Karasek—682

Mathematics
Closed expansion of the convolution integral (a generalization of servomechanism error coefficients), E. Arthurs and L. H. Martin—58
Kramers-Kronig relations, M. K. Brachman—497
Nonlinear transfer system, I. Flügge-Lotz and W. S. Wunch—484
Qualitative evaluation of correlation coefficients from scatter diagrams, T. M. Burford—56
Solution of an integral equation arising in optical studies of oriented filaments, E. F. Gurnee—918(L)

Metallurgy
Condition of high-velocity ductile fracture, E. Orowan—900
Creep of aluminum under cyclotron irradiation, M. R. Jeppson, R. L. Mather, A. Andrew, and H. P. Yockey —365
Creep of zinc crystals, E. P. T. Tyndall, R. A. Artman, C. A. Wert, and R. Eisner—286
Dislocations in germanium, S. G. Ellis—1140
Energy relations in cold working an alloy at 78°K and at room temperature, J. S. L. Leach, E. G. Loewen, and M. B. Bever—728
Interpretation of the strain broadening components in x-ray diffraction patterns, J. C. Bowman, J. A. Krumhansl, and J. R. Stock—1057(L)
Nucleation of lead with preferred orientation, H. A. Atwater and B. Chalmers—918(L)
Nucleation of lead with preferred orientation, H. A. Atwater and B. Chalmers—1284 (erratum)
Removal of copper from germanium, Katharine B. Blodgett—1520(L)
Small-angle x-ray scattering from precipitates in cold-worked Al-Ag and Al-Zn, J.-P. Jan—1291
Specification of thermally and mechanically induced non-equilibrium states in AuCu by the resistivity and magnetoresistivity, B. Wiener, G. Groetzinger, and R. McCollum—857
"Spiral polygon" tin whiskers, P. W. Levy and O. F. Kammerer—1182(L)
Study of the initial stages of sintering solids by viscous flow, evaporation-condensation, and self-diffusion, W. D. Kingery and M. Berg—1205

Metallurgy (continued)
Study of the kinetics of ordering in the alloy AuCu, G. C. Kuczynski, R. F. Hochman, and M. Doyama—871
Temperature dependent creep in zinc crystals, D. O. Thompson—280
Theory of steady-state creep based on dislocation climb, J. Weertman—1213
Transformations in plain carbon steels, F. C. Frank and K. E. Puttick—1522(L)
X-ray measurements of particle size and strain distribution in cold worked silver, F. R. L. Schoening and J. N. van Niekerk—726
Zone refining, J. L. Birman—1195

Meteorology
Rocket measurements of upper atmosphere ambient temperature and pressure in the 30- to 75-kilometer region, H. S. Sicinski, N. W. Spencer, and W. G. Dow—1284 (erratum)

Noise
Barkhausen noise from a cyindrical core, D. Haneman—355(L)
Cross correlation between velocity and current fluctuations in tube noise, S. V. Yadavalli—605
Cross correlation between velocity and current fluctuations in tube noise, S. V. Yadavalli—1523 (erratum)
Hysteresis effect in multiplier phototube noise, C. A. Ziegler and H. H. Seliger—1225
Noise at the potential minimum in the high-frequency diode, D. A. Watkins—622
Noise in one-dimensional electron beams, H. A. Haus—560
Noise measurements in semiconductors at very low frequencies, T. E. Firle and H. Winston—716
Power spectra and the minimum detectable signal in measurement systems, J. J. Freeman—236
Qualitative evaluation of correlation coefficients from scatter diagrams, T. M. Burford—56
Radiation of plasma noise from arc discharge, T. Takakura, K. Baba, K. Nunogaki, and H. Mitani—185
Relative influence of majority and minority carriers on excess noise in semiconductor filaments, L. Bess—1377
Relaxation oscillations and noise from low-current arc discharges, M. I. Skolnik and H. R. Puckett, Jr.—74
Short-time frequency measurement of narrow-band random signals by means of a zero counting process, H. Steinberg, P. M. Schultheiss, C. A. Wogrin, and F. Zweig—195
Signal-to-noise improvement and the statistics of track populations, Nelson Wax—586
Theory of frequency modulation noise in tubes employing phase focusing, J. L. Stewart—409
Variation of noise with ambient in germanium filaments, T. G. Maple, L. Bess, and H. A. Gebbie—490(L)

Nuclear Physics
Analysis of scintillation spectrometer observations of the penetration of Cs^{137} gamma radiation through water, R. B. Theus, L. A. Beach, and W. R. Faust—294
Some Monte Carlo calculations of gamma-ray penetrations, J. F. Perkins—1372

Nuclear Reactor
Angular distribution of multiply scattered gamma radiation from a plane isotropic source, M. J. Berger—1504
Anisotropic diffusion lengths in diffusion theory, B. I. Spinrad—548
Diffusion of decaying particles, L. Gold—233
Effect of asymmetric oxygen scattering on the slowing-down length of neutrons in water, H. C. Volkin—127(L)
Effect of delayed fission neutrons on reactor kinetics, L. B. Robinson—52
Effect of geometry on resonance absorption of neutrons by uranium, E. Creutz, H. Jupnik, T. Snyder, and E. P. Wigner—271
Effect of temperature on total resonance absorption of neutrons by spheres of uranium oxide, E. Creutz, H. Jupnik, and E. P. Wigner—276
Intentional explosion of a nuclear reactor, W. H. Zinn and L. C. Furney—1286
Moderation of neutrons in SiO_2 and $CaCo_3$, Jay Tittman—394
Monte Carlo calculation of gamma-ray albedos of concrete and aluminum, J. F. Perkins—655
Some Monte Carlo calculations of gamma-ray penetrations, J. F. Perkins—1372
Neutron absorption in a semi-infinite region, J. S. Dwork and H. Hurwitz, Jr.—642(L)
Resonance absorption of neutrons by spheres, E. P. Wigner, E. Creutz, H. Jupnik, and T. Snyder—260
Review of measurements of the resonance absorption of neutrons by uranium in bulk, E. Creutz, H. Jupnik, T. Snyder, and E. P. Wigner—257
Slowing down distribution of U^{235} fission neutrons from a point source in light water, J. E. Hill, L. D. Roberts, and T. E. Fitch—1013
Slowing down distribution to indium resonance of U^{235} fission neutrons from a point fission source in two aluminum light water mixtures, L. D. Roberts, J. E. Hill, and T. E. Fitch—1018
Slowing down of neutrons by hydrogenous moderators, H. Hurwitz, Jr., and P. F. Zweifel—923
Spatial distribution of thermal neutrons from a polonium-beryllium source in water-zirconium mixtures, W. Baer—1235

Oceanography
Reflection of sound in the ocean from a continuous stratum containing a velocity extremum, E. O. Cook and H. S. Heaps—429

Optical Properties
Apparatus for making simultaneous stress and birefringence measurements on polymers, E. F. Gurnee, L. T. Patterson, and R. D. Andrews—1106
Birefringence and crystallization in elastomers, G. R. Taylor and S. R. Darin—1075
Photoelectric yields in the vacuum ultraviolet, W. C. Walker, N. Wainfan, and G. L. Weissler—1366
Relation of antimony transmission and the photoelectric yield of Cs-Sb, M. Rome—166
Theory of scattering by an inhomogeneous solid possessing fluctuations in density and anisotropy, M. Goldstein and E. R. Michalik—1450
Total emissivities and absorptivities of some commercial surfaces at room and liquid-nitrogen temperatures, F. J. Zimmermann—1483

Phase Transformations
Cubic to orthorhombic diffusionless phase change—experimental and theoretical studies of AuCd, D. S. Lieberman, M. S. Wechsler, and T. A. Read—473
Effect of reactor irradiation on the white-to-grey tin transformation, J. Fleeman and G. J. Dienes—652
Thermionic emission microscopy of metals. II. Transformations in plain carbon steels, R. D. Heidenreich—879
Transition structure of nickel, G. I. Finch, K. P. Sinha, and A. Goswami—250(L)

Plastic Deformation
Approximate theory of armor penetration, W. T. Thomson—80
Condition of high-velocity ductile fracture, E. Orowan—900

Deformation of an explosively loaded aluminum single crystal, J. S. Rinehart—1315
Experimental investigation of the mechanics of plastic deformation of metals, E. G. Thomsen, C. T. Yang, and J. B. Bierbower—920
Properties of elastic and plastic waves determined by pin contactors and crystals, Stanley Minshall—463
Short-time stress relaxation behavior of plastics, M. T. Watson, W. D. Kennedy, and G. M. Armstrong—701

Polymers
Apparatus for making simultaneous stress and birefringence measurements on polymers, E. F. Gurnee, L. T. Patterson, and R. D. Andrews—1106
Application of the superposition principle and theories of mechanical equation of state, strain, and time hardening to creep of plastics under changing loads, W. N. Findley and G. Khosla—821
Birefringence and crystallization in elastomers, G. R. Taylor and S. R. Darin—1075
Crystallization kinetics in high polymers. II. Polymer-diluent mixtures, Leo Mandelkern—443
Effect of molecular weight distribution on the creep behavior of cellulose acetate, D. L. Swanson and J. W. Williams—810
Electron microscopy of monodisperse latexes, E. B. Bradford and J. W. Vanderhoff—864
Experimental examination of the statistical theory of rubber elasticity. Low extension studies, F. P. Baldwin, J. E. Ivory, and R. L. Anthony—750
Extension of the Hertz theory of impact to the viscoelastic case, Yoh-Han Pao—1083
Extension of the Rouse theory of viscoelastic properties to undiluted linear polymers, J. D. Ferry, R. F. Landel, and M. L. Williams—359
Friction of Teflon sliding on Teflon, D. G. Flom and N. T. Porile—1088
Glass transitions in polymer-plasticizer systems, L. Breitman—1092
Isothermal viscosity-molecular weight dependence for long polymer chains, T. G. Fox and S. Loshaek—1080
Measurements of electrical polarization in thin dielectric materials, R. W. Tyler, J. H. Webb, and W. C. York—61
Preferred orientation in stark rubber studied with an automatic integrating pole figure goniometer, C. J. Newton, L. Mandelkern, and D. E. Roberts—1521(L)
Preliminary results in measuring dynamic compressibilities, W. Philippoff and J. Brodnyan—846
Proton magnetic resonance in polyamides, W. P. Slichter—1099
Retraction of oriented polystyrene monofilaments, R. D. Andrews—1061
Short-time stress relaxation behavior of plastics, M. T. Watson, W. D. Kennedy, and G. M. Armstrong—701
Solution of an integral equation arising in optical studies of oriented filaments, E. F. Gurnee—918(L)
Tensile strength of plastics above the glass temperature, F. Bueche—1133
Theory of non-Newtonian flow. I. Solid plastic system, T. Ree and H. Eyring—793
Theory of non-Newtonian flow. II. Solution system of high polymers, T. Ree and H. Eyring—800
Theory of scattering by an inhomogeneous solid possessing fluctuations in density and anisotropy, M. Goldstein and E. R. Michalik—1450
Unilateral compression of rubber, M. J. Forster—1104
Viscoelasticity of poly methacrylates, F. Bueche—738
X-ray diffraction studies of crystallization in elastomers, L. E. Alexander, S. Ohlberg, and G. R. Taylor—1068

Radiation Effects in Solids
Creep of aluminum under cyclotron irradiation, M. R. Jeppson, R. L. Mather, A. Andrew, and H. P. Yockey—365
Effect of reactor irradiation on the white-to-grey tin transformation, J. Fleeman and G. J. Dienes—652
Neutron irradiation effects upon Young's modulus and internal friction of copper, D. O. Thompson, D. K. Holmes, and T. H. Blewitt—1188(L)
Radiation induced changes in the electrical resistivity of α brass, D. B. Rosenblatt, R. Smoluchowski, and G. J. Dienes—1044

Resonant Cavities
Circularly polarized cavities for measurement of tensor permeabilities, E. G. Spencer, R. C. LeCraw, and F. Reggia—354(L)
Collapsed toroidal springs as contact elements in microwave cavities, C. L. Andrews—777(L)
Measurement of susceptibility tensor in ferrites, J. O. Artman and P. E. Tannenwald—1124
Representation of electromagnetic fields in cavities in terms of natural modes of oscillation, S. A. Schelkunoff—1231
Resonant-cavity field measurements, S. W. Kitchen and A. D. Schelberg—618
Wall effects on microwave measurements of ferrite spheres, E. G. Spencer and R. C. LeCraw—250(L)

Rheology
Application of the superposition principle and theories of mechanical equation of state, strain, and time hardening to creep of plastics under changing loads, Wm. N. Findley and G. Khosla—821
Contribution to the study of transport phenomena in gases at high densities, A. Michels, J. A. M. Cox, A. Botzen, and A. S. Friedman—843
Diffusion controlled stress relaxation, R. H. McMickle and E. T. Kubu—832
Effect of molecular weight distribution on the creep behavior of cellulose acetate, D. L. Swanson and J. W. Williams—810
Effect of pressure on sound propagation in water, T. A. Litovitz and E. H. Carnevale—816
Preliminary results in measuring dynamic compressibilities, W. Philippoff and J. Brodnyan—846
Rheological equation of state which predicts non-Newtonian viscosity, normal stresses, and dynamic moduli, T. W. DeWitt—889
Society of Rheology, Annual Meeting—785
Theory of non-Newtonian flow. I. Solid plastic system, T. Ree and H. Eyring—793; II. Solution system of high polymers, T. Ree and H. Eyring—800
Vibroscope measurements of the elastic moduli of nylon 66 and dacron filaments of various draw ratios, J. H. Wakelin, E. T. L. Voong, D. J. Montgomery, and J. H. Dusenbury—786
Viscosity and elasticity of oil surfaces and oil-water interfaces, D. W. Criddle and A. L. Meader, Jr.—838

Semiconductor Devices
Anomalous forward switching transient in *p-n* junction diodes, N. T. Jones, R. H. Kingston, and S. F. Neustadter—210
Capacitance measurements on alloyed indium-germanium junction diodes, D. R. Muss—1514
Effect of water vapor on grown germanium and silicon *np* junction units, J. T. Law and P. S. Meigs—1265
Forward characteristic of germanium point contact rectifiers, Melvin Cutler—949
"Gate modulation" of electromagnetic radiation, Kurt Lehovec—495

Semiconductor Devices (continued)
Novel microwave attenuator using germanium, J. B. Gunn and C. A. Hogarth—353(L)
Observation of circular patterns in the vicinity of small-area alloyed germanium *p-n* junctions, Nick Holonyak, Jr.—121
Optical determination of base width in grown *n-p-n* silicon crystals, A. Fowler and P. Levesque—641(L)
Rate-grown germanium crystals for high-frequency transistors, H. E. Bridgers and E. D. Kolb—1188(L)
Rectification properties of metal semiconductor contacts, E. H. Borneman, R. F. Schwarz, and J. J. Stickler—1021
Reverse current and carrier lifetime as a function of temperature in germanium junction diodes, E. M. Pell—658
Shot noise in *p-n-p* transistors, G. H. Hanson—1388(L)
Silicon *n-p-n* grown junction transistors, M. Tanenbaum, L. B. Valdes, E. Buehler, and N. B. Hannay—686
Silicon solar energy converters, M. B. Prince—534
Thermal effects in point-rectifiers, R. E. Burgess—1058(L)
Transient behavior of semiconductor rectifiers, B. R. Gossick—1356

Semiconductors
Calculation of the space charge, electric field, and free carrier concentration at the surface of a semiconductor, R. H. Kingston and S. F. Neustadter—718
Dislocations in germanium, S. G. Ellis—1140
Elastic constants of germanium between 1.7° and 80°K, M. E. Fine—862
Excess Ba content of practical oxide coated cathodes and thermionic emission, G. E. Moore, L. A. Wooten, and J. Morrison—943
Injected current carrier transport in a semi-infinite semiconductor and the determination of lifetimes and surface recombination velocities, W. van Roosbroeck—380
Ion bombardment-cleaning of germanium and titanium as determined by low-energy electron diffraction, H. E. Farnsworth, R. E. Schlier, T. H. George and R. M. Burger—252(L)
Measurement of carrier lifetimes in germanium and silicon, D. T. Stevenson and R. J. Keyes—190
Measurement of excess Ba in practical oxide coated cathodes, L. A. Wooten, G. E. Moore, and W. G. Guldner—937
Measurement of the lifetime of minority carriers in germanium, W. G. Spitzer, T. E. Firle, M. Cutler, R. G. Shulman, and M. Becker—414
Noise measurements in semiconductors at very low frequencies, T. E. Firle and H. Winston—716
Properties of pore conductors, R. Forman—1187(L)
Relative influence of majority and minority carriers on excess noise in semiconductor filaments, L. Bess—1377
Removal of copper from germanium, Katharine B. Blodgett—1520(L)
Restoration of resistivity and lifetime in heat treated germanium, R. A. Logan and M. Schwartz—1287
Sparked hydrogen treatment of germanium surfaces, N. Holonyak, Jr. and H. Letaw, Jr.—355(L)
Thermionic emission from semiconductors, E. O. Kane—784
Variation of noise with ambient in germanium filaments, T. G. Maple, L. Bess, and H. A. Gebbie—490(L)
Zone refining, J. L. Birman—1195

Shock Waves
Asymptotic spherical shock decay, L. M. Tannenwald—551
Effects of attenuating materials on detonation induction distances in gases, M. W. Evans, F. I. Given, and W. E. Richeson, Jr.—1111
Elastic description of a high-amplitude spherical pulse in steel, W. A. Allen and W. Goldsmith—69
Electrical conductivity of highly ionized argon produced by shock waves, S.-C. Lin, E. L. Resler, and A. Kantrowitz—95
Electron beam method of determining density profiles across shock waves in gases at low densities, D. Venable and D. E. Kaplan—639(L)
Experimental and theoretical aspects of shock-wave attenuation, I. I. Glass and W. A. Martin—113
Experimental and theoretical aspects of shock-wave attenuation, I. I. Glass and W. A. Martin—1187 (errata)
Improved wave diagram procedure for shock reflection from an open end of a duct, G. Rudinger—1339
Interaction of two similarly facing plane shock waves, C. A. Ford and I. I. Glass—643 (erratum)
Measurement of detonation velocity by Doppler effect at three-centimeter wavelength, M. A. Cook, R. L. Doran, and G. J. Morris—426
Measurement of wall temperature and heat flow in the shock tube, A. J. Chabai and R. J. Emrich—779(L)
Numerical solutions of spherical blast waves, H. L. Brode—766
Propagation of shock waves in aluminum, H. D. Mallory—555
Properties of elastic and plastic waves determined by pin contractors and crystals, S. Minshall—463
Reflection of shock waves from an open end of a duct, G. Rudinger—981
Shock waves in air produced by elastic and plastic waves in a plate, W. A. Allen, J. M. Mapes, and E. B. Mayfield—125(L)
Shock waves in air produced by waves in a plate, W. A. Allen, J. M. Mapes, and E. B. Mayfield—1173
Similarity solution for a spherical shock wave, R. Latter—954
Spectroscopic studies of highly ionized argon produced by shock waves, H. E. Petschek, P. H. Rose, H. S. Glick, Anne Kane, and A. Kantrowitz—83
Transition through a contact region, J. G. Hall—698
Weak detonations and condensation shocks, W. H. Heybey and S. G. Reed, Jr.—969

Sound Wave Propagation
Backscattering from wide-angle and narrow-angle cones, L. B. Felsen—138
Effect of pressure on sound propagation in water, T. A. Litovitz and E. H. Carnevale—816
Electromagnetic and acoustic scattering by a semi-infinite body of revolution, C. E. Schensted—306
Electromagnetic and acoustical scattering from a semi-infinite cone, K. M. Siegel, J. W. Crispin, and C. E. Schensted—309
Geometrical acoustics. II. Diffraction, reflection, and refraction of a weak spherical or cylindrical shock at a plane interface, K. O. Friedrichs and J. B. Keller—961
Reflection of sound in the ocean from a continuous stratum containing a velocity extremum, E. O. Cook and H. S. Heaps—429

Space Charge
Influence of space charge on the potential distribution in mass spectrometer ion sources, W. M. Brubaker—1007
Potential distribution as a function of current in the spherical diode, A. Dunkuls and E. Zwicker—779(L)
Space-charge distribution in a static magnetron, H. C. Nedderman—1420
Space-charge effects in electron optical systems, K. T. Dolder and O. Klemperer—1461
Space-charge-limited current between nonsymmetrical electrodes, G. E. O'Neill—1034

Space-charge-limited current between nonsymmetrical electrodes, D. G. O'Neill—1522 (errata)
Space-charge waves in crossed electric and magnetic fields, S. S. Solomon—1443
Use of space charge in electron optics, E. A. Ash—327

Spectra and Spectroscopy
Spectroscopic studies of highly ionized argon produced by shock waves, H. E. Petschek, P. H. Rose, H. S. Glick, Anne Kane, and A. Kantrowitz—83

Surface Properties
Barium getters in carbon monoxide, J. Morrison and R. B. Zetterstrom—437
Calculation of the space charge, electric field, and free carrier concentration at the surface of a semiconductor, R. H. Kingston and S. F. Neustadter—718
Effect of water vapor on grown germanium and silicon *np* junction units, J. T. Law and P. S. Meigs—1265
Gettering of gas by titanium, V. L. Stout and M. D. Gibbons—1488
Growth of anodic Ta_2O_5 films during illumination with ultraviolet light, D. A. Vermilyea—489(L)
Injected current carrier transport in a semi-infinite semiconductor and the determination of lifetimes and surface recombination velocities, W. van Roosbroeck—380
Ion bombardment-cleaning of germanium and titanium as determined by low-energy electron diffraction, H. E. Farnsworth, R. E. Schlier, T. H. George, and R. M. Burger—252(L)
Measurement of the lifetime of minority carriers in germanium, W. G. Spitzer, T. E. Firle, M. Cutler, R. G. Shulman, and M. Becker—414
Oxidized copper single crystal sphere, F. W. Young, Jr.—644
Rate of formation of film on metals and alloys, G. P. Chatterjee—363
Small-angle scattering and surface structure, Yin-Yuan Li and R. Smoluchowski—128(L)
Sparked hydrogen treatment of germanium surfaces, N. Holonyak, Jr., and H. Letaw, Jr.—355(L)
Sputtering of metal single crystals by ion bombardment, G. K. Wehner—1056
Total emissivities and absorptivities of some commercial surfaces at room and liquid-nitrogen temperatures, F. J. Zimmerman—1483

Thermal Conductivity and Thermal Conduction
Analog methods for study of transient heat flow in solids with temperature-dependent thermal properties, N. E. Friedmann—129(L)
Analog methods for study of transient flow in solids with temperature-dependent thermal properties, N. E. Friedmann—783 (erratum)
Contribution to the study of transport phenomena in gases at high densities, A. Michels, J. A. M. Cox, A. Botzen, and A. S. Friedman—843

Thermoelectricity
Thermoelectric power and electrical resistivity of dilute alloys of silicon in copper, nickel, and iron, C. A. Domenicali and F. A. Otter—377

Thin Films
Preparation of thin magnetic films and their properties, M. S. Blois, Jr.—975
Rate of formation of film on metals and alloys, G. P. Chatterjee—363

Transmission Lines and Wave Guides
Azimuthal surface waves on circular cylinders, R. S. Elliott—368
Extension of nonreciprocal ferrite devices to the 500–3000 megacycle frequency range, R. H. Fox—128(L)
Low magnetic saturation ferrites for microwave applications, L. G. Van Uitert—1289
Magnetically controlled microwave directional coupler, R. W. Damon—1281(L)
Methods of measuring dielectric constants based upon a microwave network viewpoint, A. A. Oliner and H. M. Altschuler—214
New ferrite mode configurations and their applications, B. Lax and K. J. Button—1186(L)
New type ferrite microwave switch, R. F. Sullivan and R. C. LeCraw—1282(L)
Theory of new ferrite modes in rectangular wave guide, B. Lax and K. J. Button—1184(L)
Time delay in high-speed ferrite microwave switches, R. C. LeCraw and H. B. Bruns—124(L)

Turbulence
Analysis of turbulent density fluctuations by the shadow method, M. S. Uberoi and L. S. G. Kovasznay—19

Vacuum Technique
Barium getters in carbon monoxide, J. Morrison and R. B. Zetterstrom—437
Gettering of gas by titanium, V. L. Stout and M. D. Gibbons—1488
Ionic pumping mechanism of helium in an ionization gauge, L. J. Varnerin, Jr., and J. H. Carmichael—782(L)
Outgassing of glass, B. J. Todd—1238

Vibrations
Calculation of the complex modulus of linear viscoelastic materials from vibrating reed measurements, D. R. Bland and E. H. Lee—1497
Effect of air damping on transverse vibrations of stretched filaments, D. W. Stauff and D. J. Montgomery—540
Thickness-shear and flexural vibrations of rectangular crystal plates, R. D. Mindlin and H. Deresiewicz—1435

Viscosity and Viscoelasticity
Calculation of the complex modulus of linear viscoelastic materials from vibrating reed measurements, D. R. Bland and E. H. Lee—1497
Contribution to the study of transport phenomena in gases at high densities, A. Michels, J. A. M. Cox, A. Botzen, and A. S. Friedman—843
Effect of air damping on transverse vibrations of stretched filaments, D. W. Stauff and D. J. Montgomery—540
Equivalent-radius method for determination of non-Newtonian flow curves from viscometric data, K. H. Cram and J. C. Whitwell—613
Extension of the Hertz theory of impact to the viscoelastic case, Yoh-Han Pao—1083
Extension of the Rouse theory of viscoelastic properties to undiluted linear polymers, J. D. Ferry, R. F. Landel, and M. L. Williams—359
Low shear capillary viscometer with continuously varying pressure head, S. H. Maron and R. J. Belner—1457
Preliminary results in measuring dynamic compressibilities, W. Philippoff and J. Brodnyan—846
Rheological equation of state which predicts non-Newtonian viscosity, normal stresses, and dynamic moduli, T. W. DeWitt—889
Theory of non-Newtonian flow. I. Solid plastic system, T. Ree and H. Eyring—793
Theory of non-Newtonian flow. II. Solution system of high polymers—800
Viscosity and elasticity of oil surfaces and oil-water interfaces, D. W. Criddle and A. L. Meader, Jr.—838
Viscoelasticity of poly methacrylates, F. Bueche—738

X-Rays and X-Ray Diffraction

Correlation of diffraction and transmission experiments for x-ray and neutron elastic scattering, D. T. Keating and J. J. Antal—1041

Hexagonal microstructure of ice crystals grown from the melt, F. K. Truby—1416

Interpretation of the strain broadening components in x-ray diffraction patterns, J. C. Bowman, J. A. Krumhansl, and J. R. Stock—1057(L)

Mass absorption coefficient of carbon for CuKα radiation, D. R. Chipman—1387(L)

Method for obtaining complete quantitative pole figures for flat sheets using one sample and one sample holder, M. Schwartz—1507

Methods for the correction of x-ray intensities for primary and secondary extinction in crystal structure analysis, V. Vand—1191

Preferred orientation in stark rubber studied with an automatic integrating pole figure goniometer, C. J. Newton, L. Mandelkern, and D. E. Roberts—1521(L)

Preferred orientation of platelets in x-ray diffractometer powder samples, J. E. Manson—1254

Small-angle scattering and surface structure, Yin-Yuan Li and R. Smoluchowski—128(L)

Small-angle x-ray scattering from precipitates in cold-worked Al-Ag and Al-Zn, J.-P. Jan—1291

Small particle x-ray scattering by fibers, size and shape of microcrystallites, A. N. J. Heyn—519

Small particle x-ray scattering by fibers. II. Radial distribution of microcrystallites, A. N. J. Heyn—1113

Submicroscopic structure determination by long wavelength x-ray diffraction, B. L. Henke and J. W. M. Dumond—903

X-ray diffraction studies of crystallization in elastomers, L. E. Alexander, S. Ohlberg, and G. R. Taylor—1068

X-ray diffraction study of silver iodide aerosols, J. E. Manson—423

X-ray measurements of particle size and strain distribution in cold worked silver, F. R. L. Schoening and J. N. van Niekerk—726

X-ray path through calcite in Laue diffraction, G. L. Rogosa and G. Schwarz—967

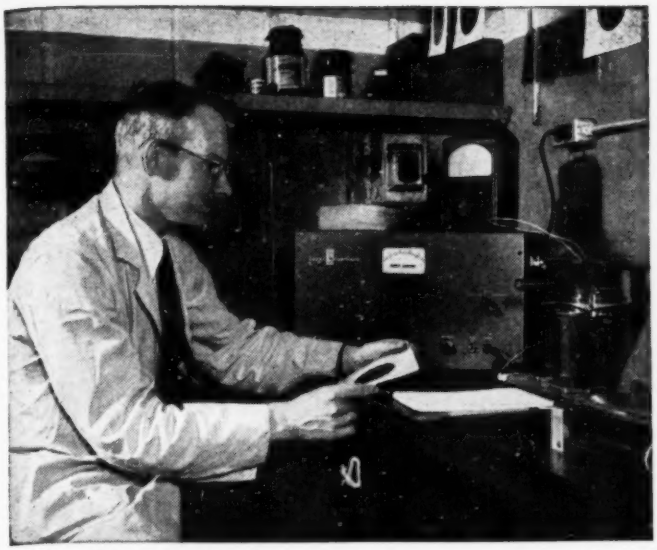

As a Direct-Reading Instrument *The extreme sensitivity of the d-c amplifier is utilized to check plasticizer insulation resistance values in the megamegohm range.*

As a Recorder Preamplifier *The rack-mounted amplifier above is being used to increase the sensitivity of a recorder in running special tests of switches.*

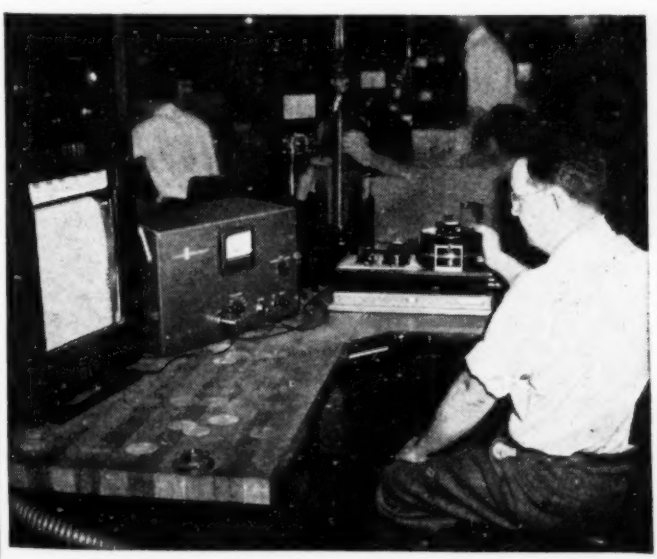

As a Null Detector *The d-c Amplifier is being used above for factory checking and calibration of instruments.*

L&N Low Level d-c Amplifiers are

Triple Purpose... for Triple Service

• In response to the constant demand for versatility in precision instruments, these d-c Indicating Amplifiers combine the functions of three useful instruments in one:

1. A Direct-Reading Instrument that is always ready to use . . . never any readjusting of zero, either initially or during a series of readings. Simply select the range in which you want to work by turning scale-multiplier knob.

2. A Recorder Preamplifier — Values measured by Stabilized d-c Amplifiers can be recorded directly on Speedomax recorders.

3. A Null Detector more sensitive than most reflecting galvanometers, yet with full scale response time of only 2 to 3 seconds. These instruments are unaffected by vibration; leveling is not necessary. At the turn of a range knob, a wide choice of sensitivities can be obtained without external shunts. A non-linear response characteristic is also available for easy balancing.

These amplifiers are suitable for handling low level measurements with thermocouples, strain gages, bolometers—bridge and potentiometer circuits—ionization, leakage and phototube currents—almost any measurement of extremely small direct current or voltage.

Self-contained, the unit can either be used "as is" or removed from case and mounted on a 19″ relay rack.

For details, including complete specifications, send for Folder EM9-51(1). Write our nearest office, or 4978 Stenton Ave., Phila. 44, Penna.

LEEDS LN NORTHRUP

instruments automatic controls • furnaces

Stokes vacuum brazing furnace at Pratt & Whitney Aircraft offers complete accessibility to work area and simplicity in material handling. These three simple operations are involved: (1) placing of work (2) covering work with retort and (3) lowering the furnace shell.

Pratt & Whitne

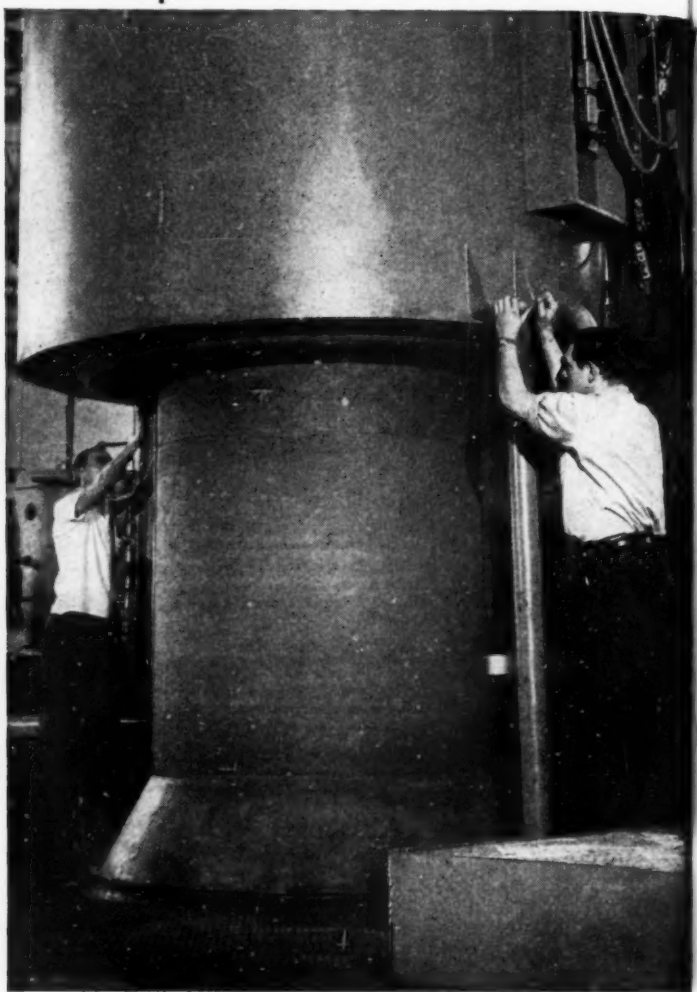

THE COMPLETE LINE OF STOKES V

Stokes manufactures a complete line of vacuum pumping equipment. This includes mechanical vacuum pumps, diffusion and booster pumps, vacuum valves and gages, and complete vacuum instrumentation. In engineered high vacuum equipment, Stokes builds vacuum metallizers, vacuum furnaces and other vacuum processing equipment.

Stokes has for many years been active in vacuum research. Vacuum experience among our engineers covers the range from laboratory equipment to some of the largest vacuum equipment in service. This experience is available to help solve your vacuum problems.

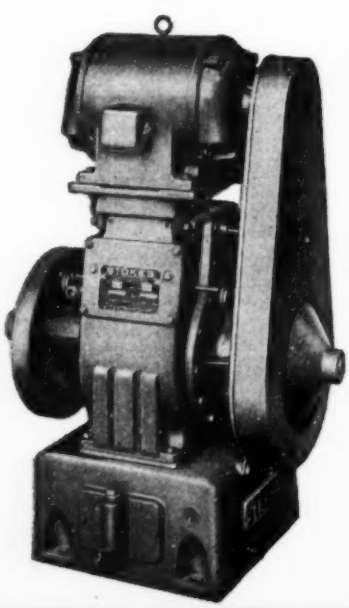

STOKES MECHANICAL VACUUM PUMPS

For vacuum processing systems and for maintaining low forepressures in high-vacuum systems, the Stokes Microvac pump provides efficient, economical operation. Designed with fully automatic lubrication and a long-lasting exhaust valve assembly, every Microvac pump is assured of smooth, trouble-free operation. Six sizes give capacities from 15 to 500 cfm. Send for catalog listed at right.

ne ircraft Uses Stokes Furnace to Investigate

acuum-Brazing of Jet Engine Components

Versatile new furnace design also can be used for heat-treating and outgassing at high vacuum or under controlled atmospheres.

A logical development of vacuum metallurgy, high-vacuum brazing, presently being investigated by numerous firms throughout the country, promises to produce superior products more economically than brazing methods used heretofore. Tests of vacuum brazed components indicate the greater strength, ductility and uniformity of assemblies produced by this method.

Typical of firms currently carrying on investigations in this field is Pratt & Whitney Aircraft, East Hartford, Conn. The firm is using a Stokes furnace in experimental work on the application of vacuum brazing to the production of jet engine components.

Stokes' furnace design for vacuum brazing is practical . . . takes into account the problems of large-scale production. The Stokes dual-chamber design, with a smooth-contour retort completely enclosing the work, permits faster vacuum pumping cycles; provides complete accessibility of the work area and a large, uniform temperature zone.

Stokes engineers have a wealth of practical experience in the field of vacuum metallurgy. We'll be glad to discuss the application of this fast-growing science to your production. Write for Catalog 790 containing valuable information on Stokes High-Vacuum Furnaces.

F. J. STOKES MACHINE COMPANY, 5504 TABOR ROAD, PHILADELPHIA 20, PA.

SEND FOR TECHNICAL LITERATURE:

- Microvac Pumps—Catalog 750
- Diffusion and Booster Pump Specification sheets and performance curves
- The Story of the Ring-Jet Pump
- Complete Vacuum Processing Systems—Catalog 730
- How to Care for Your Vacuum Pump—Booklet 755
- Vacuum Impregnation—Catalog 760
- Vacuum Drying—Catalog 720
- Vacuum Furnaces—Catalog 790
- Vacuum Metallizing—Catalog 780
- Vacuum Calculator Slide Rule

ES VACUUM EQUIPMENT

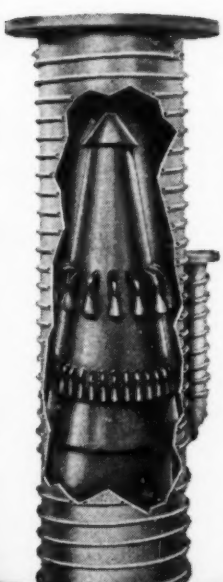

STOKES RING-JET DIFFUSION AND BOOSTER PUMPS

The new Stokes Ring-Jet Pumps embody a new concept of the diffusion principle. Size for size, they have pumping speeds of 10% to more than 100% above any other diffusion pump for a given heat input. Ring-Jet Diffusion Pumps are available in sizes of 4, 6, 10, 14 and 16 inches; Booster Pumps in sizes of 4, 6, 10 and 16 inches. Send for information listed.

STOKES VACUUM VALVES

To control vacuum safely and surely, Stokes vacuum valves are available in 4, 6, 10 and 16-inch standard flange sizes.

STOKES-McLEOD VACUUM GAGES

For measuring vacuums from fractions of a micron up to 50 mm, Stokes-McLeod gages are the standard of reference. Four sizes available.

STOKES

OFFICES IN PRINCIPAL CITIES, REPRESENTATIVES THROUGHOUT THE WORLD

HIGH VOLTAGE POWER SUPPLIES!

in harmony with your power needs

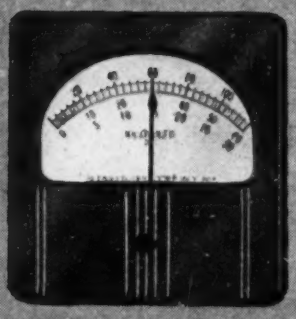

- ✔ safety
- ✔ economy
- ✔ reliability

RACK MOUNTED SERIES 1000

Whatever your power requirements may be, BETA's Series 1000 DC Power Supplies are the perfect high voltage source for complete satisfaction. Whether needed in the lab, or for production testing, these versatile and dependable power unit fills the bill for a wide variety of power problems.

Write TODAY for technical data on the complete BETA line of Power Supplies up to 300 kv, and other HV instruments.

BETA Field Engineers are available for consultation in major American and Canadian industrial centers.

SPECIFICATIONS

VOLTAGE OUTPUT—1 kv to 60 kv, in 11 continuously variable ranges
CURRENT OUTPUT—600 ma to 0.5 ma; can be drawn continuously
INPUT VOLTAGE—105-125 v, 50/60 cycle, or to order
OUTPUT VOLTAGE CONTROL—0.5%
RIPPLE—0.1 – 0.001%, depending on rating
POLARITY—negative, positive or reversible, to order
CORONA LEVELS—low, maintained to 100% rated voltage

FEATURES

- **Current and voltage overload relays**
- **Provision for auxiliary external interlock**
- **Automatic output short mechanism**
- **Line voltage regulator (optional)**
- **Automatic HV period timing (optional)**
- **Zero start interlock (optional)**

Many other features available

BETA ELECTRIC CORPORATION
333 East 103 Street; Dept. RS, New York 29, N. Y.

THE "STANDARD" IN HIGH VOLTAGE

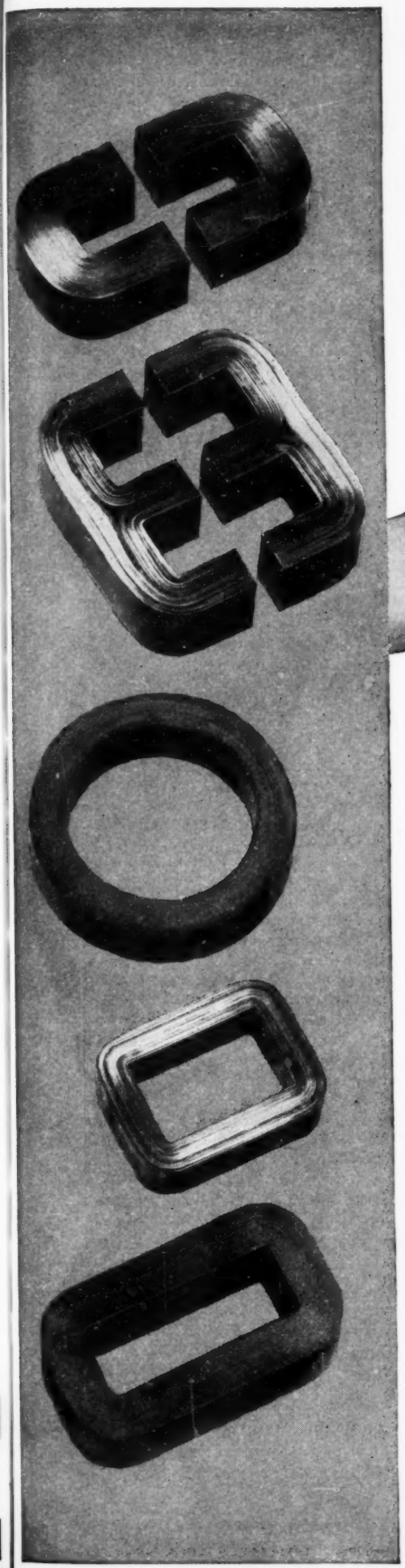

For all your Tape Wound Core Requirements, specify "CORES by ARNOLD"

You'll be *assured* of the performance and uniformity you want, when you use Arnold Cores as magnetic components in your amplifier, transformer and reactor assemblies.

Our facilities for production and testing are highly modern and complete. Arnold is a fully integrated company, controlling every manufacturing step from the raw material to the finished core, and therefore best able to maintain high quality control. You'll have at your command the most complete line in the industry . . . containing every type, shape or size core you may require to meet design needs or electrical characteristics.

Many sizes of Arnold Tape-Wound Cores are carried in stock for immediate delivery. ● *Write for additional information*, and let us quote on your requirements and help solve your problems.

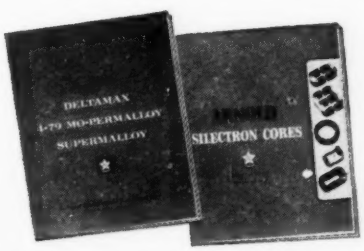

HERE'S DATA YOU NEED...
Write for these Booklets

1 *BULLETIN TC-101A* . . . "Properties of Deltamax, 4-79 Mo-Permalloy and Super-malloy"—28 pages of technical data on Arnold Tape-Wound Cores of high-permeability alloys.

2 *BULLETIN SC-107* . . . "Arnold Silectron Cores"—round, square, rectangular, or C and E cores; 52 pages of data on shapes, sizes, properties, etc.

ADDRESS DEPT. J-512

W&D 5648

THE ARNOLD ENGINEERING COMPANY

SUBSIDIARY OF ALLEGHENY LUDLUM STEEL CORPORATION

General Office & Plant: Marengo, Illinois

DISTRICT SALES OFFICES . . . New York: 350 Fifth Ave.

Los Angeles: 3450 Wilshire Blvd. Boston: 200 Berkeley St.

for the scientist or engineer who has *more to offer...*

A LIMITED NUMBER OF POSITIONS OF UNUSUAL RESPONSIBILITY

IBM, long a leader in the growing field of digital computers for business, science, and government, offers a limited number of long-range creative assignments to outstanding men with Master's or Doctor's Degrees in Electrical Engineering, Physics, Mathematics, Chemistry or Physical Chemistry.

- **Research in solid state materials**
  Investigation of electronic phenomena in solids
  Study of ferrite and semi-conductor characteristics
  Study of the role of surface effects in semi-conductor device characteristics
  Evaluation of sample semi-conductor or ferrite components

- **Development of new concepts, new approaches to internal handling of information in computer systems**
  Information Theory
  Research in Machine Organization
  Theory of Control of Digital Devices
  Switching Circuit Theory
  Digital Data Transmission

- **Circuit Design, Systems Design and Analysis**
  Electronic pulse circuits for accounting and data processing machines—arithmetic switching and logical circuitry—pulse amplifiers, shapers, gates, etc.—magnetic storage—transistor circuitry—input-output device controls.

If you have more to offer, IBM offers you

• Stimulation . . . Satisfaction
At IBM, men find the kind of facilities, associates and climate which stimulate achievement.

• Professional Growth
In Company growth lies personal opportunity, and IBM has an enviable record of steady growth. Over the past quarter century IBM's business has doubled every five years.

Out of respect for the unusual man's talent and promise, IBM encourages qualified candidates to visit its Poughkeepsie, N. Y. laboratory—at their convenience, and IBM's expense. Write, outlining your qualifications, to: William M. Hoyt, International Business Machines, Room 3812, 590 Madison Avenue, New York, N. Y.

IBM®

Producer of electronic data processing machines, electric typewriters, and electronic time equipment.

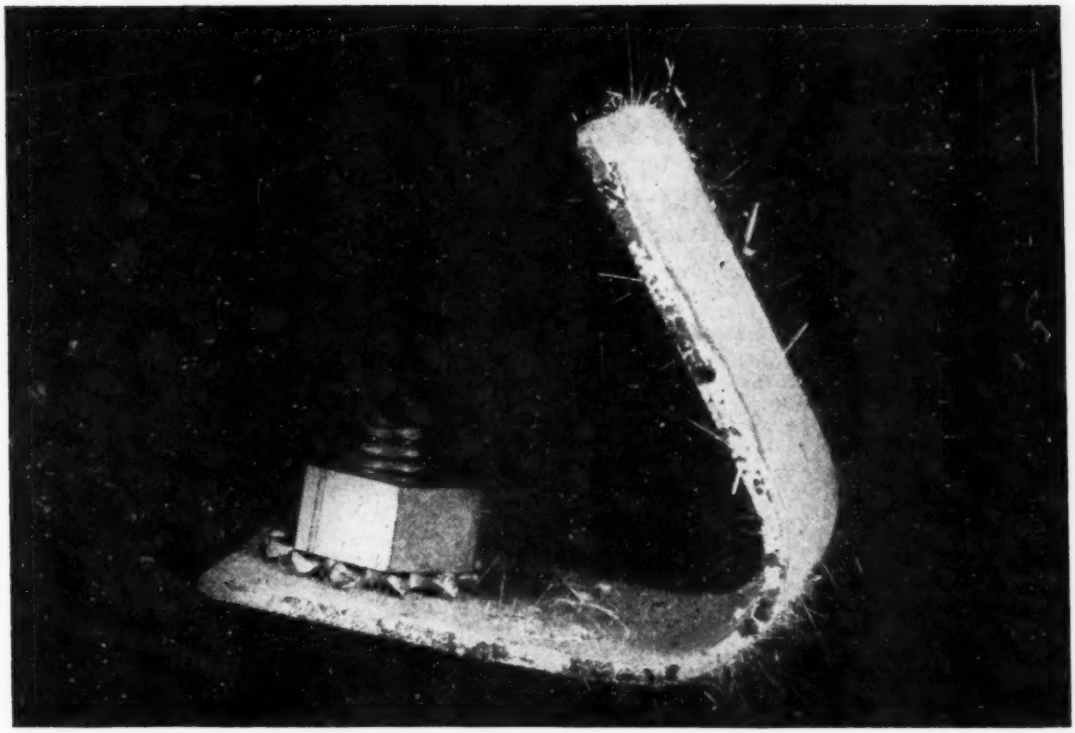

Whiskers on tin-plated steel, enlarged 6 times. Immense yield strength of metals in whisker form was discovered by Bell scientists.

The clue of the metal whiskers

The habit of close observation at Bell Laboratories often turns "tremendous trifles" into important scientific progress. Such a case occurred when unexplained short circuits in wave filters seemed to be associated with a small zinc-plated mounting bracket.

Close scrutiny disclosed a whiskery growth on the zinc plating. Similar whiskers of tin were found growing on tin-plated equipment. Studies showed the whiskers to be tiny single crystals of metal.

Suspecting that these unusual crystals might be of essentially perfect structure, alert Laboratories scientists saw an opportunity at last to test an important metallurgical theory.

The scientists studied the whiskers, grew larger ones, and showed that the crystals had enormously high yield strength as predicted by the theory for perfect crystals – a strength far greater than for the same metal in any other known form. This clue has opened new frontiers in the study of what makes metals strong or weak, and has excited metallurgists all over the world.

Thus, another new advance comes from the Bell Telephone Laboratories practice of scrutinizing *everything* that means better telephone service.

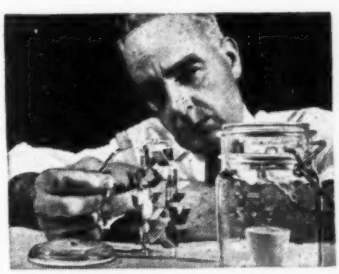

Through the study of thousands of specially cultivated whiskers, Bell scientists seek to prevent treacherous growths in telephone equipment.

BELL TELEPHONE LABORATORIES

IMPROVING TELEPHONE SERVICE FOR AMERICA PROVIDES CAREERS FOR CREATIVE MEN IN SCIENTIFIC AND TECHNICAL FIELDS

Now available for the first time . . .

RESEARCH AND ENGINEERING METHODS AND DATA

to aid in greater development of

SCIENTIFIC AND INDUSTRIAL USES OF ATOMIC ENERGY

SIX VOLUMES
on the peaceful use of
ATOMIC ENERGY
Prepared by
THE U. S. ATOMIC ENERGY COMMISSION

Here is an immensely valuable reference for the scientist and engineer working with nuclear energy. Information released by the Atomic Energy Commission shows much concerning the ways in which fissionable materials can be put to work in nuclear reactors for research purposes and for the production of power and radioisotopes.

The materials range from descriptions of research reactors now in use to a catalogue of special laboratory equipment, and includes a three-volume handbook on reactor physics, technology, and materials. These works are representative of the great strides already made in putting atomic energy to work in industry, agriculture, medicine, and research. They contain technical information and ideas that can contribute to even greater progress in the future.

RESEARCH REACTORS
406 pages, $6.50
Detailed descriptions, complete with selected design drawings of six types of U. S. research reactors now in use.

REACTOR HANDBOOK: PHYSICS
804 pages, $12.00
Discussion of reactor physics and nuclear-design data, including shielding theory and calculating techniques.

REACTOR HANDBOOK: ENGINEERING
1088 pages, $15.00
Review of reactor technology, including basic reactor systems applicable to power development and a summary of experimental reactor designs.

REACTOR HANDBOOK: MATERIALS
614 pages, $10.50
Data and background information on reactor materials; fuels and moderators, shielding, structural and miscellaneous materials.

NEUTRON CROSS SECTIONS
363 pages, $12.50
Recent compilations of neutron cross-section data affecting reactor design.

CHEMICAL PROCESSING AND EQUIPMENT
316 pages, $6.00
Process and engineering description of a separation system, together with a catalogue of special equipment for the safe handling of radioactive materials.

Announcing . . . an outstanding new series

PROGRESS IN NUCLEAR ENERGY

Published by special arrangement with the Pergamon Press of London

This new series represents the most complete selection of the latest up-to-date information and data on nuclear energy available.

In order to make the series reasonably self-contained, the necessary historical background will be included the first time a particular subject is discussed. Subsequent articles on such subjects will generally only cover the more recent progress.

PROGRESS IN NUCLEAR ENERGY aims to make it easier for scientists and engineers to obtain information outside their special field.

PHYSICS AND MATHEMATICS
to be edited by
R. A. CHARPIE — D. J. LITTLER
D. J. HUGHES — S. HOROVITZ

REACTORS
to be edited by
R. A. CHARPIE — D. J. LITTLER
D. J. HUGHES — M. TROCHERIS

ECONOMICS OF NUCLEAR POWER
to be edited by
J. GUERON — I. R. MAXWELL
J. A. LANE — J. MENKE

PROCESS CHEMISTRY
to be edited by
F. R. BRUCE — H. H. HYMAN
J. M. FLETCHER — J. J. KATZ

TECHNOLOGY, MATERIALS AND METALLURGY
to be edited by
H. M. FINNISTON — R. HURST
S. MCLAIN

BIOLOGICAL SCIENCES AND MEDICINE
to be edited by
J. COURSAGET — J. BUCHER
J. F. LOUTIT

SEND FOR COPIES ON APPROVAL

McGRAW-HILL BOOK COMPANY, INC.
330 WEST 42ND STREET NEW YORK 36, N.Y.

SIDELIGHTS ON THE SCIENTISTS *number* **2** *of a series*

How many patents per Ph. D.?

Some of the young fellows on our staff have been analyzing our files of personal data regarding scientists and engineers here at Hughes. What group characteristics would be found?

With additional facts cheerfully contributed by their colleagues they have come up with a score of relationships—some amusing, some quite surprising. We shall chart the most interesting results for you in this series.

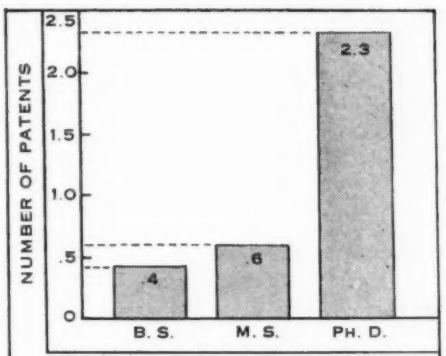

Data obtained from a 20% random sample of the 2,200 professional engineers and scientists of Hughes Research and Development Laboratories.

In our laboratories here at Hughes, more than half of the engineers and scientists have had one or more years of graduate work, one in four has his Master's, one in 15 his Doctor's. The Hughes research program is of wide variety and scope, affording exceptional freedom as well as exceptional facilities for these people. Indeed, it would be hard to find a more exciting and rewarding human climate for a career in science. Too, the professional level is being stepped up continually to insure our future success in commercial as well as military work.

Hughes is pre-eminent as a developer and manufacturer of airborne electronic systems. Our program includes military projects in ground and airborne electronics, guided missiles, automatic control, synthetic intelligence. Projects of broader commercial and scientific interest include research in semiconductors, electron tubes, digital and analog computation, data handling, navigation, production automation.

SCIENTIFIC STAFF RELATIONS

Hughes

RESEARCH AND DEVELOPMENT LABORATORIES

Culver City, Los Angeles County, California

RIGHT NOW *the Laboratories in Culver City, California, and the Missile Production facility in Tucson, Arizona, have positions open for engineers who are experienced in any or all phases of Test Equipment Design.*

Reinhold Books for Physicists, Physical Chemists, Engineers

(4) INSTRUMENTS FOR MEASUREMENT & CONTROL

By WERNER G. HOLZBOCK, Development Engineer, Askania Regulator Co.

First to describe and illustrate all the recent devices for measuring and controlling temperature, moisture, pressure, flow, uniformity, etc. In non-mathematical language. Shows how the various instruments compare with each other; discusses factors influencing choice of instruments for particular jobs.

1955 416 pages $10.00

(5) PROBLEMS & CONTROL OF AIR POLLUTION

Edited by FREDERICK S. MALLETTE, Executive Secretary, Committee on Air Pollution Controls, The American Society of Mechanical Engineers.

Presents the proceedings of the First International Congress on Air Pollution, held in March under the sponsorship of the ASME. Contains papers by the world's foremost experts, and even a chapter on management aspects telling ways of avoiding pitfalls in community relations over air-pollution problems.

1955 320 pages $7.50

(6) HAWLEY'S TECHNICAL SPELLER

By GESSNER G. HAWLEY and ALICE M. HAWLEY

A boon to everyone who must use hard-to-spell scientific terms in his work. Contains over 8,000 words selected from the vocabularies of chemistry, physics, electronics, and many other fields. Clear type. Many easy-to-use features.

1955 160 pages $2.95

(7) MATERIALS FOR NUCLEAR POWER REACTORS

By HENRY H. HAUSNER and STANLEY B. ROBOFF, of Atomic Energy Div., Sylvania Electric Products, Inc.

The very first book to describe the basic types of materials used in nuclear reactors, their functions, and the problems associated with their use. Covers materials for shielding, cladding fuel elements, moderators, reflectors—for all the most important parts of a reactor.

1955 240 pages $3.50

(8) THE TECHNICAL REPORT

Edited by B. H. WEIL

Every phase of the technical report, from the conception of its need to final destination and use, is fully covered in this exceptional new book. Goes into the fundamentals of editing, illustrating, duplicating, binding, distribution, security filing, and putting the report files to work. All aspects of writing are carefully surveyed, too.

1954 492 pages $12.00

(1) TEMPERATURE

Its Measurement and Control in Science and Industry

VOLUME 2

Edited by HUGH C. WOLFE, Sponsored by the American Institute of Physics, the National Bureau of Standards, and Office of Ordnance Research, U.S. Army

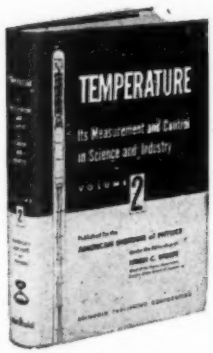

Presents the proceedings of the 3rd International Symposium on Temperature, with significant material about temperature concept and the phenomena on the basis of which temperature can be determined over the range of from .001°K to the temperatures at the core of an atomic explosion. Experts of many nations who prepared the papers cover not only their own work, but that of many others in the same fields.

1955 480 pages $12.00

(2) TEMPERATURE

Its Measurement and Control in Science and Industry

Volume I

World-wide acclaim as the outstanding reference work of its field has been accorded this encyclopedic volume. Presents thorough-going descriptions of all phases of temperature technique.

1941 1,362 pages $18.00

(3) FIFTH SYMPOSIUM (*INTERNATIONAL*) ON COMBUSTION

Combustion in Engines and Combustion Kinetics

By The Standing Committee on Combustion Symposia, The Combustion Institute, Pittsburgh, Pa.

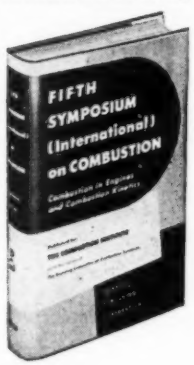

Available for the first time in bound form are all of the 101 papers presented at the Fifth International Combustion Symposium; the work of 182 contributors from many parts of the world. This timely book presents a large and important body of new knowledge on combustion problems involved in the efficient operation of all kinds of engines. Adding to the book's interest and scope is a section of round table discussions among outstanding authorities.

1955 848 pages 6⅞" x 10" $15.00

USE THIS COUPON FOR FREE 10-DAY EXAMINATION

REINHOLD PUBLISHING CORP., Dept. M-857
430 Park Ave., New York 22, N. Y.

Rush me the book(s) encircled below for 10 days FREE examination. In 10 days, I will either return the book(s) and owe you nothing, or will send purchase price plus postage.

1 2 3 4 5 6 7 8

Name.....

Address.....

City.....Zone.....State.....

☐ SAVE MONEY! Enclose purchase price now and Reinhold pays all shipping charges. Same return privileges; refund guaranteed. Please include 3% sales tax on New York City orders.

Here is one of a series of advertisements we are running in FORTUNE and BUSINESS WEEK to acquaint company managements with our interest and our experience in the field of automation and data-processing.

We believe we are making good progress in developing activities that should ultimately give us a strong position in the tremendously important and rapidly growing field of automation.

Positions are available for scientists and engineers in these fields of current activity:

Business Data Systems Development

Digital Computer Research and Development

Radar and Control System Development

Communication Systems Development

Guided Missile Research and Development

The Ramo-Wooldridge Corporation

8820 BELLANCA AVENUE
LOS ANGELES 45, CALIF.

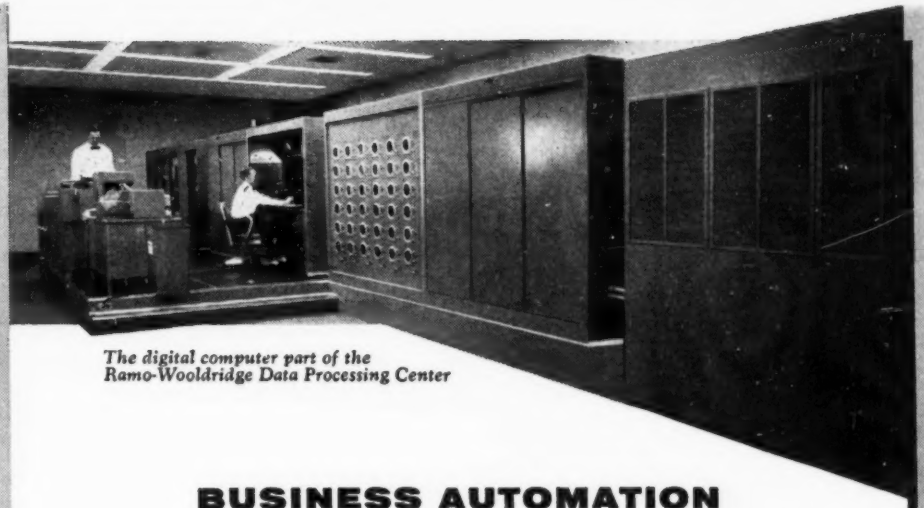

The digital computer part of the Ramo-Wooldridge Data Processing Center

BUSINESS AUTOMATION and MILITARY ELECTRONICS

The problem confronting many company managements today in deciding what course to follow in applying the new techniques of automation and data processing is similar to the problem faced in recent years by the leaders of our military organizations in arranging for efficient application of the same powerful tools of electronics to the art of war.

At Ramo-Wooldridge the difficult demands of major military systems responsibility have been met successfully by the placing of heavy dependence upon teams of unusually well-qualified, mature and experienced scientists, operational procedures experts, and engineers. These teams deal with the technical and non-technical portions of a project as inseparable and interrelated aspects of a single problem.

Similarly, work has been done in the last two years by this company on systems problems of non-military clients from such diverse fields as manufacturing, banking, transportation and public utility. The results strongly support the conclusion that many of the difficult problems in automation that face business and industry today can be economically solved by teams that include a breadth of technical and non-technical competence which permits them to conduct a highly objective, scientific analysis of a client's operations and requirements.

One important advantage to the client of such a broad and objective approach to his problems is the possibility of recommendations that realistic operational needs can be met without the necessity for investment in any additional machines or equipment. Nevertheless, the technical strength of The Ramo-Wooldridge Corporation, provided by its hundreds of scientists and engineers, is such that it can also undertake successfully the development of entirely new equipment and techniques, if required. As an example, major programs are currently under way on the development of an advanced type of digital computer and control system, and on the automation of large-scale data processing activities.

To a surprisingly great extent, military electronics experience has charted the course for non-military automation. A major objective of The Ramo-Wooldridge Corporation is to assist business and industry in moving rapidly, yet realistically and economically, to take advantage of the great benefits of the new techniques.

The Ramo-Wooldridge lecture hall during a lecture on Operations Research, as applied to the solution of management problems.

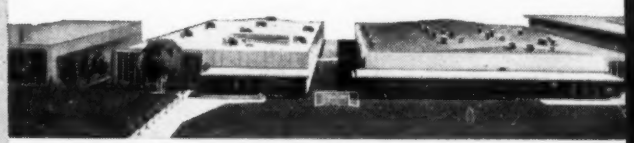

PACIFIC SEMICONDUCTORS, INC., *a subsidiary devoted to the development and manufacture of advanced types of semiconductor devices such as diodes and transistors... of great importance in the future apparatus of automation.*

The Ramo-Wooldridge Corporation

8820 BELLANCA AVENUE • LOS ANGELES 45 • CALIF.

Dear wife and kids:

Got here o.k. today. Couldn't wait to tell you what I think of Farnsworth and Fort Wayne. It's more than a place to work .. it's a way of life! Most of the folks here own their own homes. There are no row houses and that cottage in the country is <u>real</u> and only 10 minutes from everywhere.

Schools? There are 50 of them (full time .. no half day shifts!) 5 beautiful High Schools <u>and</u> I can take grad work at Purdue here at Farnsworth's expense!

This is also a town of churches ... 132 in a town of 135,000 that boasts one of the lowest juvenile delinquency rates in the country.

There's also a full size, full season symphony orchestra ... World championship basketball and hockey in a new 3 million dollar coliseum that's out of this world. (Are you listening, Jackie?)

Tell Joe and his wife to start packing because there's plenty of room here for more engineers like him in R and D and systems engineering in missiles, radar, antennas, microwaves, test equipment, countermeasures, transistor applications and other phases. Tell him to write the Technical Employment Manager, Farnsworth Electronics Co. (a division of IT & T) at Fort Wayne, Ind. He'll be glad he did.

I can't wait until you and the kids get here ... I <u>know</u> you'll love it. And, like they say at Farnsworth, "Very, very few ever leave it."

Love Jack

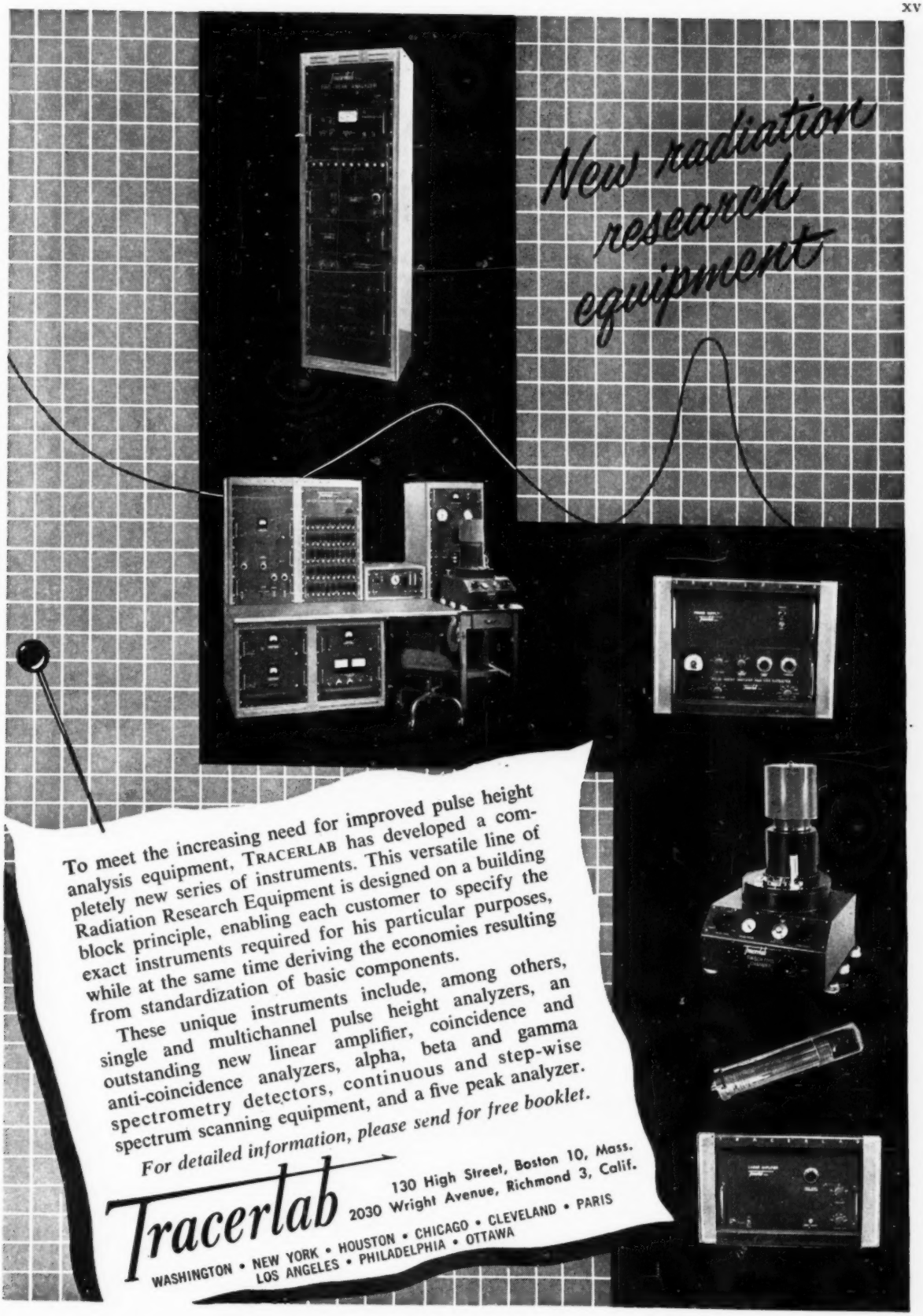

To meet the increasing need for improved pulse height analysis equipment, TRACERLAB has developed a completely new series of instruments. This versatile line of Radiation Research Equipment is designed on a building block principle, enabling each customer to specify the exact instruments required for his particular purposes, while at the same time deriving the economies resulting from standardization of basic components.

These unique instruments include, among others, single and multichannel pulse height analyzers, an outstanding new linear amplifier, coincidence and anti-coincidence analyzers, alpha, beta and gamma spectrometry detectors, continuous and step-wise spectrum scanning equipment, and a five peak analyzer.

For detailed information, please send for free booklet.

Tracerlab

130 High Street, Boston 10, Mass.
2030 Wright Avenue, Richmond 3, Calif.

WASHINGTON • NEW YORK • HOUSTON • CHICAGO • CLEVELAND • PARIS
LOS ANGELES • PHILADELPHIA • OTTAWA

Polio Vaccine

CAN'T HELP HER...

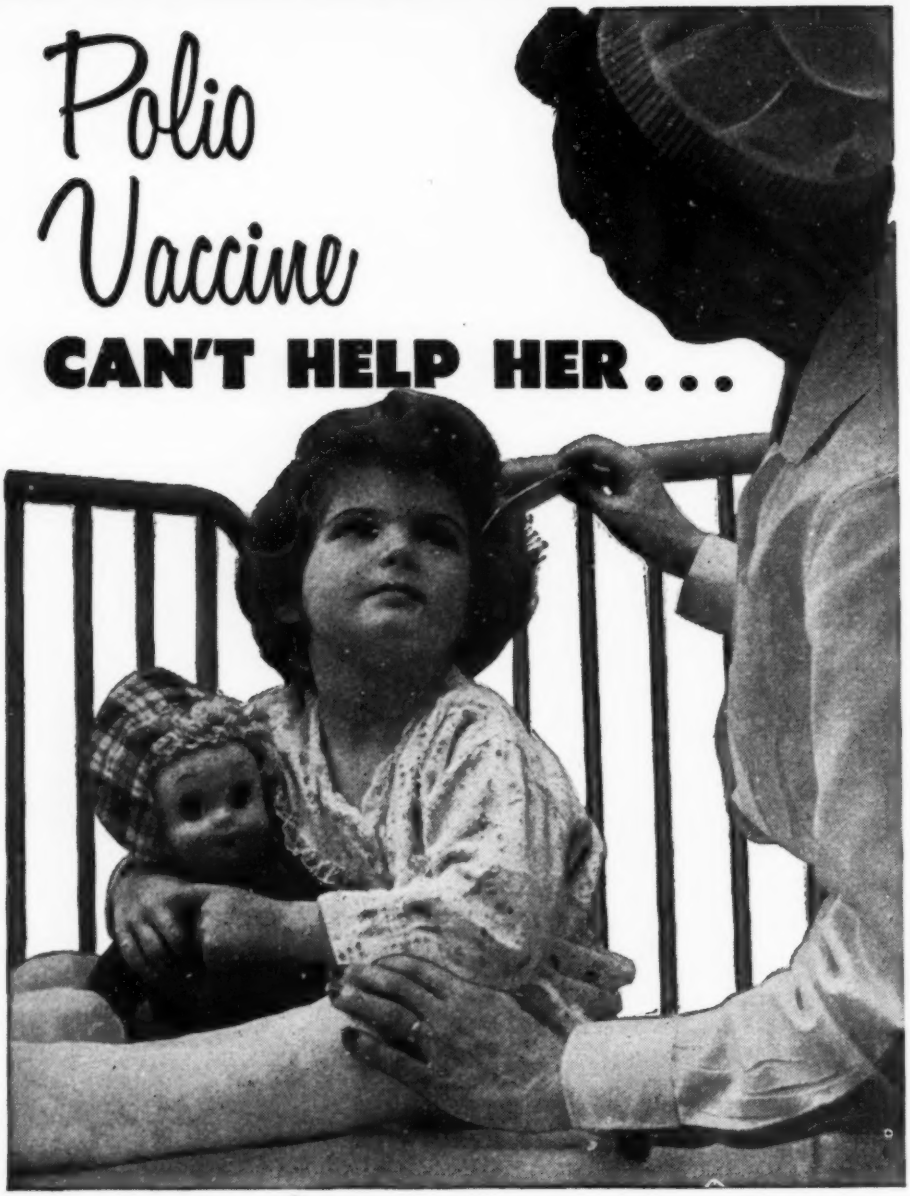

only YOU can

Your March of Dimes funds are providing the care she needs. For she is one of the tens of thousands of polio victims "born too soon"—before the epic polio vaccine. Today, March of Dimes funds which developed and tested the vaccine are financing research to improve it. But there still are polio victims who need help. And there will be tens of thousands more stricken before the nation has its blanket of protection. March of Dimes plus the hearts and hands of polio fighters everywhere must continue to provide our main bulwark against polio.

Polio isn't licked yet

Join the **MARCH OF DIMES**

January 3 to 31

physicists mathematicians

You're invited to participate in the pioneering of...

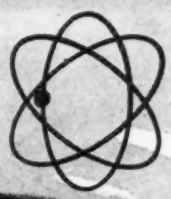

the development of

ATOMIC POWER

at **Westinghouse**

Requirements:

Research in Applied Mathematics. Numerical Analysis & Digital Computing Techniques Relating to Nuclear Power Reactors; Experimental Physicists-Research studies with Nuclear Reactors; Theoretical Physicists for General Development Reactor Theory & Dynamics.

NEW FELLOWSHIP PROGRAM —

. . . in conjunction with the University of Pittsburgh, this new Westinghouse program enables qualified candidates to attain their M.S. and Ph.D. degrees on release time, WHILE ON FULL PAY.

SALARIES OPEN —

Ample housing available in modern suburban community 15 minutes from our new plant. Ideal working conditions. Excellent pension plan. Education program. Health & Life Insurance.

Send Complete Resume To:

MR. A. M. JOHNSTON, WESTINGHOUSE BETTIS PLANT

P.O. Box 1468, Pittsburgh 30, Penna.

Westinghouse *First in Atomic Power*

NO. 3830A DENSICHRON PATENT NO. 2424933

PROBE

The Welch DENSICHRON®

ELECTRONIC DENSITOMETER

A Versatile Instrument for the Measurement of Reflectance and Transmittance

Makes Precision Light Measurements—Quickly—Accurately

The Welch Densichron is an electronic densitometer of good sensitivity and unusually high stability. It can be employed either for quantitative measurement of optical density, or as a sensing device for automatic control of various industrial processes in which constancy of transmitted or reflected light is a criterion of the quality or uniformity of the product.

It consists essentially of a probe unit containing a photoelectric tube for detecting light energy and an amplifier to which it is connected by a flexible cable. The amplifier incorporates a milliammeter calibrated to indicate either optical density on a "log" scale or percent transmission on a "linear" scale, depending upon the model.

The logarithmic optical-density scale extends from 0 to 1.5 and density is readable to 0.01. A three-step range switch increases the range to a maximum density of 4.5 with no loss in sensitivity or precision of readings. This range represents a linear response of the receiver to variations in light intensity of over 30,000 to 1.

The meter movement used in the log-scale model of the amplifier is designed in such a manner that the deflections are very nearly proportional to the logarithm of the reciprocal of the activating photoelectric current. This is advantageous in both densitometry and photometry inasmuch as optical density in both cases is this same function of photoelectric current and the scale can therefore be calibrated in essentially uniform increments of optical density. A lower scale on this meter is used for determining photographic exposure times.

The meter in the percent-transmission model uses a standard meter movement and indicates percent transmission on a linear scale. This may also be considered as percent reflectance or percent incident light upon the phototube. The full range of the scale for the first position of the range switch is from 0 to 100% transmission. Other positions of the switch provide ranges of 0 to 10%, 0 to 1% and 0 to 0.1%, respectively. The lower scale on this meter is calibrated to read directly the optical density corresponding to the percent transmission indicated on the upper scale.

The amplifier also produces an A.C. output signal, the voltage of which is a measure of the light intensity, and provision is made for utilizing the direct current of the ammeter circuit in an external circuit. The instrument therefore supplies a voltage which can be used to operate either a control mechanism or a standard ink recorder.

Principle of Operation

The outstanding feature of the Densichron is its patented system for magnetically modulating the space current in a phototube.* This is accomplished by applying a 60-cycle alternating magnetic field across the path of the electron beam, thereby deflecting the electrons from their path to the anode 120 times per second. The output current of the tube is thus changed from its normal steady value to a pulsating output with a frequency of 120 cycles per second. When the usual direct-current output of a phototube is amplified, the measuring instrument is subject to severe zero drift necessitating frequent recalibration, and its response is slow. The pulsating output from the Densichron phototube, however, is capable of stable, high-gain amplification with rapid response.

Although the Densichron can be used in a wide variety of ways it is a simple device to use and requires no special operator skill. It will perform satisfactorily in routine operations for long periods of time with little or no servicing, yet is readily adaptable to innumerable types of special measuring techniques.

* Henry P. Kalmus and George O. Striker, Rev. Sci. Inst. **19**, 79 (1948).

3830A. DENSICHRON WITH BLUE PROBE. This consists of the amplifier with logarithmic-scale meter, blue-sensitive probe, metal probe support, five different measuring apertures, a cone with ⅛-inch aperture, and a set of instructions. The amplifier operates on 115 volts, 60-cycle A.C., only, except on special order. **Each, $225.00**

3830B. DENSICHRON WITH RED PROBE. This is identical with No. 3830A except that a red-sensitive probe is furnished in place of the blue-sensitive probe. **Each, $225.00**

NO. 3832A REFLECTION UNIT

3832A. REFLECTION UNIT. When coupled to the Densichron amplifier, this unit becomes a convenient reflectance meter. It has a self-contained light source, filter wheel, and phototube. Power for the lamp is taken from the amplifier through the same connector normally used for the probe. A viewing port permits the head to be correctly placed over the area to be measured. The unit includes optics for both small and large spot work, a calibrated gray scale, and three vitrolite working standards. **Each, $110.00**

W. M. WELCH SCIENTIFIC COMPANY

DIVISION OF W. M. WELCH MANUFACTURING COMPANY

ESTABLISHED 1880

1515 Sedgwick Street, Dept. C-1 Chicago 10, Illinois U. S. A.

Manufacturers of Scientific Instruments and Laboratory Apparatus

Douglas announces...

the formation of a separate Missiles Engineering Department

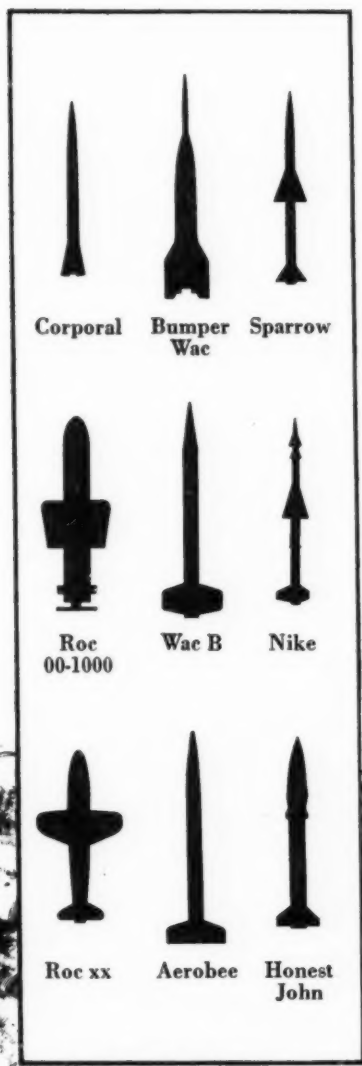

Growing importance of missiles in the nation's defense has led to the separation of missiles engineering from aircraft engineering functions at Douglas Aircraft Company.

Leadership in this important field has been won by Douglas in 14 years of development and design of guided missiles for the Armed Forces. Douglas is currently engaged in eight major missiles projects, under contracts from the Air Force, Army and Navy.

Formation of the new department at Douglas opens new opportunities for engineers and scientists interested in the missiles field. Write to: E. C. Kaliher, Engineering Personnel Manager, Missiles, Douglas Aircraft Co., Santa Monica, California.

Missiles by *DOUGLAS* **First in Aviation**

MISSILE SYSTEMS

PHYSICISTS

■

Research and development in the technology of guided missiles is not confined to any one field of physics. Broad interests and exceptional abilities are required by the participants. Typical areas at Lockheed Missile Systems Division include:

- Neutron and reactor physics
- Advanced electronics and radar systems
- Applied mathematics such as the numerical solution of physical problems on complex computers
- Analytical systems analysis of guidance and control problems
- Ballistics and the integration of ballistic type missiles with vertical guidance
- Electromagnetic properties of the upper atmosphere
- RF propagation in microwaves as concerned with antenna and radome research
- Experimental laboratory instrumentation

Continuing developments are creating new positions for those capable of significant contributions to the technology of guided missiles.

■

MISSILE SYSTEMS DIVISION | *research and engineering staff* | LOCKHEED AIRCRAFT CORPORATION | VAN NUYS • CALIFORNIA

Specify RCA Vacuum Gauge Tubes

"Application-proved" in laboratory and industrial systems, RCA's diversified line of gauge tubes meets virtually every vacuum measuring requirement. For example, RCA-1945 responds to a change of hydrogen pressure of 0.0001 micron, and even lower—is used to detect very small leaks. Thermocouple-type 1946 is highly sensitive over the pressure range of 1000 microns to 1 micron—is useful down to 0.1 micron. Pirani-type 1947 is highly sensitive over the range of 500 to 10 microns. Ionization-types 1949 and 1950 are especially useful for pressures below 0.1 micron, and on down to 0.0001 micron—are used to detect minute leaks. RCA Vacuum Gauge tubes—*and all types of RCA Tubes for laboratory work*—are available from your RCA Tube Distributor. He is listed in the Thomas' Register.

RCA, Commercial Engineering
Section L-25-U, Harrison, New Jersey

FREE
Technical Bulletins

Please send me free technical bulletins on RCA Vacuum Gauge Tubes.

NAME_____

FIRM_____

ADDRESS_____

CITY_____ STATE_____

RCA RADIO CORPORATION of AMERICA
ELECTRON TUBES HARRISON, N.J.

ENGINEERS Electronic • Mechanical DESIGNERS • DRAFTSMEN

How do you Measure success?

Some measure success only by money; others by the enjoyment they get out of their work. But the true measure of success is a combination of both *plus* the knowledge that your efforts are recognized and appreciated.

Melpar engineers find diversity and opportunity for professional growth; they enjoy being part of a highly creative staff without losing their individuality; and they benefit from Melpar's completely integrated facilities for system responsibility from design concept through production.

To learn how Melpar measures up to your own standards send complete resume to

- Network Theory
- Systems Evaluation
- Automation
- Microwave Technique
- UHF, VHF or SHF Receivers
- Analog Computers
- Digital Computers
- Magnetic Tape Handling Equipment
- Radar and Countermeasures
- Packaging Electronic Equipment
- Pulse Circuitry
- Microwave Filters
- Flight Simulators
- Servomechanisms
- Subminiaturization
- Electro-Mechanical Design
- Quality Control & Test Engineers

Technical Personnel Representative

melpar, inc.

Subsidiary of Westinghouse Air Brake Co.

3000 Arlington Blvd., Dept. JA-19, Falls Church, Va.

11 Galen Street, Watertown, Mass. • 99 First St., Cambridge, Mass.

Radioelements FOR RESEARCH

high specific activity

PILE-PRODUCED ISOTOPES

naturally radioactive materials

RADIUM • RADIUM D • POLONIUM

ALPHA • BETA • GAMMA AND NEUTRON SOURCES

ATOMIC ENERGY OF CANADA LIMITED

COMMERCIAL PRODUCTS DIVISION • P.O. BOX 93 — OTTAWA, CANADA

the future resides IN MEN WITH IMAGINATION!

los alamos
scientific laboratory

... the nation's most important institution for the development of nuclear and thermonuclear weapons is seeking professional engineers and scientists, particularly those vitally interested in the development of the atomic age.

In addition to its continuing and ever-expanding achievement in weapons research, the Laboratory is now pioneering in the fascinating fields of nuclear and thermonuclear power and nuclear propulsion.

At the Laboratory, staff members have the opportunity of associating with leaders in research and experimentation... of working with some of the Western World's finest equipment and facilities... of winning recognition ... of achieving advancement commensurate with ability.

If you would like more information about the Laboratory's career opportunities which are not civil service... about the delightful climate and area in which Los Alamos is located, send your inquiry to

DEPARTMENT OF SCIENTIFIC PERSONNEL Division 311

los alamos
scientific laboratory
OF THE UNIVERSITY OF CALIFORNIA
LOS ALAMOS, NEW MEXICO

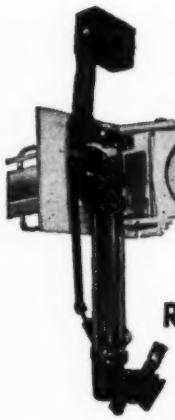

Periscopes For "HOT SPOT" Remote Observation

A custom designed industrial periscope is very often the answer to "Hot Spot" remote control handling, instrumentation and observation. We have designed and manufactured many such periscopes.

If you have a problem calling for a periscope or for any precision optical system, check with us. For nearly half a century Kollmorgen has designed, developed and manufactured precision optical products including Industrial and Naval Periscopes, Fire Control Devices, Projection Lenses and Navigational Instruments for Industry and for the Armed Services.

Send for Bulletin 301

KOLLMORGEN *Optical* **CORPORATION**

Plant: 347 King Street Northampton, Mass.
New York Office: 30 Church Street, New York 7, N. Y.

physicist

MS or PhD

OPERATIONS RESEARCH

The inauguration of greatly expanded research and development facilities at Electric Boat Division of General Dynamics Corporation calls for scientists of the utmost skill. As designers and builders of the world's first atomic submarines, Nautilus and Sea Wolf, Electric Boat has extensive knowledge in the application of nuclear energy for propulsion. This new department will delve deep into more advanced nuclear submarine design and a variety of other new fields as well.

This is a permanent position for a Physicist with a thorough background in both the mathematical and practical aspects of operations research. He will occupy a position of leadership.

Electric Boat is building for the future, and offers talented researchers a chance to grow with it. Please write complete details, including salary requirements, to Peter Carpenter.

Electric Boat Division
GENERAL DYNAMICS CORPORATION
GROTON CONNECTICUT
near New London on the Connecticut shore

LINDE
Trade-Mark

synthetic sapphire
FOR
OPTICAL SYSTEMS

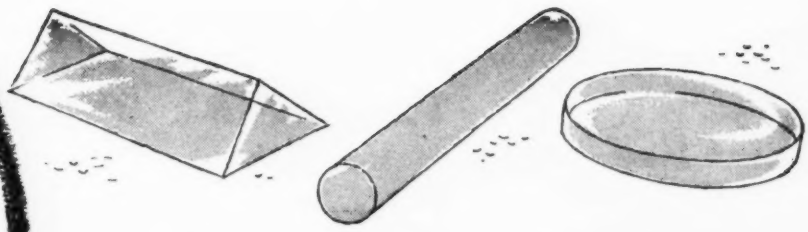

In the important infra-red and ultra-violet regions, sapphire transmits a high percentage of radiation. This excellent optical transmission, combined with physical strength and chemical inertness, makes sapphire an ideal material for optical systems that require resistance to abrasion and corrosion as well as good transmission properties.

Sapphire has been used for prisms, flats, light pipes, and windows for combustion and chemical vessels. Now that sapphire disks can be produced in diameters up to 2 inches, it is being used in many important new applications.

For further information, call or write your nearest LINDE office.

LINDE AIR PRODUCTS COMPANY
A Division of Union Carbide and Carbon Corporation
30 East 42nd Street UCC New York 17, N. Y.
Offices in Other Principal Cities

"Linde" is a registered trade-mark of Union Carbide and Carbon Corporation.

MATHEMATICAL PHYSICIST
or
APPLIED MATHEMATICIAN

Involves research and application of information theory, probabilistic logic and theory of games. A laboratory environment is combined with an industrial salary scale and benefits.

Location: Northeast. Candidate should have a doctoral degree, 3 to 5 years experience and both aptitude and liking for consultation. Replies held in strict confidence.

Write to:

BOX 1255A
JAP, 57 East 55 St.
New York 22, N.Y.

SENIOR PHYSICIST

Highly responsible position in an expanding research and development laboratory.

The work requires an MS or PhD, with several years of experience, including a combined experimental and theoretical background in one or more of the following: electromagnetic theory, sound propagation, infra-red techniques and solid state physics.

This is an unusual opportunity for an ambitious technical man who likes dealing with people to build an interesting, worthwhile future. The location in a suburban New Jersey community provides easy access to the educational and cultural facilities of New York City. Extensive employee benefits include a liberal educational assistance program.

All replies in confidence. Please write complete details, including salary requirements, to Donald R. Cordisco.

VITRO LABORATORIES
Division of Vitro Corporation of America
200 Pleasant Valley Way West Orange, N.J.

Continuing growth of

TECHNICAL OPERATIONS'
staff at the
Combat Operations Research Group

of the Continental Army Command increases our need for above-average

■ **physicists** ■ **mathematicians** ■ **physical chemists**
■ **experimental psychologists** ■ **and others**

Employment with Technical Operations at Fort Monroe, Virginia, offers above-average rewards in a new and growing field to scientists who can qualify. Write for our brochure.

Address Mr. R. A. Langevin

TECHNICAL OPERATIONS, Inc.
777 14th STREET, N. W. WASHINGTON 5, D. C.

VARIABLE SPEED CONTROL
LABORATORY MODELS

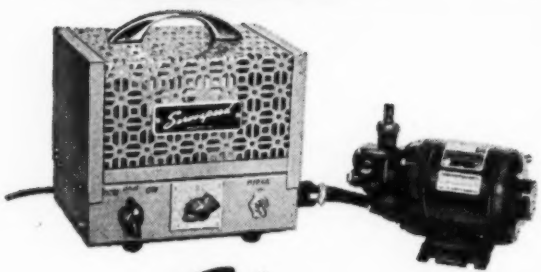

- Assures proper process speed
- Permits 40:1 speed range while in motion
- Constant torque capability
- Fingertip control from remote point
- Electronic "Servo" control
- Wide range of available gearmotors
- 115 volt 50-60 cycle operation
- Reversible direction of rotation
- "Dynamic" fast stop "braking"

Uses: Laboratory agitators, running torque testers, life test fixtures, recording chart drivers, timers, etc.

MODEL 2792 with 1/50 h.p. motor 100-5000 r.p.m. **$89.50**

MODEL 2792-G with 1-40 r.p.m. 3 in./lb. gearmotor **$95.00**

Also available with other motors • O.E.M. models for mounting into your enclosures

Servospeed DIV. of ELECTRO DEVICES, Inc.
4 Godwin Ave. Paterson, N. J.

ATOMIC'S MODEL 131 SCALER

offers greater versatility for Geiger, Scintillation or Proportional Counting

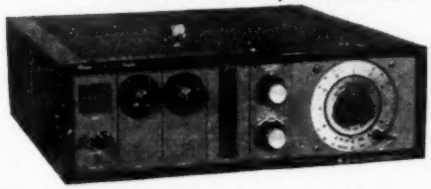

The Model 131 is a basic scaler available in combination with different High Voltage Supplies to energize detectors. It uses new simplified circuits with cold cathode glow tubes for extreme reliability and improved counting techniques.

Scale of 1000 and 4-digit register
Maximum input sensitivity, −0.25 volts
Resolution for pulse pairs, 5 microseconds
Preset time up to 1 hour
Precision Calibrated Adjustable Discriminator

Model 131 Scaler is available with H.V. power supplies as: Model 1031 — H.V. +2500V. Model 1032 — H.V. ±1400V or Model 1035 — H.V. +5000V.

For complete details request Bulletin 131-3
Representatives in principal cities — U.S. and abroad.

ATOMIC INSTRUMENT COMPANY
84 MASSACHUSETTS AVE. CAMBRIDGE 39, MASS.

PHYSICISTS

Optics and Radiation Detection

Permanent positions are available in research programs concerned with applications of optical systems and related detectors throughout the infrared, visible and ultraviolet spectrum to various research problems for industry and government.

Design and Analysis of Optical Systems

Study of Detectors and Detection Schemes

These activities are carried on in close cooperation with other groups representing all fields of the physical sciences and engineering. Location at Technology Center offers excellent opportunity for professional development and participation in scientific activities.

Send resume to Personnel Manager
Armour Research Foundation of Illinois Institute of Technology
Technology Center, Chicago 16, Illinois

NEW
developments
AT AIL

While the greatest portion of our laboratory's staff and facilities is involved in operations along the broad traditional base of electronics, we have a growing group of scientists concerned with medical electronics and physics.

Our aim in this field is the application of modern methods of physics, electronics, and data handling to problems of medical and biological investigation.

There are several positions available in our current research and development program. These are permanent positions, requiring people with extensive backgrounds of education and experience in physics and biology. Applicants who can qualify will find the best opportunities for technical and professional growth at Airborne Instruments Laboratory. Send resumes to Howard Gresens, Director of Personnel or Call PIoneer 2–0600 for interview appointment.

AIRBORNE INSTRUMENTS LABORATORY INC

160 OLD COUNTRY ROAD
MINEOLA, L. I., N. Y.

microwave dielectrometer

for measurement of dielectric constant and loss

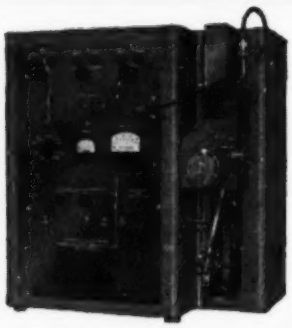

Ideal for investigating all types of dielectric materials in the microwave region, Dielectrometers designed by Central Research Laboratories, give definite aid in research on new materials, the propagation and utilization of microwave energy, and the correlation of dielectric-loss data with other properties.

Microwave Dielectrometers measure the dielectric constant and loss of materials at 1, 3 and 8.5 kilomegacycles. Range of measurement extends from 1 to 100; of dissipation factor, from 0.0001 to 1.0. Accuracy can be kept within 2 per cent.

Controls and meters are designed to eliminate complicated, time-consuming operations. Easy to service. Includes built-in test features for checking and adjusting critical circuit parameters. Electrical components are assembled in functional groups easily removable for further testing. Handsome cabinet 28″ x 17″ x 32″. Weight: 300 pounds. Power required: 115 volts, 60 cycles, 500 volt amperes—other voltage and frequency specifications to order.

For complete information, write to

Central Research

laboratories, inc.

Dept. 202 Red Wing, Minn.

Semiconductor Engineers and Scientists

GENERAL MOTORS offers exceptional opportunities in this field as a result of newly expanded programs of research and development—and now, also, pilot plant production.

These are permanent programs of great and increasing importance to General Motors in its electronic, automotive, aircraft engine, locomotive, household appliance and military activities—not just temporary study or short-term development programs.

Physicists, physical chemists and electronic engineers with baccalaureate or advanced degrees and those with transistor, diode, photo-cell, other semiconductor and related experiences in research, development or process and production will find:

- Important, interesting and challenging problems
- Modern facilities
- Congenial association with others skilled in these sciences

Resulting in maximum personal satisfaction, development and recognition.

Upper-level positions for those shown to qualify.

The unusual employe benefits of General Motors are provided by this 20-year-old GM electronics division. Relocation expenses are paid. Pleasant Indiana community with excellent living conditions, schools and many other advantages. Letters held in complete confidence. Give information on education, experience, military duty and personal data.

GM GENERAL MOTORS

Address: Personnel Director, Department SS

Delco Radio

DIVISION OF

GENERAL MOTORS

KOKOMO, INDIANA

Gaertner OPTICAL INSTRUMENTATION

10 x 10 Inch COORDINATE COMPARATOR
For Photographic Plate Measurement

READS TO 1 MICRON

The M1233 is a high quality instrument designed to permit highly accurate measurements on photographic films and plates. Readings can be made to 1 micron by means of a full length precision lead screw. A rotary stage of full 360° rotation is built in. Modifications can usually be made to meet many special requirements.

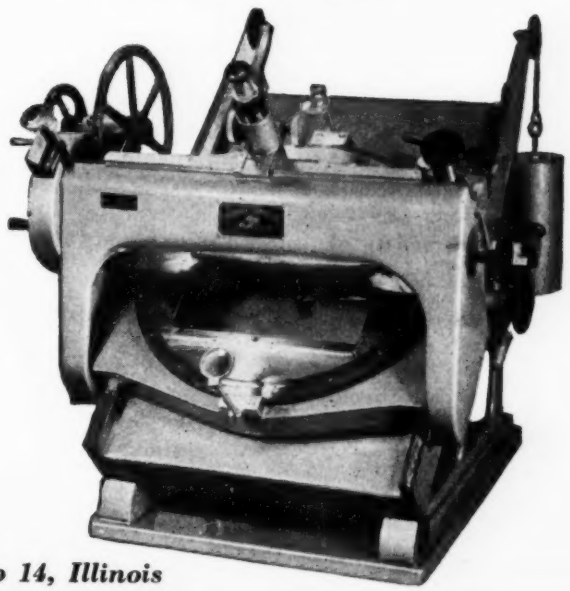

The Gaertner Scientific Corporation

WRITE FOR BULLETIN 191-53

1246 Wrightwood Avenue, Chicago 14, Illinois

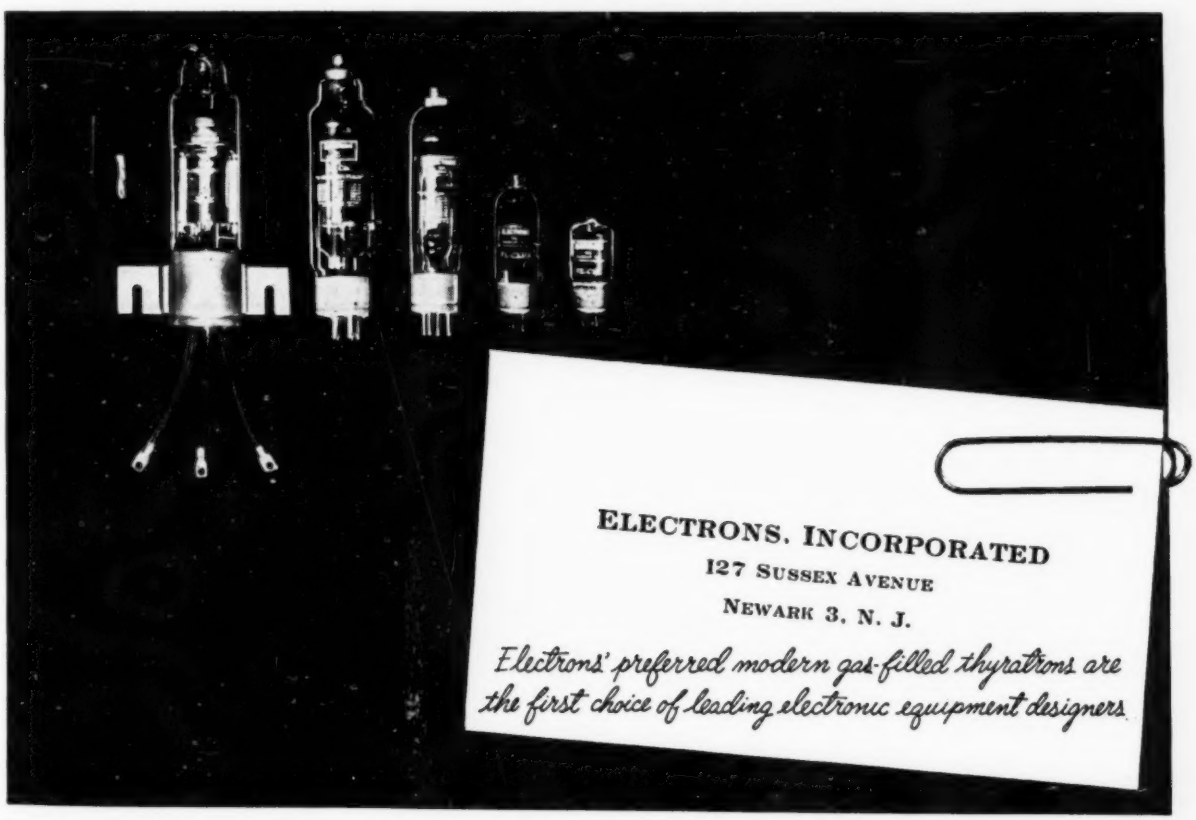
ELECTRONS, INCORPORATED
127 SUSSEX AVENUE
NEWARK 3, N. J.
Electrons' preferred modern gas-filled thyratrons are the first choice of leading electronic equipment designers.

AMERICAN INSTITUTE OF PHYSICS—25

January 31 to February 4, 1956

ADVANCE PROGRAM

—

American Physical Society—Thirty-eight sessions scheduled, January 31 through February 3rd.

American Association of Physics Teachers—Four sessions scheduled, January 30 and 31st.

Optical Society of America—One session, February 1st.

Acoustical Society of America—One session, February 1st.

Society of Rheology and American Physical Society High Polymer Division—One session, February 3rd.

American Institute of Physics—Special Anniversary Session

Thursday afternoon, February 2nd—Speakers:

J. ROBERT OPPENHEIMER, *Institute for Advanced Study*

J. A. STRATTON—*Massachusetts Institute of Technology*

H. B. G. CASIMIR—*Philips Research Laboratories, Eindhoven, Netherlands*

American Physical Society—American Association of Physics Teachers—Joint Ceremonial Session, Thursday Morning, February 2nd.

Joint Banquet—All Societies: Wednesday Evening, February 1st. Speakers: I. I. Rabi, *Columbia University;* Jerome Schweitzer

Exhibit—Open January 31 through February 3rd. Hours 9 a.m. to 5 p.m. daily.

Evening Sessions may be scheduled.

Placement Register
In session, January 30 through February 2nd, 9 a.m. to 5 p.m. daily.

Full details of sessions will be published in PHYSICS TODAY, January issue, and various Society Bulletins.

Exhibitors:

Academic Press, Inc.—Booth #15
"Solid State Physics" edited by Seitz and Turnbull, and the completing volume of the English version of Sommerfeld's "Lectures on Theoretical Physics," "Thermodynamics and Statistical Mechanics." Preliminary information on "Nuclear Science and Engineering," other texts.

Addison-Wesley Publishing Co.—Booth #1
Latest A-W texts and reference books in physics and related fields. Representatives will be on hand to discuss these books with physicists, and to furnish information about forthcoming publications.

Allegany Instrument Company, Inc.—Booth #34
Portable potentiometers, Millivolt Sources, D.C. Amplifiers for stress analysis and bridge calibrators for wire strain gages and transducers. Also, Type C, Calibrator for the standardization of transducers and Type K-7 Error Computor which permits the calculation of errors in systems employing transducers.

Barnes Engineering Company—Booth #26

Beckman & Whitley, Inc.—Booth #13
Framing Camera, Model 189 taking 1.2 million frames per second, Drum Camera Model 224, new Pressure Recorder, Model 216.

Brailsford & Company, Inc.—Booth #37
Several models of sub-fractional watt D.C. miniature motors and timers, primarily used in meteorological work where low power drain is of utmost importance. Also, Commutatorless D.C. Motor using transistors.

Cambridge Instrument Company, Inc.—Booth #33
Lindemann-Ryerson Electrometer, Microscope for L-R Electrometer, Portable Projector, Pocket Dosimeters, Charges for Pocket Dosimeters, Flik Galvanometer, Lamp and Scale Outfit, Spot Galvanometer, Pot Galvanometer, Universal Bridge, Research Model pH Meter, Rocking Microtome, Helium Indicating Outfit.

Cambridge University Press—Booth #45
Many texts including latest works by Bondi, Gamow, Jeans, Jeffreys, Klemperer, Rutherford, Schrodinger, J. J. and G. P. Thomson, and A. H. Wilson.

Central Scientific Company—Booths #3, #4
New line of Cenco Hyvac Pumps that feature compactness and quiet operation, new unique clamps, support rods and bases; new radioactivity demonstrator with helpful teaching accessories; a new line of laboratory balances, concentrated arc lamps, the "Lab-Jack" and other apparatus of interest to physicists.

Ealing Corporation—Booth #46
Research and students optical benches, Courtauld Atomic models; ripple tank; spectroscopes and spectrometers; cathetometers; vernier microscopes; electroscopes; unit system of electrical measurement; research and students microscopes; galvanometers; balances; optical demonstration apparatus and other items for education and research as manufactured in Great Britain.

Federal Telephone & Radio Company—Booth #44
Precision Bridges for resistance and inductance. Tuned Detector amplifiers, precision attenuators for h.f. and v.h.f., Capacitance standards fixed and variable, teraohmmeters for insulation measurement up to 500 million megohms, and multiflex galvanometers.

Gaertner Scientific Company—Booth #30

General Electric Research Laboratory—Booths #27, #28, #29
Man-made diamonds, High-strength whisker crystals, 4-MEV x-ray tube (and other x-ray tubes), Ionic pump, New light amplifier and a new kind of electronic tube destined to play an important role in the future of electronics.

General Radio Company—Booth #22
Variac Autotransformers, Impedance Bridges, Stroboscopes, Oscillators, Sweep Drives and other electronic instruments.

Instruments Publishing Company—Booth #42
Publications—Instruments and Automation, Instrument and Apparatus News, the 1956 Instrument and Automation Catalog and Index, Buying Directories. Books—The Automatic Factory, An Introduction to Process Control System Design, other books on instrumentation and electronics.

25TH ANNIVERSARY MEETING

Hotel New Yorker New York City

Exhibitors:

Interscience Publishers—Booth #23
Interscience Tracts on Physics and Astronomy edited by R. E. Marshak, Methods of Mathematical Physics by Courant and Hilbert, and other books on physics and applied mathematics. Also, new Nuclear Physics journal.

Jarrell-Ash Company—Booth #19
Hilger Microfocus X-ray unit and the Hilger Abbe Refractometer and Hilger Photometer. Also the Jarrell-Ash Grating Monochromator and Fluorimeter for uranium assay work, and JAco Spec Lab, a complete spectrochemical lab offered in a packaged form.

Kay Electric Company—Booth #2
Various instruments for recording and measuring audio and subaudio frequency waves, including the Vibralyzer, the Sonograph, and the Echo-Vox.

Keithley Instruments—Booth #17
Vacuum tube electrometers, microammeters, kilovoltmeters, static detectors, meg-megohm-meters, high gain dc amplifiers, dc vacuum tube voltmeters, high input impedance ac isolation amplifiers.

Walter Kidde Nuclear Laboratories, Inc.—Booth #5
The display illustrates Pressurized light water power plant for moderate power range (35,000 kw to 125,000 kw), suitable as a stationary unit for use in a utility network, or as a package unit to furnish power to isolated regions. The display includes a reactor model.

J. Klinger Scientific Apparatus—Booth #7
Rotating mirror, Gravitation torsion balance, Franck-Hertz tube with mercury atoms, Photo-electric cell, Demountable transformer, Belt generator, Model for demonstrating group velocity, Model separator tube for isotopes, Wulf's electroscope, Apparatus for demonstrating the kinetic theory of gases.

H. W. Leighton Laboratories—Booth #12
Portable type counters, metal walled GM type counter tubes, video sweep generator, count rate meter, other items.

McGraw-Hill Book Company—Booth #20
Titles in the International Series in Pure and Applied Physics, the six volumes in the U. S. Atomic Energy Commission series, the third and final volume on Radiation Biology, and the commemorative volume for Niels Bohr.

NRD Instrument Company—Booth #21
Detectors and circuits covering a wide variety of industrial and research uses. Scintillation counters of many types for gammas, as well as beta counters and windowless alpha counters. Circuits include scalers, precision count rate meters, and combinations with both instruments in one cabinet. Single channel pulse height analyzers will also be shown, plus shields and counting accessories.

National Radiac, Inc.—Booth #25
Complete scintillation methods. Scintillation crystals, including largest crystal ever grown, scintillation counter heads, power supplies and count rate meters, detection equipment, aerial scintillation counter, and other items.

North American Aviation, Inc.—Booths #35, #36

North American Philips Co.—Research and Controls Division—Booths #38, #39
New Flame Photometer, the X-ray Microradiograph, the Dual Decade Scaler and Timer, and Scintillation and Proportional Counter Equipment. The Norelco EM-75 Electron Microscope will be exhibited and a complete line of Norelco X-ray Analysis Units comprising the Wide-Range Diffractometer, 90-degree Diffractometer, the Spectrograph and Wide-Range Goniometer plus Powder Cameras and Accessories.

Nuclear Development Corporation of America—Booth #14
Reactor Model—one of the first to be designed for the chief purpose of research in neutron therapy.

Opplem Company, Inc.—Booth #47
Opplem Time Lapse Cine-Photomicrographic Apparatus with provision for High Speed Photomicrography, and accessories for Micro-Schlieren and Multiple beam Interferometry, also, High Precision Nuclear-Track Microscopes and accessories.

Optical Film Engineering Company—Booth #24
A complete line of high vacuum equipment, vacuum metallizing systems, packaged pumping system and portable power supplies. Also, dichroic filters, front surface mirrors with reflectance of 95%, electrically conductive transparent coatings on glass and plastics, ultra low reflection films and specialized thin films of descriptions.

The Perkin-Elmer Corporation—Booth #48

Prentice-Hall, Inc.—Booth #43
"Elements of Physics," 2nd Ed. by Shortley & Williams, "Introduction to Physics" by Durbin, "Elements of Atomic Physics" by Peaslee, "Electricity and Magnetism" by Winch, "Fundamental Formulas of Physics" by D. H. Menzel, et al; other P.H. texts.

RMC Associates, Inc.—Booths #8, #9, #10
Representing the following:
Beta Electric—Low, high, ultra high voltage power supplies
Budd-Stanley—Microwave transmission equipment
John Fluke Mfg—VAW Meters, precision supplies, differential voltmeter
Hewlett-Packard—Complete Electronic Measuring Instruments
Kay Lab—Absolute Supplies, Microvoltmeters, Industrial TV Systems
Pimex—Reflecting galvanometers, bridges, decade boxes
Sorenson & Co.—Electronic Voltage Regulators, Nobatrons, Frequency Changers
Varian Associates—Klystrons, Laboratory Magnets, Graphic Recorders

Rubicon Co.—Booth #32
Precision electrical measuring instruments consisting of Resistance Standards and Bridges, Potentiometers and Galvanometers. New equipment will be the laboratory type High Precision Kelvin Bridge, a radical departure from the older classical form; and a Portable Precision Thermocouple Potentiometer.

Sound Apparatus Company—Booth #31
Model SL-4, Frequency Response Recorder, utilizing a sliding-coil for operation of the pen movement and a feed-back coil to assure stability and accuracy, and other special features. Model PR-1, Polar Recorder, is designed especially for recording of antenna and other directional device patterns.

Springer Publishing Co.—Booth #6
New Encyclopedia of Physics (S. Fluegge, Editor), published in 54 volumes by Springer-Verlag, Germany. All completed volumes will be shown plus other important Springer books in physics.

Tracerlab, Inc.—Booths #40, #41
Complete new line of radiation research equipment built on building block principle, including alpha gridded ionization chamber, gamma scintillation spectrometer detector, new non-overloading linear amplifier, and many other components. This new line of radiation research equipment represents Tracerlab's experience of 10 years in providing research physicists with these tools.

Vacuum-Electronic Engineering Company—Booth #11
Full line of high vacuum equipment, including the model MS-8 Mass Spectrometer Leak Detector. On display will be Veeco Diffusion Pumps; Thermocouple Ionization Gauges (featuring the non-burnout ionization gauge type RG75; Philips Gauge; Bellows Sealed Valves; Vacuum Solenoid Valves; Veeco Leak Detector; and a group of vacuum accessories.

D. Van Nostrand Company, Inc.—Booth #18
Pioneer titles in many branches of physics, including Glasstone's Principles of Nuclear Reactor Engineering, Locke's Guidance, the initial volume in the series Principles of Guided Missile Design; and a revised edition of Timoshenko's Strength of Materials, Volume II.

W. M. Welch Manufacturing Company—Booth #16
New high vacuum Duo-Seal pump with vented exhaust for pumping condensable vapors; Densichron Transmission Densitometer for measuring optical density of glass, photographic film, plastics, paper; Welch stainless steel laboratory balances, and Welch Master portable electric meters.

John Wiley & Sons, Inc.—Booth #49
Displaying a wide range of technical, reference, and textbooks by specialists in the field of physics and related sciences.

★ ULTRA LOW capacitance & attenuation

TYPE	μμF/ft	IMPED.Ω	O.D.
C 1	7.3	150	.36"
C 11	6.3	173	.36"
C 2	6.3	171	.44"
C 22	5.5	184	.44"
C 3	5.4	197	.64"
C 33	4.8	220	.64"
C 4	4.6	229	1.03"
C 44	4.1	252	1.03"

WE ARE SPECIALLY ORGANIZED TO HANDLE DIRECT ORDERS OR ENQUIRIES FROM OVERSEAS
SPOT DELIVERIES FOR U.S.
BILLED IN DOLLARS—SETTLEMENT BY YOUR CHECK
CABLE OR AIRMAIL TODAY

TRANS T RADIO

NEW 'MX and SM' SUBMINIATURE CONNECTORS
Constant 50Ω 63Ω 70Ω impedances

TRANSRADIO LTD. 138A Cromwell Rd. London SW7 ENGLAND CABLES: TRANSRAD, LONDON

JET PROPULSION LABORATORY
of the
CALIFORNIA INSTITUTE OF TECHNOLOGY
Pasadena, California

Excellent opportunities exist for professional growth in research atmosphere for Engineers and Physicists of all grades. Facilities and equipment are superior.

Airmail your summary of qualifications to:

CALTECH
JET PROPULSION LABORATORY
4800 Oak Grove Drive
Pasadena, California

NEW PHYSICS JOURNAL . . . SOVIET PHYSICS—JETP
Complete English translation of all articles appearing in Russian Journal of Experimental and Theoretical Physics. Published bimonthly by
AMERICAN INSTITUTE OF PHYSICS
57 East 55 Street, New York 22, N.Y.
$30.00 per year U.S. and Canada $32.00 Elsewhere

POSITIONS AVAILABLE

GRADUATE ELECTRONIC ENGINEER OR PHYSICIST needed for opening in design of magnetic amplifiers and servo controls. Working knowledge of electronic circuitry necessary. Excellent opportunity for advancement to responsible position in this rapidly growing field. This is a growing engineering and production organization. Send resume to Penn-East Engineering Corp., Kutztown 2, Penna.

POSITIONS OPEN

Our Physics Group Needs Experimental Or Theoretical Physicists For Interesting Problems Concerned With High Temperatures

For Further Details Write:
Allied Research Associates, Inc.
43 Leon Street, Boston, Massachusetts
Garrison 7–8170

Specialists in the *Unusual*

DIRECT TEMPERATURE MEASUREMENT UP TO **3700°F.**

IRIDIUM vs. RHODIUM IRIDIUM THERMOCOUPLE WIRE

The only thermocouple material which may be used at these very high temperatures in an oxidizing atmosphere.

Ductile wire made possible by high purity and our advanced melting and drawing techniques.

Output: Over 10 milivolts at **3700°F.**

UNIFORM · REPRODUCIBLE

SINCE 1901

Write for List of Products

SIGMUND COHN CORP.

Metallurgists and Producers of Small Wire

121 South Columbus Avenue

Mount Vernon, N. Y.

GEOPHYSICS

A Journal of General and Applied Geophysics

Published Quarterly by

SOCIETY OF EXPLORATION GEOPHYSICISTS

624 South Cheyenne Tulsa 3, Oklahoma

- The official journal of the leading international group of prospecting geophysicists
- Devoted to current problems in seismograph, gravity, magnetic and other methods of geophysical prospecting for oil and other minerals
- Covers geophysical instrumentation

SUBSCRIPTION RATES

ONE YEAR (4 issues) $9.00, foreign $9.50

ALSO AVAILABLE ON MICROCARDS

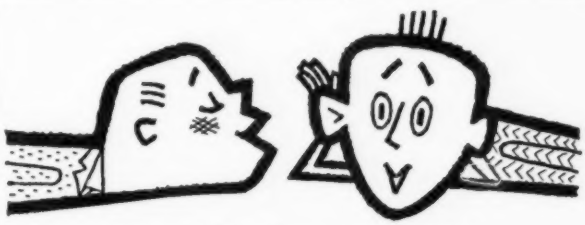

IT'S AN OPEN SECRET

. . . That originality, creativeness, imagination, resourcefulness, versatility find expression and encouragement at ADL. . . . That positions ARE NOW OPEN for men with university training and appropriate experience. . . . That if you want professional diversity, opportunity for responsibility in client relationships, you can find both at ADL. . . . Than ADL is located in an area of the finest educational, cultural and recreational activities.

Chemistry and Physics—Pure and Applied
Physical Chemistry
Solid State Physics
Radio-Chemistry
Thermodynamics and Heat Transfer
Cyrogenic Engineering
Electronics Research
Process Engineering
Metallurgy
Petro-Chemical Technology
Food and Flavor Research
Biology
Operations Research
Industrial Economics and Management Services
Regional Development
Numerical Analysis and Data Processing

Write to

PERSONNEL DIRECTOR —PROFESSIONAL STAFF

Dept. 12

Arthur D. Little Inc.
Established 1886
28 Memorial Drive
Cambridge 42, Mass.

INDEX TO ADVERTISERS

Name	Page
AIRBORNE INSTRUMENTS LABORATORY	xxv
ARMOUR RESEARCH FOUNDATION	xxv
THE ARNOLD ENGINEERING COMPANY Alnico Permanent Magnets.	vii
ATOMIC ENERGY OF CANADA LTD.	xxi
ATOMIC INSTRUMENT COMPANY Quality Instrumentation for Nuclear Research; Scalers; Linear Amplifiers; Radio Activity Demonstrators; Regulated High-Voltage Supplies; Oscilloscopes; Pulse Generators; Counting Rate Meters; Radiation Meters; and Special Electronic Equipment.	xxv
BECKMAN & WHITLEY, INC. Manufacturers of high-speed research cameras—both framing and sweeping-image types; specialized meteorological instruments; recorders for rapid pressure transients; heatflow transducers; and explosive-actuated mechanism.	Cover 2
BELL TELEPHONE LABORATORIES	ix
BETA ELECTRIC COMPANY High Voltage DC power supplies, kilovoltmeters, electronic microammeters, portable projection oscilloscopes and regulated DC power supplies of all types.	vi
CENTRAL RESEARCH LABORATORIES, INC. Chemistry, physics, electrical engineering. Consultation, research, development, production. High-speed microoscillograph. Microwave dielectrometers, double monochromators, X-Ray and electron-diffraction cameras.	xxvi
SIGMUND COHN CORP.	xxxi
DELCO RADIO DIVISION	xxvi
DOUGLAS AIRCRAFT COMPANY	xix
ELECTRIC BOAT DIVISION, GENERAL DYNAMICS CORP.	xxii
ELECTRONS, INC. Designers and manufacturers of inert gas filled rectifiers and grid controlled rectifiers (Thyratrons).	xxvii
FARNSWORTH ELECTRONICS COMPANY	xiv
THE GAERTNER SCIENTIFIC CORP. Spectroscopes, spectrometers, spectrographs, spectrophotometers, heliostats, measuring microscopes, comparators, cathetometers, reading telescopes, interferometers, chronographs, dividing machines, etc.	xxvii
GENERAL RADIO COMPANY Manufacturers of electronic measuring instruments; vacuum-tube voltmeters, amplifiers, and oscillators; wave analyzers, noise meters and analyzers, stroboscopes, laboratory standards of capacitance, inductance and frequency; impedance bridges, decade resistors and condensers, air condensers and variable inductors; rheostats, variacs, transformers; other laboratory accessories.	Cover 3
HUGHES RESEARCH & DEVELOPMENT LABS. Airborne fire control radar systems, digital data handling and processing equipment, guided missiles, microwave and display tubes, semiconductor products, and field service engineering.	xi
INTERNATIONAL BUSINESS MACHINES CORP.	viii
KEPCO LABORATORIES	Cover 4
KOLLMORGEN OPTICAL CORP. Manufacturers of industrial periscopes, boroscopes, projection lenses, optical systems, fire control and navigational instruments. Also precision machine work and special engineering and design projects.	xxii

INDEX—*Continued*

Name	Page
LEEDS & NORTHRUP COMPANY Manufacturers of galvanometers, resistors, bridges, condensers, inductances, potentiometers, testing sets, temperature measuring, recording, and controlling apparatus; instruments for measuring and controlling conductivity of electrolytes and hydrogen ion concentrations.	iii
THE LINDE AIR PRODUCTS COMPANY, UNIT OF UNION CARBIDE AND CARBON CORP. Oxygen, Argon, Helium, Krypton, Neon, Xenon, Rare Gas Mixtures, Nitrogen, Hydrogen, Calcium, Carbide, Acetylene, equipment for Oxy-Acetylene welding and cutting.	xxiii
ARTHUR D. LITTLE, INC. Industrial research and consulting in virtually all fields of science; business research; design, development and manufacture of equipment for production and storage of liquid helium and other low-boiling liquified gases; prototype development services.	xxxi
LOCKHEED AIRCRAFT CORP.	xx
LOS ALAMOS SCIENTIFIC LABORATORY is the Nation's principal institution for the development of nuclear and thermonuclear weapons, and is also devoted to research on the peace time application of atomic energy.	xxii
McGRAW-HILL BOOK COMPANY, INC. Text and reference books for classroom and laboratory—for scientist, engineer, and student. Publishers, International Series in Pure and Applied Physics. Distributors of educational films, textfilms.	x
MELPAR, INC.	xxi
RADIO CORP. OF AMERICA	xx
THE RAMO-WOOLDRIDGE CORP. Research, development, and manufacture in the field of electronic systems for commercial and military applications, and in the field of guided missiles.	xiii
REINHOLD PUBLISHING CORP.	xii
SERVOSPEED, INC.	xxiv
F. J. STOKES MACHINE COMPANY Manufacturers of high-vacuum processing equipment, including McLeod type vacuum gages, "Microvac" rotary mechanical vacuum pumps, "Ring-Jet" diffusion and booster pumps, vacuum melting, sintering, and heat treating furnaces, rotary and rotating vacuum dryers, shelf-dryers, and freeze-dryers. Also plastics molding presses, pharmaceutical machinery, and industrial and powder metal presses.	iv, v
TECHNICAL OPERATIONS, INC.	xxiv
TRACERLAB, INC. Suppliers of instruments for measuring, detecting, health monitoring and surveying radioactive materials, and radioactive tracer analyses, isotype processing, synthesis, consulting and industrial research in radioactivity.	xv
TRANSRADIO LTD. Air-insulated articulated ultra-low capacitance high impedance coaxial cables. NC precision connectors; matched impedances 20–200 ohms.	xxx
VITRO LABORATORIES	xxiii
W. M. WELCH SCIENTIFIC COMPANY Manufacturers of high-vacuum pumps, both mechanical and diffusion; vacuum gauges; electrical measuring instruments; physics equipment; and other items for the physical and chemical laboratories.	xviii
WESTINGHOUSE ELECTRIC CORP.	xvii

NEW A-C/DC VACUUM-TUBE VOLTMETER

0.1-1500 VOLTS AC
0.02-500 VOLTS DC

The new G-R Type 1803-B VTVM is an improved version of the well known "A" model, popular for its accuracy, convenience in use and reliability.

This instrument will measure a-c voltages between 0.1 and 150 volts with a basic accuracy of 3%. With the 10:1 multiplier, now permanently attached to the cabinet, direct-reading measurements can be made to 1500 volts. A distinct new feature is the provision for measuring d-c voltages from 0.02 to 500 volts. With this added facility, this voltmeter becomes as useful for every-day laboratory work as the more elaborate models available at much greater cost.

The Type 1803-B Vacuum-Tube Voltmeter has a single zero adjustment — continual resetting is not required when switching from one voltage scale to another. For greatest accuracy, four meter scales are provided to cover the five ranges.

Type 1803-B
Vacuum-Tube
Voltmeter
$180.00

A-C ACCURACY: ±3% of full scale on all ranges, subject to frequency correction (curve supplied) above 50 Mc; additional ±1% error with multiplier

D-C ACCURACY: ±3% of full scale for 1.5, 5, 15, and 50-volt ranges; ±4% of full scale for 150 and 500-volt ranges

GOOD FREQUENCY RESPONSE: Resonant frequency is 410 Mc

A-C INPUT IMPEDANCE: 7.7 megohms in parallel with 11.5 $\mu\mu$f; parallel resistance decreases at higher frequencies

D-C INPUT IMPEDANCE: 111 megohms; open-grid input can be obtained for 1.5 to 50-volt ranges by unsoldering internal connection

COMPLETELY SHIELDED PROBE: contains twin diode; one section for rectifying a-c voltage under measurement, other half for balancing out effects of transients and line-voltage changes on first tube. Probe plugs into 1:1 or 10:1 jacks under multiplier box, making for neat appearance and convenience in transit

POLARITY SWITCH: permits voltages of either + or − polarity to be applied to the high input terminal

INTERNAL CALIBRATION CONTROL: a-c and d-c calibration easily corrected if tube is changed

CORD STORAGE: probe cable conveniently stores within instrument housing

SMALL—LIGHT WEIGHT: only 9½ lbs.

WE SELL DIRECT—Prices are net, FOB Cambridge or West Concord, Mass.

GENERAL RADIO Company

275 Massachusetts Avenue, Cambridge 39, Massachusetts, U.S.A.

90 West Street NEW YORK 6
8055 13th St., Silver Spring, Md. WASHINGTON, D. C.
920 S. Michigan Avenue CHICAGO 5
1000 N. Seward Street LOS ANGELES 38

1915-1955
40 Years of Pioneering
in Electronics

KEPCO

KR SERIES

VOLTAGE REGULATED POWER SUPPLIES *for powering electronic equipment*

MODEL KR4-MC

MODEL KR7

save time ...*and* money...

Build these compact Power Supplies into your equipment!

Kepco Voltage Regulated Power Supplies are conservatively rated and are designed for continuous duty at 50°C ambient.

REGULATION: Specified for each unit is available throughout its output voltage range and is less than 0.2 volts for line fluctuation from 105-125 volts and less than 0.2 volts for load variation from 0 to maximum current.

RIPPLE: Less than 3 mv. rms.

FEATURES:

- Superior Regulation.
- Ultra-Stable 85A2/OG3 Reference Tube.
- Low Ripple.
- Low Output Impedance.
- Fast Recovery Time, Suitable for Square Wave Pulsed Loading.
- Voltage Range continuously variable without Switching.
- Either Positive or Negative may be Grounded.
- Oil Filled Condensers.
- Wire Harness and Resistor Board Construction.
- Power Requirements 105-125 volts, 50-60 cycles.
- Terminations and locking type voltage control on rear of unit.
- AC, DC Switches, Fuses, and Pilot Lights on Front Panel.
- Color Grey Hammertone.
- Guarantee One Year.

600 ma. KR SERIES

Model	Volts	6.3V AC	Rack Mount W	H	D	Price
KR 8	0-150	Each supply	19"	10½"	13"	$330
KR 5	100-200	has two	19"	10½"	13"	$240
KR 6	195-325	10 Amp.	19"	10½"	13"	$240
KR 7	295-450	outputs	19"	10½"	13"	$250

300 ma. KR SERIES

Model	Volts	6.3V AC	Rack Mount W	H	D	Price
KR 12	0-150	Each supply	19"	7"	11"	$270
KR 3	100-200	has two	19"	7"	11"	$180
KR 4	195-325	5 Amp.	19"	7"	11"	$180
KR 10	295-450	outputs	19"	7"	11"	$190

125 ma. KR SERIES

Model	Volts	6.3V AC	Rack Mount W	H	D	Price
KR 11	0-150	Each supply	19"	7"	11"	$180
KR 1	100-200	has one	19"	7"	7½"	$ 90
KR 2	195-325	3 Amp.	19"	7"	7½"	$ 90
KR 9	295-450	output	19"	7"	7½"	$ 97

To Include 3" Current and Voltage Meters, Add M to Model number (e.g. KR 1-M) and Add $30.00 to the Price.
To include Dust Cover and Handles for Table Mounting, Add C to Model number (e.g. KR1-C) and Add $10.00 to the Price.
To Include Meters, Dust Cover and Handles, Add MC to Model number (e.g. KR-1MC) and Add $40.00 to the Price.
PRICES F.O.B. Flushing

A LINE OF 45 MODELS
Available from Stock – Catalog on Request

RESEARCH • MANUFACTURING
KEPCO Laboratories

KEPCO LABORATORIES

131-38 SANFORD AVENUE • FLUSHING 55, N.Y. • INDEPENDENCE 1-7000